Coherent X-ray diffraction applied to metal physics

Maxime Dupraz

▶ **To cite this version:**

Maxime Dupraz. Coherent X-ray diffraction applied to metal physics. Materials. Université Grenoble Alpes, 2015. English. NNT : 2015GREAI103 . tel-01285735

HAL Id: tel-01285735
https://theses.hal.science/tel-01285735

Submitted on 9 Mar 2016

HAL is a multi-disciplinary open access archive for the deposit and dissemination of scientific research documents, whether they are published or not. The documents may come from teaching and research institutions in France or abroad, or from public or private research centers.

L'archive ouverte pluridisciplinaire **HAL**, est destinée au dépôt et à la diffusion de documents scientifiques de niveau recherche, publiés ou non, émanant des établissements d'enseignement et de recherche français ou étrangers, des laboratoires publics ou privés.

UNIVERSITÉ GRENOBLE ALPES

THÈSE

Pour obtenir le grade de

DOCTEUR DE L'UNIVERSITÉ GRENOBLE ALPES

Spécialité :

Arrêté ministériel : 7 août 2006

Présentée par **Maxime Dupraz**

Thèse dirigée par **Marc Verdier** et codirigée par **Guillaume Beutier**

préparée au sein du **Laboratoire de Science et Ingénierie des Matériaux et Procédés**
dans **l'École Doctorale d'Ingénierie – Matériaux Mécanique Energétique Environnement Procécés Production**

Diffraction des rayons X cohérents appliquée à la physique du métal

Thèse soutenue publiquement le **17 Novembre 2015**,
devant le jury composé de :

Mme. Virginie Chamard Chargée de recherche au CNRS, Institut Fresnel, Marseille, Rapportrice

Mr. Sylvain Ravy Directeur de recherche au CNRS, Laboratoire de Physique des Solides, Orsay, Rapporteur

Mr. Ian Robinson, Professeur à l'University College of London (UCL), Examinateur

Mr. Alain Marty, Chargé de recherche à l'Institut des Nanosciences et Cryogénie (INAC), Grenoble, Examinateur et président du Jury

Mr. Guillaume Beutier, Chargé de recherche au Laboratoire de Science Ingénierie Materiaux et Procédés (SIMAP), Co-encadrant de thèse

Mr. Marc Verdier, Directeur de recherche au Laboratoire de Science Ingénierie Materiaux et Procédés (SIMAP), Directeur de thèse

Remerciements

Avant toute chose je voudrais remercier chaleureusement les membres de mon jury de thèse pour avoir accepté de lire et critiquer ces travaux de thèse. Merci donc à Sylvain Ravy, Virginie Chamard, Ian Robinson et Alain Marty pour avoir siégé à ma soutenance, et plus particulièrement à Sylvain Ravy et Virginie Chamard pour avoir accepté de rapporter ma thèse. Ce fût pour moi un grand honneur d'avoir un jury aussi prestigieux, et j'espère avoir sû me montrer à la hauteur de l'évenement.

Ces travaux de thèse n'auraient bien sûr pas été possibles sans l'encadrement et les enseignements de mon directeur de thèse Marc Verdier et de mon co-encadrant Guillaume Beutier. Présents quotidiennement à mes côtés, ils ont été pour moi d'une aide très précieuse absolument tous les aspects couverts dans cette thèse, qu'ils soient expérimentaux ou théoriques/simulation.

J'ai connu Marc il y a quelques années lors de mon stage de Master 1, effectué au SIMaP avec Fabien Volpi. Ce stage fût ma première véritable expérience dans le milieu de la recherche et a largement contribué à me pousser à poursuivre en thèse. Marc fait partie de personnes qui ont fait naître en moi cet attrait pour la recherche et dès qu'il m'a proposé un sujet de thèse je n'ai pas donc pas hésité très longtemps avant de me lancer dans l'aventure... grand bien m'en a pris! Le courant est également très rapidement passé avec Guillaume, avec qui j'ai participé à des expériences synchrotron dès mes tous premiers mois de thèse. Il a su rapidement me transmettre ce qu'on pourrait appeler le « virus du synchrotron », et m'a donné l'opportunité de découvrir un environnement que je ne connaissais absolument pas avant le début de ma thèse.

De manière plus générale, je voudrais les remercier pour leur très grande implication dans mon travail. Un exemple très simple concerne l'analyse de données synchrotron qui a été considérablement facilitée par les programmes MATLAB de Guillaume et il est donc évident que leur encadrement a constitué une base essentielle à la réussite de ces travaux de thèse.

Au delà de l'aspect scientifique je voudrais aussi retenir tous les bons moments que nous avons pu passer ensemble, aussi bien au SIMaP que lors de nos nombreuses campagnes synchrotron. Avant d'être des chercheurs de grand talent, Guillaume et Marc sont surtout des personnes très agréables à vivre, et je crois que notre complicité fût un des ingrédients essentiels à la réussite de cette thèse. Je retiendrai en particulier les expériences à Diamond où nous aurons réussi à trouver le temps pour passer quelques soirées au Pub à Oxford ou dans la campagne anglaise.

En bref, un grand MERCI pour ces trois dernières années et j'espère sincèrement que nous aurons l'occasion de travailler ensemble à l'avenir!

Je tiens également à remercier chaleureusement David Rodney qui m'a permis de mener à bien la grande majorité des simulations de dynamique moléculaire présentées dans ce manuscrit de thèse. Il a été ma porte d'entrée vers le monde des simulations atomistiques qui ont joué un rôle très important dans ma thèse (et auront vraisemblablement un rôle important à jouer à l'avenir). Il aura été également mis à contribution pour la correction d'articles ou de certains chapitres de ma thèse, ce dont je lui suis très reconnaissant. Un grand merci également à Roberta Poloni pour son implication sur l'étude de l'interface Cu/Ta qui a grandement bénéficiée de ses calculs *ab initio*. Roberta s'est toujours montrée motivée et enthousiaste, et j'ai beaucoup apprécié notre collaboration

Comment pourrais-je aussi oublier Frédéric Livet ? Le doyen du groupe PM est une source inépuisable de connaissances sur la cohérence et ce fût toujours un très grand plaisir de discuter avec Frédéric, que ce soit de science ou d'autres sujets (et ils furent variés!). Sa présence fût également grandement appréciée sur plusieurs expériences synchrotron, où son expertise sur la cohérence (les fameux calculs du degré de cohérence) et sa bonne humeur communicative auront contribué à en faire des moments très agréables.

Je voudrais aussi saluer l'implication de Bruno Gilles, le spécialiste de la MBE, pour la préparation des

échantillons, et pour nos collaborations fructueuses sur les expériences de diffraction de surface. Merci aussi à Guillaume Parry dont l'expertise dans les simulations éléments finis auront contribué de manières significative à l'interprétation des mesures synchrotron. J'exprime également ma gratitude à Marc De Boissieu pour ses conseils et nos discussions enrichissantes autour des simulations atomistiques ou encore de diffraction cohérente.
Mention spéciale à Fabien Volpi qui fût ma porte d'entrée au SIMaP il y a quleques années. Ce fût toujours un plaisir de travailler avec Fabien, en particulier sûr les expériences synchrotron à l'ESRF ou à Diamond. Je le remercie également de m'avoir donné l'opportunité d'encadrer les travaux pratiques des étudiants PHELMA.
Je tiens également à exprimer ma gratitude à Alexis Deschamps le directeur du groupe PM, pour son dynamisme et sa gentillesse. Si le groupe PM constitue aujourd'hui un environnement idéal pour s'épanouir dans une thèse, une bonne partie du mérite lui en revient.
Pour finir, merci également à tous les autres permanents que j'ai pu croiser au cours de ces trois dernières années. Je pense en particulier à François Chiarutini dont la motivation et l'implication dès qu'il se lance dans un projet font plaisir à voir (il fallait le voir s'entraîner pour son marathon), Patricia Donnadieu ou encore Yves Bréchet qui aura réussi à trouver quelques minutes dans son cmploi du temps surchargé pour assister à ma répétition de soutenance.

J'en ai déjà parlé, mais cette thèse a été placée sous le signe du synchrotron. Au cours de ces trois dernières années j'aurai donc participé à pas moins d'une vingtaine d'expériences. Je tenais donc tout d'abord à remercier les personnes avec qui nous avons pu collaboré que ce soit à l'ESRF, SOLEIL ou encore à DIAMOND. J'aimerais commencer par Feodor Ogrin de l'université d'Exeter avec qui j'ai participé à plusieurs expériences d'holographie magnétique. Au sein de cette équipe il convient aussi de saluer l'implication des différents thésards de Féodor: Thomas Duckworth (présent pour ma première expérience d'holographie à Diamond) et beaucoup plus tard Nick Bukin et Eric Burgos. J'exprime également ma gratitude à Gerrit Van Der Laan dont la très grande expérience dans le dichroisme des rayons X auront été d'une aide précieuse. Merci également à Pierre Godard avec qui nous avons collaboré sur une expérience de ptychographie sur la ligne CRISTAL.
Je tiens aussi à remercier le staff des lignes sûr lesquelles ont été réalisées les expériences présentées dans ce manuscrit. Merci donc à Gilbert Chahine et Tobias Schülli de la ligne ID1, Maurizio De Santis et Jean-Sébastien Micha de BM32, Felisa Berenguer et Sylvain Ravy de CRISTAL, Christophe Rau et Aaron Parsons de I13, Steve Collins et Gareth Nisbet de I16, Sarnjeet Dhesi et Stuart Cavill de I06, Horia Popescu et Christophe Jaouen de SEXTANTS et pour finir Erika Jimenez et Floria Yakhou de la ligne ID32.

Je tiens aussi à exprimer ma gratitude à nos partenaires Marseillais, Grenoblois, Parisiens et Allemands impliqués dans l'ANR Mecanix. Merci donc à Olivier Thomas, Thomas Cornelius, Cédric Leclere, Ren Zhe, Anton Davydok, Francesca Mastopietro, Stéphane Labat, Marc Gailhanou, Joël Eymery, Marie Ingrid Richard, Vincent Favre-Nicolin, Sara Fernandez, Vincent Jacques ou encore David Le Bolloc'h.
Ces trois années auront été l'occasion de collaboration fructueuses et de moments très sympathiques!

Mais cette thèse n'aurait pas été la même sans tous les bons moments passés entre thésards. Je retiendrais en particulier nos parties de Tarot à la pause de midi, tradition qui s'est malheureusement un peu étiolée sur la fin de ma thèse. Les repas chez les uns et les autres et les soirées au bar ou au cinéma resteront aussi d'excellents moments qui ont contribué à rendre très agréables ces 3 dernières années à Grenoble. Le groupe des thésards ne manquait également pas de sportifs accomplis, je pense en particulier à Fanny (méfiez vous si elle vous propose d'aller faire un footing), Nico et Eva et ce fût toujours été un grand plaisir d'aller se dégourdir les jambes avec eux au bord de l'Isère. Mais si il y avait un seul moment à retenir, ce serait sans doute cette semaine que nous avons passé à Séville dans le cadre de la conférence EUROMAT (mention spéciale à Thomas Dorin).
Mes chers co-thésards, vous auriez tous mérité un paragraphe entier de remerciements,

malheureusement ma thèse faisant déjà 300 pages, j'aimerais éviter d'en rajouter 10 de plus, et je vais devoir me contenter de quelques lignes...

Merci donc à tous les anciens :
Fanny et Nico (sportifs mais bien plus encore), Laurent et Thomas (toujours partant pour une bière à la bobine ou au shannon), Dan et Simon (mes collègues de bureau et « accessoirement » colocataire pour ce dernier), Olivier (mon « compatriote » Savoyard) et Quing Quan.
Les moins anciens :
Audrey et Eva qui auront été mes copines de galère (*i.e.* de rédaction). ainsi que Kitti et Pierre-François eux-aussi de la génération 2012.
Les encore moins anciens :
Rosen (Le Bulgaro-Chiprio-Canadien qui nous aura fait le plaisir de poser un moment ses valises en France), Solène, Mahmoud et Hassan
et pour finir les petits nouveaux que je n'aurais malheureusement pas eu suffisament le temps de connaître !

Pour finir, la thèse ne se vit pas qu'au laboratoire, et j'ai eu la chance d'être très bien entouré par mes proches. A ce titre je voudrais remercier ma famille pour son soutien, en particulier au cours des derniers mois de thèse qui furent pour le moins intenses (en témoigne le matelas gonflable dans mon bureau, et mes réserves de nourriture dans la cuisine des thésards...). Merci donc à mes parents, à mes à mon frère Valentin, ma sœur Julie, mais aussi à mes grands-parents, oncles et tantes qui ont su trouver les mots justes pour exprimer leur fierté ou leurs encouragement. Evidemment, ces trois dernières années n'auraient pas eu la même saveur sans les amis Grenoblois (ou d'un peu plus loin): Tinmar, Emmanuelle, Gouze, Grunge, Fanny, Bastoune, Audrey, Catel, Salah, Nina, Antonin, David, Eric, Yvon, Raph et Piotr. Je voudrais en particulier vous remercier d'avoir été si nombreux à ma soutenance. Et puis merci à tous les autres que je ne peux malheureusement pas énumérer tous individuellement!
Et puis le meilleur pour la fin, je voudrais bien sûr remercier ma copine Clémentine. Nous nous sommes rencontrés au milieu de ma thèse et cette rencontre restera sans aucun doute la plus belle chose qui me soit arrivé au cours de ces années de thèse. Tu as su être là pour moi au cours de ces derniers mois de rédaction, et accepter de me voir passer quasiment tous les week-end de 2015 à travailler. Tu m'as donné envie de donner le meilleur de moi même et d'aller puiser dans mes ressources et nul doute que sans toi cette thèse n'aurait pas été aussi réussie. Bref merci pour tous ces bons moments passés avec toi et pour tous ceux à venir!

Voilà c'est donc la fin d'une belle aventure au SIMaP, laboratoire que je quitte à regrets (c'est d'ailleurs pour ça que j'y ai joué les prolongations). Une nouvelle page débute pour moi en Suisse au Paul Scherrer Institut et j'espère qu'elle sera tout aussi réussie!

Résumé étendu

Ce chapitre résume, en Français, le manuscrit de thèse qui est écrit en anglais. Chaque chapitre est résumé de manière à faire ressortir les principaux résultats et conclusions importantes. Le choix d'effectuer la rédaction du manuscrit entièrement en anglais a été motivé par différentes raisons. Tout d'abord, certains chapitres de la thèse sont écrits sous forme d'articles et il a donc semblé cohérent d'écrire l'ensemble de la thèse en anglais pour assurer une continuité au manuscrit. Ensuite, ayant pour objectif de poursuivre ma carrière dans le milieu académique, il me paraissait important de favoriser la diffusion internationale de ce manuscrit. Enfin, un des rapporteurs du jury de thèse qui est un spécialiste dans le domaine provient d'un pays anglophone.

Plan

Introduction générale....2
Motivations....2
Contexte de l'étude....3
....3
Méthodes expérimentales et numériques....3
Présentation du manuscrit....4
Chapitre I: Concepts de base sur la diffraction des rayons X cohérents....5
Chapitre II: Méthodes expérimentales et échantillons....5
Chapitre III : Signature de dislocations et de fautes d'empilement dans des nanocristaux cubiques face centrée étudiée par diffraction des rayons X cohérents: une étude numérique....6
Simulations sur un nanocristal cubique face centrée....6
Chapitre IV: La diffraction des rayons X cohérents appliquée à des systèmes modérément complexes. 8
Cas d'un système modérément complexe: nanoindentation simulée d'un film mince de nickel....9
Chapitre V: L'imagerie de défauts individuels et d'une microstructure de défauts par diffraction des rayons X cohérents....10
Étude d'une dislocation mixte germée au cours d'une simulation de nanoindentation....10
Cas d'un système modérément complexe: nanoindentation simulée d'un film mince de nickel....12
Chapitre VI: Étude des propriétés mécaniques d'un nanocristal d'or par nanoindentation in situ et imagerie par diffraction des rayons X cohérents....14
Détails expérimentaux....15
Comparaisons des figures de diffraction à différents stades du cycle d'indentation....15
Reconstruction de la densité électronique diffractante....16
Imagerie d'une boucle de dislocation prismatique 17
Évolution des champs de déformation et de déplacement au cours du cycle d'indentation....17
Chapitre VII: Étude de la distribution tri-dimensionnelle de la déformation dans une particule d'or maclée de taille submicronique par diffraction des rayons X cohérents et simulations de statique moléculaire....19
Détails expérimentaux....20
Simulations de statique moléculaire....21
Chapitre VIII : Étude d'une interface bi-métallique hétérogène (Cu-Ta) par diffraction de surface,

calculs ab-initio et dynamique moléculaire....23
Calculs DFT....25
Comparaison entre les calculs DFT et les données de diffraction de surface....26
Chapitre IX: Interface des cristallites de cuivre démouillés en phase solide sur une surface de Ta(0 0 1) étudiée par diffraction des rayons X cohérents et simulations de dynamique moléculaire....27
Simulations de dynamique moléculaire de l'interface CuTa....27
Observation de l'interface par microscopie électronique en transmission à haute résolution....29
Chapitre X: Étude de la distribution tri-dimensionnelle de domaines d'inversion de polarité dans des fils de GaN....30
Expérience de CXD....30
Chapitre XI: Étude de la structure magnétique et de la dynamique d'éléments magnétiques submicroniques par holographie par transformée de Fourier....31
L'Holographie de Gabor (Fourier Transform Holography)....32
Étude de la magnétisation dans le plan de nanostructures magnétiques....32
Imagerie en temps résolu des dynamiques de magnétisation du vortex....33
Conclusions et perspectives....35
Défauts structuraux et effets de taille sur les propriétés mécaniques....35
Bibliographie....38

Introduction générale

Motivations

Ces travaux de thèse portant sûr la diffraction des rayons X cohérents couvrent un spectre assez large qu'il convient de définir. Au sein du laboratoire SIMaP dans lequel ce travail de thèse a été mené à bien, un intérêt tout particulier est donné à la relation entre microstructure et propriétés physiques. La motivation principale de cette étude consiste à déterminer comment un rayonnement synchrotron et en particulier des rayons X cohérents peuvent nous aider à comprendre cette relation.

Notre étude s'intéresse en particulier à la relation entre microstructure et la réponse mécanique d'objets de taille micrométrique. Cette thématique est corrélée à l'étude des défauts cristallins et des propriétés structurelles aux petites échelles. Elle a été initiée par les travaux de Brenner dans les années 1950 (Brenner 1956), qui constata une augmentation de la résistance mécanique associée à une diminution de la taille de fils de cuivre monocristallins soumis à un essai de traction. Plus récemment, les 10 dernières années ont été marquées par un regain d'intérêt autour de cette thématique, notamment motivé par les travaux de Uchic *et al.* (2004) où sont mis en évidence une réponse mécanique aux petites échelles de longueur qui diffère fortement de celle observée dans le matériau massif.

La tendance générale est donc une augmentation de la résistance mécanique avec une diminution de la taille de l'objet. Cependant, l'existence d'une loi d'échelle est sujette à débats. La compréhension détaillée de ces effets de taille peut-être uniquement obtenue si la microstructure initiale de l'échantillon est connue (Bei *et al.* 2008). En effet, la densité initiale de défauts est dépendante du procédé d'élaboration de l'échantillon. Elle doit être mesurée *a priori* et de manière non destructive comme elle contrôle la réponse mécanique de l'échantillon.

Pour répondre à ces différentes questions, notre objectif est la caractérisation non destructive du champ de déformation 3D dans des cristaux submicroniques (îlots / fils). Ce champ de déformation est associé à la présence de défauts structuraux qui peuvent être classés par leur dimensionnalité, à savoir 1D (lignes de dislocations) ou 2D (interfaces: fautes d'empilement, surface libres ….).

La microscopie électronique en transmission (MET) est une technique particulièrement adaptée à l'étude de défauts cristallins. Elle permet d'obtenir une image directe de la structure de défauts avec une résolution atomique, actuellement inaccessible avec des rayons X, et permet la détermination du champ de déplacement avec une précision de l'ordre du picomètre. Cependant, la technique est limitée par la profondeur de pénétration des électrons et ne permet pas l'étude d'objets dont l'épaisseur excède la centaine de nanomètres. Elle nécessite dans la grande majorité des cas la préparation de lames minces dont la préparation (généralement par faisceau focalisé d'ions) introduits des défauts additionnels et des conditions aux limites très spécifiques (les surfaces libres des lames minces).
Les techniques de diffraction de rayons X sont très complémentaires du MET; elles permettent l'étude d'objets sans nécessiter aucune préparation au préalable du fait de la faible interaction des rayons X avec la matière. Elles laissent donc entrevoir la possibilité d'une étude d'objets 3D couplée avec de la caractérisation *in situ.* La diffraction des rayons X est par nature très sensible aux déformations cristallines en géométrie de Bragg et des mesures très précises de la déformation peuvent être réalisées. Pour les techniques classiques de diffraction de rayons X, la résolution est contrôlée par la taille du faisceau, qui atteint quelques dizaines de nanomètres sur certaines lignes dédiées dans les synchrotrons de 3ème génération. Cette limite de résolution peut être améliorée par l'utilisation d'un faisceau de rayons X cohérents qui permet de retrouver numériquement l'information de phase encodée dans l'intensité diffractée. Cela permet la reconstruction en 3 dimensions d'objets submicroniques avec une résolution de l'ordre de la dizaine de nanomètres, et une précision sur le champ de déplacement de l'ordre du picomètre.

Contexte de l'étude

Ces travaux de thèse a été réalisé dans le groupe Physique du Métal (PM) au sein du laboratoire SIMaP. Ses activités se concentrent sur les matériaux métalliques, avec un accent mis sur les transformations de phase, les propriétés mécaniques et les matériaux complexes. Les activités de recherche sont conduites en synergie avec l'élaboration, la caractérisation (en particulier avec des grands instruments) et des activités de modélisation. Ma bourse de thèse a été financée par l'agence nationale de la recherche (ANR) dans le cadre du projet MecaNIX dont l'objectif principal est la compréhension des propriétés mécaniques de nanostructures isolées et l'influence de la taille sûr les propriétés mécaniques. Ce projet a bénéficié de l'expertise des partenaires impliqués dans ce projet conjointement avec le SIMaP:

- la laboratoire IM2NP à Marseille. Dans le cadre du projet MecaNIX ils ont développé un AFM compact qui a été utilisé pour les expériences de nanoindentation *in situ* présentées dans le chapitre VI de ce manuscrit.
- L'institut INAC institut du CEA Grenoble, en charge de l'élaboration et de la caractérisation des nanostructures de semiconducteurs (GaN et GaAs).
- La ligne de lumière ID01 de l'ESRF (European Synchrotron Radiation Facility), où une grande partie des expériences de Diffraction des rayons X cohérents ont été effectuées.
- L'institut Max Plank de Stuttgart qui a fourni les nanofils métalliques utilisés pour plusieurs expériences de diffraction des rayons X cohérents (CXD).
- Le LPS (laboratoire de Physique du Solide), pionnier dans l'étude de défauts cristallins par diffraction des rayons X cohérents.

Méthodes expérimentales et numériques

La majorité de la partie expérimentale de ces travaux de thèse a été réalisée dans des synchrotrons de 3ème génération. Les expériences présentées dans ce manuscrit se divisent en 3 groupes principaux:

- La diffraction des rayons X cohérents pour l'étude de défauts cristallins et l'imagerie de champs de déplacement 3D.

- L'holographie de Gabor (Fourier Transform Holography: FTH) couplée au dichroïsme magnétique circulaire dans la gamme des rayons X mous (XMCD), afin d'étudier la configuration magnétique et la dynamique de nanostructures à l'aide d'expériences résolues en temps.
- Des techniques complémentaires de diffraction de rayons X comme la micro-diffraction Laue ou des techniques de diffraction de surface *in situ* sous ultra vide pour caractériser plus finement les échantillons d'intérêt

Un grand nombre d'outils numériques ont été également utilisés pour mener à bien l'analyse des données expérimentales. La majorité de ces outils ont été développé au sein du laboratoire, comme la procédure de reconstruction de phase des donnés expérimentales (et simulées), ainsi que l'imagerie de nanostructures magnétiques par holographie magnétique.
Des échantillons modèles ont été élaboré et utilisés dans ces travaux de thèse. Pour l'étude de la stabilité structurelle et les propriétés mécaniques, deux systèmes ont été principalement étudiés: des cristaux 3D submicroniques d'or et de cuivre. Ces cristaux sont mis en œuvre par la technique de démouillage en phase solide et ont une orientation spécifique vis à vis de leurs substrats respectifs: des monocristaux de Ta (0 0 1) et de Al_2O_3 (saphir) (0 0 0 1). Des techniques de caractérisation standard comme la microscopie optique, électronique ou à force atomique ont été utilisées. La sollicitation mécanique locale a été réalisée par nanoindentation aussi bien *in situ* que *ex situ* au laboratoire. Les échantillons pour l'étude des propriétés fonctionnelles, à savoir les nanofils de GaN et les éléments de permalloy (Fe-Ni) ont été élaborées par nos collaborateurs.
L'originalité principale de ces travaux de thèse réside dans le fait que la grande majorité des expériences présentées dans ce manuscrit est supportée par une grande quantité de simulations numériques: des simulations atomistiques utilisant la statique et la dynamique moléculaire pour l'étude de défauts cristallins individuels et la reproduction du procédé d'indentation, des calculs *ab initio* pour la détermination précise de la structure de surfaces et d'interfaces et enfin des méthodes d'éléments finis pour des calculs d'élasticité continue. En effet des calculs systématiques de diffraction de rayons X pour ces simulations dans l'approximation cinématique fournissent des données de diffraction simulées qui permettent une meilleure compréhension des données expérimentales dans l'espace réciproque, mais permettent également d'évaluer la robustesse des algorithmes de reconstruction de phase.

Présentation du manuscrit

Le manuscrit de thèse est rédigé entièrement en Anglais, et certains chapitres important de la thèse (Chapitre III, VII et VIII) sont écrits sous forme d'article. Il se divise en 4 grandes parties :

- Les 2 premiers chapitres présentent les concepts théoriques ainsi que les méthodes expérimentales utilisées dans ces travaux de thèse. Le premier chapitre présente les bases de la diffraction des rayons X cohérents et le chapitre II présente les méthodes et techniques expérimentales. Les configurations expérimentales utilisées pour réaliser les expériences de diffraction cohérente et de surface sont tout d'abord décrites puis les échantillons ainsi que leurs techniques de préparation et de caractérisation sont présentés.
- La deuxième partie se concentre sur l'étude de dislocations dans des micro/nanocristaux cubiques face centrés (f.c.c.) par diffraction des rayons X cohérents. Dans un premier temps le Chapitre III présente un catalogue des signatures de dislocations individuelles dans l'espace réciproque. Par la suite, les effets dans l'espace réciproque d'une microstructure de défauts est évaluée, en s'intéressant en particulier au cas de l'indentation d'un film mince, chapitre IV. Le chapitre V présente des reconstructions numériques permettant l'étude dans l'espace réel de dislocations individuelles et d'une assemblée de dislocations. Pour finir, le Chapitre VI détaille des expériences d'indentation *in situ* d'un microcristal d'or, aboutissant à l'observation et à la reconstruction de défauts germés couplé à un phénomène de recuit mécanique.

- La troisième partie (Chapitres VII-IX) est dédiée à l'étude de l'influence de surfaces et d'interfaces sur les champs de déplacement au sein de cristallites de petite taille: elle débute dans le Chapitre VII par l'étude d'une particule d'or maclée, permettant de mettre en évidence la sensibilité de la CXD aux déformations de surface induites par la relaxation des surfaces libres. Les Chapitres VIII et IX se focalisent sur l'étude de l'interface bi-métallique Cu-Ta, obtenue par démouillage en phase solide. Dans un premier temps, le Chapitre VIII combine des expériences de diffraction de surface *in situ* et des calculs *ab initio* permettant la détermination de la structure de la couche de mouillage de Cu. Par la suite, la structure de l'interface au sein des cristallites est étudiée à l'aide de simulations de dynamique moléculaire. L'impact de la structure atomique sur cette interface et son influence sur la distribution du champ de déplacement obtenu par diffraction cohérente est discutée.
- La dernière partie regroupe les résultats liés à l'imagerie de défauts concernant les propriétés fonctionnelles et se focalise en particulier à nos contributions à ces expériences. Le Chapitre X s'intéresse à l'imagerie de domaines d'inversion de polarité dans des nanofils de GaN semiconducteurs. Le Chapitre XI présente l'étude de configuration magnétiques et leur dynamique au sein de nanostructures de permalloy (Fe/Ni). L'holographie de Gabor est utilisée pour caractériser ces nanostructures, et leur dynamique de magnétisation est étudiée grâce à des expériences synchrotron en temps résolu.

Chapitre I: Concepts de base sur la diffraction des rayons X cohérents

Ce chapitre permet d'introduire les bases théoriques de la diffraction cohérente ainsi que certaines de ses utilisations.
Dans une première partie le concept de cohérence est détaillé tout comme les propriétés caractéristiques d'un faisceau de rayons X cohérents.
Dans la deuxième partie de ce chapitre, la sensibilité des faisceau de rayons X cohérents aux défauts et déformations cristallines est expliquée. Les stratégies pouvant être mises en œuvre pour l'étude de systèmes très déformées ou présentant une structure de défaut complexe sont ensuite discutées, et des exemples numériques sur des systèmes présentant une structure de défauts très simple sont également présentées.
L'imagerie par diffraction cohérente (CDI) qui s'appuie sur des algorithmes de reconstruction de phase est introduite dans la troisième partie. Le concept de sur-échantillonnage (Sayre 1952) est expliqué en détails et les récents progrès dans les algorithmes de reconstruction phase sont également présentés. Des exemples de reconstruction focalisées sur le cas de défauts uniques permettent de conclure ce chapitre

Chapitre II: Méthodes expérimentales et échantillons

Ce chapitre présente les techniques expérimentales et les échantillons utilisés au cours de ces travaux de thèse. Les techniques de diffraction des rayons X permettent d'accéder à une grande variété de propriétés structurales dans des objets submicroniques. Plus particulièrement la diffraction des rayons X cohérents permet d'accéder au champ de déplacement 3D, tandis que les techniques de diffraction de surface permettent la détermination de la structure atomique de surfaces ou d'interfaces. Ces techniques requièrent l'utilisation d'une source de rayons X de forte brillance et la partie expérimentale de ces travaux de thèse a donc été principalement effectuée dans des synchrotrons de 3ème génération.
Dans une première partie de ce chapitre sont présentés les montages synchrotron permettant de réaliser des expériences de diffraction cohérente et de surface. Les méthodes d'acquisition des données sont également discutées.
Dans une deuxième partie, nous nous intéressons aux échantillons étudiés au cours de ces travaux de thèse. Sont décrites aussi bien les méthodes d'élaboration que de caractérisation. Certaines d'entre elles sont très

conventionnelles (microscopie optique, électronique à balayage ou à force atomique) tandis que d'autres sont plus spécifiques à ces travaux de thèse (*ex situ* nanoindentation, diffraction μ-Laue, diffraction des rayons X à balayage...). Le chapitre se conclut par un exemple de caractérisation complète d'un échantillon utilisé pour les expériences de diffraction cohérente.

Chapitre III : Signature de dislocations et de fautes d'empilement dans des nanocristaux cubiques face centrée étudiée par diffraction des rayons X cohérents: une étude numérique

Le but de ce chapitre est d'établir un catalogue des signatures dans l'espace réciproque de défauts cristallins typiques (dislocations, fautes d'empilement) dans des nanocristaux cubiques faces centrées (f.c.c.), et d'établir les meilleures conditions expérimentales (choix du vecteur de diffraction $\boldsymbol{g}$) permettant de mettre en évidence ces défauts cristallins. Cette approche est ensuite illustrée sur un cas réaliste de germination de dislocations au cours de la nanoindentation simulée d'une nanoparticule d'or.
Les nanocristaux sont modélisés avec des potentiels interatomiques réalistes (Mishin *et al.* 1999, Mishin *et al.* 2001, Grochola *et al.* 2005) à l'aide du code de simulation atomistique MERLIN (Rodney 2010) et relaxés après introduction d'un défaut unique. Le recours à des simulations à l'échelle atomique est requise pour tenir compte de tous les effets physiques qui entrent en jeu: la dissociation de la dislocation parfaite en dislocations partielles (dépendante de l'énergie de faute d'empilement du cristal), l'effet de la structure du cœur des dislocations et enfin l'influence des conditions aux limites (surfaces libres / facettes des nanocristaux en forme d'équilibre de Wulff : Winterbottom 1967). Les figures de diffraction sont calculés dans l'approximation cinématique grâce à la librairie PyNX (Favre-Nicolin *et al.* 2010). Les calculs sont effectués au voisinage de différentes réflexions de Bragg, et l'influence des conditions de diffraction sûr les signatures des défauts dans l'espace réciproque est étudiée.

Simulations sur un nanocristal cubique face centrée

Dans un premier temps, nous nous intéressons à des cas génériques de défauts, comme des dislocations vis, coins ou encore des boucles de dislocations prismatiques. La figure 1 présente un exemple des signatures obtenues pour une dislocation vis introduite au centre d'un nanocristal de cuivre de 30 nm (~1 million d'atomes), pour différents vecteurs du réseau réciproque $\boldsymbol{g}$. Il est démontré qu'à chaque type de défaut cristallin correspond une signature dans l'espace réciproque et que cette signature dépend des conditions de diffraction (choix du $\boldsymbol{g}$).
Cette étude systématique permet d'identifier les conditions de diffraction les plus adaptés à l'étude de défauts uniques typiques. Par exemple la dissociation d'une dislocation vis ou coin sera particulièrement bien mise en évidence pour un vecteur du réseau réciproque satisfaisant les conditions d'invisibilité dans le cas d'une dislocation parfaite (Volterra) : $\boldsymbol{g}.\boldsymbol{b} = \boldsymbol{0}$ ($\boldsymbol{g}$ = 2 2 4 par exemple).

Application à un cas plus réaliste: nanoindentation simulée d'une nanoparticule d'or

Les conditions d'invisibilité établies pour les défauts uniques dans la première partie du chapitre sont ensuite utilisées pour l'analyse d'un cas plus réaliste et complexe: la nanoindentation simulée d'une nanoparticule d'or (collaboration avec Dan Mordehai de l'institut Technion d'Haifa). Dans un premier temps sont mis en évidence la variété des figures de diffraction obtenues pour différents arrangements de dislocations obtenus à différents stades de la simulation. Nous nous focalisons ensuite sur une étape particulière de la simulation, pour laquelle une seule dislocation mixte est présente dans la particule d'or. Quatre vecteurs du réseau réciproque de type 1 1 1 sont utilisés pour l'étude de cette configuration d'intérêt. La dislocation produite une signature claire et distincte pour deux d'entre eux, alors que la figure de diffraction est très similaire au cas -

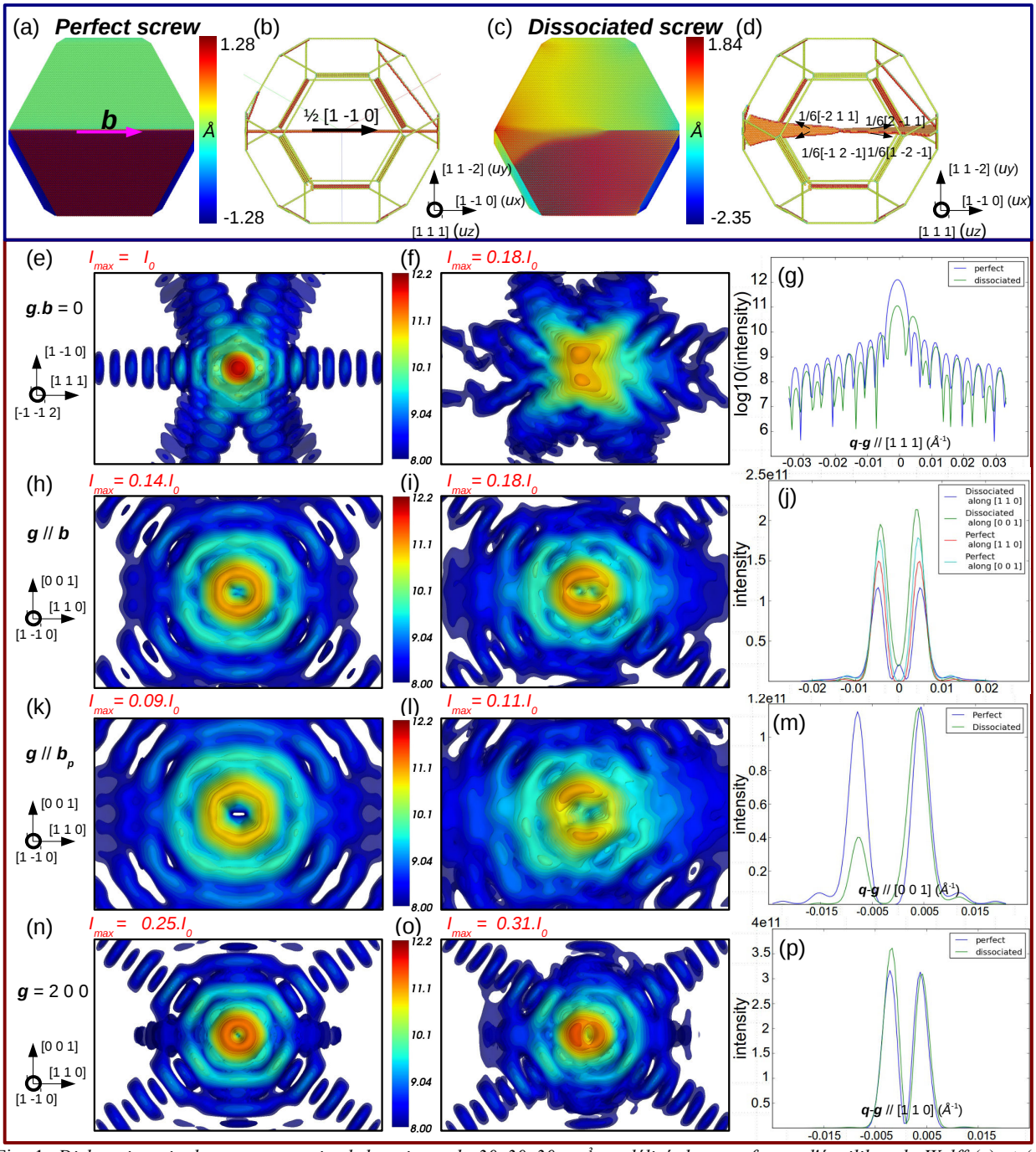

Fig. 1: *Dislocation vis dans un nanocristal de cuivre de 30x30x30 nm³ modélisé dans sa forme d'équilibre de Wulff* (a) et (c) L'échelle de couleur montre le composant u_x du champ de déplacement pour les configurations initiales et relaxées (b) et (d) Dislocation vis parfaite (Volterra) avec $\boldsymbol{b} = 1/2[1\ \bar{1}\ 0]$ et dissociation de cette dislocation en 2 jeux de dislocations partielles de Shockley dans les plans (1 1 1) et (1 1 $\bar{1}$). Sont uniquement représentés les atomes défectueux ou situés sur les coins et arêtes de la cristallite. Calcul des figures de diffraction cohérente pour $\boldsymbol{g}.\boldsymbol{b} = 0$ ($\boldsymbol{g} = 2\ 2\ \bar{4}$) pour une dislocation Volterra (e) et des dislocations dissociées (f). (g) Intensité selon la direction [1 1 1] (échelle logarithmique). Figures de diffraction calculées pour $\boldsymbol{g}$ // $\boldsymbol{b}$ ($\boldsymbol{g} = 2\ \bar{2}$ 0) pour une Volterra (h) et des dislocations partielles de Shockley (i). (j) Intensité selon [0 0 1]. Cas de la Volterra (k) des partielles de Shockley (l) et intensité selon [0 0 1] (m) pour $\boldsymbol{g}$ // $\boldsymbol{b_p}$ ($\boldsymbol{g} = 2\ \bar{4}\ 2$)**.** Cas de la Volterra (n), des partielles de Shockley (o) et intensité (p) selon [1 1 0] pour un $\boldsymbol{g}$ quelconque ($\boldsymbol{g} = 2\ 0\ 0$) . *Le volume de l'espace réciproque représenté est ici toujours le même c'est à dire 0.045x0.045x0.0675 (1/ Å)³*

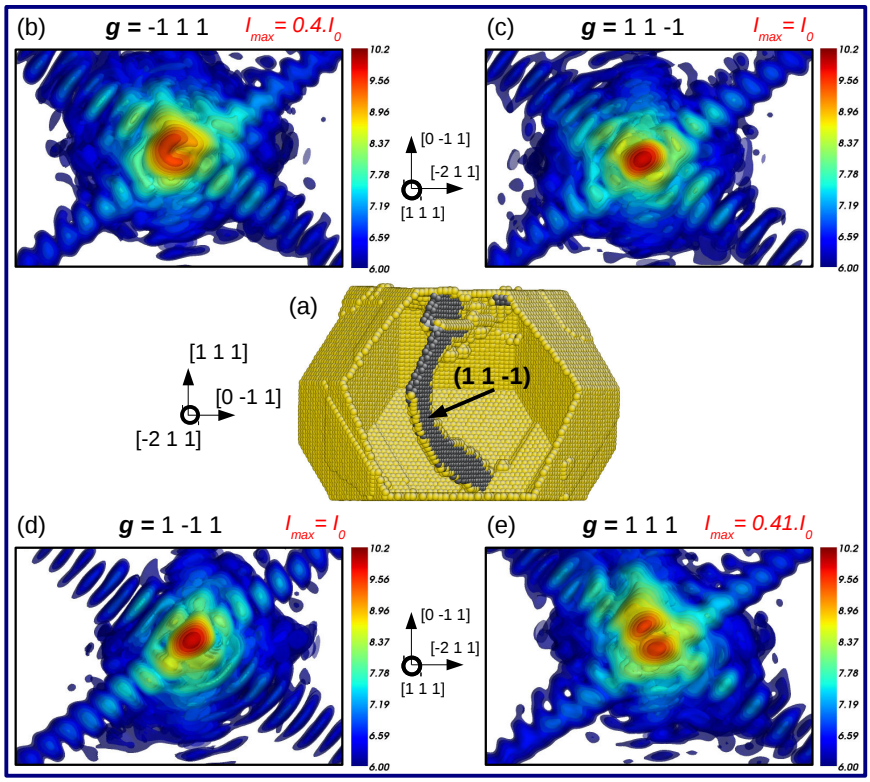

Fig. 2: (a) Nanoparticule d'or après 650000 indentation pas de simulation. Une dislocation mixte présentant un vecteur de Burgers ***b*** de type ½ <1 1 0> peut-être observée. (b) to (e) Calcul des figures de diffraction pour quatre vecteurs de diffraction de type <1 1 1>. *Le volume de l'espace réciproque représenté est ici toujours le même c'est à dire 0.08x0.08x0.12 (1/ Å)³*

- du cristal parfait pour les deux autres (Fig. 2). Ces deux vecteurs satisfont les conditions d'invisibilité $\boldsymbol{g.b} = 0$, permettant de déterminer le vecteur de Burgers de la dislocation. Une analyse plus approfondie de la figure de diffraction (perturbations dans périodicité des franges d'interférence produites par les facettes du nanocristal …) et l'utilisation de vecteurs de diffraction supplémentaires permettent d'obtenir une bonne approximation de la largeur de dissociation ou de la position de la dislocation dans la cristallite.

Ce chapitre démontre donc l'utilité et la pertinence de l'analyse des figures de diffraction cohérente dans l'espace réciproque. Dans des cas expérimentaux, cette méthode requière des temps de comptage significativement plus faibles que les méthodes d'imagerie et s'avère donc très adaptée pour des expériences ou les défauts cristallins sont germés *in situ* (nanoindentation *in situ* par exemple)

Chapitre IV: La diffraction des rayons X cohérents appliquée à des systèmes modérément complexes.

Le Chapitre III démontre que la diffraction des rayons-X cohérents est particulièrement adaptée à l'étude de défauts individuels, cependant le cas des défauts multiples n'y est pas traité.
Dans le chapitre IV présentant uniquement des études numériques, nous cherchons à démontrer que la diffraction des rayons X cohérents est également adaptée à l'étude d'un système modérément complexe (*i.e.* un arrangement de quelques défauts cristallins). Dans une première partie nous utilisons la procédure décrite par Erhart *et al.*

(1982) et Larson & Young (1987) pour mettre en évidence la sensibilité de la CXD à la taille, mais également au caractère lacunaire ou interstitiel d'une boucle de dislocation individuelle. Cette méthodologie est ensuite étendue au cas des fautes d'empilement. Le cas d'une assemblée de défauts est illustré à travers deux systèmes: la nanoindentation d'un film mince de nickel, où des boucles de dislocation prismatique sont germées au sein de différents systèmes de glissement, et le démouillage en phase solide du démouillage en phase solide d'une particule de cuivre sur un substrat de tantale, induisant un réseau complexe de fautes d'empilement.

Cas d'un système modérément complexe: nanoindentation simulée d'un film mince de nickel

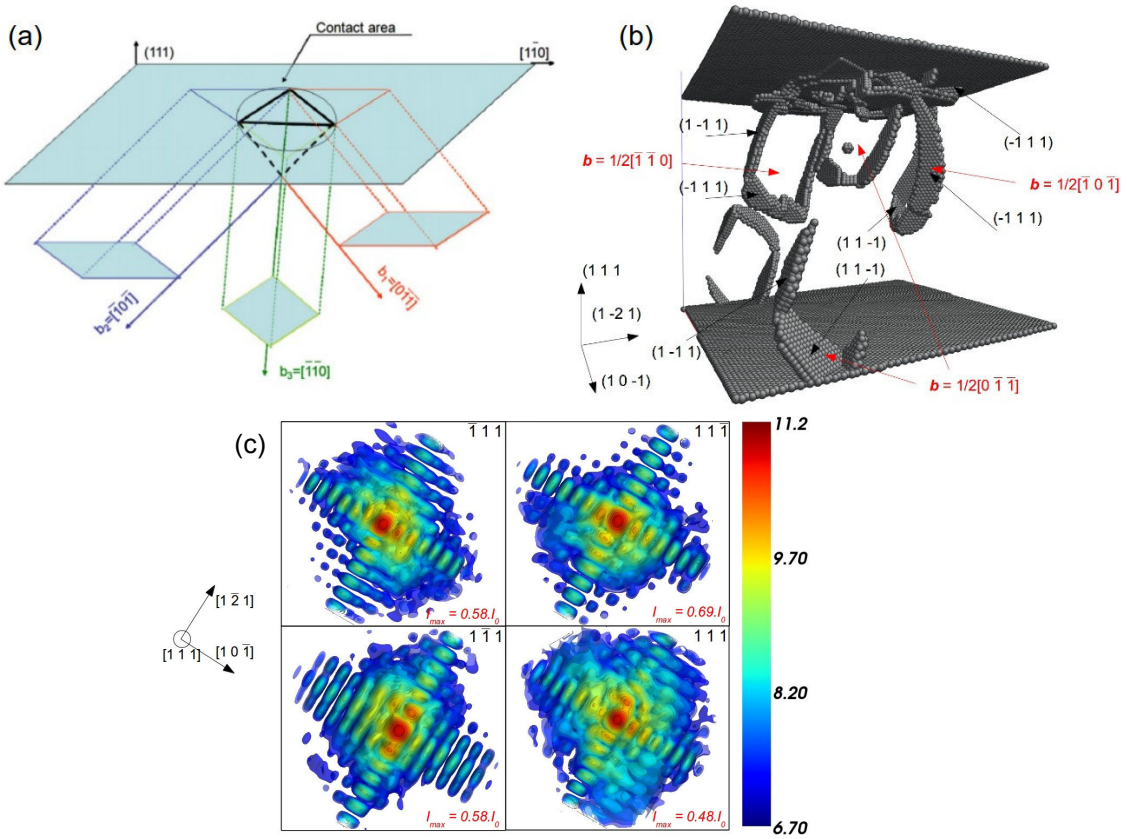

Fig. 3: (a) Description schématique du processus de germination des boucles prismatiques pendant l'indentation [1 1 1]. (b) Configuration atomistique à la fin de la nanoindentation simulée, seuls les atomes défectueux sont représentés. (c)(c) Figures de CXD calculées pour 4 vecteurs ***g*** de type 1 1 1. *Le volume représenté de l'espace réciproque est égal à 0.09x0.09x0.09 (1/ Å)*^{3}

La figure 3.a permet d'illustrer la germination des boucles de dislocation prismatiques dans un système sollicité par indentation. Selon le mécanisme décrit décrit par Ashby dans les années 1960 (Ashby 1971), les boucles de dislocation prismatique sont germées dans trois systèmes de glissement équivalents (de type 1/2<1 1 0>{1 1 1}) pour accommoder le déplacement dans la direction d'indentation. Ce mécanisme est très bien reproduit dans une simulation de nanoindentation sur un film mince de Nickel, réalisée avant ces travaux de thèse (Chang *et al.* 2010). L'indentation du film dans la direction [$\bar{1}$ $\bar{1}$ $\bar{1}$] conduit à la germination de quatre boucles de dislocations prismatiques présentant trois vecteurs de Burgers distincts correspondant aux trois systèmes de glissement (Fig.3.b).

Comme dans le cas d'un défaut unique, la signature observée dans l'espace réciproque dépend de ***g***, nous cherchons donc à déterminer si la méthode éprouvée dans le chapitre III (utilisation de plusieurs ***g*** de type 1 1 1)

permet de déterminer les caractéristiques de toutes les dislocations présentes dans la structure. Pour $\boldsymbol{g}$ = 1 1 1, sensible aux trois variants de boucle prismatique présents dans la structure, une diffusion diffuse plus prononcée, ainsi qu'une diminution sensible de l'intensité maximale (par comparaison avec un cristal parfait comportant le même nombre d'atomes) sont observées. Pour les autres $\boldsymbol{g}$ deux variants satisfont systématiquement les conditions d'invisibilité. Les perturbations observées sur la figure de diffraction dépendent donc principalement de la taille et de la position du seul variant de boucle prismatique visible.Cette méthodologie, efficace dans le cas de défauts uniques est cependant inadaptée à l'étude d'un système modérément complexe. Les interférences entre les différentes boucles conduisent à des figures de diffraction très complexes et une détermination fine de la microstructure (détermination du nombre de dislocations ainsi que leur vecteur de Burgers) est inenvisageable à partir de l'analyse seule de l'espace réciproque.
L'analyse directe de l'espace réciproque s'avère plus concluante dans le cas d'un réseau complexe de fautes d'empilement. L'intensité des franges d'interférence dans les directions perpendiculaires aux fautes d'empilement procure une bonne estimation de la densité de fautes d'empilement dans un plan de glissement donné. Dans le cas d'un faible nombre de fautes d'empilement il est également possible de déduire la distance entre deux fautes d'empilement successives.

Particulièrement adaptée à l'étude de défauts uniques, l'analyse de l'espace réciproque s'avère plus délicate dans le cas d'une assemblée de défauts. Dans ce cas, d'autres méthodes comme la reconstruction de la structure de défauts dans l'espace réel peuvent être envisagés (Chapitres V à VII).

Chapitre V: L'imagerie de défauts individuels et d'une microstructure de défauts par diffraction des rayons X cohérents.

Dans le chapitre V nous cherchons à tester et valider la méthode de reconstruction des figures de CXD 3D pour étudier la microstructure de nanocristaux isolés. Les cas du défaut unique et d'un arrangement de défauts sont tous deux envisagés. A l'image du Chapitre III, la première section du chapitre se focalise sur des cas simples et typiques de défauts individuels. L'utilisation de configurations atomistiques permet la détermination et l'analyse du champ de déplacement au voisinage de lignes de dislocation (de type vis ou coin). Dans une seconde partie le champ de déplacement est reconstruit pour des structures de dislocations plus complexes: dislocations mixtes, boucles de différent type et un arrangement de dislocations germées au cours de la nanoindentation simulée d'un nanocristal d'or initialement vierge de défaut. Le chapitre se conclut par l'analyse de la microstructure d'un film mince de nickel au cours de sa nanoindentation simulée, permettant de confirmer que l'imagerie par diffraction des rayons X cohérents (CDI) peut-être utilisée sur des systèmes modérément complexes contenant un réseau de dislocation germées sur plusieurs systèmes de glissement.

Étude d'une dislocation mixte germée au cours d'une simulation de nanoindentation

Dans la dernière section du Chapitre III nous démontrons qu'il est possible de déterminer le vecteur de Burgers et plus généralement le système de glissement d'une dislocation mixte générée au cours de la nanoindentation simulée d'une nanoparticule d'or à partir de quelques réflexions dans l'espace réciproque.
Dans cette section, nous utilisons les algorithmes de reconstructions de phase pour reconstruire le champ de déplacement 3D dans la particule et obtenir une description plus précise de la microstructure. En bon accord avec les résultats du Chapitre III la dislocation est invisible pour les $\boldsymbol{g}$ qui satisfont la condition d'invisibilité $\boldsymbol{g}.\boldsymbol{b} = 0$ ($\boldsymbol{g}$ = 1 $\bar{1}$ 1 et $\boldsymbol{g}$ = 1 1 $\bar{1}$, Fig 4.d et 9.e) alors qu'elle est clairement visible pour $\boldsymbol{g}.\boldsymbol{b} \neq 0$ ($\boldsymbol{g}$ = 1 1 1 et $\boldsymbol{g}$ = $\bar{1}$ 1 1, Fig 4.b et 4.c). Pour ces dernières la présence de la dislocation mixte se traduit dans les deux cas par un saut de phase de π entre les deux portions du cristal de part et d'autre de la ligne de dislocation. En revanche, la localisation de cette discontinuité de phase dépend du vecteur du réseau réciproque considéré. Pour $\boldsymbol{g}$ = $\bar{1}$ 1 1 elle est située au voisinage de la dislocation partielle de vecteur de Burgers $\boldsymbol{b}_{p1}$ = 1/6[$\bar{1}$ 2 1] alors qu'elle est

localisée autour de la seconde dislocation partielle ($\boldsymbol{b}_{p2}$ = 1/6[1 1 2]) pour la réflexion 1 1 1. Dans les deux cas seule la dislocation partielle dont le vecteur de Burgers est quasiment parallèle au $\boldsymbol{g}$ considéré est donc visible.

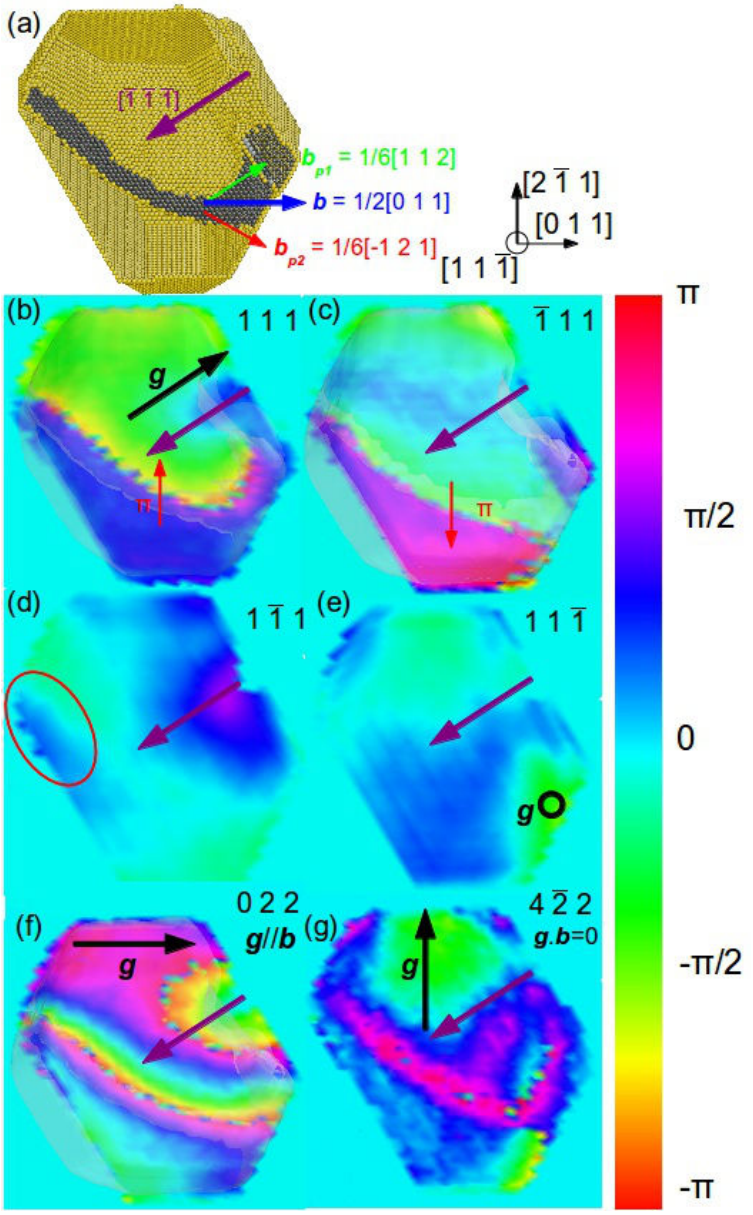

Fig. 4 *Reconstruction du champ de déplacement autour d'une dislocation mixte pour différents* $\boldsymbol{g}$ (a) Nanoparticule d'or au cours d'une nanoindentation simulée vue depuis la direction [1 1 $\bar{1}$]. Seuls les atomes défectueux et les atomes de surface sont représentés. Les directions des vecteurs de Burgers sont indiqués respectivement par une flèche bleue (dislocation parfaite) et rouge et verte (dislocation partielle). (b) à (g) Champ de déplacement reconstruit dans le plan de glissement (1 1 $\bar{1}$) de la dislocation pour différents $\boldsymbol{g}$: 1 1 1 (b), $\bar{1}$ 1 1 (c), 1 $\bar{1}$ 1 (d), 1 1 $\bar{1}$ (e), 0 2 2 (f) et 4 $\bar{2}$ 2 (g). La direction de $\boldsymbol{g}$ est indiquée par une flèche noire tandis que la direction de l'indentation est indiquée par une flèche violette.

Pour $\boldsymbol{g}$ = 0 2 2 parallèle à $\boldsymbol{b}$ les deux dislocations partielles sont en revanche visibles et induisent toutes les deux un saut de phase de π. La phase reste relativement constante dans la faute d'empilement entre les deux partielles. Si les chapitres III et IV démontrent que l'analyse de l'espace réciproque au voisinage de différents pics de Bragg permet d'obtenir une quantité significative d'information sur un défaut unique (vecteur de Burgers, système de glissement,...) la reconstruction du champ de déplacement 3D permet donc d'obtenir une description plus précise de ce dernier. En particulier elle permet la détermination de sa forme et de son orientation (largeur de la faute d'empilement, confirmation du caractère mixte d'une dislocation). A partir de la seule figure de l'espace réciproque, il s'avère également délicat de distinguer les contributions respectives des champs de déplacement au voisinage de l'indent et de la dislocation mixte. La reconstruction du champ de déplacement 3D dans la particule permet de quantifier ces deux contributions.

Cas d'un système modérément complexe: nanoindentation simulée d'un film mince de nickel

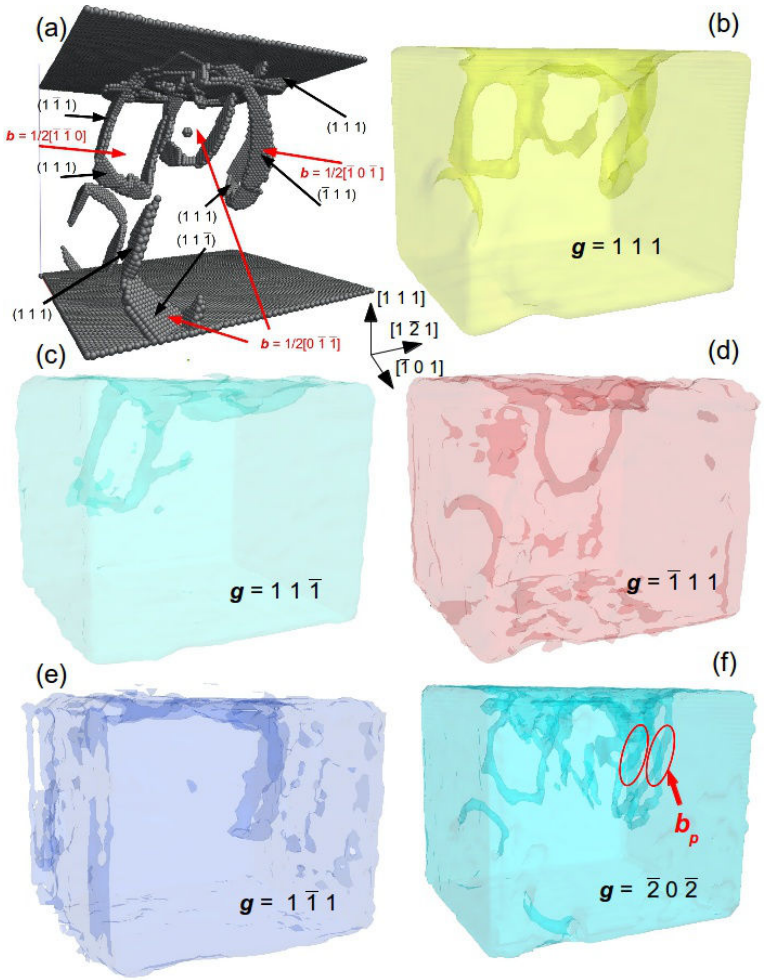

Fig. 5 Densité électronique diffractante dans le film mince de Nickel reconstruite pour différents vecteurs $\boldsymbol{g}$. (a) Configuration atomistique à l'issue de la simulation de nanoindentation du film mince de Nickel. Seuls les atomes défectueux sont représentés. Des boucles prismatiques germées dans trois systèmes de glissement sont observées dans la structure. (b) à (f) Isosurface de la densité électronique diffractante reconstruite à 65% du maximum de densité pour différents $\boldsymbol{g}$

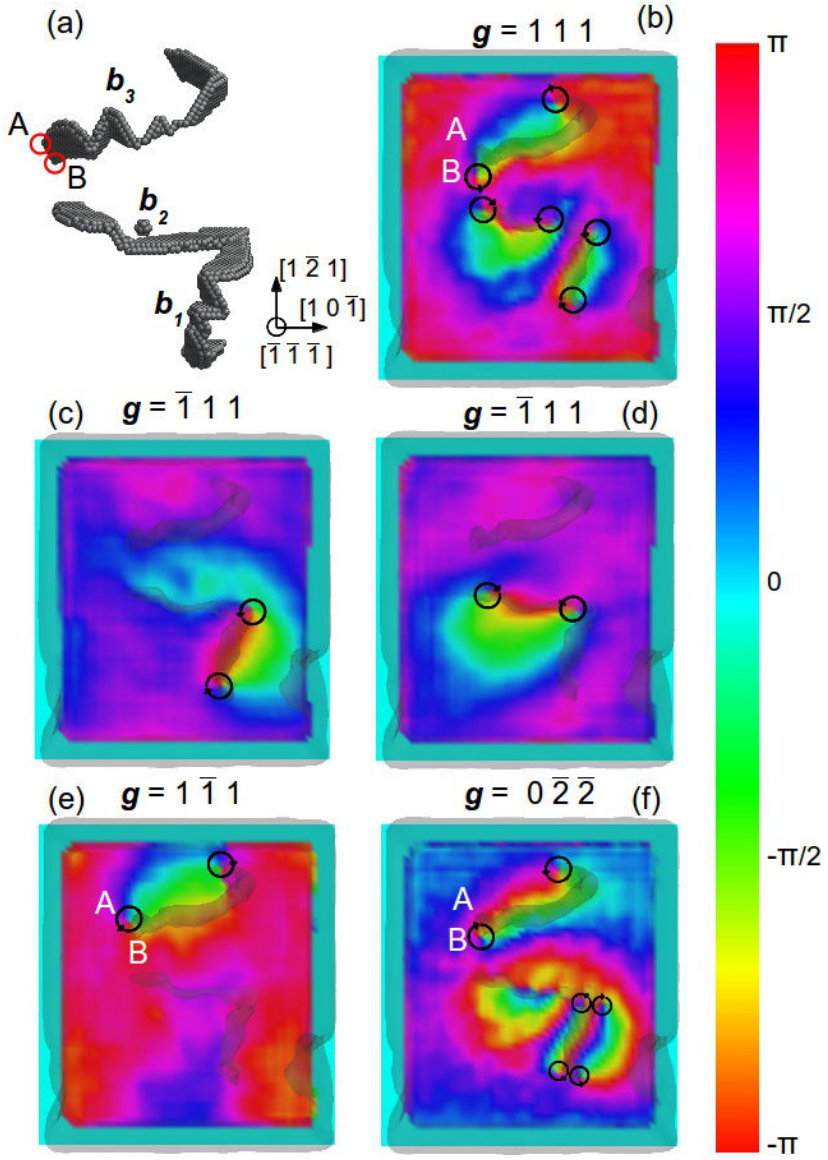

Fig. 6 *Champ de déplacement reconstruit dans le plan* $(\bar{1}\ \bar{1}\ \bar{1})$ *pour différents* $\boldsymbol{g}$ (a) Configuration atomistique vue depuis la direction $[\bar{1}\ \bar{1}\ \bar{1}]$. Sont visibles la position des dislocations dans la structure, ainsi que la localisation du plan $(\bar{1}\ \bar{1}\ \bar{1})$ qui intercepte les dislocations partielles et dans lequel le champ de déplacement est reconstruit. (b) à (f) Reconstruction du champ de déplacement pour quatre $\boldsymbol{g}$ de type 1 1 1 : (b) $\boldsymbol{g} = 1\ 1\ 1$, (c) $\boldsymbol{g} = \bar{1}\ 1\ 1$, (d) $\boldsymbol{g} = 1\ \bar{1}\ 1$ et $\boldsymbol{g} = 1\ 1\ \bar{1}$ (e) et pour $\boldsymbol{g} = 0\ \bar{2}\ \bar{2}$

Le Chapitre IV nous a démontré qu'une assemblée de boucles prismatique germée au cours de la nanoindentation simulée d'un film mince de nickel produit une signature très complexe et difficilement interprétable sur une figure de diffraction cohérente. En plus d'être difficilement réalisable expérimentalement (mesure d'un grand nombre de réflexions de Bragg sur une particule unique) cette approche ne conduit pas à une détermination précise et complète de la microstructure. Comme illustré sur les figures 5et 6 la reconstruction de la densité électronique diffractante et du champ de déplacement pour plusieurs réflexions de Bragg s'avère être une approche nettement plus pertinente pour de tels systèmes (présence de plusieurs boucles de dislocations

prismatiques dans les trois systèmes de glissement).
La présence de défauts se traduit par des chutes dans la densité électronique diffractante qui peuvent être utilisés pour déterminer avec précision la position et le vecteur de Burgers des dislocations présentes dans la structure. Pour $\boldsymbol{g}$ = 1 1 1 par exemple, aucune des boucles prismatiques ne satisfait les conditions d'invisibilité. Les chutes de densité sont donc observées au voisinage de toutes les boucles de dislocation, avec une parfaite correspondance avec la configuration atomique. Dans le cas des autres vecteurs 1 1 1 deux variants satisfont les conditions d'invisibilité, les chutes de densité électronique sont donc observées autour d'un seul variant de boucle prismatique. Enfin, $\boldsymbol{g} = \bar{2}\ 0\ \bar{2}$ ne satisfait aucune des conditions d'invisibilité susmentionnées, les boucles de dislocations sont donc toutes visibles. De plus, ce vecteur de diffraction est parallèle au vecteur de Burgers d'une des boucles ($\boldsymbol{b} = 1/2[\bar{1}\ 0\ \bar{1}]$), et les variations de densité électronique sont donc observées au voisinage de toutes les dislocations partielles de cette boucle (entourées en rouge sur la Fig. 5.f), permettant de les distinguer individuellement.
La reconstruction de la phase permet de mettre en évidence le champ de déplacement caractéristique au voisinage d'une boucle prismatique. Sur la figure 6 il est représente dans un plan $(\bar{1}\ \bar{1}\ \bar{1})$ qui intercepte les trois variants de boucles de dislocations prismatiques pour différents vecteurs du réseau réciproque.
Pour $\boldsymbol{g}$ = 1 1 1, sensible à tous les variants de boucle prismatique, le profil du champ de déplacement consiste en trois paires de vortex de phase de chiralité opposée (correspondant aux trois boucles de dislocation).
A l'image de nos observations pour la densité électronique diffractante, les trois autres vecteurs de type 1 1 1 permettent d'observer ces vortex de phase uniquement au voisinage de la boucle de dislocation qui ne satisfait pas les conditions d'invisibilité. La localisation de la singularité de phase autour de l'une ou l'autre partielle de chacun des segments de dislocation qui forme la boucle dépend également du vecteur de diffraction considéré, tout comme dans le cas de la dislocation mixte.
Enfin pour $\boldsymbol{g} = 0\ \bar{2}\ \bar{2}$ parallèle à $\boldsymbol{b_2}$, les trois variants de boucles sont visibles. Comme $\boldsymbol{g}$ n'est ni parallèle $\boldsymbol{b_1}$ ni à $\boldsymbol{b_3}$ seule une des deux dislocations partielles est observée pour ces boucles (une seule paire de vortex de phase pour ces deux boucles). Pour le variant $\boldsymbol{b_2}$, les deux dislocations partielles du segment de dislocation interceptant le plan $(\bar{1}\ \bar{1}\ \bar{1})$ dislocation sont toutes deux visibles, se traduisant par la présence de deux paires de vortex de phase de chiralité opposée.

Les différents cas présentés dans de chapitre permettent donc de démontrer que l'imagerie par diffraction des rayons X cohérents s'avère être une méthode parfaitement adaptée à l'étude de systèmes modérément complexes, contenant par exemple un arrangement de dislocation. La reconstruction de la densité électronique et de la phase permet de déterminer toutes les caractéristiques de chaque dislocation présente dans la structure (géométrie, position, vecteur de Burgers, système de glissement,...). La pertinence de cette approche dans le cas d'une étude expérimentale est discutée dans le Chapitre VI.

Chapitre VI: Étude des propriétés mécaniques d'un nanocristal d'or par nanoindentation *in situ* et imagerie par diffraction des rayons X cohérents.

Dans ce chapitre nous appliquons les méthodes décrites dans les chapitres III à V pour analyser l'évolution de la microstructure d'une cristallite d'or submicronique indentée *in situ.* A notre connaissance, l'imagerie d'un défaut germé *in-situ* par sollicitation mécanique n'a pas été reportée dans la littérature.
Ce chapitre débute par une description de la préparation et du choix de l'échantillon pour cette expérience. Les détails expérimentaux sont donnés dans la seconde partie de ce chapitre tandis que la troisième partie s'intéresse à l'influence de la présence de déformations interfaciales ou d'un contenu initial de défauts sur les figures de CXD obtenues expérimentalement. Cette section permet d'illustrer les difficultés d'obtenir un échantillon présentant à la fois une faible déformation résiduelle et une faible densité de défauts dans son état initial.
La présentation des résultats les plus marquants de cette expérience conclut ce chapitre. Dans un premier temps

nous utilisons la méthodologie d'analyse de l'espace réciproque présentée dans les chapitres III et IV, puis nous utilisons les méthodes de reconstruction de phase pour analyser l'évolution de la forme de la particule et pour visualiser le champ de déplacement autour d'une boucle prismatique germée au cours de l'expérience d'indentation. Pour finir l'évolution des champs de déplacement et de déformation au cours de l'expérience est discutée et interprétée dans la dernière section de ce chapitre.

Détails expérimentaux

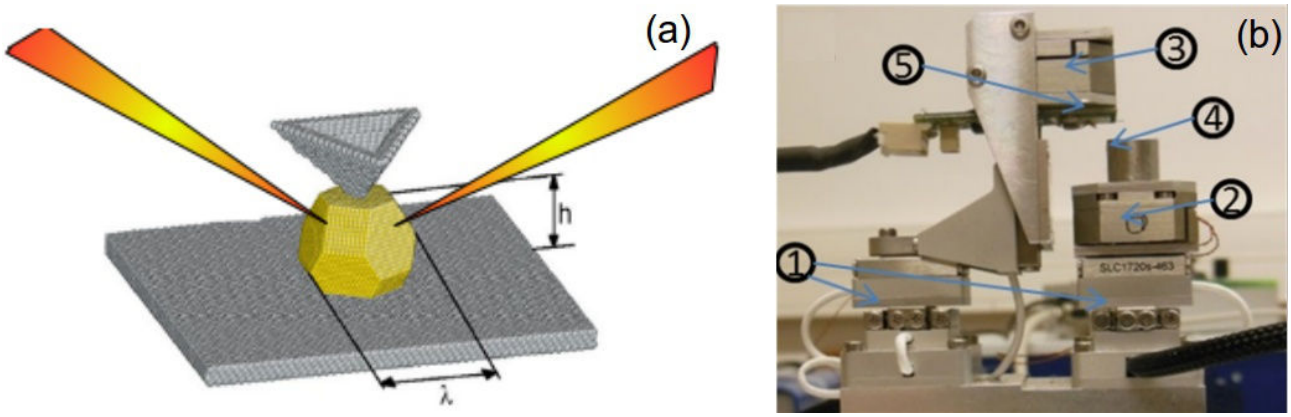

Fig. 7 (a) Principe de l'expérience. La cristallite d'or est illuminée par un faisceau de rayons X cohérents tandis qu'elle est indentée par une pointe d'AFM Berkovitch. (b) Photographie de “SFINX” représentant (1) les deux empilements de piezo longue course (2) le scanner piezo xy (3) le scanner piezo-z (4) l'échantillon (5) la poutre AFM.

L'expérience a été réalisée sur la ligne ID01 de l'ESRF. Un faisceau de rayons-X cohérents est utilisé pour illuminer les cristallites d'or. Ces dernières sont obtenues par démouillage en phase solide sur un substrat de saphir (0 0 0 1). Des diamètres et hauteurs moyennes de 700 et 400 nm respectivement sont généralement obtenus. Pour collecter une figure de diffraction 3D au voisinage de la réflexion 1 1 1, l'échantillon est pivoté dans le faisceau par +/- 0.5°. Une des premières difficultés expérimentales est la sélection d'un bon candidat pour l'expérience d'indentation *in situ.* La plupart des figures de diffraction mesurées indiquent une forte densité de défauts et/ou une large déformation interfaciale dans les cristallites. Le choix se porte sur une cristallite dont la figure de diffraction apparaît la plus parfaite possible (faible densité de défaut et faible déformation interfaciale). L'indentation *in situ* est réalisée à l'aide de l'AFM *in situ* SFINX (Zhe *et al.* 2014) développé dans le cadre du projet ANR Mecanix. L'enregistrement simultané de cartographies AFM et SXDM permet d'aligner la pointe de l'AFM avec les cristallites d'or et le faisceau focalisé de rayons X. Le schéma de l'expérience est illustré sur la figure 7.a, après l'alignement de pointe de l'AFM sur la cristallite d’intérêt, l'indentation est réalisée en abaissant cette dernière à une vitesse de 2 nm/s. La pointe est rétractée à la même vitesse dès qu'un changement est détecté sur les figures de diffraction collectées pendant l'approche de la pointe. Un total de 6 itérations de charge-décharge est réalisé et une figure de CXD 3D est collecté après chaque décharge. Pour finir une dernière figure de CXD est collectée après 24h d'illumination sous le faisceau.

Comparaisons des figures de diffraction à différents stades du cycle d'indentation

L'analyse directe des figures de diffraction fournit plusieurs renseignements très utiles sur l'évolution de la forme et de la déformation résiduelle dans la particule. Tout d'abord, un changement dans l'orientation des franges associées aux facettes de la cristallite révèle une modification de la particule après 24h de vieillissement sous faisceau de rayons X. Il apparaît aussi assez clairement que la figure de diffraction est plus parfaite après quelques itérations dans le cycle de charge-décharge. Cette évolution suggère une relaxation de la déformation

résiduelle selon le phénomène de recuit mécanique décrit par Matthews & Blakeslee (1974). Les boucles de dislocation susceptibles d'être germées étant de très petite taille par rapport au volume total de la cristallite, elles ne produisent pas de signature facilement identifiable sur les figures de diffraction. Seule la reconstruction de la densité électronique et de la phase peuvent donc confirmer la présence de boucles de dislocation dans la cristallite.

Reconstruction de la densité électronique diffractante

Le champ de déplacement $u_{l\,1\,1}$ est reconstruit à chaque itération du cycle de charge-décharge en utilisant les techniques classiques de reconstruction de phase. Les densités électroniques reconstruites sont moyennés sur les 10 meilleures reconstructions (sélectionnés à partir de l'erreur métrique et de l'homogénéité de la densité électronique diffractante).

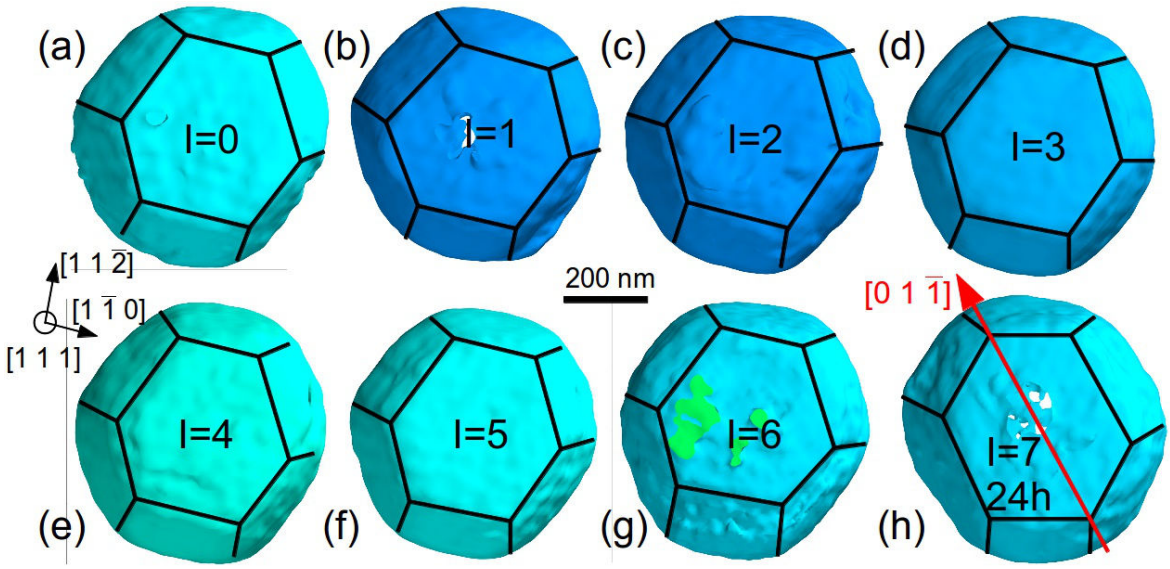

Fig. 8: *Reconstruction de la densité électronique diffractante représentée à 25% de la densité maximale pour chaque itération du cycle de charge-décharge.* La densité est moyennée sur les 10 meilleures reconstruction après chacune des étapes du cycle. (a-g) Indentations itératives, (h) 24 h de vieillissement sous le faisceau à température ambiante.

La cristallite reconstruite est fortement facettée, les facettes {1 0 0} et{1 1 1} étant connectées par des interfaces arrondies, en bon accord avec les observations de Sadan & Kaplan (2006), Malyi *et al.* (2012).
Les reconstructions pour les six premières étapes du cycle de charge-décharge sont très reproductibles et semblables aux images en microscopie électronique à balayage réalisées avant l'expérience.
En revanche après 24h d'illumination sous le faisceau, la forme de la particule évolue drastiquement (Fig.8). Sa hauteur reste constante, mais les surfaces respectives pour les facettes {1 1 1} et {1 0 0} sont complètement modifiées, notamment du fait d'un allongement de la particule dans la direction [0 1 $\bar{1}$]. De plus une rotation de la cristallite d'environ 5-10° est clairement visible. Plusieurs mécanismes peuvent être envisagés pour expliquer cette évolution, ils impliquent tous de la diffusion de surface qui n'est pas négligeable à température ambiante sur une période de 24h. L'hypothèse la plus probable est une rotation induite par la plasticité cristalline: un déplacement non compensé d à l'interface avec le substrat est induit au cours du régime de déformation plastique (dû à une activation majoritaire de certains systèmes de glissement). Ce déplacement après réorganisation de la structure atomique à l'interface induit une rotation de la cristallite. Ce réarrangement n'est pas immédiat car non observé pendant les différentes itérations du cycle charge-décharge, mais après 24h de recuit à température

ambiante, les mécanismes de diffusion peuvent entraîner une modification de cette interface substrat/cristallite.

Imagerie d'une boucle de dislocation prismatique

La modification la plus significative de la forme du pic de Bragg intervient après 3 itérations du cycle charge-décharge. La présence de défauts dans la cristallite est donc suspectée à cette itération du cycle. La figure 9.a montre l'isosurface de la densité électronique diffractante reconstruite représentée à 25% du maximum de densité. Une chute de densité ayant la forme d'une boucle d'environ 50 nm de diamètre est clairement visible approximativement 100 nm au dessus de l'interface particule-substrat. Ces perturbations dans la densité électronique sont très similaires à celles observées au voisinage des dislocations dans nos simulations.
La reconstruction du champ de déplacement $u_{1\,1\,1}$ représenté ici dans les plans (y,z) (1 $\bar{1}$ 0) (Fig. 9.b), (x,z) (1 1 $\bar{2}$) (Fig. 9.c) and (x,y) (1 1 1) (Fig. 9.d) qui interceptent la boucle en deux points, montre à chaque fois la présence de deux vortex de chiralité opposée. Ce profil du champ de déplacement, en tout point similaire à celui observé autour des boucles prismatiques, simulées permet de conserver la nature prismatique de la boucle germée au cours de l'indentation de la cristallite.

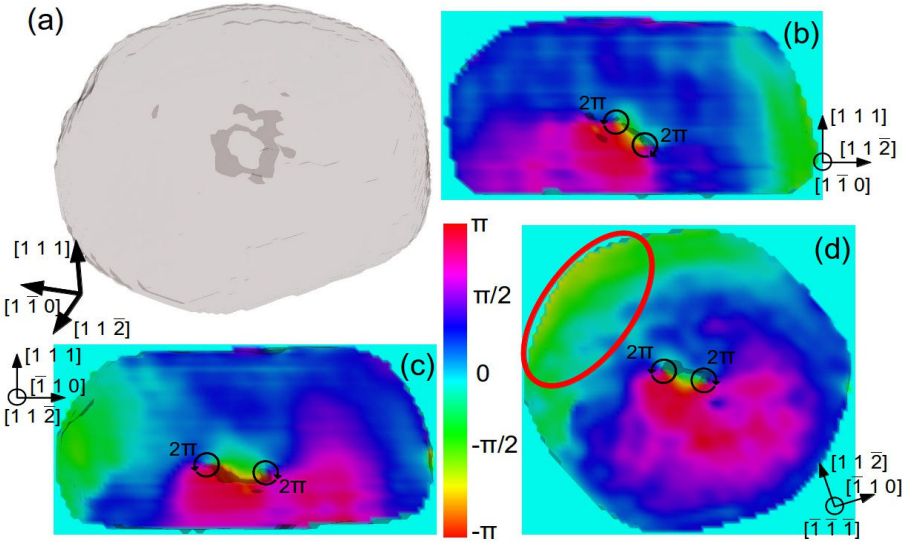

Fig. 9 *Reconstruction du champ de déplacement autour d'une boucle de dislocation prismatique après quatre itérations dans le cycle de charge-décharge.* (a) Densité électronique diffractante représentée à 15% du maximum de densité. Les chutes de densité électronique indiquent la position des boucles. Champ de déplacement $u_{1\,1\,1}$ reconstruit dans les plans (1 $\bar{1}$ 0) (b), (1 1 $\bar{2}$) (c) et (1 1 1) (d) interceptés par la boucle de dislocation en 2 points. La densité électronique diffractante est également représentée en transparence pour permettre une localisation précise de la boucle.

La présence d'une unique boucle dans la structure peut s'expliquer par le fait que les boucles régulièrement émises au cours de l'indentation depuis la région situé sous la pointe sont annihilées sur les surfaces libres de la cristallite. Par ailleurs le retrait de la pointe avant l'acquisition de la figure de diffraction 3D entraîne des évolutions supplémentaires dans la microstructure. La stabilisation d'une boucle dans la particule est donc un événement plutôt rare. Dans notre cas la présence d'une boucle prismatique n'est avérée qu'à une seule itération du cycle charge-décharge. En résumé, la germination d'une boucle de dislocation prismatique est avérée par la reconstruction de la densité électronique et du champ de déplacement $u_{1\,1\,1}$. Son diamètre de 50 nm équivaut à un rayon de contact de 3nm, valeur correspondant à l'initiation de la déformation plastique.

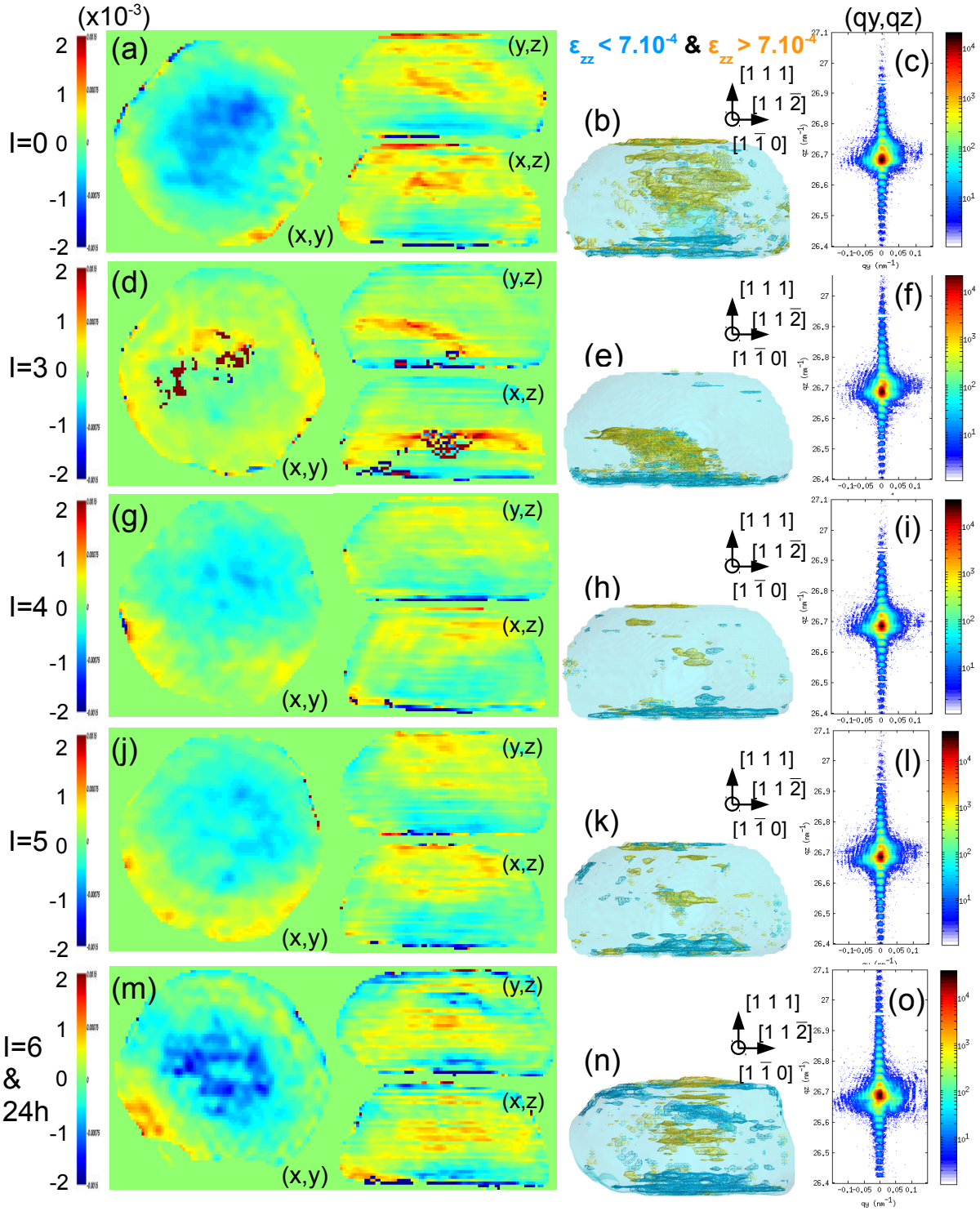

Fig. 10: *Reconstruction du champ de déformation ε_{zz} pour des itérations successives du cycle de charge-décharge* (a) Reconstruction du champ de déformation ε_{zz} dans les plans (x,y), (x,z) and (y,z) correspondant respectivement aux plans (1 1 1), (1 1 $\bar{2}$) et (1 $\bar{1}$ 0). (d), (g), (j) et (m) champ de déformation dans ces mêmes plans après 3, 4, 5 et 6 itérations (24 h vieillissement) dans le cycle de charge-décharge. Isosurface des déformations représentées pour $\varepsilon_{zz} < 7.10^{-4}$ (bleu) et $\varepsilon_{zz} > 7.10^{-4}$ (orange) dans l'état initial (b), après 3 itérations (e), après 4 itérations (h), après 5 itérations (k) et après 6 itérations et 24 h vieillissement (n). Figures de diffraction correspondantes dans les plans (qy,qz) dans l'état initial (c), après 3 itérations (f) après 4 itérations (l) et après 6 itérations et 24 heures de vieillissement (o)

Évolution des champs de déformation et de déplacement au cours du cycle d'indentation

La reconstruction du champ de déplacement $u_{1\,1\,1}$ pour chaque itération du cycle de charge-décharge permet d'évaluer l'évolution de la déformation résiduelle dans la cristallite. Nous espérons ainsi confirmer le phénomène de recuit mécanique, dont l'occurrence est suggérée par l'analyse des figures de diffraction. Pour avoir une idée plus claire de l'évolution de la déformation résiduelle, la composant ε_{zz} du tenseur de déformation est dérivé à partir du champ de déplacement. ε_{zz} est représenté à chaque étape du cycle dans les plans $(1\ \bar{1}\ 0)$ (coupe y-z), $(1\ \bar{1}\ 2)$ (coupe x-z) et (1 1 1) (coupe x-y). La distribution volumique de ε_{zz} est également représentée sur les figures (Fig. 10.b, 10.e …, 10.n) . Seules les régions soumises à une large compression ($\varepsilon_{zz} < -7.10^{-4}$) ou tension ($\varepsilon_{zz} > 7.10^{-4}$) sont représentées, respectivement par des isosurfaces bleues et oranges.
En résumé, trois différentes distributions de la déformation résiduelle sont observés au cours des itérations de charge, et une importante évolution à la fois de la forme mais aussi de la distribution de la déformation résiduelle est observée après 24h de vieillissement.
État initial de la déformation résiduelle:
La plus grande valeur de déformation résiduelle est observée lors de l'état initial. L'interface substrat/cristallite correspond à une région de compression quand le centre de la particule correspond à une zone de tension.
Présence de boucles dislocations prismatiques:
Après 3 itérations de charge, la déformation compressive à l'interface cristallite/substrat est affectée de manière marginale. En revanche, dans la région centrale la déformation résiduelle a quasiment complètement disparu et est désormais localisé au voisinage de la boucle de dislocation.
Recuit mécanique
Pour I=4 et I=5, la déformation compressive à l'interface cristallite/substrat est toujours présente bien que légèrement réduite en comparaison de l'état initial. En revanche la région de déformation en tension a presque complètement disparue: c'est le phénomène de recuit mécanique associé à la germination de boucles prismatiques.
24 h de vieillissement:
Une profonde modification de la distribution de la déformation résiduelle, associée à l'évolution de la forme de la particule est observée après 24h de vieillissement à température ambiante. En particulier, au centre de la cristallite, des régions successives de déformation en tension et en compression sont observées.

En conclusion de ce chapitre, nous avons appliqué les méthodes décrites dans les chapitres III à V pour étudier l'évolution de la microstructure d'une cristallite d'or au cours d'une expérience d'indentation *in situ*. La germination d'une boucle de dislocation prismatique a été mise en évidence, ce qui constitue à notre connaissance, la première identification d'une boucle de dislocation prismatique par CDI. La relaxation de la contrainte résiduelle par recuit mécanique a également été clairement démontrée.

Chapitre VII: Étude de la distribution tri-dimensionnelle de la déformation dans une particule d'or maclée de taille submicronique par diffraction des rayons X cohérents et simulations de statique moléculaire

Ce chapitre est consacré à l'étude du champ de déformation d'une particule d'or submicronique présentant un joint de macle, par l'utilisation combinée de la diffraction des rayons X cohérents et de simulations atomistiques. Comme illustré dans les chapitres précédents, la CDI peut-être utilisée pour imager le champ de déplacement 3D autour d'un défaut unique ou d'un réseau de dislocations. Cependant, la technique étant sensible aux déviations par rapport au cristal parfait, elle n'est pas uniquement sensible à la présence de défauts cristallins, mais également à toutes les sources de déformation résiduelle dans la particule: la déformation interfaciale pour les particules en épitaxie, la déformation thermoélastique induite par le traitement thermique de

la particule mais également la déformation produite par la relaxation des surfaces libres. Dans ce chapitre, la technique est utilisée pour étudier la distribution du champ de déplacement 3D dans la particule maclée qui dépend de toutes ces contributions.
Le procédé d'élaboration de la particule d'or et les détails expérimentaux sont présentés dans les deux premières parties de ce chapitre. Dans la dernière partie, des simulations de dynamique moléculaire sont utilisées pour analyser et comprendre la distribution 3D de la déformation résiduelle dans la particule. Les effets de taille et l'influence des conditions aux limites sur cette distribution sont notamment discutés.

Détails expérimentaux

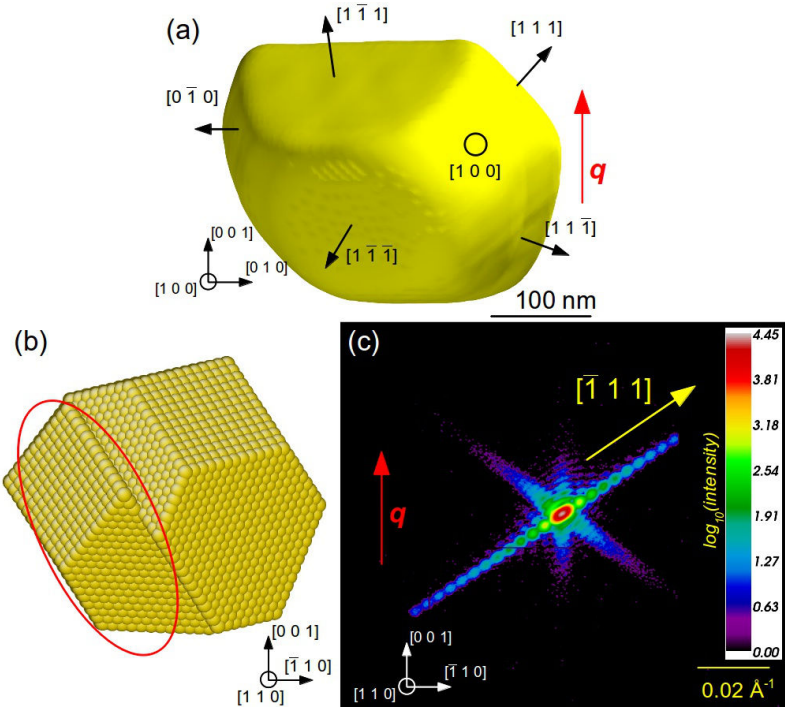

Fig. 11 *Particule d'or maclée mesurée expérimentalement (*a) Isosurface de la densité électronique diffractante reconstruite représentée à 50% du maximum de densité (b) Modélisation de la particule maclée. La région entourée en rouge correspond à celle mesurée expérimentalement (c) Coupe (1 1 0) de la figure de diffraction cohérente utilisée pour la reconstruction

Les cristallites d'or sont mis en forme par la technique de démouillage en phase liquide sur un substrat de saphir (0 0 0 1) (axe-c). Le démouillage du film mince d'or polycristallin est réalisé par chauffage du film mince d'or pendant 10h à 1100°C. Ce procédé d'élaboration permet l'obtention de particules très facettées de diamètre compris entre 200 et 800 nm et séparées par une distance typique de 2 µm. Elles adoptent la forme d'équilibre de Winterbottom (Winterbottom 1967) qui se caractérise par la présence de facettes {1 0 0} et {1 1 1} séparées par des régions rugueuses et arrondies (Heyraud & Métois 1982, Sadan & Kaplan 2006).
La mesure des cristallites d'or est réalisée sur la ligne I13-1 de la Diamond light source. Une faisceau de rayons-X cohérents d'énergie 9.7 keV est focalisé sur l'échantillon grâce à des miroirs Kirkpatrick-Baez (KB) permettant d'obtenir une taille de faisceau d'approximativement 8 x 6 µm^2 sur l'échantillon. En dépit de la large taille du faisceau, il est possible d'isoler une cristallite d'orientation hors plan (0 0 1) dont l'occurrence est moins fréquente que l'orientation (1 1 1). La réflexion 0 0 2 de Bragg de cette cristallite est mesurée en géométrie spéculaire. L'acquisition d'une cartographie 3D de la réflexion de Bragg est effectué par une mesure en

bercement (rocking curve) sur +/- 0.5° par pas de 0.005°.
La Fig. 11 montre une coupe perpendiculaire à l'axe (1 1 0) de la figure de CXD. La direction du vecteur $\boldsymbol{g}$ = 0 0 2 est indiquée par une flèche rouge. Des franges d'interférences sont observées dans les directions normales aux facettes de la cristallite. D'autre part, une asymétrie est observée le long de la direction [0 0 1], où les franges au dessus de la positon de Bragg sont plus intenses que celles en dessous. Une figure de diffraction mesuré sur un cristal parfait (pas de déformation) apparaîtrait parfaitement centrosymétrique (Robinson *et al.* 2001). Huang *et al.*(2008) ont mis en évidence qu'une telle distribution de l'intensité diffractée est associée à des phénomènes de contraction de surface, la direction de l'asymétrie étant le long de la facette subissant la contraction maximale.).
A partir des données de diffraction, la densité électronique diffractante et le champ de déplacement $u_{0\,0\,2}$ sont tous deux reconstruit, en utilisant les algorithmes classiques de restitution de phase: Error reduction (Gerchberg et Saxon 1972), Hybrid Input Output (Fienup 1982) et Shrink-Wrap (Marchesini 2003).
La Fig. 11.a montre la densité électronique diffractante. La région maclée ne satisfait pas les conditions de Bragg et est donc absente de la reconstruction. Le modèle atomistique présenté sur la Fig. 11.b illustre la proportion relative (estimée) entre les deux grains. En bon accord avec les observations en microscopie électronique à balayage, la particule obtenue est fortement facettée avec des régions rugueuses de petite taille entre les facettes {1 0 0} et {1 1 1}. La reconstruction du champ de déplacement $u_{0\,0\,2}$ révèle une distribution assez complexe vraisemblablement influencée par plusieurs sources de déformation.

Simulations de statique moléculaire

Afin d'analyser et de comprendre la distribution de la déformation résiduelle dans la particule, la cristallite maclée est modélisée grâce au code de simulation atomistique MERLIN (Rodney 2010). Un potentiel EAM (Embedded Atom Method, Grochola *et al.* 2005) est utilisé pour décrire les forces entre les atomes. Ce dernier reproduit avec précision les énergies de surface et les propriétés élastiques de la cristallite. Les particules sont modifiés selon la forme d'équilibre de Wulff, et les aires des différents plans cristallographiques sont ensuite ajustées afin de reproduire le plus fidèlement possible la forme de la particule expérimentale. Évidemment la taille de la particule expérimentale (360x270x270 nm^3) n'est pas atteignable par des simulations atomistiques, aussi l'effet de la taille sur la distribution de la déformation résiduelle est analysé par la modélisation de cristallites de taille comprises entre 25 et 170 nm (respectivement 15 fois et 2 fois plus petites que la cristallite expérimentale). Les cristallites sont relaxées dans leur forme d'équilibre de Wulff par minimisation d'énergie à 0K. La cristallite relaxée est ensuite coupée selon le plan de macle ($\bar{1}$ 1 1) pour reproduire la forme observée expérimentalement. L'analyse de la distribution de la déformation résiduelle est conduite à la fois dans l'espace réciproque (calcul des figures de diffraction associées aux cristallites relaxées avec la librairie PyNx : Favre-Nicolin *et al.* 2010) et dans l'espace réel (reconstruction du champ de déplacement u_{002} à partir des données de diffraction simulées).
Ces deux approches permettent d'établir que la distribution de la déformation résiduelle n'est que faiblement affectée par la taille de l'objet et dépend d'avantage de sa géométrie, même si de manière attendue, les effets de relaxation de surface sont plus prononcés pour les particules de petite taille. La modélisation de cristallites de taille modeste apparaît donc comme une approche valide pour analyser la distribution expérimentale du champ de déplacement 3D. Cependant l'accord avec les données expérimentales est loin d'être satisfaisant et suggère la présence d'une autre source de déformation probablement liée au procédé d'élaboration de la particule. La présence d'une déformation thermoélastique associée au refroidissement au refroidissement de la particule à température ambiante est suspectée.

Pour déterminer l'influence du substrat et du joint de macle sur la distribution de la déformation résiduelle, des cristaux de 50 nm présentant des conditions aux limites variables sont modélisés et relaxés à 0K. Plusieurs cas sont considérés: (b) particule non relaxée (cas du cristal parfait) de géométrie similaire à la particule expérimentale, (c) particule relaxée dans sa forme d'équilibre de Wulff puis coupée selon le plan de macle, (d)

particule maclée relaxée (e) particule coupée selon le plan de macle puis relaxée → le plan de macle est donc une surface libre. (f) particule mise en contact avec un substrat dont le paramètre de maille est ajusté pour simuler une quantité définie de déformation interfaciale.

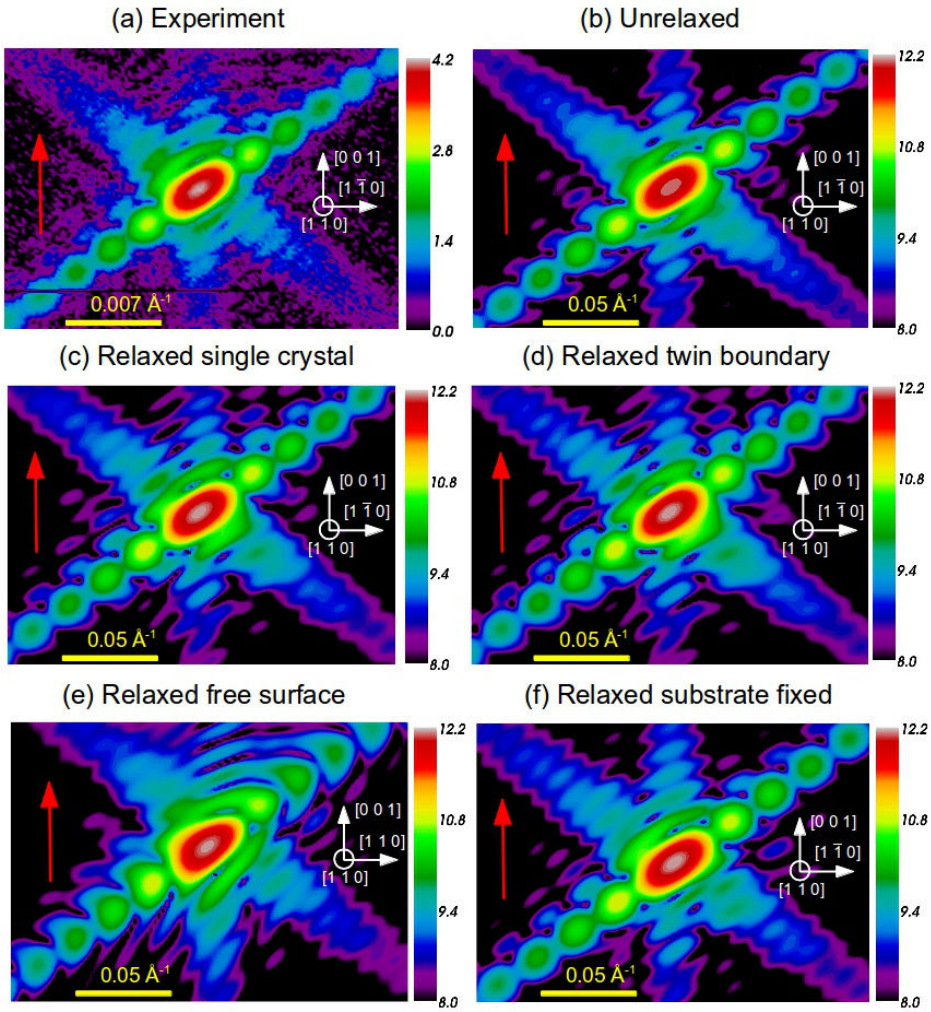

Fig. 12 : *Influence des conditions aux limites sur les figures de diffraction cohérentes pour* ***g*** *= 0 0 2.* Cristallite expérimentale (a) et cristallites modélisées (b-e). (b) Forme d'équilibre de Wulff, avant relaxation des surfaces libres. (c) Forme d'équilibre de Wulff, relaxation des surfaces libres, pas de déformation interfaciale (d) Particule maclée, relaxation des surfaces libres, pas de déformation interfaciale. (e) Particule maclée, joint de macle considéré comme une surface libre, pas de déformation interfaciale. (f) Forme d'équilibre de Wulff, relaxation des surfaces libres et prise en compte de la déformation interfaciale.

Les figures de diffraction sont calculées pour ces différentes configurations au voisinage de la réflexion de Bragg 0 0 2. Plusieurs enseignements peuvent être déduits de l'étude de ces figures de diffraction:

- la cristallite de Wulff tronquée (c) et la cristallite maclée (d) produisent des figures de diffraction très similaires. Cela suggère qu'aucune déformation résiduelle n'est générée au voisinage du joint de macle, un résultat finalement peu surprenant puisqu'un joint de macle est une interface cohérente.
- Si le joint de macle est considéré comme une surface libre (f), la forme du pic de Bragg est

profondément affectée. La surface libre subit en effet une forte contraction qui affecte fortement la distribution de la déformation résiduelle. Il est donc clair que la cristallite mesurée expérimentalement est une particule maclée et non un monocristal coupée le long de son plan ($\bar{1}$ 1 1).

– le meilleur accord avec la figure de diffraction expérimentale est obtenu (et de loin) quand la particule est contrainte par un substrat.

La reconstruction du champ de déplacement permet d'établir des conclusions similaires à l'analyse des figures de l'espace réciproque. Un bon accord avec les résultats expérimentaux est obtenu quand l'influence de la déformation interfaciale est prise en compte dans les configurations atomistiques (Fig. 13)

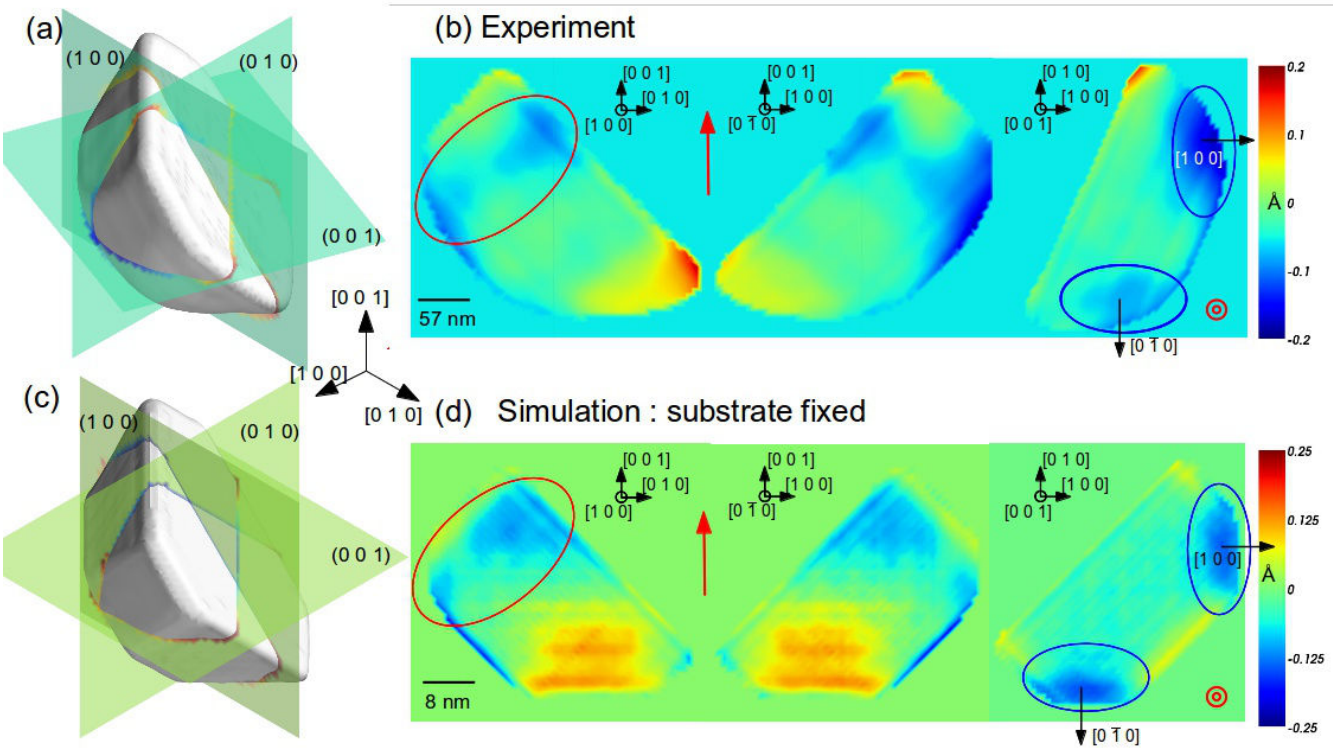

Fig. 13 *Comparaison entre la reconstruction des données expérimentales et simulées.* Reconstruction de la densité électronique diffractante (isosurface 50% de la densité maximale) pour la particule expérimentale (a) et simulée (c) indiquant la position des coupes pour lesquelles le champ de déplacement est reconstruit. Coupes (100), (010) et (001) du champ de déplacement pour la particule expérimentale (b) et simulée (d)

Cette exemple de reconstruction expérimentale d'une particule d'or maclée démontrent que la diffraction cohérentes est sensible aux différentes sources de déformation résiduelle dans la cristallite: la déformation interfaciale , la déformation thermoélastique induite par le traitement thermique de la particule mais également la déformation produite par la relaxation des surfaces libres. L'utilisation de simulations de dynamique moléculaire permet de quantifier l'influence de ces contributions et d'obtenir une distribution de la déformation résiduelle en bon accord avec les résultats expérimentaux.

Chapitre VIII : Étude d'une interface bi-métallique hétérogène (Cu-Ta) par diffraction de surface, calculs *ab-initio* et dynamique moléculaire

Dans ce chapitre, l'interface hetero-épitaxiale formée par un film mince de cuivre déposé sur un substrat de Tantale est étudiée par diffraction de surface et calculs *ab initio*. Ces deux outils permettent de déterminer la structure atomique de la couche de mouillage sur la surface (0 0 1) du Tantale.
L'évolution du signal de diffraction de surface (SXRD) est mesuré *in situ* pendant le dépôt et la démouillage de la couche de Cu. Ces mesures permettent d'identifier sans ambiguïté la présence de deux couches de Cu pseudomorphes (PM) sur la surface de Tantale. La distance inter planaire entre les plans de Cu et les plans de Ta de surface est également déterminée avec précision. Des calculs de théorie de la fonctionnelle de la densité (DFT) dans l'approximation locale sont ensuite utilisés pour calculer l'énergie d'interface d'excès d'un ensemble de configurations atomistiques, présentant un nombre variable de couches PM ainsi que des structures atomiques différentes. Ces deux approches conduisent à des résultats remarquablement similaires.

Expérience de diffraction de surface (SXRD)

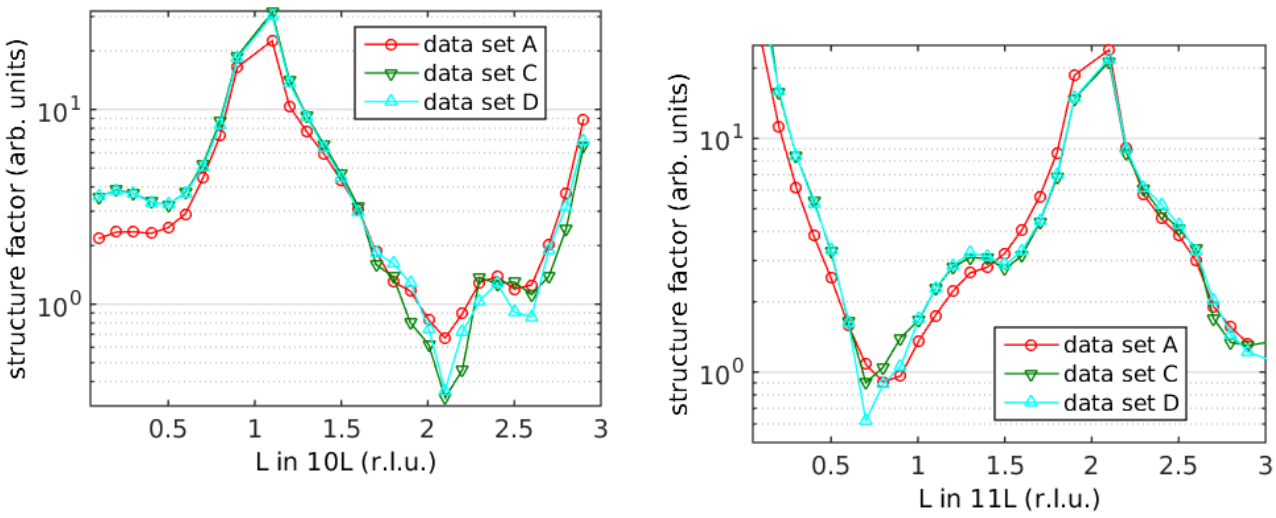

Fig. 14 *Comparaison entre le CTR 1 0 L (a) et le CTR 1 1 L (b) pour les deux campagnes expérimentales, réalisées avec des niveaux différents de contamination.* Les barres d'erreur ne sont pas visibles pour faciliter la visualisation.

La diffraction de surface est un outil puissant pour sonder la structure de surfaces cristallines (Robinson & Tweet 1992). Des interfaces avec une terminaison nette donnent naissance à des tiges de troncature du cristal (CTR) dans l'espace réciproque (Andrews & Cowley, 1985). Ces CTR s'avèrent particulièrement efficace pour l'étude de couche de mouillage pseudomorphes (Ball *et al.* 2002). En effet, l'amplitude diffractée par les couches pseudomorphes est renforcée par phénomène d'interférence avec l'amplitude diffractée par le substrat, au voisinage des réflexions dans le plan de ce dernier. Ces interférences permettent une détermination quantitative du nombre de couches pseudomorphes et leur distance inter planaire.
L'expérience a été réalisée sur la ligne BM32 de l'ESRF. Cette dernière contient une chambre à ultra vide (UHV) équipée pour la préparation d'échantillon et montée sur un diffractomètre. Le dépôt du cuivre et le démouillage peuvent donc être réalisés *in situ,* en revanche la préparation de la surface (0 0 1) du Ta requièrent des température de recuit à des températures supérieures à 2000 K qui ne peuvent être atteinte dans la chambre. La préparation de la surface de Ta (0 0 1) est donc réalisée *ex situ.*
Une couche de protection de cuivre de 5 nm est déposée pour couvrir la surface de Ta pendant le transfert sur la chambre de la ligne, principalement réalisé sous vide primaire avec une très courte exposition à l'air. Cette couche est ensuite retirée par évaporation à 1300 K, permettant d'obtenir une surface de Ta très faiblement contaminée.
Quatre jeux de données (A, B, C et D par la suite) ont été collecté au cours de deux sessions expérimentales. Les

conditions de préparation de la surface de Ta, de déposition et de démouillage de Cu diffèrent pour ces quatre jeux de données, cependant ils conduisent tous à l'obtention d'une surface de Ta propre dans l'état initiale.
La contamination de l'interface intervient principalement lors de la mesure des CTR. L'ordre de mesure des CTR variant selon la session expérimentale, des mesures ont donc été réalisées avec des niveaux de contamination de surface variables. Par exemple, le CTR *1 1 L* a été mesuré sur une surface ne présentant aucune contamination au carbone et une contamination d'oxygène très limitée pour les jeux de données C et D, tandis que la contamination de surface (oxygène et carbone) est prononcée dans le cas du data set A. Les différences observées entre le jeu de données A d'une part et les jeux de données C et D d'autre part (Fig. 14) sont donc vraisemblablement liés à cette contamination de surface. Des constatations similaires peuvent être effectuées dans le cas du CTR *1 0 L*.

Calculs DFT

A partir des mesures des CTR, la détermination précise de la structure de l'interface est en principe obtenu par un fit des données expérimentales. Dans ces travaux de thèse, nous utilisons des calculs DFT afin d'établir si cette méthode permet d'obtenir une description de l'interface en bon accord avec les résultats expérimentaux.
Afin de déterminer la structure et la stabilité d'un film mince de Cu sur la surface de Ta(0 0 1) plusieurs systèmes d'interfaces contenant un nombre variables de couches PM (1 à 6) sont modélisées. L'influence de la structure cristalline sur la stabilité du film mince est également évaluée à travers deux configurations supplémentaires contenant une couche f.c.c. de Cu, déposée sur la surface de Ta dans un cas, et sur deux couches PM. La stabilité thermodynamique des films minces de Cu est déterminée par calcul de l'énergie d'excès d'interface représentant la différence entre une configuration complètement relaxée et une configuration avec le même nombre d'atomes dans l'environnement du matériau massif. L'énergie d'excès d'interface est la somme de l'énergie de l'interface film/substrat γ_i, et de l'énergie de surface libre du film mince γ_f *i.e.* $\gamma = \gamma_{i+} \gamma_f$. La contribution de l'énergie de déformation élastique est également implicitement contenue dans cette équation, sa contribution augmentant avec le nombre de couches de Cu et devenant rapidement prédominante à partir d'un faible nombre de couches de Cu. La stabilité et le mode de croissance d'un film mince sur un substrat peut-être évaluée à partir de la différence d'énergie entre une configuration contenant uniquement des surfaces libres et une configuration contenant des interfaces. Cela se traduit en équation par (Freund & Suresh 2003, Wuttig & Liu 2004) :

$$\delta = \gamma_i + \gamma_f - \gamma_s \quad (1)$$

où γ_s est l'énergie de surface libre du substrat. Le mode de croissance du substrat dépend du signe de δ. Pour $\delta <$ 0 l'interface film/substrat est thermodynamiquement stable et la croissance s'effectue couche par couche (mode de croissance Frank-van-der-Merwe: Frank & Van der Merwe 1949, Van der Merwe 1963). A partir de $\delta = 0$, une croissance de type Stranski-Krastanov correspondant à une croissance 3D sur le film mince.
Les énergies d'interface calculées pour 1 à 6 PM sont modélisés dans le tableau 1.

	0 PM (dewetting)	1 PM	2 PM	3 PM	4 PM	5 PM	6 PM
γ (J/m^2)		2.50	2.19	2.63	2.78	3.13	3.32

Tab. 1: Comparaison des énergies d'excès d'interfaces calculées pour 1 à 6 couches PM sur la surface de Ta (0 0 1)

Notre énergie de surface libre calculée est égale à γ_s is 3.18 J/m^2 une valeur supérieure aux estimations expérimentales de 2.5 J/m^2 (Tyson & Miller 1977), mais proche d'autres valeurs théoriques de 3.10 J/m^2 (Vitos *et*

al. 1998) et de 3.14 J/m^2, (Aqra & Ayyad 2011). L'énergie de surface libre du Ta(0 0 1) est supérieure à l'énergie d'excès d'interface ($\delta < 0$) pour jusqu'à 5 couches PM. La configuration contenant deux couches PM est donc la plus stable alors que 1, 3, 4 et 5 couches de Cu PM sont métastables. Un mode de croissance de type Frank-van-der-Merwe est ainsi attendu jusqu'à 5 couches PM avant de basculer dans un mode Stranski-Krastanov. Ces résultats sont en bon accord avec des données expérimentales reportant la présence d'une à deux couches de mouillage (Venugopal *et al.* 2009).
Les configurations contenant des couches de Cu f.c.c. n'ont en revanche pas convergé vers des structures «acceptables» avec une forte tendance à former des couches PM. Il a donc été impossible de déterminer l'énergie d'excès d'interface pour ces configurations.

Comparaison entre les calculs DFT et les données de diffraction de surface

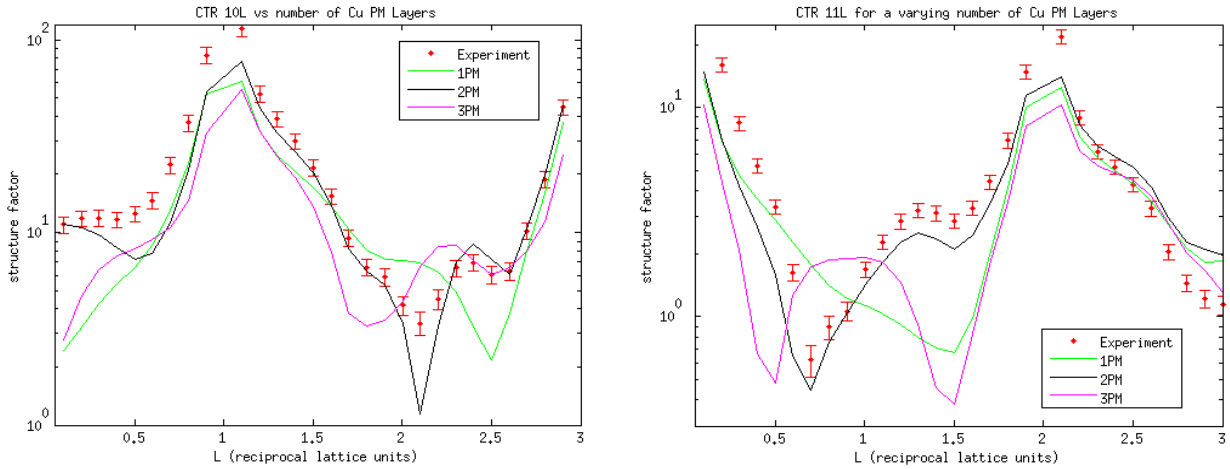

Fig. 15 *Comparaison des facteurs de structure calculés 1 0 L (a) et 1 1 L(b) avec les données expérimentales pour un nombre variable de couches pseudomorphes.*

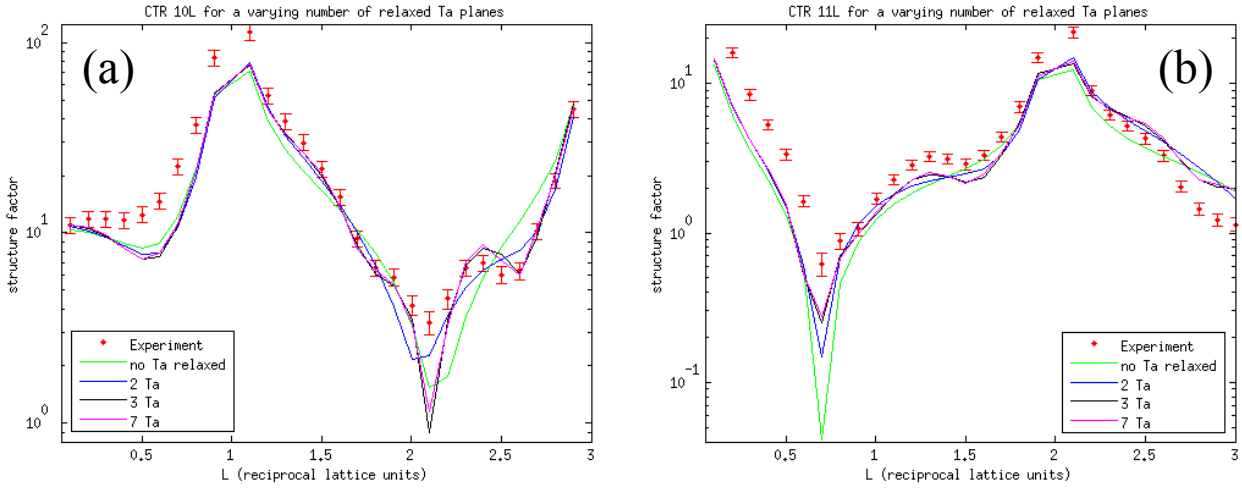

Fig. 16 *Influence du nombre de plans de Ta relaxés sur les facteurs de structure 10L (a) et 11L(b) calculés.*

La comparaison entre les calculs DFT et les calculs de diffraction de surface peut-être vérifié par le

calcul des facteurs de structure pour les configurations relaxées. Ces calculs sont effectuées grâce au logiciel ROD (Vlieg 2000). La figure 15 présente plusieurs comparaisons entre des CTR mesurés sur des surfaces de Ta propres, et les CTR calculés pour 1,2 et 3 couches PM. Pour les CTR *1 1 L* et *1 0 L,* le meilleur accord est trouvé pour 2 couches PM. Cet accord est renforcé quand la surface de Ta(0 0 1) est vierge de contamination, confirmant l'importance des effets de contamination discutés dans la section précédente.
Afin de quantifier l'importance de la prise en compte des effets de relaxation de surface du Ta, les facteurs de structure sont calculés pour quatre configurations avec un nombre variable de plans de Ta pris en compte pour la relaxation. Comme illustré sur la figure 16 pour les deux CTR, un bon accord avec les résultats expérimentaux est uniquement obtenu à partir de 3 plans de Ta relaxés. Ces calculs confirment donc l'importance de la prise en compte des effets de relaxation de surface du Ta pour une description précise de l'interface Cu-Ta.

Cette étude de l'interface Cu/Ta (0 0 1) combinant mesures de SXRD et calculs DFT démontre donc la présence de deux couches pseudomorphes de cuivre après démouillage du cuivre. Les deux approches conduisent à des résultats remarquablement similaires, en particulier pour une faible contamination de surface. Les deux couches de cuivre ont une structure b.c.c. avec une distance inter planaire $d_{1\text{-}2}$ = 1.035 Å qui permet de maintenir une distance avec le plus proche voisin équivalente à celle de la structure f.c.c. du matériau massif. Cette configuration minimise l'énergie élastique des liaisons Cu-Cu et est uniquement possible en l'absence d'une troisième couche de cuivre.

Chapitre IX: Interface des cristallites de cuivre démouillés en phase solide sur une surface de Ta(0 0 1) étudiée par diffraction des rayons X cohérents et simulations de dynamique moléculaire.

Dans le chapitre VIII nous avons étudié la structure atomique de la couche de mouillage de Cu sur la surface (0 0 1) du Tantale. Les calculs DFT ont permis de prédire une interface en très bon accord avec les résultats expérimentaux. Du fait du très grand nombre d'atomes nécessaires pour modéliser l'interface Cu-Ta dans les cristallites de cuivre, il est malheureusement impossible de déterminer la structure de cette interface dans les cristallites par des calculs *ab-initio.* Pour des systèmes de cette taille, le recours a des simulations de dynamique moléculaire utilisant des potentiels interatomiques constitue un outil puissant pour la prédiction de cette interface.
Ce chapitre débite par la description de la préparation de l'échantillon, nous permettant de détailler la géométrie de la cristallite de cuivre et son influence sur l'importante déformation interfaciale induite par le procédé de démouillage en phase solide. La seconde partie de ce chapitre est consacrée à des simulations de dynamique moléculaire que nous allons détailler par la suite. Dans un premier temps, l'orientation et la forme d'équilibre des cristallites est discuté et comparé avec les observations expérimentales. Les interfaces obtenues avec les conditions expérimentales simulées sont ensuite présentées et comparées avec des images de l'interface obtenues par microscopie électronique en transmission à haute résolution. Pour finir, l'influence de la structure atomique de l'interface sur la distribution du champ de déplacement dans la particule est discutée dans la dernière section de ce chapitre.

Simulations de dynamique moléculaire de l'interface CuTa

Le potentiel utilisé pour les simulations de MD est un potentiel à dépendance d'angle (angular dependant potential : ADP) développé par Hashibon, Lozovoi *et al.* (2008). Dans le chapitre VIII il est démontré qu'en dépit de certaines limitations, ce potentiel parvient à prédire le nombre correct de couches PM à l'interface Cu-Ta. Dans un premier temps, nous vérifions si le potentiel parvient à reproduire l'orientation et la forme des particules observées expérimentalement. Plusieurs simulations de démouillage en phase solide conduisent, -

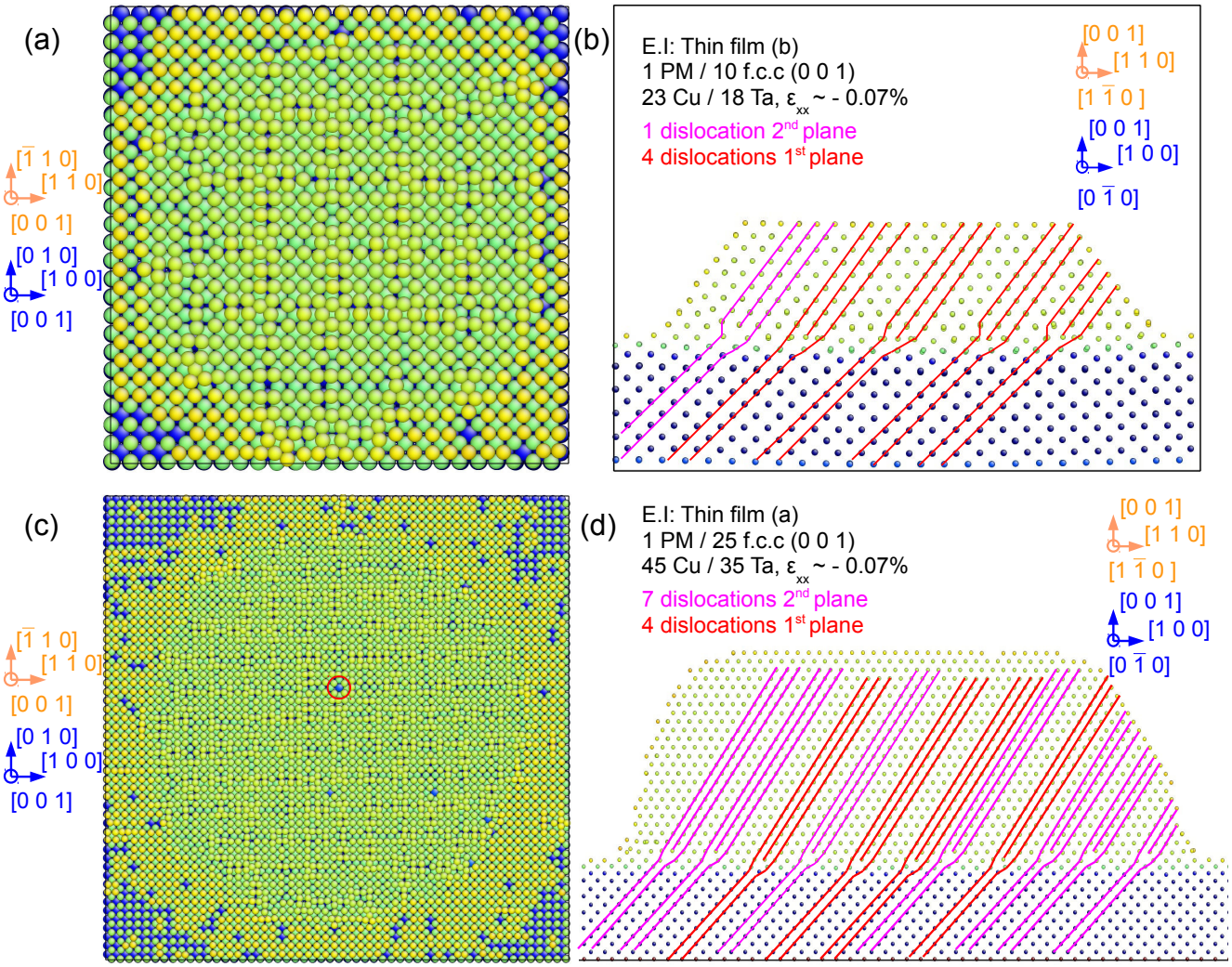

Fig. 17: *Effet de taille sur l'interface Cu-Ta.* (a) Structure atomique de la 2ème couche de cuivre dans une particule de petite taille. (b) Vue en coupe de l'interface Cu-Ta, les dislocations initiés sur la première couche de cuivre sont prédominantes. (b) Structure atomique de la 2ème couche de cuivre dans une particule de plus grande taille. (d) Vue en coupe de l'interface Cu-Ta, les dislocations initiés sur la deuxième couche de cuivre sont prédominantes.

- indépendamment des conditions initiales (film mince, forme d'équilibre de Wulff tronquée, nombre variable de couches PM), et de manière reproductible, à une orientation similaire à celle établie expérimentalement, à savoir Cu (0 0 1)[1 1 0] // Ta (0 0 1)[1 0 0] (Beutier *et al.* 2013a). Dans l'état final, une forme d'équilibre de Winterbottom (Winterbottom 1967) est systématiquement obtenue. Cette forme d'équilibre étant obtenue par une minimisation de l'énergie de surface par optimisation des surfaces des différents cristallographiques, il est clair que le potentiel parvient donc à prédire des énergies de surface en bon accord avec les observations expérimentales.

Le nombre de couches de mouillage pseudomorphes est également indépendant des conditions initiales et toujours égal à 2. La structure atomique de l'interface dépend en revanche en partie des conditions initiales de la simulation. L'évolution de cette interface quand la cristallite est soumise à des temps de recuit prolongés est illustrée à travers deux exemples présentés sur la figure 17. Une cristallite de petite taille issue du démouillage en phase solide d'un film mince f.c.c. de Cu, et une particule de plus grande taille, également issue du démouillage d'un film mince f.c.c. Dans le cas de la particule de petite taille, le film mince repose sur la surface libre du

Tantale dans les conditions initiales, alors que pour la particule de grande taille, une couche de mouillage PM de Cu est insérée entre le substrat de Tantale et le film mince de Cu. La figure 17 présente la structure atomique après des temps de recuit respectifs de 23 et 15 ns pour la petite et la grande cristallite. Comme illustré sur la Fig. 17.a, la structure atomique de la 2ème couche est assez fortement ordonnée. La structure peut-être décrite comme intermédiaire entre b.c.c. et f.c.c., mais cette dernière domine clairement la tendance. La plupart des dislocations d'interface débutent sur la première couche de Cu (en rouge sur la Fig. 17.b). Pour la particule de plus grande taille, la structure de la 2ème couche de Cu est encore une fois intermédiaire entre b.c.c. et f.c.c, mais c'est cette fois ci la structure b.c.c. qui prédomine. Associé à cette prédominance, la majorité des dislocations d'interface débutent à partir de la deuxième couche de Cu (en violet sur la Fig. 17.d).

En résumé, les configurations atomistiques recuites en dessous de la température de fusion du cuivre conduisent à une interface Cu-Ta très reproductibles. Pour accommoder la grande différence de paramètre de maille, un réseau de dislocations orthogonales est toujours obtenu. L'intervalle entre ces dislocations est régulier (une dislocation tous les 4.5 plans de Cu). D'autre part, ni le nombre de couches PM (0,1 ou 2), ni les conditions aux limites (film mince ou cristallite) dans l'état initial ont une influence marquée sur la forme d'équilibre ou l'interface Cu-Ta obtenue après recuit.

Observation de l'interface par microscopie électronique en transmission à haute résolution

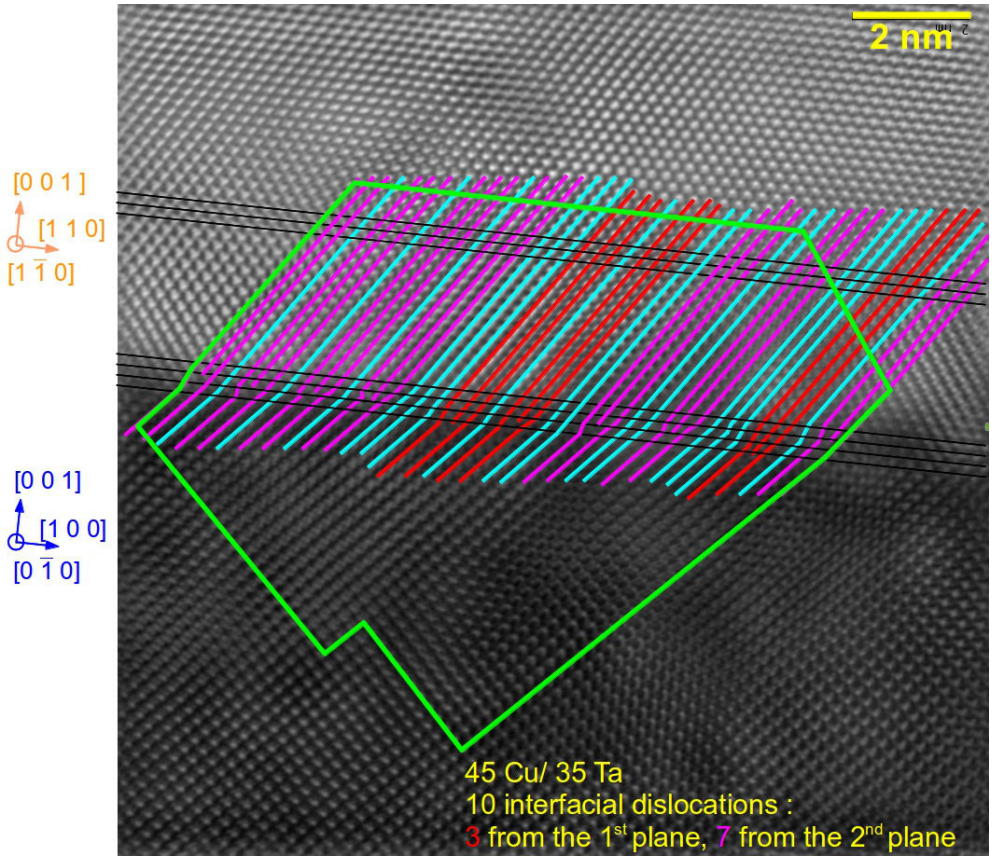

Fig. 18: *Micrographie en microscopie électronique en transmission à haute résolution (HR-TEM) illustrant la structure atomique de l'interface Cu-Ta.*

En dessous de la température de fusion du cuivre, l'interface obtenue avec le potentiel Cu-Ta est très reproductible, ce qui ne signifie pas pour autant qu'elle est en bon accord avec les résultats expérimentaux.
Pour l'étude d'interfaces avec une résolution atomique, la microscopie électronique en transmission à haute résolution (HR-TEM) est une bonne alternative aux techniques de diffraction des rayons X. La figure 18 illustre la structure atomique détaillée de l'interface vue depuis la direction [0 $\bar{1}$ 0] du substrat (direction [1 $\bar{1}$ 0] de la cristallite). Cette micrographie permet de confirmer que la grande différence de paramètres de maille est accommodée par des dislocations de « misfit ». L'intervalle entre ces dislocations est en très bon accord avec les prédictions du potentiel ADP, avec une distribution des dislocations tous les 4 à 5 plans. En particulier, la région délimitée par le contour vert correspond à 45 plans de Cu sur 35 plans de Ta, correspond très exactement au ratio déterminé avec le potentiel pour minimiser la déformation dans le plan à 0 K.

Des simulations de grande taille utilisant un potentiel Cu-Ta à dépendance angulaire se sont donc avérées être un outil efficace pour prédire la structure atomique de l'interface entre une surface de Ta (0 0 1) b.c.c. et une cristallite de cuivre (0 0 1) f.c.c. Aussi bien la structure de l'interface que la forme d'équilibre de la particule sont très reproductibles en dessous de la température de fusion du cuivre, indépendamment des conditions initiales de la simulation, et sont en très bon accord avec les observations expérimentales.

Chapitre X: Étude de la distribution tri-dimensionnelle de domaines d'inversion de polarité dans des fils de GaN

Ce court chapitre permet d'illustrer la capacité de l'imagerie par diffraction des rayons X cohérents (CDI) à mettre en évidentce des domaines d'inversion de polarité (IDB, Northrup *et al.* 1996) dans des fils de nitrure de Gallium (GaN). Ces domaines d'inversion peuvent être décrits comme des défauts planaires (d'interface) localisés dans des plans (0 1 $\bar{1}$ 0), parallèles à la direction de croissance [0 0 0 1] (axe-c). Localement, l'occupation des sites de Ga et de N est inversée, résultant en une inversion de la polarité du GaN, définie par la liaison Ga-N, de part et d'autre de l'interface.
Si ces IDB peuvent être imagés par microscopie électronique à balayage après attaque chimique du fil, l'imagerie par diffraction des rayons X cohérents (CDI) permet de les caractériser de manière non destructive. (pour des diamètres compris entre 100 nm et 1 μm) et de révéler l'arrangement spatial des IDB. La technique est particulièrement adaptée à l'étude de ces défauts planaires, ces derniers pouvant être décrits comme des interfaces cohérentes, de basse énergie et donc exemptes de déformation interfaciale.
L'absence d'une déformation interfaciale inhomogène pouvant altérer la distribution de la phase permet de mesurer très précisément le saut de phase entre les domaines d'inversion permettant d'accéder au déplacement relatif entre les deux domaines avec une précision de l'ordre du picomètre. Comme démontré par Labat *et al.* (2015), l'utilisation de plusieurs réflexions de Bragg non coplanaires permet d'extraire les déplacements dans les directions longitudinales et transverses du fil de GaN. La polarité absolue des IDB est ainsi déterminée sans ambiguïté. Cette étude se limite néanmoins à 2 dimensions, et les éventuels variations de l'arrangement spatial des IDB le long de l'axe-c n'est pas étudié. La reconstruction 3D du champ de déplacement peut-être utilisée pour analyser cette évolution.

Expérience de CXD

L'expérience est réalisé sur la ligne ID01 de l'ESRF. Les fils de GaN dans cette étude sont élaborés par la technique d'épitaxie en phase vapeur aux organométalliques (MOVPE) sur un substrat de saphir (0 0 0 1) (orienté selon l'axe-c). Les fils obtenus ont un diamètre typique de 600 nm et une hauteur comprise entre 3 et 5 μm. Sur le fil d'intérêt de diamètre 400 nm et de hauteur 5 μm, l'acquisition des données de diffraction cohérentes est effectué au voisinage de la réflexion 0 0 4 de Bragg avec un faisceau cohérent focalisé à une taille de 0,8x0,4 μm^2. Les mesures sont réalisées pour trois positions distinctes le long de l'axe de croissance du fil :

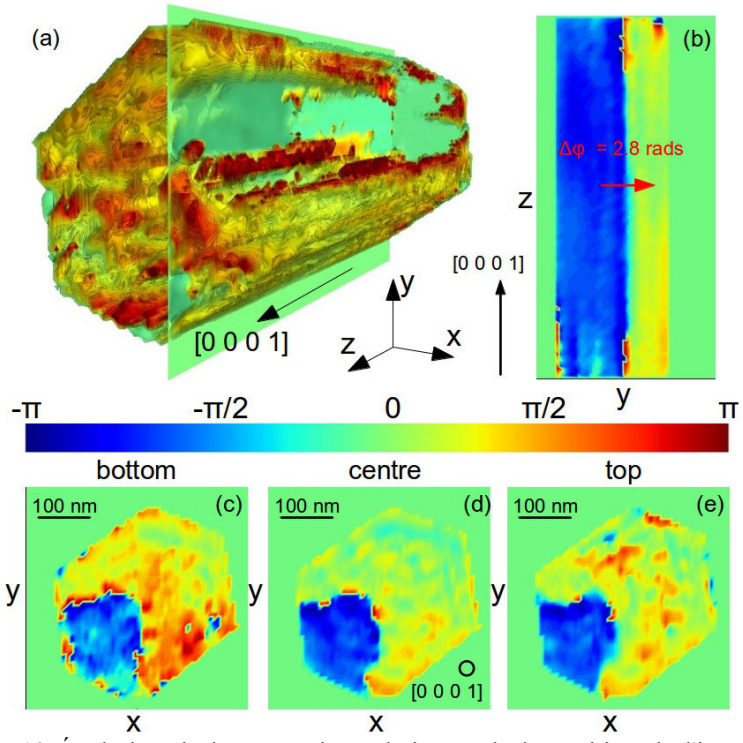

Fig. 19 Évolution de la proportion relative et de la position de l'interface entre deux domaines d'inversion de polarité (IDB) (a) Distribution 3D de la phase révélant la présence de deux IDB (c) Coupe y-z montrant l'absence de variation dans les proportions relatives des deux domaines. (c) Évolution de l'interface pour une hauteur variable.

proche de sa base, au centre et proche du sommet. Ces positions sont séparées d'approximativement 1,5 μm et des figures de diffraction 3D sont collectées pour chacune d'entre par une mesure en bercement (rockin-curve) sur 1.28° par pas de 0.05°.

Dans un premier temps des cartes d'intensité (diffractée) 2D sont extraites des données 3D pour reconstruire une image 2D de l'échantillon aux différentes positions le long de l'axe de croissance du fil (axe-c). Ces dernières correspondent à une projection du volume mesuré sur l'axe-c. Si un saut de phase constant de 2.8 radians est observé pour les trois positions, il apparaît en revanche que la distribution spatiale des IDB évolue légèrement d'une position à l'autre. La structure interne du fil n'est donc pas totalement invariante le long de l'axe-c. Les reconstructions 3D pour les 3 hauteurs permettent donc d'établir si cette invariance est visible à l'échelle du volume illuminé par le faisceau (0,4 μm de hauteur). Les Fig. 19.d-f révèlent cependant que la distribution pour spatiale des IDB est quasiment constante sur la hauteur du volume illuminé, le saut de phase restant constant et égal à 2.8 radians comme déterminé précédemment. Le recours à des reconstructions 3D n'est donc pas véritablement nécessaires pour comprendre la microstructure, et les projections 2D s'avèrent donc suffisantes une analyse fine de la microstructure.

Chapitre XI: Étude de la structure magnétique et de la dynamique d'éléments magnétiques submicroniques par holographie par transformée de Fourier

Ce chapitre est consacré à la présentation de la technique d'holographie de Gabor (Fourier-transform holography: FTH) et ses applications pour l'imagerie de structures magnétiques. En effet, si les précédents

chapitres ont permis de démontrer l'intérêt des techniques de diffraction des rayons-X et en particulier de la diffraction des rayons-X cohérents pour l'étude des propriétés structurelles d'objets submicroniques, ces techniques sont également pertinentes pour l'analyse des propriétés fonctionnelles. Parmi elles on trouve les propriétés magnétiques également sensibles aux effets de taille.

L'Holographie de Gabor (Fourier Transform Holography)

Dans le régime des X mous, l'holographie de Gabor (FTH) a été utilisée pour la première fois par Mc Nulty *et al.* (1992). Sa haute résolution spatiale couplée à son indépendance des aberrations optiques (pas de lentille) sont très propices à l'imagerie de matériaux nanostructurés. En exploitant le dichroïsme circulaire de la diffraction résonante magnétique des X mous (SXRMS), Eisebitt *et al.* (2004) ont démontré l'application de la technique aux matériaux magnétiques. L'holographie magnétique combine donc les avantages de la FTH conventionnelle (résolution spatiale de quelques nanomètres, reconstruction aisée de l'image, sensibilité aux couches enterrées) et du dichroïsme circulaire magnétique des rayons X : XMCD (contraste magnétique et chimique).
Dans une première partie de ce chapitre nous présentons tout d'abord les bases de la FTH et ses applications dans l'imagerie de structures magnétiques. Dans la section suivante, nous détaillons les spécificités des configurations expérimentale utilisée pour réaliser les expériences d'holographie magnétique. Pour imager la magnétisation dans le plan, nous employons une technique d'imagerie holographique basée sur l'utilisation d'une référence étendue : HERALDO (Guizar-Sicairos & Fienup 2007). La pertinence de l'utilisation d'une référence étendue et ses avantages est exposée brièvement dans la 3ème section. La deuxième partie est consacré à la présentation des expériences réalisées au cours de ces travaux de thèse. Dans la première section de cette seconde partie HERALDO est employée pour étudier la structure magnétique dans le plan d'un élément de Py (Fe/Ni). Les sections suivantes sont consacrées à l'étude des dynamiques de magnétisation de ces nanostructures, notamment par l'intermédiaire d'expériences résolues en temps.

Étude de la magnétisation dans le plan de nanostructures magnétiques

Dans ces travaux de thèse, la FTH fût principalement utilisée pour l'étude de la magnétisation dans le plan de films minces de permalloy (Fe/Ni). La préparation des échantillons est décrite en détails par Duckworth *et al.* (2011), et est illustré sur la figure 20. Les dimensions typiques de l'élément de Py sont de l'ordre de 600x600x50 nm^3.
Les mesures sur l'élément de Py ont été réalisées sur plusieurs lignes synchrotron parmi lesquel la ligne I06 de la Diamond light source. Comme illustré sur les Fig. 20.c et 20.d, la magnétisation dans le plan est uniquement accessible par rotation par rapport à la normale de l'échantillon par un angle compris entre 30 et 45° par rapport à la direction de propagation du faisceau de rayons X (Tieg *et al.* 2010). L'énergie des photons est sélectionnée pour correspondre au seuil de l'absorption du Fer (~708 eV).
Les hologrammes sont collectés en utilisant les deux hélicités des rayons X polarisés circulairement. Un grand nombre d'hologramme est collecté pour chaque polarisation pour améliorer le rapport signal/bruit. L'image finale est obtenue par soustraction des hologrammes accumulées pour les deux polarisations. Cela permet de supprimer la contribution de la diffusion de charge et de conserver uniquement la contribution magnétique.
La sensibilité de la technique à la magnétisation dans le plan est illustrée par la figure 21. Du fait de l'augmentation de la projection de la magnétisation dans le plan le long de la direction du faisceau, le meilleur contraste est obtenu pour une inclinaison assez large de l'échantillon (de l'ordre de 45°). La reconstruction révèle la présence de domaines de Landau qui sont typiquement observés pour des éléments de Py de cette taille. Dans un élément de forme carré, il prennent la forme de quatre domaines triangulaires. A l'intersection de ces quatre domaines se trouve un vortex de 30 nm de diamètre présentant une magnétisation hors plan. La position du cœur de vortex est susceptible d'être modifiée par l'application d'un champ magnétique externe.

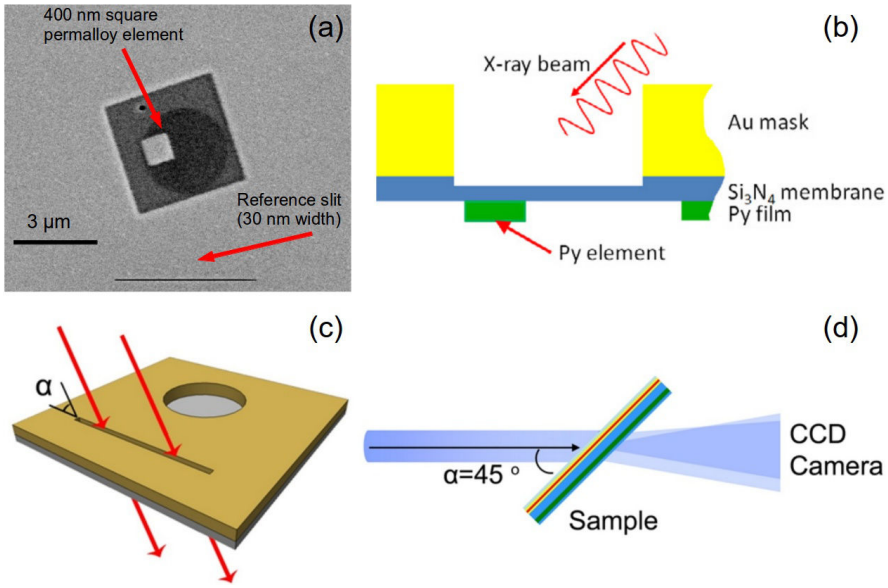

Fig. 20 *Imagerie de la magnétisation dans le plan d'un élément de Py* (a) Image MEB d'un élément de Py de 400 nm. La région circulaire et sombre est l'ouverture du masque d'or qui permet aux rayons X de traverser l'échantillon. La fente de référence est localisé à 5 µm de l'échantillon. (b) Schéma de l'échantillon (c) Design de l'échantillon, la face avant de la membrane de SiN est couverte par un masque d'or qui bloque les rayons-X excepté dans la région de l'ouverture circulaire et de la fente de référence. (d) Géométrie de l'expérience, l'échantillon est tourné dans le faisceau pour imager la magnétisation dans le plan.

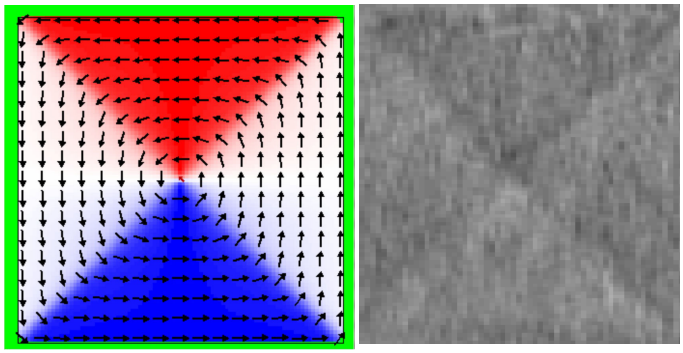

Fig. 21: *Organisation des domaines magnétiques (domaines de Landau) dans un élément de Py à la rémanence magnétique. Obtenue par des simulations micromagnétiques (gauche) tel qu'observée expérimentalement dans un élément de 2x2 µm²*

Imagerie en temps résolu des dynamiques de magnétisation du vortex

Si dans un premier temps les éléments de Py ont été employé comme des objets modèles pour démontrer la capacité de la FTH couplé avec le XMCD pour l'étude de structures magnétiques dans le plan, il s'avère également que ces éléments possèdent également un grand intérêt technologique. L'étude de leur dynamique de magnétisation est donc de première importance. L'holographie magnétique est donc utilisée dans cette section en temps résolu permettant l'analyse de la précession du cœur vortex induite par de courts pulses magnétiques.

L'expérience est conduite sur la ligne ID32 de l'ESRF sur un élément de Py de 2 x 2 μm^2 . Pour fournir le champ haute fréquence (RF), des guides d'onde coplanaires (CPW) sont intégrés sur la membrane de Si_3N_4 en utilisant des procédures lithographiques (Fig. 22.c). L'échantillon est également incliné à 45° dans le faisceau pour accéder à la magnétisation dans le plan (Fig. 22.d).
Pour l'analyse des dynamiques de magnétisation des vortex, les mesures sont réalisées dans un mode stroboscopique utilisant une excitation pulsée haute fréquence (RF). Les pulses de rayons X sont fournis par le mode 16 bunch, dont les paquets d'électrons sont séparés par 176 ns (Fig. 22.a). Les pulses de champ RF induisent la précession du vortex (pompe) quand les pulses de rayons X (sonde) permettent d'imager une phase particulière de la précession (Fig. 22.b) et servent de déclencheur pour les pulses de champ RF (Fig. 22.a).
Au total, le vortex est imagée pour 7 positions avec des temps de retard compris entre 0 et 8 ns. Ce retard correspond à l'intervalle de temps entre le front montant du pulse de champ RF et (pompe) et le pulse de rayons-X (sonde).

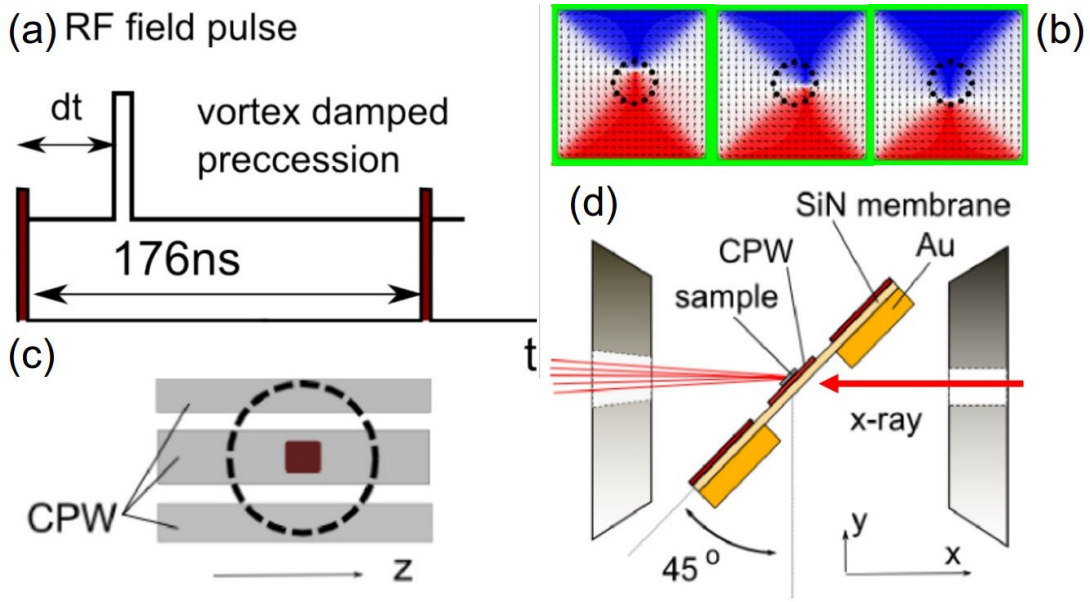

Fig. 22: *Schéma de l'expérience en temps résolu* . (a) Imagerie stroboscopique par excitation pulsée en mode 16 bunch. Le pulse magnétique est déclenché par le paquet de rayons X et retardé de *dt.* (b) Simulations micromagnétiques de la précession du coeur du vortex dans un élément de Py de 500x500 nm^2, pour 3 différentes étapes de la précession (c) Élément de Py et guide d'onde coplanaire situé de l'autre côté de la membrane, derrière l'ouverture circulaire. (d) Orientation de l'échantillon par rapport au faisceau de rayons X.

La Fig. 23 illustre l'évolution de la position du cœur du vortex pour différents retards. Le déplacement est quantifié précisément en traçant des profiles verticaux et horizontaux à travers le cœur du vortex (Fig. 23.d). La précession du cœur est clairement visible (Fig. 23.c) en bon accord avec les prédictions des simulations micromagnétiques (Fig. 23.b). L'asymétrie de la giration et sa faible amplitude ne peuvent pas être expliqués de manière satisfaisante à l'heure actuelle. Ces effets peuvent être liés à la structure du pulse ou encore à des effets de couplage induit par le réseau de vortex.

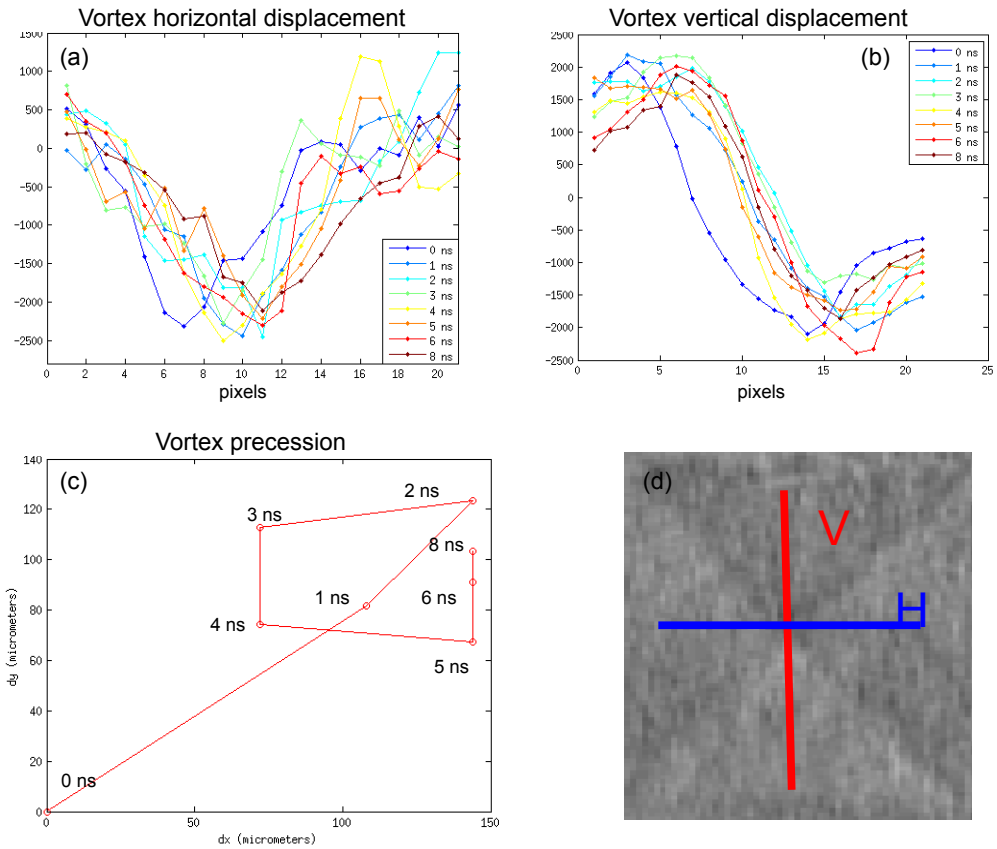

Fig. 23: *Position du cœur du vortex pour différentes étapes de sa précession.* (a) et (b) profiles montrant l'évolution des positions horizontales et verticales du cœur du vortex. Ces profiles sont tracés pour les positions indiquées sur la figure (d). (c) Position du cœur du vortex pour différentes valeurs du décalage temporel.

En résumé ce chapitre démontre donc que la FTH appliquée à des systèmes magnétiques est une technique très puissante pour l'étude de structures magnétiques et de leurs dynamiques. L'utilisation d'une référence étendue permet d'améliorer la résolution des données reconstruites et d'imager à la fois les dynamiques de magnétisation dans les éléments du Py constitue un résultat important et novateur.

Conclusions et perspectives

La perspective choisie pour ces travaux de thèse s'inscrit dans une approche physique du métal / métallurgie et est basée sûr l'étude de la relation entre la microstructure cristalline (présence de défauts), les propriétés physiques et l'élaboration. Dans ce cadre nous avons utilisé un outil expérimental, la radiation synchrotron, et plus spécifiquement les techniques de diffraction des rayons X cohérents, pour répondre à plusieurs questions fondamentales

Défauts structuraux et effets de taille sur les propriétés mécaniques

La réponse mécanique d'un objet cristallin dépend de la nature, de la densité et du comportement des

défauts qu'il contient. Les échantillons submicroniques ont une réponse différente du matériau massif à cause d'une modification des mécanismes prédominants de déformation à ces échelles de longueur.
La sélection du mécanisme de déformation est contrôlé par l'état de contrainte interne du système (la quantité d'énergie élastique stockée étant la force motrice), et la capacité du système à nucléer un type spécifique de dislocation (cinétique de la déformation).

- Le niveau de contrainte résiduelle dans des structures de petite taille est très différent de celui observé dans le matériau massif: d'une part la proximité des conditions aux limites tend à augmenter cette dernière (rôle des surfaces libres, étendue et relaxation de la déformation interfaciale), d'autre part le chemin d'élaboration de l'objet va également conduire à une contrainte résiduelle plus ou moins relaxée pour une géométrie donnée. L'un des principaux challenge expérimental est de mesurer ce niveau de contrainte résiduelle interne et d'être capable d'identifier les paramètres la contrôlant (la densité de défauts ou la relaxation de l'interface par exemple).
- La seconde question fondamentale concerne le mécanisme de nucléation des défauts: quel type/arrangement de dislocation est capable de relaxer (et dans quelle proportion) une contrainte mécanique extérieure imposée sur une quantité initiale de déformation. Ces considérations contrôlent le niveau de contrainte mécanique pour lequel un objet entre dans un régime de déformation irréversible.

.
Ces travaux de thèse permettent de répondre à certaines de ces questions:

Identification quantitative et imagerie des défauts

- Nous avons développé dans les chapitres III et IV des méthodes et outils numériques pour identifier la plupart des caractéristiques (vecteur de Burgers, système de glissement, caractère parfait ou dissocié de la dislocation) d'un défaut unique (dislocation, faute d'empilement) à partir de la signature qu'il produit dans l'espace réciproque. Les condition de diffraction optimales (choix du vecteur du réseau réciproque $\boldsymbol{g}$) sont déterminés et discutés pour chaque type de défaut.
- L'imagerie par reconstruction de la phase et de la densité électronique s'avère être une technique très puissante pour l'identification et l'analyse d'une microstructure de défauts. Utilisant la reconstruction nous avons pu établir, pour la première fois sur une liste exhaustive de défauts cristallins, une méthodologie qui permet l'identification quantitative de la nature physique et géométrique du défaut:
  - la densité électronique diffractante locale permet de déterminer la localisation de la ligne de dislocation
  - les variations de phase et leur chiralité permettent l'identification sans ambiguïté de la nature du défaut.
- L'extrême sensibilité de la CXD aux imperfections cristallines et un outil puissant pour évaluer rapidement la qualité d'un cristal. Nous démontrons que des variations assez large dans la qualité cristalline pour des structures de forme équivalente (observée par MEB ou AFM) sont obtenues par le procédé de démouillage. Le caractère non destructif de la CXD permet de s'assurer que la caractérisation mécanique est effectuée sur des objets équivalents dans leur état initial, un pré-requis essentiel pour caractériser les effets de taille sur la réponse mécanique.
- Une expérience originale de déformation *in-situ* par indentation d'une particule d'or quasiment vierge de défauts dans son état initiale a été réalisée. L'utilisation des méthodologies décrites dans les chapitres III-V a permis de déterminer avec succès la stade de germination d'une dislocation prismatique. En utilisant des reconstructions à différents étapes de la sollicitation mécanique:
  - une boucle de dislocation prismatique est clairement identifiée.
  - Nous démontrons l'interaction entre les défauts germées et la déformation interfaciale conduisant à un 'recuit mécanique'

Les interfaces et conditions aux limites ont été également étudiées avec succès sur différents systèmes:

- Dans une cristallite d'or maclée, la sensibilité de la reconstruction de phase à la relaxation des surfaces libres a été mise en évidence. L'absence de déformations longue distance aux voisinage du joint de macle a été également confirmée.

- Un cas plus complexe d'interface d'un système bi-métallique Cu-Ta a été revisité. Des expériences *in situ* de diffraction de surface ont permis la mesure quantitative de deux couches pseudomorphes de Cu sur le substrat de Ta. Des calculs ab-initio montrent un excellent accord avec ces mesures expérimentales. L'influence de la structure de l'interface Cu (f.c.c.) et Ta (b.c.c.) dans les cristallites de Cu présentant une forte déformation interfaciale est également évaluée à l'aide de simulations de statique et de dynamique moléculaire.

- La CDI est enfin utilisée avec succès pour reconstruire en 3 dimensions des domaines d'inversion de polarité le long de fils de GaN.

La possibilité de mesurer quantitativement à la fois la microstructure de défauts et le champ de déplacement interne, possiblement *in situ* mais également dans des structures enterrées, fait de la diffraction des rayons X cohérents un outil unique pour résoudre des problèmes mécaniques fondamentaux. La CXD peut ainsi permettre de répondre à des questions de longue date concernant par exemple la compréhension de la déformation plastique par des mécanismes de maclage ou encore des problèmes de fracture/relaxation plastique. Enfin, la technique pourrait être utilisée pour des études de transformation de phase dans des systèmes de petite taille.

Configurations magnétiques et dynamiques de magnétisation en temps résolu

- Dans un élément de Permalloy (Fe-Ni) de taille micrométrique, l'holographie de Gabor (Fourier Transform Holography) permet de démontrer avec succès l'effet de taille sur l'organisation des domaines magnétiques est démontré avec succès. Dans un second temps, des mesures en temps résolu à la nanoseconde permettent l'étude des dynamiques de magnétisation dans ce système. Ces mesures ouvrent la perspective de l'étude d'effets de couplage dans des systèmes de petite taille, en particulier concernant le couplage ferroélectrique-ferromagnétique dans des multicouches.

Les perspectives scientifiques présentées dans cette conclusion devraient bénéficier des améliorations constantes des sources de rayons-X cohérents. L'augmentation de la brillance des sources permet d'accéder à une plus large portion de l'espace réciproque, permettant une amélioration de la résolution des reconstructions. Les mises à jour des sources de synchrotron de 3ème génération devraient permettre une augmentation d'un facteur x10 de la brillance. Encore plus impressionnant, les lasers à électrons libres de rayons-X permettent une augmentation de la brillance d'environ 9 ordres de grandeur, permettant d'envisager une large gamme d'expériences en temps résolue, comme déjà démontré à travers des expériences d'holographie magnétique par von Korff Schmising et al. (2014) ou par l'imagerie d'ondes acoustique dans des cristallites de taille micrométrique Clark *et al.* (2013).

Bibliographie

Andrews, S. R. & Cowley, R. A. (1985) *J. Phys. C* **18**, 6247

Aqra, F. & Ayyad, A. (2011) *Appl. Surf. Science* **257***,* 6372-6379

Ashby, M.F. (1971) Strengthening methods in crystals, Chapter 3, edited by Kelly A.and Nicholson R.B., John Wiley & sons, inc, New York

Ball, M. J., Lucas, C. A., Markovic, N. M., Stamenkovic, V. & Ross, P. N. (2002) *Surface Science* **518**, 201.

Bei, H., Shim, S., Pharr, G. M., & George, E. P. (2008). *Acta. Mater.* **56**, 4762-4770.

Beutier, G., Verdier, M., Parry, G., Gilles, B., Labat, S., Richard, M. I., Cornelius, T., Lory, P. -F., Vu Hoang, S., Livet, F., Thomas, O. & De Boissieu, M. (2013a). *Thin Solid Films* **530**, 120-124.

Brenner, S. S. (1956). *J. Appl. Phys.* **27**, 1484.

Chang, H. J., Fivel, M., Rodney, D. & Verdier, M., (2010). *C. R. Physique* **11**, 285-292

Clark, J. N., Beitra, L., Xiong, G., Higginbotham, A., Fritz, D. M., Lemke, H. T., … Robinson, I. K. (2013). . *Science **341***, 56–59.

Duckworth, T. A., Ogrin, F., Dhesi, S.S., Langridge, S., Whiteside, A., Moore, T., Beutier, G. & Van der Laan G (2011) *Optics Express* **19**, 16223.

Ehrhart, P., Trinkaus, H., & Larson, B. C. (1982). *Phys. Rev. B* **25**, 834-848.

Favre-Nicolin, V., Richard, M. I. & Renevier, H. (2011). *J. Appl. Cryst.* **44**, 635-640.

Fienup, J. R. (1982). *Appl. Opt.* 21, 2758-2769

Frank, F. C. & Van Der Merve, J. H. (1949). *Proc. Roy. Soc. Lond. Ser. A* **198**, 205-216.

Freund, L. B. & Suresh, S. (2003) Thin Film Materials: Stress, Defect Formation and Surface Evolution, edited by Cambridge University Press, Cambridge, England

Gerchberg, R. W. & Saxton, W. O. (1972). Optik (Stuttgart) 35, 237–246.

Grochola, G. S., Russo, P. & Snook, I. K. (2005). *J. Chem. Phys.* **123**, 204719.

Guizar-Sicairos, M. & Fienup, J. R. (2007) *Opt. Express* **15**, 17592.

Hashibon, A., Lozovoi, A. Y., Mishin, Y., Elsässer, C. & Gumbsch, P. (2008) *Phys. Rev. B* **77**, 0941131.

Heyraud, J. C. and Métois, J. J. (1982) *Surf. Sci* **128**, 334.

Huang, W. J., Sun, R., Tao, J., Menard, L. D., Nuzzo, R.G. & Zuo, J. M. (2008). *Nature Materials* **7**, 308-313.

Labat. S., Richard, M-I., Dupraz, M., Gailhanou, M., Beutier, G., Verdier, M., Mastropietro, F., Cornelius, T. W., Schülli, T. U., Eymery, J. & Thomas, O. (2015) *ACS Nano* **9**

Larson, B. C. & Young, F. W. (1987). *Phys. Stat. Sol. A* **104**, 273-286.

Malyi, O. & Rabkin, E. (2012) *Acta Materiala* **60**, 261-268

Marchesini, S. (2003). *Phys. Rev. B* **68**, 140101

Matthews, J.W. & Blakeslee, A. E. (1974) *J. Crystal Growth* **27**, 118.

McNulty, I., Kirz, J., Jacobsen, C., Anderson, E. H., Howells, M. R. & Kern, D. P (1992). *Science* **256**, 1009–1012

Mishin, Y., Farkas, D., Mehl, M. J. & Papaconstantopoulos, D. A. (1999). *Phys. Rev. B* **59**, 3393-3407.

Mishin, Y., Mehl, M. J., Papaconstantopoulos, D. A., Voter, A. F. & Kress, J. D. (2001). *Phys. Rev. B* **63**, 224106.

Northrup, J. E., Neugebauer, J., & Romano, L. T. (1996) *Phys. Rev. Lett.* **77**, 103–106.

Robinson, I. K. & Tweet, D. J. (1992) *Rep. Prog. Phys.* **55***,* 599-651 .

Robinson, I. K. & Vartanyants, I. A. (2001). *Applied Surface Science* **182**, 186-191.

Rodney, D. (2010), Merlin in a Nutshell, non publié

Sadan, H. & Kaplan, W. D. (2006). *J. Mater. Sci.* **41**, 5099-5107.

Sayre, D. (1952) *Acta. Cryst.* 5, 843.

Tieg, C., Frömter, R., Stickler, D., Hankemeier, S., Kobs, A., Streit-Neirobisch, S., Gutt, C., Grübel, G. & Oepen, H. P., *Opt. Express* **18**, 27251.

Tyson, W. R. & Miller, W. A. (1977). *Surf. Sci.* **62**(1), 267-276.

Uchic, M. D., Dimiduk, D. M., Florando, J. N. & Nix, W. D. (2004). *Science* **305**, 986-989.

Van der Merwe, J. H. **1963** *J. Appl. Phys.* **34**, 123

Venugopal, V. & Thijsse, B. J. (2009) *Thin solid Films* **517***,* 5482-5488.

Vitos, L., Ruban, A. V., Skriver, H., L. & Kollár, J. (1998) *Surface Science* **411***,* 186-202.

Vlieg, E. (2000) *J. Appl. Cryst.* **33***,* 401-405

Von Korff Schmising, C., Pfau, B., Schneider, M., Günther, C. M., Giovannella, M. Perron, J. Vodungbo, B.

Müller, L., Capotondi, F. Pedersoli, E. Mahne, N., Lüning, J. & Eisebitt, S. (2014) *Phys. Rev. Lett.* **112**, 217203

Wuttig, M. & Liu, X. (2004) Ultrathin Metal Films, edited by Springer-Verlag, Berlin

Zhe, R., Mastropietro, F., Davydok, A., Langlais, S., Richard, M.-I., Furter, J.-J., Thomas, O., Dupraz, M., Verdier, M., Beutier, G., Boesecke, P. & Cornelius, T. W. (2014). *J. Synchrotron Rad.* **21**, 1128-1133.

Table of contents

Introduction.....1

Chapter I: Basics of Coherent X-ray Diffraction

Introduction.....5
I.1 Coherence.....5
I.1.1 Mutual coherence.....5
I.1.2 Coherence lengths.....6
1.2 Scattering of a coherent X-ray beam.....8
1.2.1 General case.....8
I.2.2 Exploiting Coherent X-ray Diffraction.....9
I.2.3 Coherent X-ray Diffraction in Bragg geometry.....10
I.3 Modelling Coherent X-ray Diffraction from micro- and nanoscale crystals.....12
I.3.3 Advantages of the atomic description 13
I.3.4 Fast Fourier Transform vs direct computation of the kinematic sum for the study of crystal defects 15
I.4 Coherent Diffraction Imaging.....19
I.4.1 The phase problem.....19
I.4.2 Holography.....20
I.4.3 Coherent Diffraction Imaging with phase retrieval algorithms.....20
I.4.3.1 Oversampling.....20
I.4.3.2 General formalism of phase-retrieval algorithms.....21
I.4.3.3 Finite support constraint and Error-Reduction (ER algorithm).....22
I.4.3.4 Hybrid-Input-Output (HIO) algorithm.....23
I.4.3.5 Support determination, Shrink wrap algorithm.....23
I.4.3.6 Recent improvements on the phase retrieval procedure.....24
I.4.4 Correction for artefacts related to experimental conditions.....25
I.4.4.1 Reciprocal space offsets.....26
I.4.4.2 Refraction effects.....26
I.4.4.3 The wavefront problem.....26
I.4.5. Numerical study, case of defective samples.....27
I.4.5.1 Comparisons between reconstructions for several Bragg reflections 27
I.4.5.2 Extent of the reciprocal space pattern, resolution and oversampling conditions.....32
Conclusion 36
Bibliography.....37

Chapter II: Experimental methods and samples

Introduction.....41
II.1. Synchrotron Sources.....41
II.1.1. Description of the coherence set-up.....42

II.1.1.1 Slits and focusing optics....42
II.1.1.2 Kirkpatrick-Baez (KB) mirrors....43
II.1.1.3 Fresnel zone plates (FZP)....44
II.1.1.4 Coherence set-up, photon flux and degree of coherence....45
II.1.2. Detectors....47
II.1.2.1 Correction of the defects for 2D detectors....48
II.1.3 Diffractometers and sample stage....49
II.1.4 Measurements in the reciprocal-space using diffractometers - Isolation of a single island....50
II.1.5 Collection of 3D reciprocal space maps from isolated objects....51
II.1.6 Reconstruction of the 3D diffraction pattern in the sample orthonormal basis....52
II.2. Surface diffraction....54
II.2.1 Crystal truncation rods....54
II.2.2 X-ray diffraction from the surface region....56
II.2.3 Surface X-ray diffraction experimental set-up....56
II.2.4 Measurement of the rod intensities....58
II.3. Samples....58
II.3.1. Islands....59
II.3.1.1 Solid-state dewetting....59
II.3.1.2 Equilibrium shape of the particles....61
II.3.2 Nanowires....64
II.4. Sample characterization....66
II.4.1 Ex situ indentation....66
II.4.2. Synchrotron characterization....72
II.4.2.1 Laue microdiffraction....72
II.4.2.2 Finding the sample of interest: 2D fast-mapping of the sample....76
II.4.2.3 Mapping the sample strain and tilt: Scanning-X-ray Diffraction Microscopy (SXDM)…78
II.4.3 Multi-characterization of a sample....83
Bibliography....86

Chapter III : Signature of dislocations and stacking faults of *fcc* nanocrystals in coherent X-ray diffraction patterns: a numerical study

Abstract....90
III.1. Introduction....90
III.2. Tools and methods....92
III.3. Simulations on fcc nanocrystals....94
III.3.1. Screw dislocations....95
III.3.3. Stacking faults....100
III.3.4. Frank loops....104
III.3.5. Prismatic loops....106
III.3.6. Influence of the crystal size and shape....109
III.3.7. Influence of the defect position....111
III.4. Application to a complex case: indentation of a gold nanocrystal....112
III.5. Discussion....116
III.6. Conclusions....118
Bibliography....119

Chapter IV: Coherent X-ray diffraction applied to moderately complex systems. Comparison of the direct analysis of the CXD patterns and reconstruction of the displacement field methods.

Introduction....123
IV.1. Case of quantitative determination of a loop size and geometry....123
IV.1.1. Determination of the interstitial or vacancy character of a defect....123
IV.1.2. Determination of the size of a dislocation loop....126
IV.2. Analysis of the CXD pattern of a moderately complex system: nanoindentation of a Nickel thin film....127
IV.3. Case of a system with multiple stacking faults in equivalent slip planes....133
Conclusion....137
Bibliography....139

Chapter V: Coherent Diffraction Imaging of single defects and of a small assembly of defects

Introduction....140
V.1. Reconstructed of the displacement field from single dislocation lines and comparison with their signature on CXD patterns....140
V.1.1. Simple case of a perfect screw dislocation....141
V.1.2 Dissociation of an edge dislocation....142
V.2. Comparison between calculated and reconstructed displacement fields and visibility of dissociated defects in experimental reconstructions....148
V.3. Single mixed dislocation in the course of nanoindentation of a gold nanoparticle....150
V.4. Displacement fields from individual dislocation loops....155
V.4.1. Frank dislocation loops....155
V.4.2. Prismatic dislocation loops....160
V.5. Case of a moderately complex system : simulated nanoindentation of a nickel thin film....162
Conclusion....167
Bibliography....168

Chapter VI: Investigation of the mechanical properties of a single gold crystal by in-situ nano-indentation in combination with coherent Bragg diffraction imaging

Introduction....169
VI.1 Sample preparation....169
VI.2 Coherent X-ray diffraction experiment....174
VI.3 Selection of the gold particle and importance of the preparation conditions....176
VI.4 Simple model of the thermoelastic strain with molecular statics simulations....179
VI.5 Results....180
VI.5.1 Analysis of the CXD patterns at various iteration of the loading unloading cycle....180
VI.5.2 Reconstruction of the electron density....183
VI.5.3 Imaging of the displacement field around a prismatic dislocation loop....185

VI.5.4 Evolution of the displacement and strain fields in the particle during the loading-unloading iterations....187
Conclusion....193
Bibliography....195

Chapter VII: Investigation of the three-dimensional strain distribution in a sub-micron twinned gold island by coherent X-ray diffraction and molecular statics simulations

Abstract....198
Introduction....198
VII.1 Sample preparation....199
VII.2 CXD experiment....200
VII.2. Molecular statics simulations....204
VII.2.1 Size effects....204
VII.2.2 Influence of the boundary conditions....207
Conclusion....211
Bibliography....212

Chapter VIII : Study of an heterogeneous bi-metallic interface (Cu-Ta) investigated by surface diffraction, ab-initio and molecular dynamics calculations

Introduction....214
VIII.1. Experiment....215
VIII.1.1. Experimental details....215
VIII.1.2. Comparisons between different surface states....218
VIII.2. Density Functional theory calculations....219
VIII.2.1. Computational method....219
VIII.2.2. Supercell configuration....219
VIII.2.3. Calculation of the excess interface energies....220
VIII.2.4. Calculation of the structure factors....221
VIII.2.5. Fitting of the experimental data....224
VIII.3. Atomistic simulations with an angle-dependent potential for the Cu-Ta system....225
VIII.3.1. Calculation of the excess interface energies....226
VII.3.2. Calculation of the structure factors....228
VIII.3.3. Testing the potential....230
VIII.3.4. Application to the solid state dewetting of a Cu thin film....231
Conclusions....233
Bibliography....235

Chapter IX: Interface of copper islands dewetted in the solid state on the Tantalum (0 0 1) surface studied by coherent X-ray diffraction and molecular dynamics simulations

Introduction....237
IX.1. Sample preparation and description....238
IX.2. Molecular dynamics simulations of the Cu-Ta interface using the angle-dependent potential....239
IX.2.1. Simulation of the solid-state and liquid-state dewetting....239
IX.2.2. Interfaces obtained with simulated experimental conditions....244
IX.2.3. Evolution of the interface for longer annealing times....245
IX.3. HR-TEM observation of the Cu-Ta interface....247
IX.4. Influence of the atomic structure of the interface on the distribution of the displacement field. .248
Conclusion....254
Bibliography 255

Chapter X: Investigation of the three-dimensional distribution of Polar Inversion Domain Boundary in GaN wires

X.1 GaN nanowires and Inversion Domain Boundaries Sample preparation and description....257
X.2 CXD experiment 258
Conclusion....260
Bibliography 261

Chapter XI: Investigation of the magnetic structure and dynamics of sub-micron magnetic elements using Fourier Transform Holography

Introduction....262
X.1 Fourier Transform Holography....263
X.1.1 Basics of Fourier Transform Holography....263
X.1.2 Experimental set-up....265
XI.1.3 Magnetic contrast polarization and interference....266
XI.1.4 Investigation of in-plane magnetic scattering....270
XI.1.5 Extended reference....271
XI.2 Investigation of the in-plane magnetization of nanostructures and their dynamics....273
XI.2.1 Determination of the magnetic structure of a permalloy thin film....273
XI.2.2 Experimental considerations and correction of the experimental data....276
XI.2.3 Field dependence measurements....279
XI.2.4 Time resolved imaging of the magnetic vortex dynamics....281
XI.2.5 Observation of the resonance gyration of the magnetic vortex in a nano-contact spin torque oscillator....285
Conclusions....287
Bibliography....288

Conclusions and perspectives....290

Appendix A1: Study of the Cu/Tantalum (0 0 1) interface

A1.1 Calculation of the excess interface energies for several Cu-Ta interfaces.....293
A1.2 Atomic structure of the Cu-Ta interface in solid state dewetted particles.....301
Bibliography 305

Appendix A2: Inversion Domain Boundaries in GaN Wires Revealed by Coherent Bragg Imaging

Results and discussions 306

Table of Figures

Chapter I

Fig. I.1 Illustration of the coherence length....7
Fig. I.2 Differences in the scattering of an incoherent X-ray beam (a) and a coherent X-ray beam (b)....9
Fig. I 3 Sensitivity of coherent x-ray diffraction to lattice displacements....11
Fig. I.4 Comparison of the computing speed for a single CPU and a GPU depending on the number of atoms and reflections....14
Fig. I.5 Computation of the scattering from an edge dislocation using a FFT....16
Fig. I.6 Enhancement of the resolution in the resolution of the reciprocal space by padding the computing cell in the real space with zeros....17
Fig. I.7 Scattering from an edge dislocation with b = 1/2[1 1 0] and g = 2 0 2 obtained by two distinct methods of computation....21
Fig. I.9 General architecture of phase retrieval algorithms 22
Fig. I.10 Phase retrieval from samples containing individual defects 28
Fig. I.11 Comparison between the calculated and reconstructed displacements around a perfect edge dislocation introduced at the centre of the reference copper nanocrystal 29
Fig. I.12 Case of sharp and large phase jumps ($>2\pi$) 31
Fig. I.13 Shape of the Error-metric for a failed and successful reconstruction 32
Fig. I.14 Enhancement of the resolution in the real space reconstruction by increasing the spatial extent in the reciprocal space....33
Fig. I.15 Resolution of the reconstruction given by the phase retrieval transfer function (PRTF) 35

Chapter II

Fig. II.1 Layout of the experimental setup on the ID01 beamline....41
Fig. II.2 Focusing of the X-ray beam with Kirkpatrick-Baez mirrors....43
Fig. II.3 Focusing of the X-ray beam with a Fresnel-Zone-Plate....44
Fig. II.4 Coherence setup on the ID01 beamline....45
Fig. II.5 Schematic of typical CXD experiments with focusing optics....46
Fig. II.6 Six circle diffractometers 49
Fig. II.7 Real space lattice and reciprocal space lattice of a f.c.c material: direction of the incident, diffracted wave vectors and of the scattering vector for a specular and an off-specular reflection....50
Fig. II.8 Measurement of 3D reciprocal-space maps....52
Fig. II.9 Detector plane in the reciprocal space 53
Fig. II.10 (a) SXRD dedicated experimental set-up at BM32 (b) Schematic of the z-axis diffractometer....57
Fig. II.11 Ewald construction which summarizes the geometry of the experiment 57
Fig. II.12 Schematics of the solid-state dewetting process....59
Fig. II.13 Schematic of the growth mechanism of holes....60
Fig. II.14 Wulff plot of the equilibrium shape (γ-plot)....62
Fig. II.15 γ^* and corresponding equilibrium shape for different wetting behaviours....63
Fig. II.16 Secondary Electron Microscopy image of the dewetted islands....63
Fig. II.17 Morphology of gold nanowires (NW)....65
Fig. II.18 Force-displacement curves for different mechanical behaviours....68
Fig. II.19 Experimental set-ups to carry out the in-situ nanoindentation experiments....69
Fig. II.20 Comparison between a CXD pattern obtained from a pristine particle, and from a particle where few dislocations have been nucleated....70
Fig. II.21 Nanoindentation of a gold nanowire....71
Fig. II.22 2D Laue micro-diffraction from a gold particle with a twin-boundary 74

Fig. II.23 2D Laue micro-diffraction from a gold nanowire with a twin-boundary.....75
Fig. II.24 Macroscopic markers on the sample, to locate the crystals of interest.....76
Fig. II.25 Illustration of the SXDM technique to localize the islands of interest 78
Fig. II.26 Catalog of the distribution of sizes and geometries of the particles obtained by solid-state dewetting. 80
Fig. II.27 Determination of the out-of-plane strain of a population of islands by SXDM.....81
Fig. II.28 Rocking-curve for several particles determined from the integrated intensities at various angular positions 82
Fig. II.29 Example of a multi-characterization of a gold particle.....84

Chapter III

Fig. III.1 Defect free gold nanocrystal of Wulff geometry and size 30x30x30nm^3.. 94
Fig. III.2 Screw dislocation in a 30x30x30 nm^3 copper crystal with a Wulff geometry.....96
Fig. III.3 Edge dislocation in a 30x30x30 nm^3 copper crystal with a Wulff geometry.....99
Fig. III.4 (1 1 1) Stacking fault in a silver crystal with a Wulff geometry induced by the complete relaxation of a perfect edge line dislocation.....101
Fig. III.5 Influence of the Stacking Fault Energy.....103
Fig. III.6 Relaxation for a crystal with a low SFE (silver).....104
Fig. III.7 Relaxed Frank dislocation loop with $\boldsymbol{b}$ = ⅓ [1 1 1] in the centre of a 30x30x30nm^3 Wulff silver crystal. 105
Fig. III.8 Relaxed prismatic dislocation loop with $\boldsymbol{b}$ = ½ [1 0 1] at the centre of a 30x30x30nm^3 Wulff copper crystal.....107
Fig. III.9 Defect free copper spherical crystal with r = 14.1nm.....110
Fig. III.10 Effect of the position of a perfect screw dislocation in a 30x30x30nm^3 copper crystal in a Wulff geometry.....112
Fig. III.11 Simulation of the indentation of a 12.1 nm high gold nanoparticle by a cube-corner indenter.....113
Fig. III.12 Gold nanoparticle after 650000 indentation steps.....115

Chapter IV

Fig .IV. 1 Calculated CXD pattern from an interstitial (a) and a vacancy (b) Frank dislocation loop with b = 1/3[1 1 1] and g // b (g = 1 1 1).....124
Fig. IV.2 Calculated CXD pattern from a 25 nm (a) and a 10 nm (c) Frank dislocation loop with b = 1/3[1 1 1] and g // b (g = 1 1 1).....126
Fig. IV.3 Schematic description of loop nucleation process during [1 1 1] indentation.....128
Fig. IV.4 Calculated CXD patterns from the simulated indented for four different 1 1 1-type diffraction vectors. 129
Fig. IV.5 Calculated diffraction patterns from the simulated indented nickel crystal for g = 1 1 1 (a), g = 1 1 1 (b) and g = 1 1 1 (c).....131
Fig. IV.6 Calculated diffraction patterns from the simulated indented nickel crystal for g = 2 2 0 (a), g = 2 0 2 (b) and g = 0 2 2 (c).....131
Fig. IV.7 (a) 10.5 x 10.5 x 4.1 nm and (b) 18.6 x 18.6 x 6.7 nm Copper particles dewetted on a Tantalum substrate above the melting temperature. 134
Fig. IV.8 Calculated CXD diffraction patterns from the small (10.5 x 10.5 x 4.1 nm) copper particle.....135
Fig. IV.9 Calculated CXD diffraction patterns from the small (18.6 x 18.6 x 6.7 nm) copper particle. (a) to (d) Calculations for four 1 1 1-type diffraction vectors. If possible, the direction of the diffraction vector is indicated by a red arrow.....136

Chapter V

Fig. V.1 Case of the perfect screw dislocation. 142

Fig. V.2 Case of the edge dislocation line, perfect (top) and dissociated (bottom), for $\boldsymbol{g} = 2\ \bar{2}\ 0$ ($\boldsymbol{g}$ // $\boldsymbol{b}$).....143
Fig. V.3 Case of the edge dislocation line, perfect (top) and dissociated (bottom), for $\boldsymbol{g} = 2\ \bar{4}\ 2$ ($\boldsymbol{g}$ // $\boldsymbol{b}_p$).....144
Fig. V.4 Case of the edge dislocation line, perfect (top) and dissociated (bottom), for $\boldsymbol{g} = 2\ 0\ \bar{2}$.....145
Fig. V.5 Case of the dissociated dislocation line for $\boldsymbol{g} = 2\ 2\ \bar{4}$ ($\boldsymbol{g}.\boldsymbol{b} = 0$ and $\boldsymbol{g}.\boldsymbol{b}\mathrm{x}\boldsymbol{t} = 0$).....146
Fig. V.6 Case of the dissociated dislocation line for $\boldsymbol{g} = 2\ 2\ 4$ ($\boldsymbol{g}.\boldsymbol{b} = 0$ and $\boldsymbol{g}.\boldsymbol{b}\mathrm{x}\boldsymbol{t} \neq 0$).....147
Fig. V.7 Comparison between the calculated and reconstructed displacements around a perfect edge dislocation introduced at the centre of the reference copper nanocrystal for $\boldsymbol{g} = 2\ 2\ 4$ 149
Fig. V.8 Identification of dissociated edge dislocations with $\boldsymbol{g}$ // $\boldsymbol{b}$ for low and high real-space resolution data. 150
Fig. V.9 Reconstructed displacement field of the mixed-dislocation for several **g** 152
Fig. V.10 Comparison between reconstructed displacement field and calculated CXD patterns for several $\boldsymbol{g}$.....153
Fig. V.11 Variations in the reconstructed electron density at the vicinity of a Frank dislocation loop 156
Fig. V.12 Reconstructed displacement field from loops of varying size and type for $\boldsymbol{g} = 1\ 1\ \bar{1}$.....157
Fig. V.13 Reconstructed displacement field from a 20 nm Frank interstitial loop for several $\boldsymbol{g}$.....158
Fig. V.14 Reconstructed $u_{2\,2\,0}$ displacement field from the 20nm interstitial loop in the (2 2 0) plane.....159
Fig. V.15 Reconstruction of the displacement field from a diamond shaped prismatic loop for several $\boldsymbol{g}$ 160
Fig. V.16 Reconstructed displacement field from the diamond shaped prismatic dislocation loop for $\boldsymbol{g} = 2\ 0\ 2$ and $\boldsymbol{g} = 1\ 1\ 1$ in the $(\bar{1}\ 0\ 1)$ plane 161
Fig. V.17 Reconstructed electron density in the nickel thin film for several reflections 163
Fig. V.18 Reconstructed displacement field in the (1 1 1) plane for several reflections.....164
Fig. V.19 Reconstructed displacement field around the $\mathbf{b}_3$ loop ($\mathbf{b}_3 = 1/2[\ \bar{1}\ 0\ \bar{1}]$) in the $(1\ \bar{2}\ 1)$ plane.....166
Fig. V.20 Reconstructed displacement field from four crystallographic variants of prismatic loops 166
.....

Chapter VI

Fig. VI.1 Summary of the possible orientation relationship between the gold particle and the sapphire substrate. 171
Fig. VI.2 SEM picture of a population of solid state dewetted gold islands 172
Fig. VI.3 SEM pictures of the solid state dewetted particles from Technion Inst. 173
Fig. VI.4 CXD diffraction patterns from the two crystals with the least estimated residual strain and defect content.....175
Fig. VI.5 Principle of the experiment and description of the *in situ* AFM 176
Fig. VI.6 CXD patterns measured at other Bragg reflections.....176
Fig. VI.7 Signature of the thermoelastic strain on the CXD pattern.....178
Fig. VI.8 Thermoelastic strain modeled with molecular statics simulations.....179
Fig. VI.9 CXD patterns at different stages of the indentation experiment measured around $\mathbf{g} = 1\ 1\ 1$.....182
Fig. VI.10 Reconstructed electron density isosurface drawn at 30% of the maximum density.....173
Fig. VI.11 Reconstructed electron density isosurface drawn at 25% of the maximum density for each iteration of the loading-unloading cycle.....184
Fig. VI.12 Reconstruction of the displacement field around a prismatic dislocation loop nucleated after four iterations in the loading-unloading cycle.....186
Fig. VI.13 Comparison between the $u_{1\,1\,1}$ displacement fields from the experimental loop and from the dislocation loops nucleated during the simulated nanoindentation of a nickel thin film 187
Fig. VI.14 Reconstructed φ_{111} phase field for increasing iterations of the loading-unloading cycle.....189
Fig. VI.15 Phase profile along z (the [1 1 1] direction) at each iteration of the loading-unloading cycle.....190
Fig. VI.16 Reconstructed εzz strain field for increasing iterations of the loading-unloading cycle. 192
Fig. VI.17 Evolution of the "elastic strain energy" stored in the particle versus the number of loadings of the particle.....193

Chapter VII

Fig. VII.1 SEM picture of Au particles dewetted at 1100°C on a (0001) sapphire substrate.....199

Fig. VII.2 Twinned gold particle considered in this experiment 200
Fig. VII.3 Reconstructed electron density and $u_{0\,0\,2}$ displacement for the twinned gold particle.....203
Fig. VII.4 Effect of the correction for refraction.....203
Fig. VII.5 Influence of the size of the particle on the calculated CXD patterns and the reconstructed $u_{0\,0\,2}$ displacement fields. 205
Fig. VII.6 Dependence of the CXD patterns on the boundary conditions for $\boldsymbol{g}$ = 0 0 2.....207
Fig. VII.7 Distribution of the $u_{0\,0\,2}$ displacement field depending on the boundary conditions.....209
Fig. VII.8 Comparison between experimental and simulated reconstructions.....210

Chapter VIII

Fig. VIII.1 Auger spectra showing the surface contamination at various stages of the experiment 216
Fig. VIII.2 Geometry of the experiment 218
Fig. VIII.3 Comparison of the 1 0 L rod (a) and 1 1 L rod (b) for two different experimental runs with different state of surface contamination.....219
Fig. VIII.4 Configurations considered for the DFT calculations.....220
Fig. VIII.5 1 0 L (a) and 1 1 L(b) calculated structure factors for a varying number of PM Cu layers compared with experimental data.....222
Fig. VIII.6 Interplanar spacing versus plane index for 2 and 7 relaxed Ta planes.....223
Fig. VIII.7 Influence of the number of relaxed Ta planes on the calculated 10L (a) and 11L(b) structure factors 223
Fig. VIII.8 1 0 L(a) and 1 1 L(b) calculated structure factors, before and after fitting.....224
Fig. VIII.9 Atomic structures from a different set of initial Cu thin films obtained by energy minimization at 0K with the ADP potential.....227
Fig. VIII.10 Calculated structure factors with the ADP potential.....228
Fig. VIII. 11 Interplanar spacing versus plane index for the ADP and DFT calculations.....229
Fig. VIII.12 Simulation of the solid state dewetting of Cu islands on a (0 0 1) Ta surface for a varying number of PM layer in the initial configuration.....232

Chapter IX

Fig. IX.1 Secondary Electron Microscopy of the solid state dewetted copper islands.....238
Fig. IX.2 Comparison of the simulated solid state and liquid state dewetting for various initial configurations. 240
Fig. IX.3 Comparisons of the shape of experimental and simulated particles obtained by solid-state dewetting. 242
Fig. IX.4 Evolution of the structure of the interface of particle (c) after 1 ns of annealing at 1000K.....244
Fig. IX.5 Size dependency of the Cu-Ta interface.....246
Fig. IX.6 HR-TEM micrograph illustrating the atomic structure of the Cu-Ta interface (FIB cross section of typical Cu island).....247
Fig. IX.7 (a) Distribution of the u_z displacement field in a 40x40x15 Cu particle relaxed by energy minimization. 249
Fig. IX.8 Comparison of the 0 0 2 Bragg reflection from a typical experimental island, from FEM simulations and from MS simulations.....251
Fig. IX.9 (x,z) slice through a 40x40x15 nm Cu island showing the strain field εzz for $\Delta\alpha\Delta T$ = 1.13%.....252
Fig. IX.10 Comparison of the distribution of the u_z displacement field for the 1 PM and 2 PM configurations 253

Chapter X

Fig. X.1 3D representation of an Inversion Domain Boundary or Wall (IDB) in the [0 1 1 0] separating two-oppositely polarized GaN domains.....257
Fig. X.2 Scanning electron microscopy pictures of GaN wires obtained by MOVPE.....258

Fig. X.3 2 D and 3 D reconstruction of the u_{004} displacement field at several positions along the GaN wire.....259
Fig. X. 4 Evolution of the relative proportion and position of the interface between two IDB along the c-axis. 259

Chapter XI

Fig. XI.1 Schematics of the interferences between the wavefront scattered by the object and a reference wavefront.....263
Fig. XI.2 Schematics of the Fourier Transform Holography (FTH) technique.....264
Fig. XI.3 Schematics of the experimental set-up on the I06 beamline (Diamond Light Source).....265
Fig. XI.4 Illustration of the X-ray circular magnetic dichroism (XMCD).....267
Fig. XI.5 Real and imaginary parts of (a) the charge scattering F_0 and (b) the magnetic scattering F_1 at the Fe $L_{2,3}$ edges.....268
Fig. XI.6 Imaging the in-plane magnetisation with FTH.....271
Fig. XI.7 HERALDO schematics.....272
Fig. XI.8 Imaging the in-plane magnetisation in a Py square element. 274
Fig. XI.9 Influence of the tilt angle for the imaging of the in-plane magnetisation.....275
Fig. XI.10 Vortex closure domain in a Py square element at the remanence.....276
Fig. XI.11 Influence on the ratio between the intensity scattered by the slit and the sample.....276
Fig. XI.12 Effect of the "phase optimization" 279
Fig. XI.13 Kerr-hysteresis loop in square Py element.....280
Fig. XI.14 Field-induced displacement of the vortex core and comparisons with micromagnetic modeling.....280
Fig. XI.15 Schematics of the time-resolved experiment 281
Fig. XI.16 Field induced displacement of the vortex core.....282
Fig. XI.17 Reconstruction of the magnetic flux closure for different delays from the rise point of the magnetic pulse.....283
Fig. XI.18 Position of the vortex core for different stages of the precession 284
Fig. XI.19 Nano-contact spin torque oscillator (STO).....286
Fig. XI.20 HERALDO reconstructed image of the magnetisation in the single layer structure for several DC currents applied.....287

Appendix A1

Fig. A1.1 Geometries considered in the simulations. 294
Fig. A1.2 Excess interface energies calculated from various Cu-Ta interface, with a (1 0 1) or (0 0 1) orientation and a varying number of PM layers in the initial configuration.....295
Fig. A1.3 Structure of the most stable Cu-Ta interfaces determined from the values of the excess interface energies.....297
Fig. A1.4 Network of interfacial dislocations for the most stable Cu-Ta interfaces 298
Fig. A1.5 Explanation of the presence of two regimes in the excess interface energy vs number of planes curve for the (1 1 0) orientation.....302
Fig. A1.6 Network of interfacial dislocations in the dewetted islands, for a varying number of PM layers.....303

Introduction

Motivations

This work entitled “Coherent X-ray diffraction applied to metal physics” covers a large scope which needs to be defined. In the approach of the Metal Physics group of SIMaP lab., in which this PhD work is undertaken, a special interest is given to the relationship between the microstructure and the physical properties. The basic motivation of this study consists in asking what can we learn in the light of synchrotron radiation, particularly with coherent X-rays, regarding this relationship.

Indeed, accompanying the technological driving force towards length scale reduction of devices, several fundamental questions arise. In general, modifications of physical properties from bulk behaviour appear when the size of the system is of the same order of magnitude as the characteristic length scale associated with the underlying physical mechanism being probed (*e.g.* mean free path of dislocations in the case of mechanical strength of ductile crystalline materials, or the size of magnetic domains in ferromagnetism, *etc.*).

Our study focuses particularly on the relationship between the structural stability / mechanical response of sub-micron size crystals. This topic is linked to the understanding of crystal defects and structural properties at small scale. Initiated by the seminal work of Brenner in the late 1950's (Brenner 1956) who measured an increase in strength of single crystal metals with decreasing size (mm to a few µm), the interest in small scale materials emerged with the thin film technology, industrially mature in the late 1960's. Understanding the structural stability and mode of growth of thin films is for example well understood through the modelling of defects nucleation (dislocations) and propagation as a function of the layer thickness, in the classical problem of hetero-epitaxial growth of a layer on a substrate with small lattice misfit (Frank & Van der Merwe 1949). More recently, there has been in the last 10 years a renewal of interest in this topic, since it has been evidenced by dedicated mechanical tests and sample preparation that sub-micron size crystals exhibit a different mechanical behaviour as compared to their bulk counterparts (typical length scale between a few µm down to 100 nm, Uchic *et al.* (2004)). The general trend is that reducing the characteristic length scale leads to an increased strength (so called 'smaller is harder'), but a general scaling law is still under debate. In fact, a complete understanding of the scaling law of mechanical stability/resistance can only be obtained if the initial microstructure of the sample is well known, as recalled and well demonstrated by Bei *et al.* (2008). Indeed the initial density and nature of defects in the samples (microstructure) is dependent on the processing route of the sample. It requires to be measured *a priori* and in a non destructive way, since it controls the mechanical response and plastic deformation under a given loading.

To address these questions, we aim at characterizing non destructively the 3D strain field in sub-micron size crystallites (islands / wire shapes), with the ability to identify structural defects and their nucleation in complex mechanical loading. Structural defects will be considered here classically following their characteristic dimension, namely of 1D type (dislocation lines) and 2D (interface such as stacking fault planes, free surface (crystallite - vacuum), heterophase interface (crystallite - substrate)).

Similarly to structural properties, functional properties also exhibit some size dependence. Among them we focus on 2D defects, more precisely the presence and structure of polarity inversion domain boundary in the case of nitride semiconductor and ferromagnetic domain microstructure and dynamics in the case of ferromagnetic materials.

For many years, Transmission Electron Microscopy (TEM) remained almost unchallenged for investigating defects in crystals. Electronic lenses provide direct imaging of the defect structure with a sub-Angstrom resolution which is currently out-of-reach with X-rays and give access to the displacement field with a picometre resolution. However, transmission electron techniques are limited by the weak penetration depth of electrons in the matter which makes difficult the study of objects thicker than 100 nm or buried / embedded in a functional device. The preparation of the required thin sections is somehow destructive and can introduce additional unwanted features, such as specific boundary conditions (free surfaces of the foils) and damage (especially with the use of Focus Ion Beam milling). Additionally, 3D analysis is difficult to carry out, and the

quantitative analysis of the data can be complicated by dynamical effects.
X-ray diffraction techniques are very complementary to TEM techniques; they allow to study objects without any preparation due to the weak interaction of X-rays with matter, foreseeing the possibility to study 3D objects and coupled *in situ* characterization. X-ray diffraction is by nature very sensitive to lattice deformations in Bragg geometry, and very precise strain measurements can be achieved. In X-ray scanning microscopy, the resolution in the direct space is controlled by the size of the beam: In third-generation synchrotron facilities, focused beams of the order of a few tens of nm can be obtained. On the other hand, classical X-ray imaging techniques lack resolution in the real space. The limited resolution of X-ray techniques in the real space can be overcome by the use of Coherent X-ray Diffraction (CXD) which allows to retrieve numerically the lost phase information of the diffracted intensity. This allows to reconstruct 3D sub-micron objects with a spatial resolution of the order of 10 nanometres. In Bragg geometry, the technique is not only sensitive to the electron density of the object but also to the inner displacement field of the object which corresponds to the phase of the complex electron density. From the perspective of solving mechanical equilibrium problems, it gives access to the complete solution of the differential equations of mechanical equilibrium, namely the displacement field. This is enriched by identifying the microstructure of defects which inherently generate phase field discontinuities in the regular crystal lattice.

Experiments and methods

Most of the experimental part of this work was carried out in third-generation synchrotron sources. The experiments can be divided in three main groups:

- Coherent X-ray diffraction for the study of crystal defects and the imaging of 3D displacement fields,
- Fourier Transform Holography coupled with X-ray Magnetic Circular Dichroism in the soft X-ray range to study the magnetic configuration and its dynamics in nanostructures with time resolved experiments.
- Complementary advanced diffraction techniques to characterize the samples like Laue micro-diffraction and *in situ* UHV surface diffraction techniques.

A large number of numerical tools have been used to carry out the analysis of the experimental data. A significant part of them were home-made such as the phase retrieval procedure for the reconstruction of the experimental data or the procedure for the imaging of the magnetic nanostructures by Fourier Transform Holography. Alternatively, some softwares available to the users community such as Rod for the analysis of surface diffraction, LaueTools for Laue micro-diffraction were used.

Model samples have been processed and used in this work. For the study of structural stability and mechanical properties, two systems are mainly investigated: 3D sub-micron crystallites of Cu and Au. They are obtained by controlled solid state dewetting technique, and have specific crystalline orientation relationship with their respective substrates, single crystal Ta (0 0 1) and Al_2O_3 (sapphire) (0 0 0 1). Standard characterization techniques have been used such as optical, electron and atomic force microscopies. Local mechanical loading is achieved by contact mechanics (nanoindentation) either *in situ* or *ex situ* at the laboratory. Samples for the study of functional properties, namely GaN nanowires on Si and permalloy (Fe-Ni) nanostructures are processed by our collaborators.

The originality of this work also lies in the fact that almost all the experiments are supported and somehow transposed numerically by a large amount of numerical simulations: atomic simulations using molecular statics and dynamics (MD) for the study of individual crystal defects and reproducing nucleation in the indentation process, *ab initio* calculations for the precise atomic structure determination of surfaces or interfaces and finite element method for continuum elasticity calculations. Indeed systematic calculations of X-ray scattering from these simulations in the kinematic approximation provides simulated diffraction data to design experiments and better understand the experimental data in reciprocal space but also to evaluate the robustness of phase retrieval algorithms.

Context

This PhD work was carried out in the Metal Physics (PM) group of the laboratory SIMaP. Its activities are focused on metallic materials, dealing mainly with phase transformation, mechanical properties and complex structure materials. Research activities are carried out in synergy with processing, characterization (especially with large scale instruments) and modelling activities. My PhD grant was founded by the Agence Nationale de la Recherche (ANR) in the framework of the MecaNIX project which aims at understanding the mechanical properties of single isolated nanostructures and the influence of size on mechanical properties. It benefits from the partners involved in this project with the SIMaP:

- the laboratory IM2NP in Marseille. Relevant to this work, they developed a portable AFM which was used for the *in situ* nanoindentation experiments described in the Chapter VI of this manuscript,
- the INAC institute of the CEA in Grenoble, in charge of the processing and characterization of the semiconductor nanostructures (GaN, GaAs).
- Beamline ID01 of the European Synchrotron Radiation Facility, where most of the CXD experiments were performed,
- the Max Plank Institute (Stuttgart) which provided metallic nanowires for several CXD experiments,
- the LPS (Laboratoire de Physique du Solide), which pioneered the study of crystal defects by CXD.

Outline of the manuscript

This manuscript is divided in four parts:

- The first two chapters present the theoretical concepts and experimental methods. The first chapter introduces the basics of Coherent X-ray Diffraction, with a focus on Coherent Diffraction Imaging (CDI) technique to reconstruct 3D displacement fields of isolated samples in Bragg geometry. In the Chapter II, the experimental methods and techniques are presented. Typical experimental set-ups to perform CXD experiments and surface diffraction experiments are described. The samples are then presented along with their processing and characterization techniques.
- The second part deals with a study of dislocations in face-centred cubic crystals using CXD (Chapter III to VI). At first a complete survey of signatures of individual dislocations in reciprocal space are established in Chapter III. Then the effect of microstructures of dislocations are evaluated in reciprocal space, specifically in the case of indentation of a crystallite, Chapter IV. In Chapter V numerical reconstruction for real space evaluation of individual and collective dislocations are presented and discussed. Chapter VI details experiments of *in situ* indentation of a gold crystallite, with the observation and reconstruction of defect nucleation and 'mechanical annealing'.
- The third part (Chapter VII-IX) is dedicated to the induced effect of surface and interfaces on the displacements field in small particles: it starts in Chapter VII by a detailed study of a twinned gold particle, where the sensitivity of CXD to the surface strain induced by free surfaces relaxation is discussed. Chapter VIII and IX concern a detailed study of the specific hetero-epitaxial interface (f.c.c./b.c.c.) of the Cu/Ta system obtained by dewetting. Epitaxial Cu crystallites on Ta were previously studied by CXD in the lab. (Beutier *et al.* 2013a) and exhibit very large residual stress associated with the interfacial strain. At first, Chapter VIII gathers experiments of *in situ* surface diffraction experiments and *ab initio* calculations to determine the structure of the Cu wetting layer in this Stransky-Krastanov system. Then the structure of the interface within the crystallites is investigated by MD simulations and the impact of the atomic structure of this interface on the distribution of the displacement field obtained by CXD is discussed.
- The last part gathers the results related to defect imaging for functional properties and focuses on our contribution to these experiments. Chapter X concerns the imaging of polarity inversion domain boundary in GaN semiconductor nanowires, and essentially consists in a 3D reconstruction of the domain structure along the wire. Chapter XI deals with magnetic configuration and dynamics in in-plane

magnetized permalloy (Fe/Ni) nanostructures, which are investigated by Fourier Transform Holography. In a first part of this Chapter, the technique is briefly presented and the detailed magnetic configuration of the permalloy layer is presented. Then the magnetization dynamics of the system are studied by time-resolved synchrotron experiments.

Bei, H., Shim, S., Pharr, G. M., & George, E. P. (2008). *Acta. Mater.* **56**, 4762-4770.

Beutier, G., Verdier, M., Parry, G., Gilles, B., Labat, S., Richard, M. I., Cornelius, T., Lory, P. -F., Vu Hoang, S., Livet, F., Thomas, O. & De Boissieu, M. (2013a). Thin Solid Films 530, 120-124.

Brenner, S. S. (1956). *J. Appl. Phys.* **27**, 1484.

Frank, F. C. & Van Der Merve, J. H. (1949). *Proc. Roy. Soc. Lond. Ser. A* **198**, 205-216.

Uchic, M. D., Dimiduk, D. M., Florando, J. N. & Nix, W. D. (2004). *Science* **305**, 986-989.

Contents

Introduction....5
I.1 Coherence....5
I.1.1 Mutual coherence....5
I.1.2 Coherence lengths....6
1.2 Scattering of a coherent X-ray beam....8
1.2.1 General case....8
I.2.2 Exploiting Coherent X-ray Diffraction....9
I.2.3 Coherent X-ray Diffraction in Bragg geometry....10
I.3 Modelling Coherent X-ray Diffraction from micro- and nanoscale crystals....12
I.3.3 Advantages of the atomic description....13
I.3.4 Fast Fourier Transform vs direct computation of the kinematic sum for the study of crystal defects....15
I.4 Coherent Diffraction Imaging....19
I.4.1 The phase problem....19
I.4.2 Holography....20
I.4.3 Coherent Diffraction Imaging with phase retrieval algorithms....20
I.4.3.1 Oversampling....20
I.4.3.2 General formalism of phase-retrieval algorithms....21
I.4.3.3 Finite support constraint and Error-Reduction (ER algorithm)....22
I.4.3.4 Hybrid-Input-Output (HIO) algorithm....23
I.4.3.5 Support determination, Shrink wrap algorithm....23
I.4.3.6 Recent improvements on the phase retrieval procedure....24
I.4.4 Correction for artefacts related to experimental conditions....25
I.4.4.1 Reciprocal space offsets....26
I.4.4.2 Refraction effects....26
I.4.4.3 The wavefront problem....26
I.4.5. Numerical study, case of defective samples....27
I.4.5.1 Comparisons between reconstructions for several Bragg reflections....27
I.4.5.2 Extent of the reciprocal space pattern, resolution and oversampling conditions....32
Conclusion....36
Bibliography....37

Chapter I: Basics of Coherent X-ray Diffraction

Introduction

Coherent X-ray Diffraction (CXD) is the central technique used in most of the experiments presented in this manuscript. The main concept of CXD are exposed in this chapter. In a first part, the concept of coherence is discussed, and the detailed characteristics of a coherent X-ray beam are presented. In the following section, the sensitivity of coherent X-ray beams to crystal defects and strain is explained. The best strategies to compute the diffraction from highly strained and defective crystals are discussed. Numerical examples of systems containing simple defects are given.
The technique of Coherent Diffraction Imaging which relies on phase retrieval algorithms is presented in section I.3. The concept of oversampling is explained in extensive details, and conventional phase retrieval algorithms as well as recent improvements with the technique are given. Numerical examples of reconstructions focused on the case of single defects conclude this chapter.

I.1 Coherence

Simply speaking, coherence is the ability of a wave packet to produce interference. It requires that the different waves in the packet have a finite phase relationship. To take two extreme cases, the light from a bulb is highly incoherent while that of a laser beam is highly coherent. The emission process is at the origin of coherence. In the X-ray range, we can find also two extreme cases: the X-ray tube and the Free-Electron Laser.
Electromagnetic beams are in the general case neither fully incoherent nor fully coherent: there is always some degree of coherence. This is for instance the case of X-ray tubes, otherwise crystallographic diffraction would not be possible at all.
The coherence of a beam is by nature anisotropic in space: the propagation direction of the beam has coherence properties differing from those of the transverse directions. Moreover, the coherence can also be anisotropic in the plane transverse to the propagation direction, if the emission process is anisotropic (such is the case for undulators).

I.1.1 Mutual coherence

A general way to quantify the coherence of the beam is the mutual coherence function (Born & Wolff, 1980):

$$\Gamma(\rho_1,\rho_2,\tau)=\langle E(\rho_1,t)E^*(\rho_2,t+\tau)\rangle \quad \text{(I.1)}$$

where $E(\rho,t)$ is the electromagnetic field at position ρ and instant t. The brackets denote the time-averaging (or expectation value if we consider a quantum description of the electromagnetic field). The mutual coherence is thus the autocorrelation in time and space of the electromagnetic field. $\Gamma(\rho, \rho, \tau)$ is the auto-correlation in time of the field at position ρ; if the delay τ is set to zero, $\Gamma(\rho, \rho, 0)$ is simply the intensity $I(\rho)$.
The normalized version of the mutual coherence function (MCF), also known as the complex degree of coherence, can be defined as:

$$\gamma(\rho_1,\rho_2,\tau) = \frac{\Gamma(\rho_1,\rho_2,\tau)}{\sqrt{\langle I(\rho_1,t)\rangle\langle I(\rho_2,t)\rangle}} \quad \text{(I.2)}$$

where $\langle I(\rho,t)\rangle$ is the expectation value of the intensity at the position ρ of the field. The complex degree of coherence $\gamma(\rho_1, \rho_2, \tau)$ has values between zero and one. If it is equal to zero, the points ρ_1 and ρ_2 are mutually incoherent (no interference at all) while full coherence is achieved when it is equal to one. In practice, when the electromagnetic field is generated by a single stable source (which can be extended), one considers that the degree of coherence is homogeneous in space and time, *i.e.* $\gamma(\rho, \rho+\delta, \tau) = \gamma(0, \delta, 0)$ for any ρ and τ (note that it does not apply to Γ, otherwise the beam would be infinite).
The 2D mutual coherence can be measured in experiments of the type of Young's double slit experiment. The visibility of the interference fringes is proportional to the complex-degree of coherence. Such measurement is well suited to undulator radiation (Takayama *et al*, 1998). A more refine way to perform this measurement by scanning a large range of separation δ in a single measurement is to use a uniformly redundant array (Lin *et al*, 2003).
There are alternative ways to characterize the coherence of the beam, for instance by measuring the diffraction from a pinhole (Beutier *et al*, 2007) or the speckle pattern from random scatterers (Livet, 2007).

I.1.2 Coherence lengths

The complex degree of coherence provides a comprehensive measurement of the coherence, but it is a 7-dimensional quantity according to Eq. (I.2) (2x3 space coordinates and 1 time coordinate). It is convenient to refer to simpler scalar quantities, and it is actually possible to define such quantities when dealing with a 'nice' beam (a Gaussian beam for instance, which is not a bad approximation for undulator radiation). In such case, one can consider that the complex degree of coherence $\gamma(\rho, \rho+\delta, \tau)$ is homogeneous and decreasing in the 3 space directions (*x*,*y*,*z*), which are decoupled. Then it is possible to define coherence lengths, for instance as the half width at half maximum (Lin *et al*, 2003). Alternatively to such interferometric measurements, the coherence lengths can be estimated (and even defined) in the framework of geometrical optics, as presented below.
The coherence along the propagation direction is called the longitudinal (or temporal) coherence length. In the case of synchrotron radiation, the anisotropy of the source requires separating the horizontal and vertical coherence lengths.

The longitudinal coherence of the beam is related to the monochromaticity of the X-ray beam. If two waves with a wavelength differing by Δλ are in phase at a given position, the phase-shift between them gradually increases with the distance, eventually reaching a distance where they are in phase opposition (Fig. I.1.a). It is usual to define this distance as the longitudinal coherence length ξ_l, if Δλ if the spread of the wave packet:

$$\xi_l = \frac{\lambda^2}{2\Delta\lambda} = \frac{1}{2}\frac{\lambda}{\Delta\lambda}\lambda \quad \text{(I.3)}$$

It can be understood in the following way: if all the amplitudes (assumed with equal magnitude) within the spread Δλ are summed, the total amplitude vanishes at $2\xi_l$ and the phase is undefined.
According to Eq. (I.3), the better the monochromaticity, the larger the longitudinal coherence. Similarly, the larger the wavelength, the larger the longitudinal coherence: it is advantageous to use softer X-rays if possible. In a typical synchrotron experiment at mid energy (λ~1 Å), with a Si(111) double crystal of bandwidth $\Delta\lambda/\lambda \sim 10^{-4}$, the longitudinal coherence length is $\xi_l \sim 0.5$ µm. It can be increased by using monochromators with narrower bandwidth such a Si(311), but at the price of flux.

The transverse coherence lengths can be defined from the diffraction limit: a linear source of size *S* scatters in

the far field a cone of emission of opening λ/S, which has size $\lambda L/S$ at a distance L (Fig. I.1.b). A common definition of the transverse coherence length is thus:

$$\xi_t = \frac{\lambda L}{S} \tag{I.4}$$

This definition can be extended to the case of a two-dimensional source by considering two distinct coherence lengths. Eq. (I.4) shows that the coherence length:

- increases with the distance, which is a motivation for building long beamlines,
- decreases with the source size, which is a motivation for reducing the horizontal spread of electron bunches in storage rings
- increases with the wavelength, which is again in favour of softer X-rays.

If we consider a source size of 100(H)x10(V) µm² (it is the order of magnitude for sources in 3rd generation storage rings), at λ=1Å and 100 m from the source, we have coherence lengths of 100 µm (H) and 1 mm (V). In practice, these are optimistic estimates.

In order to better control the transverse coherence, it is common to define a secondary source by inserting slits (Robinson 2008).

Moreover, when focusing optics are used, the transverse coherence lengths are reduced by the same demagnification factor as the size of the beam (Schroer *et al.* 2008).

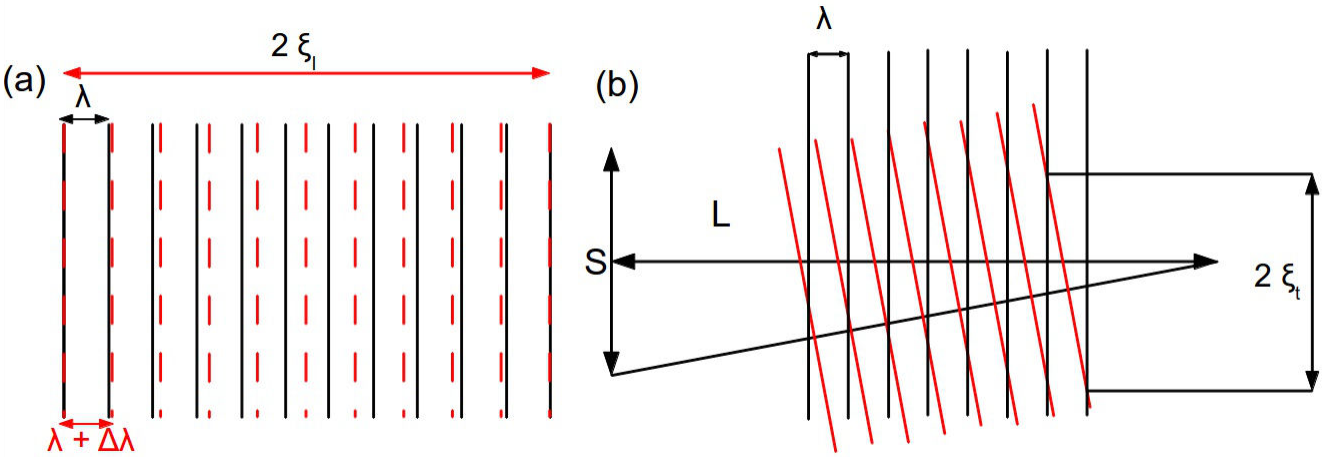

Fig. I.1 *Illustration of the coherence length.* (a) Longitudinal (temporal) coherence (b) Transverse (spatial) coherence

In this manuscript we will thereafter call incoherent a beam which is much larger than its transverse coherence lengths, and coherent a beam with coherence lengths at least of the same order as its size. The case of partial coherence is not considered here, although it is relevant for applications such as X-ray Photon Correlation Spectroscopy, because the best compromise between flux and coherence is usually far from the optimal coherence. In the case of Coherent Diffraction Imaging, it has been shown that the effect of partial coherence can be corrected (Clark *et al*, 2012), in particular in the more particular case of ptychography (Burdet *et al*, 2015). The best compromise between flux and coherence is much debated and depends on the sample, in particular when it is sensitive to radiation damage or if the stability of the set-up becomes a limiting factor. In the work presented here, we always used a very coherent beam, because the reduced flux was not a problem and the measurements could be done in a reasonable amount of time.

Synchrotron radiation is a poorly coherent source: while individual electrons emit coherent radiation at each pole of the undulator, there is little coherence between the waves emitted by the different electrons in a bunch, and

none between different bunches. This is the big difference with a Free-Electron Laser, in which the Self-Amplified Stimulated Emission (SASE) ensures a good coherence between the electrons of a bunch, providing an increase of several orders of magnitude of the brilliance (Pellegrini & Stöhr, 2003). All the work reported in this manuscript was performed at 3rd generation synchrotron facilities, and it was therefore necessary to extract a coherent X-ray beam out a very poorly coherent beam. This is done by inserting slits whose gaps match the transverse coherence lengths. Since the transverse coherence lengths is reduced by focusing, the slits are usually inserted before the microfocusing optics (Mastropietro *et al*, 2011).

1.2 Scattering of a coherent X-ray beam

1.2.1 General case

One can define a coherence volume according to the three coherence lengths. Roughly speaking, when a sample scatters an incoherent beam, one can consider that a large number N of 'domains' defined by the coherence volume scatter incoherently: the waves $A_i(\boldsymbol{q})$ scattered by the different domains are summed in intensity, not in amplitudes (Fig. I.2.a):

$$I(\boldsymbol{q}) = \sum_{i}^{N} |A_i(\boldsymbol{q})|^2 \tag{I.5}$$

Such measurement provides statistical information on the measured property (the lattice spacing in the case of diffraction), such as its mean value and its standard deviation, but the properties of individual domains are lost.

Conversely, using a coherent beam is equivalent to selecting a single coherence volume, hence (Fig. I.2.b):

$$I(\boldsymbol{q}) = |A(\boldsymbol{q})|^2 \tag{I.6}$$

such that the property of the selected volume is measured. In principle, the inhomogeneity of this property is encoded in the scattering pattern, and we discuss later in this chapter how to retrieve it. Because of the absence of averaging effect, the pattern displays sharp intensity fluctuations: if the sample consists of an assembly of random scatterers, the scattering pattern is an isotropic 'speckle' pattern (Sutton *et al*, 1991). When the sample is smaller than the coherent beam, fringes related to the shape of the object can also be observed.

In the kinematic approximation of scattering, which is justified in our case because we study small crystals (<1 μm) with a distorted lattice, the scattered amplitude is the Fourier transform of the atomic scattering factor *f* and the intensity is its square modulus:

$$I(\boldsymbol{q}) = |A(\boldsymbol{q})|^2 = |FT\{f(\boldsymbol{r})\}|^2 = \left|\int f(\boldsymbol{r}) e^{2i\pi \boldsymbol{q}.\boldsymbol{r}} \boldsymbol{dr}\right|^2 \tag{I.7}$$

where the integration is performed on the illuminated volume. Refraction and absorption effects are left aside of this discussion.
Note the convention for the sign and the 2π factor in the complex exponential of Eq. I.7: this convention is used throughout the manuscript. The numerical values of $\boldsymbol{q}$ given in this document follow this convention, i.e. the 2π factor is not included. It should be noted that the sign is opposite to that used in the definition of the Fourier transform in most computational packages (Matlab, numpy for python...) and this difference is taken into

account in the results presented in this document (i.

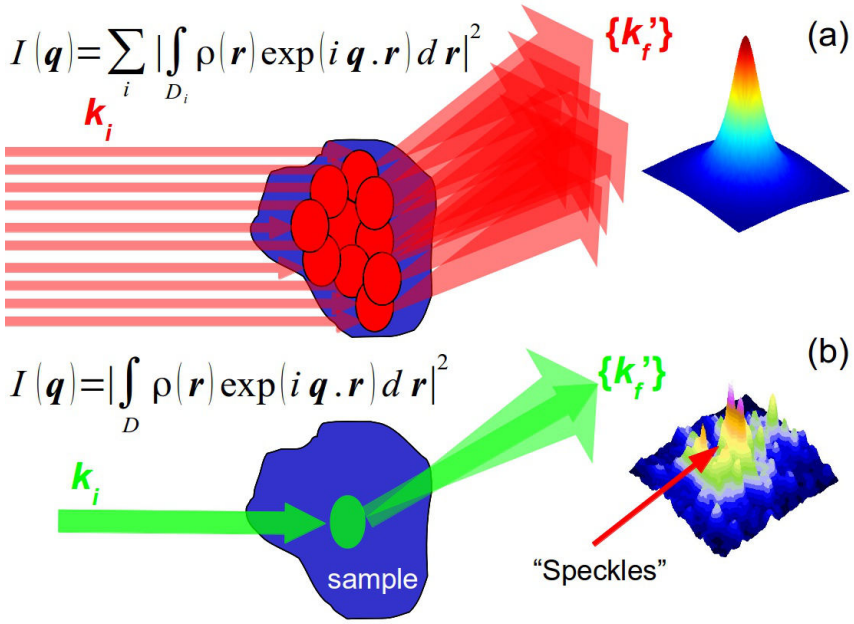

Fig. I.2 *Differences in the scattering of an incoherent X-ray beam (a) and a coherent X-ray beam (b)*

Coherent X-rays can be used in various geometries, depending on the problem to investigate.
In the small angle regime, the speckle pattern usually reveals inhomogeneities of the electronic density, such as the case of particles embedded in a matrix (Mainville *et al*, 1997). However, it is also possible to observe the inhomogeneity of magnetisation in a ferromagnetic material by tuning the energy of the beam to an appropriate absorption edge (Eisebitt *et al*, 2003). This combination of coherence and resonance is exploited in Chapter XI to image magnetic vortices in nanostructures.
The reflection geometry is well suited to the study of surfaces (Pierce *et* al, 2009, Livet *et al*, 2011). Again, it can be used at a resonant edge to study magnetic nanostructures (Chesnel *et* al, 2002, Beutier *et al*, 2009). The Grazing incidence geometry (GISAXS) can also be exploited for nanoparticles on a surface (Streit *et al*, 2007).
Finally, in Bragg geometry, coherence is useful to study the inhomogeneity of crystalline order, such as chemical order (Brauer *et al*, 1995), strain (Robinson & Harder, 2009), polarity (Labat *et al*, 2015) and magnetic order (Yakhou *et al*, 2001).

I.2.2 Exploiting Coherent X-ray Diffraction

Coherent X-ray scattering methods were first developed for the study of speckle dynamics, in technique called X-ray Photon Correlation Spectroscopy (XPCS): based on an assumption of bijection between the scattering function and its Fourier transform, the dynamics in real space can be inferred from the dynamics measured in reciprocal space (Sutton, 2008). This technique is well suited to the study of slow dynamics, since it is measured in the time domain, hence bounded by the time scale of the measurements. It is complementary to inelastic scattering techniques, which access faster dynamics by measuring in the energy domain. In practice, the bijection is not true if the incident beam is not perfectly coherent, which is common in XPCS because it is more

efficient to increase the flux at the price of coherence. The partial coherence is nevertheless accounted for in the data analysis.
There is also an interest in studying static systems, because the CXD pattern reveals the inhomogeneity of the scattering function: in simple cases, defects can be identified directly from their reciprocal space signature (Le Bolloc'h *et al*, 2005). This is the subject of Chapters III & IV, in which we provide an extensive study of the signature of typical crystal defects.
A third way to exploit CXD is to retrieve the phase of the scattered amplitude in order to turn it into an imaging technique. This can be done essentially in two different manners: either by encoding the phase by interference with a reference wave (holographic method, Eisebitt *et al*, 2004, Chamard *et al*, 2010b), or by using phase retrieval algorithms in combination with a sufficiently oversampled diffraction pattern (Miao *et al*, 1999, Williams *et al*, 2003). The holographic case is discussed in details in Chapter XI, where it is applied to image magnetic systems. The algorithmic method, known as Coherent Diffraction Imaging (CDI), is presented in this chapter and used throughout this manuscript.
Finally, X-ray Free-Electron Lasers now allow the combination of real space imaging using CDI with dynamical measurements, so far only in pump-probe mode (Clark *et al*, 2013).

I.2.3 Coherent X-ray Diffraction in Bragg geometry

The Bragg geometry probes the crystalline order. Coherent X-rays can be shined in Bragg geometry to investigate the deviation of the sample to a perfect crystal order.
If the crystal is not perfect, we define $\boldsymbol{r_0}$ the positions of a perfect lattice that approximates the crystal and $\boldsymbol{u}(\boldsymbol{r})$ the displacement of the atoms from this perfect lattice, such that $\boldsymbol{r} = \boldsymbol{r_0} + \boldsymbol{u}(\boldsymbol{r})$. Now we consider a Bragg reflection with a diffraction vector $\boldsymbol{g}$ (defined on the perfect lattice which approximates the crystal) and we focus on the region of reciprocal space in the vicinity of $\boldsymbol{g}$. We can decompose the phase factor in the exponential of Eq. I.7:

$$\boldsymbol{q}.\boldsymbol{r} = \boldsymbol{q}.\boldsymbol{r_0} + \boldsymbol{g}.\boldsymbol{u}(\boldsymbol{r}) + (\boldsymbol{q}-\boldsymbol{g}).\boldsymbol{u}(\boldsymbol{r}) \tag{I.8}$$

The third term of Eq. I.8 can be neglected in the exponential of Eq. I.7 if $|(\boldsymbol{q}-\boldsymbol{g}).\boldsymbol{u}(\boldsymbol{r})| \ll 1$ (Takagi's approximation), which is equivalent to assuming small distortions of the lattice and a restricted extent of the reciprocal space. This approximation is discussed later in this Chapter. Following Takagi (1969), Eq. I.7 can now be approximated by:

$$I(\boldsymbol{q}) = |A(\boldsymbol{q})|^2 = \left|\int \tilde{f}(\boldsymbol{r_0}) e^{2i\pi \boldsymbol{q}.\boldsymbol{r_0}} \boldsymbol{dr_0}\right|^2 = |FT\{\tilde{f}(\boldsymbol{r_0})\}|^2 \tag{I.9}$$

with the modified scattering factor:

$$\tilde{f}(\boldsymbol{r}) = f(\boldsymbol{r}) e^{2i\pi \boldsymbol{g}.\boldsymbol{u}(r)} \tag{I.10}$$

in the work presented here, the Bragg case is used only in non-resonant scattering, such that the atomic scattering factor is essentially the electronic density $\rho(\boldsymbol{r})$, which is a real scalar, and the modified scattering factor is referred as the complex electronic density $\tilde{\rho}(\boldsymbol{r})$: its modulus is the real electronic density and its phase encodes the projection of the displacement field $\boldsymbol{u}(\boldsymbol{r})$ onto the diffraction vector $\boldsymbol{g}$.
The phase term can be understood simply by considering a block of material which is displaced from the rest of the lattice by a vector $\boldsymbol{u}(\boldsymbol{r})$ (Fig. I.3). The phase of the X-ray wave scattered by this block of atoms is shifted relative to the rest of the reference crystal by an amount $\varphi/2\pi = \boldsymbol{k_f}.\boldsymbol{u} - \boldsymbol{k_i}.\boldsymbol{u} = \boldsymbol{g}.\boldsymbol{u}$. Provided that a complex image of the sample is obtained (for instance by Coherent Diffraction Imaging, as described later on), the phase shift

appears in the final image as a region of complex density with the same magnitude as the rest of the crystal (same electronic density) but a different phase.

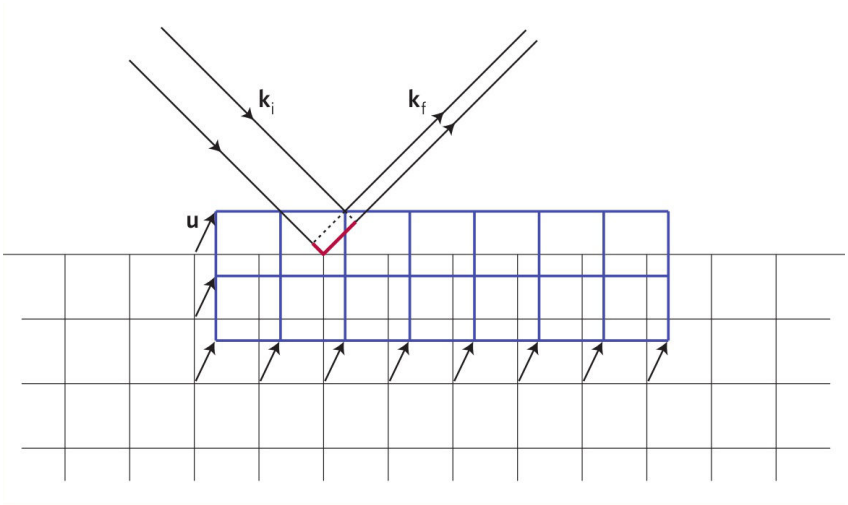

Fig. I 3 *Sensitivity of coherent x-ray diffraction to lattice displacements* (from Robinson & Harder, 2009)

The effect of the displacement field and of the corresponding phase on the CXD pattern can be understood as follows. For an ideal crystal which can be described by a perfect lattice, the intensity distribution is a periodic function of the reciprocal space: the intensity distribution is identical around every Bragg peak. Moreover, if the atomic scattering factor is real (to a constant phase), which is the case in non-resonant conditions, the diffraction pattern is symmetrical about the origin of the reciprocal space, therefore also about each node of the reciprocal lattice. These local inversion symmetries are lost (except around the origin) with the introduction of an inhomogeneous displacement field, which can be mathematically understood from the inhomogeneous phase of the complex electronic density. When non-symmetric diffraction patterns are observed around a Bragg reflection $\boldsymbol{g}$, it can be decomposed into symmetric and antisymmetric parts. The symmetric part can be considered to originate from the average electron density $\overline{\rho(\boldsymbol{r})}$ while the antisymmetric part is associated with the real space phase, equal to the displacement field projected onto the reciprocal lattice vector $\boldsymbol{g}$ of the local Bragg peak (Vartanyans & Robinson 2001). The asymmetry of the Bragg peak induced by the displacement field is illustrated in Chapter III and IV of this manuscript.

Since the phase depends on the projection of the displacement field onto the Bragg reflection, non-coplanar Bragg reflections give access to distinct components of the displacement field. In the 3D case, 3 non-coplanar reflections are needed to perform a full vectorial analysis of the displacement field.

For a Bragg peak symmetric to the crystal surface (specular reflection), the diffraction peak will only be sensitive to the $u_z(x,y,z)$ component of the displacement field (z is the direction normal to the substrate surface). This geometry is employed in most of the experimental studies presented in this manuscript (Chapter VI and VII).

For a (1 1 1) out-of-plane orientation (case of the gold islands on the sapphire substrate, Chapter VII), the (1 1 1) planes are parallel to the surface of the sample, it gives :

$$\boldsymbol{g}.\boldsymbol{u} \;=\; g_{111}.u_z(x,y,z) \tag{I.11}$$

The intensity measured at the vicinity of the 1 1 1 Bragg reflection is thus given by:

$$I(\boldsymbol{q}) \simeq |FT\{\rho(\boldsymbol{r})e^{i\frac{2\pi}{d_{111}}u_z(x,y,z)}\}|^2 \quad \text{(I.12)}$$

where d_{111} is the distance between two successive (1 1 1) planes.

The only assumption on the displacement field made so far is that it fulfils Takagi's approximation: $|(\boldsymbol{q}-\boldsymbol{g}).\boldsymbol{u}(\boldsymbol{r})| \ll 1$, but there is no restriction on its nature and origin: it concerns continuous displacement fields such as elastic strain as well as discontinuous fields such as stacking faults, dislocation cores and chemical inversion domains.
In the case of a crystal with many defects, the interference between the waves scattered by each perfect domain of the crystal produces a complex speckle pattern such as that shown in Fig I.2.b. In crystals containing a low density of defects, only few domains of the particle are phase shifted with respect to each other. The diffraction pattern is far less complex and the complete identification of the defect becomes possible by analysing its fingerprint on the diffraction pattern. This is object of Chapter III and IV.

I.3 Modelling Coherent X-ray Diffraction from micro- and nanoscale crystals

Modelling of CXD from a micro- or nanoscale crystal consists mainly in two separate tasks:

1) Modelling the crystal, including its shape, strain and defects. This task is explained in more details in Chapter III.
2) Modelling the diffraction itself, *i.e.* computing Eq. I.7. This is the point that we address here.

Eq. I.7 relies on the Fourier transform and implies a continuous integration in the illuminated volume. It is necessary for computation to adopt a discrete description of the crystal. While the atomic description is the most natural choice, the size of the system to describe is at the limit of what modern personal computers can handle. This is nevertheless the method that has been used in most of the calculations of this work. As we show below, a crystal of a few tens of nanometres in size (~10^6 atoms) can be handled by modern Graphical Processing Units (parallel computing cores). In that case, Eq. I.7 is computed directly using the discrete expression of the Fourier transform:

$$I(\boldsymbol{q}) = |A(\boldsymbol{q})|^2 = |FT\{f(\boldsymbol{r})\}|^2 = |\sum_j f_j e^{2i\pi \boldsymbol{q}.\boldsymbol{r}_j}|^2 \quad \text{(I.13)}$$

where the index j runs over the atoms of the crystal.

Note that for larger systems, the scale of discrete description of the crystal must be larger than the atomic distance. In that case it is necessary to model the crystal on a larger periodic grid and to use Eq. I.9 (Takagi's approximation) with the help of a Fast Fourier Transform (FFT):

$$I(\boldsymbol{q}) = |A(\boldsymbol{q})|^2 = |FFT\{\tilde{f}_j\}|^2 = |\sum_j \tilde{f}_j e^{2i\pi \boldsymbol{q}.\boldsymbol{r}_j}|^2 \quad \text{(I.14)}$$

Here the description on a grid of larger period than the crystallographic cell implies a redefinition of the complex scattering factor:

$$\tilde{f}_j = \sum_{a \in supercell_j} f_a e^{2i\pi \boldsymbol{g}.\boldsymbol{u}_a} \approx N_j S_j(\boldsymbol{g}) e^{2i\pi \boldsymbol{g}.\boldsymbol{u}_j} \quad \text{(I.15)}$$

where N_j is the number of crystallographic cells in the supercell j, $S_j(\boldsymbol{g})$ is the structure factor of the crystallographic cell et u_j is the average displacement of the supercell. The second part of Eq. (I.15) assumes that the displacement field is locally constant and that the crystal structure is locally homogeneous. In fact, the structure factor is often independent of the supercell and can be factorised out of the sum in Eq. (I.14). In that case N_j is also independent of the cell j.
In the case of f.c.c. crystals reported here, $S(\boldsymbol{g}=(h,k,l))$ vanishes if h, k and l are not all of the same parity.

I.3.3 Advantages of the atomic description

The calculation speed of FFT is optimal for the calculation of the scattering from large crystalline structures. For N points in the real space, N points in the reciprocal space are calculated with a cost proportional to $N.log(N)$ instead of N^2 for the direct computation of the kinematic sum. As discussed above, the Takagi approximation is limited to a very small extent of the reciprocal space for highly strained crystals.
It is thus interesting to consider the direct computation of Eq. (I.13) since it allows the computation of any assembly of points in the reciprocal space, and of any structural model (no matter how severely strained or disordered they are).
The direct calculation of the kinematic sum can be achieved in a reasonable amount of time using a Graphical Processing Unit (GPU) for the computation (Favre-Nicolin *et al.* 2011). In a few words, it is possible to considerably increase the calculation speed of any calculation provided that it is highly parallel (same formula applied to large amount of data), the number of memory transfers is much smaller than the number of mathematical operations. It is clear that Eq. I.13 fulfils all the requirement for a GPU implementation, provided that both the number of atoms and reciprocal space points are large (>> 1000). A significant part of the scattering simulations presented within this work has been performed using the software PyNX (Favre-Nicolin *et al.* 2011), based on this GPU implementation.

The speed achieved with the GPU calculation is shown in Fig. I.4. A strong dependency of the speed of the GPU calculations with the number of reflections and the number of atoms per-second is observed. The maximum calculation speed is reached for a number larger than 10^4 for both quantities. Depending on the GPU, the calculation speed is between 2 and 3 orders of magnitude faster than a calculation performed using a single CPU. The calculation speed increases linearly with the number of cores for the GPU.

Most of the calculations presented in this work were performed using two different GPU's:

- a Geforce GTX 580, slightly more powerful than the GTX 295 which was employed for Fig. I.4
- a Quadro 2000M, a GPU from a relatively powerful laptop.

The Quadro 2000M has 192 cores while the GTX 580 has 512 cores. A maximum calculation speed of 5.2×10^{10} reflections.atoms.s^{-1} is achieved by the latter, while the calculation speed is "only" 1.9×10^{10} reflections.atoms.s^{-1} for the Quadro 2000M. This confirms the linear increase of the calculation speed with the number of GPU cores.

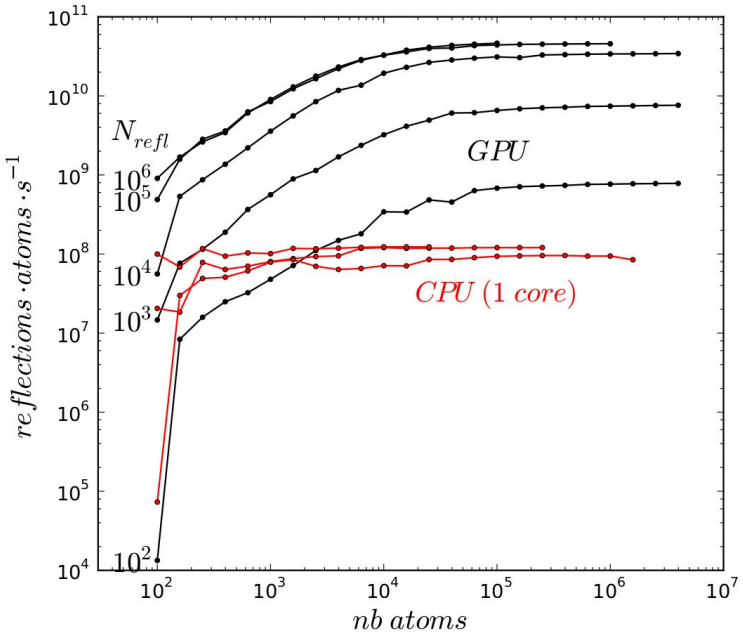

Fig. I.4 *Comparison of the computing speed for a single CPU and a GPU depending on the number of atoms and reflections (from Favre-Nicolin, 2011)*

A typical configuration used in this work (Chapter III) contains approximately 10^6 atoms, and the scattering from such structure is calculated on an extent of 100x100x100 reciprocal space points. This corresponds to 10^{12} atoms.reflections. The calculation is achieved for this configuration in 25 seconds with the GTX 580 and 60 seconds with the Quadro 2000M. These values are in good agreement with the calculation speeds given above.
Even for large systems, Eq. (I.13) can thus be computed in a very reasonable amount of time, including with a laptop equipped with a suitable GPU.

However, for very large systems, the FFT calculation is still significantly faster. It is thus important to determine if the direct computation of the kinematic sum is necessary to obtain a precise computation of the scattering.
It is clear that the scattering from highly disordered systems can only be obtained by the computation of Eq. (I.13). However, such systems are not addressed in this manuscript. The case of highly strained systems is presented in Chapter VIII and IX which are dedicated to the Cu-Ta system.
For this highly strained system, the criterion $|(\boldsymbol{q}-\boldsymbol{g}).\boldsymbol{u}(\boldsymbol{r})| \ll 1$ is not valid for some combinations of $\boldsymbol{q}$ and $\boldsymbol{r}$ for this system. .Nevertherless, the computation of Eq. (1.9) with a FFT gives a result in reasonably good agreement with the direct computation of Eq. (I.7) as shown by Beutier (2013a).
Most of the configurations considered in this manuscript exhibit a residual strain significantly smaller than the Cu-Ta system, and it is a reasonable assumption to consider that the FFT calculation is adapted to such weakly strained systems.
A significant part of this manuscript (Chapter III to VII) is dedicated to the study of typical crystal defects using coherent X-ray diffraction. An atomistic description of the matter is provided, relying on the use of interatomic potentials combined with molecular dynamics calculations. An important question to address is to determine the best and most efficient computation method for the study of such defects.
It is clear that large strain fields are induced at the vicinity of crystal defects. However, this does not necessarily prevent the use of Eq. (I.14) to compute the scattering. If the analytical expression of the displacement field of the defect is already known, this method can be in fact very efficient. This will be discussed in the next section.

However, in most of the cases presented in the next chapter, the displacement field is obtained from the positions of the atoms, after the relaxation of the atomic configurations. In this case, the analytical expression of the displacement field is unknown.
In order to compute the scattering using Eq. (I.14)., the displacement field would need to be interpolated on a regular grid. Given the number of atoms in the simulations (up to 10^7) , this grid would not be fine enough to resolve the atomic positions. Additionally, given the large strain fields involved in the vicinity of the dislocations, the calculation method would be probably less precise than the direct computation of the kinematic sum given in Eq. (I.13). Given the short calculation times achieved thanks to the GPU implementation of the computation of Eq. (I.13), the interpolation procedure itself would take more time than the direct calculation of the scattering using the kinematic sum. In the case of an atomistic model is used in the simulations, the direct computation of the kinematic should be obviously preferred. The only case where the use of the FFT method could become more adapted would be for very large systems (more than 10^7 atoms), when the computation of Eq. (I.13) becomes time consuming, even using modern GPU's.

I.3.4 Fast Fourier Transform vs direct computation of the kinematic sum for the study of crystal defects

In this sub-section, the scattering from systems containing simple crystal defects, whose displacement field can be calculated analytically, are computed using Eq. (I.14) (FFT calculation). The results are compared to the scattering obtained from the computation of Eq. (I.13).
We consider a model 2D crystal of square shape with x and y axes corresponding to the [1 1 0] and [1 1 1] f.c.c. crystallographic directions respectively. The crystal is described by a 256 x 256 grid with a period corresponding to the crystallographic unit cell. An infinite z direction parallel to $[\bar{1}\ \bar{1}\ 2]$ is implicitly considered.
A perfect edge dislocation is introduced at the centre of the crystal, with a Burgers vector $\boldsymbol{b} = ½[1\ \bar{1}\ 0]$ parallel to x and the dislocation line $\boldsymbol{t}$ runs along the infinite direction z. We use the analytical formula of the displacement field given by Hirth and Lothe (1968) in the hypothesis of an isotropic and semi-infinite volume. Here the latter hypothesis is not fulfilled but it is not important for the question addressed here. The analytical displacement field is constant along the dislocation line: $u_z = 0$ and depends only on two components:

$$u_x = u\|b = \frac{b}{2\pi}\left[\tan^{-1}\frac{y}{x} + \frac{1}{2(1-\nu)}\frac{xy}{(x^2+y^2)}\right] \quad \text{(I.16)}$$

$$u_y = u\|(b\times t) = -\frac{b}{8\pi(1-\nu)}\left[(1-2\nu)\ln(x^2+y^2) + \frac{(x^2-y^2)}{(x^2+y^2)}\right] \quad \text{(I.17)}$$

where ν is the Poisson ratio.
The phase $\varphi_{20\bar{2}} = \boldsymbol{g}_{20\bar{2}}.\boldsymbol{u}$ corresponding to the projection of the displacement field onto the 2 0 $\bar{2}$ Bragg reflection is shown in the (x,y) plane (Fig. I.5.a).
As seen in Fig. I.5.a, the phase is continuous everywhere, except for a singularity in the vicinity of the dislocation line. A phase vortex is thus observed around the dislocation line.
The phase shift between the two parts on each side of the singularity is equal to π. This phase discontinuity induces large perturbations in the CXD pattern calculated with Eq. (I.14).
At the theoretical position of the Bragg peak, the intensity is equal to zero. This is the characteristic signature induced by a π phase defect which has been reported by Jacques *et al.* (2011). The detailed calculations to

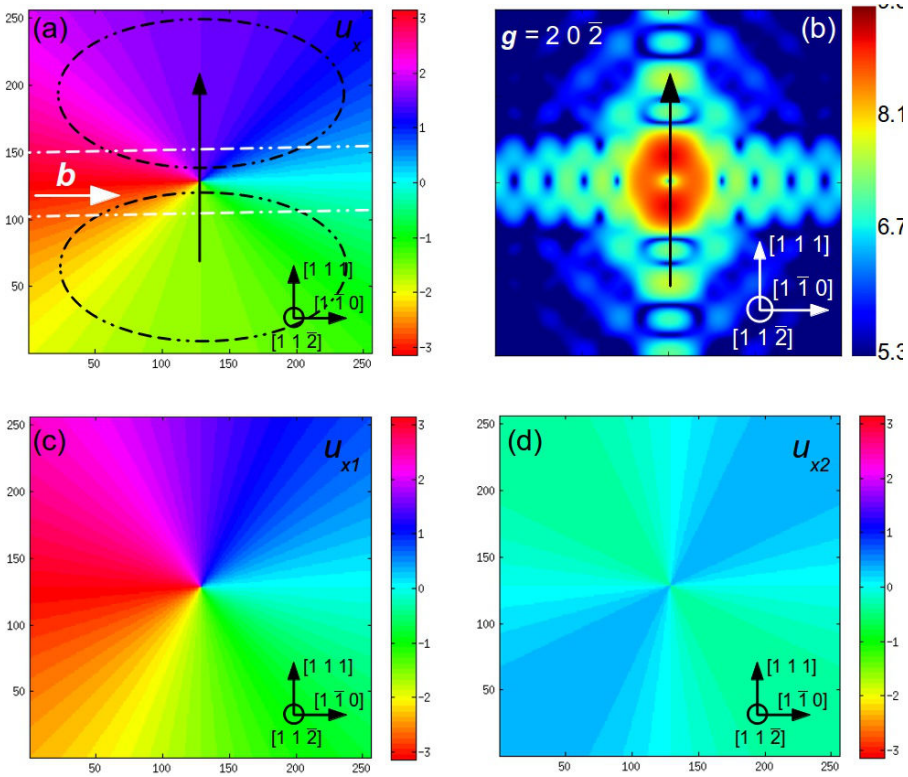

Fig. I.5: *Computation of the scattering from an edge dislocation using a FFT.* (a) Angular distribution of $\varphi_{20\bar{2}}$ in the plane perpendicular to a single straight edge dislocation with $\boldsymbol{b}$ = ½[1 $\bar{1}$ 0] . (b) Corresponding CXD pattern in the (1 1 $\bar{2}$) plane of the reciprocal space for $\boldsymbol{g}$ = $\bar{2}$ 0 2.

explain this peculiar distribution of the diffracted intensity can be found elsewhere (Jacques 2009).

As illlustrated in Fig. I.5.a, and contrary to the case of a screw dislocation, the angular phase distribution is anisotropic. This difference between the two type of defects can be used to identify them, as illustrated later in this manuscript (Chapter V).

Here, the phase variations are concentrated in the region between the two white dashed lines, parallel to the [1 $\bar{1}$ 0] direction, *i.e.* the direction of the Burgers vector of the dislocation. Conversely, the phase is almost constant in the two regions circled in black which are connected by a black arrow along the [1 1 1] direction. This anisotropy of the phase variations is reflected in the shape of the Bragg peak. It is slightly elongated along the same [1 1 1] direction which connects the two largest phase shifted volumes.

$g_{20\bar{2}}$ is perpendicular to y and is thus insensitive to the u_y component of the displacement field. Since u_z=0, it is only sensitive to u_x which probably explains why the phase variations are concentrated along the direction of the Burgers vector. Alternatively, the anisotropy in the displacement field can be understood from Eq. (I.16). u_x is the sum of two terms, one increasing uniformily with the azimuthal angle $\theta = \tan^{-1}(y/x)$ and an additional periodic modulation which depends on the Poisson ratio The two terms of the u_x component of the displacement field are shown in Fig. I.5.c & d.

The selected pixel size in the real space δl determines the extent of the reciprocal space pattern Δq. Conversely the total size of the computing box in the real space L can be arbitrary extended with zeros (zero-padding) to enhance the resolution of the reciprocal space pattern δq.

$$\delta q = \frac{2\pi}{L} \quad \& \quad \delta l = \frac{2\pi}{\Delta q} \quad \text{or} \quad \delta q = \frac{1}{L} \quad \& \quad \delta l = \frac{1}{\Delta q} \tag{I.18}$$

depending on the convention used for the Fourier Transform. For the chosen convention in this manuscript the term, *i.e.* the 2π factor is not included in $\boldsymbol{q}$ (crystallographic convention) the pixel size in the real space is given by $\delta l = \frac{1}{\Delta q}$ (and the resolution of the reciprocal space by $\delta q = \frac{1}{L}$).

Note that this consideration is only valid for the FFT computation (Eq. 1.17) and obviously does not apply for the direct computation of the kinematic sum which compute the scattering from the atomic positions. (Eq. I.13)

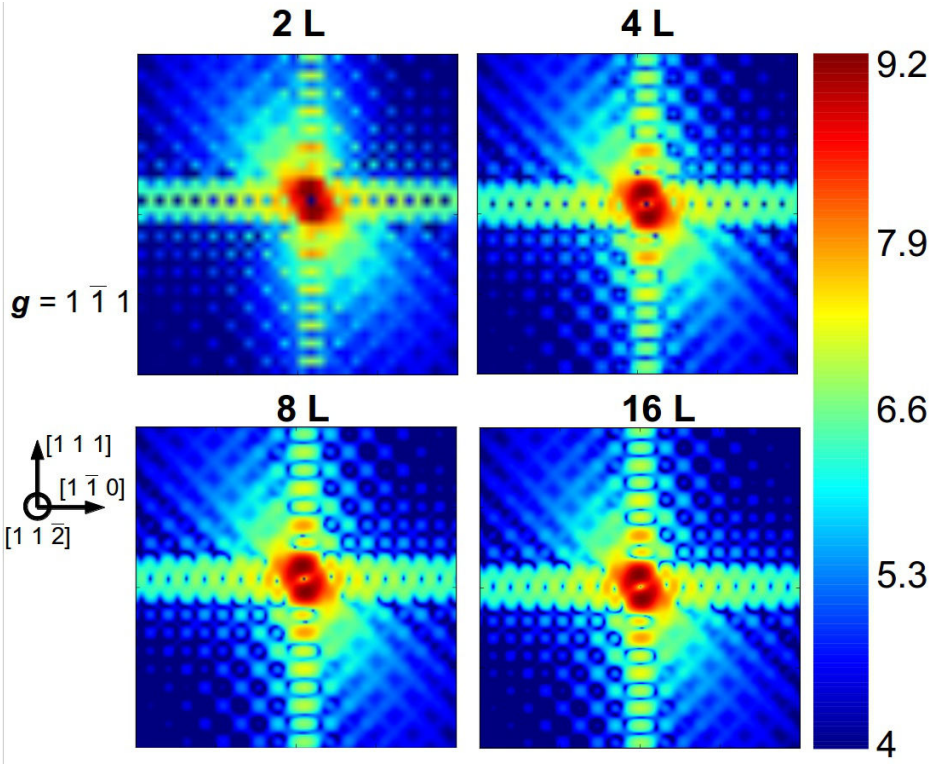

Fig. I.6 *Enhancement of the resolution in the resolution of the reciprocal space by padding the computing cell in the real space with zeros*

Fig. I.6 shows the effect of zero-padding to compute the diffraction pattern. An enhancement of the resolution in the reciprocal space is observed. The diffraction pattern is calculated in the vicinity of $\boldsymbol{g}$ = 1 $\bar{1}$ 1. When the resolution of the reciprocal space is good enough, a splitting of the Bragg peak is also observed for this reflection. It correspond to the π phase jump induced by the phase singularity in the vicinity of the dislocation line.

The 1 $\bar{1}$ 1 reflection allows to illustrate the effect of the u_y component of the displacement field on the scattering pattern. While the Bragg peak was purely elongated along the [1 1 1] direction for $\boldsymbol{g}$ = 2 0 $\bar{2}$, corresponding to the fact that the reflection is only sensitive to the u_x component of the displacement field, it is slightly distorted here and the split of the Bragg peak is not oriented along a specific direction. This comes to the fact that $\boldsymbol{g}$ = 1 $\bar{1}$ 1 is sensitive to both component of the displacement field (parallel and perpendicular to the Burgers vector of the dislocation). The bending of the lattice along z induced by the extra-half plane forming the dislocation induces supplementary perturbations in the CXD pattern.

These two examples provide a first insight in the variety of signature induced by a single crystal defects, depending on the Miller index of the Bragg reflection. This topic is addressed in extensive details in Chapter III of this manuscript.

In order to test the accuracy of the calculation using the FFT, it has been tested against the computation of the kinematic sum for the same type of defect.

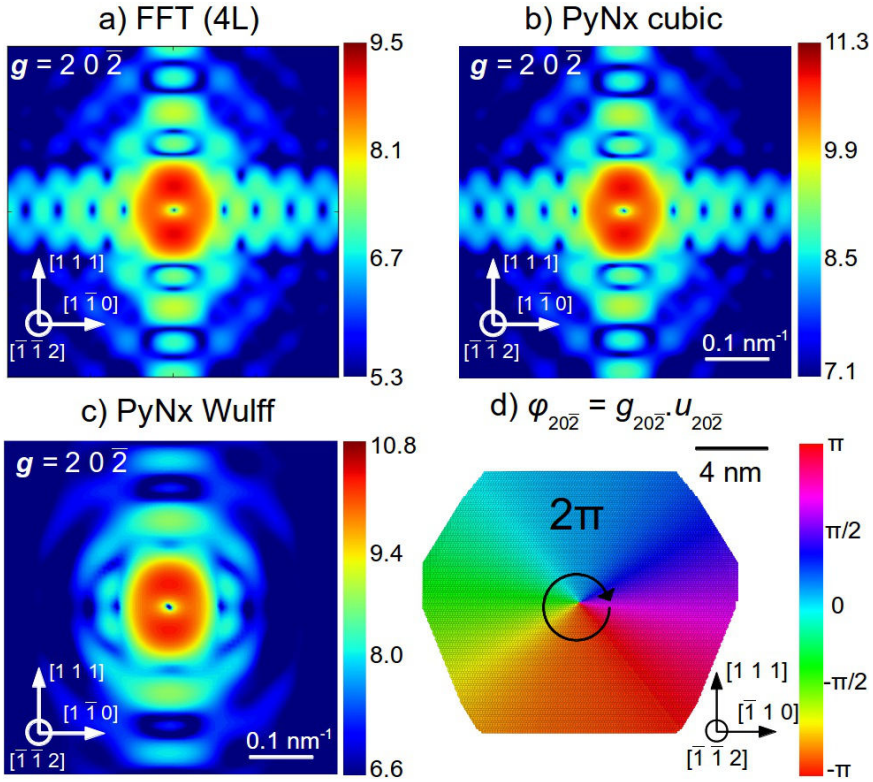

Fig. I.7 *Scattering from an edge dislocation with* $\boldsymbol{b}$ = 1/2[1 $\bar{1}$ 0] *and* $\boldsymbol{g}$ = *2 0* $\bar{2}$ *obtained by two distinct methods of computation.* (a) FFT calculation (Eq. I.14) (b) Direct calculation of the kinematic sum (Eq. I.13). (c) Calculation of the kinematic sum for an object with different boundary conditions (Wulff equilibrium shape). (d) Angular distribution of the phase $\varphi_{20\bar{2}}$ for the particle in a Wulff geometry).

A perfect edge dislocation with its corresponding displacement field (Eq. I.16 & I.17, hypothesis of an isotropic and semi-infinite volume) is introduced at the centre of a 20x20x20 nm^3 copper crystal, modelled with realistic inter-atomic potentials (Mishin *et al.* 2001), using the home-made atomistic simulation code MERLIN. More details about these simulations are found in Chapter III. The dislocation has the same Burgers vector equal to ½[1 $\bar{1}$ 0]. A cubic shape, with the x,y and z axis corresponding to the [1 $\bar{1}$ 0], [1 1 $\bar{2}$] and [1 1 1] directions is considered. The cubic shaped crystal is equivalent to the 2D crystal presented at the beginning of this section except for the number of atoms.

The effect of the shape of the particle is also evaluated in this calculation by considering a particle in the Wulff shape (Winterbottom 1967) corresponding to an equilibrium crystal shape (ECS). For both cubic and Wulff crystal (Chapter II, III & VII for more details). The scattering is computed with Eq. (I.13), using the software PyNx (Favre-Nicolin *et al.* 2011) presented above. The results are compared with the scattering from the 2D

crystal computed with Eq. (I.14).
As illustrated in Fig. I.7.a & Fig. I.7.b, the computation from Eq. (I.13) and Eq. (I.14) gives the exact same result. One can conclude that the strain field at the vicinity of the dislocation line is not large enough to invalidate the use of a Fast Fourier Transform for computing the scattering from a simple defect structure. When the displacement field from the defect is known analytically this method of computation is straightforward. As discussed previously, when the displacement field is obtained for relaxed atomic positions, there is in principle no reason that the displacement field surrounding the defect dramatically increases upon relaxation (see Chapter III and VI). It is also possible to compute the displacement field from Eq. (I.14) by interpolating the relaxed atomic positions on a regular grid. However given the very short computation times needed to compute Eq. (I.13) with PyNx, there is no interest in using such method of calculation.
The influence of the boundary conditions of the simulation *i.e.* the shape of the particle are discussed in extensive details in Chapter III. Here it is clear that the signature of the edge dislocation in the cubic and in the Wulff particle only slightly differs. The elongation along the [1 1 1] direction is found for both particles, so is the general shape of the Bragg peak. Obviously, the fringes induced by the finite size of the particle differ between the two geometries, but this does not induce large modifications of the shape of the Bragg peak.

I.4 Coherent Diffraction Imaging

I.4.1 The phase problem

The phase problem has been a widely studied subject since the middle of the last century. It is the name given to the problem of loss of information concerning the phase of an electromagnetic wave that can occur when making a physical measurement.
Several successful attempts have been made for extracting phases from diffraction intensities such as holography (Gabor 1948, Gabor 1949) using electrons (Mulvey 1952) or photons at the visible or X-ray spectral range. This ability to extract the phase has revolutionized the imaging science.
Coherent X-ray Diffraction Imaging (CDI) is a lensless imaging technique that has opened up a new way of accessing the phase information by using iterative algorithms (see section I.4.3) based on the Sayre's oversampling principle (Sayre 1952): it states that the loss of the phase information can be compensated by a measurement of the intensities with a spatial frequency at least twice the Nyquist frequency. Algorithms can then be used to recover the phase of the measured electromagnetic wave. In practice, the difficulty is to find a combination of experimental conditions and algorithms that actually provides a successful reconstruction. The most common implementation of Sayre's principle is a measurement in the far field of the exit wave from a sample of finite extent, with the phase retrieval performed by algorithms that iterate between real space and reciprocal space with appropriate constraints applied in both spaces.
The technique has been used successfully in the last decade to image the 3D strain-field and defect structure in a variety of systems. The most significant achievements of CDI are presented in the introduction of Chapter III.
The principle of the technique is rather simple. When a crystal is fully illuminated by a coherent X-ray beam, the scattered waves from all parts of the sample interfere in the diffraction pattern. Provided that the intensity scattered by the sample is measured in the far-field (Fraunhofer) regime, a real-space image (in general complex) of the sample may be reconstructed from the diffraction data using phase retrieval algorithms.
In diffraction geometry and non-resonant conditions, the real-space image corresponds to a complex density function (Eq. I.10).
The amplitude of the complex-valued density corresponds to the electron density of the sample. It gives access to the shape and density of the object, and can provide a precise location of the defective part of the crystal. A void in the electron density is indeed observed for the parts of the crystal which do not perfectly satisfy the

Bragg conditions (Williams *et al*, 2003). As a consequence, twin domains are for instance invisible in the reconstructed electron density, while voids of density are commonly observed in the vicinity of crystal defects, such as dislocations, where the crystal lattice is highly distorted. This voids or dips in the electron density can be exploited to determine the nature of the defect as shown in Chapter V & VI.
The phase of the complex electron density is related to the displacement field $\boldsymbol{u}$ via $\varphi = 2\pi.\boldsymbol{g}.\boldsymbol{u}$. The image of the reconstructed phase displays the encoded displacement field of the crystal.

I.4.2 Holography

In the following sections is presented the most conventional method to address the phase problem. It relies on the use of phase retrieval algorithms to retrieve numerically the phase of oversampled diffraction patterns. However, phase retrieval methods are not the only option to access the phase information. Provided that a reference wavefield from a suitable scatterer interferes at the detector plane with the wave scattered by the object, the phase information can be sufficiently preserved such that an image of the object can be reconstructed from the measured intensity pattern. Using this method, the phase of the object wavefield is encoded by the reference wave-field in the far-field scattered intensity collected by an area detector. Both amplitude and phase of the complex image are simply obtained using a single inverse Fourier transform. This method is illustrated in Chapter XI, to image the magnetic structure and dynamics of sub-micron magnetic elements an won't be further detailed in this section.

I.4.3 Coherent Diffraction Imaging with phase retrieval algorithms

I.4.3.1 Oversampling

The phase retrieval technique is based on the central notion of oversampling of the diffraction data. “Oversampling” is defined by the Nyquist-Shannon theorem (Shannon 1949). It states that in order to retrieve the signal correctly from a set of sample points, the sampling frequency has to be higher than the Nyquist sampling frequency.
In the case of a rectangular function (typically a slit), whose Fourier transform is the 'sinc' function, the Nyquist (Shannon) sampling frequency corresponds to at least one point per fringe. Below this sampling frequency, the fringes of the sinc function is not resolved, which leads to the loss information on the scattering object.
When only the modulus of the Fourier transform of the signal is available (as in the case of diffraction), half of the information on the object is lost.
Sayre proposed a criterion for the retrieval of the signal based on the Nyquist frequency: the signal can be retrieved only if the intensity of the Fourier transform of the signal is sampled at least at twice the Nyquist frequency. If the objects have N unknown values, the number of measurement points on the amplitude of the Fourier transform of the object needs to be at least 2N to reconstruct the signal. For the simple example of a rectangular function (Fig. I.8.a), the diffracted intensity is a squared 'sinc' function. To retrieve all the information, the signal has to be sampled by at least two points per fringe.
This criterion can be extended to 2D or 3D systems. In this case, a condition σ of oversampling has been defined by Miao *et al.* (1998). It corresponds to the ratio between the total number of points of measurements, and the number of unknown values. It was concluded that the oversampling condition $\sigma>2$ is the same for 1D, 2D and 3D systems and that the requirement of phase retrieval by oversampling the magnitude of a Fourier transform by 4 for 2 D reconstruction and by 8 for 3 D (by a factor 2 in each direction) reconstruction is unnecessary. The requirement of $\sigma>2$ corresponds to $> 2^{1/2}$ in each dimension for a 2D square object and $> 2^{1/3}$ in each dimension

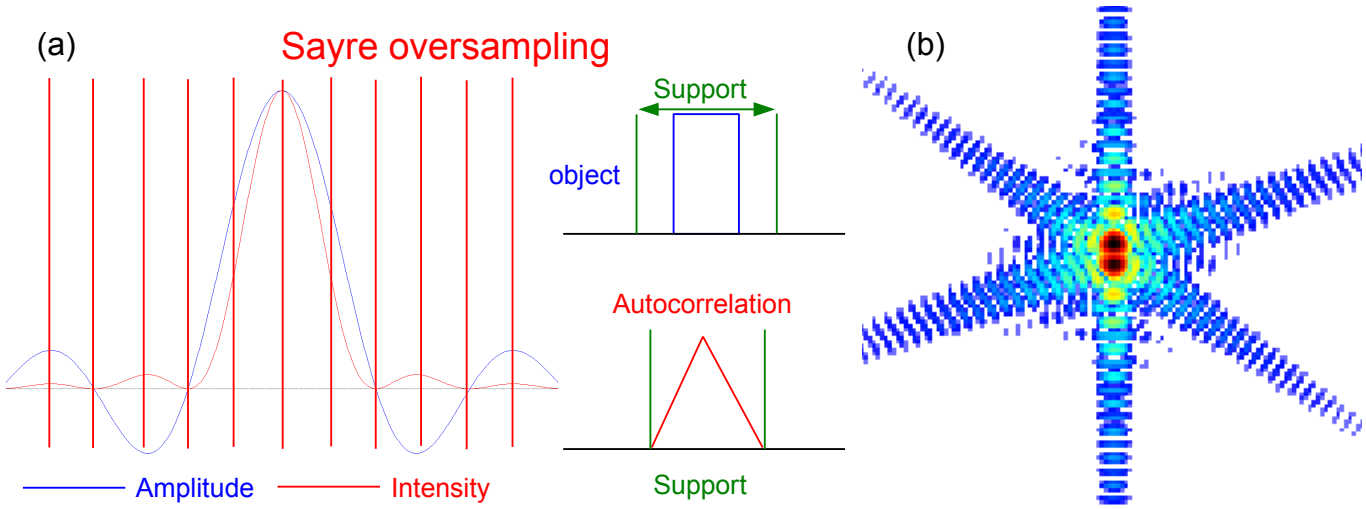

Fig. I.8 *Illustration of the oversampling criterion.* (a) Sayre oversampling of a 1D 'sinc' function, Fourier transform of a rectangular function. The oversampling condition is fulfilled for the sampling of at least two points per oscillation fringe. (b) Illustration of an oversampled diffraction pattern from a Wulff crystal. The two pixels per fringe ensure that the oversampling conditions are largely satisfied (2x2 oversampling)

for a 3 square object but it was evidenced that slightly higher values are needed in order to ensure the phase can be perfectly retrieved.
Regarding experimental matters, the criterion of two pixels per fringe defined for the rectangular function can be applied to the diffracted intensity from an isolated crystal. The finite size of the crystal induces fringes normal to the crystallographic directions of its facets, with periodicity equal to the inverse of the distance between two parallel facets (Fig. I.8.b). If the diffracted intensity is sampled with at least two points per fringe, both the density and phase of the crystal can be retrieved (Williams *et al.* 2003). As discussed above, this criterion is even too strong since an oversampling of 2 along each direction of the space is not needed for 2D or 3D system.

I.4.3.2 General formalism of phase-retrieval algorithms

Provided that the diffraction data is oversampled, and that the sample is isolated (finite support constraint), the phase can in principle be retrieved. The first iterative algorithm, error-reduction (ER), was proposed by Gerchberg & Saxton (1972) (Fig. I.9) and was initially successfully used in Electron Microscopy to obtain the missing phase information in both direct and reciprocal space. It relies on the fact, that the amplitude and phase of the complex-valued scattering function $f(\mathbf{r})$ in real and reciprocal space are linked by direct or invert Fourier transform (Fig. I.9). In the case of electron microscopy, both the amplitudes in the reciprocal space (electron diffraction) and in the real space (image of the sample) are accessible experimentally.
The basic phase retrieval process begins with a guess of the diffracted phase of the object. A first estimate of the complex object is obtained by applying an inverse Fourier transform. This first estimate does not necessarily correspond to the shape of the object. At this stage, the amplitude of the object is corrected to match the experimental data. This new iterate with a "corrected shape" is in turn Fourier transformed to yield a new guess for the diffracted wavefield. The consistency with the reciprocal space constraint, *i.e.* the diffracted amplitude is then enforced while retaining the current phase. This process known as phase-retrieval algorithm is then repeated until both the amplitude (density) and phase of the object are reconstructed.
We call *g*k the object guess at th k-th iteration, Gk its Fourier transform, G'k a modification of Gk according to the reciprocal space constraints, and g'k its inverse Fourier transform. The next iteration of the guess, g(k+1), is obtained by applying the real space constraints to g'k. Most iterative algorithms used for phase-retrieval are just different strategies to apply the real space and reciprocal space constraints to g'k and Gk respectively.

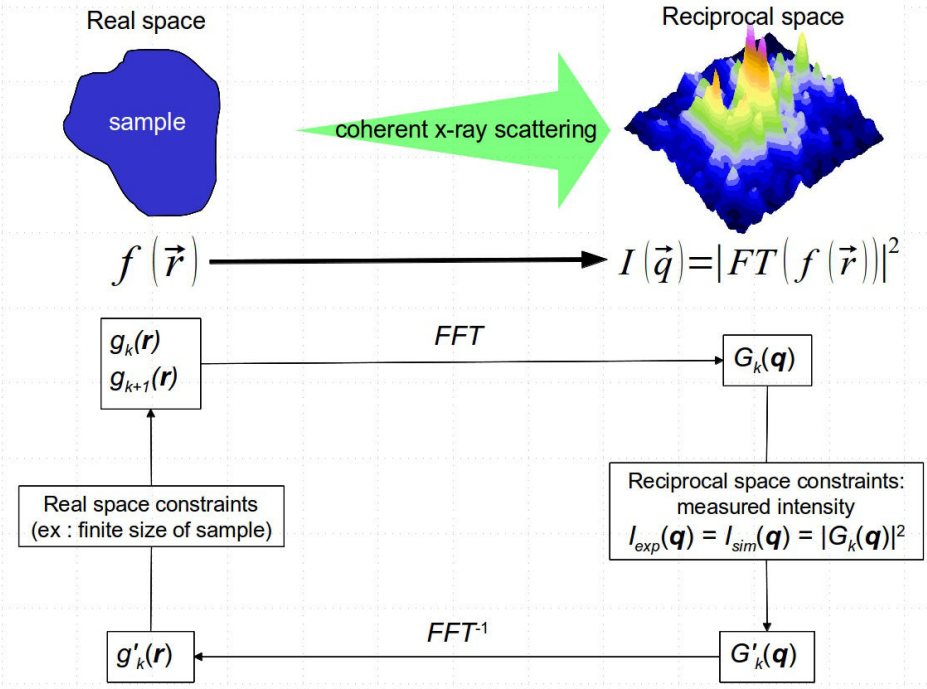

Fig. I.9 *General architecture of phase retrieval algorithms*

I.4.3.3 Finite support constraint and Error-Reduction (ER algorithm)

To deal with the cases when only the amplitude in the reciprocal space (the diffracted intensity) is available, and there is no information on the real space object. Fienup introduced the notion of finite-support in the Error-reduction (ER) algorithm (Fienup 1978). The support corresponds to a shape when the object is included. The density of the object is thus equal to zero outside the support. Following the formalism introduced in Fig. I.9, this condition can be written as following:

$$\begin{cases} g_{k+1}(\boldsymbol{r}) = g'_k(\boldsymbol{r}) & \text{if } \boldsymbol{r} \text{ is } \in \text{Support} \\ g_{k+1}(\boldsymbol{r}) = 0 & \text{if } \boldsymbol{r} \text{ is } \notin \text{Support} \end{cases} \tag{I.19}$$

In the reciprocal space (Fourier space), the condition on the reconstructed amplitude (the modulus constraint) is given in Fig. I.9 :

$$|G'_k(\boldsymbol{q})| = \sqrt{I_{\exp}(\boldsymbol{q})} \tag{I.20}$$

The agreement between the retrieved amplitude and the measured amplitude is evaluated by the mean squared error between the two amplitudes:

$$E_r^2 = \frac{\sum \left(|G_k(q) - \sqrt{I_{\exp}}(q)| \right)^2}{\sum I_{\exp}(q)} \tag{I.21}$$

This parameter is a good indicator of the quality of the reconstruction. It is used to monitor the convergence of the algorithm. In practice, a slow convergence of the ER algorithm is often observed. The error-metric does not evolve and the algorithm is sort of stuck in a local minimum.

I.4.3.4 Hybrid-Input-Output (HIO) algorithm

To overcome the problem of stagnation in local minima of the ER algorithm, an enhanced algorithm was introduced by Fienup (Fienup 1982), the Hybrid-Input-Output algorithm (HIO). It differs in the application of the real space constraints. Contrary to the ER algorithm, the retrieved informations outside the support are kept and subtracted during the next iteration after having been multiplied by a feedback parameter β:

$$\begin{cases} g_{k+1}(\boldsymbol{r}) = g'_k(\boldsymbol{r}) & if \ \boldsymbol{r} \ is \in Support \\ g_{k+1}(\boldsymbol{r}) = g_k(\boldsymbol{r}) - \beta g'_k(\boldsymbol{r}) & if \ \boldsymbol{r} \ is \notin Support \end{cases} \quad \text{(I.22)}$$

β is generally selected between 0 and 1 with typical value of 0.5 to 0.9. In some particular cases, it can be selected to be bigger than 1 (Kohl & Baumbach 2012).
In practice, this adaptation is efficient and significantly enhances the convergence speed. It can be seen as a little perturbation that allows to leave a local minimum. However, the HIO algorithm still fails sometimes, and this explains why the ER and HIO algorithms are generally used in combination.

On top of the conventional support constraint, additional real-space constraints can be added to the algorithm.
A good illustration of the application of these additional real-space constraints is the Phase-Constraint HIO (PCHIO) algorithm that was proposed by Harder *et al* (2010). In this algorithm, the real-space phases are constrained to be within a range with minimum and maximum phase values. Typical values are $\pm\pi/2$.
In the case of limited phase variations it can significantly improve the data convergence :

$$\begin{cases} g_{k+1}(\boldsymbol{r}) = g'_k(\boldsymbol{r}) & if \ \boldsymbol{r} \ is \in Support \cap \Phi_{min} < \Phi < \Phi_{max} \\ g_{k+1}(\boldsymbol{r}) = g_k(\boldsymbol{r}) - \beta g'_k(\boldsymbol{r}) & if \ \boldsymbol{r} \ is \notin Support \cap \Phi_{min} < \Phi < \Phi_{max} \end{cases} \quad \text{(I.23)}$$

An extensive comparison of the modern algorithms has been realized by Marchesini (2007), and in particular their ability to avoid stagnation in local minima has been evaluated. It was concluded that the combination ER + HIO is particularly robust. This combination is used in most of the reconstruction presented in this work.

I.4.3.5 Support determination, Shrink wrap algorithm

There are several techniques to estimate the support. In some cases, the shape and dimensions of the object have been already determined by other techniques (such as SEM or AFM for instance), and a support can be built from this knowledge. When the shape of the object is unknown, a rough estimate of the support can be obtained from the diffraction signal using the autocorrelation function (Marchesini 2003). It is based on the Patterson function which can be defined as the invert Fourier transform of the diffracted intensity. This function can be expressed as the convolution of the complex electron density :

$$\begin{aligned} Patterson(\boldsymbol{r}) &= TF^{-1}\{I(\boldsymbol{q})\} \\ &= TF^{-1}\{A(\boldsymbol{q})A^{*}(\boldsymbol{q})\} \\ &= TF^{-1}\{TF(\rho(\boldsymbol{r}))TF(\rho(-\boldsymbol{r}))\} \\ &= \rho(\boldsymbol{r}) \otimes \rho(-\boldsymbol{r}) \end{aligned} \quad \text{(I.24)}$$

It comes from Eq. (I.22) that the Patterson function contains a strong signature of the shape of the object, unless the strain is so high that the characteristic features of the shape disappear from the diffraction signal (Beutier *et al.* 2013a). The size of the crystal is overestimated by the Patterson function, since it provides its autocorrelation. In practice, a non uniform density leads to a non-trivial shape of the autocorrelation. The function needs to be threshold to start with a reasonable approximation. In most of the reconstructions in this manuscript, the threshold was set to 2% of the maximum of the Patterson function.
As discussed by Vaxelaire (2011), the method is not adapted to highly strained objects. For such objects, the Patterson function can be written as:

$$Patterson(\boldsymbol{r}) = \rho(\boldsymbol{r})e^{i\boldsymbol{q}.\boldsymbol{u}(\boldsymbol{r})}\rho(-\boldsymbol{r})e^{-i\boldsymbol{q}.\boldsymbol{u}(-\boldsymbol{r})} \quad \text{(I.25)}$$

It is clear from Eq. (I.23) that the inhomogeneity of the displacement field plays an important role in the shape of the autocorrelation function. For large strain, the diffraction pattern has a large extent in the reciprocal space (Beutier *et al.* 2013a). As a consequence, the Patterson function underestimates the size of the object, preventing any chance of success in the phase-retrieval procedure. In summary, if the shape and size of the object is unknown, it is not recommended to use the autocorrelation function as a first estimate of the support in the case of an highly strained system.

In combination of the ER and HIO algorithms, a third algorithm is routinely used for CDI. It is known as the shrink wrap (SW) algorithm and allows to update the support during the reconstruction. It was first introduced by Marchesini (2003) and has proven to greatly improve the convergence of the procedure. In practice, the estimate is smoothed by convolution with a Gaussian. After convolution, a thresholding is applied to the smoothed image to a typical value of 10% of the maximum value of the amplitude. Values above the threshold are set to 1 and values below are set to 0. The threshold is generally set to such low values to avoid to suppress too large parts of the support. Nevertheless, the convolution step allows to recover from a support that has been reduced too much.

I.4.3.6 Recent improvements on the phase retrieval procedure

The combined use of ER, HIO and SW has proven to reach data convergence, especially in the case of weakly-strained crystallites, which are studied within this work (Pfeifer *et al.* 2006, Robinson & Harder 2009, Watari *et al.* 20111). However, there is no combination of the existing algorithms that guarantees a successful reconstruction. This is especially true in the case of highly strained objects where conventional iterative algorithms often fail when phasing the diffraction pattern of such objects. Some improvements in the phase-retrieval procedure have been recently proposed in order to improve the convergence of the results.

Guided phase retrieval method

The guided phase retrieval method (Chen *et al.* 2007) is particularly effective, and its successful use has been reported in several recent publications (Clark *et al.* 2015, Ulvestad *et al.,* 2015). It is described in extensive details elsewhere (Clark *et al.* 2015). In short the procedure works by generating several initial random guesses to start the iterative procedure. Each initial guess is then transmitted to a phase retrieval algorithm, and after a

predefined number of iterations, a set of potential solutions is obtained. The algorithm then selects the best solution according to specific criteria such as the metric-error for instance, to guide the next round of iterations. After several rounds/generation, the solutions usually converges regardless of the initial random starts.

Sharp metric error

As already discussed in section I.4.3.5 the diffraction patterns from strained crystals has a large spatial extent. This results in a narrow autocorrelation which underestimates the size of the object. Even if the initial support is selected to be sufficiently large, the choice of the best solution according to the conventional metric-error (mean-squared error between the measured and retrieved amplitude) does not guarantee a successful reconstruction.
It is well known that the width of the diffraction peak of a crystal depends on the size of the crystal and of the level of strain (Williamson & Hall 1953, see Chapter II). A given width of the Bragg peak can be obtained either by a large strained crystal or by a smaller unstrained crystal. There is the possibility during the phase retrieval procedure of stagnation in a local minimum with largely underestimated dimensions of the crystal. To promote the reconstructions with a larger spatial extent, Clark *et al.* 2015 proposed to select the best values according to a different form of metric error, namely the sharp metric error which is given by:

$$E_s = \sum_{l=1}^{L} |\rho(l)|^4 \tag{I.26}$$

where l is the pixel index, so that the metric-error selects estimates which have a more uniform distribution of amplitude values, corresponding to a larger spatial extent of $|\rho|$. It was shown that in a highly strained systems, the choice of the best solution according to the conventional metric-error usually fails to reconstruct the original sample, while the selection based on the sharp metric-error systematically yields successful reconstructions.

Low-to-high resolution phasing implantation

Another suggestion of improvement was the use of a Low-to-High resolution phasing implantation (McCallum & Bates 1989). This consists in first phasing a low resolution data set by limiting the extent of the reciprocal space pattern before using it to seed the phasing of progressively higher resolution data. This results in smoother and less pronounced phase features than the original object and greatly facilitates the reconstruction.

Partial coherence effects

Finally, the reconstruction of the experimental data can be improved by taking partial coherence effect into account (Clark *et al.* 2012). In the Schell model, the effect of partial coherence is to convolve the diffracted intensity with a function $\gamma(\mathbf{q})$ which is the Fourier transform of the normalized mutual coherence function given by Eq. (I.5).During the iterative routine the estimate of the diffracted intensity : $|G(\mathbf{q})|^2$ is replaced with :

$$|G(\boldsymbol{q})|'^2 \quad = \quad |G(\boldsymbol{q})|^2 \otimes \gamma(\boldsymbol{q}) \tag{I.27}$$

I.4.4 Correction for artefacts related to experimental conditions

The phase of the retrieved complex-valued electron density often presents some variations that are related to the experimental conditions rather than to the crystal structure (Diaz *et al.* 2009, Harder *et al.* 2007). These artefacts can complicate the analysis of the reconstructed data. Here we briefly describe some of these artefacts. Among them are the reciprocal space offsets, refraction effects and curved illumination wavefront. The

effect of these artefacts on the reconstructed data is illustrated through several examples in Chapter VI and Chapter VII.

I.4.4.1 Reciprocal space offsets

A slight mis-centring of the diffraction data before phase retrieval results in a linear phase ramp in the real space reconstruction. This is a consequence of the Fourier shift theorem. This phase ramp is particularly problematic because it is equivalent to an uniform expansion/contraction of the crystal lattice.
In order to remove any real space phase ramp in $f(\boldsymbol{r})$, its Fourier transform $F(\boldsymbol{q})$ needs to be re-centred. This can be done through the use of the centre of mass of $|F(\boldsymbol{q})|$ but as discussed by Clark *et al.* (2015) this choice might not be appropriated for complex-objects with a non-negligible phase. An alternative consists in centring $F(\boldsymbol{q})$ based on the centre of mass of $|F(\boldsymbol{q})|^4$. The sub-pixel shift is achieved by multiplying $f(\boldsymbol{r})$ by the appropriate phase ramp determined from the centre of mass. This procedure has been used in this work for the reconstruction of both experimental and simulated data and has proven to be very efficient.

I.4.4.2 Refraction effects

Although the real part of the refractive index, 1-δ, is close to unity, refraction effects may become non-negligible because the wave propagation distance is much larger than the wavelength λ. Refraction causes the waves travelling inside the crystal to have a different wavelength from those travelling in the vacuum outside. The real part of the refractive index n corresponds to the ratio between these two wavelengths. Over a distance d which corresponds to the diameter of the sample, the wave field propagating into the sample is experiencing a phase shift with regards to the wave field propagating in the absence of matter, for both incident and scattered waves. This phase shift is given by :

$$\Delta\varphi_{0\,ref} = 2\pi k \delta d \tag{I.28}$$

Where k is the wave vector corresponding to the vacuum wavelength.
Harder *et al.* (2007) evidenced that in a large (d = 750 nm) and weakly strained Pb crystal, the phase variations induced by the strain and the phase shift accounting for refraction effects is of the same order of magnitude. The latter needs to be taken in account in order to provide a precise description of the distribution of the displacement field. They model the phase shift due to refraction in a spherical Pb crystal. It relies on the fact that the refraction phase shift simply accumulates along the path of the incident wave-vector $\boldsymbol{k_i}$, and that the contributions from all points $\boldsymbol{r}$ within the crystal are detected along the exit wave direction $\boldsymbol{k_f}$ after experiencing a phase shift due to refraction along its exit path. This model is in the Born approximation and thus supposes only one scattering event. It is thus possible to assign a phase shift to every point $\boldsymbol{r}$ in the crystal providing the knowledge of $\boldsymbol{k_i}$ and $\boldsymbol{k_f}$. For a sphere, the phase shift at a point $\rho = \boldsymbol{r}/r_0$ where r_0 is the radius of the crystal is given by:

$$\Delta\varphi_{ref} = \frac{\Delta\varphi_{0\,ref}}{2} \sum_{j=i,\,f} \left(\hat{\boldsymbol{k}}_j . \rho - \sqrt{1-|\hat{\boldsymbol{k}}_j . \rho|^2 - |\rho|^2} \right) \tag{I.29}$$

where $\boldsymbol{k}$'s are unit vectors pointing toward the centre of the sphere in the direction of the incident and diffracted beams. This model is used in Chapter IV to correct the refraction effect in a weakly strained gold crystal. We will also see in Chapter VI that for defective crystals experiencing larger amount of strain, the phase-shift accounting for refraction effects become negligible in regard to other variations.

I.4.4.3 The wavefront problem

Both the curvature and the inhomogeneities in the wavefront are critical issues when using CDI for the imaging of strain field within crystallites. These modifications in the wavefront profile are mainly introduced by the optics used to improve the focusing of the beam at the sample position (Fresnel-zone plates, K-B mirrors...). They are thus especially critical for sub-micron beam sizes. Polishing imperfections are also a common issue and occur frequently with channel-cut monochromators (the geometry of the double crystal, etched in a single block, does not allow a high-quality surface polishing).
The wavefront profile can be described as a complex-valued function $P(\mathbf{r})$. The magnitude of the illumination is usually described by a Gaussian profile, while the phase depends on the nature of the focusing elements. For instance the phase of the wave front is supposed to be flat in the focus with a Fresnel Zone Plate (Schroer *et al.* 2008, subssection II.1.1.3).
As a consequence, the scattered wavefield in the Fraunhofer region is the Fourier transform of the exit wavefield given by the product $P(\boldsymbol{r})f(\boldsymbol{r})$ and the retrieved phase at the sample is a mixture of the phase of the illumination wave-front and of the phase complex electron density. This mixing of the phase is particularly well illustrated in the Chapter VII of this manuscript.
To disentangle the contributions from the illumination wavefront and from the sample itself, the wavefront illumination needs to be finely characterized. The difficulty is largely increased by the small size of the beam at the focus and the need to characterize it at the same length scale (a few nanometers) as the sample. This can be done either using dedicated optics such as a Hartmann wavefront sensor (Mercère *et al.* 2003) (so far not available for hard X-rays), or using a lensless approach: a common method is to apply CDI methods to a measurement of the direct beam in the far field of the focus (Quiney, Nature Phys 2006); alternatively, ptychography can be used to reconstruct the probe and this difficult approach can be eased by using a known sample (Kewish, Ultramicroscopy 2010).

I.4.5. Numerical study, case of defective samples

I.4.5.1 Comparisons between reconstructions for several Bragg reflections

The ability of phase retrieval algorithms to handle systems containing sharp and possibly large phase jumps is evaluated here on simulated data. In this introduction, we focus the study on the case of perfect dislocations whose displacement field can be calculated analytically as discussed in sub-section I.3.4. This short subsection can be seen as an introduction of Chapter V where reconstruction of the displacement field for more complex defect structures (relaxed defects, assembly of defects) are presented.
Similarly to the example in sub-section I.3.4, copper crystallites are modelled using the atomistic simulation MERLIN. They are all in a Wulff geometry which is the equilibrium shape of the particle (Chapter II-VII) and measure 30x30x30 nm^3 which corresponds to slightly more than 10^6 atoms. A perfect edge dislocation is introduced at the centre of the particles, with a Burgers vector equal to $\boldsymbol{b} = \frac{1}{2}[1\ \bar{1}\ 0]$.
The diffraction patterns are calculated by computing Eq. (I.13) with PyNx, and the displacement field for various Bragg reflections is reconstructed from these calculated diffraction patterns. In the first set of simulations, the extent of the reciprocal space is selected to achieve a high resolution (of the order of the nanometer), while ensuring that Sayre's oversampling conditions are satisfied.
The scattering is computed on 128x128x128 reciprocal space points corresponding to an extent Δq of 0.14x0.14x0.14 $Å^{-3}$. The voxel size in the real space is thus equal to $\delta l = 1/\Delta q = 0.7$ nm. In the case of simulated data, the pixel size roughly gives the resolution. It is thus clear that the resolution for these simulations is of course not achievable experimentally. Here it is needed to perform quantitative comparisons with the displacements calculated from the atomic position.
Over a first phase we aim at ensuring the accuracy of the reconstruction of the displacement field. To do so, the reconstructed displacement field is compared to the atomic displacement field directly calculated from the relaxed configurations in the atomistic configurations. The atomic displacements are calculated from a perfect

crystal with the same number of atoms. The displacement field surrounding the defect is reconstructed for $\boldsymbol{g} = 1\ \bar{1}\ 1$, for which the phase jump induced by the dislocation is equal to π (sub-section I.3.4), and the profile of the displacement field is expected to be rather simple. This Bragg reflection is sensitive to both components of the displacement field but is almost parallel to the Burgers vector of the dislocation so that the u_y component produces only little perturbations on the CXD pattern as illustrated in Fig. I.10.

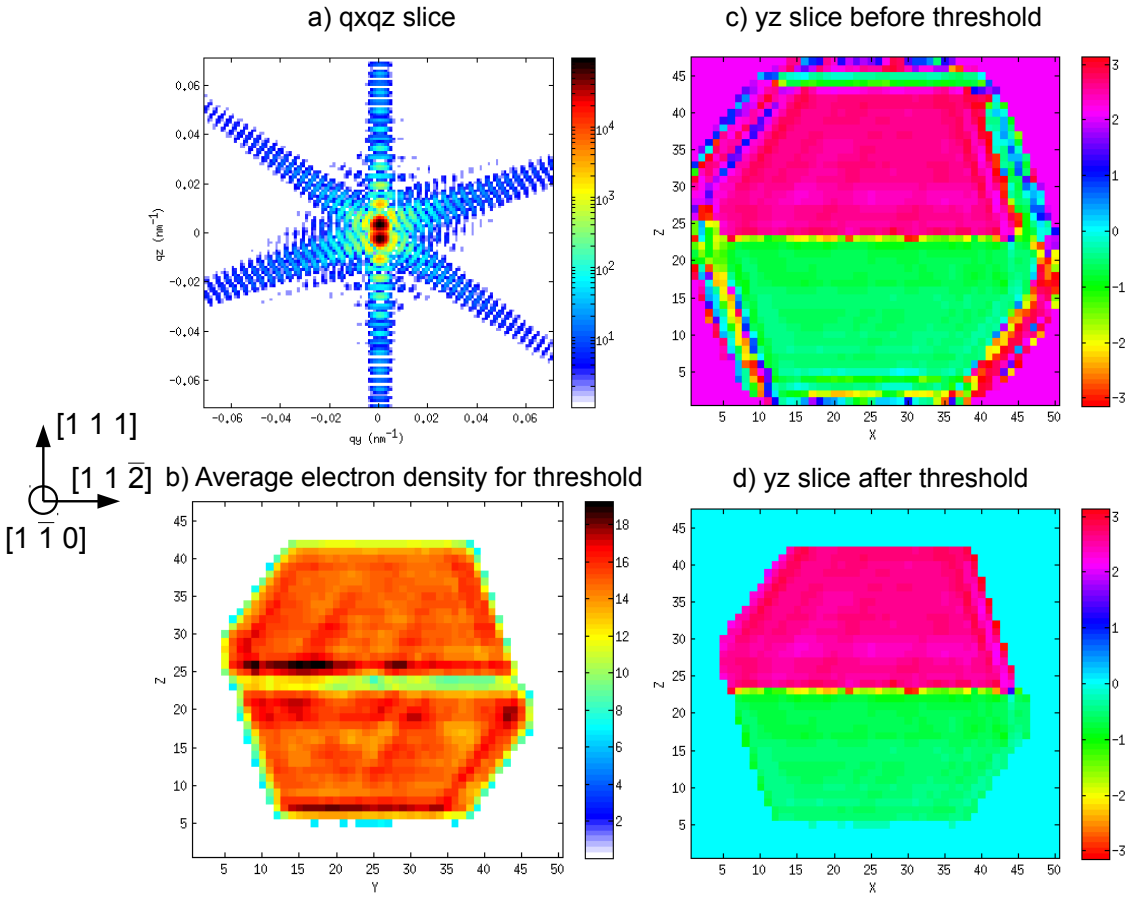

Fig. I.10 *Phase retrieval from samples containing individual defects* (a) (qy,qz) slice of a CXD pattern from a 30x30x30 nm^3 Wulff crystal. A single edge dislocation with $\boldsymbol{b} = 1/2[1\ \bar{1}\ 0]$ is introduced at the centre of the crystal, and the calculation is performed at the vicinity of the $1\ \bar{1}\ 1$ reciprocal lattice point. (b) Reconstructed phase $\varphi_{1\ \bar{1}\ 1}$ with the support obtained from the SW algorithm (c) Final support obtained by averaging the reconstructed electron density over 10 reconstructions. The pixels with $\rho < 0.35\ \rho_{max}$ are set to zero. (d) Reconstructed phase constrained to the support defined in (c).

The reconstruction of the diffracted data is carried-out using the standard phase retrieval algorithms described in the previous section, namely the ER, HIO and SW algorithms.
The sample complex density is constrained in a support which is given by the Patterson function (autocorrelation of the intensity). Since the sample is strain-free, except at the vicinity of the dislocation where large strain fields can be found, this gives a reasonably good approximation of the shape of the particle. To ensure that the initial support is sufficiently large, the threshold for the Patterson function is set to a very low value (2% of the maximum of the function), as discussed in subsection I.4.3.5. The dynamical range in the diffraction pattern is limited to 4.5 decades of intensity, which is the typical dynamical range of our experimental data sets obtained

on our gold particles with a 1s exposure time.
The procedure itself consists of an alternation of 50 HIO and 100 ER repeated 15 times, with an update of the support using SW at the end of every series of (50 HIO + 100 ER). The feedback parameter for the HIO algorithm β is set to 0.9 while the threshold for the SW algorithm is equal to 10% of the maximum of the electron density. These are typical values as discussed previously. To characterize its convergence, the procedure is used over 20 random starts. For all 20 random starts the convergence is rapidly achieved and a minimum is reached after only 3 series of (50 HIO + 100 ER). The reproducibly of the solutions can be evaluated through their error-metric. Here the error-metric is remarkably reproducible and all 20 reconstructions lead to the same metric error with an average value of 1.634×10^{-2} and a standard deviation of the order of 10^{-4}.
In Chapter VI & VII, we will see that the reconstructed images are generally averaged over a rather large number of reconstructions which correspond to the best solutions, as evaluated from their metric error and the homogeneity of the retrieved electronic density. This allows to obtain smoother representations, and reduce the noise inherent to experimental measurements.
For simulated data, there is thus no need for such averaging. As already discussed, the final support shape which contains all the complex electron density is obtained using the SW algorithm. It is known that crystal defects induce voids in the electron density (Takahashi *et al.* 2013, Labat *et al.* 2015). In order to insure that the support is not set to zero in regions that correspond to parts of the crystal, the threshold for the SW algorithm is set to a low value: 10% of the maximum of the electron density. As a consequence, the support obtained by SW is significantly larger than the actual size of the crystal. At the end of the reconstructions, the support is adjusted by averaging the electron densities obtained from the best reconstructions. This procedure allows to obtain a support very consistent with the atomistic simulations, after removing the voxels of the support below 35% of the maximum value of the electron density. As illustrated in Fig. I.10.d, all the complex electron density values are contained in this support, which allows to obtain a very clean representation.

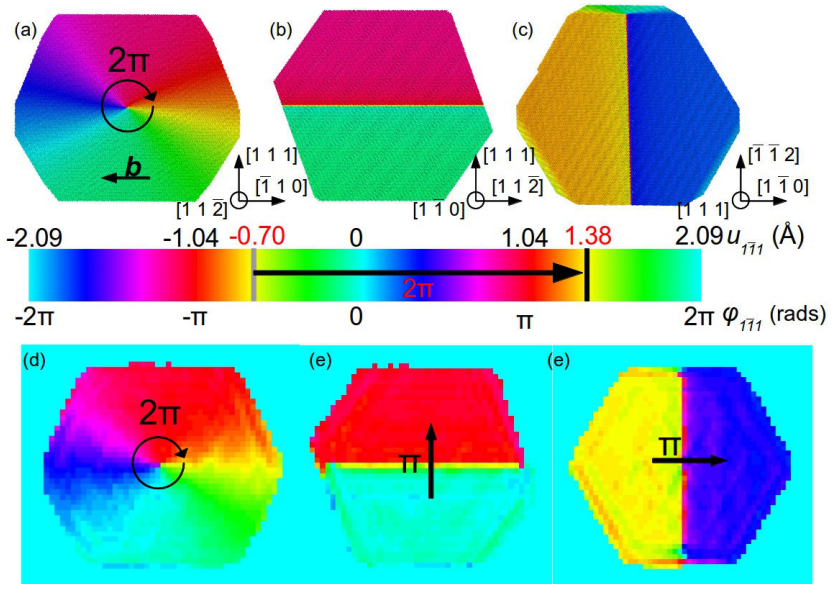

Fig. I.11 Comparison between the calculated and reconstructed displacements around a perfect edge dislocation introduced at the centre of the reference copper nanocrystal for $\boldsymbol{g}$ = 1 1̄ 1 (a) to (c) Calculated $u_{1\bar{1}1}$ displacement in the (1 1 2̄) (a), (1 1̄ 0) (b) and (1 1 1) planes (c). (d) to (f) Reconstructed $u_{1\bar{1}1}$ displacement in the (1 1 2̄) (a), (1 1̄ 0) (b) and (1 1 1) planes (c).

From this first series of simulations, all the reconstructions have converged to the same minimum. The remaining question is to determine whether this minimum corresponds to the actual phase field in the particle, or to a local minimum.
Fig. I.11 shows the phase reconstructed from the simulated data with $\boldsymbol{g} = 1\ \bar{1}\ 1$ (Fig. I.11.a) compared to the phase calculated from the atomic positions. As illustrated in Fig I.10.a, the total amplitude of displacements in the $(1\ 1\ \bar{2})$ plane perpendicular to the dislocation line is exactly equal to the spacing between two successive $(1\ \bar{1}\ 1)$ planes and corresponds to a phase variation of 2π (Fig. I.10.a). For all the crystallographic planes which contain the dislocation line, including the $(1\ \bar{1}\ 0)$ and $(1\ 1\ 1)$ planes (Fig I.10.b and I.10.c), a π phase jump occurs at the dislocation line position. The reconstructed displacement field (Fig I.10.d to I.10.f) is very similar to the calculated one. Both the 2π vortex in the plane perpendicular to the dislocation line, and the π phase jumps in the $(1\ \bar{1}\ 0)$ and the $(1\ 1\ 1)$ planes are well reproduced. Our phase retrieval procedure systematically converges towards the good solution, with a success rate of 100%.

Fig. I.12.b shows the case of the 2-2 0 reflection, which is parallel to $\boldsymbol{b}$ for the same atomic configuration. In this case ($\boldsymbol{g} /\!/ \boldsymbol{b}$), the displacements around the dislocation line vary linearly as a function of the azimuthal angle θ.
Similarly to the $2\ 0\ \bar{2}$ reflection, which is only sensitive to the u_x component of the displacement field, rapid phase variations are observed in the regions directly on the right and the left of the dislocation line which are both along the $x = [1\ \bar{1}\ 0]$ direction. Conversely, the phase remains relatively constant on the top and on the bottom of the dislocation line which are connected by the $y = [1\ 1\ 1]$ direction (Fig. I.12.a). This results in the anisotropy of the diffracted intensity which is elongated along the [1 1 1] direction. The phase distribution is not affected by u_y since $\boldsymbol{g}$ has no projection on this part of the displacement field.
For $\boldsymbol{g} = 2\ \bar{2}\ 0$, a phase variation of 2π corresponds to half the lattice spacing between two $(1\ \bar{1}\ 0)$ planes, *i.e.* the magnitude of the Burgers vector. As seen in Fig. I.12a which shows $\varphi_{2\bar{2}0} = \boldsymbol{g}_{2\bar{2}0}.\boldsymbol{b}$ in the $(1\ 1\ \bar{2})$ plane perpendicular to the dislocation line, the minimum and maximum displacements along $[1\ \bar{1}\ 0]$ with respect to the atomic positions in the perfect crystal are respectively -1.28 Å and 1.28 Å. The displacement amplitude is thus exactly equal to one lattice spacing between two $(1\ \bar{1}\ 0)$ planes and corresponds to an overall phase variation of 4π.
This implies that the phase difference between the two parts of the crystal on each side of the dislocation line is equal to 2π (Fig. I.12.b): the dislocation line does not induce any phase jump. Only the atoms on the dislocation itself are phase-shifted by π with respect to the surrounding atoms. Due to the absence of phase jump, the calculated intensity is not equal to zero at the Bragg position (Fig. I.12a). The reconstruction of the displacement field is performed using the same procedure as for $\boldsymbol{g} = 1\ \bar{1}\ 1$. However, contrary to the latter, the phase retrieval procedure does not systematically lead to the same solution. Two families of solution are obtained. For about 1/3 of the reconstructions (6 out of 20), the phase retrieval converges to a solution very close to the true displacement field.
For the other 14 reconstructions, a completely different solution is obtained. The reconstructed phase consists of two regions phase shifted by π. Inside these regions, the phase is homogeneous. Since the atomic displacement field is known, it is clear that the second set of solutions does not correspond to the actual phase distribution in the sample. However, an important question is to find out if the correct set of solution can be determined without the prior knowledge of the atomic displacement field.
A good criterion to evaluate the success or the failure is to rely on the metric error. As illustrated in Fig. I.13, the two sets of solutions correspond to two different values for the metric error. The solutions which correspond to the true displacement field have an average metric error of $1.65.10^{-2}$ with a standard deviation of 2.10^{-4}. The second set of values gives an average metric error of $2.27.10^{-2}$ with a standard deviation of $3.5.10^{-4}$. As expected, a lower error-metric is obtained for the set of values which correspond to the good solution. Also interesting, the values of the errors-metrics are very reproducible for the two sets of solutions. On experimental data, a larger dispersion of error-metrics is generally observed for the solutions which correspond to local minima (Labat *et al.*2015).

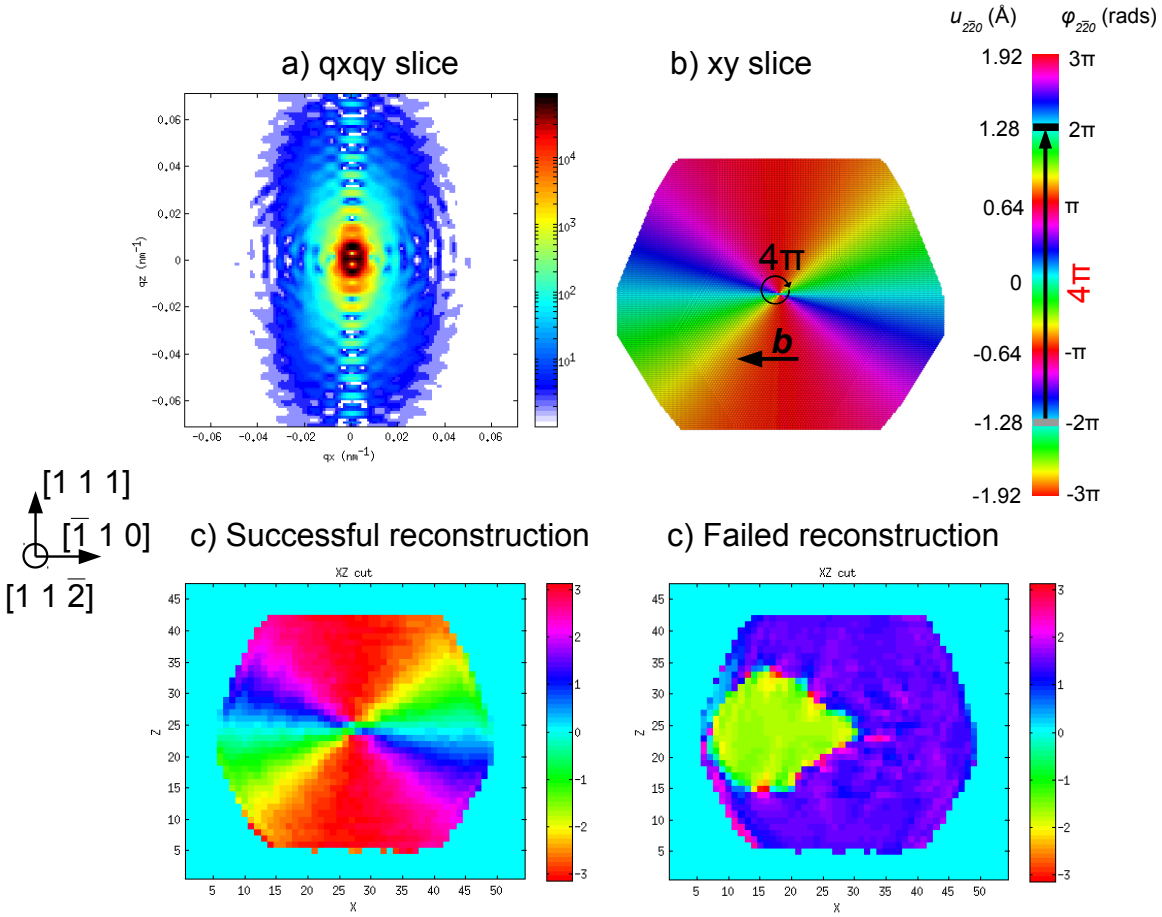

Fig. I.12 *Case of sharp and large phase jumps (>2π)* (a) (q_x,q_z) slice of a CXD pattern from a 30x30x30 nm^3 Wulff crystal. A single edge dislocation with $\boldsymbol{b}$ = 1/2[1 $\bar{1}$ 0] is introduced at the centre of the crystal, and the calculation is performed in the vicinity of the 1 $\bar{1}$ 1 reciprocal lattice point. (b) Phase $\varphi_{2\,\bar{2}\,0}$ calculated from the atomic position shown in the (1 1 $\bar{2}$) plane. (c) Successful reconstruction of the $\varphi_{2\,\bar{2}\,0}$ phase shown in the same (1 1 $\bar{2}$) plane. (d) Failed reconstruction of the $\varphi_{2\,\bar{2}\,0}$ phase shown in the (1 1 $\bar{2}$) plane.

An additional criterion was proposed by Labat *et al.* (2015) to discriminate between the solutions of the phase retrieval. It is based on the homogeneity of the reconstructed electron density. For the set of solutions with the largest metric error, large variations in the electron density are observed between the two phase shifted regions. The associated density in the small green region is approximately four times larger than the density in the purple region (not shown here). The variations in the electron density are much smaller in the set of solutions with the lowest metric error, confirming that this criterion is also reliable to discriminate between different solutions. The reconstruction of the displacement field for $\boldsymbol{g}$ = 2 $\bar{2}$ 0 is thus a good illustration of the risk of stagnation of phase retrieval algorithms in local minima. Here it should be noted that the number of iterations for the HIO algorithm are only half the number of iterations for the ER algorithm. A larger number of HIO iterations might help to prevent this phenomena, but this has not been tested. In any case, the success rate of the phase retrieval procedure drops from 100% for $\boldsymbol{g}$ = 1 $\bar{1}$ 1 to only 30% for $\boldsymbol{g}$ = 2 $\bar{2}$ 0. This is an indication that large values of sharp phase jumps ($\Delta\varphi > 2\pi$) seem to be difficult to handle by conventional phase retrieval algorithms. It is well known that the convergence of standard phase retrieval algorithms is difficult in systems with large phase variations (>> 2π, Diaz *et al.* 2010). However, the difficulties of convergence in the presence of large and sharp phase jump have not been reported to our knowledge. We will see in Chapter VI and VII that they are not very

common in our experimental systems, where the dislocations are often dissociated into partials (Chapter III). When the dislocation is dissociated, the overall phase jump is kept to the same value, but spatially divided between the two partials, so that it is generally below 2π unless Bragg reflections with high (h,k,l) indexes are used.

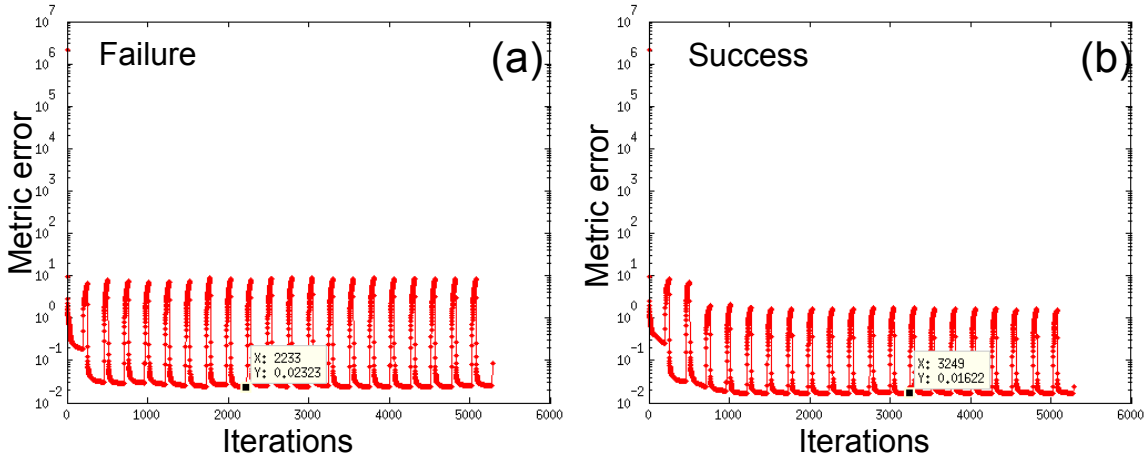

Fig. I.13 *Shape of the Error-metric for a failed and successful reconstruction*

I.4.5.2 Extent of the reciprocal space pattern, resolution and oversampling conditions

The resolution in real space is inversely proportional to the extent of the reciprocal space; the latter can be adjusted in order to improve the resolution. In the following we try to evaluate to which extent the resolution can be increased, for a given particle size.

Coherent Diffraction Imaging is a reciprocal-space based imaging technique as compared to most of its counterpart imaging method. The maximum attainable resolution is not limited by the optics and depends on the maximum extent of the Brillouin zone measurable with a sufficient signal-to-noise ratio. With a typical coherent flux of the order of 10^{10} photons/s at 3rd generation synchrotron sources, CDI experiments require long exposure times to improve the spatial resolution. There is thus a trade-off between the best achievable resolution and measurement time. With the help of nanofocusing the coherent flux on the sample can be efficiently increased, reducing considerably the exposure time needed to reach high spatial resolution. Schroer *et al.* (2008) reported a resolution of 5 nm in a reconstructed gold nanoparticle using a nanofocused beam.

On simulated data, the photon flux is not a problem, and the resolution is theoretically unlimited. It is actually limited by the limit of size of the computational arrays used for the phase retrieval which depends on the computational power. We have seen in sub-section I.4.3.1 that the diffraction data needs to be oversampled to allow the retrieval of the complex density. A commonly reported criterion for the case of nanocrystals is the number of pixel per fringe in the reciprocal space pattern. 2 pixels per fringe ensure that the CXD pattern is oversampled (Williams *et al.* 2003). This criterion is even too strong since an oversampling of a factor 2 along each direction of the space is not needed for 2 D and 3 D systems (Miao *et al.* 1998). For a given number of points in the computational array, the extent of the Brillouin zone that can be selected and the corresponding resolution in the real space depends on the size of the simulated particle. The smaller is the particle, the larger is the period of the corresponding fringes, and the easier it is to fulfil the oversampling conditions.

Here the diffraction patterns are calculated from the same 30x30x30 nm^3 copper particle using Eq. (I.13) around the 1 $\bar{1}$ 1 reciprocal lattice point. This Bragg reflection is chosen because of its high success rate for the inversions. Four different ranges are selected for the extent of the reciprocal space patterns, which all consist of 128x128x128 points.

The smallest extent is 0.07 nm^{-1}, giving a pixel size of 1.4 nm in every direction of the space, while the largest is

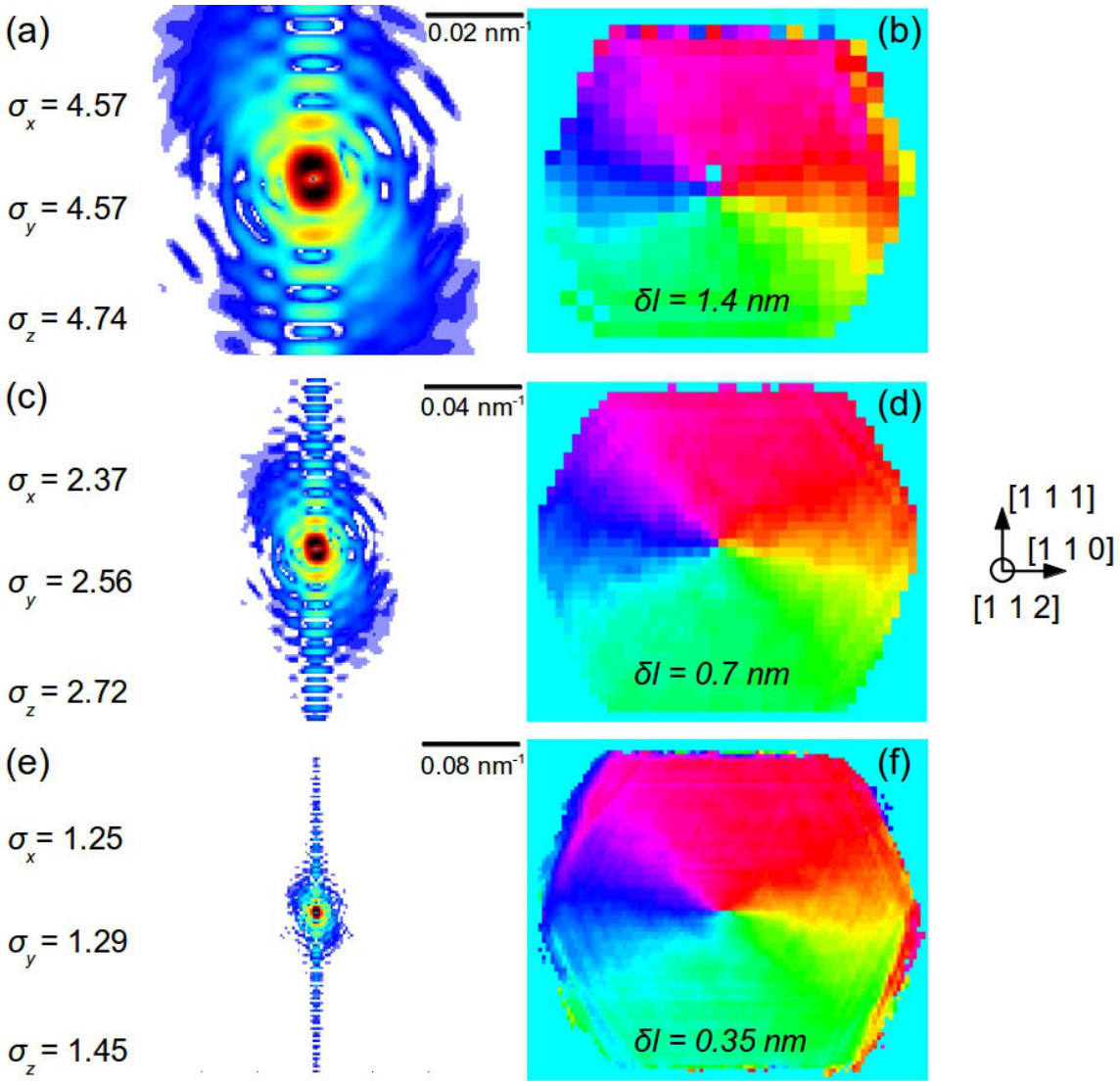

Fig. I.14 *Enhancement of the resolution in the real space reconstruction by increasing the spatial extent in the reciprocal space.* The σ values denote the oversampling ratio. (a) Δq = 0.07 nm^{-1} corresponding to δl = 1.4 nm. (b) Δq = 0.14 nm^{-1} corresponding to δl = 0.7 nm. (c) Δq = 0.28 nm^{-1} corresponding to δl = 0.35 nm.

0.35 nm^{-1} giving a pixel size of 0.28 nm. In between, two intermediate ranges are selected : 0.14 nm^{-1} (pixel size of 0.7nm) and 0.28 nm^{-1} (pixel size of 0.35 nm^{-1}). For each spatial extent, the phase retrieval is carried out using the procedure described previously using only 5 random starts. For the two smallest spatial extents, the reconstructions are successful for all five random starts. For Δq = 0.28 nm^{-1}, the success rate drops to 60% (3 out of 5), while the reconstructions systematically fail for the largest spatial extent.

Since it was shown in the previous section that a 100% success rate for the phase retrieval for $\boldsymbol{g} = 1\ \bar{1}\ 1$ if the oversampling conditions are fulfilled, the success or failure of the phase retrieval is here related to the oversampling conditions. Independently of the extent of the reciprocal space extent, the computational array for the complex sample density is equal to the number of reciprocal space points (*i.e.* 128x128x128 points). Following the definition of the oversampling ratio, the number of points in the finite sample which contains all the unknown values of the complex-electron density can be used to calculate the oversampling ratio. The initial support is estimated by the Patterson function, and the final support has a shape which is close to the crystal

equilibrium shape. For the sake of simplicity, a cubic support is considered for the calculation of σ.
For the smallest spatial extent, all the complex densities values are contained in a support which consist of 28x28x27 points. This gives the following values for the oversampling ratio in the three directions of the space: $\sigma_x = \sigma_y = 4.57$ and $\sigma_z = 4.74$ and an overall oversampling ratio $\sigma = \sigma_x \sigma_y \sigma_z = 99$! The oversampling conditions are thus largely fulfilled.

The values for the other spatial extents are presented in Tab. I.1 :

	σ_x	σ_y	σ_z	σ
$\Delta q = 0.07$ nm^{-1}, $\delta l = 1.4$ nm	4.57	4.57	4.74	99
$\Delta q = 0.14$ nm^{-1}, $\delta l = 0.7$ nm	2.37	2.56	2.72	16.5
$\Delta q = 0.28$ nm^{-1}, $\delta l = 0.35$ nm	1.25	1.29	1.45	2.34
$\Delta q = 0.35$ nm^{-1}, $\delta l = 0.28$ nm	1.05	1.08	1.11	1.26

Tab. I.1 *Oversampling ratio obtained for different spatial extent in the reciprocal space*

Note that σ is calculated for a cubic sample, the oversampling ratios are thus underestimated.
For the intermediate spatial extent ($\Delta q = 0.14$ nm^{-1}), the overall oversampling ratio is still largely fulfilled as well as along the three directions of space. This explains the 100% success rate for the two largest ratios.
For $\Delta q = 0.28$ nm^{-1} both the overall oversampling ratio and the oversampling ratios along each direction are satisfied ($\sigma_i > 2^{1/3}$), but only by a very slight margin. σ is even below the empirical limit value of 2.57 that was given by Miao *et al.* (1998). As discussed above, the number of unknown values is overestimated and σ is in fact probably very close to this value.
For the larger value of the spatial extent, the oversampling conditions are not satisfied, explaining the systematic failure of the reconstructions.
We conclude that the value of 0.28 nm^{-1} corresponds to the upper limit of the spatial extent for this particle size and this number of reciprocal space points. Provided that the diameter of the particle is increased and that the reciprocal space sampling is increased, it is likely that a reciprocal space extent which cover the full Brillouin zone is reachable.
The increase of the spatial extent and the corresponding improvement of the resolution is illustrated in Fig. I.14. It is shown that the resolution can be improved by a factor 2 in each direction of space as compared to the previous reconstructions presented in this manuscript (Fig. I.11 and Fig. I.12). As illustrated in Fig. I.14e-f, the oversampling criterion defined by Williams *et al.* 2003 (2 pixels per fringe) is overestimated. This is another evidence that the oversampling conditions are relaxed for 3D systems.

We stated in the introduction of this section that the resolution corresponds to the pixel size for the case of simulated data. This can be attributed to the fact that the retrieved phases are extremely reproducible. This is a different story for experimental data, where the noise inherent to experimental measurement and the partial coherence effects induce a resolution significantly larger than the pixel size. For experimental data, the resolution of the final reconstruction can be estimated using the phase retrieval transfer function (PRTF) (Chapman *et al.* 2006). This function can be used to assess the reproducibility of the retrieved phase and hence the resolution at which features are reliably reproduced. It is defined as :

$$PRTF(\boldsymbol{q}) = \frac{|\langle F(\boldsymbol{q})\rangle|'}{\sqrt{I(\boldsymbol{q})}} \tag{I.30}$$

where $I(\boldsymbol{q})$ is the measured intensity for the diffraction pattern and $|\langle F(\boldsymbol{q})\rangle|'$ is the amplitude of the Fourier

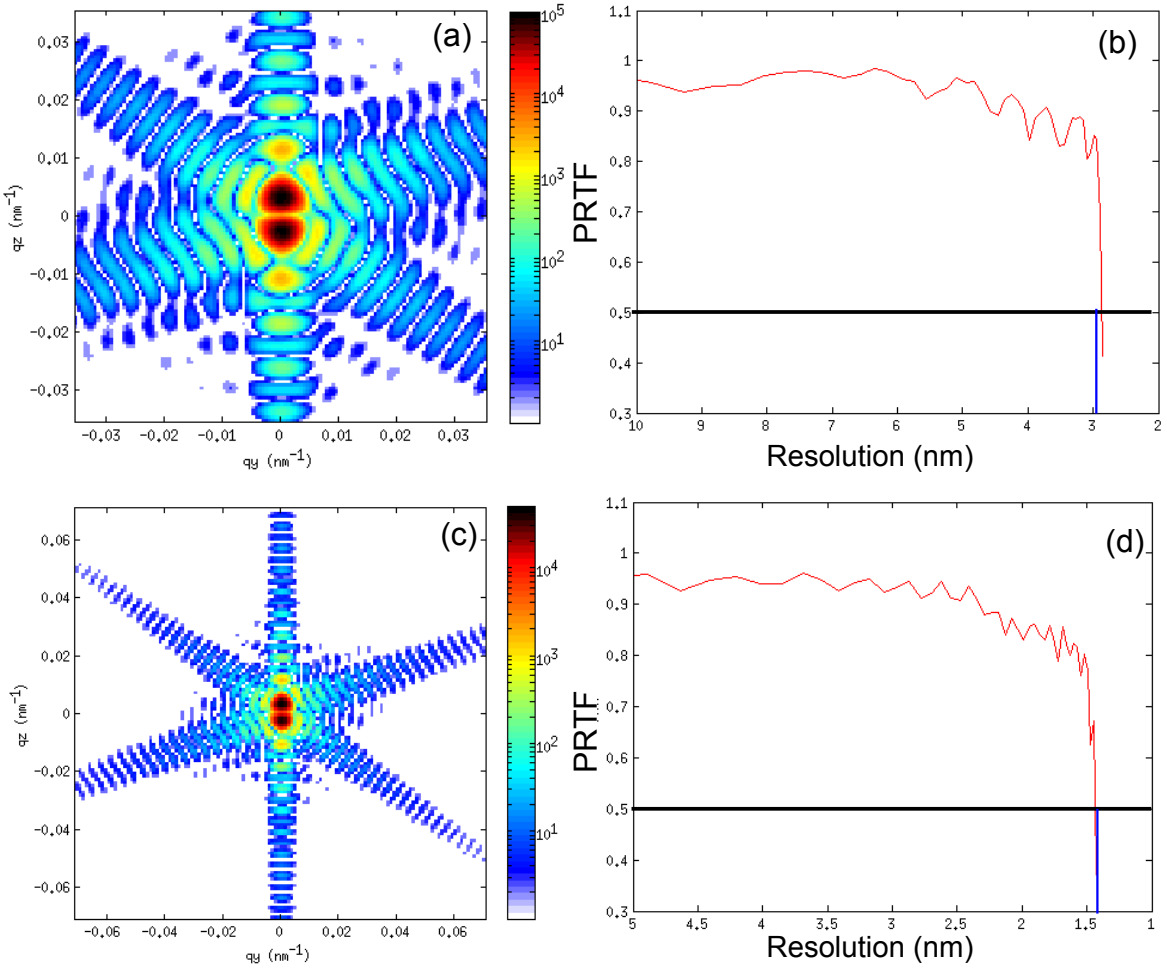

Fig. I.15 *Resolution of the reconstruction given by the phase retrieval transfer function (PRTF)*(a) – (c) Calculated CXD pattern from a perfect edge dislocation introduced at the centre of a copper Wulff crystallite. This diffractions pattern are used for the reconstruction of the displacement field for two spatial extents (a) Δq = 0.07 nm^{-1} (c) Δq = 0.14 nm^{-1} (b) and (d) Corresponding phase retrieval transfer function which gives the resolution.

transform of the average of the complex-sample densities retrieved $|\langle f(\boldsymbol{r})\rangle|$, after convolution with the normalized MCF, which gives the complex degree of coherence. It is equal to 1 for simulated data.
The function is plotted as a function of the real space resolution for two distinct spatial extents corresponding to pixel sizes of 1.4 nm and 0.7 nm. Here $|\langle f(\boldsymbol{r})\rangle|$ is averaged over only 5 estimates for both resolution values. The resolution is indicated by the drop of the PRTF at a particular value. A conservative estimate is a value of 0.5 (Chapman *et al.* 2006). This gives a resolution of 3 nm for the small spatial extent and 1.5 nm for the intermediate one. These values are slightly larger than the pixel size, but only by a slight margin.

Conclusion

In this chapter, basics of Cohenrent X-ray diffraction are introduced, along with the requirements for Coherent X-ray imaging. In particular, we focus on reviewing the different algorithm for reconstruction: a special attention is given to the ability to handle large local phase jump associated with crystal discontinuities, and the choices we make in our approach. The discussion is extended to the range of reciprocal space to be measured and the resulting resolution.

Bibliography

Beutier *et al* (2009) New J. Phys. **11**, 113026.

Beutier, G., Verdier, M., Parry, G., Gilles, B., Labat, S., Richard, M. I., Cornelius, T., Lory, P. -F., Vu Hoang, S., Livet, F., Thomas, O. & De Boissieu, M. (2013). *Thin Solid Films* **530**, 120-124.

Born, M. & Wolf, E. (1980). *Principles of Optics*, 6th ed. Oxford: Pergamon Press

Brauer *et al* (1995) *Phys. Rev. Lett.* **74**, 2010.

Burdet *et al* (2015) Optics Express **23**, 5452.

Chamard., V, Dolle, M., Baldinozzi, G., Livet, F., de Boissieu, M., Labat, S., Picca, F. , Mocuta, C. Donnadieu, P. and Metzger, T.H. (2010) *Journal of Modern Optics* **57**(9), 816–825

Chamard *et al* (2010b) *Phys. Rev. Lett.* **104**, 165501.

Chapman, H. N. *et al*. (2006) *J. Opt. Soc. Am.* **A 23**, 1179–1200 .

Chen, C.-C., Miao, J., Wang, C. W. & Lee, T. K. (2007). *Phys. Rev. B* **76**, 064113.

Chesnel *et al* (2002), Phys. Rev. B **66**, 172404.

Clark *et al* (2013) Science **341**, 56.

Clark, J. N., Huang, X., Harder, R. & Robinson, I. K. (2012) . *Nature Comm.* **3**, 993 .

Clark, J. N., Ihli, J., Schenk, A., Kim, Y-Y., Kulak, A. N., Campbell, J. M., Nisbet, G., Meldrum, F. C. & Robinson, I. K (2015) *Nature materials* **14**

Diaz, A., Chamard, V., Mocuta, Stangl, J., Mandl, B., Vila-Comamala, J., Metzger, T.H. & Bauer, G. (2009) *Phys. Rev. B.* **79**, 125324.

Diaz, A., Chamard, V., Mocuta, C., Magalhaes- Paniago, R., Stangl, J., Carbone, G., Metzger, T.H., Bauer, G. (2010) *New J. Phys.* **12**, 035006.

Eisebitt, S. , Lörgen, M., Eberhardt, W., Lüning, Stöhr, J., Rettner, C., T., Hellwig, O., Fullerton, E. E. & Denbeaux, G. (2003). Phys. Rev. B. 68, 104419

Eisebitt, S., Luning, J., Schlotter, W. F., Lorgen, M., Hellwig O., Eberhardt, W. & Stohr, J. (2004) Nature 432, 885

Favre-Nicolin, V., Richard, M. I. & Renevier, H. (2011). *J. Appl. Cryst.* **44**, 635-640.

Fienup. J. R. (1978) *Optics Letters* **3**(1), 27–29.

Fienup, J. R. (1982). *Appl. Opt.* **21**, 2758–2768.

Harder, R., Pfeifer, M. A., Williams, G. J., Vartaniants, I. A. & Robinson, I. K. (2007). *Phys. Rev. B* **76**, 115425

Harder, R., Liang, M., Sun, Y., Xia, Y. & Robinson, I. K. (2010). *New Journal of Physics* **12**, 035019

Hirth, J. & Lothe, J. (1968). *Theory of dislocations*, edited by McGraw-Hill, New York.

Gabor, D. A. (1948). *Nature* **161**, 777-778.

Gabor, D. A. (1949) *Proc. Royal Soc. A* **197**, 454-487.

Gerchberg, R. W. & Saxton, W. O. (1972). *Optik (Stuttgart)* **35**, 237–246 .

Jacques ,V. L. R. (2009) PHD thesis : *Application de la diffraction cohérente des rayons X à l'étude de défauts topologiques dans les structures atomiques et électroniques*

Jacques, V. L. R., Ravy, S., Le Bolloc'h, D., Pinsolle, E., Sauvage-Simkin, M. & Livet, F. (2011). *Phys. Rev. Lett.* **106**, 065502.

Kohl, M. & Baumbach, T. (2012). *Optics Express* **20**, 17093-17106.

Labat. S., Richard, M-I., Dupraz, M., Gailhanou, M., Beutier, G., Verdier, M., Mastropietro, F., Cornelius, T. W., Schülli, T. U., Eymery, J. & Thomas, O. (2015) *ACS Nano*

Le Bolloc'h *et al* (2005) Phys. Rev. Lett. **95**, 116401.

Lin *et al* (2003) Phys. Rev. Lett. **90**, 074801.

Livet, F. (2007). *Acta. Cryst.* **A63**, 87-107.

Livet *et al* (2011) Surface Science **605**, 390–395

Marchesini, S. (2003). *Phys. Rev. B* **68**, 140101

Marchesini. S (2007) *Review of Scientific Instruments* **78**(1), 011301.

Mainville *et al* (1997) J. Appl. Cryst. **30**, 828-832.

Mastropietro, F., Carbone, D., Diaz, A., Eymery, J., Sentenac, A., Metzger, T. H., Chamard, V. & Favre-Nicolin, V. (2011). *Optics Express* **19**, 19223

McCallum, B. C. & Bates, R. H. T. (1989). *Journal of Modern Optics* **36**, 619–648.

Mercère, P., Zeitoun, P., Idir, M., Le Pape, S., Douillet, D., Levecq, X., Dovillaire, G., Bucourt, S., Goldberg, K. A., Naulleau, P. P. & Rekawa, S." (2003) *Opt. Lett.* **28**, 1534-1536

Miao, J., Sayre, D. & Chapman. H., N. (1998) *Journal of the Optical Society of America* **15** (6), 1662–1669.

Miao *et al* (1999) *Nature* **400**, 342.

Mulvey, M. E. (1952) *Journal of the Optical Society of America* **42**, 763-769.

Panzner, T., Leitenberger, W., Grenzer, J., Bodenthin, Y., Geue, T., Pietsch, U. & Mohwald, H. (2003). *J. Phys. D Appl. Phys.* **36**, A93.

Pellegrini & Stöhr (2003) Nuclear Instruments and Methods in Physics Research A **500**, 33–40.

Pierce *et al* (2009) Phys. Rev. Lett. **103**, 165501.

Pfeifer, M. A., Williams, G. J., Vartanyants, I. A., Harder, R. & Robinson, I. K., (2006). *Nature* **442**, 63-66.

Robinson (2008) Z. Kristallogr. Suppl. **27**, 27-35

Robinson, I. & Harder, R. (2009). *Nature Materials* **8**(4), 291–298.

Rodenburg, J. M. & Faulkner, H. L. M. (2004). *Appl. Phys. Lett.* **85**, 4795-4797

Sayre, D. (1952) *Acta. Cryst.* **5**, 843.

Schroer, C.G., Boye, P., Feldkamp, J.M., Patommel, J., Schropp, A., Schwab, A., Stephan, S., Burghammer, M., Schoder, S. & Riekel, C.(2008) *Phys. Rev. Lett.* **101**, 090801.

Shannon, C. (1949). *Proc. Inst. Radio Engineers* **37**, 10–21.

Stadler, L. -M., Harder, R., Robinson, I. K., Rentenberger, C., Karnthaler, H. -P., Sepiol, B. & Vogl. G. (2007). *Phys. Rev. B* **76**(1), 014204.

Streit *et al* (2007) Phys. Rev. Lett. **98**, 047801.

Sutton, M., Mochrie, S. G. J., Greytak, T., Nagler, S. E., Berman, L. E., Held, G. E. & Stephenson, G. B. (1991). *Nature (London)* **352**, 608–610.

Sutton (2008) C. R. Physique **9**, 657–667.

Takagi, S. (1969). *J. Phys. Soc. Jpn.* **26**(5), 1239–1253.

Takahashi, Y., Suzuki, A., Furukatu, S., Yamauchi, K., Kohmura,Y. & Ishikawa, T. (2013). *Phys. Rev. B* **87**, 121201.

Takayama *et al*, J. Synchrotron Rad. (1998). 5, 456 – 458

Toellner, T. S., Hu, M. Y., Sturhahn, W., Bortel, G., Alp, E. E. & Zhao, J. (2001). *J. Synchrotron Rad.* **8**, 1082–1086.

Ulvestad, A., Clark, J. N., Harder, R., Robinson, I. K. & Shpyrko, O. G. (2015), *Nanoletters* **15**

Vartanyants, I. A. & Robinson, I. K. (2001) *J. Phys. Condens. Matter* **13**, 10593–10611.

Vartanyants & Singer (2010), New J. Phys. **12**, 035004.

Vaxelaire N. (2011) PHD Thesis: *Etude des Inhomogénéités de déformation dans les films minces polycristallins par diffraction X cohérente*

Verbeni, R., Sette, F., Krisch, M. H., Bergmann, U., Gorges, B., Halcoussis, C., Martel, K., Masciovecchio, C., Ribois, J. F., Ruocco, G. & Sinn, H. (1996). *J. Synchrotron Rad.* **3**, 62–64.

Williams, G. J., Pfeifer, M. A., Vartanyants, I. A. & Robinson, I. K. (2003). *Phys. Rev. Lett* **90**(17),175501

Watari, M., McKendry, R. A., Vögtli, M., Aeppli, G., Soh., Y- A., Shi, X., Xiong, G., Huang, X., Harder, R., and Robinson, I., K. .(2011), *Nature Materials* **10**, 862-866

Yakhou *et al* (2001), *J. of Magnetism and Magnetic Materials* **233**, 119–122.

Contents

Introduction....41
II.1. Synchrotron Sources....41
II.1.1. Description of the coherence set-up....42
II.1.1.1 Slits and focusing optics....42
II.1.1.2 Kirkpatrick-Baez (KB) mirrors....43
II.1.1.3 Fresnel zone plates (FZP)....44
II.1.1.4 Coherence set-up, photon flux and degree of coherence....45
II.1.2. Detectors....47
II.1.2.1 Correction of the defects for 2D detectors....48
II.1.3 Diffractometers and sample stage....49
II.1.4 Measurements in the reciprocal-space using diffractometers - Isolation of a single island....50
II.1.5 Collection of 3D reciprocal space maps from isolated objects....51
II.1.6 Reconstruction of the 3D diffraction pattern in the sample orthonormal basis....52
II.2. Surface diffraction....54
II.2.1 Crystal truncation rods....54
II.2.2 X-ray diffraction from the surface region....56
II.2.3 Surface X-ray diffraction experimental set-up....56
II.2.4 Measurement of the rod intensities....58
II.3. Samples....58
II.3.1. Islands....59
II.3.1.1 Solid-state dewetting....59
II.3.1.2 Equilibrium shape of the particles....61
II.3.2 Nanowires....64
II.4. Sample characterization....66
II.4.1 Ex situ indentation....66
II.4.2. Synchrotron characterization....72
II.4.2.1 Laue microdiffraction....72
II.4.2.2 Finding the sample of interest: 2D fast-mapping of the sample....76
II.4.2.3 Mapping the sample strain and tilt: Scanning-X-ray Diffraction Microscopy (SXDM)…78
II.4.3 Multi-characterization of a sample....83
Bibliography....86

Chapter II: Experimental methods and samples

Introduction

X-ray diffraction (XRD) methods are very efficient to characterize the strain or defect content of crystals. We used several XRD techniques to access a large range of structural properties in sub-micrometer crystals. Among them, coherent X-ray diffraction (CXD) gives access to the 3D displacement field, while surface diffraction techniques enable the determination of the atomic structure of surfaces and interfaces. These techniques usually require the use of a high brilliance X-ray source and the experimental part of this work was mostly carried out in 3rd generation synchrotron facilities.
In a first section of this chapter, we present the experimental set-up required to perform synchrotron CXD and Surface X-Ray Diffraction (SXRD) experiments. For the case of CXD, the preparation of the beam is a critical issue. The coherence set-up needed to obtain a beam with good coherence properties is thus presented in details in section II.1.2. For CXD experiments or even for conventional XRD experiments, the collection of 3D Reciprocal Space Maps is also essential to measure structural properties such as the strain. This requires the use area detectors which are presented in section II.1.3. The methods to collect these 3D maps, using six-circles diffractometers and to represent them in the orthogonal reference laboratory frame are described in the last two sections of this first part.
In a second part of this Chapter, the emphasize is put on the samples that were used during this work. Both processing and characterization methods are described. Some of them are very usual (SEM and AFM) while others are more specific to this work (*ex situ* nanoindentation, µ-Laue diffraction, scanning X-ray diffraction microscopy …). The chapter is concluded by an example of a complete characterization of a sample used for CXD experiments.

II.1. Synchrotron Sources

The diffraction experiments presented in this manuscript have been carried-out on several synchrotron beamlines in three different 3rd generation synchrotron facilities. In this section, we present the set-up of two beamlines where CXD experiments can be performed: the ID01 beamline at the ESRF (Grenoble) and the CRISTAL beamline of the French synchrotron SOLEIL.

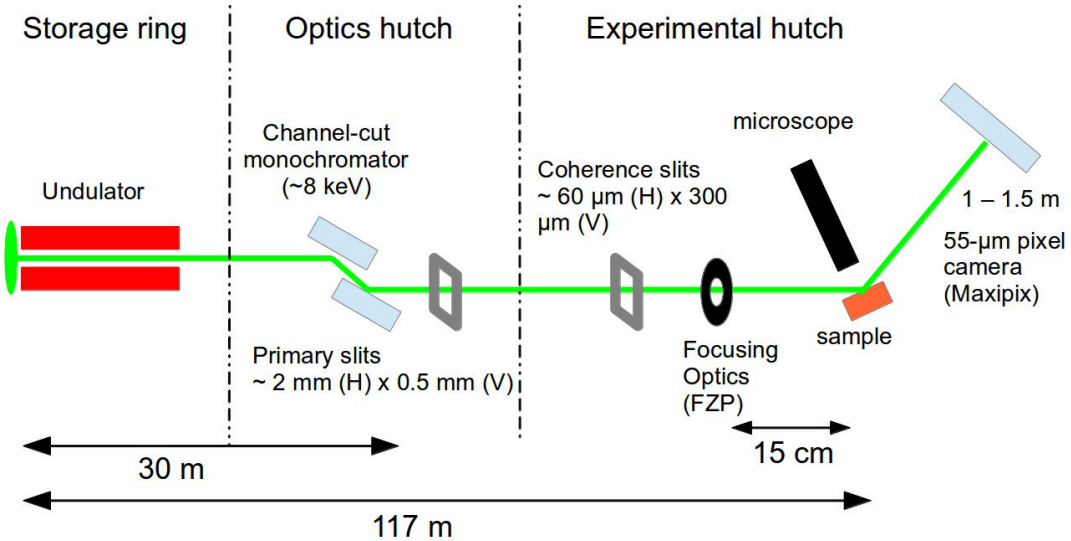

Fig. II.1: *Layout of the experimental set-up on the ID01 beamline*

Fig. II.1 shows the general layout of the ID01 beamline. The set-up has some particularities that will be discussed later in this section. Note that the ID01 beamline was upgraded in 2014 and that CXD experiments were carried out before and after the upgrade in this beamline.
Here we only describe the upgraded set-up that consists of three main parts. The undulator located in the storage ring which is the source of the beam, the optics hutch where the beam is monochromatized and the experimental hutch where the CXD experiment itself is carried-out. The constituting elements of these three parts are described in the following.
Although in principle a coherent X-ray beam can be obtained from a bending magnet source, the high brilliance needed for the experiments reported here requires using undulator sources. Indeed, all beamlines which have developed a CXD set-up are built on an undulator.
The CRISTAL and ID01 beamlines differ in the properties of the source, *i.e.* its size and divergence, which essentially depends on the electron beam in the undulator. For the ID01 beamline the source size and divergence are respectively equal to 0.134 (H) x0.024 (V) mm^2 (FWHM) and 0.140 (H) x0.009 (V) $mrad^2$ (FWHM). For the CRISTAL beamline, values of 0.84 (H) x 0.019 (V) mm^2 (FWHM) and 0.047 (H) x 0.031 (V) $mrad^2$ (FWHM) are obtained for the source size and divergence respectively.
At 30 metres from the source, which corresponds roughly to the exit of the primary slits, beam sizes of 1.7 (H) x 0.85 (V) mm^2 and 8.7 (H) x 0.55 (V) mm^2 are obtained for CRISTAL and ID01 respectively.
The two X-ray sources can be compared in terms of brilliance B. This quantity takes into account the number of photons produced per second, the angular divergence of the photons and the cross-sectional area of the beam and is thus given by:

$$B = \frac{photons}{s.mrad^2.mm^2.0.1\%BW} \quad \text{(II.1)}$$

where the term 0.1% BW means that only the photons within a bandwidth of 0.1% of the central wavelength are counted. In third-generation synchrotron facilities, undulators typically provide a brilliance of 10^{20} ($ph.s^{-1}.mm^{-2}.mrad^{-2}$).
At the energy considered in this work (> 8 keV), the ESRF is already providing a larger brilliance than SOLEIL, and the brilliance of the source will be further improved (by approximately one order of magnitude) with the 2015-2019 upgrade of the facility.
For both beamlines the monochromatization of the beam is ensured by a channel-cut double crystal Si (1 1 1) monochromator. At 8 keV the monochromaticity of the beam $\Delta\lambda/\lambda$ is of the order of 10^{-4}. For the CRISTAL beamline, a second double crystal Si(3 1 1) monochromator is also available. It can be used for the larger energy ranges (up to 60 keV).
In term of flux, a value of $5x10^{13}$ photons.s^{-1} flux is measured for the ID01 beamline, with primary slits closed to 2.0 (H) x 0.5 (V) mm^2 (FWHM). It should be noted that the large value for the horizontal divergence implies a large horizontal beam size in the optic hutch (approximately 5.5 mm). A significant part of the beam is thus lost before which results in a decrease of the total photon flux.
The horizontal divergence is less pronounced for the CRISTAL beamline, and a beam-size of 2.0 mm (H) x 1.2 mm (V) is measured 40 m downstream the source, when the primary slits are fully opened. The corresponding photon-flux is slightly smaller with a value of $2.3x10^{13}$ photons.s^{-1}.

II.1.1. Description of the coherence set-up

II.1.1.1 Slits and focusing optics

In a synchrotron experiment, the source sample distance is generally of the order of 50 m. However, for

the three beamlines we used for CXD experiments, this distance greatly varies, ranging from 36 m on the CRISTAL beamline, to 220 m in the I 13-1 coherence beamline at the Diamond Light Source.
At the upgraded ID01 beamline, this distance is intermediate, with a value of 117 m (Fig. II.1). Using Eq. (I.4), this gives respective horizontal and vertical transverse coherence lengths at 8keV of ξ_{th}= 135 µm and ξ_{tv} = 755 µm. These values suppose that there are no optics inserted in the path of the X-ray beam. In practice, the imperfections in the focusing optics (errors in the slope of the mirrors of the order of the micro-radian) tend to reduce the transverse coherence length. In order to clean the beam from the imperfections as well as reducing the source size seen from the sample, slits are inserted just after the optics to select an homogeneous part of the beam (Fig. II.1). In this document we call them primary slits. They are generally opened to values between 100 to 200 µm. To control the beam size and coherence properties of the beam, an additional set of slits is put close to the sample (Fig. II.1). The aperture of the slits needs to be carefully chosen, a too large sample slit is likely to affect the coherence properties of the beam resulting in reduced fringe visibility of the diffraction data. Conversely, decreasing the slits aperture ensures to extract the coherent part of the beam at the expense of the flux. It should be also noted that the scattering from the slits will tend to increase the size of the beam if the slits are closed to a too small value. In set-ups without microfocusing optics, the slits aperture was adjusted to obtain good coherence properties and to adjust the beam size. Current synchrotron beamlines are equipped with focusing optics (see next section) which allow to obtain sub-micrometer beam size at the focal spot. The only requirement for the sample slits is now to find a compromise between the flux and good coherence properties. Both the transverse dimensions of the focal spot and the focal depth are strongly influenced by the aperture of the sample slits. The smaller is the opening, the larger are these two quantities (Mastropietro *et al.* 2011). Typical values of (20x60 µm^2, HxV) were chosen on the ID01 beamline before the upgrade. After the upgrade, due to the increase in the transverse coherence length, the slits are now open to larger values of 60x300 µm^2 (HxV) in order to maximize the flux.
Also important, it is clear that for the sub-microns objects studied in this work, a vertical transverse coherence-length of 300 µm is not needed. When the beam is focused, the flux density is increased in the same proportion as ξ_{tv} is decreased (Livet 2007). For the study of small objects a reduced beam size is thus desirable in order to maximize the flux as discussed in section II.1.1.4 of this chapter. To obtain sub-micrometer beam sizes, high quality focusing elements have been developed, such as Kirkpatrick-Baez (KB) mirrors and Fresnel-zone plates (FZP).

II.1.1.2 Kirkpatrick-Baez (KB) mirrors

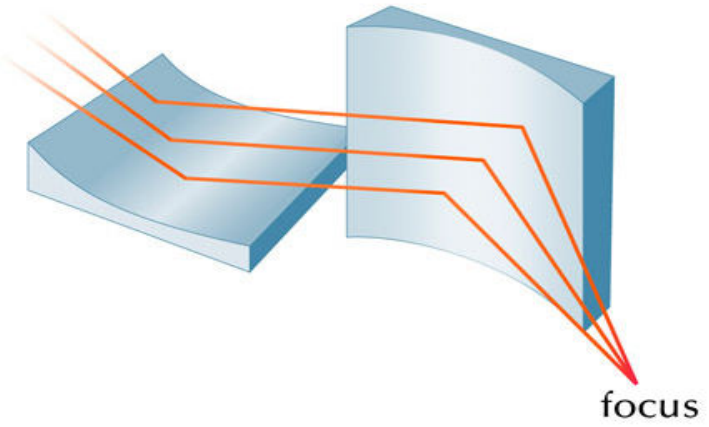

Fig. II.2 *Focusing of the X-ray beam with Kirkpatrick-Baez mirrors*

The system proposed by Kirkpatrick & Baez (1948) consist of two total reflection elliptical mirrors having two focal points; one at the light source and the other at the focal point. One mirror is used for vertical focusing and the other for horizontal focusing. A KB system is achromatic, and due to the high reflectivity of the mirrors, X-ray can be focused efficiently over a large energy range. KB-mirrors systems have a high efficiency and use the grazing incidence of the horizontal and vertical mirrors to focus, using the small refractive index of X-rays.

II.1.1.3 Fresnel zone plates (FZP)

Fresnel zone plates (FZP) are diffractive lenses. They consist of circular diffraction gratings made of a set of concentric rings, which alternate between opaque (or phase-shifting) and transparent material. The zones are spaced so that the X-rays constructively interfere at the desired focal length. The diameter of the focal spot is proportional to the width of the outer ring. With current FZP, diameters as small as a few nanometres can be obtained. However, since they are diffractive optics, FZP have chromatic aberrations, and their focal distance has a λ^{-1} dependence.

A Fresnel-zone plate has *m* diffraction orders (*m* being an odd integer) that lead to multiple focusing point at distances *f/m* with respect to the optical element (*f* being the focal length). Since the FZP is used as a focusing lens, only the first diffraction order is exploited and all the other orders are blocked by a beam-stop for the zeroth order and a pinhole, called order sorting aperture (OSA), for the higher ones ($m>1$). Both KB mirrors and FZP curve the wavefront of an incident plane-wave illumination. The degree of curvature of the wavefront is inversely proportional to the distance from the focusing optics. However, if the sample is small enough, the wavefront can be locally considered as a plane wave (Schroer *et al.* 2008, Mastropietro *et al* 2011).

The two types of focusing optics are fundamentally different in overall efficiency and aberration effects. The overall efficiency of a typical Fresnel-zone plate is rather low compared to that of KB mirrors. Their initial efficiency of the order of 10% (Yun *et al.*, 1999) can be raised by a suitable use of material (David *et al.* 2001). Complex multilevel zone plates can reach 50% efficiency (Fabrizio *et al.* 1999).

On the other hand, due to the extremely small focal spot produced by a FZP, the X-ray flux density at the focal spot is relatively higher (Schroer *et al.* 2008). That being said, a focal spot as small as few nanometres can be obtained with some sophisticatedly designed KB mirrors (Mimura *et al.* 2010). Additionally, as reflective focusing optics, they have much less optical aberrations than the FZP.

Both types of focusing optics have thus advantages and drawbacks, and their use depends on the requirements for the experiment.

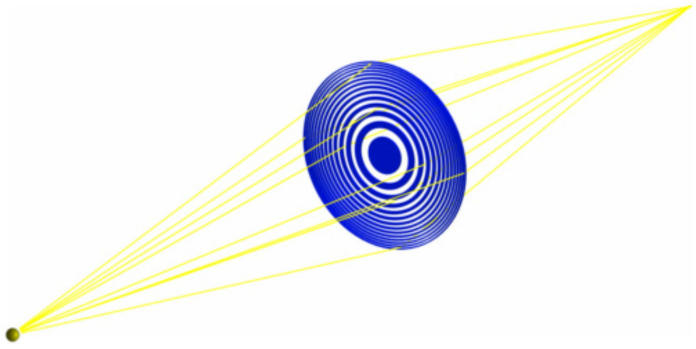

Fig. II.3 *Focusing of the X-ray beam with a Fresnel-Zone-Plate*

II.1.1.4 Coherence set-up, photon flux and degree of coherence

The FZP, OSA combination has been used for focusing of the beam spot for almost all the CXD experiment carried out during this work. KB mirrors have been used in only one CXD experiment on the I13-1 beamline. The coherence set-up on the CRISTAL beamline (coherence slits + FZP + OSA) allows to obtain a typical beam size of 2x0.5 (HxV) μm^2 (FWHM) at the sample. On the ID01 upgraded beamline, the coherence set-up allows to focus the beam on the sample to a smaller values of 0.150 (H)x0.100 (V) μm^2 (FWHM) (Fig. II.4). Given the size of the samples considered in this work (between 0.3 and 1 µm for the lateral dimensions), this beam size is too small if a reconstruction of the 3D displacement field by classical Coherent Diffraction Imaging (CDI) is intended. The full illumination of the sample, and thus the finite support constraint is not satisfied. For CXD experiments on the ID01 beamline, the FZP was generally translated to move the sample out-of the focal spot. This way, typical values of 0.8x0.5 (VxH) μm^2 (FWHM), ensuring the full illumination of the sample. Out of focus, the phase of the wave-front is in principle relatively constant.

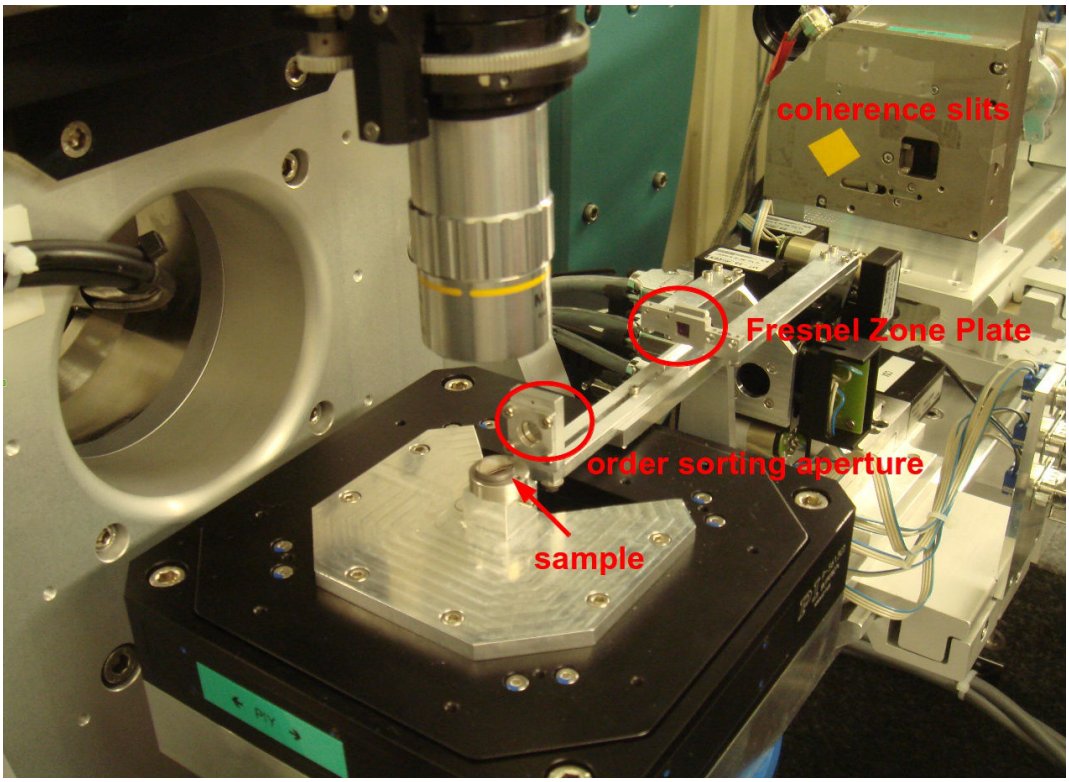

Fig. II.4 *Coherence set-up on the ID01 beamline*

The total number of photons available in the coherence volume is connected to the average source brilliance B (Livet 2007, Schroer *et al.* 2008):

$$D_c = F_c T = \mathrm{B}\left(\frac{\lambda}{2}\right)^2\left(\frac{\Delta\lambda}{\lambda}\right)T \qquad \text{(II.2)}$$

where F_c is the coherent flux, B is the brilliance of the source, T the total exposure time and $(\Delta\lambda/\lambda)$ is the degree of monochromaticity which impacts the longitudinal coherence length.
At 8 keV a brilliance of ~ 10^{20} is obtained with an undulator from a third generation synchrotron and using a Si

(1 1 1) crystal monochromator, typical values of 10^{-4} are achieved for the energy bandwidth. This gives an expected value of 10^{11} *photons.s*$^{-1}$ for the coherent flux. The total coherent flux also depends on the aperture of the coherence slits which generally match the transverse coherence of the beam. Given the larger size of the source and the smaller distance of the sample from the source at CRISTAL, the transverse coherence is approximately one order of magnitude smaller than that of the upgraded ID01 beamline. Hence, the coherence slits are closed to a much smaller value than at ID01. Typically the whole set-up gives a coherent flux of about 1 to 5 10^9 ph.s^{-1} in the 6-12 keV energy range used for CXD experiments.
On the upgraded ID01 beamline, a value of $6.2.10^{11}$ ph.s^{-1} is obtained for slits closed at 0.4x0.4 μm^2. This value does not correspond to the coherent flux on the sample, but it is clear that its value is currently at least one order of magnitude larger on the ID01 beamline than that of CRISTAL.
It should be noted that the photon-flux on the sample was generally not an issue in this work. The relatively large size of the samples and the strong scattering power of gold (and to a less extent of copper) insured a strong diffraction signal (typical dynamical range of 4 to 5 decades of intensity for the 1 1 1 Bragg reflection of 1 μm gold islands at 8 keV). However, a high photon-flux is desirable for CDI, unless the sample suffers from radiation damage.
As discussed in Chapter I, the resolution of the reconstructed image depends on the spatial extent of the diffraction data. A strong decay of the diffracted intensity is indeed observed with increasing scattering vector $\boldsymbol{q}$. The diffraction intensity decays with a power law $\boldsymbol{q}^{-\alpha}$ with α equal to 4 for a generic object.
It is thus clear that the coherent dose on the sample needs to be maximized on the sample. From Eq. (II.2), it comes that the number of photons in the coherence volume increases linearly with the exposure time, however, and as stated by Schroer *et al.* (2008), longer exposure time only provide a small gain in resolution as the exposure time grows with the fourth power of the resolution.
Much more can be gained by efficiently focusing the coherent flux onto the sample. With increasing gain g on the focusing set-up, the diffraction density is increased linearly, improving the spatial resolution as $\boldsymbol{g}^{1/\alpha}$ (Schroer *et al.* 2008). It is thus clear that the focusing optics (FZP, KB mirrors) play an important role in the expected spatial resolution, and explain why a particular effort is put in the focusing of the X-ray beams in recent coherent set-ups.

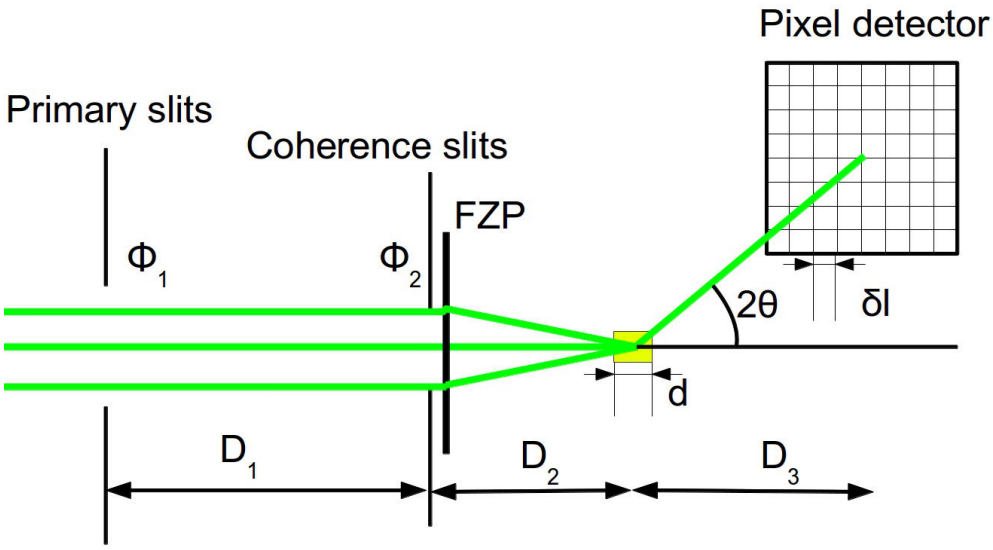

Fig. II.5 *Schematic of typical CXD experiments with focusing optics*

Another very important consideration for CXD experiments is the degree of coherence of the X-ray beam. As

discussed in Chapter I, it can be evaluated by the normalized mutual coherence function. Alternatively, the degree of coherence can also be simply expressed as the ratio between the coherent part of the X-ray beam ξ_t and the size of the beam σ at a certain distance of the optics (the origin $x = 0$ is the last optical element of the beamline before the sample) :

$$\beta(x) = \frac{\xi(x)}{\sigma(x)} \tag{II.3}$$

From Eq. (II.3) it comes that after the last optical element, the degree of coherence is kept independently of the distance *x*, and is characteristic of the X-ray beam.
Livet (2007) evidenced that the quality of the coherence set-up can be estimated by the calculation of an experimental degree of coherence which depends on the optics of the beamline.
Let us consider a beam between two sets of square slits of respective apertures Φ_1 and Φ_2 and separated by a distance D. The degree of coherence can be calculated by a series of expansion in the variable $z = \pi\Phi_1\Phi_2 / \lambda D$

$$\beta(z) = \left\{\sum_{n=0}^{\infty}(-1)^n 2^{2n+2} z^{2n}/[(2n+1)(2n+2)^2(2n+1)!]\right\}^2 \tag{II.4}$$

For the CXD experiments presented in this manuscript, Φ_1 is the aperture of the primary slits which acts as a secondary source (Fig. II.5). Φ_2 is the aperture of the coherence slits. This allows to define $z_1 = \pi\Phi_1\Phi_2 / \lambda D_1$ and the degree of coherence $\beta(z_1)$ between the source and the coherence slits/FZP where Φ_2 also corresponds to the illuminated fraction of the FZP. If the aperture is not square but rectangular, the square in Eq. (II.4) is replaced by the product of 2 equivalent expressions with appropriate values.
Similarly, the degree of coherence between the FZP and the sample is given by $\beta(z_2)$ with $z_2 = \pi\Phi_2 d / \lambda D_2$ where *d* the size of the diffracting sample defines the sample aperture.
Finally, a third term $\beta(z_3)$ allows to measure the detection contrast where $z_2 = \pi\delta l\, d / \lambda D_3$ where δl is the pixel size of the detector which defines the detector aperture. A very good approximation for the overall value of degree of coherence is given by the product of the contrast of the beam $\beta(z_1)$ with the diffraction contrast $\beta(z_2)$ and the detector contrast $\beta(z_3)$.
For the CXD experiments presented in this work, it was ensured that a degree of coherence of at least 0.75 was obtained with the coherence set-up with values generally superior to 0.9 (0 being an incoherent beam and 1 a fully coherent beam). It is a safe assumption to state that the X-ray beam illuminating the sample is not perfectly coherent, but we will see in the next chapters that successful reconstruction were possible for a variety of samples in this work. It should be noted that it is possible to take into account partial coherence effects to improve the convergence of the reconstructions (Clark *et al.* 2012), but this was not implemented in our reconstruction procedure.

II.1.2. Detectors

For X-ray imaging of the scattered intensities and for slow processes with low counting statistics, 2D area detectors are currently used. Three main type of detectors can be used for hard X-ray experiments. For most of the CXD experiments carried out during this work a pixel detector is used.
The "indirect" CCD detectors use a scintillator to convert the X-rays into visible light which can be detected by the CCD. The main advantage of these cameras relies in their ability to work at high energies (>20 keV range) and their reasonably good dynamical range (which is however significantly lower than that of pixel detectors). On the other hand, the requirement to convert the incident photon has some disadvantages: the conversion

process is inefficient, and since the photon is not directly detected, there is no ability to correlate the number of electrons to the incident energies. Another problematic issue is the CCD read-out noise. This kind of detector has not been used during this PhD.
In the case of a direct illumination CCDs (DI-CCD) the photons are directly collected on the CCD chip. They provide a good detection quantum efficiency in the 0.1-12 keV energy range. The DI-CCD are divided in two types: the front-illuminated 'deep-depletion' CCD (DD-CCD) and the back-illuminated CCD (BI-CCD).
In DD-CCD, the photons are detected close to the integrated circuit surface, at the vicinity of the CCD cell. For the detection of hard X-rays, the weak absorption by the silicon chip is overcome by increasing its thickness, hence the 'deep-depletion' appellation.
For the BI-CCD, the Si wafer is thinned down to about 50 µm and X-rays are absorbed on the opposite side and detected at the surface. It is possible to work with a very small pixel size (13.5 µm for the 2048x2048 chip of the CCD presented in Chapter X) which is interesting for high resolution measurements. However, the dynamical range of the CCD is very poor. A CCD cell saturates at about 200000 electrons, *i.e.* 100 photons.pixel^{-1} at 8 keV (Livet 2007). It is necessary to read the CCD frequently in order to avoid saturation. The chip is also very fragile, and it is quite easy to damage pixels if attenuators are not used. The other major issue with the DI-CCD detector is the slow readout. It is thus clear that both CCD detectors have some potentially problematic drawbacks: the readout noise for the indirect CCD detectors, and the potentially limited lifetime of the sensors and the slow read-out of DI-CCD.
A need therefore existed for detectors with faster readout and higher dynamical range yet providing noise-free detection and high spatial resolution. Fortunately, the pixel detectors can meet both this requirements. For these detectors, each pixel has its own sensor and amplifier, providing very fast readout times. This fast readout time and large dynamical range come at the price of the pixel size which is significantly larger than in the case of DD-CCD detectors (55 µm *vs*. 13 µm). Examples of these detectors are the Maxipix / Medipix (Ponchut *et al.* 2007), the XPAD (Bérar *et al.* 2002) and the Pilatus. Next generation single-photon counting detector are currently in development, such as the EIGER (Johnson *et al.* 2014) and XCALIBUR.
A typical chip size for these detectors is 256x256 pixels. The MAXIPIX detector is an assembly of 2x2 Medipix chips for a total of 516x516 pixels (there are 4 dead lines between two adjacent chips). It is the detector used for all the CXD measurements reported in this document, although other detectors have been used for measurements not reported here.

II.1.2.1 Correction of the defects for 2D detectors

The 2D detectors are never perfect and there are always some imperfections in the collected data. In the case of CCD cameras, the electronic noise and potentially defective pixels needs to be corrected.
For pixel detectors, the electronic noise is suppressed by an appropriate calibration, but the presence of “hot pixels” on the detector, *i.e.* pixels reading high values while no photons are collected is a common issue. If they are limited in number, they can simply be removed manually by setting their value to zero. Alternatively, a more efficient and reliable strategy is to record a dark image, *i.e.* the image collected by the detector when it is not exposed to any photon. An acquisition time similar to the acquisition time used for the measurement of the data is generally selected. In any case, this acquisition time needs to be large enough to provide good statistics. Each diffraction pattern collected is then corrected by the subtraction of this dark image.
For the diffraction data used for reconstruction (see Chapter VI and VII), a threshold is applied to the data set, *i.e.* all the pixels in the detector with less than a specific number of photons (for instance 2) are set to zero. This correction is critical when a flight tube is not used (*i.e.* a tube between the sample and detector which is under primary vacuum), due to the large amount of air scattering. This procedure is very efficient to reduce the noise on the reconstructed data.
Several algorithms have also been developed for the data correction, among them is the droplet algorithm (Livet 2000) which is able to perform several corrections simultaneously, among them are the removal of the cosmic X-rays subtraction of the background noise dark and the correction of the dispersion of photons on several pixels (a

common issue with DI-CCD cameras).

II.1.3 Diffractometers and sample stage

The diffractometers at ID01, CRISTAL and I13-1 use different geometries. They can all be described in the framework of the '4S+2D' geometry proposed by You (1999, Fig. II.6.c): there are 2 perpendicular detector axes ν (horizontal) and δ (vertical) and 4 perpendicular sample axes (μ, η, χ and φ).
ID01's diffractometer (Fig. II.6.b) is very similar to You's '4S+2D' diffractometer, except that there is no χ axis. However, the hexapod mounted on the diffractometer can act as such, on a small angular range (±5°).
CRISTAL's diffractometer (Fig. II.6.a) has a slightly different geometry: the traditional χ axis is replaced by a so-called κ axis, which is at 50° to the η axis: this geometry gives more free space for the sample environment. Angles calculations directly encoded in the control software allow to use it in the traditional Euler geometry.
The case of I13-1 (not shown here) is also different, since there is no proper diffractometer: the detector is mounted on an articulated robot arm, such as those used in the car industry, such that there are no physical ν and δ axes; moreover the η and χ axis are provided by tilted stages with range only ±15° and there is no φ axis above the tilt stages.

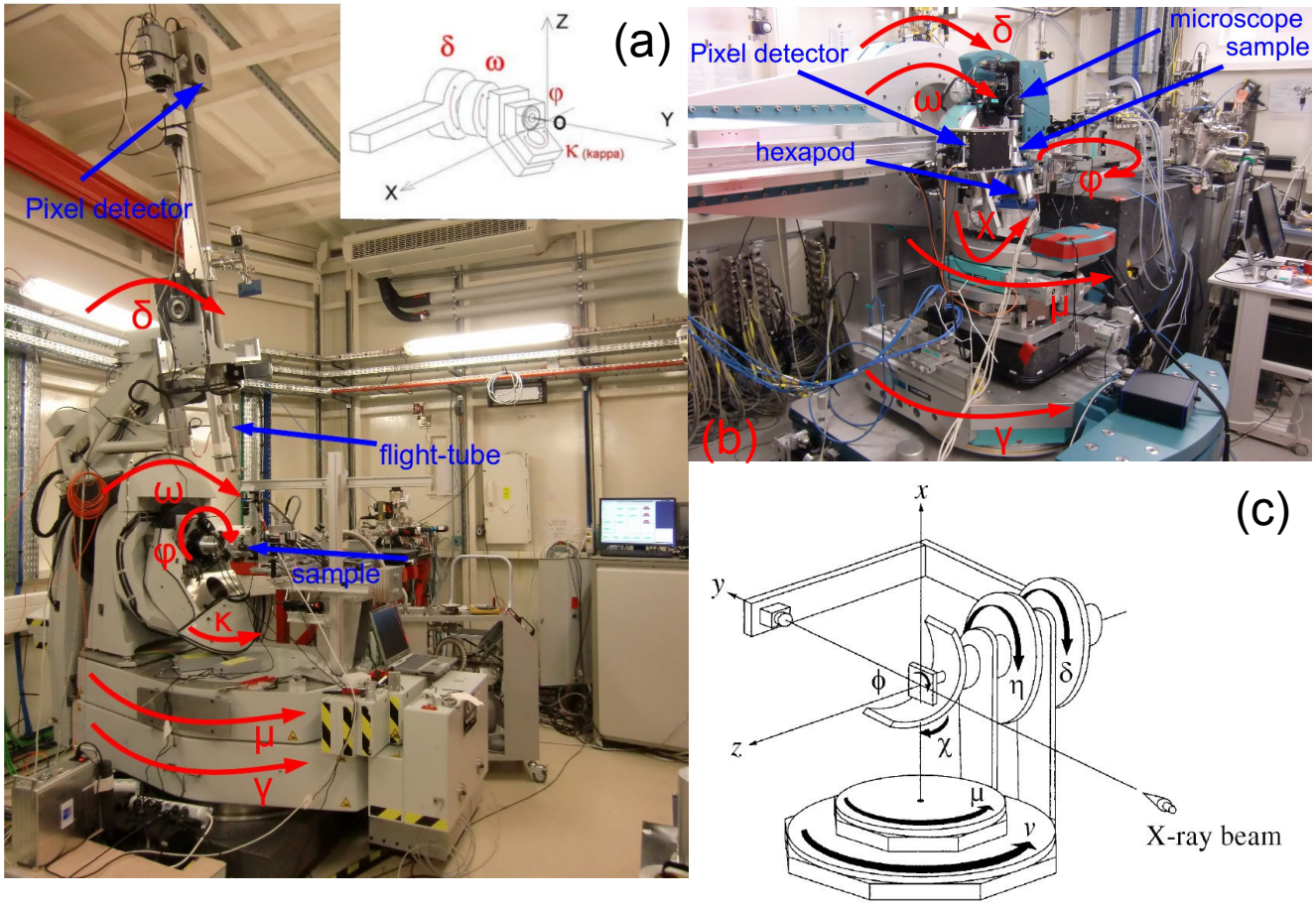

Fig. II.6 *Six circle diffractometers* (a) Six-circles diffractometer on the CRISTAL beamline (SOLEIL). (b) 2+4 circles diffractometer on the ID01 beamline (ESRF). (c) Schematic of a '4S+2D' diffractometer (from You, 1999).

The precision of a diffractometer is characterized by its 'sphere of confusion', which is a sphere inside which all rotation axes intersect. It should be as small as possible, and ideally smaller than the beam size or the sample.

This requirement is not met for our typical measurements, which are performed with beams and crystals of the order of the micron. For the 6C diffractometer on the CRISTAL beamline, the sphere of confusion is equal to 53 µm and 64 µm for the horizontal and vertical plane respectively. No data is available for the ID01 2+4C diffractometer, but a value larger than 20 µm can be estimated. These values are much larger than the ideal (~1 µm) but nevertheless good enough for our typical measurements, which consist mostly in a rocking curve (~1°) on a single reflection, if the beam and the crystal are carefully aligned at the centre of rotation. Several reflections from the same microcrystal can be measured after manual alignment of the crystal at each reflection.
The alignment of the sample in the beam is thus a critical step, and is performed with piezo-translation stages.
For the ID01 beamline for instance, the alignment is achieved thanks to a compact hexapod sitting on the diffractometer and a stack of three piezo-motors. The hexapod is typically used to align the substrate (tilts and height) as well as for the coarse in plane alignment of the microcrystal, while the piezo-motors are used for the fine alignment.

II.1.4 Measurements in the reciprocal-space using diffractometers - Isolation of a single island

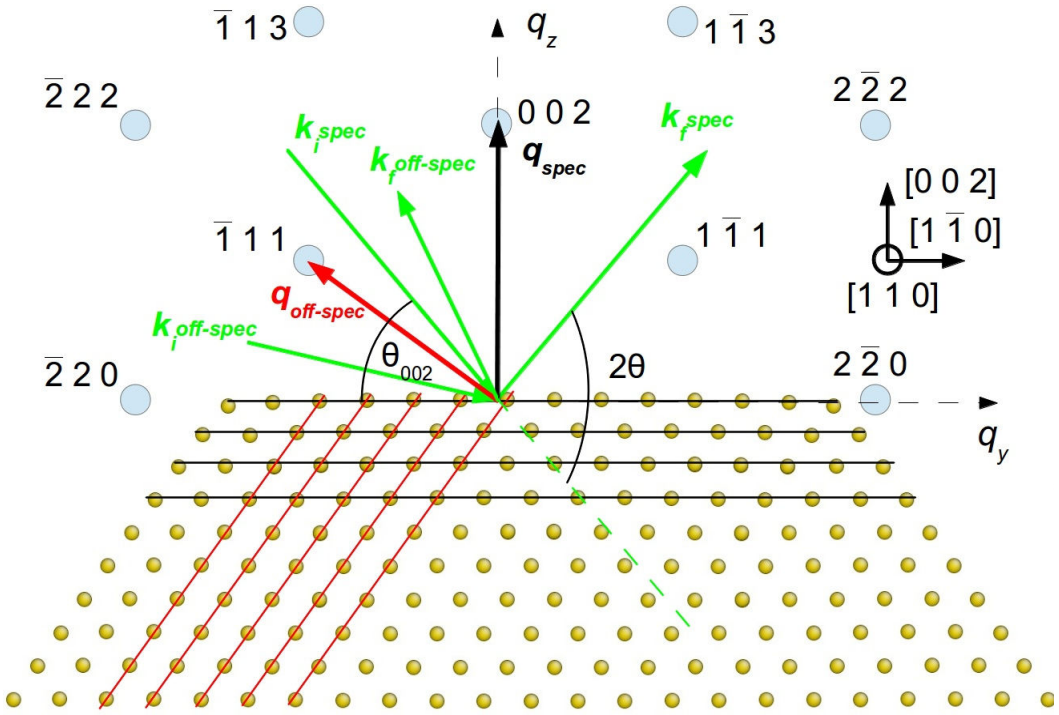

Fig. II.7 *Real space lattice (yellow) and reciprocal space lattice (blue) of a f.c.c. crystal, in the [1 1 0] zone axis: direction of the incident, diffracted wave vectors and of the scattering vector for a specular and an off-specular reflection.*

Experimentally, a given Bragg reflection (*h*,*k*,*l*) is measured by aligning the scattering vector $\boldsymbol{q}$ with the reciprocal lattice point $\boldsymbol{g}_{hkl}$, using the diffractometer axes.
The reflection is said 'specular' when $\boldsymbol{q}$ is parallel to the normal of the crystal surface (the normal to the surface is the bisecting direction between $\boldsymbol{k}_i$ and $\boldsymbol{k}_f$). This is the case of the 0 0 2 reflection in Fig. II.7. All the other reflections are said 'off-specular'. The 1 $\bar{1}$ 1 reflection shown in Fig. II.7 is a particular case of such reflection, for which the surface normal is in the scattering plane.
Specular reflections are usually easier to measure than off-specular ones: they require the use of mostly two axes

of the diffractometer, namely $\omega = \theta$ and $\delta = 2\theta$ (in vertical scattering geometry), where θ is the Bragg angle determined with the Bragg law, and small adjustments of the other axes if the sample surface is not exactly parallel to the reference surface of the sample stage.
The measurement of an off-specular reflections is not always straightforward, and the measurement procedure depends on the geometry of the diffractometer. For a six-circles diffractometer putting an off-specular reflection into a diffracting position implies the combined rotation of several axes of the diffractometer, It is thus necessary to determine the combination of sample and detector angles which bring the scattering vector $\boldsymbol{q}$ in coincidence with the chosen Bragg vector $\boldsymbol{g}_{hkl}$. The determination of the angles is achieved thanks to the orientation matrix $\boldsymbol{UB}$ which describes the sample orientation with respect to the diffractometer angles. The matrix $\boldsymbol{B}$ transforms the given (h,k,l) into an orthonormal coordinate system fixed in the crystal while the matrix $\boldsymbol{U}$ rotates the crystal reference Cartesian frame into the laboratory frame of reference. In other words it corrects the misalignment between the Cartesian axes of the reciprocal space and those of the laboratory frame of reference. Details on the angle calculations for the '4S+2D' diffractometer are given by You (1999). The orientation matrix is obtained experimentally by the determination of the diffractometer angles for two non parallel Bragg reflections.

II.1.5 Collection of 3D reciprocal space maps from isolated objects

The CXD experiments presented in this manuscript are focused on sub-micron crystals exhibiting a certain amount of strain and defects. Owing to the the small size and the possible heterogeneous strain distribution, a sub-micron structure is expected to exhibit an extended three-dimensional diffraction pattern. Area detectors can be used to efficiently record the diffracted intensity, however, the two-dimensional XRD images represent only one specific cut through reciprocal space. A classical method to obtain three-dimensional intensity distributions consists in performing rocking-curves through the selected Bragg peak, while simultaneously recording 2D diffraction patterns at each step of the scan (Fewster *et al.* 1997). As illustrated in Fig. II.8, a variation of the scattering angle θ corresponds to a translation of the detector plane in the reciprocal space. The detector plane intercepts the 3D Bragg peak at discrete positions, and all the recorded 2D diffraction patterns can be aggregated together to form a single 3D diffraction pattern. This method is reliable and reasonably fast, however, it is not well adapted in some particular situations. As discussed previously, the sphere of confusion of the 6C diffractometers is particularly large (a few tens of micrometers). When both the beam and sample size are almost two orders of magnitude smaller than the sphere of confusion, as in the case of nanostructures imaged with a nanofocused beam, this large sphere of confusion might become problematic. Even with a rocking-curve range of 1°, the investigated nanostructure might move out of the beam. Additionally, when CDI is performed, small movements of the sample can be an issue since different parts of the beam, having different wavefronts are diffracted. As discussed in Chapter I and Chapter VI, variations in the wavefront may complicate the reconstruction of the image of the sample.
In the CXD studies presented in this manuscript, the typical sample and beam sizes are respectively around 500 nm and 1x1 μm^2. The 3D CXD pattern are systematically collected by rotating the crystal through its rocking-curve and it is shown for instance in Chapter VI that this method of collection is generally not an impediment for the reconstruction of the complex electron density. More problematic is a complex sample environment for *in situ* XRD measurements since it may demand a limitation of sample movement to reduce or avoid any vibrations induced by the diffractometer movement. A typical example are the *in situ* nanoindentation experiments presented in the Chapter VI. If the tip of the AFM or of the nanoindentor is in contact with the nanostructure under investigation, any movement or vibration must be avoided, to prevent the sample surface or the tip itself from being damaged during the rocking curve.
To overcome such potential issues, an alternative method of collection of the 3D-reciprocal space maps has been proposed by Cornelius *et al.* (2011). The main advantage of this method is that it does not require any movement of the sample. It consists in tuning the energy of the X-rays, typically on a range of ± 100 eV with steps of 1 eV for an energy of 10 keV . Since the undulator gap needs to be adjusted while scanning the energy to keep the incident intensity constant, this method is significantly slower than a conventional rocking-curve. Despite this

issue, the obtained 3D-RSM maps are consistent with the ones obtained by the conventional method and avoid any noise/motion on the sample.

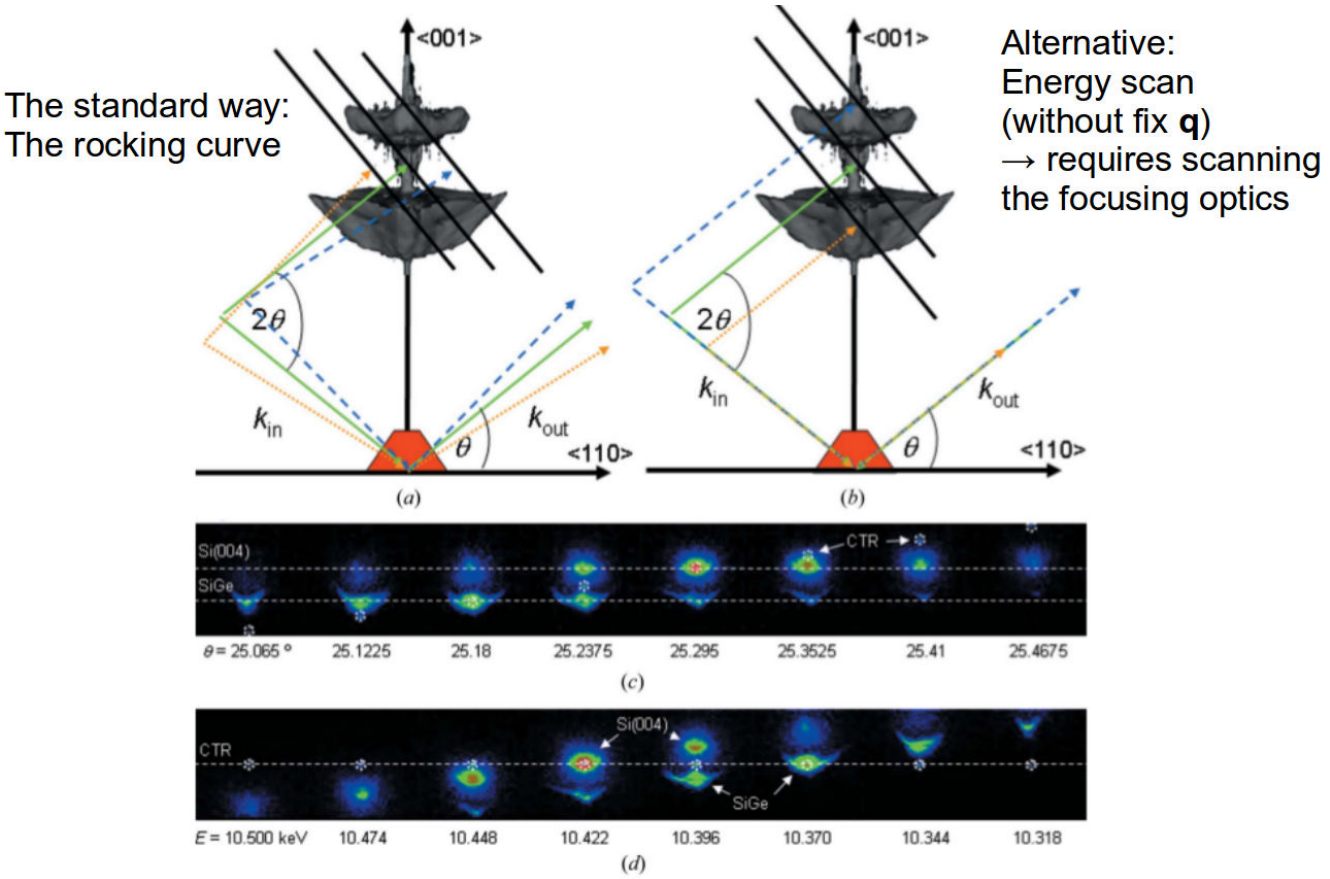

Fig. II.8 *Measurement of 3D reciprocal-space maps.* (a) Collection of a 3D Bragg peak by rotating the sample along its rocking-curve. (b) Collection of the 3D Bragg peak by scanning the energy of the incident X-ray beam. (c) 2D slices of the reciprocal space intercepted by the detector plane during a rocking-curve. (d) 2D slices of the reciprocal space intercepted by the detector plane during an energy scan. (from Cornelius *et al*, 2011)

II.1.6 Reconstruction of the 3D diffraction pattern in the sample orthonormal basis

As discussed above, the acquisition of 2D CXD patterns around a given Bragg reflection with an area detector allows to measure a slice through the 3D Bragg peak. However, this data is not directly usable, and the obtaining of the 3D data is not straightforward. Rather than simply stacking the 2D slices together, it is necessary to affect to each pixel of the collected data a value of $\boldsymbol{q}$ = (qx,qy,qz). In other words, a coordinate change has to be performed in order to depict the 3D -RSM in the orthogonal reference laboratory frame. The latter corresponds to the frame of the sample where all the diffractometer circles are set to zero.

The mathematical formalism won't be described in details in this manuscript. In short, it can be divided in two steps: convert the pixels positions of the detector into angles, and convert the diffractometer angles into reciprocal space coordinates. The coordinate transformation uses the formalism introduced by You (1999) for the angle calculations in a '4S+2D' diffractometer.

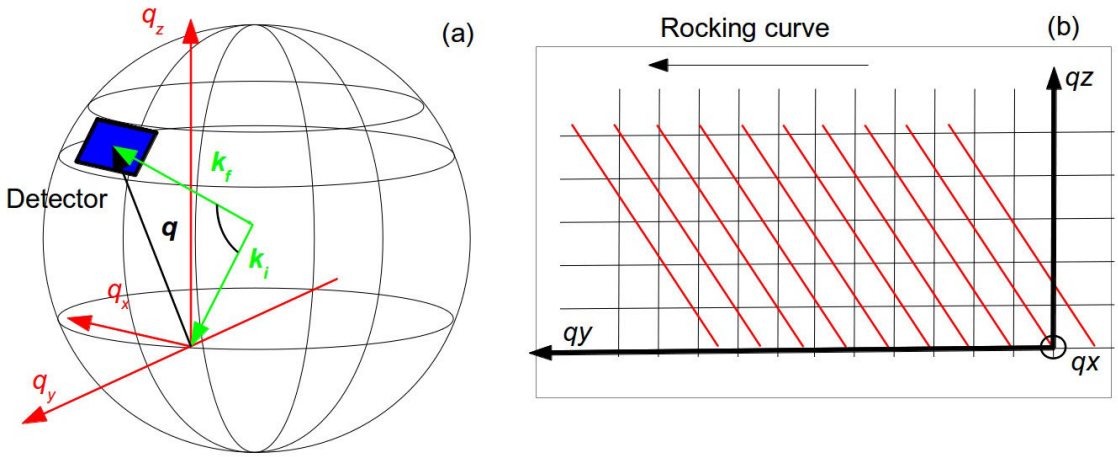

Fig. II.9 *Detector plane in the reciprocal space* (a) Representation of the detector plane on the Ewald sphere (b) Representation of the translation of the detector plane in the orthogonal laboratory frame of reference during a rocking curve. The q_y and q_z coordinates are obtained by a linear interpolation on a regular grid

Several approximations are used for the coordinate change. As illustrated in Fig. II.9.a, the detector plane corresponds to a portion of the Ewald sphere. In our formalism, the curvature of the Ewald sphere is not taken into account. Considering the angular opening of the detector (which depends on the sample to detector distance), and the energy ranges considered for most of the CXD experiments presented in this manuscript, this approximation is perfectly acceptable. For experiments in the soft X-ray range (< 1 keV), it might worth considering a correction for the curvature of the Ewald sphere.
As shown in the previous section, the acquisition of a 3D RSM is carried out by rotating the sample along its rocking-curve. The latter corresponds to a translation in the reciprocal space along the q_y direction. Experimentally, this translation is slightly curved. This curvature is here not taken into account and the translation is described with a linear approximation. Fig. II.9.b shows the orientation of the detector in the orthogonal laboratory frame of reference. It is slightly misoriented with respect to the (q_x,q_z) plane. The q_x direction corresponds to one of the two directions of the detector plane, but the q_y and q_z positions need to be interpolated on a regular grid. In our case, a linear interpolation is used. Using this method we obtain 3D-RSM that can be used for the reconstruction of the experimental data.

Chapters I and II are mostly dedicated to the introduction of the coherent X-ray diffraction technique which is employed in many experimental and numerical studies presented in this manuscript. It gives access to the 3D displacement field of isolated objects and is thus well adapted to the investigation of the crystal plasticity in such objects. It does not provide any information on the detailed atomic structures of surfaces or interfaces, but reflects the strain they may induce. The heteroepitaxial of f.c.c. Cu(0 0 1) on b.c.c. Ta(0 0 1) system studied in this work exhibits a large amount of residual strain (around 0.6 % , Beutier *et al.* 2013a), induced at the Cu crystallite – substrate interface. The growth of islands of Cu on Ta follows the so-called Stransky-Krastanov mode (Rodriguez & Goodman 1991) characterized by a wetting layer of a few atomic Cu planes between the 3D f.c.c. strained crystallites. The detailed atomic structure of this wetting layer and at the interface in the crystallites is not known but accommodates the large misfit strain (around 31% total lattice misfit) to produce nearly defect free but strained Cu crystallites. The atomic structure of this wetting layer is only accessible through surface X-ray diffraction techniques which are presented in the next section.

II.2. Surface diffraction

II.2.1 Crystal truncation rods

In the classical derivation of the diffraction pattern of a crystal lattice, it is frequently assumed that the crystal is infinite in-extent; the diffraction patterns are then perfect δ functions. When finite size effects are included, the peaks are found to be broadened by an amount inversely related to the dimensions of the diffracting region of the crystal. For crystal with sharp boundaries, a significant amount of the intensity is always scattered far away from the Bragg peaks and spreads across the Brillouin zone. The order of magnitude of this intensity is similar to that arising from a single layer of atoms. X-ray experiments with monolayers (ML) sensitivity are thus able to detect it.
Let us consider a block shaped crystal. The periodic repetition of the unit-cell us defined by three vectors, $\boldsymbol{a_1}$, $\boldsymbol{a_2}$ and $\boldsymbol{a_3}$ which correspond to the crystal axes. The bulk unit cell structure factor $F_u(\boldsymbol{q})$ can be defined as :

$$F_u(\boldsymbol{q}) = \sum_{j}^{unit\ cell} f_j(q) e^{\frac{-B_j q^2}{16\pi^2}} e^{i\boldsymbol{q}.\boldsymbol{r}_j} \tag{II.5}$$

where $\boldsymbol{q}$ is the scattering vector (momentum transfer), $\boldsymbol{r_j}$ position of the atom j and $f_j(q)$ is the atomic form factor (defined as the Fourier transform of the electron density of atom j). Here a damping term parameter B_j has been added. This is the temperature dependent Debye parameter proportional to the mean square displacements from the equilibrium atomic position.
The scattering amplitude $A(\boldsymbol{q})$ is obtained by a summation over the Bravais lattice:

$$A(\boldsymbol{q}) = F_u(\boldsymbol{q}) \sum_{n_1=0}^{N_1-1} \sum_{n_2=0}^{N_2-1} \sum_{n_3=0}^{N_3-1} e^{i\boldsymbol{q}(n_1\boldsymbol{a_1}+n_2\boldsymbol{a_2}+n_3\boldsymbol{a_3})} \tag{II.6}$$

This sum can be easily calculating yielding the following expression for the scattering intensity:

$$I(\boldsymbol{q}) = |A(\boldsymbol{q})|^2 = |F_u(\boldsymbol{q})|^2 \prod_{j=1}^{3} \left(\frac{\sin^2 N_j \boldsymbol{q} \frac{\boldsymbol{a_j}}{2}}{\sin^2 \boldsymbol{q} \frac{\boldsymbol{a_j}}{2}} \right) \tag{II.7}$$

If The scattering vector is now written in the basis of the reciprocal vector :

$$\boldsymbol{q} = h\boldsymbol{b_1} + k\boldsymbol{b_2} + l\boldsymbol{b_3} \tag{II.8}$$

Replacing in (II.7) it comes that the three terms of the product have a maximum for integer h, k and l respectively. This is equivalent to the Laue conditions which define the reciprocal lattice.

Let us now consider an X-ray beam impinging on the surface of a semi-infinite single crystal which corresponds to the ($\boldsymbol{a_1}$, $\boldsymbol{a_2}$) plane. For integer h and k values, and in the limit of large N_3 we obtain from Eq. (II.8) :

$$|A(h,k,q_3)|^2 \;=\; N_1^2 N_2^2 |F_u(h,k,q_3)|^2 \left| \frac{1}{2\sin\frac{1}{2}\boldsymbol{q}\,\boldsymbol{a_3}} \right|^2 \tag{II.9}$$

Remembering that $\boldsymbol{q}\,\boldsymbol{a_3} \;=\; l\,\boldsymbol{b_3}\boldsymbol{a_3} \;=\; 2\pi l$ it can be rewritten as

$$|A(h,k,q_3)|^2 \;=\; N_1^2 N_2^2 |F_u(h,k,l)|^2 \left| \frac{1}{2\sin\pi l} \right|^2 \;=\; I_{CTR} \tag{II.10}$$

where l takes non-integer values.
Eq. (II.9) and Eq. (II.10) show a characteristic variation of the scattered intensity from a crystal surface as function of the scattering vector perpendicular to the surface. It demonstrates that the diffraction intensity of finite-sized crystals has diffuse streaks connecting all the Bragg points. These diffuse streaks of intensity are called the Crystal Truncation Rods (CTR).
An alternative way to understand the scattering vector dependency of Eq. (II.10) is to use the Fourier transform (FT) properties. A semi-infinite crystal can be seen as the product of an infinite lattice and a step function. The scattering amplitude is thus the convolution of the reciprocal lattice with the FT of a step function. The latter has a $1/q$ dependence and decreases slowly with q resulting in a detectable intensity along the CTR.
It is quite obvious that any surface roughness has a strong effect on the CTRs inducing a reduced intensity in between the Bragg peaks (Robinson 1986). A commonly used approximation proposed by Robinson 1986 (so-called the β model) describes the surface roughness with an occupancy distribution β^n for the layer n and above the last fully occupied one, resulting in pyramidal islands. The attenuation of the CTR intensity is given by:

$$R_\beta \;=\; \frac{(1-\beta)^2}{(1-\beta)^2 + 4\beta\sin^2\;\dfrac{\pi(l-l_{Bragg})}{M_{layers}}} \tag{II.11}$$

where l_{Bragg} is the l value of the nearest Bragg peak and M_{layers} is the number of layers in the unit cell. From Eq. (II.11), one can understand that the relatively large value of the intensity measured in-between the Bragg peak along the CTRs is predominantly due to the fact that the surface is almost atomically flat and not due to the fact that the crystal has a finite-size.
Robinson (1986) evaluated the expected intensity from a CTR by considering a semi-infinite crystal measured with an incident and diffracting beams passing through its surface (Bragg geometry). In this case, five out six of the parallelepiped crystal becomes indistinct. Four because of the soft edges of the beam and the fifth because of its limited penetration in the sample. The strength of a truncation rod can be evaluated by including the X-ray coherence length, m (measured in unit cells) in Eq. (II.12).
It comes that the Bragg points have an intensity of $N_1N_2N_3m^3$ while the diffuse intensity is given by $N_1N_2m^2$.
With a penetration depth taken to be 1 μm corresponding to ~ 10^3 unit cells for N_3 and m = 100 unit cells, this gives a relative intensity of:

$$\frac{I(\,Bragg\;point\,)}{I(CTR)} \;=\; N_3\,m \;\simeq\; 10^5 \tag{II.12}$$

Intensities of this order of magnitude were confirmed experimentally. It implies that synchrotron radiation is generally mandatory for measuring such low intensities. However, it should be noted that experiments involving heavy atomic elements were performed using rotating anode X-ray generators (Meyerheim *et al.* 1998).

II.2.2 X-ray diffraction from the surface region

The X-ray scattering amplitude from a film deposited onto a substrate can be simply written as the sum of the scattering from the substrate and from the atoms close to the surface:

$$A(\boldsymbol{q}) = A_{bulk}(\boldsymbol{q}) + A_{surf}(\boldsymbol{q}) \quad \text{(II.13)}$$

where the first term contains all substrate atoms in bulk positions and the second term contains the deposited atoms and the substrate atoms close to the surface with displaced positions with respect to the bulk. In the relatively simple case of pseudomorphic epitaxy, the sum on the Bravais lattice gives delta-like functions, the scattering is thus observed at integer h and k value. This case is illustrated in Chapter VIII by the study of the Cu-Ta interface.
Perpendicular to the surface, an intensity distribution is observed. It can be described through a generalized structure factor F which is the coherent sum of both bulk and surface contributions :

$$F(h,k,l) = F_{Bulk} + \sum_{j}^{surface\ unit\ cell} f_j \theta_j e^{\frac{-B_j q^2}{16\pi^2}} e^{2\pi i(hx_j + k y_j + l z_j)} \quad \text{(II.14)}$$

where $(xyz)_j$ is the position of atom j in fractional coordinates. An occupancy parameter θ is included because in the surface unit cell not all the positions need to be fully occupied.
F_{bulk} describes the bulk-unit-cell structure factors F_u summed from the top layer to $-\infty$. Because of the attenuation factor α, only a finite amount of unit cells contributes to F_{bulk} and it can be expressed as follows:

$$F_{bulk} = \frac{F_u}{1 - e^{-2\pi i l} e^{-\alpha}} \quad \text{(II.15)}$$

Not that in this formalism, the bulk and surface contributions can only be added coherently (Vlieg *et al.* 1989). The coordinates of the surface and bulk atoms are expressed with respect to a common origin.

II.2.3 Surface X-ray diffraction experimental set-up

The surface X-Ray Diffraction (SXRD) experiment discussed in the chapter VIII of this manuscript was performed at the SUV-BM32 (CRG-IF) beamline at ESRF. Fig. II.10.a shows the experimental station. It consists of a ultrahigh vacuum chamber, fully equipped for sample preparation, mounted on a Z-axis diffractometer. A complete description of the set up has been done by Baudoing-Savois *et al.* (1999). The diffractometer axes are sketched in Fig. II.10.b. The sample is in vertical position, α is the angle of incidence of the X-ray beam. The base table also called α support two rotary tables ω and δ with their axis parallel to the z axis. ω is the azimuthal angle while δ is the in-plane scattering angle. The detector arm supports a movable system which allows for the emergence of the out – of plane scattering angle γ. The γ angle is achieved by the combination of two motions: a translation along the detector arm is synchronized with a rotation. This induces a change in the sample-detector distance during a γ scan: the angular acceptance of the detector slits decreases with an increasing angle. Finally two further axis χ_1 and χ_2 "the cradle axis" allows the alignment to the surface normal $\hat{\boldsymbol{n}}$ parallel to z.

The angular settings of the diffractometer allows to measure the intensity at a well defined scattering $\boldsymbol{q} = \boldsymbol{k}_f - \boldsymbol{k}_i$ vector as shown by the Ewald construction in Fig. II.11.
The $\boldsymbol{q}$ vector is expressed in a Cartesian coordinate frame attached to the reciprocal lattice. To find the

corresponding settings for the diffractometer, it is necessary to express the incoming and scattering wave vector and outgoing wave vector in the same frame of axis. This is done by performing a coordinate transformation from the laboratory frame (x,y,z) to the ($X^{\omega},Y^{\omega},Z^{\omega}$) frame attached to the circle ω. Details on the calculation of the coordinate transformations are available elsewhere (Lohmeier & Vlieg 1993).

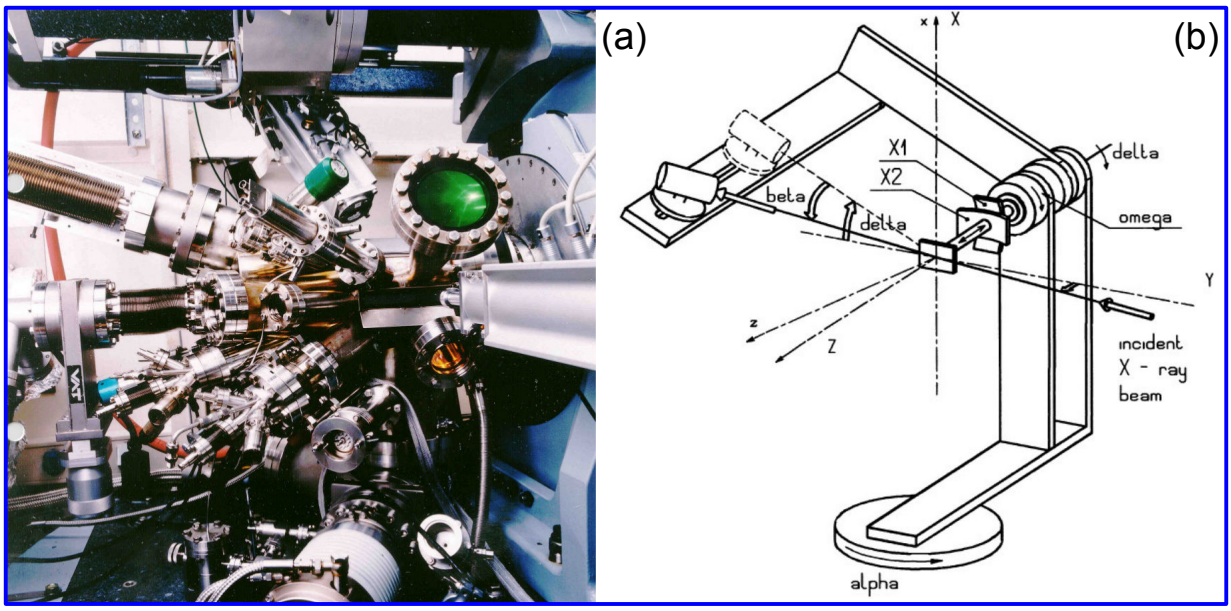

Fig. II.10 (a) SXRD dedicated experimental set-up at BM32 (b) Schematic of the z-axis diffractometer

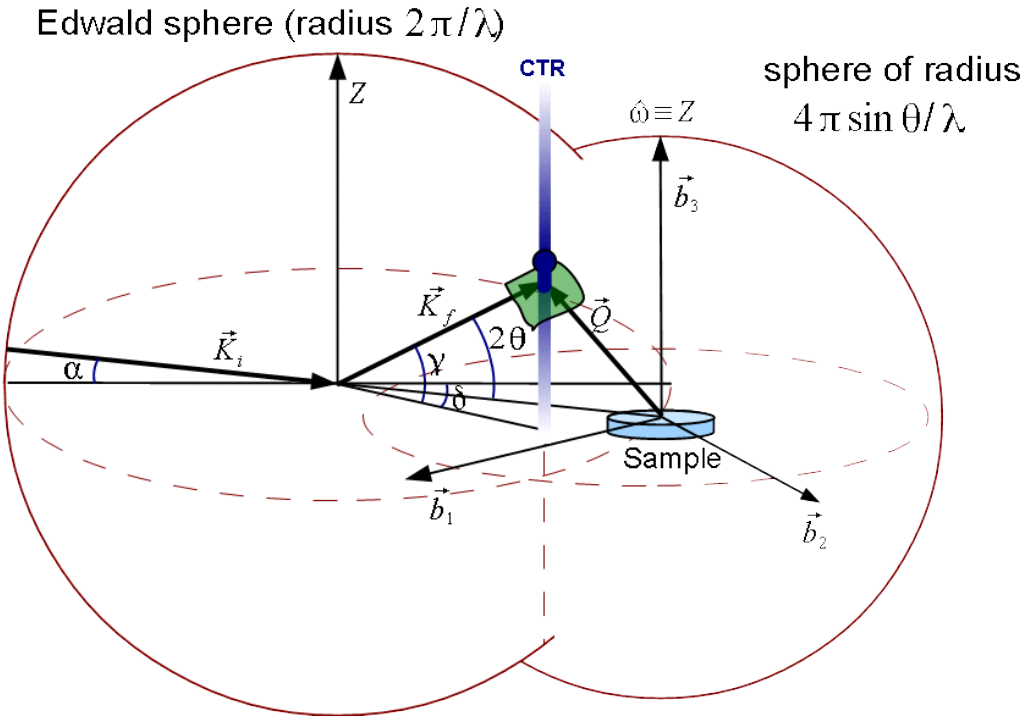

Fig. II.11 *Ewald construction which summarizes the geometry of the experiment (courtesy to M. De Santis)*

II.2.4 Measurement of the rod intensities

A detector placed on the diffractometer arm integrates the scattering cross section over the solid angle $d\Omega$ which is given by the pixels included in the region of interest in 2D CCD detectors (as in the case of the experiment presented in Chapter VIII). The scattering cross section derived from the classical formula of Thompson scattering.

$$d\sigma = \frac{|A(\boldsymbol{q})|^2 e^4}{m^2 c^4} \sin^2\theta \, d\Omega \tag{II.16}$$

where m is the mass of the particle, c the speed of light and θ defines the angle between the electric field of the incoming photon and the scattering direction.
The atomic structure of thin films and of 2D surface layers is generally solved through a fit of the experimental structure factor amplitudes $|F(h,k,l)|$ with the expression given by Eq. (II.14). In Chapter VIII the determination of the surface structure through the fit of the experimental data is tested against first-principle and Molecular Dynamics calculations. To get the correct amplitudes several geometric correction factors need to be applied to the measured intensities. In the following we summarize them quickly but extensive details on the application of the correction factors can be found elsewhere (Vlieg 1997).
Among the correction factors are the correction of the polarisation factor which is the classical angular dependence in the dipole scattering ($\sin^2\theta$ in Eq. (II.16)); the Lorentz factor which can be described as the geometrical correction in the integration volume. The rod correction which aims at determining precisely the range of l values that are accepted by the detector. In other words, this correction factor depends on the way the rod cylinder intersect the lines that define the detector aperture.
Additional correction include the linear γ table correction which takes into account the fact that the rotation γ is composed of a translation and a rotation yielding an increasing sample-detector distance when increasing angle and a subsequent decrease of the acceptance angle of the detector. The area correction depends on the illuminated area on the sample which is defined by the opening of the vertical slits of the incoming beam.
Finally, a detector corrections need to be applied when he diffraction peak is too wide and the complete integrated intensity is not measured. This occurs in particular when the coherence between the substrate and the surface is partially lost.

All the aforementioned correction allow to obtain a total correction factor. It is applied at the integrated intensity measured by rocking the sample azimuth to obtain the structure factor given by:

$$|F(h,k,l)|_2 \propto \frac{\int I_{h,k}(\omega)\, d\omega}{L \times C_{rod} \times C_{pol} \times C_{area} \times C_{table} \times C_{Det}} \tag{II.17}$$

Provided a careful acquisition of the experimental data, this allows to obtain a precise measure of the structure factor amplitudes which can be used for the determination of the atomic structure of the surface.

II.3. Samples

To investigate the structural and mechanical properties of sub-micron crystals, several samples have been studied during this work. They can be divided in two main groups: the particles (islands) and the nanowires.

II.3.1. Islands

The particles were obtained by the solid state dewetting technique. This technique has the advantage to produce a series of similar objects in term of size, geometry and orientation, which is particularly convenient for X-ray diffraction studies. The choice of gold and copper is justified by the fact that the plasticity mechanism in bulk f.c.c. metals is well known.

II.3.1.1 Solid-state dewetting

For both Cu an Au particles, the dewetting occurs from a continuous thin film. The deposition method and structure of the two thin films varies slightly between the two systems. The gold thin film is deposited using Electron Beam physical vapor deposition (EBPVD) on a sapphire (0 0 0 1) substrate in a high vacuum chamber. A polycrystalline thin film of typically 20 nm with a pronounced {1 1 1} texture is obtained. The Cu thin film is deposited using Molecular Beam Epitaxy on an atomically flat Ta (0 0 1) substrate. The thin film is in hetero-epitaxy with the substrate, and a 5 nm thick thin single-thin film with a (0 0 1) out of plane orientation is obtained. In both cases, the deposition is carried-out at room temperature. More details on the sample preparation can be found in Chapters VI and VII (gold islands) and Chapters VIII and IX (copper islands).
As shown on Fig. II.12, the process of formation of the islands is similar for the two systems. Due to large surface energy difference between the film and its substrate (either the refractory metal Ta or the oxide sapphire), the metallic thin film breaks up upon heating well below the melting temperature, and agglomerate into regularly distributed sub-micron islands with a well defined orientation with respect to the underlying substrate.

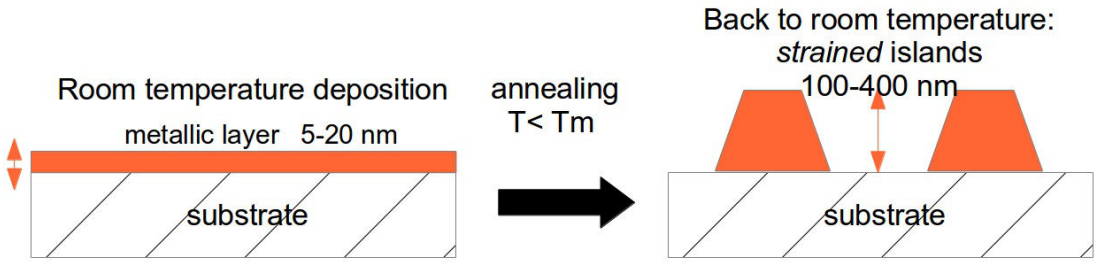

Fig. II. 12 *Schematics of the solid-state dewetting process.*

An important question to address is to determine what triggers the particles formation?
Thin films are generally formed under conditions for which atomic motion is limited and non-equilibrium structures are obtained. This is particularly true for films formed through vapour deposition, for which atoms arriving at the surface of a substrate or growing film can often move over distances limited to a nanometre or less (as in the case of formation of amorphous films). As a result, most films are unstable, or at best metastable, and spontaneously dewet to form islands when heated to temperatures at which the mobility of the constituent atoms is sufficiently high.
The driving force for dewetting is minimization of the total energy of the free surfaces of the film and substrate, and of the film-substrate interface. This force increases with decreasing film thickness resulting in an increasing dewetting rate. As a consequence, the temperature at which dewetting occurs decreases with film thickness.
Dewetting generally progresses through at least three distinct stages: hole formation, hole growth and impingement, and ligament breakup (Thompson 2012).
The dewetting either occurs at pre-existing holes or at film edges or requires the formation of new holes. These holes then grow to form dewetted regions that eventually overlap so that the entire film is dewetted.
In polycrystalline films, grain boundaries and grain boundary triple junctions play an important role in the hole

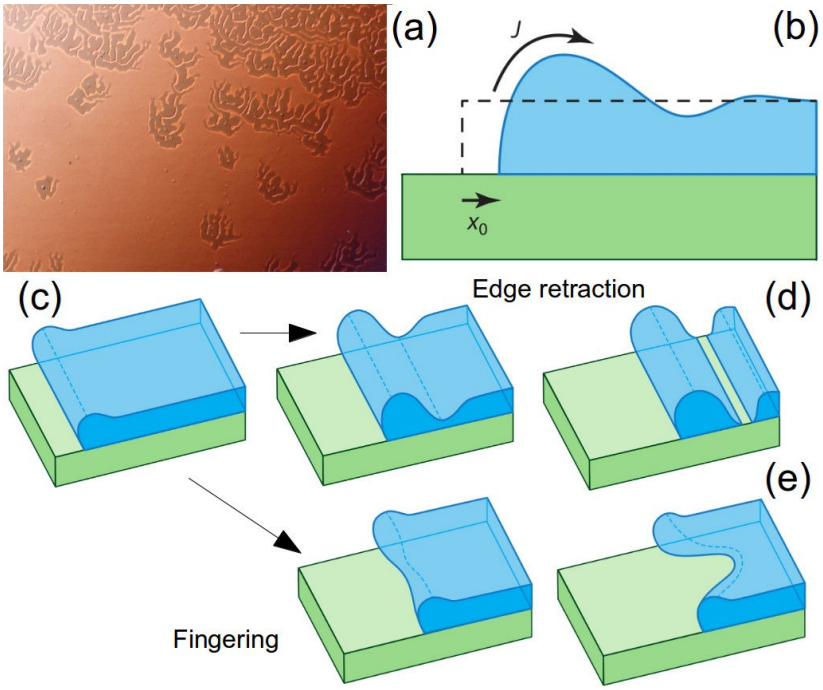

Fig. II.13 *Schematic of the growth mechanism of holes.* (a) Optical microscope image of a Cu thin film undergoing solid-state dewetting. (a) Cross-sectional view of a retracting edge-film. (c)-(d) Illustration of the pinch-off mechanism – (c) – (e) Illustration of the fingering instability (Fig. 12. (b) to 12.(e) are taken from Thompson (2012))

formation. For single-crystal film, the dewetting of a continuous thin film also seem to require pre-existing holes or defect that promote local thinning and hole formation (Freund & Suresh 2003, Chapter IX), however no clear mechanism of formation that leads to dewetting has been clearly identified. Candidate possibilities include pinholes in the initial films, localized impurities on the substrate or film surface that react locally to make the film discontinuous or defects such as dislocations that cause local pit formation (Thompson 2012) or even local fluctuations of thickness for very thin film.

Once a hole of critical size has formed, capillary energies will drive the retraction of its edges and the hole will grow. As illustrated on Fig. II.13, the growth of the hole is driven by two main distinct processes that are initiated in the same way. If we consider a hole at a sharp corner, material will be transported from the corner to reduce its curvature. However, since the curvature of the edge of the thin film is always higher than that of the film surrounding the hole, there will be a continuing net flux of material from the edge over the rim of the hole, and into the flat area surrounding the hole. This flux leads to retraction of the edge and to corresponding hole growth. As the edge-retracts, the rim thickens, and the valley ahead of the rims deepens (Fig. II.13.b and II.13.d). At some point, the valley makes contact with the substrate, leading to the creation of two sharp edges (Fig. II.13.d). A wire (or strand) is then formed from the isolated rim. This process called pinch-off can repeat, leading to the creation of new wires (Thompson 2012)

Alternatively, in some cases a retracting edge undergoes a so-called fingering instability, *i.e.* the breaking up of the thin film into fingers upon retraction of the edge. These fingers are also unstable and break up into islands at later stages of the dewetting process. The fingering instability is commonly observed in single crystal thin films (Fan *et al.* 2008, McCarthy *et al.* 2009), and is illustrated in Fig. II.13.a which shows the dewetting of the copper islands from a 5nm single-crystal thin film. At late stages of dewetting, the break-up of the rim leads to wire-like strands (Fig. II.13.a). These strands have radii that scales with the film thickness. They are subject to the so

called Rayleigh-Plateau-like instability: free standing cylinders of radius r_R are unstable with respect to radial perturbations of wavelength greater than $2\pi r_R$ and tend to break up into spheres at spacings $2\sqrt{2}\pi\ r_R$. The radii of the resulting particles scale with r_R.

II.3.1.2 Equilibrium shape of the particles

At the end of the dewetting process, the shape of a particle equilibrated on a substrate reflects the anisotropy of the surface energy of a particle and the influence of the substrate.
The example of the liquid droplet in a contact with a substrate provides an illustration of the manner in which the substrate-droplet binding can influence the shape.
Once the thermodynamic equilibrium is achieved, and provided that the interface remains flat and coplanar with the substrate, the contact angle (θ) can be used via Young's equation as a measure of the substrate vapour (γ_{SV}), liquid vapour (γ_{LV}) and substrate liquid interfacial energies (γ_{SL}) of the droplet:

$$\gamma_{SV} = \gamma_{SL} + \gamma_{LV}\cos\theta \qquad \text{(II.18)}$$

Through Eq.(II.18), it can be seen that the shape of a droplet can be related to the binding between the liquid and the surface, characterized by γ_{SV}, and the surface tension of both the liquid and the substrate.
Similarly to a liquid droplet, the shape of solid particle on a substrate must reflect the influence of these surface quantities. The solution to the problem of determining the equilibrium shape of a free-standing particle has been available since the beginning of the 20th century (Wulff 1901). Wulff proposed a graphical manner of determining a crystal shape from a free-energy plot also known as a γ plot. 50 years later, Herring (Herring 1953) proved that Wulff's construction led to an absolute minimum for all possible energy plots.
For a free particle, the Wulff solution requires that the equilibrium shape of the particle be such that:

$$\gamma_{hkl} = \lambda h_{hkl} \qquad \text{(II.19)}$$

i.e. the perpendicular distance h_{hkl} of a (*hkl*) surface from the centre of the body (referred as the Wulff point) is directly proportional to the surface tension γ_{hkl} of that surface. This agrees with the fact that crystallographic planes with lower surface energies are closer to the origin of the crystal and thus give larger facets (see Chapter VII).
The result in Eq. (II.19) can expressed graphically by means of the Wulff plot shown of Fig. II.14. This plot begins with a radial plot of the surface tension of the crystal (in green on Fig. II.7). Planes (or lines in the 2D case) are drawn through each point on the surface, perpendicular to the line connecting that surface point and the Wulff point O that define the centre of the crystal. The equilibrium shape (in red) is given by the area internal to all planes. It comes that low energy orientations will have large flat facets while higher energy orientations will only exist in planes that are tangent to the shape at a single point or will be missing entirely from the boundary of the crystal planes. Closed packed planes tend to have a low energy (the (1 1 1) and (1 0 0) planes for a f.c.c. structure) because the atoms on the surface have the most neighbours and fewest broken bonds. This topic is extensively discussed in the Chapter VII of this manuscript.
To take into account the presence of a solid-solid interface, *i.e.* the presence of an underlying substrate. Winterbottom (1967) developed the concept of general surface tension. If P corresponds to a single crystal particle, S to the substrate and V to the vapor phase surrounding the particle, this general surface tension is defined by $\gamma^* = \gamma_{PV}$ for all orientations corresponding to the free surfaces (particle - vapour surface), and $\gamma^* = \gamma_{SP} - \gamma_{SV}$ for the particle-substrate interface in common with the substrate.
For a planar substrate-particle interface, it is thus possible to determine the equilibrium shape of the Winterbottom particle by considering an equivalent free particle with a surface tension γ^*.

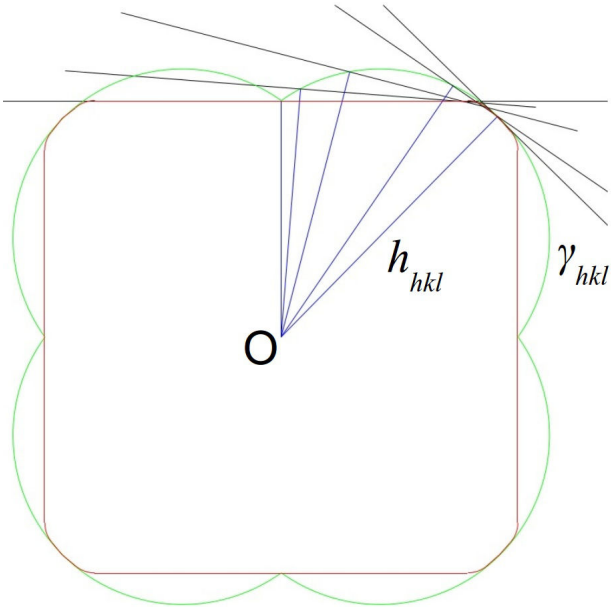

Fig. II.14 *Wulff plot of the equilibrium shape* (γ-plot). The free-energy is plotted as a function of the orientation in green. The equilibrium shape (in red) is given by the volume (area) internal to all crystallographic planes (in black)

The shape of the particle can be determined from the γ* plot construction which is a generalization of γ plot described above. The only difference lies in the fact that negative values of γ* are possible. For positive values, the equilibrium shape is still given by the inner envelope developed of the Wulff construction while for negative values of γ* the Wulff point no longer fall within the inner envelope of the construction (Fig. II.15)

The binding or degree of wetting between the particle and the substrate can be measured from the value of $\gamma_{SP}-\gamma_{SV}$. Winterbottom considered four possible cases ranging from the non-wetting of the particle to a complete wetting. The latter is still characterized by a zero contact angle (θ) as defined by Young's equation, while for a non-wetting, the equilibrium shape corresponds exactly to that of a free particle.

In between, these two extrema, a partial wetting of the particle is observed. In this case, two configurations are possible. If $\gamma_{PV} > \gamma_{SP}-\gamma_{SV} > 0$, the equilibrium shape differs from that of a free-particle and the construction plane for $\gamma^* = \gamma_{SP}-\gamma_{SV}$ represents the substrate surface and the base of the equilibrium shape. As illustrated in Fig. II.15.b, the Wulff point lies within the equilibrium shape, and can be precisely determined from the geometry of the particle.

It is also possible to determine the substrate-particle interface energy by measuring the distances R_1 and R_2 corresponding respectively to the substrate-to-Wulff point and the Wulff point-to-top facet distances

$$\frac{R_1}{R_2} = \frac{\gamma_{SP}-\gamma_{SV}}{\gamma_{PV}} \qquad \text{(II.20)}$$

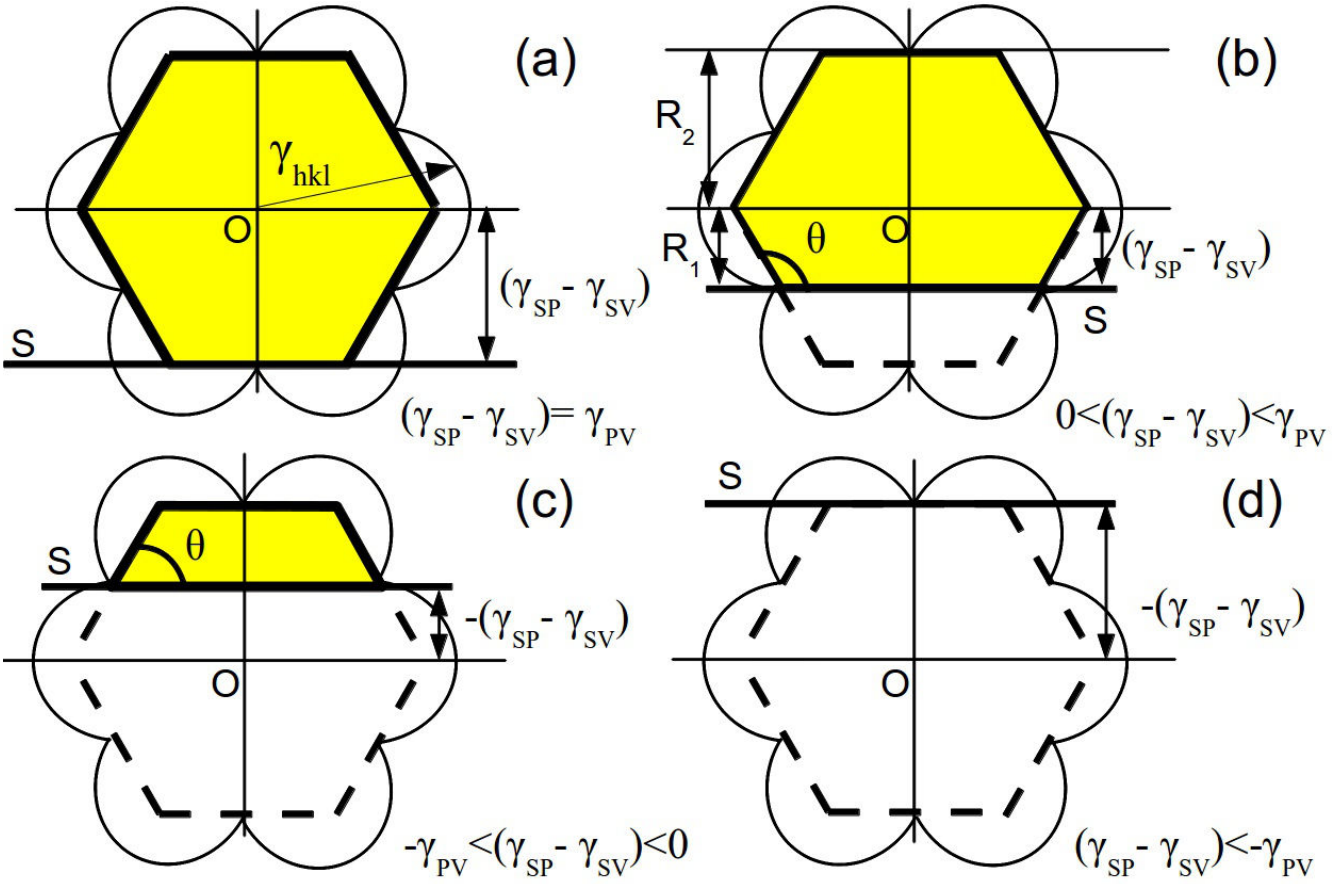

Fig. II.15 *γ* and corresponding equilibrium shape for different wetting behaviours.* (a) non-wetting (b) partial wetting with $\gamma_{SP}-\gamma_{SV}>0$. (c) partial wetting with $\gamma_{SP}-\gamma_{SV}<0$. (d) Total wetting

The contact angle θ used to define the wetting behaviour of a liquid droplet is not as significant in the case of a single-crystal particle since γ is not isotropic.
When $\gamma_{SP}-\gamma_{SV}$ becomes negative, the Wulff point no longer lies within the equilibrium shape of the particle. It is generally not possible to determine the equilibrium shape of the free particle from the geometry of the particle on the substrate, unless the value of $\gamma_{SP}-\gamma_{SV}$ is known.

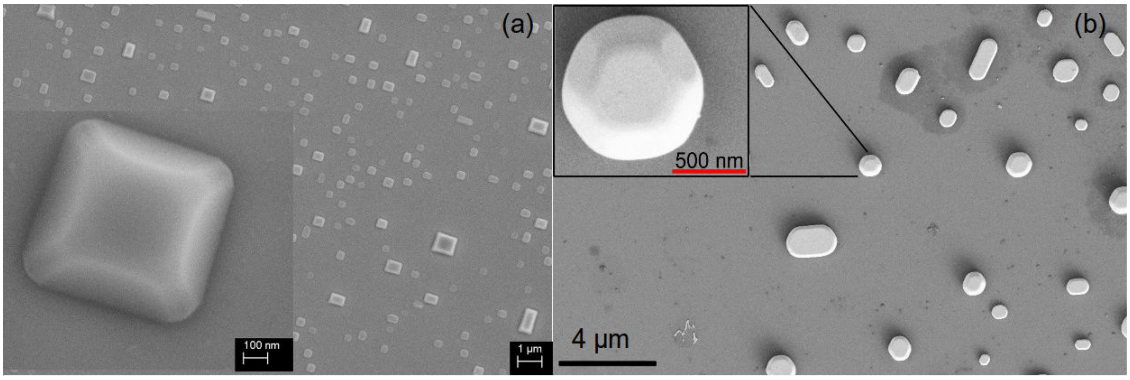

Fig. II.16 *Secondary Electron Microscopy image of the dewetted islands.* (a) Copper islands dewetted on top of a Ta (0 0 1) surface. (b) Gold islands dewetted on top of a Al_2O_3 (0 0 0 1) surface

Fig. II.16 shows SEM pictures of the typical size, geometry and distribution of the solid-state dewetted copper (Fig. II.16.a) and gold (Fig. II.16.b) islands. A partial wetting is observed for both systems, for the gold particles the Wulff point is located inside the particle, meaning that $> \gamma_{SP} - \gamma_{SV} > 0$. It is thus possible to calculate the substrate-particle interface energy, provided that both the substrate and the particle orientation are known (Sadan & Kaplan 2006). For the copper particles, a partial wetting is also observed, but the particle is largely truncated indicating the location of the Wulff point outside the equilibrium shape. This suggests a lower value of interface energy and a stronger connection with the substrate as compared to the gold particle as well a lower interface energy. In both cases the distribution of the island is relatively regular with a typical spacing of 2 μm between the islands. Both the in-plane and out-of plane orientations are well defined with respect to the substrate. The particles are highly faceted with a shape close to the Equilibrium Crystal Shape (ECS, see next sub-section)). Note that all the flat facets correspond to low energy orientations, i.e. (1 1 1) and (1 0 0) facets where the surface atoms are densely-packed.

We should point out that the equilibrium shape discussed so far is a minimization of the surface energies for a given relaxed volume. At equilibrium, the volume energy of the particle has to be taken into account, including its elastic strain energy (due to for example to the interface that accommodates the particle/substrate lattice): deviations to the Winterbottom shape are expected and can be calculated. If r_o designate the aspect ratio of the equilibrium shape ($r_o = h/l$, where l is the lateral size of the crystal and h its height), the surface stress of the facet in contact with the substrate (s_A) contributes to the aspect ratio so that:

$$r = r_0 + \frac{2(s_A - \gamma_{PV})m}{\gamma_{PV}} \qquad \text{(II.21)}$$

where m is the misfit between particle and substrate.

Hence, the general trend is that wetting tends to flattens the equilibrium shape whereas epitaxial strain acts against flattening and thus "blows up" the equilibrium shape (Muller & Kern 1998). All these considerations are discussed in extensive details in Chapters VI and VII (gold islands) and Chapter IX (copper islands).

II.3.2 Nanowires

Copper and gold islands are theoretically model objects for the investigation of the first stages of plastic deformation (nucleation) in small objects by Coherent X-ray diffraction. They are in the sub-micron range, well oriented with respect to the substrate, exhibit a reproducible size and geometry, and are in principle sufficiently well isolated to allow the imaging of their 3D displacement field by CDI. Additionally, their flat top facet parallel to the substrate are ideal for potential *ex situ* or *in situ* nanoindentation experiments. The only potential drawback with these objects lies in their strong binding with the substrate, which is prone to generate a large amount of strain, as for example thermoelastic strain due to cooling from the dewetting temperature (Beutier *et al.* 2013a). We have seen in Chapter I that even small values of strain can induce strong perturbations on CXD pattern which can make difficult the identification of crystal defects. Moreover, it is well known that large strain fields are difficult to handle for phase retrieval algorithms, even if some additional constraints in the phase retrieval algorithms can facilitate their convergence (Diaz *et al.* 2010, Minkevitch *et al.* 2008). The influence of the residual strain and his relationship with the binding between the particle and the substrate is further discussed in Chapter VI.

To limit the amount of residual strain the first strategy employed in this work was to grow islands with a weaker bounding to the substrate. This can be done by dewetting the particles above the melting temperature. The processing of such particles is presented in Chapter VII of this manuscript.

The other type of "strain-free" objects that are considered are single crystalline gold nanowires (NW). These objects are grown by physical vapour deposition on carbon-coated tungsten substrates under ultra-high vacuum and at high temperature. The method of growth of these nanowires (also referred as nanowhiskers) is described

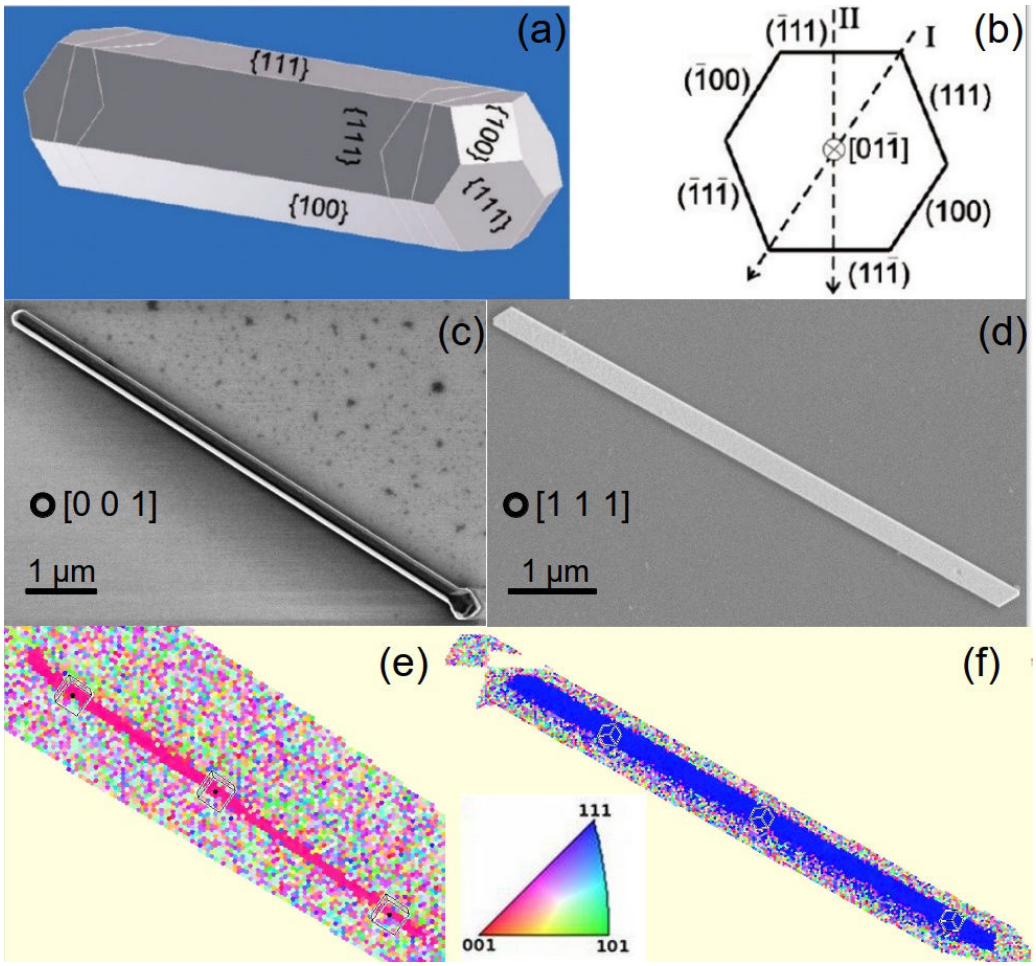

Fig. II.17 *Morphology of gold nanowires (NW).* (a) NW shape model based on the Wulff plot. Only {1 1 1} and {1 0 0} surface planes can be found. (b) Ideal whisker shape, as shown projected in the [0 1 $\bar{1}$] direction. (c) and (d) SEM images of two nanowires with a (0 0 1) (c) and a (1 1 1) (d) out-of-plane orientation. (e) and (f) Electron-back scattered diffraction from the same nanowires, revealing the (0 0 1) (e) and (1 1 1) (f) out-of plane orientation

elsewhere (Richter *et al.,* 2009). Presence of atomically smooth and faceted surfaces (Fig. II.17.a) as well as the absence of dislocations is confirmed using transmission electron microscopy investigation (Richter *et al.* 2009). Similarly to the islands, the nanowires only exhibit {1 1 1} and {1 0 0} low energy facets (Fig. II.17.a), and are elongated along the [0 1 $\bar{1}$] which corresponds to the growth direction.

For the CXD experiments the nanowires were mechanically transferred (scrubbing) on a silicon substrate, the in-plane orientation of the substrate is thus completely random while the out-of-plane orientation depends on the orientation on the facet in contact with the substrate. The four {1 1 1} lateral facets having the lower free-surface energy, they are larger than the 2 {1 0 0 } facets. {1 1 1} specular facets parallel to the substrate surface (Fig. II.17.d) are thus more frequently encountered than {1 0 0} facets (Fig. II.17.c), as confirmed by electron back-scattered measurements (EBSD, Fig. II.17.e & II.17.f). Similarly to the gold islands, the flat and reasonably large top facet (either {1 1 1} and {1 0 0}) facet is particularly convenient for the nucleation of dislocations by nanoindentation.

The typical dimensions for the nanowires are 0.15x0.15x10 µm^3. The extent in the third dimension (typically between 5 and 20 µm) is hence significantly larger than the typical beam-sizes used for CXD experiment. At the

expense of the flux, a full illumination of the sample would be certainly possible, but it is clear that the resolution of the 3D reconstruction would be rather low.
To image the 3D displacement field an alternative and far more efficient strategy is to use the scanning version of CDI, namely the 3D Bragg ptychography. In Bragg geometry, it has been demonstrated that the Bragg Projection Ptychography (BPP) technique can be used to image lattice strains in semiconductors thin films (Hruszkewycz *et al.* 2012), and can even generate maps of lattice strain and lattice tilt independently (Holt *et al.* 2014). Although impressive, this technique is limited to 2D dimensions.
To our knowledge, the experimental demonstration of 3D Bragg ptychography has been only reported once (Godard, Carbone *et al.* 2011). The ptychographic algorithms that can be used for the reconstruction of the data are well known (Faulkner *et al.* 2004, Thibaut *et al.* 2009, Maiden & Rodenburg 2009) and provided that a good data set is collected, the ptychographic approach is in principle more robust than conventional CDI especially in

- the case of highly strained systems (Godard, Allain *et al.* 2011). The rather limited use of this technique is mostly related to the experimental difficulties to collect a 3D dataset suitable for reconstruction. The technique requires to perform 2D scans at each position of the rocking-curve, hence a rather long measurement time (typically 8 hours depending on the angular step size for the rocking curve). Unless a very good stability of the set-up is ensured, the experimental data is unusable. We will see in the following that our attempts to perform 3D ptychography were not successful.

II.4. Sample characterization

II.4.1 *Ex situ* indentation

Nanoindentation tests have been widely used to study plasticity mechanisms at the nanometre scale since the mid-1990. It has been demonstrated both experimentally and in molecular dynamics simulations that for small size crystallites, in the presence of free surfaces crystal plasticity mechanisms are controlled by nucleation of dislocations at edges of faceted samples (Mordehai *et al.* 2011). In this manuscript, the detailed mechanisms of the nucleation of dislocations is detailed in Chapter IV.
A central objective of the ANR MECANIX and of this work is the *in situ* investigation of the first plastic events, *i.e.* nucleate crystal defects *in situ* while illuminating the object with a coherent X-ray beam (Fig. II.19. a). Such experiments have been carried-out at late stages of this PhD work and are presented in Chapter VI. The *in situ* nanoindentation experiment was carried-out with a compact atomic force atomic force microscope that has been developed by our collaborators from Marseille (SFINX). This set-up compatible with various synchrotron end stations allows both *in situ* imaging and some *in-situ* mechanical loading (Fig. II.19.c). Further details on this set-up can be found elsewhere (Zhe *et al.* 2014).
It should be noted that a *in situ* nanoindentation set-up is also under development in our group (Fig. II.19.d). It is a compact nanoindentor that is also compatible with synchrotron end-stations and is integrated into a Scanning Electron Microscope to combine *in situ* mechanical testing and real space imaging. Coherent X-ray diffraction experiments have not been performed with this set-up so-far, but it has been already used in combination with a micro-diffraction technique which allows the high resolution monitoring of crystal deformation with X-ray multiple scattering (Nisbet *et al.* 2015). 'Nanoindentation' performed with an AFM is rather distinct from a compact nanoindentor: in AFM, only the force applied to the sample is controlled (deflection of a calibrated cantilever), the displacement of the sample is not independently measured (only the total displacement tip+sample is controlled, not the tip depth within the sample). So AFM nanoindentation is very similar to classic indentation in metallurgy: a force is applied and if visible/created, the residual imprint can be imaged to derive the so called hardness (pressure of flow corresponding to the applied force divided by the projected imprint area). The term 'nanoindentation' usually refers to experiments carried out with a nanoindenter, basically a very stiff one axis instrumented column, to measure quantitatively and continuously the force and the tip

displacement within the sample. The advantage of instrumentation of Force and Displacement in nanoindentor is that the mechanical parameters are quantitatively and continuously measured (access to contact area through some equations) and allows to follow at least elastic (contact indentation modulus) and plastic properties (hardness) at any depth. The drawback is fine positioning of the diamond nanoindentor tip on a location: although nanoindentor equipped with a 2D XY sample translators can reproduce AFM-contact imaging mode as developed in our lab., this process is much slower and can be destructive. *In situ* SEM nanoindentation is therefore used for such characterization, but is only recently available in our lab. At a synchrotron, micro-focus beam can allow precise positioning of nanoindentor tips on a sample (using shadowing of Bragg reflection for example), but this is rather cumbersome with a diamond tip.

The *in situ* nano-indentation experiments were only possible at a late stage of this work. Hence, the nucleation of crystal defects by nano-indentation was primarily performed *ex situ* in good vibration controlled environment at the lab., using an AFM Dimension 3100 (Veeco) and a specific metrologically calibrated cantilever on which a diamond Berkovitch tip is attached.

The objective was to introduce a controlled amount of defects into the sample, and to use coherent X-ray diffraction or ptychography to characterize the nucleated defects, and the corresponding modifications in the 3D strain field. For a precise characterization of the evolution of the defect content, several sub-micron crystallites or nanowires in various loading states were generally prepared *ex situ* in the lab. The complete preparation procedure is described in the following.

After a pre-selection of the potential candidates by SEM, the AFM is used to image (with very weak mechanical interaction, in dynamic mode-tapping) the object which is to be indented. Fine AFM tapping scans are performed to enable a precise positioning of the AFM tip for indentation on top of a facet (width between 50 to 200 nm in general).

Once the location of the indent site is selected, the nano-indentation is performed by moving the cantilever downwards in the z-direction (force-approach curve, Fig. II.18). It corresponds to a classic force-approach curve in AFM, but to larger depth to induce defects in the sample. During the indentation process, the changes in the deflection of the tip are monitored and plotted against the downward (z) displacement of the cantilever. The measurement of the deflection of the tip is achieved through the well known beam deflection method (Meyer & Amer 1988). A laser light from a solid-state diode is reflected off the back of the cantilever and collected by a position sensitive photodetector composed of four photodiodes. An angular displacement of the cantilever (elastic deflection of the cantilever)produces on a position sensitive photodiode quadrant can output signal proportional to the vertical deflection of the cantilever. The deflection is measured in volts on the photodiode and is converted to nanometres through the deflection contact sensitivity calibration. This calibration is achieved at each location since it depends on the optical path arrangement between cantilever and photodiode. Basically is consist in measuring the slope of force-approach curve on a non deforming sample, typically our sapphire substrate. Then with the nanoindentation probe used in this work, we use its metrological calibration (nanobalance set-up), to calculate the force F between the tip and the sample using Eq.(II.22). The slope k of our nanoindentation probe is measured at 264 N/m (+/- 0.5)

$$F = k\,\delta \tag{II.22}$$

where δ is the deflection of the cantilever.

The general shape of the force displacement curve depends on the mechanical behaviour of the material.

During the approach from O to A, the tip goes into the sample of a depth δ, causing a deformation. During the retraction, the tip goes back from A to O. If the sample is purely elastic, it regains step by step its own shape, exerting on the tip the same force. Hence loading and unloading curve, *i.e.* the approach and retraction of the tip completely overlap (Fig. II.18.a). Conversely, if the sample is purely plastic, it undergoes a deformation a deformation during the loading curve, and when the tip is withdrawn, the sample does not regain its own shape and the load decreases whereas the penetration depth stay the same (Fig. II.18.b).

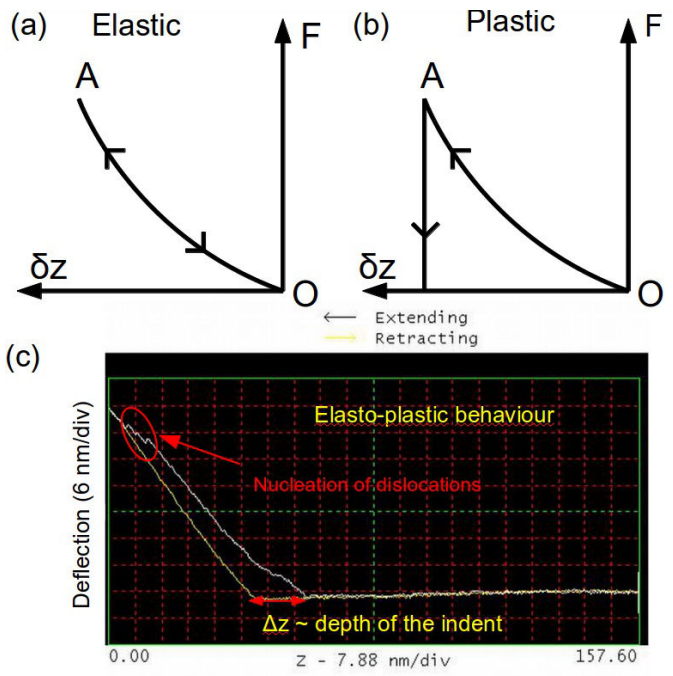

Fig. II.18 *Force-displacement curves for different mechanical behaviours.* (a) Purely elastic material. (b) Purely plastic material. (c) Force-approach curve of a gold particle revealing an elasto-discrete plastic behaviour

As illustrated in Fig. II.18.c, in practice, most samples exhibit a mixed elasto-plastic behaviour: the deformation is initially elastic, but the first stages of plasticity initiate suddenly and are easily identified on the loading curve by discontinuities a so-called "pop-in" event in nanoindentation (Fig. II.18.c, region circled in red). They appear as sudden drops in the loading curve. They mark the transition between the initial elastic behaviour to an elasto-plastic behaviour (Tromas *et al.,* 1999, Gaillard *et al.* 2003). The phenomenon is observed in a large variety of materials and is associated with dislocation activity (Gerberich *et al.* 1995, Michalske & Houston 2003). The initiation of the load drops in the indentation curves correlates abrupt surface displacements with dislocation nucleation events. As shown on Fig. II.18.c, the difference between the difference of penetration depth between the loading and unloading curves roughly gives the depth of the indent. Here, a deflection of 45 nm is observed, knowing that k = 264.5 N.m^{-1} for the diamond tip, the force applied to the particle is equal to 1.2 x 10^{-5} N. This value, for the tip geometry we used (sharpBerkovich diamond) is sufficient to enter the plastic regime and the corresponding depth of the indent is approximately 15 nm, as determined from the Force-approach curve.
Upon indentation by a sharp indenter, the first dislocations nucleate just below the indenter (Mordehai *et al.* 2011, Chang *et al.* 2010). Hence, the location of the indent has to be carefully selected. Indeed, dislocation nucleated upon indentation are glissile dislocations and might propagate in their slip plane until they are annihilated at the particle surface and interface (Mordehai *et al.*2011). The main objective of the CXD study being the investigation of the influence of crystal defects on the distribution of the 3D strain-field in the particles, it is only achievable if the nucleated dislocations are kept in mechanical equilibrium in the particle.
It is well-known that a dislocation is a thermodynamically non-equilibrium crystal defect. However, in the absence of external loading, they might stay in the small particle if the resolved shear stress due to both boundary condition and internal stress that apply on the dislocation are insufficient to overcome at least the -

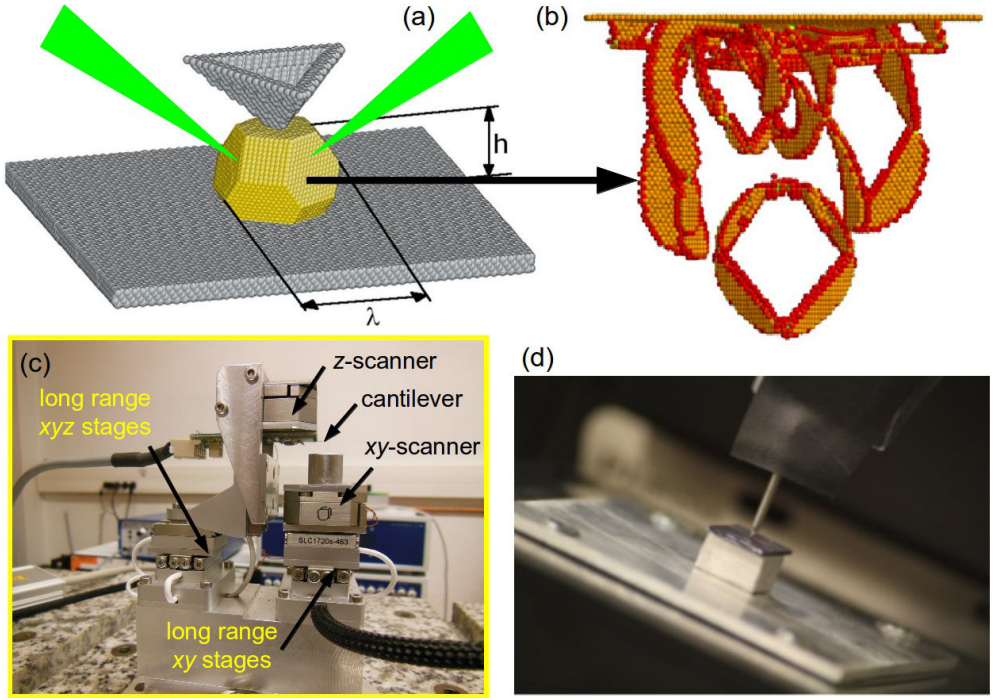

Fig. II.19 *Experimental set-ups to carry out the* in situ *nanoindentation experiments.* (a) Schematics of the *in situ* nanoindentation experiment while illuminating the particle with a coherent X-ray beam. (Fig. From Mordehai *et al.* 2011) (b) Snapshot of atomic configuration during a pop-in event in the course of a [1 1 1] indentation. Prismatic dislocation loops are nucleated. Are shown only the atoms that do not have a local f.c.c. environments. (Fig. from Chang *et al.* 2010) (c) Compact AFM "SPHINX" developed by the IM2NP in the ANR MECANIX framework. (d) Compact nanoindentor under development in our group (SIMaP). Both set-ups are designed to be adapted at a variety of synchrotron end-stations.

- lattice friction (minimum shear threshold for which a dislocation can glide on its slip system). This represents a lower bound since some dislocation-dislocations intersection can form a lock due to reaction and form sessile segments (Hirth &Lothe 1968).

Gryaznov *et al.* 1989 propose an estimate for a critical size for a free standing particle below which the rough estimate of image force that applies on the particle of size 2A: αGb/2A, systematically overcomes the lattice friction on the dislocation (determined by the Peierls barrier σ_p (Hirth & Lothe 1968)). The free particle thus becomes free from dislocations when it reaches the characteristic length:

$$l \propto \frac{\alpha G b}{\sigma_p} \tag{II.23}$$

where α is a numerical coefficient which depends on the geometry of a dislocation line and its position in the SP, G, b the shear modulus and Burgers vector of the dislocation respectively. This critical size is of the order of 100 nm for f.c.c. metals, which is well below the typical 500 nm size of the gold particles considered in this work. Additionally, it has been shown that a a glissile dislocation loop is usually unstable in a free-standing small particle (Grayznov *et al.* 1989), while dislocation loops which are localized near the centre of a crystallite that is coherently bounded with a stiff substrate are generally stable. Indeed, the correct calculation of the complete boundary conditions (free surface + particle/substrate interface) have to be carried out numerically: for example, the image force of vacuum is attractive whereas is it repulsive for the interface with a stiffer substrate (Sapphire).

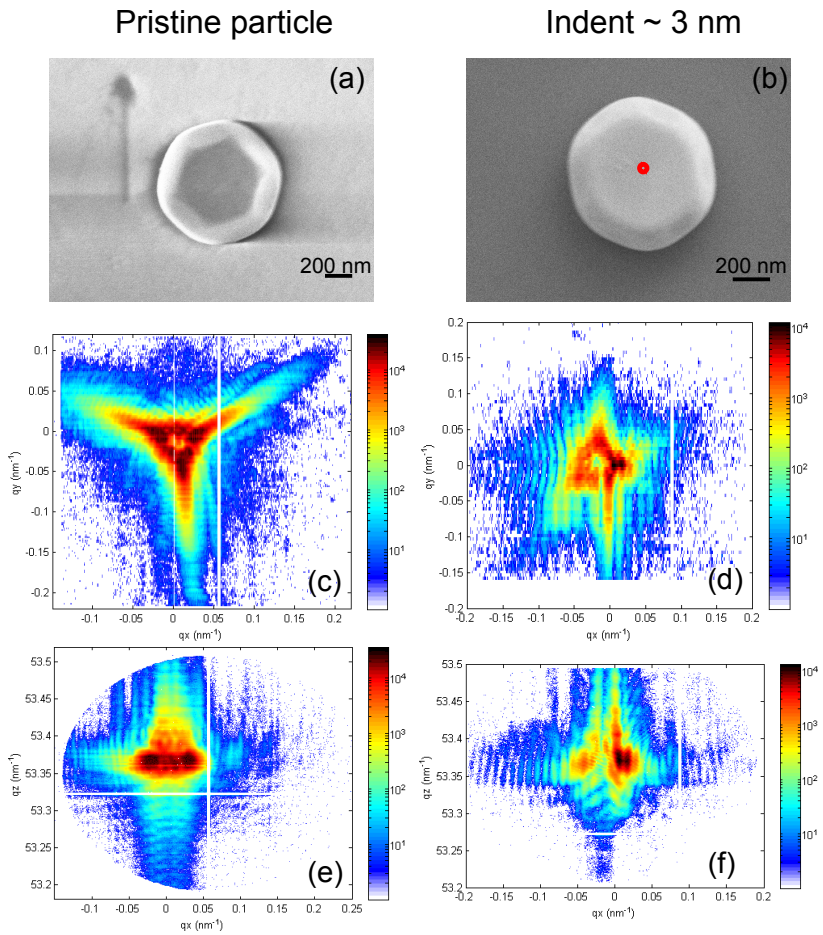

Fig. II.20: *Comparison between a CXD pattern obtained from a pristine particle, and from a particle where few dislocations have been nucleated.* The 2 2 2 Bragg reflection is measured. (a) – (b) SEM pictures of the pristine and indented particles. (c) – (d) and (e) -(f) (q_x,q_y) and (q_x,q_z) slices through the peak for the pristine (c and e) and indented (d and f) islands.

By indenting the gold particle at the centre of the flat {1 1 1} top surface, there is thus larger chance to nucleate dislocation loops that may remain stable in the particle in the unloaded state.

Fig. II.20 illustrates the effect of a gentle indentation on a gold solid-state dewetted particle close to its equilibrium shape. Both particles were measured on the CRISTAL beamline of the French synchrotron SOLEIL. The measurement was carried-out at the 2 2 2 Bragg reflection of gold using a 8.5 keV beam that was focused to 2 (H) x 0.5 (V) μm^2 with a FZP. The two island have a similar size and geometry, close to the Winterbottom equilibrium shape (Fig. II.20.a and II.20.b). Particle (b) was gently indented (~ 3 nm) prior to the experiment.

As illustrated in Fig. II.20.a, a large broadening of the Bragg peak is already visible in the pristine particle. The elongation is mainly along the {1 1 1} directions not perpendicular to the top (1 1 1) facet. The broadening of the Bragg peak is attributed to the presence of residual strain and is discussed in Chapter VI.

The indentation induces some clear effects on the CXD pattern. The most visible effect is the drop of intensity around $q = 0$. It was already present for the pristine particle but is clearly more pronounced after the nucleation of some defects into the structure (Fig. II.20.d and II.20.f). Conversely, the elongation along the {1 1 1} directions seems to decrease after indentation. This might suggest a partial relaxation of the residual strain by the

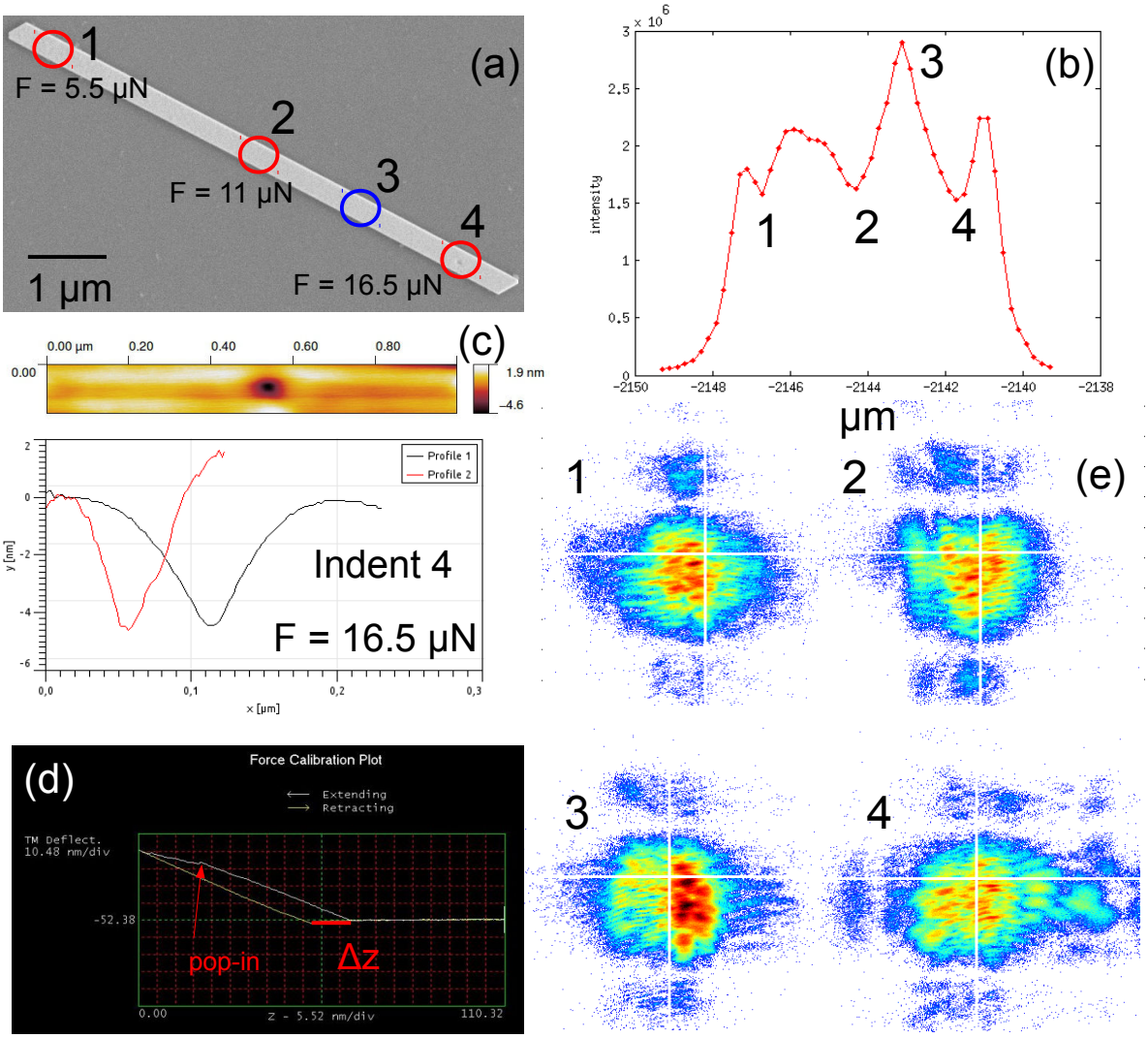

Fig. II.21 *Nanoindentation of a gold nanowire.* (a) SEM picture of a gold nanowire that was selected for nanoindentation. The regions circled in red indicate the position of the indents. The region circled in blue is left untouched. The red arrow denotes the direction of the scan during the synchrotron experiment. (b) Integrated intensity along the NW. Drops of intensity are clearly visible at the position of the indent. (c) AFM image of the NW in the region of indent (4), the depth of 5 nm is measured. (d) Force-displacement curve for indent (4). (e) 2D CXD patterns at several positions along the NW. (1), (2) and (4) correspond to indentation sites while (3) was collected in a pristine region.

- well known mechanical annealing process (Matthews & Blakeslee 1974).
Note the presence of high frequency oscillation fringes for the indented particles which suggest interferences with a neighbouring particles (a rather large beam-size was used for the experiment).

The selection of the nucleation sites for the nanowires is driven by other considerations. Given 1D long length size of the wires, it is perfectly conceivable to nucleate defects in some defined part while others are left untouched. The reconstruction of the 3D displacement field using 3D Bragg displacement field should allow a comparison between these defective and pristine regions.
The sample considered for nano-indentation is a 7.5(L)x0.3(W)x0.04(H) µm^3 ribbon shaped NW, with a (1 1 1)

out-of-plane orientation.
Following the procedure described above, dislocations were nucleated in three different regions of the NW separated by approximately 3 μm, which ensured that no interactions between the dislocations nucleated from distinct indentation sites would be observed. A gradient of increasing forces was applied from the left to the right of the NW, with values of 5.5 μN, 11 μN and 16.5 μN in (1), (2) and (4) respectively (Fig. II.21.a). The transition from the elastic to plastic regime is initiated for the three nucleation sites, with the presence of pop-in in the three-loading curves. From the difference in the penetration depth for the loading and unloading curves, it was possible to estimate indentation depths of 4 nm (1), 6 nm (2) an 11 nm (4, Fig. II.20.d).
The region around the indents was systematically imaged with the AFM tip after the indentation event. It was found that the depth of the indent is systematically lower than the value estimated from the load-displacement curve. For instance, the depth of indent (4, F = 16.5 μN) which was estimated to be 11 nm is actually only 5 nm deep. It is thus clear that a significant amount of recovery occurs after the withdrawal of the tip.
The reconstruction of the 3D displacement field by 3D Bragg ptychography was attempted in two distinct synchrotron experiments carried out on the CRISTAL beamline and on the I13-1 beamline (Diamond Light Source). These attempts failed for various reasons.
In a few words, for the CRISTAL experiment, an unexpectedly large amount of defects was found in the pristine nanowires (Fig. II.23), and no sufficient stability of the set-up was achieved. For the I13-1 experiment, the primarily issue was the weak coherence of the beam.
The NW presented in Fig. II.21 was measured during the I 13-1 experiment, with a partially coherent X-ray beam. Fig. II.21.d shows the integrated intensity along the NW, the direction of the scan is indicated by the red-arrow in Fig. II.21.a. It is clear that the drops of intensity perfectly match with the position of the indent. This indicates the large concentration of defects in the region below the indent, as well as the presence of significant lattice distortions. Fig. II.21.e shows 2D CXD patterns taken at different locations along the NW. (1), (2) and (4) correspond to the indent positions while (3) was left untouched. It is obvious that CXD patterns are affected by the presence of a localized arrangement of defects.
A speckle pattern is observed at each position, which indicate a large concentration of defects before nucleation of additional dislocations. Since these NW are supposed to be almost defect-free (Richter *et al.* 2009), this high initial concentration of defect might be related to our transfer procedure on the silicon substrate.
Additionally if the focusing set-up used during this experiment (FZP) gave a beam-size that was estimated to be in the sub-micron range (FWHM) the measurement was carried-out at the 1 1 1 Bragg reflection which correspond to an incident angle of less than 16° at 9.8 keV. Along the direction of the beam, which roughly corresponds to the orientation of the NW, the footprint of the beam is thus much larger (as much as 3.6 μm for a 1 μm beam). The untouched region of the NW (3) is only 1.5 μm away from the closest indentation sites, which means that crystal defects are probably illuminated from this position. That being said, the largest perturbations on the CXD pattern, and the minimum of the integrated intensity are found around the indent (4), where the largest mechanical solicitation was applied.

II.4.2. Synchrotron characterization

II.4.2.1 Laue microdiffraction

While monochromatic diffraction gives access to individual Bragg reflections with high resolution, methods based on polychromatic beams allow for measuring many diffraction peaks at the same time without any *a priori* knowledge about the crystallographic unit-cell orientation of the sample under investigation. Since the crystalline sample is illuminated with a white beam, a large number of atomic plane satisfies the Bragg law, and several Bragg reflections can be intercepted on a diffraction pattern by placing a 2D area detector close to the sample (typical distance of 10 centimetres).
Micro-Laue diffraction combines the oldest X-ray diffraction method – Laue diffraction – with modern X-ray

sources and detector. The technique can provide much insight on the defect and strain content of single particles.
As discussed in Chapter I, local elastic strain (or stress) can be determined from the unstrained cell parameters of a single crystal volume. Methods for determining the unit-cell parameters on single-crystal have been derived by Busing & Levy (1967). It was shown that 3 linearly independent reflections determine the 3 parameters required for crystallographic orientation and the 6 parameters for the unit cell (a, b, c, α, β, γ). Following a similar formalism Chung & Ice (1999) evidenced that 4 Laue reflections determine the 3 crystallographic orientation parameters and the unit cell shape: a/c, b/c, α, β, γ. The strain tensor can thus be determined at each point of the crystal can be determined by spatially resolved micro-Laue diffraction.
The components of the second-rank elastic strain tensor ε_{ij} can be determined from the transformation matrix that maps unstrained to strained vectors:

$$\epsilon_{ij} = (T_{ij} + T_{ji})/2 - I_{ij} \quad \text{(II.24)}$$

Similarly to the case of CXD, the presence of elastic strain distorts the angle between reflections. With a constant strain tensor throughout the sampled volume, the shape of the Bragg peak is unchanged. However, in the presence of strain gradients (changes in the elastic strain tensor within the volume probed), angular distortions are not uniform and cause a blurring and streaking of the Bragg peaks.
In many materials, streaks observed around the Laue spots can also originate from the presence of geometry necessary (GND) dislocations which dominates over the influence of elastic strain gradients. Dislocations indeed interrupt the periodicity of the crystal lattice and introduce long-range rotations between sections of the crystal lattice. The character of Laue pattern streaking changes with dislocation type. Since the commonly activated dislocation systems are known for most materials, it is in principle possible, to fit Laue patterns to evaluate the most likely slip systems in a local volume. Informations about the total dislocation density can theoretically be derived by observing the extent of the streaking of the Bragg spot (Ice *et* al. 2005, Ice *et al.* 2007, Barabash *et al.* 2003). The determination of these informations is however very challenging experimentally. Among other perturbations that can be observed on Laue micro-diffraction patterns are the the splitting of the Bragg spots in two or more parts. The splitting of the Laue spots can be induced by low angle grain boundaries (Barabash *et al.* 2002). The latter generally results in the accumulation of so-called tilt-dislocation walls (Barabash *et al.* 2002) in geometrically necessary boundaries (GNB).
In this work we did not intend to perform a detailed analysis of the Laue micro-diffraction patterns, for instance, we did not try to determine the strain tensor or the slip systems of the dislocations nucleated in the particle. The technique has been used as a preparation technique to select the best candidates for CXD experiments, and to evaluate the amount of strain that was generated by the *ex situ* indentation of particles.
As discussed above the amount of elastic strain and defects can be deduced from the shape of the Laue spots. For CXD experiments and in particular for CDI a large amount of elastic strain and a high defect concentration is not desirable, at least for a proper study of defect nucleation. In this case, the direct analysis of CXD patterns is indeed very delicate (see Chapter IV) due to the interplay between a large and heterogeneous elastic strain and the multiple crystal defect. Regarding CDI, to our knowledge, there is no experimental evidence of the reconstruction of systems exhibiting such a high density of defects.
The particles or NW with large distortions of the Laue spots were systematically discarded, while particles exhibiting a reasonably low amount of strain were selected for CXD experiments.
In practice, only one Laue micro-diffraction experiment has been carried-out during this work, so that only few samples are evaluated using this technique. For most of the CXD experiments in this PHD, the initial level of deformation and defect density in the particles or NW is generally unknown prior to the CXD experiment.
Alternatively, Laue patterns are also collected for objects which had been measured previously by CXD in order to quantify the agreement between the two techniques.
Fig. II.22 and Fig. II.23 show Laue micro-diffraction pattern from a NW and a particle exhibiting different levels of strain. The measurements are carried-out on the BM 32 beamline at the ESRF. The sub-micron size of the polychromatic beam allows to scan the samples to measure local deformations with a good spatial resolution.

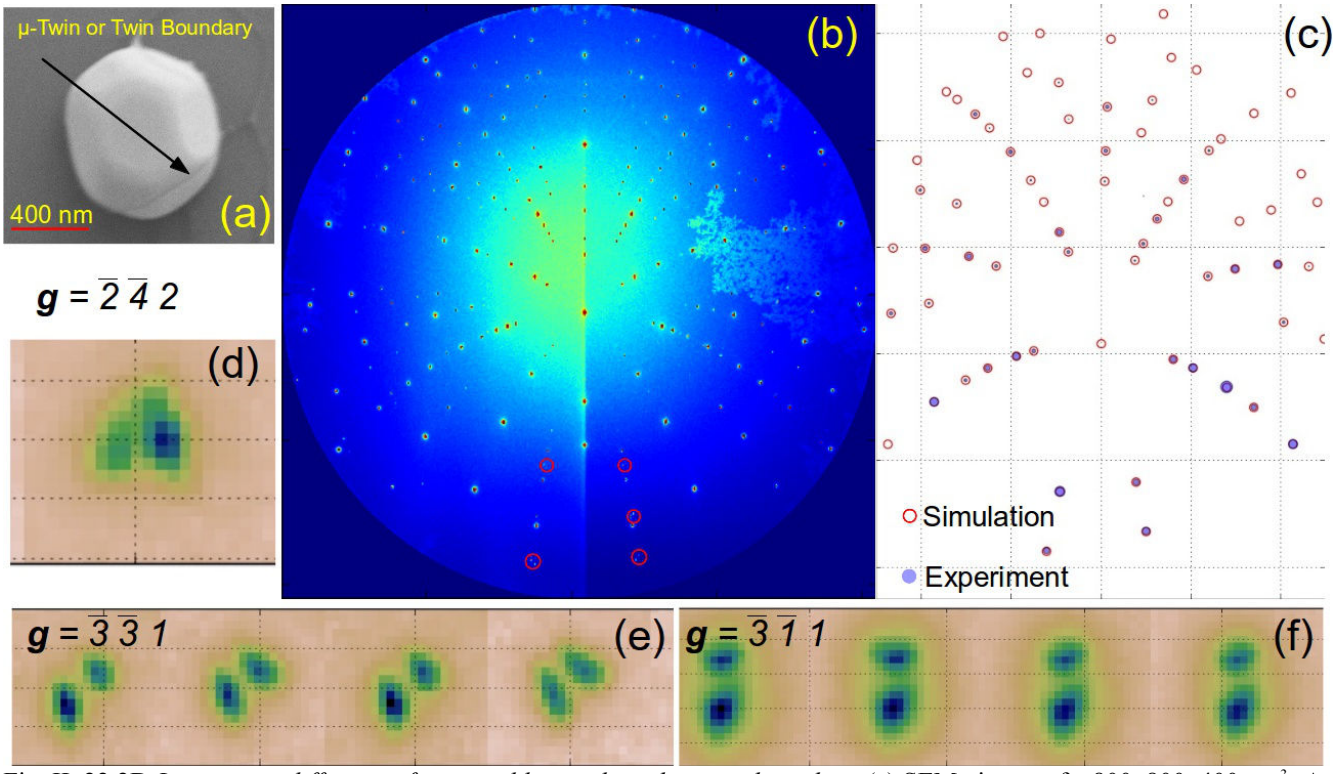

Fig. II. 22 2D *Laue micro-diffraction from a gold particle with a twin-boundary.* (a) SEM picture of a 800x800x400 nm^3 . A micro-twin or possibly a twin boundary can be identified. (c) Indexation of the Laue spots with the software Laue tools. (d)-(f) Zoom around some Laue reflections revealing a splitting of the Laue spots.

This is particularly useful when the sample is extended in one direction as in the case of the NWs. For the latter, 2D scans were performed, with a step size of 250 nm in both x and y directions of the NW. A 2D Laue micro-diffraction pattern is recorded at each scan position. For the particles, l D scan with a finer step size of 50 μm are performed.

As illustrated from the SEM picture (Fig. II.22.a), a dark line which extends over all the particle surface is clearly visible. This dark-line probably corresponds to a low-energy twin-boundary or to a micro-twin.

As a reminder, twin domains occur when two crystals share some of the same crystal lattice point and are related by symmetry operations. The twin crystal planes are rotated with respect to the parent crystal planes, and do not diffract at the same positions in the reciprocal space. Since twin-boundaries are coherent interfaces, no or very few lattice distortions are found at the vicinity the twin boundary. In presence of a single twin-boundary in the structure, two sets of isotropic Laue spots corresponding to the two crystals are expected.

A micro-twin is encountered when two twin-boundaries with a small spatial separation are found in the crystal. The two crystal volumes on both side of the twin share the same orientation and the twinned part is rotated with respect to the parent crystal. Since only a very small volume of the crystal is rotated, it should not be visible on the Laue micro-diffraction pattern. Fig. II.23.b show the 2D Laue pattern collected at the centre of the island top facet. A large number of Laue reflections are measured, coming from both the diffraction of gold island and of the underlying silicon substrate . Using the software Lauetools (Micha & Robach 2014), it is possible to index each Laue reflection originating from the gold particle. An excellent agreement is found between the simulated position of the Laue spot and the experimental data (Fig. II.22.c). From the analysis of the position of the Laue spot, it is clear that a single grain is diffracting. Hence, the dark line does not correspond to a single twin boundary. On the other hand, and as illustrated on Fig. II.22.c to II.22.e, a zoom around some of the Laue reflections reveal a splitting of the Laue spot. Such splitting is an indication of the presence of a low angle grain

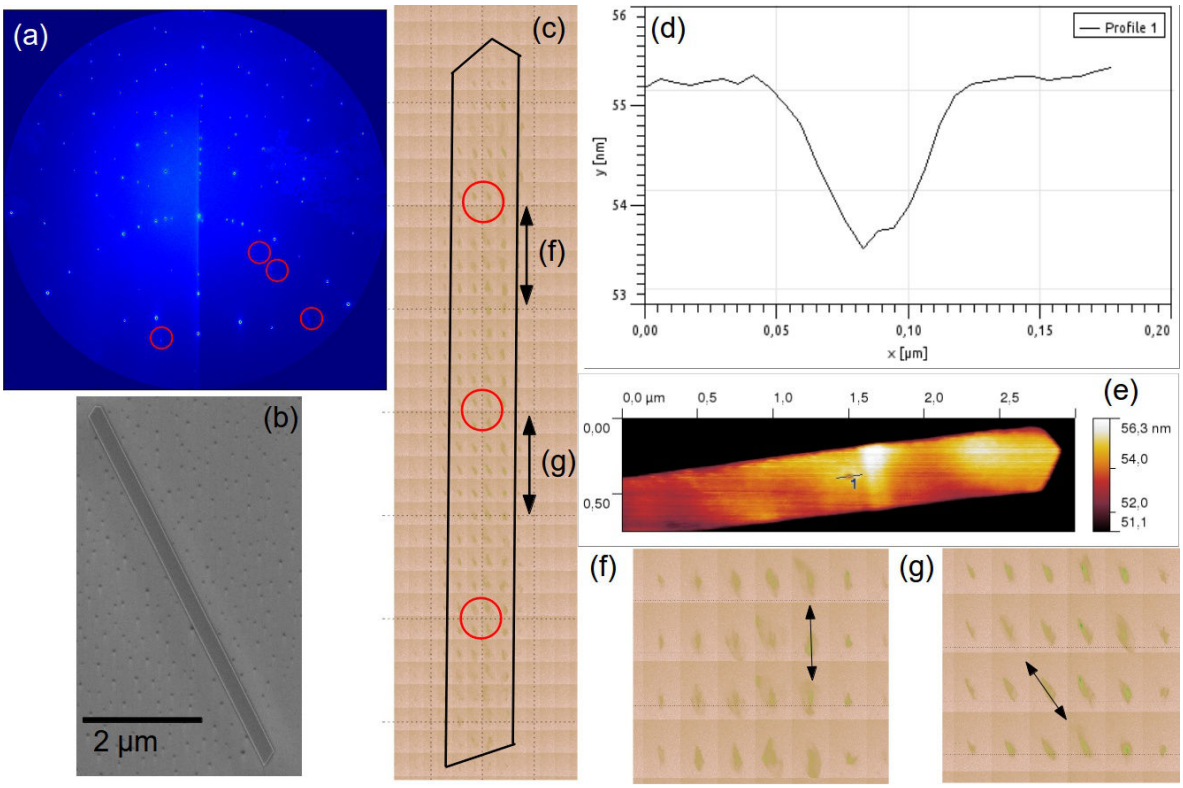

Fig. II.23 2D *Laue micro-diffraction from a gold nanowire with a twin-boundary.* (a) Laue diffraction pattern taken close to the NW centre. (b) SEM picture of a 6.6 (L) x 0.4 (W) x 0.05 (T) µm^3 Au NW that was indented at three positions with a gradient of increasing forces. (d) Scan of the NW with a white micro-beam. The location of the indents are indicated with a red circle. (e) and (d) AFM picture of the indent, showing a 2 nm deep indent. (f) and (g) zoom on specific regions of the NW, where large distorsions of the Laue spots indicate a large amount of micro-strain

boundary. It is however unclear if the dark-line visible on the SEM picture correspond to this low angle grain boundary or if it is a twin-boundary which is invisible with Laue micro-diffraction. The measurement of the particle with a Coherent X-ray beam should help to answer this question.

Fig. II.23.a show a Laue micro-diffraction pattern of an *ex situ* indented NW measured close to its centre. The NW measured previously on the CRISTAL beamline was found to be extremely defective and as a result is impossible to reconstruct by ptychographic means. The defective character of the NW is confirmed by the Laue measurements. A limited number of Laue reflections is visible and the indexation of the Laue spot is thus not possible. The Laue spots that can be identified are very diffuse, indicating the presence of large lattice distortions.

The NW was indented at several locations circled in red in Fig. II.23.c. The force applied for the indentation was rather weak in order to limit the amount of plastic deformation and the corresponding number of nucleated dislocations. As illustrated in Fig. II.23.e and II.23.f, the remaining indent depth is less than 2 nm. The analysis of the Laue spots in various regions of the NW reveals that it is very defective other its entire length and the supplementary amount of local plastic deformation brought by the nano-indentation is thus difficult to distinguish. It is however clear that the shape of the Laue spots is not constant over the NW length. In region (g) close to the central indent, the streaking of the Laue spot (indicating either the presence of heterogeneous strain or of GND) is clearly visible.

The streak direction of the Laue spot depends on the dislocation tensor and the effective strain gradient. In the case of single slip the streak direction depends on the dislocation slip system orientation. It is thus probable that

that a single slip system is largely predominant in this region of the crystal. Conversely, both a splitting and a streaking of the Laue spot are observed in region (f), this indicates an even more complex microstructure probably composed of both GNB and individual GND as suggested by Barabash *et al.* (2002).

II.4.2.2 Finding the sample of interest: 2D fast-mapping of the sample

The solid state dewetting technique produces a large number of sample with relatively similar size, geometry and out-of-plane orientation. Since the particles of interest are characterized before and/or after the synchrotron experiment, it is critical to be able to locate them easily. To locate the areas of interest, different methods can be employed. The most simple and basic one consist in drawing a network of perpendicular lines on the sample surface, using tweezers. As illustrated in Fig. II.24.a, the areas that have been scratched with the tweezers are depleted from gold particles. The regions at the intersection of two perpendicular lines are very easy to locate, and the potential candidates for CXD experiments are generally selected close to intersections, in order to retrieve them easily. Although very basic, this method proved to be efficient. A more precise and elegant method consist in patterning the gold thin film prior to dewetting, using a mask that is glued to the substrate before the gold deposition. This approach was used by a master student in our group, using a copper mask containing hexagonally arranged holes (6 µm pitch).
For the NW, the approach is noticeably different, since only a few of them are deposited on the silicon substrate. The most efficient way to locate them consist in marking the substrate with a network of indent at the vicinity of the NWs. Since all the synchrotron end-stations that we used are equipped with an optical microscope, both the indent and the trenches can be easily located.
For a synchrotron experiment, the procedure to find and measure the sample of interest can be divided in two main steps. The first step which is not necessarily the easiest one consists in locating the precise position of the beam. As discussed in section II.1.3, the alignment of the sample in the beam is a very critical step. Once the sample is in Bragg condition, the position of the beam on the sample must coincide with the centre of rotation of diffractometer. Although 6C diffractometers have a rather large sphere of confusion, this will ensure that the beam stay on the sample while acquiring a rocking-curve. For the measurement of a single sample, it is also very

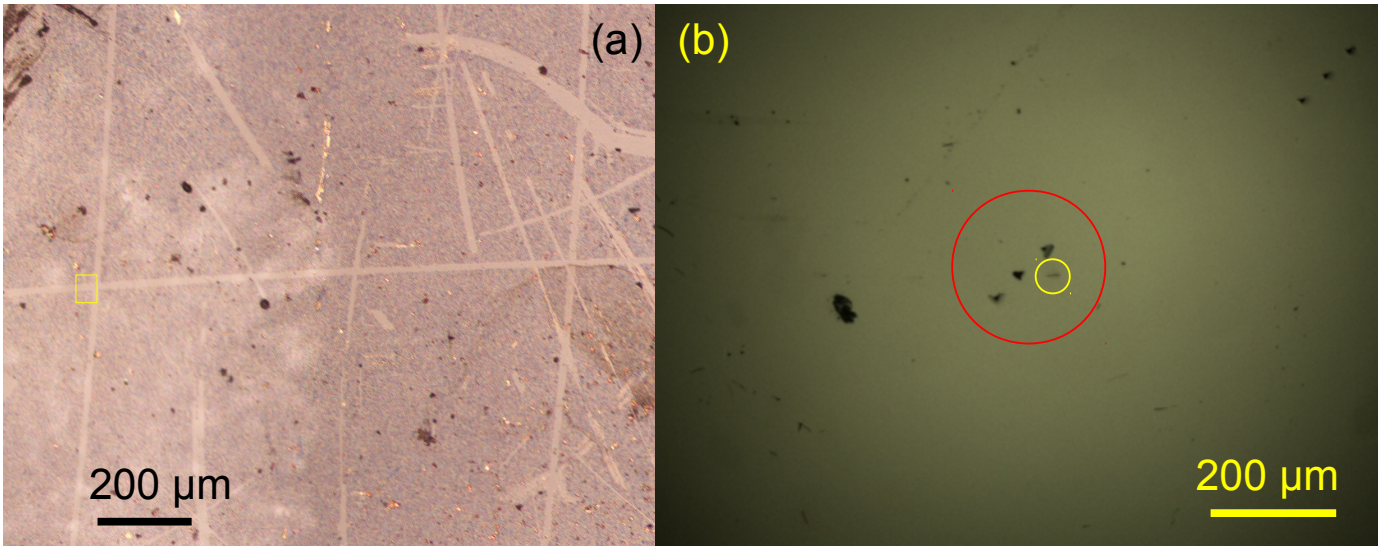

Fig. II.24:*Macroscopic markers on the sample, to locate the crystals of interest.* (a) Gold islands on a sapphire substrate. The tracking of the islands of interest is carried out in regions at the intersection between two trenches depleted from islands. The yellow rectangle indicates the extent of the region represented in Fig.25. (b) Gold nanowires on a silicon substrate. The regions of interest are marked with a network of indents. The small wire inside the yellow circle is one of the nanowires.

important that the beam does not move too much while rotating the diffractometer. Of course, due to the aforementioned large sphere of confusion, the precise alignment of the sample in the beam needs to be performed each time the Bragg angle is changed.

The gold on sapphire system is very convenient for the location of the beam. Indeed, the incident X-ray beam excite the fluorescence of the sapphire in the visible light so that the beam is always visible. It is thus particularly easy to move the X-ray beam to the region of interest.
Once the beam is roughly in the region of interest, the sample needs to be aligned precisely in the X-ray beam. To do so, we use the scanning X-ray diffraction microscopy technique (SXDM) which offers a real space mapping of the sample. A 2D scan at the vicinity of the sample of interest, and the diffracted intensity is measured at each position of the scan. All the particles obtained by solid state dewetting technique have the same out-of plane orientation, and thus satisfy the Bragg conditions for the same angle. Once the sample is rotated to Bragg conditions, a high integrated intensity is thus collected when an island is illuminated while a much lower intensity is obtained in the region in between two islands.
The resolution of the real space map depends on the step size of the scan and is limited by the beam size (see next sub-section for more details). As discussed in Chapter I, for CDI experiments, it is essential that the beam is larger than the sample, but small enough to illuminate only one island at a time. The compromise can be difficult to find, but a beam size slightly below 1x1 μm^2 is generally ideal. This matter is discussed in more details chapter VI.

In any case, the beam size is smaller than the typical spacing between two neighbouring islands and their position are clearly resolved on SXDM maps. A typical map consist of 50x50 points and could be in principle be performed using the scanning options offered by the beamline control software (for instance SPEC for the ESRF or GDA for the Diamond light source). The weak point of this scanning mode is the dead time required for positioning hardware and software triggering (data transfer, connection between program, motors and detectors). This imply measurement times that are generally not compatible with a synchrotron experiment (11 hours for 200x200 points scans!). On the ID01 beamline, the standard controlling software have thus been replaced by a hardware control system, eliminating the positioning time and greatly reducing the scanning time. In this mode, the diffracted intensity is indeed collected while continuously moving the sample.
In our case the sample of interest can be rapidly found by performing a large scan on a spatial extent of 100 x 100 µm with a 1 µm step size which is generally sufficient to distinguish the islands. The collection of such scan is a matter of minutes. Since the areas of interests are generally located at the vicinity of the trenches, the obtained SXDM map (Fig. II.25.a) can be compared with SEM / HiRes optical images collected before the experiment (Fig. 25.b). Note that the extent of the map shown on Fig. II.25.a and II.25.b correspond to the small yellow rectangle in Fig. II.24.
Once the localization of the island is roughly estimated with this coarse scan, a finer 2D map with a reduced step size is collected at the immediate vicinity of the sample. As illustrated on Fig. II.25.c and II.25.d, very good agreement is generally obtained with the SEM images, which allows to identify the exact location of all the islands of interest.
The crystallites used for the experiment presented in chapter VI are dewetted from a patterned gold thin film so that a single island is found at the centre of a 50x50 μm^2 square. Once the beam position is roughly established, the location of the island is in this case straightforward.
It is also important to mention that we initiated the implementation of a similar “fast-scan” procedure on the CRISTAL beamline and on the B-16 beamline (Diamond light-source).

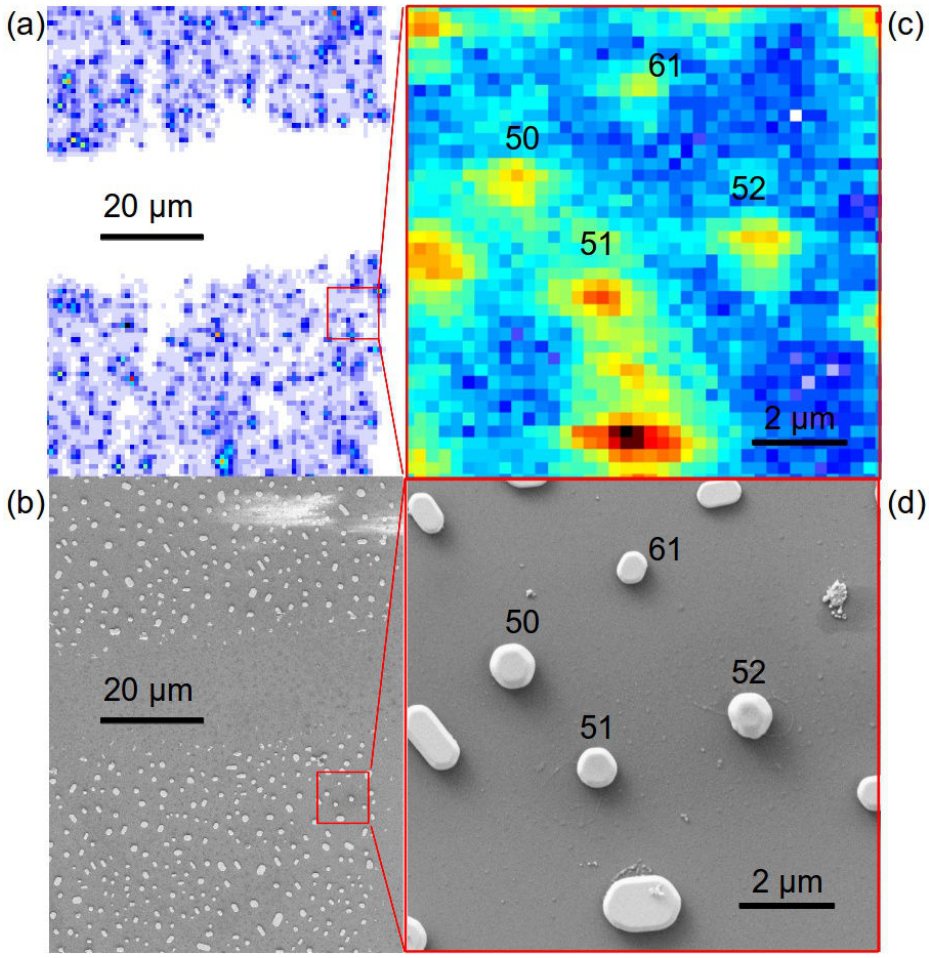

Fig. II.25 *Illustration of the SXDM technique to localize the islands of interest* (a) Coarse scan of a 80x80 µm^2 area with a 1 µm step size. (b) SEM picture of the same area allowing the detection of the island of interests. (c) Fine 10x10 µm^2 scan with a 0.250 µm step size. (d) A perfect coincidence is obtained with the SEM picture of the same region.

II.4.2.3 Mapping the sample strain and tilt: Scanning-X-ray Diffraction Microscopy (SXDM)

We have seen in the previous sections that X-rays are a powerful tool to access the strain of various materials. CXD can provide a reconstruction of the 3 dimensional strain field with a very good resolution, while Laue micro-diffraction is a powerful method for mapping the full strain tensor of single-crystal and polycrystalline materials with sub-micrometer spatial resolution.

An alternative technique for the strain characterization with a good spatial resolution is X-ray nanodiffraction. It has emerged in the past few-years, taking advantage of the modern X-ray diffractive and refractive optics which allow to obtain a beam size of a few tens of nanometres are (Vila-Comamala *et al.* 2011, Schroer *et al.* 2005). The technique has opened the possibility of measuring the lattice parameter of single nanostructures with a resolution down to 100 nm and a sensitivity to relative lattice parameters of around 10^{-4} (Chrastina *et al.* 2012). As compared to Laue micro-diffraction, the use of a monochromatic radiation enables to achieve a higher lateral resolution, and the technique also avoids the complicated analysis of Laue diffraction patterns.

The main issue of the technique lies in the need to perform point by point measurement of the strain which is

often time consuming and impede the investigation of large areas.
Additionally, in the micro XRD measurements the determination of the Bragg peak position and shape in the reciprocal space is essential for retrieving all the information related to the strain and/or tilt in the structure. This information can only be accessed by recording a 3D reciprocal space map (3D RSM) of the investigated structure. In this way, all the the component of the scattering vector $\boldsymbol{q}$ can be determined. Two parameters can be extracted and represented as a function of their spatial distribution. The length of the scattering vector $|\boldsymbol{q}|$ and its angular deviation from an orientation defined as 'normal orientation'. This allows to separate between lattice strain and the lattice rotation (lattice tilt).
The obtaining of these parameters supposes the collection of 2D maps at each point of the rocking curve, while a 2D diffraction pattern is collected at each point of the 2D maps. In other words, a 5D dataset needs to be collected with 2 dimensions corresponding to the real space positions, x and y, one for the incidence angle ω and two for the detector scattering angles δ and ν (which corresponds to γ in the description of the diffractometer given in section II.1.3). The collection of such huge dataset in a reasonable amount of time, compatible with a synchrotron experiment can be only achieved through the continuous mapping method of the sample described in the previous section.
The 3D RSM are obtained by converting the pixel positions of the detector into detector angles and to the corresponding reciprocal-space coordinates following a procedure similar to that presented in section II.1.6. The pixel position corresponding to the reciprocal space origin as well as the definition of the grid (the detector pixels per degree) are determined by the *XSOCS* package (Chahine *et al.* 2014). A 3D RSM is generated for each position on the sample. Both the strain and tilt are determined from the position of the Bragg peak with respect to a reference position calculated from the unstrained lattice.

The mapping of the average strain with a good spatial resolution is highly desirable for the case of solid state dewetting, since a rather large size distribution as well as different shapes .
For the Au/Al_2O_3 system, the gold particles can be divided in three categories. The first one corresponds to equiaxed particles with a shape close to the Winterbottom equilibrium shape (circled in red in Fig. II.26.a). A second category of particles is elongated along one of the <1 1 0> direction, with an height generally lower than that of the equiaxed Winterbottom particles (circled in green in Fig. II.26.b). The origin of this elongation, and the evolution of the particle shape for longer annealing times are discussed in more details in Chapter VI.
Finally, a third type of particles which are generally significantly larger and very flat (less than half the height of the Winterbottom particles, Fig. II.26.c) can be observed. It is unclear if these particles have well defined {1 1 1} and {1 0 0} facets corresponding to ECS. The three types of particles and their corresponding height are shown in Fig. II.26. It should be noted that the aspect ratio of the equiaxed Winterbottom particles is very reproducible while the height does not depend on the lateral size for the two other types.
Does the size and geometry of the particle influence the residual strain, and how reproducible is it ?
The question can be answered by generating a 2D map of the strain, with a large statistics. The measurement was carried-out at the 1 1 1 Bragg reflection using a monochromatic 8 keV beam. The latter is focused by a 300 μm (FZP). The zero order beam is removed by a beam stop while the higher diffraction orders are eliminated by the order sorting aperture (OSA) mounted downstream. A typical 150x100 nm^2, (FWHM) focal spot size is obtained with this set-up, but the latter was not checked. The 80x60 μm^2 area was scanned with a step size of 500 nm in both directions, corresponding to 160x120 points for each 2D map. Maps were collected at 15 angular positions within a scan range of 0.3°. A step size of 0.05° was used for the outer points of the rocking curve, while finer steps of 0.01° were used at the vicinity of the Bragg peak. Note that the measurement was not carried-out with a coherent X-ray beam.

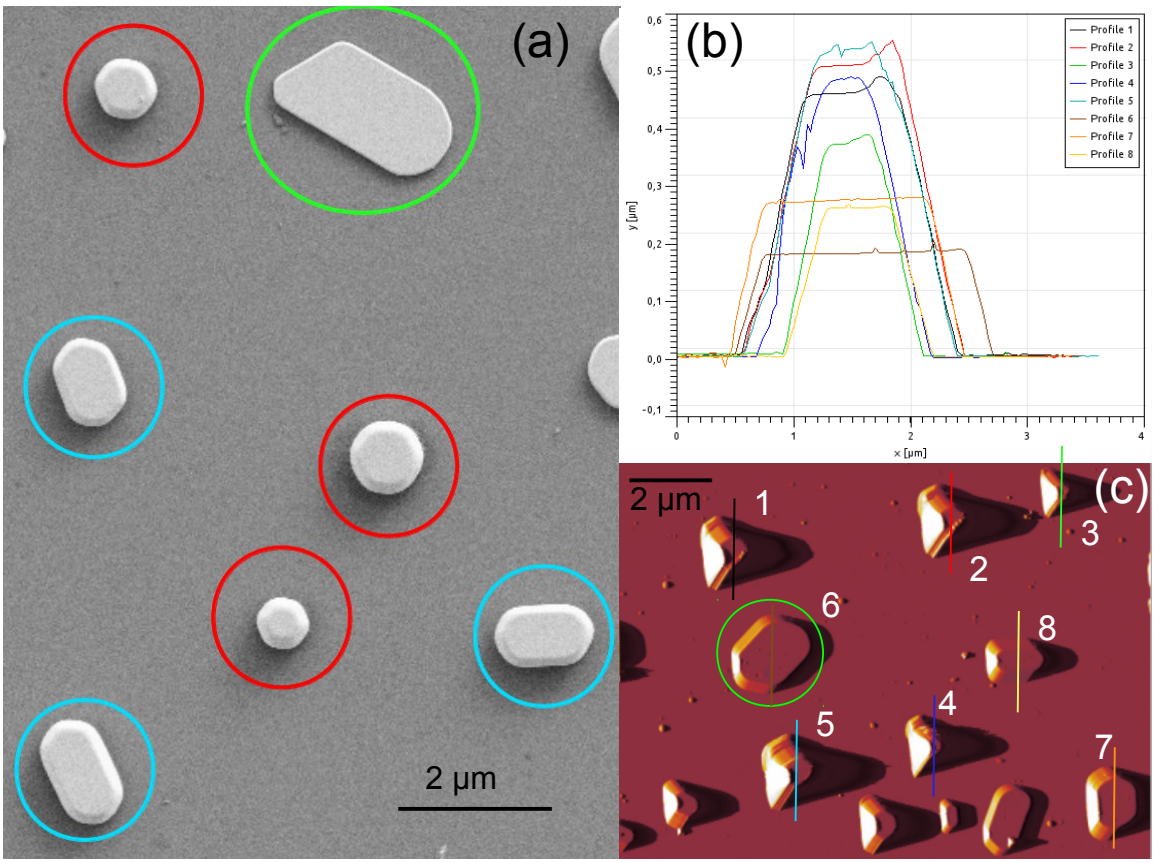

Fig. II.26: *Catalogue of the distribution of sizes and geometries of the particles obtained by solid-state dewetting.* (a) SEM pictures illustrated the three families of islands. The colour of the circles surrounding the particles depends on their geometry (see text for more details). (b) Typical distribution of particle heights. (c) AFM picture of the region where the particle heights have been measured.

Fig. II.27 show the 80x60 µm^2 region of the sample where the 2D strain map was measured. Note that this area was selected at the vicinity of a trench in order to be easily retrieved for post-characterization (Fig. II.27.a).
The region was imaged by AFM after the synchrotron measurement in order to correlate the calculated strain with the size and shape of the particles (Fig. II.27.b). A perfect coincidence is obtained with the integrated intensity map (maximum of the Bragg peak), which allows an easy identification of all the islands. The color coding for the islands is the same that that the one used in Fig. II.27. It is difficult from Fig. II.27.b to determine if one the geometry is more frequent, although it is quite clear that the Winterbottom shape which corresponds to the equilibrium shape of the crystal is the less frequent. Note that 3D CXD patterns were also collected for most of the Winterbottom particles present in this region.
The map of the integrated intensity shown in Fig. II.27.c was measured at $\theta = 19.49°$, which corresponds to the maximum of the Bragg peak as illustrated in Fig. II.28. It provides a limited amount of information on the particles. For a given particle, the integrated intensity is proportional to the diffracting volume, and it is quite straightforward to understand that the larger is the particle, the higher is the integrated intensity. Also interesting, a drop of intensity is clearly visible for some of the indented particles (particles 64 and 66 for instance). Note that the force applied for the indentation of these particles was rather large (much larger than the values described in section II.4.1), resulting in a deep indentation and a high content of defects nucleated in the particle.

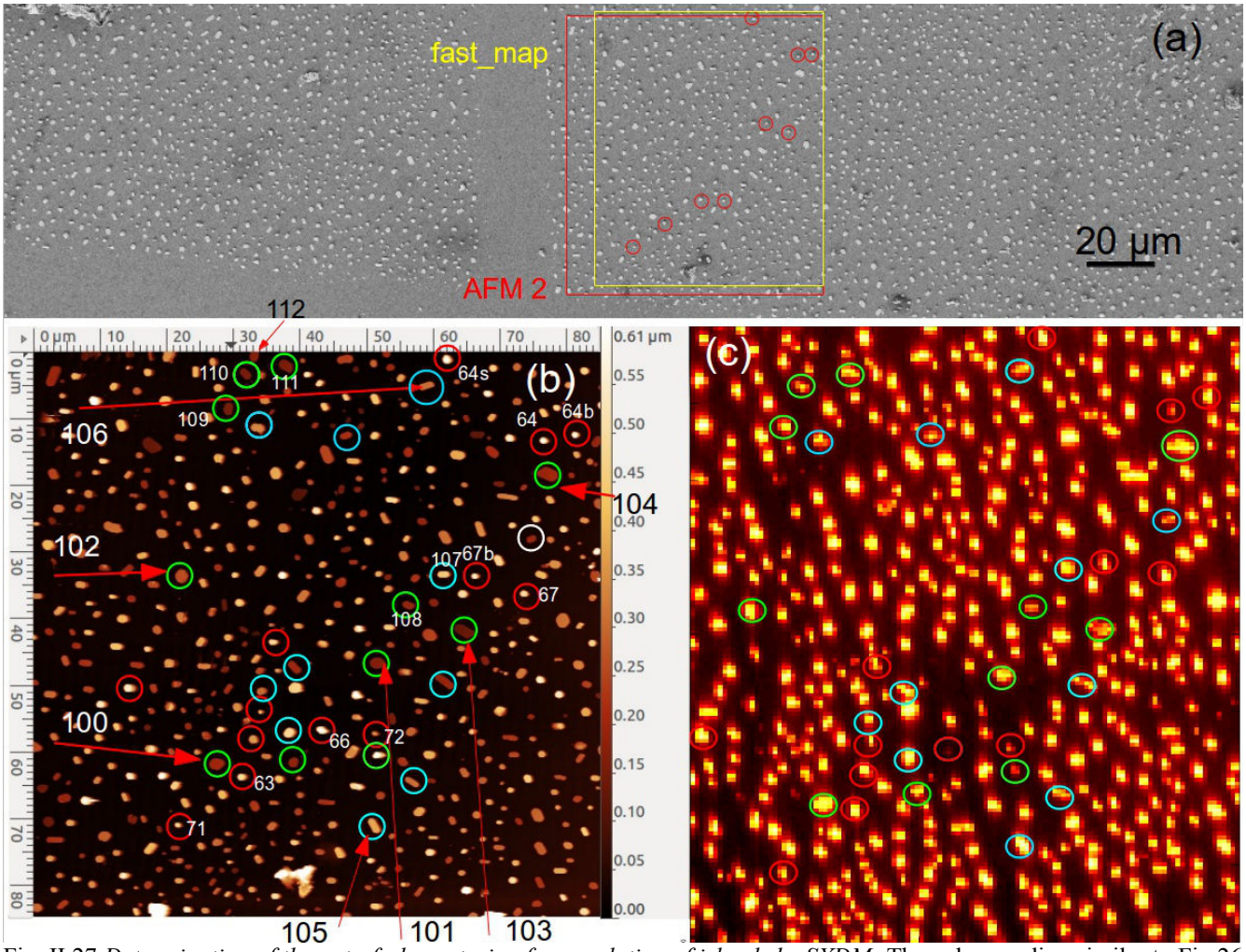

Fig. II.27 *Determination of the out-of-plane strain of a population of islands by SXDM.* The colour coding similar to Fig.26 defines the particle geometry (a) SEM picture of the region where the SXDM microscopy measurements have been carried-out. (b) AFM image of the same region. (c) Integrated intensity map at θ = 19.49° corresponding to the Au 1 1 1 Bragg peak.

A traditional approach to characterize the strain in a particle using a large parallel incoherent X-ray beam are the integral breadth (IB) methods (Klug & Alexander, 1974). As a reminder, the integral breadth β simply designate the ratio between the integral of a Bragg line and its maximum. The IB methods provide a quick-estimation of the so-called 'size-strain' line broadening effect of the Bragg peak. The broadening is caused by the average size of the crystallites and by lattice strains : *i.e.* lattice strains and distortions induced by the presence of lattice defects. The Scherrer formula (Scherrer 1918) describe the influence of a crystallite size on the broadening of a Bragg line. It simply states that the integral breadth β is inversely proportional to the size of the crystallite L.
In practice, the line broadening is rarely entirely caused by size effects, and an additional factor of broadening are the inhomogeneities of the internal strain. Simple models have been proposed to evaluate the of the internal strain, also called micro-strain ε^*. The Williamson-Hall (WH) model (Williamson & Hall 1953) states that the line broadening that can be attributed to the crystallite size is independent of q . The increasing of the integral breadth with q only depends on the internal state of deformation:

$$\beta(q) = \beta_s + \beta_d = 1/L + 2\epsilon^* q \qquad \text{(II.25)}$$

where β(q) is the total integral breadth, and β_s and β_d are respectively the component size for the size and strain. The plot of β(q) versus q called the Williamson plot provides an estimate of both the size of the crystallite (the y-intercept) and of the micro-strain ε^* (the slope of the WH plot). Obviously, this method supposes the measurement of several Bragg reflections.

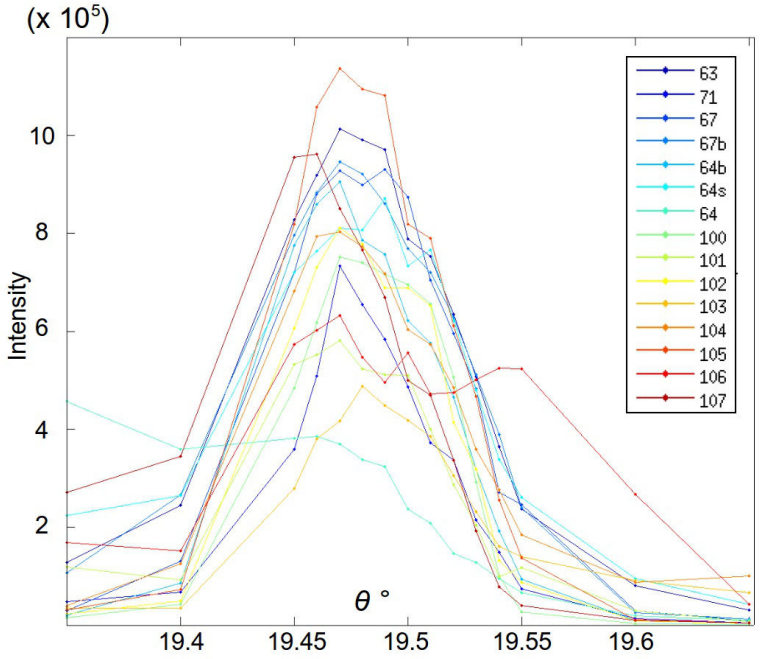

Fig. II.28 *Rocking-curve for several particles determined from the integrated intensities at various angular positions*

For the present experiment, it is clear that these approaches are not applicable since the beam size σ is significantly smaller than the particles. The broadening of the peak has thus a 1/σ dependency that is stronger than the size dependency, and that is likely to be stronger than the strain dependency, unless the particles are very defective. The analysis of the broadening of the Bragg peak or of the rocking curve is not likely to reveal any interesting information on the strain content in the particles.

As a quick check, we plotted the rocking curve for several particles. The intensity at each position being obtained from the integrated intensity maps. From Fig. II.28, it is clear that the beam size is the main factor of the peak broadening since the FWHM of the peaks are relatively constant, independently of the particle size or geometry. It is also clear from Fig. II.26 and II.27 that the size distribution of the particles is relatively large. Even if the micro-strain is assumed to be similar for all particles, which is probably not true, the size component of the integral breadth would induce large variations in the FWHM of the peaks if the beam was larger than the particles. It should be noted that for very defective particles (particle 64 and 106) the particle is so defective that the broadening that can be attributed to the micro-strain becomes larger than the broadening associated to the beam size.

The micro-strain, i.e. the lattice distortions caused by the presence of lattice defects is thus not accessible with this experiment. Using the methodology described above, it is on the other hand possible to determine the strain in the direction of the scattering vector at each position of the scan. Here we used the specular 1 1 1 Au reflection and if q_x, q_y and q_z are the reciprocal space coordinates of the 3D Bragg peak calculated for each

position of the scan, it is clear that the displacements of the Bragg peak will be limited to the z direction.
The computation of the strain maps has unfortunately not been carried-out yet at the time of the writing of this manuscript, but will be achieved in a very near future.

II.4.3 Multi-characterization of a sample

Obtaining an ideal sample for the imaging of the strain field and defects by CDI is a delicate task that requires a great deal of preparation and characterization.
The selection of a sample of interest is done in several steps that can be summarized as follows:

- 1) Put macroscopic markers on the sample, (i.e. *visible* with a conventional optical microscope). A basic and simplistic way is to draw lines on the sample surface using tweezers. A more elegant and elaborated method is to pattern the metallic thin film, hence limiting the dewetting to specific regions of the sample that are easy to localize.
- 2) Pre-selection of samples of interest by imaging the regions of interests with SEM. For the gold particles, the best candidates are equiaxed Winterbottom which are close to the ECS.
- 3) Imaging of the samples of interest with AFM in order to measure their precise dimensions (in particular their height). Nucleation of a limited amount of defects in some of them by nano-indentation. For the particles, the indent needs to be done at the centre of the top facet, to maximize the chance of nucleating metastable defects in the particle. It is also interesting to induce difference states of deformations in the particles that range from the first bursts of plastic deformation (nucleation of first dislocations) to deeply indented. For the NW, the general strategy was to apply a gradient of increasing forces along the NW length.
- 4) If possible, characterization of the indented and pristine islands by Laue microdiffraction. This allows to check on the amount of defect nucleated in the indented particles. Very defective particles are not desired for CXD experiments since it won't be possible to reconstruct their displacement field. This is also important to check the amount of micro-strain in the pristine particles as they need to be as perfect as possible. We will see in Chapter VI that a relaxation of the micro-strain can occur in the particle upon indentation, by the well known phenomenon of mechanical annealing (Matthews & Blakeslee 1974)
- 5) Proper CXD experiment: imaging of the particles were a controlled Comparison with the displacement field obtained for pristine particles. If possible, *in situ* indentation of the particles during the indentation experiments.

In practice steps it was only possible to include the step (4) of the procedure only once in this work. The latter is yet very useful and prevent for unpleasant surprises for the CXD experiments, as for instance during the CRISTAL experiment described in II.4.1 where all the pre-indented NW turned out to be very defective and thus unusable for the reconstruction of the 3D displacement field by Bragg ptychography.
Fig. II.28 show a particle that went through all the steps of the preparation process : characterization by SEM and AFM, *ex situ* indentation, μ-Laue diffraction and acquisition of the 3D CXD pattern.
The particle which exhibits a defect visible in the SEM picture (Fig. II.29.a) was already shown in the μ-Laue subsection.
The SEM and AFM characterization allow to determine the precise dimensions of the particle: 920x800x600 nm^3 which is a typical size for the equiaxed Winterbottom particle (Fig. II.29.a & II.29.b).
To nucleate a limited amount of dislocations, a force as low as 4.2 μN was applied, resulting in an indentation depth of ~ 3 nm (Fig. II.29.c).
The Laue micro-diffraction pattern reveal a splitting of several Laue reflections which could originate from a low-angle grain boundary.
The complexity of the CXD pattern measured at the 2 2 2 Bragg reflection reveals that the defect structure is not trivial. The most interesting feature is the splitting of the Bragg peak in two spots of equal intensity (Fig. II.28.i).

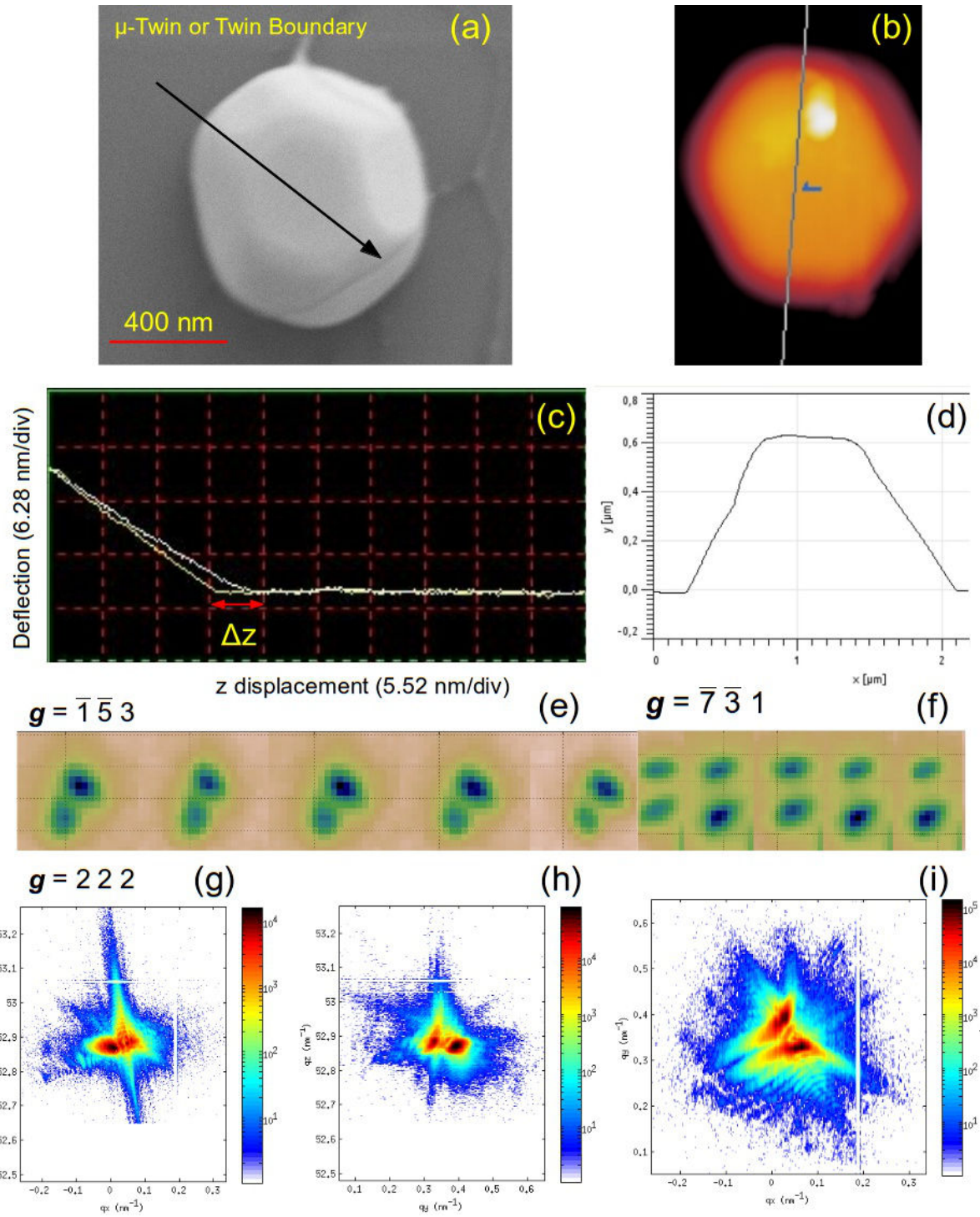

Fig. II.29: *Example of a multi-characterization of a gold particle.* (a) and (b) SEM and AFM pictures. (c) Force displacement curve recorded during the *ex situ* nanoindentation of the particle. (c) μ-Laue diffraction patterns for $\boldsymbol{g} = \bar{1}\ \bar{5}\ 3$ and $g = \bar{7}\ \bar{3}\ 1$. The five Laue spots for each reflection correspond to five positions on the island. (g-i) CXD pattern measured at the 2 2 2 Bragg reflection: (g) (q_y,q_z) slice through the Bragg peak (h) (q_x,q_z) slice (I) (q_x,q_y) slice.

This splitting could be induced by the micro-twin, however we will see in Chapter III that if a Stacking Fault or Twins can induce a splitting of the Bragg peak, the value of the phase jump does not lead to a splitting of the Bragg peak in two spots of equal intensity. Alternatively, the micro-twin could be invisible, and the splitting could be induced by a dislocation, nucleated upon indentation of the particle.
We did not manage to reconstruct the displacement field for this particle, and unfortunately, this question can not be answered with certainty.

Bibliography

Barabash, R., Ice, G.E & Walker, F. J. (2003) *J. Appl. Phys.* **93**(3), 1457-64

Baudoing-Savois, R., Renaud, G., De Santis, M., Saint-Lager, M.C., Dolle, P., Geaymond, O., Taunier, P.,

Bérar, J.-F. Blanquart, L., Boudet, N., Breugnon, P., Caillot, B., Clemens, J.-C. , Delpierre, I., Koudobine, P. Mouget, C., Potheau, R. & Valin, I. (2002) *J. Appl. Cryst* **35**(4), 471- 476.

Beutier, G., Verdier, M., Parry, G., Gilles, B., Labat, S., Richard, M. I., Cornelius, T., Lory, P. -F., Vu Hoang, S., Livet, F., Thomas, O. & De Boissieu, M. (2013a). *Thin Solid Films* **530**, 120-124.

Busing, W.R. & Levy, H.A. (1967) *Acta Cryst.* **22** , 457

Chahine, G.A., Richard, M.-I., Homs-Regojo, R.A., Tran-Caliste, T.N., Carbone, D., Jacques, V.L.R., Grifone, R., Boesecke, P., Katzer, J., Costina, I., Djazouli, H., Schroeder, T. & Schülli, T.U. (2014). *J. Appl. Cryst.* **47**, 762

Chang, H. J., Fivel, M., Rodney, D. & Verdier, M., (2010). *C. R. Physique* **11**, 285-292

Chrastina, D., Vanacore, G. M., Bollani, M., Boye, P., Schoder, S., Burghammer, M., Sordan, R., Isella, G., Zani, M. & Tagliaferri, A. (2012). *Nanotechnology* **23**, 155702.

Chung, J.S & Ice G.E. (1999). *J Appl Phys.* **86**(9), 5249–55.

Cornelius, T. W., Carbone, D., Jacques, V. L. R., Schülli, T. U., & Metzger, T. H. (2011). *J. Sync. Rad.* **18**, 413-417.

David, C., Nohammer, B., Ziegler, E. & Hignette, O. (2001). *Proc. SPIE* **4499**, 96–104.

Diaz, A., Chamard, V., Mocuta, C., Magalhães-Paniago, R., Stangl, J., Carbone, D., Metzger, T. H. & Bauer, G. (2010). *New J. Phys.* **12**, 035006.

Fabrizio, E. D., Romanato, F., Gentil, M., Cabrini, S., Kaulich, B., Susini, J. & Barett, R. (1999). *Nature* **401**, 895–898.

Fan Y, Nuryadi-Zanial, R., Burhanudin, A., Tabe, M., (2008). *J. Appl. Phys.* **47**, 1461–64

Faulkner, H. M. L. & Rodenburg & J. M. Movable (2004). *Phys. Rev. Lett.* **93**, 023903–1–4

Fewster, P. F. (1997). *Crit. Rev. Solid State* **22**, 69–110

Freund, L. B. & Suresh, S. (2003) *Thin Film Materials: Stress, Defect Formation and Surface Evolution,* edited by Cambridge University Press, Cambridge, England

Gaillard, Y., Tromas, C. & Woirgard, J. (2003) *Philos Mag Lett* **83**, 553

Gerberich, W.W., Venkataraman, S.K., Huang, H., Harvey, S.E. & Kohlstedt D.L. (1995) *Acta Metall. Mater* **43** , 1569

Godard, P., Carbone, G., Allain, M., Mastropietro, F., Chen, G., Capello, L., Diaz, A., Metzger, T.H. , Stangl, J. & Chamard, V. (2011). *Nature comm.* **2**, 568.

Godard, P., Allain, M. & Chamard, V. (2011) *Phys. Rev. B.* **84**, 144109.

Rodriguez, J.A. Goodman, D.W. (1991) *J. Phys. Chem.* **95**, 4196-4206

Gryaznov, V.G., Kaprelov, A.M & Romanov A.E. (1989) *Scripta Metall.* **23**, 1443-1448.

Herring. C. (1953) *Structure and Proper-ties of Solid Surfaces* edited by University of Chicago Press.

Hirth, J. & Lothe, J. (1968). *Theory of dislocations*, edited by McGraw-Hill, New York.

Holt, M. V., Hruszkewycz, S. O., Murray, C. E., Holt, J. R., Paskiewicz, D. M. & Fuoss, P. H. *Phys. Rev. Lett.* **112**, 165502

Hruszkewycz, S. O., Holt, M. V. , Murray, C. E., Bruley, J., Holt, J., Tripathi, A., Shpyrko, O. G., McNulty, I., Highland, M. J. & P. H. Fuoss (2012). Nano Lett. 12, 5148-5154.

Ice G. E. & Barabash, R. (2007). *Dislocations in Solids.* Edited by Elsevier, 500–601.

Ice G. E, Barabash R. & Pang (2005). *Encyclopedia of materials: science and technology updates.* Edited by Oxford: Elsevier

Jeantet, P., Roux, J.P., Barbier, A. Robach, O., Ulrich, O., Mougin, & Berard, A. G. (1999) *Nuclear Instruments and Methods in Physics Research B* **149**, 213-227.

Johnson, I., Bergamaschi, A., Billich, H., Cartier, S., Dinapoli, R., Greiffenberg, D., Guizar-Sicairos, M., Henrich, B., Jungmann, J., Mezza, D., Mozzanica, A., Schmitt, B., Shi, X. & Tintia, G. (2014) *J. Instrumentation* **9**.

Kirkpatrick, P. & Baez, V. (1948). *J. Opt. Soc. Am.* **38**, 766.

Lohmeier, M. & Vlieg, E. (1993) *J. Appl. Cryst.* **26**, 706

Maiden, A. & Rodenburg, J. M. (2009). *Ultramicroscopy* **109**, 1256–1262

Matthews, J.W. & Blakeslee, A. E. (1974) *J. Crystal Growth* **27**, 118.

McCarty, K. F., Hamilton, J. C., Sato, Y., Saa, A. & Stumpf., R (2009) *New J. Phys.* **11**, 043001.

Micha, J.S. & Robach, O. (2014) *LaueTools*

Meyer, G. & Amer, N. M. (1988). *Appl. Phys. Lett.* **53**, 2400

Meyerheim, H. L. De Santis, M. Moritz, W. & Robinson, I. K. (1998) Surf. Sci. **418**, 295

Michalske, T.A. & Houston J.E. (1998) *Acta Mater.* **46**, 391.

Mimura, H., Kimura, T., Yumoto, H., Daisuke, Y., Yokoyama, H., Inagaki K., Yamamura, K. Sano, Y.,Tamasaku, Yabashi, M., Ishikawa, T. & Yamauchi, K. (2010). *Nature Physics* **6**, 122- 125,

Minkevich, A. A., Baumbach, T., Gailhanou, M. & Thomas, O. (2008). *Phys. Rev. B* **78**, 174110

Mordehai, D., Lee, S. W., Backes, B., Srolovitz, D. J., Nix, W. D. & Rabkin, E. (2011). *Acta Mater.* **59**, 5202-5215.

Müller, P., Kern, R. (1998) *J. Cryst. Growth.* **193**, 257-270.

Nisbet, A.G.A., Beutier, G., Fabrizi, F., Moser, B. & Collins, S. P. (2015). *Acta Cryst.* **A71**, 20-25

Ponchut, C., Clément, J., Rigal, J-M., Papillon, E., Vallerga, J., LaMarra, D. & Mikulec, B. (2007). *Nuclear Instruments and Methods in Physics* **576**(1), 109-112.

Richter, G., Hillerich, K., Gianola, D., S., Mönig, R., Kraft, O. & Volkert C. A. (2009) *Nano Lett.* **9**(8), 3048-3052.

Sadan, H. & Kaplan, W. D. (2006). *J. Mater. Sci.* **41**, 5099-5107.

Scherrer, P. (1918). *Nachr. Ges. Wiss. Gottingen*, 98-100.

Schroer, C. G., Kurapova, O., Patommel, J., Boye, P., Feldkamp, J., Lengeler, B., Burghammer, M., Riekel, C., Vincze, L., van der Hart, A. & Kuchler, M. (2005). *Appl. Phys. Lett.* **87**, 124103.

Schroer, C.G., Boye, P., Feldkamp, J.M., Patommel, J., Schropp, A., Schwab, A., Stephan, S., Burghammer, M., Schoder, S. & Riekel, C.(2008) *Phys. Rev. Lett.* **101**, 090801.

Thibault, P., Dierolf, M., Bunk, O., Menzel, A. & Pfeiffer, F. (2009). *Ultramicroscopy* **109**, 338–343.

Thompson C. V. (2012). *Annu. Rev. Mater. Res*. 42, 399–434

Tromas, C., Girard, J.C. Audurier, V., Woirgard, J. J Mater Sci, (1999) **34**, 5337

Vila-Comamala, J., Gorelick, S., Farm, E., Kewish, C. M., Diaz, A., Barrett, R., Guzenko, V. A., Ritala, M. & David, C. (2011). Opt. Express **19**, 175–184.
Vlieg, E., Van der Veen, J. F., Gurman, S. J., Norris, C. & Macdonald, J. E. (1989) *Surf. Sci.* **210**, 301-321.

Vlieg, E. (1997) *J. Appl. Cryst.* **30**, 532-543

Williamson, G. K. & Hall, W. H. (1953). *Acta Metall.* **1**, 22-31.

Winterbottom, W. L. (1967). *Acta Metall.* **15**, 303.

Wulff. G. (1901). *2. Kristallow* **34**, 449

You, H., Axe, J., D., Kan, X. B., Moss, S. C., Liu, J. Z. & Lam, D. j. (1988) *Phys. Rev. B.* **37**(4), 2301.

Yun, W., Lai, B., Cal, Z., Maser, J., Legnini, D., Gluskin, E., Chen, Z., Krasnoperova, A. A., Vladimirski, Y.,

Cerrina, F., Fabrizio, E. D. & Gentili, M. (1999). *Rev. Sci. Instrum.* **70**, 2238–2241.

Zhe, R., Mastropietro, F., Davydok, A., Langlais, S., Richard, M.-I., Furter, J.-J., Thomas, O., Dupraz, M., Verdier, M., Beutier, G., Boesecke, P. & Cornelius, T. W. (2014). *J. Synchrotron Rad.* **21**, 1128-1133.

Chapter III : Signature of dislocations and stacking faults of *fcc* nanocrystals in coherent X-ray diffraction patterns: a numerical study

Contents

Abstract....90
III.1. Introduction....90
III.2. Tools and methods....92
III.3. Simulations on fcc nanocrystals....94
III.3.1. Screw dislocations....95
III.3.3. Stacking faults....100
III.3.4. Frank loops....104
III.3.5. Prismatic loops....106
III.3.6. Influence of the crystal size and shape....109
III.3.7. Influence of the defect position....111
III.4. Application to a complex case: indentation of a gold nanocrystal....112
III.5. Discussion....116
III.6. Conclusions....118
Bibliography....119

This Chapter is the article that was published in the June 2015 issue of Journal of Applied Crystallography: Dupraz, M. *et al.* (2015) *J. Appl. Cryst.* ***48****(3).*

It was slightly modified to be integrated into this manuscript

Chapter III: Signature of dislocations and stacking faults of *fcc* nanocrystals in coherent X-ray diffraction patterns: a numerical study

Maxime Dupraz[1,*], Guillaume Beutier[1], David Rodney[1,2], Dan Mordehai[3], Marc Verdier[1]

[1] *SIMaP, Univ. Grenoble Alpes & CNRS, F-38000 Grenoble, France*
[2] *Institut Lumière Matière, Université Lyon 1, CNRS, UMR 5306, F-69622 Villeurbanne, France*
[3] *Department of Materials Engineering, Technion—Israel Institute of Technology, 32000 Haifa, Israel*

Abstract

Crystal defects induce strong distortions in diffraction patterns. A single defect alone can yield strong and fine features that are observed in high-resolution diffraction experiments such as coherent X-ray diffraction. The case of face-centred cubic nanocrystals is studied numerically and the signatures of typical defects close to Bragg positions are identified. Crystals of a few tens of nanometres are modelled with realistic atomic potentials and 'relaxed' after introduction of well defined defects such as pure screw or edge dislocations, or Frank and prismatic loops. Diffraction patterns calculated in the kinematic approximation reveal various signatures of the defects depending on the Miller indices. They are strongly modified by the dissociation of the dislocations. We provide selection rules on the Miller indices to observe the maximum effect of given crystal defects, in the initial and relaxed configurations. The effect of several physical and geometrical parameters such as stacking fault energy, crystal shape and defect positions are discussed. The method is illustrated on a complex structure resulting from the simulated nanoindentation of a gold nanocrystal.

III.1. Introduction

The microstructure of materials plays a large role in their physical properties (Hull & Bacon 2001, Hirth & Lothe 1968). Even in a small crystallite, elastic strain and crystal defects are of primary importance, in particular in small scale structures: for instance, electron transport properties and superconductivity (Ying *et al.* 2013) are strongly affected by dislocations; the mechanical response of crystals is driven by dislocation motion, such that the presence of a few dislocations and their nature strongly impact mechanical properties of sub-micron crystals (Bei *et al*. 2008). Tailoring and monitoring the microstructure of materials is therefore of primary importance in order to guarantee the best performance of nanodevices.

A variety of experimental techniques are available for evidencing and identifying crystal defects. Among them, Transmission Electron Microscopy (TEM) is routinely used to produce various imaging contrasts of dislocations in real space by selecting pertinent diffraction vectors, according to well known invisibility criteria (Williams & Carter 1996). It has atomic resolution and thus can evidence individual crystal defects. However, the use of TEM is hindered by strong experimental constraints on the sample environment and thickness. These restrictions are relaxed for X-rays, which thus have a great potential for the study of defects in crystals.

Elastic diffuse scattering of X-rays (Krivoglaz 1969), neutrons (Moisy-Maurice & De Novion 1981) or electrons (Zhou *et al.* 2005) has been used since the 70's to study crystals containing defects with displacement fields. Near Bragg positions (Huang diffuse scattering), it provides valuable information on long range lattice distortions, far away from defects. Further away from Bragg peaks, Asymptotic Diffuse Scattering (also known as Stokes-Wilson scattering) can in some cases provide information on shorter range lattice distortions (Dederichs 1971). However, the signature of defect cores, so-called Laue scattering (Larson & Schmatz 1980) or structural Diffuse scattering (Ehrhart *et al.* 1982), whose extent is limited in the real space, is very diffuse in reciprocal space (Krivoglaz 1969, Fultz & Howe 2007) and orders of magnitude weaker than the Huang diffuse scattering. Despite this limitation, it has been used successfully on a large number of systems. In the early 70's

X-ray scattering from single and clusters of point defects has been investigated theoretically (Dederichs 1973, Trinkaus 1972). Few years later, Huang Diffuse Scattering from dislocation loops has been considered, both experimentally (Larson & Schmatz 1980, Larson & Young 1987) or numerically (Ehrhart *et al.* 1982). More recently, the calculated and measured X-Ray diffuse scattering from threading dislocations in epitaxial GaN layers provided a precise estimation of the dislocation density and their relative proportion (edge or screw type) in good agreement with already existing destructive methods (Barchuk *et al.* 2010). Since neutrons and X-rays probe large volumes of materials containing many defects of various types, the interpretation of diffuse scattering usually assumes a model for the dominant defects and a rather large density of them. In the case of dislocation loops or stacking faults, diffuse scattering has to be averaged over all possible loop orientations. Interpreting correctly the shape and symmetry of the elastic diffuse scattering requires the use of single crystals and careful averaging procedures. The smaller probe size (~50 nm) achievable with electron beams has allowed the measurement of electron diffuse scattering from single defects and individual dislocation loops (Kirk *et al.* 2005, Kirk *et al.* 2006). Similar studies with X-rays are now being developed thanks to the progress of X-ray focusing optics.

In the past decade, the availability of intense coherent X-ray beams from third generation synchrotron facilities has allowed the emergence of a very attractive technique to probe the microstructure of crystals: Coherent X-ray Diffraction (CXD) (Livet 2007, Sutton 2008). In Bragg geometry, it probes the deviation from the perfect crystal lattice and has been successfully used to characterize elastic strain in isolated crystals (Beutier *et al.* 2012) or to evidence the presence of crystal defects such as stacking faults (Chamard *et al.* 2008, Favre-Nicolin *et al.* 2010) and dislocation loops (Jacques *et al*. 2011). Recently, the same principles have been applied to electrons, and first measurements of coherent electron diffraction have been reported (Huang *et al.* 2008).

Following Sayre's principle (Sayre 1952), CXD has been turned into an imaging technique known as Coherent Diffraction Imaging (CDI) (Miao *et al.* 1999): by oversampling the diffraction pattern and with the help of iterative phase retrieval algorithms, the scattering function which encodes the crystal density and, in the Bragg case, a projection of the displacement field (Robinson & Harder 2009, Pfeifer *et al.* 2006), can be recovered. In the latter case, the tridimensional (3D) measurement of the reciprocal space in the vicinity of a Bragg reflection yields a 3D image of the strained crystal (Pfeifer *et al.* 2006) with a typical resolution of a few nanometers and a strain sensitivity better than 10^{-3} (Newton *et al.* 2010). Several Bragg reflections can be combined to recover all the components of the displacement field (Newton *et al.* 2010). While this method of characterization is now well established for weakly strained systems, its application to highly strained systems has so far been successful only for a limited number of cases due to the strong inhomogeneity of the phase to be recovered (Minkevich *et al.* 2008, Diaz *et al.* 2010, Vaxelaire *et al.* 2010). In its original version, CDI was restricted to finite objects, because phase retrieval algorithms need a real-space constraint (such as a finite support constraint) in order to converge. In recent years, this limitation has been lifted by the introduction of ptychography, a scanning version of CDI: with scanning steps smaller than the beam size, sufficient redundancy is obtained in the data to allow the reconstruction of extended objects with the help of dedicated algorithms (Rodenburg & Faulkner 2004). In Bragg conditions it has been used to reconstruct the strain field of extended objects (Hruszkewycz *et al.* 2012, Godard *et al.* 2011) and to reconstruct a single dislocation and its associated strain field (Takahashi *et al.* 2013), however the case of multiple defects is still out of reach.

CDI and ptychography often fail to provide quickly a real space reconstruction, while a rapid evaluation of data might be needed during experiments. This is particularly true in the case of Bragg ptychography which requires a considerable amount of data. Moreover, for both CDI and ptychography the definition of a good input for the initialization of the inversion cycles is of primary importance. There is thus an interest in understanding qualitatively diffraction patterns and interpreting them directly in the reciprocal space. In particular, during *in situ* mechanical loading of a sample (Beutier *et al.* 2013, Zhe *et al.* 2014), one would like to witness the first plastic events by measuring a CXD pattern and interpreting it on the fly. Here we use this direct approach, which consists in first modelling the object in the real space and second computing the corresponding reciprocal space pattern and try to identify characteristic signatures of defects that can be observed in experimental CXD data. While obtaining the displacement field of the sample in the real space provides a more comprehensive picture,

all the information is present in the reciprocal space and it should in principle be possible to extract valuable information on the defect nature within the sample, without the difficulty of reverting to the real space.
So far only few studies were carried out on individual defects with CXD: misfit dislocations in an epitaxial SiGe thin film (Robinson *et al.* 2005), Frank dislocation loops in silicon (Jacques *et al*. 2011), a single dislocation in silicon (Takahashi *et al.* 2013), stacking faults in semiconductor nanowires (Chamard *et al.* 2008, Favre-Nicolin *et al.* 2010) and dislocations in charge and spin density waves (Le Bolloc'h *et al.* 2005, Jacques *et al.* 2009). In the present paper, focused on common face-centred cubic (*fcc*) metals, we demonstrate that CXD can be used to identify single defects directly from their signature in the diffraction pattern, provided the Bragg reflection is well chosen. Similarly to TEM (Williams & Carter 1996), we establish that the careful choice of diffraction conditions is essential when it comes to highlight specific defects.
We consider first the cases of single defects: a single defect can induce strong modifications of the diffraction pattern and therefore a good understanding of these elementary cases is necessary before investigating crystals with multiple defects. There is a large variety of crystal defects. We focus here on the most common ones for *fcc* crystals. After introducing the tools and methods used for this study in section III.2, we start with the screw and edge dislocations (subsections III.3.1 and III.3.2 respectively), then the stacking fault (subsection III.3.3), and finally the Frank and prismatic dislocation loops (subsections III.3.4 and III.3.5 respectively), crystalline defects commonly introduced in metals by irradiation (Stoller *et al.* 1992), rapid thermal treatments (quench) or mechanical loading (indentation). In subsection III.3.6 we investigate the effect of the size and shape of the crystal, and in subsection III.3.7 we discuss the effect of the position of the defect in the crystal. Finally, we apply our methodology in section III.4 to the analysis of a more complex structure resulting from the simulated nanoindentation of a gold nanocrystal .

III.2. Tools and methods

A common method to analyse CXD measurements is to model the diffracting object with a Finite Element Method (FEM) and to calculate the CXD pattern by Fourier transforming a modified electronic density (Diaz *et al.* 2010, Beutier *et al.* 2013a). FEM uses a continuous description of matter and thus has the advantage to allow modelling large crystals. However, this continuous description is not able to deal with plasticity, despite a possible correction of the elastic strain by taking into account the plastic relaxation (Proudhin *et al.* 2010). It is therefore not well suited to the study of faulted crystals. Alternatively, analytical models have been used to explain the effect of 'perfect' crystal defects in CXD patterns. While such simple model gives a reasonable description of defects in electronic crystals (Le Bolloc'h *et al.* 2005, Jacques *et al.* 2009), it does not take into account the dissociation of dislocations into partials, which can have a strong effect on the CXD patterns. In this study we use an atomistic description of matter, in order to accurately model crystal defects. This comes at the price of the size of the studied objects, but progresses of atomic-scale modelling and of x-ray focusing optics has allowed a convergence of the scales of individual objects that these techniques can study (Schroer *et al.* 2008). With an electron beam it is possible to deal with even smaller scales, and using coherent electron diffraction beams Huang *et al.* were able to extract valuable information on the surface relaxation of gold nanocrystals with less than 5 nm in diameter (Huang *et al.* 2008). Here we deal with crystals of typical size of the order of a few tens of nanometres.
Molecular statics is used to simulate nanocrystals of common *fcc* transition metals (aluminium, copper, silver, gold and nickel) modelled with embedded atom method (EAM) potentials (Mishin *et al.* 1999, Mishin *et al.* 2001, Williams *et al.* 2006, Grochola *et al.* 2005) that reproduce accurately elastic properties as well as surface and stacking fault energies. The geometry considered here consists in a free-standing equilibrium-shaped crystallite, which minimizes the surface energy through a Wulff construction (Winterbottom 1967) (see Fig. III.1.a). Due to the low surface energy of its {1 1 1} and {1 0 0} facets, this geometry exhibits a remarkable stability and is commonly observed experimentally (Mordehai *et al.* 2011a, Sadan & Kaplan 2006). Since we want to highlight the effect of defects we do not consider here the case of pre-strained particles, for instance

when a crystallite is in epitaxial relationship with a substrate. The reference crystallite considered throughout this study contains 10^6 atoms and measures approximately 30x30x30 nm^3. The defects are introduced with defined characters: edge or screw dislocations, Frank and prismatic dislocation loops and stacking faults. The system is relaxed by energy minimization at 0 K . The large difference between the Stacking Fault Energies (SFE) of the selected materials, is expected to strongly influence the characteristics of the crystalline defects (Rodney *et al.* 2005, Groves & Kelly 1963, Smallman & Green 1964). Understanding the influence of this parameter on relaxation and its corresponding effect on diffraction patterns is one of the goals of the present study. We also focus on the ability of CXD to determine the parameters which define a dislocation, its Burgers vector, line direction and slip and dissociation planes. The 3D CXD patterns are calculated by summing the amplitudes scattered by each atom with its phase factor, following a kinematic approximation:

$$I(\boldsymbol{q}) = \left|\sum_j \exp(2i\pi \boldsymbol{q}.\boldsymbol{r}_j)\right|^2 \quad \text{(III.1)}$$

where $\boldsymbol{q}$ is the scattering vector and $\boldsymbol{r}_j$ the position of atom j. Here we discarded the atomic scattering factor as we are dealing with mono-element materials. The kinematic approximation is justified by the relatively small size of the crystals studied here and the large perturbation of the perfect lattice caused by the defects in such small volumes. Eq. (III.1) assumes a plane wave illumination, which is a reasonable approximation for most experimental conditions on such small objects at synchrotron radiation facilities, even with microfocusing optics (Mastropietro *et al.* 2011). Eq. (III.1) also assumes fully coherent scattering. Absorption and refraction effects are not considered in this study.

For objects of size L and lattice parameter a, the reciprocal space must be probed with a step no larger than $a/2L$ in reciprocal lattice unit (r.l.u.) in order to resolve the smallest possible features in the reciprocal space. In the case of 30 nm crystals of common *fcc* transition metals, $a/2L \sim 0.02$ r.l.u. (0.006 $Å^{-1}$ in the case of a 30nm copper nanocrystal), but we typically sample the diffraction pattern with a step size of 0.0015 r.l.u. (0.00045 $Å^{-1}$) to obtain smoother representations. Given the large number of atoms ($\sim 10^6$) and the similarly large number of points in reciprocal space for which the calculation is performed (typically 100x100x100=10^6 for each pattern), the computation is performed with a graphical processing unit (GPU), which allows massive parallelism. Current GPUs which include up to 2500 cores are particularly efficient for computing large diffraction maps. Eq. (III.1) was computed with the PyNX code (Favre-Nicolin *et al.* 2011) on a NVidia GTX 580 GPU which achieves a speed of calculation of up to $4*10^{10}$ *atoms.reflections.*s^{-1}. This is almost 3 orders of magnitude higher than with a single core central processing unit (CPU). For our usual calculations (sum in Eq. (III.1) for 10^6 atoms and 10^6 points in reciprocal space), the calculation of the 3D CXD pattern around a Bragg position takes about 25-30 seconds. Such calculations can easily be performed during experiments to help data evaluation.

In the present study, all the calculations are carried out in the vicinity of Bragg positions $\boldsymbol{g}$ defined by their Miller indices *hkl*. $\boldsymbol{g}$ is a particular case of the generic scattering vector $\boldsymbol{q}$, and in the following it will be referred as the diffraction vector. The effect of dislocations on CXD patterns arises from their corresponding atomic displacement field $\boldsymbol{u}(\boldsymbol{r})$ with respect to the lattice of the perfect crystal. A commonly reported method in electron microscopy is to use a diffraction vector parallel to the dislocation line (Williams & Carter 1996). The invisibility condition $\boldsymbol{g}.\boldsymbol{b} = 0$ (Williams & Carter 1996, Head *et al.* 1967, Steeds 1966), where $\boldsymbol{b}$ is the Burgers vector of the dislocation, is also extensively employed in this study, in particular to evidence the effect of dissociation. According to Eq. (III.1), it is clear that crystal defects distort the diffraction pattern when they produce a displacement field, which is not perpendicular to the diffraction vector $\boldsymbol{g}$, and conversely one can expect a maximal effect when the main direction of the displacement field is parallel to $\boldsymbol{g}$. However in most cases, the detailed distortion cannot be predicted easily: already in infinite or semi-infinite isotropic materials the displacement field can have a complex analytical form, and the situation is further complicated by the relaxation of the system, which is affected by the interatomic potentials and the tension free mechanical equilibrium conditions at the free surfaces. All these considerations explain the need to rely on an atomistic description with reliable inter-atomic potentials for a more complete and accurate description of the problem.

III.3. Simulations on *fcc* nanocrystals

Fig. III.1 illustrates a 30x30x30nm^3 perfect (strain and defect-free) copper nanocrystal in Wulff geometry after relaxation (Fig. 1.a) and the corresponding 3D intensity map of its reciprocal space calculated according to Eq. (III.1) (Fig. III.1.b). In the following it will be referred as the reference nanocrystal.
It is important to notice that the assumption of a strain free and defect free object for the reference nanocrystal is only valid in the initial state, *i.e.* before the nanocrystal has been relaxed by energy minimization. Upon relaxation a contraction of the surface atoms towards the bulk can be observed (Huang *et al.* 2008). As illustrated on Fig. III.1.a the motion of the surface atoms is strongly correlated to their coordination number explaining why such high displacement is observed for corner and edges atoms. Additionally, since the {1 0 0} surface atoms are less coordinated than the {1 1 1} surface atoms, the {1 0 0} facets tend to contract more towards the bulk than the {1 1 1} facets. Coherent X-ray diffraction is very sensitive to the atomic structure of the nanocrystal surfaces and characteristic features due to the contraction of nanocrystals facets during relaxation can be observed on the calculated CXD patterns. They also depend on the *hkl* indices of the Bragg reflection. However, we will see in the next section that the introduction of a single defect within the crystallite produces an even stronger signature on CXD patterns. As a result in the case of the defective nanocrystals, even if the contraction of surface atoms still have some effects on the calculated diffraction patterns, it can be assumed negligible in comparison to the features associated to the defect and its corresponding displacement field. Since we deal only with defective nanocrystals in the next sections, the effect of the displacement of surface atoms and the corresponding surface strain is not further addressed in this work.
If we were dealing with a perfect crystal, the CXD patterns around all allowed Bragg reflections would be -

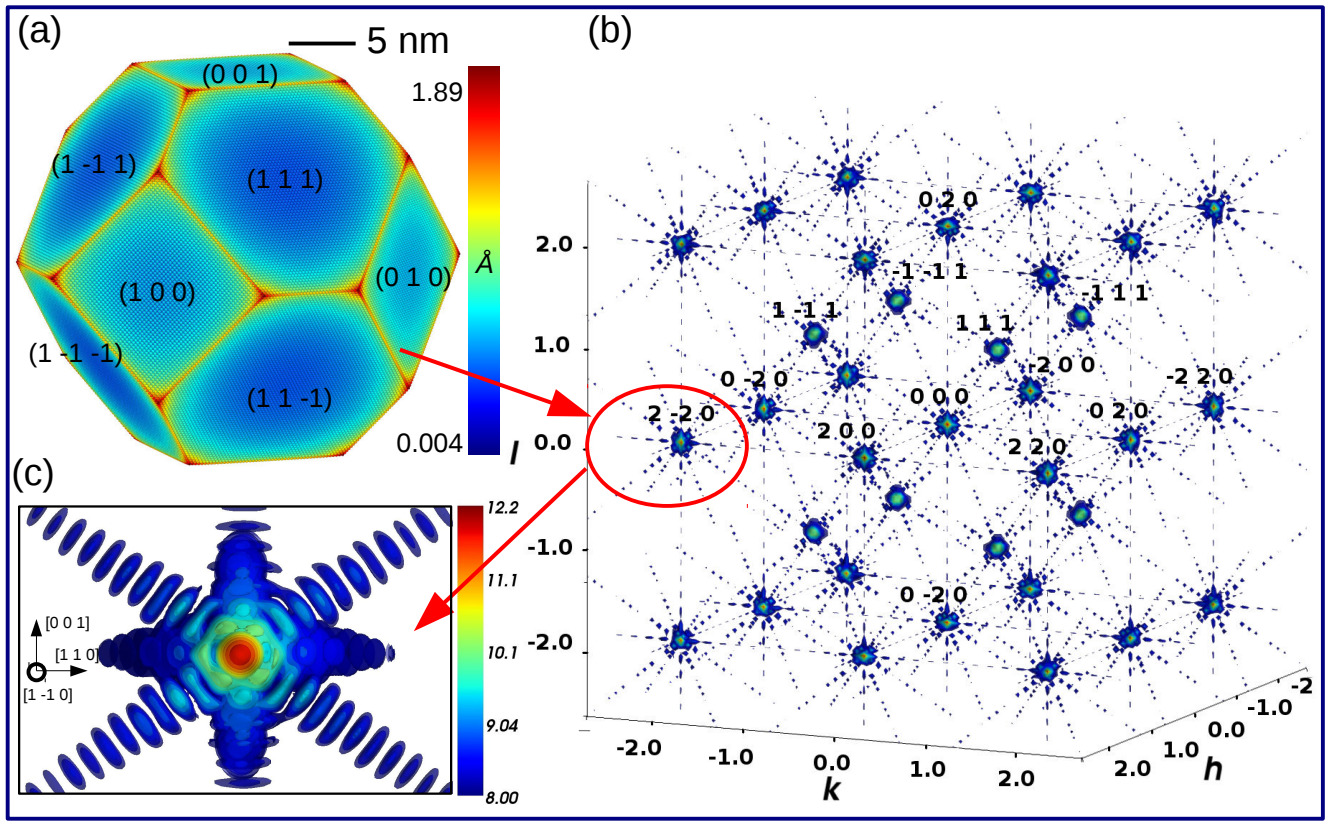

Fig. III.1 (a) Defect free gold nanocrystal of Wulff geometry and size 30x30x30nm^3. The colour scale encodes the magnitude of displacements of the surface atoms after relaxation. (b) 3D intensity map of the corresponding reciprocal space. (c) Zoom on the Bragg reflection $\mathbf{g} = 2\,\bar{2}\,0$. *The area of the reciprocal space is kept to the same value in all figures and is equal to 0.045x0.0675 (1/ Å)^2*

- identical to the CXD pattern at the origin of the reciprocal lattice. Here the surface relaxation is weak enough so that the CXD patterns still display essentially the same features, which can be observed for instance around $\boldsymbol{g} = 2\ \bar{2}\ 0$ (Fig. III.1.c): intensity is maximal at the Bragg position; the diffraction pattern forms streaks along the {1 1 1} and {1 0 0} directions due to the crystal facets, and these streaks are fringed because of the finite size of the crystal. We call $I_0 = N^2$, where N is the number of atoms in the nanocrystal, the intensity scattered at the exact Bragg position by the perfect crystal. In the following we will use this reference intensity to quantify the effect of crystal defects. For the reference nanocrystal all the calculations around a given Bragg reflection are performed in a reciprocal space volume of 0.045x0.045x0.0675 (1/ Å)^3. Since all the calculations presented in section III.3 are performed on crystals whose size and number of atoms are similar to the reference crystal, the investigated area of the reciprocal space in this section is always the same and equal to 0.045x0.0675 (1/ Å)^2 (area within the black rectangle surrounding a CXD pattern (such as Fig. III.1.c)). Consequently, in order to simplify the figures, axis are not shown on reciprocal space figures. Additionally, the dynamical range of intensities is limited to 4.2 decades which is typical for a CXD experiment. Similarly, the intensity dynamical range is kept to the same value all along section 3.

III.3.1. Screw dislocations

For a screw dislocation, the displacement field $\boldsymbol{u}(\boldsymbol{r})$ is parallel to the dislocation line and the Burgers vector $\boldsymbol{b}$, such that $\boldsymbol{u}$ is proportional to $\boldsymbol{b}$ and $\boldsymbol{g}.\boldsymbol{b} = 0$ is an invisibility condition for a perfect screw dislocation. However, this condition is not strictly fulfilled in the vicinity of $\boldsymbol{g}$ ($\boldsymbol{q} \neq \boldsymbol{g}$), such that a weak distortion of the Bragg spot cannot be excluded. This distortion could lead to strong diffuse scattering in the case of many defects measured with an incoherent x-ray beam.

The screw dislocation simulated here has a Burgers vector $\boldsymbol{b} = ½\ [1\ \bar{1}\ 0]$. It is introduced at the centre of the nanocrystal with its associated displacement field in an infinite isotropic medium: $u_x = u // \boldsymbol{b} = b\theta/2\pi$. The initial configuration is relaxed by quenched molecular dynamics simulations to get the relaxed positions and the corresponding atomic displacement field. Fig. III.2.a and III.2.c show the u_x component of the atomic displacement field, *i.e.* parallel to the Burgers vector and line direction, for both the initial and the relaxed configuration: it is exactly equal to $\pm\ b/2$ in the initial configuration, while it increases during the relaxation process partly due to the dissociation into partial dislocations but also to the contraction of surface atoms described in the previous section. On Fig. III2.b and III.2.d, atoms are color-coded according to their coordination number and only the defective, corner and edge atoms are shown. The dislocation dissociates in both {1 1 1} planes that contain the Burgers vector, *i.e.* the (1 1 1) and (1 1 $\bar{1}$) planes and thus adopts a non-planar configuration (Fig III.2.d). At the end of the relaxation process two sets of two partial Shockley dislocations (Hull & Bacon 2001) are stabilized within the nanocrystal with respective Burgers vector of 1/6[$\bar{2}$ 1 1] and 1/6[$\bar{1}$ 2 $\bar{1}$] in the (1 1 1) plane and 1/6[2 $\bar{1}$ 1] and 1/6[1 $\bar{2}$ $\bar{1}$] in the (1 1 $\bar{1}$) plane. This crossed configuration is more energetically favourable than the configuration with coplanar stacking faults because of the negative energy of the intersecting node (Rasmussen *et al.* 1997). The u_x component of the atomic displacement field is exactly equal to $b/4$ within the (1 1 1) stacking fault ribbon. The contraction of the surface atoms towards the bulk, which is particularly high for corner and edge atoms due to their low coordination number, is similar to the case of the defect-free crystal.

The invisibility criterion $\boldsymbol{g}.\boldsymbol{b} = 0$ is selected to evidence the effect of dissociation. With such a diffraction condition, when the dislocation is not-dissociated (Fig. III.2.e), the Bragg peak is undistorted compared to that of a perfect crystal. This is not the case for the dissociated dislocation, which yields a splitting of the Bragg peak along $\boldsymbol{b}$ (Fig. III.2.f). For low h, k, l values (typically for $h+k+l < 4$) no splitting can be evidenced but the elongation of the Bragg peak along $\boldsymbol{b}$ is clearly visible. This demonstrates that dissociation can be unambiguously evidenced using CXD. For this particular diffraction vector, interferences between the faulted planes and the facets also induce strong distortions in the fringes along the [1 1 1] and [1 1 $\bar{1}$] directions. It is well known that stacking faults create - streaks along the normal of their plane, but here it is modulated by the -

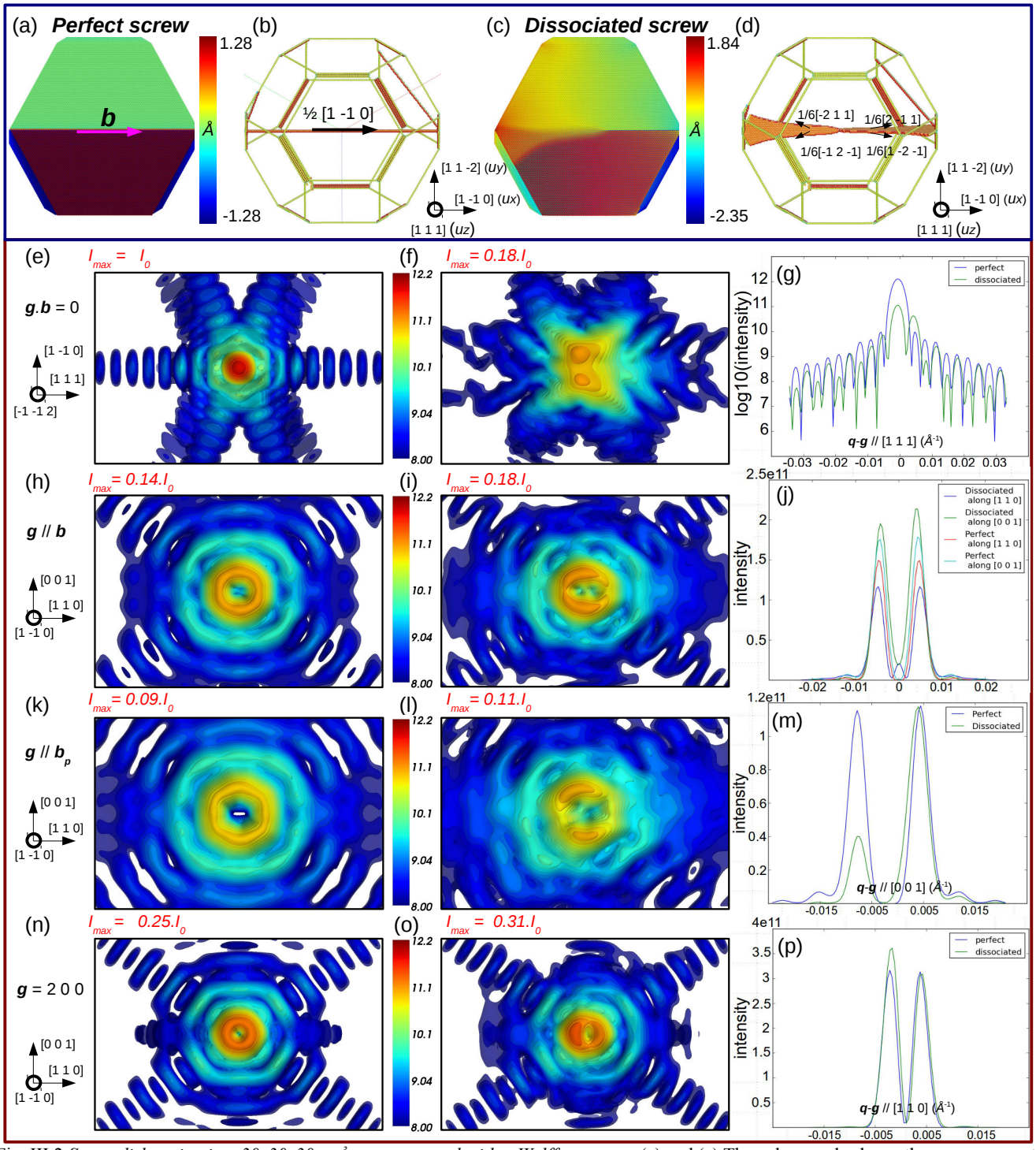

Fig. III.2 *Screw dislocation in a 30x30x30 nm³ copper crystal with a Wulff geometry.* (a) and (c) The colour scale shows the u_x component of the atomic displacement field for both initial and relaxed configurations. (b) and (d) Perfect screw dislocation with $\boldsymbol{b} = 1/2[1\ \bar{1}\ 0]$. and dissociation of the perfect dislocation in 2 sets of Shockley partials in the (1 1 1) and (1 1 $\bar{1}$) planes Only the defective, edge and corner atoms are shown. Calculated CXD patterns with $\boldsymbol{g}.\boldsymbol{b} = 0$ ($\boldsymbol{g} = 2\ 2\ \bar{4}$) for a perfect (e) and dissociated dislocations (f). (g) Intensity along [1 1 1] (log scale). Calculated CXD patterns with $\boldsymbol{g}$ // $\boldsymbol{b}$ ($\boldsymbol{g} = 2\ \bar{2}\ 0$) for a perfect (h) and dissociated dislocations (i). (j) Intensity along [0 0 1]. Perfect (k) dissociated (l) and intensity along [0 0 1] (m) with $\boldsymbol{g}$ // $\boldsymbol{b}_p$ ($\boldsymbol{g} = 2\ \bar{4}\ 2$)**.** Perfect (n), dissociated (o) and intensity (p) along [1 1 0] for general $\boldsymbol{g}$ ($\boldsymbol{g} = 2\ 0\ 0$) . *The area of the reciprocal space is kept to the same value in all figures and is equal to 0.045x0.0675 (1/ Å)²*

- form factor of the crystal. A closer look at the intensity profile along the [1 1 1] direction (Fig. III.2.g) reveals that the fringes intensity decrease steadily as we move away from the Bragg position in the case of a perfect dislocation while the intensity profile is more erratic in the case of a dissociated dislocation with a drop of intensity every two fringes. The doubling of the fringes periodicity can be explained by the position of the stacking fault at the centre of the crystallite, which implies that the distance between two (1 1 1) facets is twice the distance between a (1 1 1) facet and the (1 1 1) faulted plane. As the extent in the reciprocal space is inversely proportional to the one in the real space, the period of the fringes produced by the stacking fault fringes is therefore twice the period of the fringes induced by the crystal facets.

The case $\boldsymbol{g}$ // $\boldsymbol{b}$ shown in Fig. III.2.h and III.2.i for a perfect and a dissociated dislocations exhibits a very characteristic signature on the CXD pattern: at the Bragg position, the intensity vanishes (completely for the perfect dislocation, almost completely for the dissociated dislocation). Instead we observe a ring-shape distribution of intensity around the Bragg position. For a perfect screw dislocation at the centre of an isotropic material, the symmetry would impose an uniaxial distribution of intensity with axis parallel to the dislocation line. Here the anisotropy of the elasticity tensor slightly distorts the perfect ring (Fig. III.2.h). The ring size is strongly dependent on the Miller indexes of the reflection and on the crystal size. For $\mathbf{g} = 2\ \bar{2}\ 0$ and a 30x30x30 nm^3 crystallite, the ring diameter is d = 0.01 $Å^{-1}$. Micro or nanocrystals observed experimentally are often one order of magnitude larger (Beutier *et al.* 2013a, Mordehai *et al.* 2011a), resulting in a ring diameter 10 times smaller in the reciprocal space. Our ability to resolve such features experimentally will be discussed in the last section. For a dissociated dislocation (Fig. III.2.i.), a ring shaped pattern is still obtained but the distribution of intensity in the ring is more contrasted and the intensity at the centre does not completely vanish anymore (it is in fact not strictly zero in the case of the perfect dislocation, but it increases by a factor of 25 when the dislocation dissociates). Due to the dissociation in partials, the strain around the dislocations is inhomogeneous but one can assume that this inhomogeneity does not produce a sufficient effect to affect the shape of the CXD pattern. However the effect of dissociation can clearly be seen in the distribution of intensity on the CXD pattern. A tetragonal distribution, typical of the $1\bar{1}0$ zone axis, is observed in both cases, but in the case of the perfect dislocation it looks almost hexagonal, reflecting the crystal shape projected along the dislocation axis, since the latter induces no strong asymmetry. In the dissociated case, the symmetry of the defect structure induces a significant change of distribution and its anisotropy dominates the symmetry of the crystal shape. For the latter, the maxima of intensity are along the [0 0 1] which is a good indication of the anisotropy of the strain along the [0 0 1] and [1 1 0] axes. The intensity profile along [0 0 1] (Fig. III.2.j) reveals an increase of the maxima of intensity of about 20%, while the intensity of the maxima along [1 1 0] decreases by 25%.

When $\boldsymbol{g}$ is parallel to a partial Burgers vector $\boldsymbol{b}_\mathbf{p}$ (Fig. III.2.k & III.2.l) the resulting diffraction pattern for a perfect dislocation is very similar to the case $\boldsymbol{g}$ // $\boldsymbol{b}$, with a ring shaped pattern oriented along $\boldsymbol{b}$. After dissociation, a ring shaped pattern is still observed, but now oriented along the partial Burgers vector $\boldsymbol{b}_\mathbf{p}$. For these particular diffraction conditions, we can infer that the Shockley partial is seen as a single perfect dislocation with a signature independent of the other partial and of the stacking fault.

Finally, for a general $\boldsymbol{g}$ (Figs. III.2.n & III.2.o), a perfect screw dislocation still produces a ring shaped diffraction pattern with an axis along $\boldsymbol{b}$. A relaxed system yields a distorted and disoriented ring-shaped pattern. Under such diffraction conditions, all 4 Shockley partials contribute to the diffraction pattern but unlike the particular cases detailed above, the ring axis is dependent on $\boldsymbol{g}$ but not directed along any particular direction.

The screw dislocation is therefore a relatively simple case to understand. For a perfect dislocation, only two cases are possible. When the extinction condition $\boldsymbol{g}.\boldsymbol{b} = 0$ is fulfilled, the dislocation remains invisible and the resulting pattern is similar to that of a perfect crystal. For any other diffraction vector, the characteristic signature of a perfect dislocation is a ring shaped pattern oriented along $\boldsymbol{b}$. Analysis of CXD patterns produced by a dissociated dislocation is not as straightforward, but it appears very clearly that the diffraction conditions where $\boldsymbol{g}$ is *perpendicular* to $\boldsymbol{b}$ or *parallel* to a potential $\boldsymbol{b}_\mathbf{p}$ are best suited to evidence the effect of dissociation. For diffraction vectors yielding a ring-shaped pattern, the anisotropic distribution of intensity and the increase of the maximum of intensity (by approximately 20%) and of the intensity in Bragg position are also good indicators of a dissociation.

III.3.2. Edge dislocations

Now we introduce an edge dislocation at the centre of the reference crystal. The Burgers vector is $\boldsymbol{b} = ½ [1\ \bar{1}\ 0]$ which is by definition perpendicular to the dislocation line direction $\boldsymbol{t} = [1\ 1\ \bar{2}]$. Similarly to a perfect screw dislocation, an edge dislocation dissociates during relaxation in two Shockley partials, but the dissociation is now planar and constrained to the (1 1 1) slip plane of the dislocation (Fig. III.3.c and III.3.d).
The analysis of the CXD pattern is less straightforward in this case than for a screw dislocation because of the strain component normal to the slip plane. We use Cartesian coordinates x, y, z so that the z-axis is along the dislocation line $\boldsymbol{t}$ and the x-axis is along the Burgers vector $\boldsymbol{b}$ (y-axis is along a third direction $\boldsymbol{b}\times\boldsymbol{t}$). In the approximation of an isotropic and infinite material, the symmetry of the problem constrains the displacement field in the x-y plane and it is independent of z. Furthermore, an analytical expression can be derived (Hull & Bacon 2001, Hirth & Lothe 1968):

$$u_x = u\|b = \frac{b}{2\pi}\left[\tan^{-1}\frac{y}{x} + \frac{1}{2(1-\nu)}\frac{xy}{(x^2+y^2)}\right] \quad \text{(III.2)}$$

$$u_y = u\|(b\times t) = \frac{b}{8\pi(1-\nu)}\left[(1-2\nu)\ln(x^2+y^2) + \frac{(x^2-y^2)}{(x^2+y^2)}\right] \quad \text{(III.3)}$$

where ν is the Poisson Ratio.This analytical displacement field is injected in the perfect nanocrystal as the initial state of the edge dislocation before relaxation.The u_x component of the atomic displacement field is shown in Fig. III.3.a and III.3.c for the initial and relaxed configurations respectively. Similarly to the case of the screw dislocation, it is equal to $\pm\ b/2$ for a perfect edge dislocation. Upon relaxation it slightly increases due to the dissociation into partials and to the contraction of surface atoms. For atoms within the (111) stacking fault ribbon $u_X = b/4$. From Eq. (III.2) and Eq. (III.3), one can easily understand that complete invisibility of an edge dislocation may only be achieved when $\boldsymbol{g}.\boldsymbol{b} = 0$ and $\boldsymbol{g}.(\boldsymbol{b}\times\boldsymbol{t}) = 0$, satisfied only if $\boldsymbol{g}$ is parallel to the dislocation line. As illustrated in Fig. III.3.e, when the diffraction vector fulfils this invisibility condition, the dislocation remains indeed invisible and the resulting CXD pattern is similar to that of a perfect crystal. As revealed by the intensity profile along the [1 1 1] direction, dissociation of the dislocation (Fig. III.3.g) results in the appearance of intense fringes along [1 1 1] with twice the period of the crystal finite-size fringes. As shown in the previous section, this is a clear evidence of the presence of a stacking fault in the (1 1 1) plane located at the centre of the crystallite. In the vicinity of $\boldsymbol{g} = 2\ 2\ \bar{4}$, the invisibility condition is not strictly fulfilled resulting in a large decrease of the maximum intensity of the central spot (around 35%, Fig III.3.f). However, in such diffraction conditions, only displacements parallel to the dislocation line can be detected. They are not strictly equal to zero when the dislocation is relaxed but they remain very limited and the effect produced by the dissociation on the calculated CXD pattern remains relatively weak. The conditions $\boldsymbol{g}.\boldsymbol{b} = 0$ with $\boldsymbol{g}$ not parallel to $\boldsymbol{t}$ are more suited to evidence the effect of the dissociation. In this configuration (Fig. III.3.h), a perfect dislocation yields a CXD pattern elongated along $\boldsymbol{b}$ with a strong decrease of intensity of the Bragg spot (40% of the perfect crystal) consistent with the fact that this diffraction condition is sensitive to the displacements in the planes perpendicular to the dislocation line (Hull & Bacon 2001, Williams & Carter 1996). The CXD pattern obtained for the dissociated dislocation (Fig. III.3.i & III.3.j) is very similar to that of a dissociated screw dislocation, with a split of the Bragg peak along $\boldsymbol{b}$ and fringes along the [1 1 1] direction associated to the (1 1 1) stacking fault (Fig. III.3.j). Similarly to the screw dislocation, the split of the Bragg peak is not visible for low h, k, l values ($h+k+l < 4$) which only induce an elongation along $\boldsymbol{b}$. The correlation between the intensity and spacing of Bragg spots and the crystal SFE is addressed in more details in subsection III.3.3.

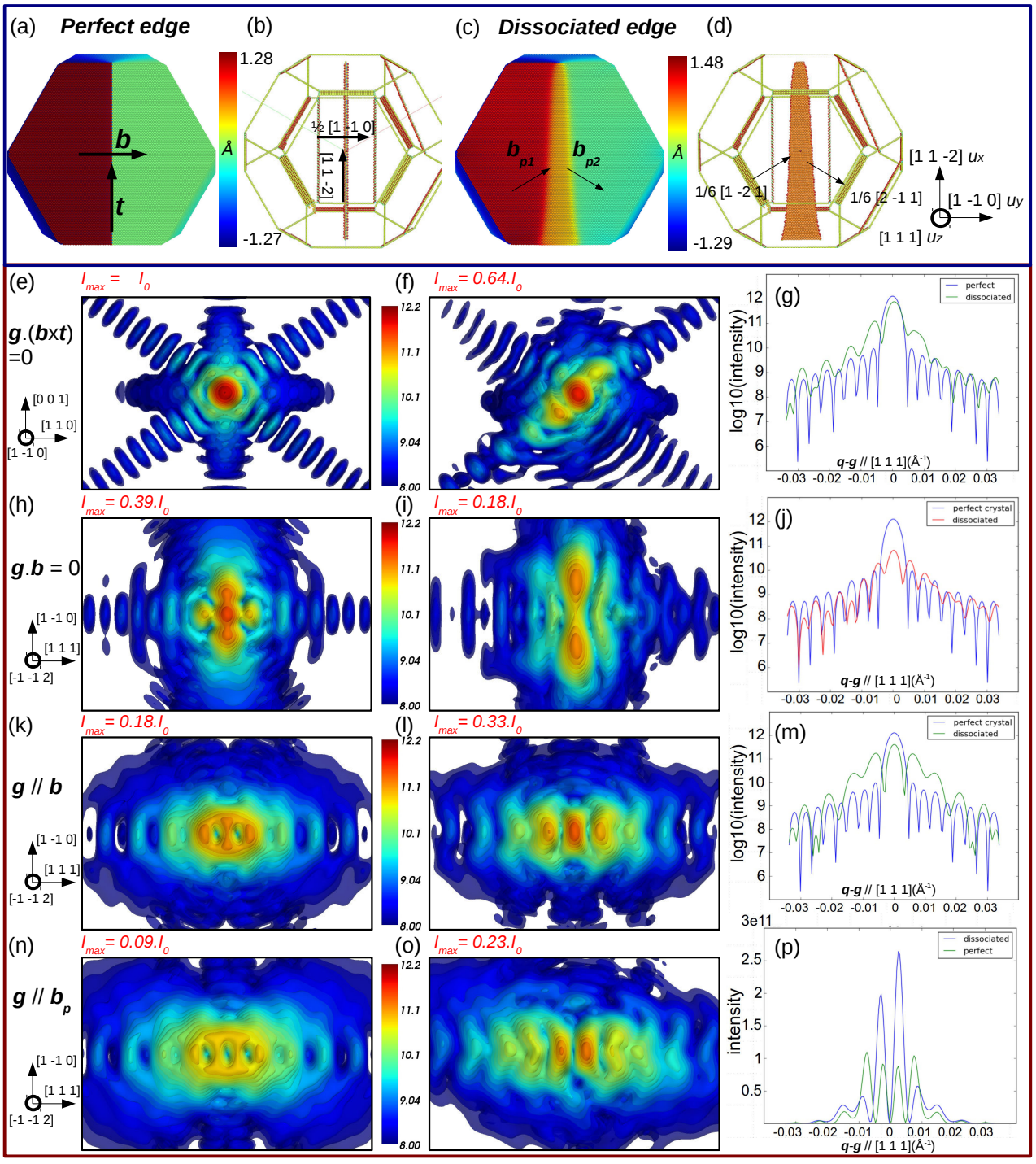

Fig. III.3: Edge dislocation in a 30x30x30 nm^3 copper crystal. (a) and (c) u_x component of the atomic displacement field for both initial and relaxed configurations. (b) and (d) Perfect edge dislocation with $\boldsymbol{b}$ = 1/2[1 $\bar{1}$ 0] and $\boldsymbol{t}$ = [1 1 $\bar{2}$] and dissociation of the perfect dislocation in 2 Shockley partials in the (1 1 1) plane. Only the defective, edge and corner atoms are shown. Calculated CXD pattern for a perfect (e) and dissociated (f) dislocations. (g) Intensity along [1 1 1] for perfect and dissociated dislocations (log scale) with $\boldsymbol{g}.\boldsymbol{b} = 0$ and $\boldsymbol{g}.(\boldsymbol{b}\times\boldsymbol{t}) = 0$ ($\boldsymbol{g}$ = 2 2 $\bar{4}$). Perfect (h), dissociated (i) and intensity along [1 1 1] for both cases (j) with $\boldsymbol{g}.\boldsymbol{b} = 0$ and $\boldsymbol{g}.(\boldsymbol{b}\times\boldsymbol{t}) \neq 0$ ($\boldsymbol{g}$ = 2 2 4). Perfect (k), dissociated (l) and intensity along [1 1 1] for a defect-free crystal and dissociated dislocation (log scale) (m) with $\boldsymbol{g}$ // $\boldsymbol{b}$ ($\boldsymbol{g}$ = 2 $\bar{2}$ 0). Perfect (n), dissociated (o) and intensity along [1 1 1] for both cases (p) with $\boldsymbol{g}$ // $\boldsymbol{b}_p$ ($\boldsymbol{g}$ = 2 $\bar{4}$ 2). *The selected area of the reciprocal space is kept to the same value in all figures and is equal to 0.045x0.0675 (1/ Å)^2*

When $\boldsymbol{g} \,//\, \boldsymbol{b}$ (Fig. III.3.k & III.3.l), as in the case of a screw dislocation, an edge dislocation produces a strong and characteristic signature, but the effect of dissociation is not as significant. Close to the Bragg position one can notice the elongation of the Bragg spot intensity along **b** for perfect and dissociated dislocations. The effect of dissociation is reflected by an increase of the Bragg spot intensity by a factor of 2 during relaxation. Both perfect and dissociated dislocations also induce intense fringes along the [1 1 1] direction with an apparent doubling of the fringes period. This doubling of the period has also been reported by (Wilson 1952), (Wilson 1955) and (Gailhanou & Roussel 2013) in the case of a perfect screw dislocation. It is not related to a (1 1 1) stacking fault since it is observed for both perfect and dissociated dislocations. For $\boldsymbol{g} \,//\, \boldsymbol{b}_p$ (Fig. III.3.n & III.3.o), similar fringes along [1 1 1] and an elongation along $\boldsymbol{b}$ can be observed for both perfect and dissociated dislocations. A more surprising result is the vanishing intensity at the exact Bragg peak position probably related to the 3π phase jump induced by the dislocation for the $2\,\bar{4}\,2$ reflection. As in the $\boldsymbol{g} \,//\, \boldsymbol{b}$ case, the intensity of the central spots increases by a factor 3 during relaxation. For any other selected diffraction vector, the calculated CXD pattern results in two clear and identifiable effects, a splitting or at least an elongation along $\boldsymbol{b}$ and intense fringes along [1 1 1] (*i.e.* the direction perpendicular to the dissociation plane).

III.3.3. Stacking faults

Similarly to dislocations, stacking faults induce a global shift of one part of the crystal with respect to another and thus appear as phase defects in diffraction. But, while dislocations induce a long distance heterogeneous strain field, elastic strain caused by a stacking fault remains limited to the vicinity of the fault (Hirth & Lothe 1968). According to Eq. (III.1), CXD is sensitive to the displacement field, even in the absence of elastic strain, and in fact the stacking fault is the case that can produce the maximum interference contrast. The relative simple signature on CXD patterns combined with their frequent occurrence in nanowires with low SFE (1D systems) have already motivated numerous studies of such materials using CXD (Chamard *et al.* 2008, Favre-Nicolin *et al.* 2010, Jacques *et al.* 2013): it has been used to try to evaluate the number of stacking faults in an InSb pillar (Jacques *et al.* 2013) and to get useful information about the fault sequence in a GaAs/GaP nanowire (Favre-Nicolin *et al.* 2010). While CXD has been mostly used to study systems with no or very few crystal defects, these studies demonstrate that it can be used efficiently on systems with multiple defects. This opens the perspective to apply the technique to a wider range of systems, even if the case of multiple defects is so far limited to 1D systems. In the present paper we deal with the case of stacking faults in 3D systems. Stacking faults are fairly common in *fcc* metals and usually occur in {111} crystallographic planes.

Let us start with the simple case a stacking fault completely separating the crystal in two parts either side of a (1 1 1) plane. The phase jump $\Delta\varphi$ across the stacking fault can be expressed as:

$$\Delta\varphi = 2\pi \begin{pmatrix} h \\ k \\ l \end{pmatrix} . \frac{n_{111}}{3} \begin{pmatrix} 1 \\ 1 \\ 1 \end{pmatrix} = \frac{2\pi}{3} n_{111}(h+k+l) \qquad \text{(III.4)}$$

where $n_{1\,1\,1}$ is the number of faulted planes. If it is a multiple of 3, $\Delta\varphi$ is a multiple of 2π for any Bragg reflection and it is impossible to evidence the fault in diffraction, unless the volume of the faulted part becomes comparable to that of the rest of the crystal.

A stacking fault is created by the insertion or the removal of a close packed {1 1 1} layer in the crystal. The removal of a plane is called an intrinsic stacking fault, whereas the insertion of a layer is called an extrinsic stacking fault. If the stacking fault results from the dissociation of a perfect dislocation, it is necessarily intrinsic ($n_{1\,1\,1} = 2$). Close to a Bragg position, the (h,k,l) values can be approximated by the integer values of the Bragg position. Depending on the selected diffraction vector, only two cases can occur. When $h+k+l=3n$, the resulting phase jump is a multiple of 2π and the stacking fault remains invisible (Fig. III.4.b). This invisibility condition can be exploited to hide a particular type of stacking fault and instead highlight elastic strain and other defects (Favre-Nicolin *et al.* 2010). When $h+k+l\neq 3n$, the stacking fault causes a phase shift of $\pm 2\pi/3$ between the two

parts of the crystal, inducing a strong signature in the diffraction pattern. The intensity in the vicinity of the Bragg position $\boldsymbol{g}$ can then be expressed as follows:

$$I(\boldsymbol{q}\simeq\boldsymbol{g}) \simeq \left|F_1(\boldsymbol{q})+F_2(\boldsymbol{q})e^{\frac{2i\pi}{3}}\right|^2 \quad \text{(III.5)}$$

where F_1 and F_2 are the structure factors of the crystal parts on either side of the stacking fault. At the exact Bragg position, F_1 and F_2 are essentially proportional to the respective volume fractions x and 1-x of unfaulted material either side of the stacking fault and:

$$I(\boldsymbol{g}) = x^2+(1-x)^2-x(1-x) \quad \text{(III.6)}$$

Destructive interference is maximal when the two volumes are equal: the intensity is then a quarter of the intensity diffracted by the perfect crystal which means that the best contrast is obtained when the stacking fault is located in the middle of the volume.

The complete picture of the vicinity of the Bragg position ($\boldsymbol{q} \approx \boldsymbol{g}$) is obtained with PyNX calculations performed on our model crystal after introduction of a traversing stacking fault passing through the centre (Fig. III.4.a). It confirms that the stacking fault is invisible on the 111 reflection (h+k+l=3n) (Fig. III.4.b), while it has a clear signature on the 1 1 $\bar{1}$ reflection (h+k+l≠3n) (Fig. III.4.c). The intensity at the exact 1 1 $\bar{1}$ Bragg position roughly equals ¼ of the intensity at the exact 1 1 1 Bragg position, as predicted above. The most characteristic signature of the stacking fault is the reinforcement of the intensity on the streak along [1 1 1], with a modification of its fringes, while fringes along other directions are barely changed. Here the modification of the fringes is essentially a doubling of the period, which is a consequence of the stacking fault being in the middle of the crystal.

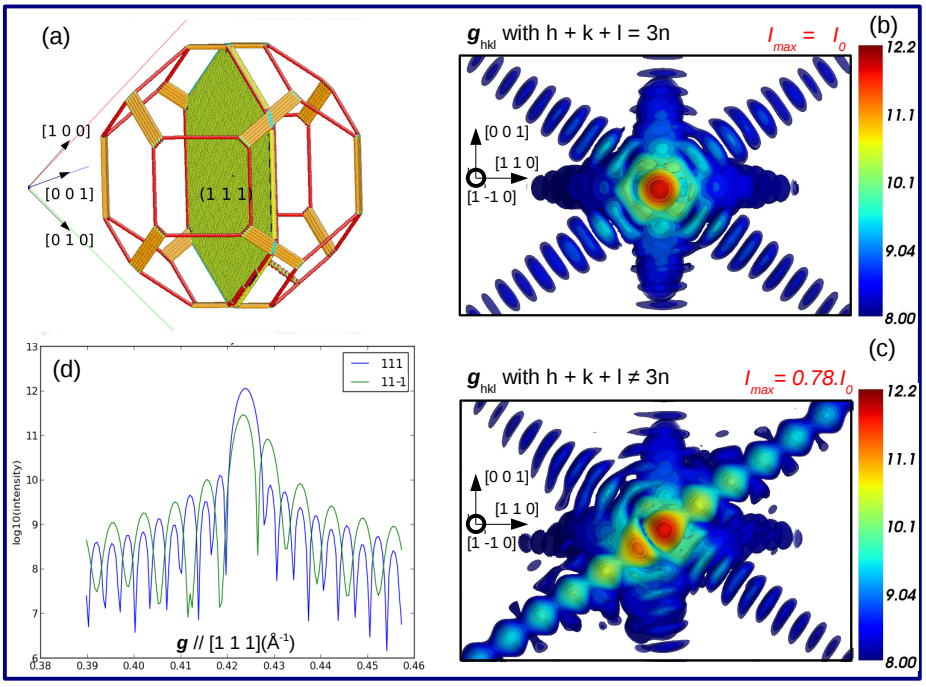

Fig. III.4 (a) (1 1 1) Stacking fault in a silver crystal with a Wulff geometry induced by the complete relaxation of a perfect edge line dislocation. (b) Corresponding CXD pattern when $\boldsymbol{g}$ fulfils the extinction conditions, *i.e.* h+k+l=3n ($\boldsymbol{g}$ = 1 1 1)**.** (c) Same CXD pattern when h + k + l ≠ 3n ($\boldsymbol{g}$ = 1 1 -1). (d) Intensity along [1 1 1] for both cases (log scale). *The selected area of the reciprocal space is kept to the same value in all figures and is equal to 0.045x0.0675 (1/ Å)²*

Traversing stacking faults are not the only common case in nanocrystals: as seen above, dissociated dislocations can stabilize in ribbon-shaped stacking faults, due to the competition between SFE and repulsive forces between the partials. It is interesting to see if one can get an idea of the extension of a single stacking fault from a CXD measurement. For a given material, the ability of a perfect dislocation to dissociate and produce a stacking fault is influenced by two main parameters, its stacking fault energy γ_s and its shear modulus μ. Physically, the dissociation length of a dislocation is represented by the dimensionless material parameter $\gamma_s/\mu b_p$, where b_p is the modulus of the partial Burgers vector of the dislocation, see for example Chassagne *et al.* 2011. Materials with a low $\gamma_s/\mu b_p$ value have widely dissociated dislocations with a high constriction stress while the occurrence of dissociated dislocations or stacking faults is less frequent in materials with a high $\gamma_s/\mu b_p$. Calculations were performed on 5 different *fcc* metals with similar size and shape (Fig. III.5, Gold and Nickel are not shown) and SFE ranging from 17.8 mJ/m^2 (silver), to 149.3 mJ/m^2 (aluminium) (Cockayne *et al.* 1971). Values given by EAM potentials and experiments are reported in Tab.1. They are in a very good agreement, except for the case of gold for which the discrepancy between EAM and experimental values is close to 25%. We use the SFE given by the EAM potentials to calculate the parameter $\gamma_s/\mu b_p$ whose values are reported in Tab.1. As illustrated in Fig. III.5.(a,b,c), the dissociation length obtained upon relaxation (1600 relaxation steps) decreases consistently when $\gamma_s/\mu b_p$ increases: the dislocation is widely dissociated in silver which has the lowest $\gamma_s/\mu b_p$ whereas the dissociation remains very limited in aluminium (highest $\gamma_s/\mu b_p$).

	Ag	Cu	Au	Ni	Al
γ_s (mJ/m^2) from EAM	17.8 (Williams *et al.* 2006)	44.7 (Mishin *et al.* 2001)	42.6 (Grochola *et al.* 2005)	125.2 (Mishin *et al.* 1999)	149.3 (Mishin *et al.* 1999)
γ_s (mJ/m^2): experiments	16 (Hirth & Lothe 1968)	45 (Westmacott & Peek 1971)	32 (Jenkins 1972)	125 (Balluffi 1978)	144 (Carter & Ray 1977)
$\gamma_s/\mu b_p$ (x10^{-3}): EAM	3.5	7.4	9.5	11.7	33.5
Average dissociation length (Å)	85	37	47	29	18
Splitting distance (x10^{-3} Å^{-1})	6.67	15.1	12.9	16.5	17.1
Maximum intensity	1.87x10^{11}	2.25x10^{11}	2.25x10^{11}	2.21x10^{11}	2.67x10^{11}

Tab. III.1. SFE of 5 fcc metals, from EAM and experiments, and their $g_s/\mu b_p$ parameter. Corresponding dissociation length in real space, as obtained after 1600 relaxation steps; splitting distance and maximum intensity in reciprocal space for $\boldsymbol{g}$ = 2 2 4.

When looking at the CXD patterns (Fig III.5.d. to III.5.f.) and the intensity profile along [1 $\bar{1}$ 0] (Fig. III.5.g.), one observes the inverse phenomena: a narrow stacking fault induces a large splitting distance (i.e, the distance between the maxima of intensity of the splitted Bragg peak) with intense maxima of intensity, a low minimum of intensity at the Bragg position and a large splitting distance of the Bragg peaks (Fig III.5.d to III.5.g), whereas a wide stacking fault induces a weak splitting, with low maxima of intensity, low intensity drop in Bragg position and a small splitting distance of the Bragg peaks. One can also notice the increasing intensity of the [1 1 1] fringes and the decreasing distance between the maxima of intensity along [1 $\bar{1}$ 0] as the stacking faults spreads into the crystallite. Copper, gold and nickel have similar $\gamma_s/\mu b_p$ values and the resulting dislocation dissociation lengths upon relaxation for these three materials are hence rather close. The case of nickel is quite interesting since it has a SFE similar to that of aluminium, however its high shear modulus allows to obtain a dissociation length equivalent to the one obtained for copper. This illustrates the influence of both parameters on the occurrence of stacking faults. Calculations of CXD patterns for nickel and gold (not shown here) logically lead to results very similar to the case of copper. Regarding experimental matters, it is then a safe assumption to expect the same kind of structural defects in these three *fcc* metals, and as a result the calculations presented for copper in this study can also be used as a reference for experimental work on gold or nickel crystallites.

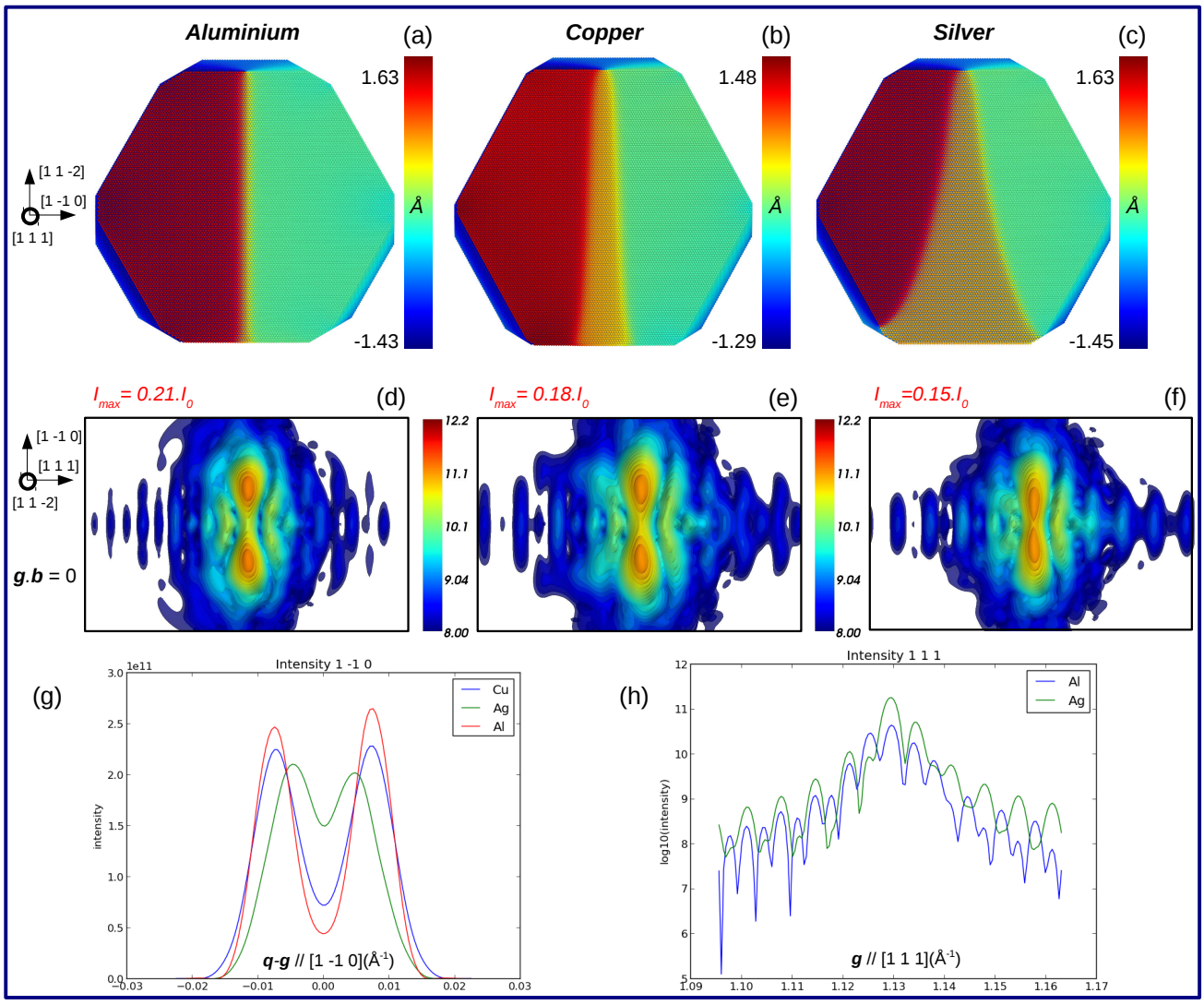

Fig. III. 5 *Influence of the Stacking Fault Energy.* Dissociated edge dislocations in 30x30x30nm^3 and corresponding displacement field (u_x component) for aluminium (a), copper (b) and silver (c) crystals with a Wulff geometry. (d-f): corresponding CXD patterns with $\boldsymbol{g}.\boldsymbol{b} = 0$ ($\boldsymbol{g}$ = 2 2 4). (g) and (h) Intensity profiles along [1 -1 0] and [1 1 1] (logarithmic scale). *The selected area of the reciprocal space is kept to the same value in all figures and is equal to 0.045x0.0675 (1/ Å)^2*

From these first conclusions, some complementary calculations on the relaxation of systems with low SFE such as silver were performed. During the first steps of relaxation (Fig III.6.a & III.6.d), the stacking fault remains rather narrow, and for $\boldsymbol{g}.\boldsymbol{b} = 0$, both partials and the stacking fault display a strong signature on the CXD pattern, with respectively a splitting of the Bragg peak along $\boldsymbol{b}$ and intense fringes along [1 1 1]. After 3000 relaxation steps, the stacking fault continues to spread and the splitting of the Bragg reflection cannot be observed any longer while the [1 1 1] fringes become more intense. As the stacking fault extends, the intensity at the Bragg position increases while the global maximum of intensity steadily decreases, and so does the splitting of the Bragg reflection (Fig. III.6.b, III.6.e & III.6.g). At this stage of relaxation, the inhomogeneous strain around the dislocation, induces a very low maximum of intensity on the CXD pattern (Fig. III.6.e & III.6.g). During the final steps of relaxation, the stacking fault continues to spread until it emerges on one of the crystal facets and the signature of the Shockley partials (*i.e.* splitting of the Bragg peak along $\boldsymbol{b}$) completely vanishes while the intensity of the [1 1 1] fringes increases with the width of the stacking fault (Fig. III.6.h). One can also notice the

sharp increase of the maximum intensity which coincides with the disappearance of the Shockley partials from the nanocrystal. One can assume that the rather large inhomogeneous strain around the partials during the dissociation (Fig III.6.a & III.6.b) results in a drop of intensity during the relaxation. As the partials leave the crystal, the strain around the stacking fault is weak and with a very limited extent (restrained to the two faulted planes of the intrinsic stacking fault) (Fig III.6.c), resulting in a larger intensity close to the Bragg position.

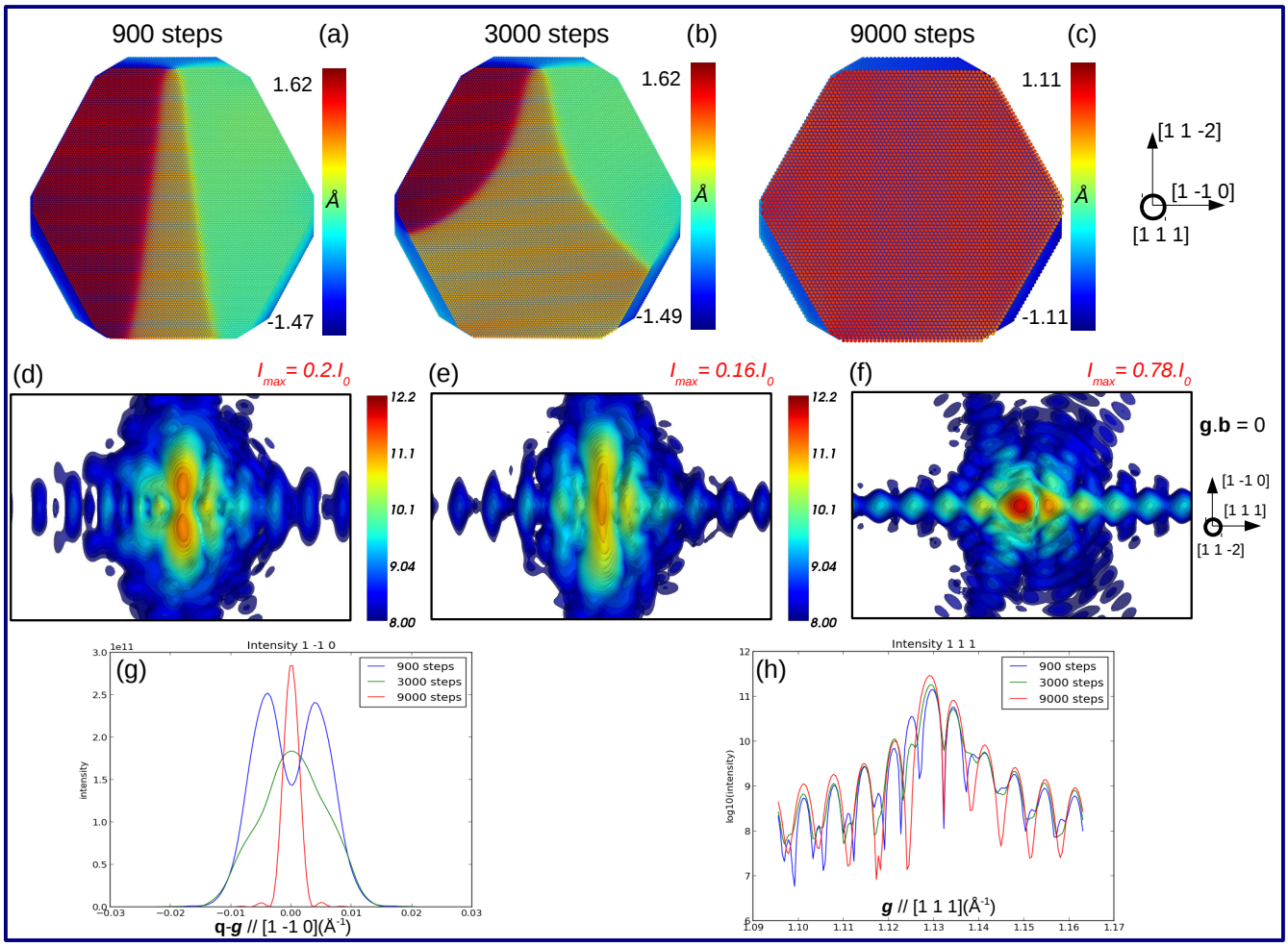

Fig. III.6: *Relaxation for a crystal with a low SFE (silver)*. u_x component of the atomic displacement after 900 relaxation steps (a), 3000 relaxation steps (b) and after full relaxation (c). (d to f) Corresponding CXD pattern for $\boldsymbol{g}.\boldsymbol{b} = 0$ ($\boldsymbol{g}$ = 2 2 4). (g and h) Intensity along [1 $\bar{1}$ 0] and [1 1 1] (log scale) *The selected area of the reciprocal space is kept to the same value in all figures and is equal to 0.045x0.0675 (1/ Å)²*

III.3.4. Frank loops

A Frank partial dislocation is formed as the boundary of a fault formed by inserting or removing a close-packed {1 1 1} layer of atoms in a perfect crystal. Geometrically, the Frank intrinsic stacking fault is identical to the intrinsic fault produced by the dissociation of a perfect dislocation, except that the bounding partial is different. An intrinsic Frank loop is often called a vacancy Frank loop whereas an extrinsic Frank loop can be referred as an interstitial Frank loop. The Burgers vector of a Frank loop is perpendicular to the {1 1 1} fault plane, with a magnitude equal to the interplanar spacing, *i.e.* $\boldsymbol{b}$ is of type 1/3<1 1 1>. Here, an extrinsic Frank

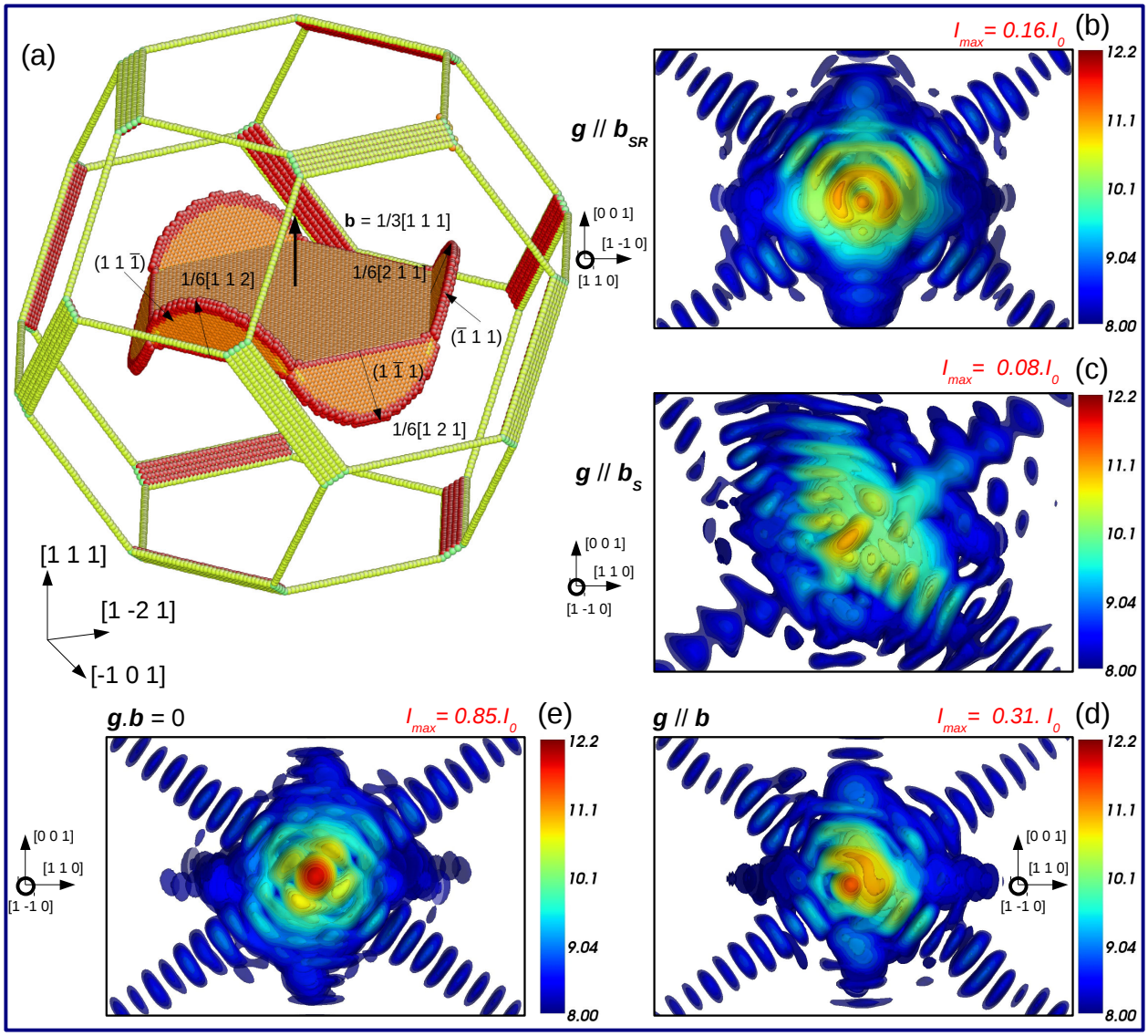

Fig. III.7 (a) Relaxed Frank dislocation loop with $\boldsymbol{b} = \frac{1}{3}[1\ 1\ 1]$ in the centre of a 30x30x30nm^3 Wulff silver crystal. The colour code represents the coordination number, such that only the defective atoms and nanocrystal edges are shown (b) Calculated CXD patterns when $\boldsymbol{g} // \boldsymbol{b}_{SR}$ ($\boldsymbol{g} = 2\ 2\ 0$) , (c) when $\boldsymbol{g} // \boldsymbol{b}_S$ ($\boldsymbol{g} = 2\ 2\ 4$), (d) when $\boldsymbol{g} // \boldsymbol{b}$ ($\boldsymbol{g} = 1\ 1\ 1$), (e) when $\boldsymbol{g}.\boldsymbol{b} = 0$ ($\boldsymbol{g} = 2\ \bar{2}\ 0$). *The selected area of the reciprocal space is kept to the same value in all figures and is equal to 0.045x0.0675 (1/ Å)*^{2}

loop with $\boldsymbol{b} = 1/3[1\ 1\ 1]$ is introduced in a 30x30x30nm^3 silver nanocrystal with a Wulff shape (Fig. III.7.a). During relaxation, the Frank partial dissociates in a low energy, so-called stair-rod dislocation (Hull & Bacon 2001), and a Shockley partial on an intersecting {1 1 1} plane according to a reaction of the type:

$$\frac{1}{3}[1\ 1\ 1] = \frac{1}{6}[1\ 0\ 1] + \frac{1}{6}[1\ 2\ 1] \qquad \text{(III.7)}$$

The hexagonal Frank loop with Burgers vector $\frac{1}{3}[1\ 1\ 1]$ can dissociate to produce a stair-rod along each edge and a Shockley partial on the three inclined {1 1 1} planes as illustrated in Fig. III.7.a.
Calculations of diffuse scattering performed on perfect (prismatic) and partial (Frank) dislocation loops in *fcc* metals (Erhart *et al.* 1982) and semiconductors (Nordlund *et al.* 2000) already provided a very accurate picture

of the scattering which can be expected from such defects. The Huang diffuse scattering of perfect and Frank dislocation loops has also been studied experimentally by Larson & Schmatz (1980) and Larson & Young (1987). They have demonstrated that Huang diffuse scattering can be used to determine the vacancy or interstitial character of a loop, to estimate their relative proportion in a given population, and to estimate their size. It is shown by Nordlund *et al.* (2000) that the general features observed in diffuse scattering patterns are mostly independent of the choice of the Bragg peak. We demonstrate in the following that in the case of CXD, the choice of the Bragg reflection is essential to evidence the characteristic signature of a Frank or a prismatic dislocation loop.

A Frank loop is a pure edge dislocation since the Burgers vector is always perpendicular to the dislocation line. Contrary to the case of a straight edge dislocation there is no diffraction condition where $\boldsymbol{g}.\boldsymbol{u} = 0$ for all the loop edges (*i.e.* $\boldsymbol{g}.\boldsymbol{b}=0$ AND $\boldsymbol{g}.(\boldsymbol{b}\times\boldsymbol{t})=0$). This particular case can be used to distinguish a Frank loop from a straight dislocation when analysing CXD patterns.

As in the case of a straight dislocation line (subsection III.3.2), $\boldsymbol{g}.\boldsymbol{b} = 0$ is a partial extinction condition, since it ignores the part of the displacement parallel to the Burgers vector, such that little perturbation is observed around these reflections (Fig. III.7.e). The other part of the displacement field and the relaxation in stair-rods and Shockley partials are responsible for the weak reduction of intensity of the central peak (85% of the perfect crystal) and the weak distortions of the pattern visible in Fig. III.7.e.

The case $\boldsymbol{g}//\boldsymbol{b}$ at the end of the relaxation (Fig. III.7.d.) also produces some interesting results with a drastic reduction of intensity of the central spot (30% of the perfect crystal) and the appearance of a satellite spot along the [1 1 1] direction. This reduction in intensity is obviously related to the presence of the loop in the centre of the volume. In agreement with the invisibility conditions for a stacking fault detailed in Section 3.3, the characteristic signature of a (1 1 1) stacking fault, *i.e.* fringes along [1 1 1], is not visible on the CXD pattern in this case. This particular reflection is also well suited to determine the interstitial or vacancy character of the Frank loop. As shown in Fig. III.7.d, the scattering is more intense for the high $\boldsymbol{q}$ values (presence of a satellite peak) with respect to the theoretical Bragg position. This distribution of the scattering is expected for an interstitial Frank loop and in good agreement with Erhart *et al.* 1982 and Nordlund *et al.* 2000. In the case of a vacancy Frank loop and for this particular reflection (not shown here), the satellite peak is located in the lower $\boldsymbol{q}$ values with respect to the theoretical Bragg position.

As illustrated on Fig. III.7.b, the dissociation in Shockley and stair-rods partials induce a very characteristic signature on CXD patterns when the diffraction vector is parallel to a <1 1 0> direction (Fig III.7.b), (but not perpendicular to $\boldsymbol{b}$, *i.e.* only the 2 2 0, 2 0 2 and 0 2 2 reflections can be used) corresponding to the Burgers vector of a partial stair-rod. The pattern then looks fairly similar to that of a screw dislocation with a ring-shaped pattern oriented along $\boldsymbol{b}_{\mathbf{SR}}$ = <2 2 0> (where $\boldsymbol{b}_{\mathbf{SR}}$ is the Burgers vector of the stair-rod dislocation). This kind of pattern is not observed when the loop is not dissociated and is a clear indication of the formation of a stair-rod dislocation during relaxation.

When looking at the other set of partials, *i.e.* when $\boldsymbol{g}$ is parallel to one of the Shockley partial ($\boldsymbol{g}//\boldsymbol{b}_{\mathbf{S}}$, $\boldsymbol{g}$ = 2 2 4 Fig. III.7.c, where $\boldsymbol{b}_{\mathbf{S}}$ is the Burgers vector of the Shockley partial dislocation), the resulting CXD pattern is very disturbed at the end of relaxation, with intense fringes along [1 1 1] and an elongated central spot with very low intensity in comparison with a perfect crystal (only 8% of the Bragg peak intensity). During the first stages of relaxation, the intensity of the central spot is similar to that of a perfect crystal, and only the fringes along [1 1 1] indicate the presence of a defect in the crystal. Hence these particular Bragg conditions appear particularly well suited to evidence the dissociation of the Frank partial in its intersecting slip planes.

III.3.5. Prismatic loops

A prismatic dislocation loop has a ½[1 0 1] Burgers vector not contained in the plane of the loop (as opposed to a shear loop whose Burgers vector is contained in the plane of the loop). We introduce a prismatic loop at the centre of a 30x30x30nm^3 copper crystal with a Wulff geometry. The Burgers vector $\boldsymbol{b}$ = ½[1 0 1]

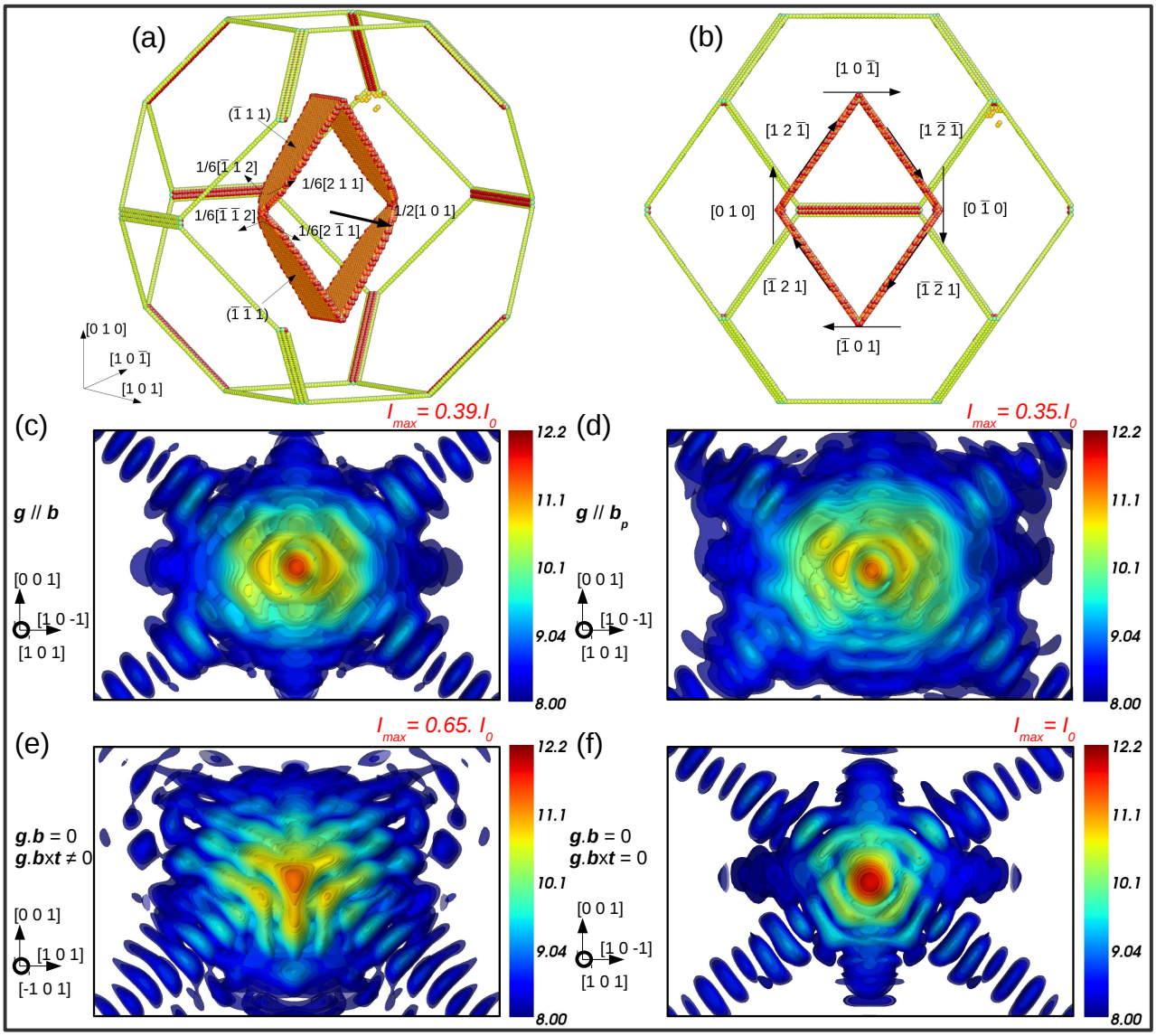

Fig. III.8 (a) Relaxed prismatic dislocation loop with $\boldsymbol{b} = \frac{1}{2}$ [1 0 1] at the centre of a 30x30x30nm^3 Wulff copper crystal. The colour code represents the coordination number, such that only the defective atoms and nanocrystal edges are shown. The loop decomposes in partial dislocations in its (1 1 $\bar{1}$) and ($\bar{1}$ 1 1) slip planes. (b) Same dislocation loop viewed along the [1 0 1] direction. Calculated CXD pattern for $\boldsymbol{g}$ // $\boldsymbol{b}$ ($\boldsymbol{g}$ = 2 0 2) (c), $\boldsymbol{g}$ // $\boldsymbol{b}_p$. ($\boldsymbol{g}$ = 4 2 2) (d), $\boldsymbol{g}.\boldsymbol{b}$ = 0 and $\boldsymbol{g}.(\boldsymbol{b}\times\boldsymbol{t}) \neq 0$ ($\boldsymbol{g}$ = 2 $\bar{6}$ $\bar{2}$) (e) and for $\boldsymbol{g}.\boldsymbol{b}$ = 0 and $\boldsymbol{g}.(\boldsymbol{b}\times\boldsymbol{t})$ = 0 ($\boldsymbol{g}$ = 0 2 0) (f). *The selected area of the reciprocal space is kept to the same value in all figures and is equal to 0.045x0.0675 (1/ Å)*^{2}

decomposes during relaxation in partial dislocations in its (1 1 $\bar{1}$) and ($\bar{1}$ 1 1) slip planes, as illustrated in Fig. III.8.a. Since the Burgers vector is perpendicular to the dislocation line, the loop edges are pure edge dislocations and the invisibility criteria, *i.e.* $\boldsymbol{g}.\boldsymbol{b}$ = 0 and $\boldsymbol{g}.(\boldsymbol{b}\times\boldsymbol{t})$ = 0 described in section III.3.2, apply for this type of defect. However, as in the Frank loop case, since the loop edges are not all aligned, there are always segments of the dislocation loop where $\boldsymbol{g}.(\boldsymbol{b}\times\boldsymbol{t}) \neq 0$, which produces a visible effect on the CXD pattern. However, when $\boldsymbol{g}.\boldsymbol{b}$ = 0 and $\boldsymbol{g}.(\boldsymbol{b}\times\boldsymbol{t})$ = 0 for two opposite segments of the loop (for instance $\boldsymbol{g}$ = 0 2 0) (Fig. III.8.f), the signature of the prismatic loop on CXD patterns is very faint, and the intensity of the Bragg spot is similar to the case of the perfect crystal, with no elongation in any particular direction. When $\boldsymbol{g}.\boldsymbol{b}$ = 0 but $\boldsymbol{g}.(\boldsymbol{b}\times\boldsymbol{t}) \neq 0$, *i.e.* $\boldsymbol{g}$ not parallel to any segment of the loop, (the case $\boldsymbol{g}$ = 2 6 $\bar{2}$ is shown in Fig. III.8.e.), the prismatic loop

Tab. III.2 Summary of all the most relevant cases that can be encountered during the study of the signature of single defects. For each case the maximum intensity calculated on the CXD pattern is compared to the intensity for a defect-free crystal with same size and shape. In the following ***n*** is the direction normal to a stacking fault, ***t*** is the dislocation line direction and ***bxt*** is the direction perpendicular to both the Burgers vector and the dislocation line direction. The best conditions to evidence the defect are highlighted in yellow, while the invisibility conditions are highlighted in pale green.

	Screw dislocation		Edge dislocation		Stacking Fault	Frank dislocation loop	Prismatic dislocation loop
	Unrelaxed	Relaxed	Unrelaxed	Relaxed			
$\boldsymbol{g}.(\boldsymbol{b}\times\boldsymbol{t})=0$	Single clean spot $I = I_0$	Single clean spot $I = I_0$	Single clean spot $I = I_0$	Single clean spot Fringes along ***n*** $I = 0.78.I_0$	not applicable (N/A)	Small drop of intensity in Bragg position: $I = 0.85.I_0$	Single clean spot slight distortion in the pattern $I = I_0$
$\boldsymbol{g}.\boldsymbol{b}=0$ $\boldsymbol{g}.(\boldsymbol{b}\times\boldsymbol{t})\neq 0$	Single clean spot $I = I_0$	Splitting along ***b*** Fringes along ***n*** $I = 0.2.I_0$	Elongation along ***b*** $I = 0.4.I_0$	Splitting along ***b*** Fringes along ***n*** $I = 0.2.I_0$	N/A	Single clean spot slight disturbances $I = 0.8.I_0$	Single clean spot Drop of intensity in Bragg position $I = 0.65.I_0$
$\boldsymbol{g}$ // $\boldsymbol{b}$	Ring-shaped pattern: ring axis along ***b*** Extinction in Bragg position $I = 0.14.I_0$	Ring shaped pattern: ring axis along ***b*** Extinction in Bragg position Maxima of intensity along [0 0 1] $I = 0.18.I_0$	Fringes along ***n*** Elongation of Bragg peak along ***b*** $I = 0.18.I_0$	Fringes along ***n*** Elongation of Bragg peak along ***b*** and increased intensity in Bragg position $I = 0.33.I_0$	N/A	Satellite spot and low intensity in Bragg position $I = 0.3*I_0$ No fringes along ***n***: ***g*** with $h+k+l = 3n$	Hexagonal shaped pattern with elongation along ***b*** Fringes along ***n*** Intensity maximal in Bragg position $I = 0.5.I_0$
$\boldsymbol{g}$ // $\boldsymbol{b}_p$	Ring shaped pattern: ring axis along ***b*** Extinction in Bragg position $I = 0.09.I_0$	Ring shaped pattern: ring axis along $\boldsymbol{b}_p$ Extinction in Bragg position $I = 0.11*I_0$	Fringes along ***n*** Elongation of fringes along ***b*** Extinction in Bragg position $I = 0.09*I_0$	Fringes and splitting along ***n*** Elongation of fringes along ***b*** $I = 0.23*I_0$	N/A	Distorted ring-shaped pattern for $\boldsymbol{g}$ // $\boldsymbol{b}_{sr}$ with ring axis along $\boldsymbol{b}_{sr}$ $I = 0.16*I_0$	Similar to $\boldsymbol{g}$ // ***b*** with a lower intensity in Bragg position $I = 0.35*I_0$
g with $h+k+l=3n$	N/A (no stacking fault (SF)).	Fringes along ***n*** disappear	N/A (no stacking fault (SF)).	Fringes along ***n*** disappear	Single clean spot. $I = I_0$	Fringes along ***n*** disappear	Fringes along ***n*** disappear
g with $h+k+l\neq 3n$	N/A	Fringes along ***n***	N/A	Fringes along ***n***	Intense fringes along ***n*** and splitting due to the $\pm 2\pi/3$ phase jump induced by the SF. Intensity in Bragg position 25% of perfect crystal	N/A	N/A
general ***g***	Ring shaped pattern. Ring diameter inversely proportional to crystal size and *hkl* indices	Ring-shaped pattern. Distortion and disorientation of the ring depending on the *hkl* indices of the diffraction vector Increase of the maxima of intensity during relaxation	Fringes and splitting along ***n*** and elongation of Bragg peak and/or of fringes along ***b***, depending on the selected diffraction vector	Fringes and splitting along ***n*** and elongation/ splitting along ***b*** depending on the selected diffraction vector Increase of the maximum intensity during relaxation	Only two possible cases (see above)	Three main effects: 1) fringes along ***n*** normal to the SF, 2) ring shaped pattern along one of the stair-rod partial and 3) decrease of the intensity of the central spot and appearance of a satellite spot depending on *hkl*	Distorted hexagonal shaped pattern not oriented along a particular direction and dependent of the *hkl* indices of ***g***. Maximum intensity lower than perfect crystal

induces some perturbation in the CXD pattern, which is expected since such conditions do not lead to a complete extinction for
an edge dislocation. The central spot intensity slightly decreases (65% of perfect crystal) and the diffraction pattern is elongated in the (1 $\bar{1}$ 0) plane along the [1 1 1], [1 $\bar{1}$ 1] and [0 0 1] directions. We now focus on diffraction conditions where the prismatic loop should produce a strong and characteristic signature, *i.e.* $\boldsymbol{g}$ // $\boldsymbol{b}$. As shown in Fig. 8.c ($\boldsymbol{g}$ = 2 0 2), one can observe an hexagonal shaped pattern with an elongation along the Burgers vector direction $\boldsymbol{b}$ = ½ [1 0 1] and a strong decrease of the intensity of the central spot (by half compared to the perfect crystal). One can also notice the increased intensity of the [1 $\bar{1}$ 1] and [1 1 $\bar{1}$] fringes, due to the stacking faults in the dissociated loop edges. Similarly to an edge dislocation, the conditions when $\boldsymbol{g}$ // $\boldsymbol{b}_p$, for instance $\boldsymbol{g}$ = $\bar{2}$ 2 4 (Fig. III.8.d), also produces a characteristic signature (Fig. III.8.e). The resulting diffraction pattern is similar to the case $\boldsymbol{g}$ // $\boldsymbol{b}$ (Fig. III.8.c) with a hexagonal-shaped pattern elongated along $\boldsymbol{b}$ and a reduction of the central spot intensity by a factor of 3. Finally, for a general diffraction vector $\boldsymbol{g}$ the defect signature can clearly be identified on the CXD pattern, but its intensity is generally lower than for the particular cases $\boldsymbol{g}$ // $\boldsymbol{b}$ and $\boldsymbol{g}$ // $\boldsymbol{b}_p$. Additionally, the hexagonal shaped pattern is slightly disoriented with respect to $\boldsymbol{b}$.
In conclusion to this section, similarly to simple dislocation lines and stacking faults, Frank and prismatic loops produce a characteristic signature strongly influenced by the choice of the diffraction vector and the invisibility conditions. The main difference between a dislocation loop and a line dislocation lies in the choice of the diffraction conditions to evidence such defects. While for the latter the case $\boldsymbol{g}.\boldsymbol{b}$=0 is an appropriate choice to evidence dissociation, this condition is less adapted to dislocation loops since it will hide their characteristic signature. However, we will see in the last section that the proper use of these invisibility conditions turns out to be particularly useful to determine the Burgers vector of any kind of dislocation.
This study of simple and ideal cases of single defects drives us to a simple conclusion: a given crystalline defect has a characteristic signature, which can be identified and interpreted using coherent x-ray diffraction. Equally important is the influence of the diffraction vector on the resulting CXD pattern, and the need to select the appropriate vector in order to highlight or hide the signature of a given crystal defect. One has to keep in mind that particular cases detailed throughout this study are not always the best suited for all types of crystalline defects. These considerations should be useful in order to select the best experimental conditions to evidence a given crystalline defect. Additionally, as illustrated in the next Section, these simple cases can be used to understand and interpret CXD patterns from more complex and realistic structures. An overview of the cases detailed throughout this study is presented in Table 2, which highlights the best diffraction conditions to evidence each type of crystalline defect.

III.3.6. Influence of the crystal size and shape

The cases detailed in subsections III.3.1 to III.3.6 share the same geometry with a single defect introduced at the centre of a Wulff crystal. However, the position of the dislocation and the boundary conditions of the crystal might have a considerable influence on the defect signature and their effect is investigated in the present section. To study the effect of the crystal shape, we compare the results obtained with a crystal of Wulff geometry with a spherical crystal. We simulated a sphere of copper with radius r = 14.1 nm (corresponding to 1.2×10^6 atoms, a number similar to the reference crystal), at the centre of which we introduce a dislocation line of pure screw or pure edge character, with Burgers vector $\boldsymbol{b}$ = ½ [1 $\bar{1}$ 0]. Similarly to what has been observed with the Wulff geometry, the perfect screw dislocation dissociates during relaxation in two sets of two Shockley partials in its two {1 1 1} slip planes, while the edge dislocation dissociates in the (1 1 1) plane only (Fig. III.9.j). As illustrated on Fig. III.9.d & III.9.g, the u_x component of the displacement field is very similar to the one obtained for a Wulff geometry. In both cases it is exactly equal to ± *b/2*. The only differences which can be expected on the calculated CXD patterns should be related to the nanocrystal shape. In the case of perfect crystals, the influence of the shape is seen in the form factor: instead of streaked fringes along the facet

directions, one observes spherical fringes, and the shape of the central spot also reveals the geometry (Fig III.9.b

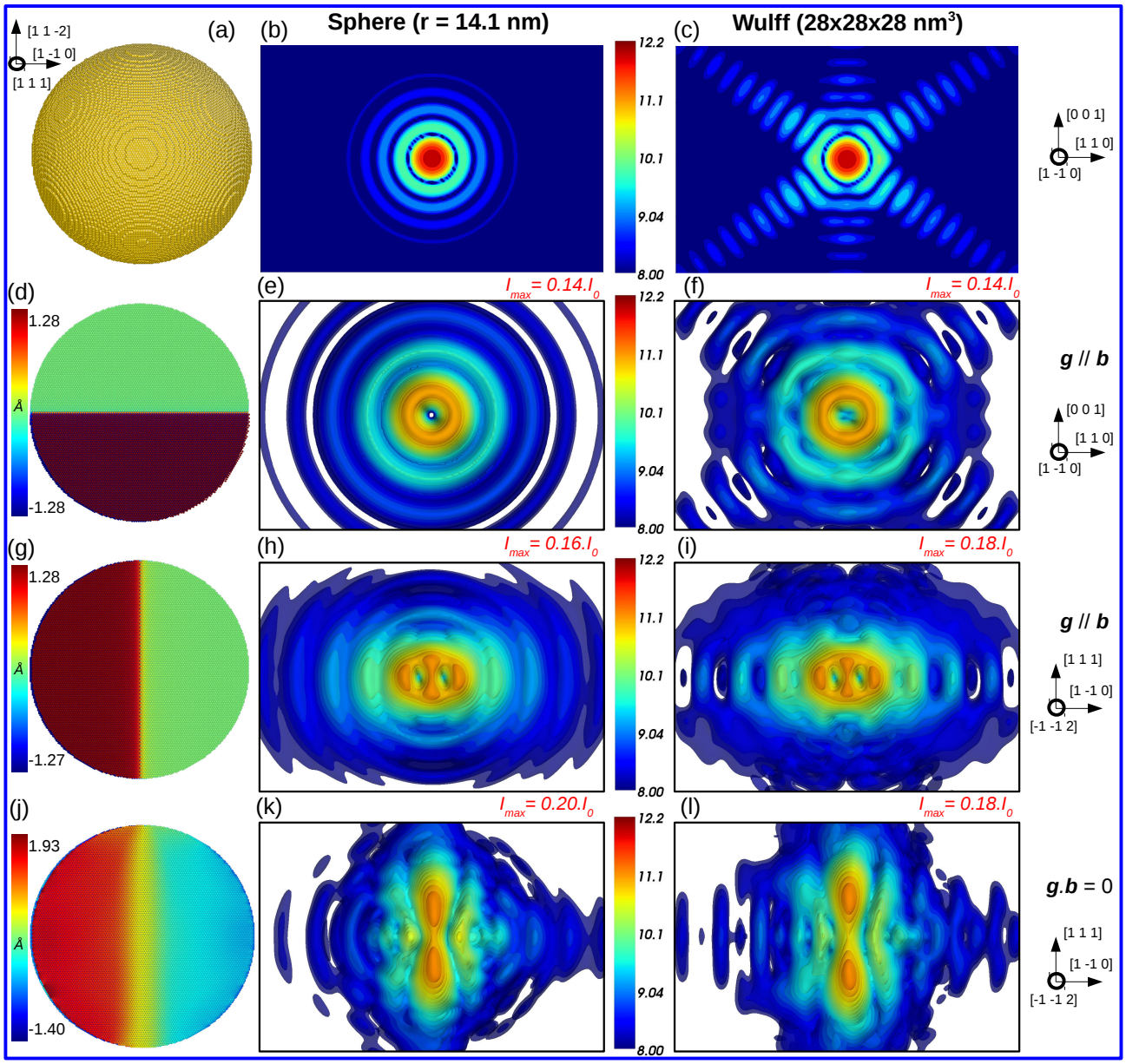

Fig. III.9 a) Defect free copper spherical crystal with r = 14.1nm. Corresponding CXD patterns with $\boldsymbol{g}$ // $\boldsymbol{b}$ ($\boldsymbol{g}$ = 2 $\bar{2}$ 0) for the sphere (b) and the reference copper crystal in Wulff geometry (c). (d) Perfect screw dislocation with $\boldsymbol{b}$ = ½ [1 $\bar{1}$ 0] at the centre of the section in the same spherical crystal. The colour scale shows the u_x component of the atomic displacement field . Corresponding CXD patterns with $\boldsymbol{g}$ // $\boldsymbol{b}$ ($\boldsymbol{g}$ = 2 $\bar{2}$ 0) for a sphere (e) and a Wulff crystal (f). (g) Perfect edge dislocation with $\boldsymbol{b}$ = ½ [1 $\bar{1}$ 0] in the same crystal. Corresponding CXD patterns with $\boldsymbol{g}$ // $\boldsymbol{b}$ ($\boldsymbol{g}$ = 2 $\bar{2}$ 0) for a sphere (h) and a Wulff crystal (i). (j) Dissociation of the perfect dislocation in 2 Shockley partials in the (1 1 1) plane with $\boldsymbol{b}_{p1}$ = 1/6[1 $\bar{2}$ 1] and $\boldsymbol{b}_{p2}$ = 1/6[2 $\bar{1}$ $\bar{1}$] in the same crystal. Corresponding CXD patterns with $\boldsymbol{g}.\boldsymbol{b}$ = 0 ($\boldsymbol{g}$ = 2 2 4) for a sphere (k) and a Wulff crystal (l). *The selected area of the reciprocal space is kept to the same value in all figures and is equal to 0.045x0.0675 (1/ Å)²*

& III.9.c). Such details are easily evidenced experimentally with decent statistics. To examine the case of the faulted crystals, we choose a diffraction vector parallel to the Burgers vector ($\boldsymbol{g}$ = 2 $\bar{2}$ 0). As illustrated in Fig.

III.9.e, the perfect screw dislocation still yields a ringshaped pattern with its axis along the Burgers vector direction. The crystal shape only affects the distribution of intensity in the ring (Figs. III.9.e and III.9.f). For the perfect edge dislocation, similar conclusions are drawn, and the calculated CXD patterns displays the same features which have been observed for the Wulff crystal such as fringes along the [1 1 1] direction and the elongation of the Bragg peak along $\boldsymbol{b}$. The distribution of intensity is very similar for both Wulff and spheric crystallites (Figs. III.9.h & III.9.i).

The effect of the crystallite size has also been investigated by comparing the obtained CXD patterns of Wulff shape crystals with size ranging from 5 to 60 nm. While this would be a simple scaling exercise in a continuous description of matter such as FEM, here the problem is not invariant because of the fundamental size of the defect, given by the modulus of the Burgers vector. Of course we evidence in the diffraction patterns the scaling of the form factor in proportion to the change of size of the crystal. But one might expect a significant effect related to the change of ratio between crystal shape and defect size. However, no significant size effects are seen on the signatures of the defects, regardless of the type of defect and the chosen Bragg reflection, in the range of sizes explored. It suggests than we are still in a size range in which a continuous description of matter would be valid, provided a sufficiently good continuous description of the defect and its strain field. An important consequence of the weak influence of size and shape of the crystal containing the defect is that the results presented above can be generally applied to a wide range of size and shapes of *fcc* crystals. This is particularly useful since samples may contain many crystals of the same materials with a wide range of size and shapes, depending of the processing route (in particular in the case of dewetting: Beutier *et al.* 2013a, Mordehai *et al.* 2011a, Mordehai *et al.* 2011b).

The edge and screw dislocations are not stable in a spherical crystallite and the Shockley partials tend to leave the crystallite during relaxation. To make relevant comparisons between relaxed dislocations in the sphere and the Wulff crystallites, the relaxation is stopped after the same number of steps in both configurations (typically 1600 steps for the copper nanocrystal) before the disappearance of the partials from the crystallite (Fig III.9.j). Additionally, the contraction of the surface atoms towards the bulk during relaxation is strongly affected by the change of geometry. For these two reasons, the obtained values of the u_x component of the atomic displacement field (Fig III.9.j) differs from the ones obtained in the Wulff geometry (section III.3.2). We use the extinction condition $\boldsymbol{g}.\boldsymbol{b} = 0$ ($\boldsymbol{g}$ = 2 2 4) to evidence the effect of dissociation. The Bragg peak splits along the Burgers vector direction, and fringes along the normal to the stacking fault ($\boldsymbol{n}$ = [1 1 1]) are clearly evidenced, even though the crystal does not have (1 1 1) facets (Fig III.9.k). Another interesting observation is the similarity of the ratio I_{defect} / I_0 between the two crystallites for all two types of defects.

From these examples, one can conclude that the boundary conditions have only limited influence on CXD patterns. While the shape determines the form factor of the Bragg reflection, yielding for instance strong fringes in faceted crystals, the shape and intensity distribution of the features induced by the defects, generally close to the Bragg position, are only marginally affected. It is important to notice that a logarithmic scale, and therefore a few decades of dynamical range in the data, are needed to characterise the form factor, whereas the defects have an obvious impact on the central part of the pattern if the Bragg reflection is well chosen.

III.3.7. Influence of the defect position

To evidence the effect of the defect position, we chose to focus on two simple defects: a perfect screw dislocation and a stacking fault, both in a 30x30x30 nm^3 copper crystal of Wulff shape. The screw dislocation is introduced at several positions in the crystal: 0, 1, 5 and 10 nm away from the centre of the crystal and the 2 $\bar{2}$ 0 reflection is used to probe the dislocation. As illustrated in Fig. III.10.a, the displacements of the dislocation line induces a considerable effect on the intensity distribution of the calculated diffraction pattern. As the dislocation moves towards the emerging facets of the crystal, the distribution of intensity in reciprocal space becomes highly anisotropic until the ring shaped pattern vanishes when the dislocation reaches one edge of the crystal. The same results could be obtained for an edge dislocation line in both its perfect and relaxed states (not shown here).

Another very important consideration is the unstable character of dislocations which are not introduced close to the centre of the crystallite. According to our calculations in the reference crystallite, for a perfect dislocation introduced more than 3 nm away from the centre, the Shockley partials always leave the crystallite during relaxation. One can then assume that the probability to probe dissociated dislocations far away from the crystallite centre in experimental crystals is very low. This strengthens the relevance of our study since most of the calculations are performed with dislocations introduced at the centre of the crystallite.
As seen in Section , a stacking fault introduced at the centre of the reference crystal leads to a splitting of the central spot and intense fringes along the normal to the (1 1 1) stacking fault plane with a doubling of spacing between fringes. When the stacking fault is placed at the centre of the crystal, the two parts of the object which interfere are equal, yielding a symmetric distribution of intensity in the fringes along the [1 1 1] direction (see Fig 10.b and 10.c.). A stacking fault off the crystal centre splits the volume in two unequal parts and yields an asymmetric distribution of intensity along the [1 1 1] axis. Fig. 10.b indeed shows that a stacking fault splitting the crystal in two volumes such that $V_1 = 4.V_2$ yields an asymmetry of the [1 1 1] fringes intensity distribution which is further increased when the stacking fault is moved towards an edge of the crystal ($V_1 = 8.V_2$). The intensity at the exact Bragg position can be evaluated and, according to Eq. (III.6), as the stacking fault moves away from the centre, the interferences become less destructive and the Bragg position becomes a peak of intensity again, like for the perfect crystal.

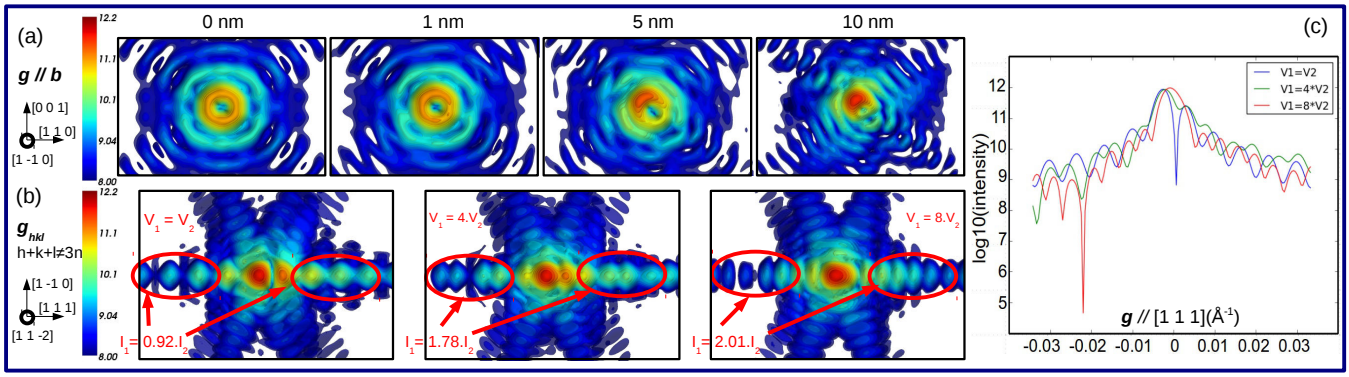

Fig. III.10: (a) Effect of the position of a perfect screw dislocation in a 30x30x30nm^3 copper crystal in a Wulff geometry. At the vicinity of the crystal centre the intensity distribution is altered, and as the dislocation moves towards an edge of the crystal its characteristic signature completely vanishes. (b) Effect of the position of a stacking fault in a 15x15x15 nm^3 copper crystal in a Wulff geometry. The stacking fault position strongly affects fringes intensity and period, and the intensity and splitting of the Bragg reflection. (c) Intensity along [1 1 1] for different positions of the stacking fault in the crystallite. *The selected area of the reciprocal space is kept to the same value in all figures and is equal to 0.045x0.0675 (1/ Å)^2*

This section confirms that the defect position has a very strong effect on the calculated CXD patterns. This effect increases with the distance between the defect and the centre of the illuminated crystal. In the vicinity of the centre, the intensity distribution is strongly altered but a given defect can clearly be identified from its signature on the diffraction pattern. However, close to an edge of the crystal, the characteristic signature of a given defect vanishes, and our ability to identify the defect from its signature in reciprocal space becomes questionable. As a consequence, it is also expected that detailed structure of interfaces (not their associated role as strain generator) will be difficult to characterize since inherently they are located at one boundary of the diffracting crystal.

III.4. Application to a complex case: indentation of a gold nanocrystal

The study of model systems is very useful to understand and interpret the signature induced by a single defect and to demonstrate the influence of the selection of the diffraction vector on CXD patterns. However, interpretations of the pattern can also be deduced for more complex and realistic configurations of defects such -

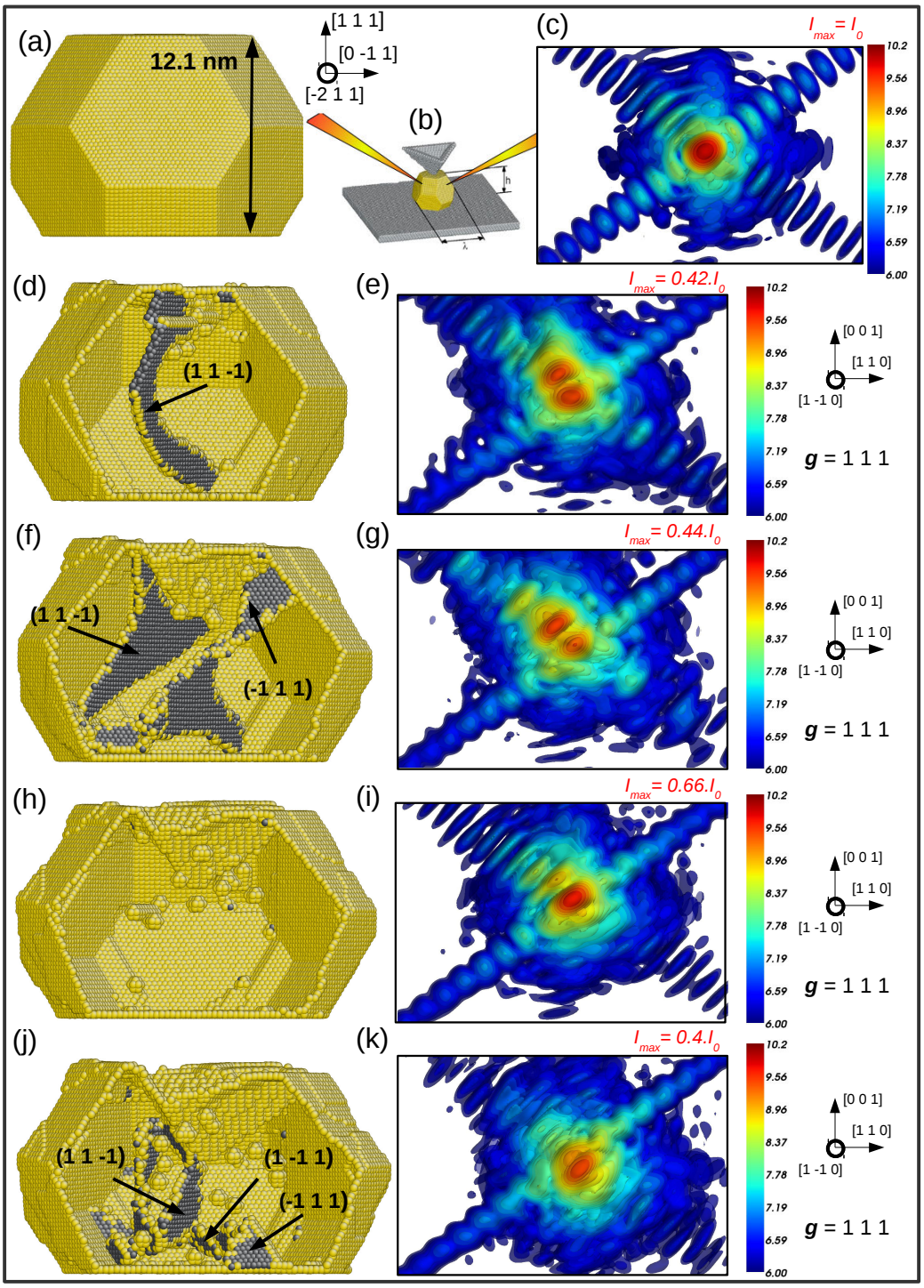

Fig. III.11 (a) Simulation of the indentation of a 12.1 nm high gold nanoparticle by a cube-corner indenter. (b) and (c) Atomistic configuration at the initial state and corresponding CXD pattern (see text for more details) The dislocations are shown in grey. (d) and (e) Gold nanoparticle after 650000 indentation steps (t = 3.25 ns) and calculated CXD pattern. (f) and (g) Gold nanoparticle after 850000 indentation steps (t = 4.25 ns) and calculated CXD pattern. (h) and (i) Gold nanoparticle at t = 5 ns and corresponding CXD pattern. (j) and (k) Gold nanoparticle at the final stages of indentation (t = 6 ns) and corresponding CXD pattern. *The selected area of the reciprocal space is kept to the same value in all figures and is equal to 0.08x0.12 (1/ Å)²*

as the one obtained during plastic indentation of a crystallite. More details concerning the dislocation mechanisms during nano-indentation are given by Mordehai *et al.* (2011b). In the present section, only few key stages of the indentation process and the corresponding CXD patterns in reciprocal space are detailed. Molecular dynamics simulations with the Large-scale Atomic/Molecular Massively Parallel Simulator (LAMMPS, Plimpton 1995) and a Au EAM potential (Grochola *et al.* 2005) are used to simulate the indentation of a 12.1 nm gold nanoparticle on a sapphire substrate (Mordehai *et al.* 2011a, Mordehai *et al.* 2011b).

The Winterbottom construction (Winterbottom 1967) is employed, considering the surface energies of the Au potential and the interface energy to initialize the particle configuration (Fig. III.11.b). The indenter in the simulation is lowered at a constant velocity and the integration step is 5 fs. To avoid the complex atomic description of the particle/substrate and indenter/particle, both the indenter and substrate are assumed non-deformable (satisfying the experimental condition of using exceptionally stiff and hard materials for the substrate and indenter, respectively sapphire and diamond) and are frozen into their perfect crystal locations (Mordehai *et al.* 2011b). The effect of the residual / processing strain induced by the substrate is thus not taken in account in this model.

Figs. III.11.a & III.11.c show the gold particle in its initial state and the corresponding CXD pattern around the Bragg position $\boldsymbol{g}$ = 1 1 1, parallel to its upper facet. These are realistic diffraction conditions. Given the smaller size of the particle compared to the reference crystallite (12.1 nm vs 30nm), the calculation of the 3D CXD pattern is done on a larger volume of the reciprocal space: 0.8x0.8x1.2 (1/ Å)^3. Additionally, the dynamic range is kept to 4.15 decades, but the maximum of intensity is decreased by a factor 100 (10 times less atoms in the particle). Since the crystal is still in its pristine state, the diffraction pattern looks very clean with a maximum intensity at Bragg positions and rather intense fringes along [1 1 1] due to the relatively large size of its (111) facet.

Fig. III.11.d illustrates the atomistic configuration and its corresponding CXD pattern after 650000 steps of indentation (t = 3.25 ns). At this stage of the indentation process, nucleation and glide of multiple dislocations already occurred, leaving short slip steps on the {1 1 1} and {1 0 0} facets. A dislocation half-loop with Burgers vector of type $\boldsymbol{b}$ = ½ <1 1 0> dissociated in partials in one of its {1 1 1} slip planes can be seen at the centre of the volume. When looking at the CXD pattern, this defect induces a strong and characteristic signature with intense fringes along [1 1 $\bar{1}$] due to the stacking fault, and a splitting related to the phase jump induced by the dislocation half loop. One can notice that the period of the defect fringes is approximately twice the period of the facet fringes. As stated in previous sections, this is a good indication of the defect location at the centre of the volume. Additionally, since the upper (1 1 1) facet is compressed, the period of the fringes along this direction slightly increases.

After 850000 steps (t = 4.25 ns) (Fig. III.11.f), dislocations left multiple slip steps on the crystal facets, and multiple dislocation half-loops are found in the crystal. The largest loop is dissociated in partials in the (1 1 $\bar{1}$) and ($\bar{1}$ 1 1) planes, with a Burgers vector along the intersection between these two planes, *i.e.* ½ [1 0 1]. Correspondingly, the CXD pattern displays intense fringes along the [1 1 $\bar{1}$] (Fig. III.11.g) and [$\bar{1}$ 1 1] (not shown) directions. The period of the fringes along [1 1 $\bar{1}$] roughly equals four times that of the facets fringes. One can guess that this is due to the decomposition of two dislocations in the (1 1 $\bar{1}$) slip plane. Similarly to the previous step, we can observe the Bragg peak splitting into two spots, probably due to the phase jump induced by the main dislocation half-loop.

After deeper indentation, around 10^6 steps (t = 5 ns), no more dislocations can be found remaining in the crystallite (Fig. III.11.h). Consequently, the calculated CXD pattern displays a single and clean spot at Bragg position, and SF fringes along [1 1 $\bar{1}$] and [$\bar{1}$ 1 1] have completely vanished. One can notice that the period of the fringes along [1 1 1] increased since the crystal went under further compression.

At the final stages of the simulated indentation process (t = 6 ns), the crystal hosts multiple dislocation loops which decomposed in partials in three out of the four available {1 1 1} slip planes (Fig. III.11.j). The diffraction pattern becomes very difficult to interpret due to the interplay of multiple defects, and the characteristic signatures such as a splitting or intense fringes along one of the <1 1 1> directions cannot be identified. At this

stage, the diffraction pattern is well "speckled" and a statistical interpretation could relay the identification of individual defects as suggested by Favre-Nicolin *et al.* (2010) and Jacques *et al.* (2013).
We now come back to an earlier stage of the indentation (t = 3.25 ns), when a single dislocation half loop can be found in the particle (Fig. III.12). Our goal is to determine the Burgers vector of this loop using the extinction conditions detailed in previous sections. Since this dislocation half-loop is a mixed dislocation, there are no conditions where $\boldsymbol{g}.\boldsymbol{u}$ is exactly zero everywhere (Hirth & Lothe 1968). However one can assume that the condition $\boldsymbol{g}.\boldsymbol{b}$ is sufficient to hide most of the dislocation signature in the dislocation pattern. The Burgers vector of the dislocation half loop is of ½<1 1 0> type, consequently two of the <1 1 1> diffraction vectors must be perpendicular to $\boldsymbol{b}$. When looking at the calculated CXD patterns for four of the eight 1 1 1-type diffraction vectors, one can notice the signature of the defect is only visible for $\boldsymbol{g} = \bar{1}\ 1\ 1$ and $\boldsymbol{g} = 1\ 1\ 1$ whereas no signature can be found for $\boldsymbol{g} = 1\ \bar{1}\ 1$ and $\boldsymbol{g} = 1\ 1\ \bar{1}$ (Fig. III.12). Both diffraction vectors fulfill the extinction criterion and there is only one possible Burgers vector perpendicular to these two directions: $\boldsymbol{b} = ½\ [0\ 1\ 1]$. This demonstrates the possibility to identify both the Burgers vector and the slip plane of a dislocation by the appropriate selection of two, or at most three, diffraction vectors. More generally, this study proves that the technique is adapted to the interpretation of CXD patterns from realistic structures. On the other hand, as shown by the atomistic configuration from the late stages of indentation, the interpretation of CXD patterns from complex structures with multiple defects remains highly challenging due to the interplay between multiple defects on the corresponding CXD pattern.

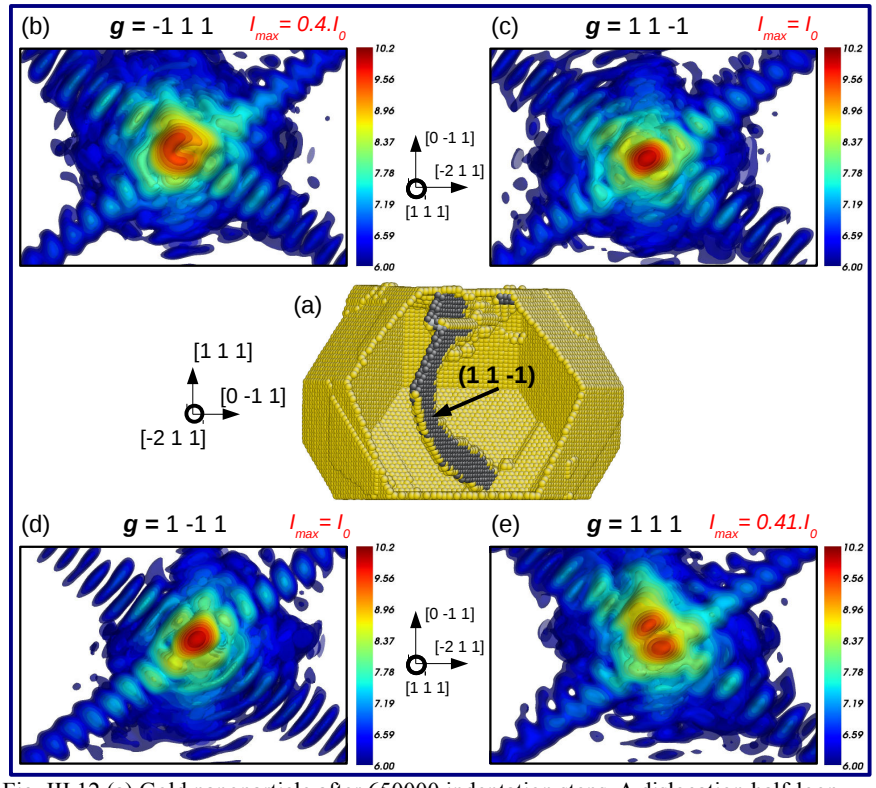

Fig. III.12 (a) Gold nanoparticle after 650000 indentation steps. A dislocation half-loop with $\boldsymbol{b}$ of type ½ <1 1 0> can be observed. (b) to (e) Calculated CXD patterns for four different 1 1 1-type diffraction vectors. *The selected area of the reciprocal space is kept to the same value in all figures and is equal to 0.08x0.12 (1/ Å)²*

III.5. Discussion

The results above show that all typical defects of *fcc* crystals induce strong distortions of the CXD patterns at most Bragg reflections. This holds both for dislocations, which induce a long distance strain field, and for stacking faults, which are nearly strain-free defects. The case of the stacking fault illustrates that coherent X-ray diffraction is properly speaking sensitive to the atomic displacement field and not just the elastic strain: in this case it extends over a semi-infinite volume, hence the localised signature at the Bragg peaks. Even better, each defect has a characteristic signature on particular Bragg peaks, such that it can in principle be unambiguously identified from the measurement of one or several reflections: for instance, the characteristic CXD pattern of a perfect screw dislocation at a Bragg reflection not perpendicular to the Burgers vector leaves no ambiguity on the nature of the defect and its Burgers vector; similarly, characteristic fringes at reflections with $h \pm k \pm l \neq 3n$ indicates the presence of a stacking fault and reveals its orientation. While these two cases are quite straightforward, the identification can be much more delicate for defects which display complex diffraction patterns such as Frank or Prismatic loop. For the latter it appears clearly that several reflections are needed in order to guess what kind of defect the system hosts. For instance, a relaxed Frank loop can be efficiently identified by using two reflections parallel to a partial stair-rod and a partial Shockley. Similarly to what has been observed from the elastic diffuse scattering of dislocation loops, the interstitial or vacancy character of a Frank loop (or the intrinsic or extrinsic character of a Stacking Fault) can also be identified using coherent X-ray diffraction.

For both screw and edge dislocations, the technique can also be used to unambiguously evidence the dissociation into Shockley partials with two very clear and identifiable effects: elongation and splitting of the Bragg peak along $\boldsymbol{b}$ and doubling of the fringes period in the direction perpendicular to the dissociation plane (sections 3.1 and). The dissociation of the dislocation is best evidenced using reflections of high indices, and preferably perpendicular to the Burgers vectors. One can infer that, more generally, such measurement is sensitive to the core structure of the dislocation, since it influences the spatial shift between two sub-volumes of the crystal.

Moreover, even reflections that do not show any distortion can be very useful in establishing the characteristic features of a crystal defect: a wise use of invisibility criteria allows the determination of a dislocation Burgers vector and dissociation plane using only a couple of well chosen reflections. This holds in principle for any kind of single defects that can be encountered in *fcc* materials.

Based on these results, we propose an experimental strategy to identify and characterize a single defect in a *fcc* crystal.

The first step would be to measure several 1 1 1-type reflections in order to distinguish between dislocations and stacking faults / Frank loops: if the defect is a stacking fault or a Frank loop, the defect signature should vanish for only one pair ($\boldsymbol{g}$,-$\boldsymbol{g}$) of these reflections and be visible for every other 1 1 1 reflection, whereas it will be invisible for two pairs ($\boldsymbol{g}$,-$\boldsymbol{g}$) if it is a dislocation. In the first case, a Frank loop is easily distinguished from the stacking faults by the strong distortion at the Bragg position. In the case of dislocations, the Burgers vector can be determined by identifying the two pairs ($\boldsymbol{g}$,-$\boldsymbol{g}$) out of four for which the signature is visible. Until this stage the character of the dislocation does not matter. Once the Burgers vector is established, the use of a reflection $\boldsymbol{g} \,//\, \boldsymbol{b}$ will allow to determine the character of the dislocation. A prismatic loop is identified by simultaneous evidence for edge and screw dislocations.

Following this procedure it is *in principle possible to determine all the characteristics of a given single defect:* for a dislocation, its type, Burgers vector, dissociation plane, dissociation length and an estimate of its position; for a stacking fault, the faulted plane, its extrinsic or intrinsic character (vacancy or interstitial type in the case of a Frank dislocation loop) and a rough estimate of its position.

Regarding experimental matters, it turns out that a high dynamical range is not needed during measurements. In cases presented here, a single decade of intensity is enough to evidence a distortion or a split of the Bragg peak, and two decades suffice to evidence a modification of fringes due to a stacking fault. The counting time can thus

be significantly reduced, making easier the live monitoring of deformation mechanisms (in such case however, the choice of the Bragg reflection for live monitoring implies that some defects remain invisible). The direct analysis of the reciprocal space is thus very complementary to real space reconstruction, which requires longer counting times.

An important concern regarding the experimental set-up is our ability to resolve the features induced by defects during coherent X-ray diffraction experiments. In fact, the fundamental size of the finest diffraction features on CXD patterns is determined by the size of the diffracting volume (*i.e*. the sample or the beam size, depending on which is the smaller one). If the experimental setup allows to sample the reciprocal space with a step size small enough to resolve the fringes induced by the finite size of a perfect crystal, it is also able to resolve any kind of defect signature in a faulted crystal of the same size, independently of the nature and the number of defects. For instance, the splitting distance (i.e, the distance between the two maxima of intensity of the splitted Bragg peak) induced by a dislocation is of the same order of magnitude as the fringe period is related to the crystal size.

Additionally, direct analysis of the reciprocal space relies on the comparison between simulation and experimental data. Even if valuable information can be already extracted from the 2D cut of the detector plane, this approach implies most of the time to record the full 3D CXD pattern in order to produce the needed 2D cuts of the reciprocal space. For typical CXD experiments in Bragg geometry with crystal whose size is around 300nm (Beutier *et al.* 2013a, Watari *et al.* 2011), the acquisition of a 3D CXD pattern which fulfills the oversampling conditions in the 3 directions of the space imply to probe the recipocal space with an extent of approximately ±0.5° and steps of 0.01° (100 points in total). To achieve a dynamical range between 4 and 5 decades of intensity, the usual exposure time lies between 2 and 5 seconds for each point of the rocking curve, and between 200 and 500 seconds for the acquisition a full 3D CXD pattern.

For a direct analysis of CXD patterns we suggested that a single decade of intensity is sufficient to evidence a distortion or a splitting of the Bragg peak while 2 decades are needed for the modification of fringes due to a stacking fault. The acquisition time can thus be reduced at least by a factor 50 (0.1s or even less per point). It would thus only need 4 to 10 seconds (50 seconds due to the detector deadtime) to perform the acquisition of a full 3D CXD pattern. With only one decade of intensity, the 3D reconstruction of the experimental data is not likely to provide a complete and accurate picture of the strain and defect distributions, while the analysis of the reciprocal space pattern can already provide some information on the latter. To obtain the same kind of dynamical range for 30 nm crystal (size comparable to the molecular statics simulations), the acquisition time has to be multiplied by 1000. However for a 300 nm crystal a 0.1s acquisition time provides almost 3 decades of intensity. In principle the acquisition time can be divided by a factor 2 or 3 if one wants to evidence the perturbations in the crystal fringes, and even 20 to 30 to highlight the splitting or distortion of the Bragg peak.

One could also wonder if these calculations, performed on *fcc* metals, are valid for other crystal structures such as hexagonal or body-centred cubic lattices. In the latter, the dislocation structure, its motion and relaxation, are very different from *fcc* crystals. The calculations performed on dissociated dislocations should in principle not be valid for such crystalline structure. However it appears reasonable to think that the simulations performed for the perfect dislocations and stacking faults are still correct: these perfect defects are described by simple geometric models; only the Burgers vector may differ in other crystal structures. In the case of stacking faults, it induces a different phase shift, hence a different contrast, but modulated streaks are still expected, provided the planar geometry of the stacking fault is stable. Different extinction conditions than $h+k+l=3n$ will apply. Several works on materials with the wurtzite and the zinc-blende structures (Chamard *et al.* 2008, Favre-Nicolin *et al.* 2010, Jacques *et al.* 2013) have shown that the phase jump induced by stacking faults in these crystal structures is the same as in *fcc* structures ($\pm 2\pi/3$ depending on the number of faulted planes and the *hkl* indices of the reflection). In the case of the perfect edge and screw dislocations, the displacement fields scale with the Burgers vector, such that the contrast of characteristic features may be different.

If this study establishes the efficiency of CXD to probe single defects, it does not address the case of multiple defects which can be encountered in various experimental samples. Very few studies have been carried out so far on multiple defects and they only focus on the case of stacking faults. In such complex systems a wise use of the

invisibility conditions can provide very useful information on the defect content and density. Alternatively, as pointed out in section and section 4, a statistical approach can be used to get relevant information about dislocation density and their distribution (Jacques *et al.* 2013) or about the stacking fault sequence (Favre-Nicolin *et al.* 2010).
A further complication is the interaction of the defects with residual strain in the sample, due for instance to the growth process. Here we discarded this complication to focus on the defects, but in many realistic cases it is a crude approximation and the calculations presented here are for instance not suited to the case of interface dislocations. The study of crystallites in epitaxial relationship with their substrate, resulting in inhomogeneous strain distribution with a significant contribution of the latter on CXD patterns (Diaz *et al. 2010,* Beutier *et al.* 2012, Mastropietro *et al.* 2014) could be a further development. This would allow to make comparisons with more realistic experimental cases even if disentangling the contributions of interface strain and defects appears quite challenging.

III.6. Conclusions

We carried a detailed numerical analysis of the effect of defects in *fcc* nanocrystals on their CXD patterns in the vicinity of allowed Bragg reflections. Realistic atomic potentials were used to equilibrate the structures. Our analysis demonstrate the *unique character of the signature* induced by a single defect and the *crucial importance of the diffraction conditions i.e.*, the selection of the diffraction vector. The relaxation of the faulted crystal structure is shown to have a large impact on CXD patterns. From these characteristic signatures, we suggest a procedure based on the measurement of a few reflections to identify a defect and its characteristics when it is known that it is alone in the structure.
We also extended the scope of this study to nanocrystals containing a few defects by analysing the case of a gold nanocrystal undergoing simulated indentation: we demonstrated that the defects generated in the early stages of indentation can in principle be identified by the study of CXD patterns at several chosen reflections. The use of invisibility conditions proves to be particularly efficient on such complex systems.
Such direct analysis of the reciprocal space requires significantly lower counting times than phase retrieval imaging methods and is well suited to the live monitoring of the nucleation of defects (for instance to study deformation mechanisms during *in situ* loading experiments).

Acknowledgements

This work was supported by the French ANR MECANIX (ANR-11-BS10-0014).

Bibliography

Balluffi, R. W. (1978). *J. Nucl. Mater.* **240**, 69-70.

Barchuk, M., Holỳ, V., Miljević, B., Krause, B., Baumbach, T., Hertkorn, J. & Scholz, F. (2010). *J. Appl. Phys.* **108**, 043521.

Bei, H., Shim, S., Pharr, G. M., & George, E. P. (2008). *Acta. Mater.* **56**, 4762-4770.

Beutier, G., Verdier, M., Parry, G., Gilles, B., Labat, S., Richard, M. I., Cornelius, T., Lory, P. -F., Vu Hoang, S., Livet, F., Thomas, O. & De Boissieu, M. (2013a). *Thin Solid Films* **530**, 120-124.

Beutier, G., Verdier, M., De Boissieu, M., Gilles, B., Livet, F., Richard, M. I., Cornelius, T. W., Labat, S. & Thomas ., O. (2013b). *J. Phys .Conf. Series* **425**, 132003.

Carter, C. B. & Ray, I. L. nF. (1977). *Phil. Mag* **35**, 189.

Chamard, V., Stangl, J., Labat, S., Mandl, B., Lechner, R. T. & Metzger, T. H. (2008). *J. Appl. Cryst.* **41**, 272-280.

Chassagne, M., Legros, M. & Rodney, D. (2011). *Acta Mater.* **59**, 1456-1463.

Cockayne, D. J. H., Jenkis, M. L. & Ray, I. L. nF. (1971). *Phil. Mag.* **24**, 1383-1392.

Dederichs, P. H. (1971). *Phys. Rev. B* **4**, 1041-1050.

Dederichs, P. H., (1973). *J. Phys.* **F3**, 471-496.

Diaz, A., Chamard, V., Mocuta, C., Magalhães-Paniago, R., Stangl, J., Carbone, D., Metzger, T. H. & Bauer, G. (2010). *New J. Phys.* **12**, 035006.

Ehrhart, P., Trinkaus, H., & Larson, B. C. (1982). *Phys. Rev. B* **25**, 834-848.

Favre-Nicolin, V., Mastropietro, F., Eymery, J., Camcho, D., Niquet, Y. M., Borg., B., Messing, M. E., Wemersson, L., Algra, R. E., Bakkers, E. P. A., Metzger, T. H., Harder, R. & Robinson, I. K. (2010). *New J. Phys.* **12**, 035013.

Favre-Nicolin, V., Richard, M. I. & Renevier, H. (2011). *J. Appl. Cryst.* **44**, 635-640.

Fultz, B. & Howe, J. (2007). *Transmission Electron Microscopy and Diffractometry of Materials*, edited by Springer Berlin Heidelberg New York, third edition ISBN: 978-3-540-73885-5.

Gailhanou, M. & Roussel, J. M. (2013). *Phys. Rev. B* **88**, 224101.

Godard, P., Carbone, G., Allain, M., Mastropietro, F., Chen, G., Capello, L., Diaz, A., Metzger, T.H. , Stangl, J. & Chamard, V. (2011). *Nature comm*. **2**, 568.

Grochola, G. S., Russo, P. & Snook, I. K. (2005). *J. Chem. Phys.* **123**, 204719.

Groves, G. & Kelly, A. (1963). *Phil. Mag.* **8**, 877-887.

Head, A. K., Loretto, M. H. & Humble, P. (1967). *Phys. Stat. Solid.* **20**, 505-519 & 521-536.

Hirth, J. & Lothe, J. (1968). *Theory of dislocations*, edited by McGraw-Hill, New York.

Hruszkewycz, S. O., Holt, M. V. , Murray, C. E., Bruley, J., Holt, J., Tripathi, A., Shpyrko, O. G., McNulty, I., Highland, M. J. & P. H. Fuoss (2012). *Nano Lett.* **12**, 5148-5154.

Huang, W. J., Sun, R., Tao, J., Menard, L. D., Nuzzo, R.G. & Zuo, J. M. (2008). *Nature Materials* **7**, 308-313.

Hull, D. & Bacon, D. J. (2001). *Introduction to dislocations,* edited by Butterworth-Heinemann, Fourth edition.

Jacques, V. L. R., Le Bolloc'h, D., Ravy, S., Giles, C., Livet, F. & Wilkins, S. B. (2009). *Eur. Phys. J. B* **70**, 317-325.

Jacques, V. L. R., Ravy, S., Le Bolloc'h, D., Pinsolle, E., Sauvage-Simkin, M. & Livet, F. (2011). *Phys. Rev. Lett.* **106**, 065502.

Jacques, V. L. R., Carbone, D., Ghisleni, R. & Thilly, L. (2013). *Phys. Rev. Lett.* **111**, 065503.

Jenkins, M. L. (1972). *Phil. Mag.* **26**, 747-751.

Kirk, M. A., Davidson, R. S., Jenkins, M. L. & Twesten, R. D. (2005). Phil. Mag. **85**, 497-507.

Kirk, M. A., Jenkins, M. L., Zhou, Z., Twesten, R. D., Sutton, A. P., Dudarev, S. L. & Davidson, R. S. (2006). *Phil. Mag.* **86**, 4797-4808.

Krivoglaz M. A., (1969). *Theory of X-Ray and Thermal Neutron Scattering by Real Crystals*, edited by New York Plenum Press.

Larson, B. C. & Schmatz, W., (1980). *Phys. Stat. Sol. B* **99**, 267-275.

Larson, B. C. & Young, F. W. (1987). *Phys. Stat. Sol. A* **104**, 273-286.

Le Bolloc'h, D., Ravy, S., Dumas, J., Marcus, J., Livet, F., Detlefs, C., Yakhou, F. & Paolasini, L. (2005). *Phys. Rev. Lett.* **95**, 116401.

Livet, F. (2007). *Acta. Cryst.* **A63**, 87-107.

Mastropietro, F., Carbone, D., Diaz, A., Eymery, J., Sentenac, A., Metzger, T. H., Chamard, V. & Favre-Nicolin, V. (2011). *Opt. Soc. of Amer.* **19**, 19223.

Mastropietro, F., Eymery, J., Carbone, G., Baudot, S., Andrieu, F. & Favre-Nicolin, V. (2013). *Phys. Rev. Lett.* **111**, 215502.

Miao, J., Charalambous, P., Kirz, J. & Sayre, D. (1999). *Nature* **400**, 342-344.

Minkevich, A. A., Baumbach, T., Gailhanou, M. & Thomas, O. (2008). *Phys. Rev. B* **78**, 174110

Mishin, Y., Farkas, D., Mehl, M. J. & Papaconstantopoulos, D. A. (1999). *Phys. Rev. B* **59**, 3393-3407.

Mishin, Y., Mehl, M. J., Papaconstantopoulos, D. A., Voter, A. F. & Kress, J. D. (2001). *Phys. Rev. B* **63**, 224106.

Moisy-Maurice, V., & De Novion, C. H., (1981). *Sol. Stat. Comm.* **39**, 661-665.

Mordehai, D., Lee, S. W., Backes, B., Srolovitz, D. J., Nix, W. D. & Rabkin, E. (2011). *Acta Mater.* **59**, 5202-5215.

Mordehai, D., Kazakevitch, M., Srolovitz, D. J. & Rabkin, E., (2011). *Acta Mater.* **59**, 2309-2321.

Newton, M. N., Leake, S. J., Harder, R. & Robinson, I. K. (2010). *Nature Materials* **9**, 120-124.

Nordlund, K., Partyka, P. R., Averback, S., Robinson, I. K. & Ehrhart, P. (2000). *J. Appl. Phys.* **88**, 2278-2288.

Pfeifer, M. A., Williams, G. J., Vartanyants, I. A., Harder, R. & Robinson, I. K., (2006). *Nature* **442**, 63-66.

Plimpton, S. J. (1995). *J. Comp. Phys.* **117**, 1.

Proudhon, H., Vaxelaire, N., Labat, S., Forest S. & Thomas, O. (2010). *C. R. Phys.* **11**, 293-303.

Rasmussen, T., Jacobsen, K. W., Leffers, T. & Pedersen, O. B. (1997). *Phys. Rev. B* **56**, 2977.

Robinson, I. K., Da, Y., Spila, T. & Greene, J. E. (2005). *J. Phys. D: Appl. Phys.* **38**, A7-A10.

Robinson, I. K. & Harder, R. (2009). *Nature Materials* **8**, 291-298.

Rodenburg, J. M. & Faulkner, H. L. M. (2004). *Appl. Phys. Lett.* **85**, 4795-4797

Rodney, D., Fivel, M. & Dendievel, R. (2005). *Phys. Rev. Lett.* **95**, 108004.

Sadan, H. & Kaplan, W. D. (2006). *J. Mater. Sci.* **41**, 5099-5107.

Sayre, D. (1952) *Acta. Cryst.* **5**, 843.

Schroer, C. G., Boye, P., Feldkamp, J. M., Patommel, J., Schropp, A., Schwab, A., Stephan, S., Burghammer, M., Schoder, S. & Riekel, C. (2008). *Phys. Rev. Lett.* **101**, 090801.

Smallman, R. E. & Green, D. (1964). *Acta Metall.* **12**, 145-154

Steeds, J. W. (1966). *Proc. Roy. Soc. Lond. Ser. A* **292**, 1430.

Stoller, R. E., Kumar, A. S., Gelles, D. S. (1992). *Effect of radiation on materials.*

Sutton, M. (2008). *C. R. Physique* **9**, 657-667.

Takahashi, Y., Suzuki, A., Furukatu, S., Yamauchi, K., Kohmura,Y. & Ishikawa, T. (2013). *Phys. Rev. B* **87**, 121201.

Trinkaus, H., (1972). *Phys. Stat. Sol. B* **51**, 307-319

Vaxelaire, N., Labat, S., Chamard, V., Thomas, O., Jacques, V. L. R., F. Picca, Ravy, S., Kirchlechner, C. & Keckes, J. (2010). *Nucl. Instr. and Meth. in Phys. Res. B* **268**, 388-393.

Westmacott, K. H. & Peek, R.L. (1971). *Phil. Mag.* **23**, 611.

Wiliams, D. B., & Carter, C. B. (1996). *Transmission Electron Microscopy*, edited by New York Plenum Press.

Williams, P. L., Mishin, Y. & Hamilton, J. C. (2006). *Model. Simul. Mater. Sci. Eng.* **14**, 817-833.

Wilson, A. J. C. (1952). *Acta. Cryst.* **5**, 318.

Wilson, A. J. C. (1955). *Nuovo Cimento* **1**, 277.

Winterbottom, W. L. (1967). *Acta Metall.* **15**, 303.

Ying, Y. A., Staley, N. E., Xin, Y., Sun, K., Cai, X., Fobes, D., Liu, T. J., Mao, Z. Q. & Liu, Y. (2013). *Nature comm*. **4**, 2596.

Zhe, R., Mastropietro, F., Davydok, A., Langlais, S., Richard, M.-I., Furter, J.-J., Thomas, O., Dupraz, M., Verdier, M., Beutier, G., Boesecke, P. & Cornelius, T. W. (2014). *J. Synchrotron Rad.* **21**, 1128-1133.

Zhou, Z., Sutton, A. P., Dudarev, S. L., Jenkins, M. L. & Kirk, M. A. (2005). *Proc. R. Soc.* A **461**, 3935-3953.

Chapter IV: Coherent X-ray diffraction applied to moderately complex systems. Comparison of the direct analysis of the CXD patterns and reconstruction of the displacement field methods.

Contents

Introduction....123
IV.1. Case of quantitative determination of a loop size and geometry....123
IV.1.1. Determination of the interstitial or vacancy character of a defect....123
IV.1.2. Determination of the size of a dislocation loop....126
IV.2. Analysis of the CXD pattern of a moderately complex system: nanoindentation of a Nickel thin film....127
IV.3. Case of a system with multiple stacking faults in equivalent slip planes....133
Conclusion....137
Bibliography....139

Chapter IV: Coherent X-ray diffraction applied to moderately complex systems : analysis of the reciprocal space patterns

Introduction

Chapter III demonstrates that coherent X-ray diffraction (CXD) is particularly suited to the study of individual defects. In particular, it is shown that single crystal defects have a unique characteristic signature on CXD patterns, and that the selection of the diffraction vector is of crucial importance in order to highlight the fingerprint of such defects. The case study of the simulated nanoindentation of a gold nanoparticle evidences that the direct analysis of CXD pattern can be used in a more complex and realistic system, however in this simulation, only one defect is present in a structure. Hence, the case of multiple defects was not adressed in the previous Chapter.

In the following, we aim at establishing that the study of the coherent X-ray scattering of a moderately complex assembly of defects can provide valuable information on the defect type, content, geometry and size distribution. In a first part, following the procedure described by Erhart *et al.* (1982) and Larson & Young (1987) we show the sensitivity of CXD to the size and vacancy or interstitial type of individual dislocation loops and we demonstrate that it can be extended to the case of stacking faults (SF). The case of multiple defects is addressed through two examples, the simulated nanoindentation of a nickel thin film which nucleate several prismatic dislocation loop types with equivalent Burgers vectors, and the simulated liquid state dewetting of a copper particle on a tantalum substrate which creates a complex network of stacking faults.

IV.1. Case of quantitative determination of a loop size and geometry

Calculations of diffuse scattering performed on perfect (prismatic) and partial (Frank) dislocation loops in f.c.c. metals (Erhart *et al.* 1982) and semiconductors (Nordlund *et al.* 2000) already provided a very accurate picture of the scattering which can be expected from such defects. The X-ray diffuse scattering of perfect and Frank dislocation loops has also been studied experimentally by Larson (Larson & Schmatz 1980), (Larson & Young 1987) and is relatively well understood. Their methodology has has been applied to the case of individual perfect and faulted dislocation loops to determine the vacancy or interstitial character of the loops, and to estimate their size.

IV.1.1. Determination of the interstitial or vacancy character of a defect

As illustrated in section III.3.4 and III.3.5, the strain field around faulted Frank and prismatic loops is rather complex, and the evaluation of the scattering from such defects can be difficult. Erhart (Erhart *et al.* 1982) and (Larson & Young 1987) considered this scattering in terms of three distinct parts:

- the Huang diffuse scattering (HDS) induced by the long range part of the strain field and thus limited to small δq in the reciprocal space.
- The asymptotic diffuse scattering (ADS) or Stockes-Wilson scattering resulting from the highly strained region in the close vicinity of the loop plane and thus located in larger δq in the reciprocal space.
- The Structural Diffuse Scattering (SDS) or Laue scattering induced by the core, *i.e* the defective region of the dislocation loop.

The expression of the diffuse scattering $\boldsymbol{A}(\boldsymbol{q})$ resulting from a dislocation loop has been formalized by Larson (Larson & Schmatz 1980, Larson & Young 1987):

$$\boldsymbol{A}(\boldsymbol{q}) = \sum_j e^{i\boldsymbol{q}.\boldsymbol{r}_j^L} + \sum_j e^{i\boldsymbol{\delta q}.\boldsymbol{r}_j}\left(e^{-i\boldsymbol{q}.\boldsymbol{u}(\boldsymbol{r}_j)} - 1\right) \quad \text{(IV.1)}$$

where $\boldsymbol{q}$ is the scattering vector and can be expressed as the sum of the reciprocal lattice vector $\boldsymbol{g}$ and a vector $\boldsymbol{\delta q}$ inside the Brillouin zone: $\boldsymbol{q} = \boldsymbol{g} + \boldsymbol{\delta q}$. $\boldsymbol{r_j}$ is the ideal position of atom j in the undistorted lattice, and $\boldsymbol{r_j} + \boldsymbol{u}(\boldsymbol{r_j})$ the position of atoms *j* in the distorted crystal at the vicinity of the dislocation loop.
The first sum so-called the Laue scattering (StructuralDiffuse Scattering) takes into account the scattering from atoms at positions $\boldsymbol{r_j^L}$ in the dislocation loop. The second sum so-called the total distortion scattering (sum of the HDS and ADS) is obtained by subtracting the scattered amplitude associated with the perfect crystal from the total scattered amplitude (hence the -1 term). The distortion scattering can be considered as two terms, with a $1/q^2$ dependence close to the Bragg peak (Huang Diffuse scattering in the $q << 1/R$ region where R is the radius of the loop) and a $1/q^4$ dependence further away from the Bragg peak (Asymptotic Diffuse Scattering (ADS) or Wilson-Stockes Scattering in the $q > 1/R$ region).

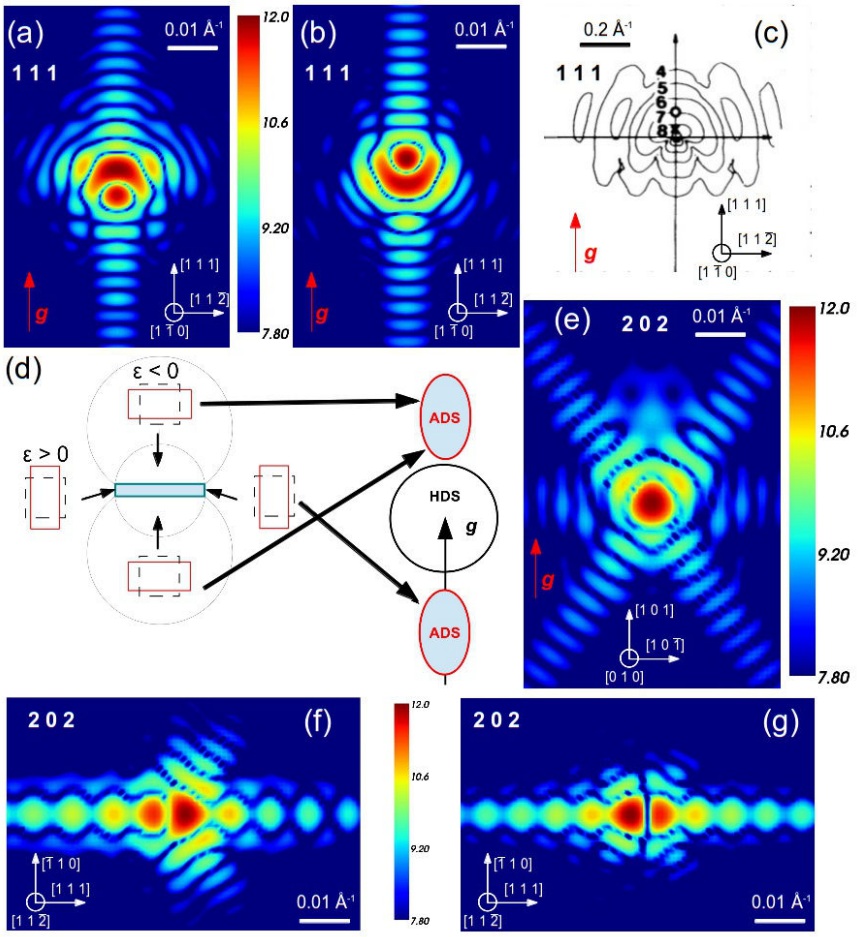

Fig. IV.1 Calculated CXD pattern from an interstitial (a) and a vacancy (b) Frank dislocation loop with $\boldsymbol{b}$ = 1/3[1 1 1] and $\boldsymbol{g}$ // $\boldsymbol{b}$ ($\boldsymbol{g}$ = 1 1 1). (c) Calculation by Erhart *et al.* (1982) of the diffuse scattering in an infinite crystal from an interstitial Frank loop with $\boldsymbol{b}$ = 1/3[1 1 1] and $\boldsymbol{g}$ // $\boldsymbol{b}$ ($\boldsymbol{g}$ = 1 1 1). (d) Scheme of the strain field around an interstitial dislocation loop and corresponding distribution of the diffuse scattering. (e) Calculated CXD pattern from an interstitial prismatic dislocation loop with $\boldsymbol{b}$ = 1/2[1 0 1] and $\boldsymbol{g}$ // $\boldsymbol{b}$ ($\boldsymbol{g}$ = 1 0 1). Calculated CXD patterns for an intrinsic (f) and extrinsic stacking fault (g) for $\boldsymbol{g}$ = 2 0 2 (h + k + l ≠ 3n)

Larson & Young (1987) gave a detailed interpretation of the ADS which allows to distinguish between vacancy and interstitial loops. Fig. IV.1.d, illustrate the lattice strain in the immediate vicinity of the dislocation loop, and the corresponding scattering induced by such lattice distortions. For an extrinsic interstitial dislocation loop, the extra plane of atoms leads to a compressed region above and below the loop and an expanded region outside the periphery of the loop (this strain distribution is discussed in further details in Chapter V, section V.3.1).
The region in compression exhibits a constant strain over a spherical-like region of diameter roughly that of the loop (Ohr 1974). This compression strain gives rise to a diffuse scattering peak at positive δq. The volume of the expanded region at the periphery of the loop is much smaller, and consequently the diffuse scattering distributed on negative δq values (*i.e* on opposite sides of the reciprocal lattice point) is less intense. Conversely, for an intrinsic vacancy dislocation loop, the missing plane of atoms leads to a tensile region above and below the loop and a compressive region at the periphery of the loop. The diffuse scattering is the most intense at negative δq values.
Erhart *et al.* (1982) evidenced the presence of oscillations in this diffuse scattering peak. They are due to the inversion symmetry of the displacement field for a dislocation loop. Given that $\boldsymbol{u}(\boldsymbol{r}) = -\boldsymbol{u}(-\boldsymbol{r})$, at least two points of the real lattice scatter into one point of the reciprocal lattice. The resulting interferences lead to oscillations in the diffuse scattering peak, the intensity of the scattering depending on the projection of $\boldsymbol{u}(\boldsymbol{r})$ on $\boldsymbol{q}$. Additionally, since the overall form of the scattering in this region (ADS or Stockes-Wilson scattering) varies as $\sim 1/q^4$. The oscillations in the diffraction pattern are best seen for a scaling of the intensity by q^4 (not shown in Fig. IV.1).
Fig IV.1.a & IV.1.b show the calculated CXD pattern from a 25 nm interstitial (Fig. IV.1.a) and a vacancy (Fig. IV.1.b) Frank dislocation loop in a 30 nm copper nanocrystal of Wulff geometry. Both loops are in the (1 1 1) plane with $\boldsymbol{b} = 1/3[1\ 1\ 1]$ and the distribution of the scattering is shown in the vicinity of $\boldsymbol{g} = 1\ 1\ 1$ in the $[1\ \bar{1}\ 0]$ plane of the reciprocal space. Unlike in Eq. (IV.1) the scattered amplitude from the perfect crystal is not removed from the calculation.
As already shown in subsection III.3.4, the signature of the [1 1 1] stacking fault is invisible on the CXD pattern for this particular $\boldsymbol{g}$ ($h+k+l = 3n$), and the spacing between the fringes due to the crystal finite-size remains undisturbed. The diffuse scattering from both loops has a distinct signature and is concentrated above and below the 1 1 1 Bragg position for the interstitial and vacancy loops respectively. Apart from the oscillation fringes along the [1 1 1] direction due to the finite size of the crystal, the calculated diffraction pattern is similar to the calculations performed by Erhart *et al.* (1982) on a Frank dislocation loop oriented along the [1 1 1] axis in an infinite crystal (Fig. IV.1.c).
The interstitial or vacancy character of a prismatic dislocation loop can also be determined from the analysis of the calculated coherent X-ray diffraction pattern. A 15 nm prismatic loop with $\boldsymbol{b} = 1/2[1\ 0\ 1]$ (similar in geometry as the one shown in section 3.5) is introduced in a 30 nm copper crystallite. The calculation of the CXD pattern for $\boldsymbol{g} = [2\ 0\ 2]$ // $\boldsymbol{b}$ (Fig. IV.1.e) reveals that the presence of diffuse scattering along the [2 0 2] direction, while almost no diffuse scattering can be found along the opposite side of the reciprocal lattice, signing the interstitial nature of the prismatic loop.
Finally, it is also possible to deduce the intrinsic or extrinsic character of a stacking fault from a single CXD pattern. The calculation presented in Fig. IV.1 is performed around the 2 2 0 reflection ($h+k+l \neq 3n$). As demonstrated in subsection III.3.3, for a given Bragg reflection, the phase jumps associated to an intrinsic and extrinsic stacking fault in the (1 1 1) plane are respectively equal to $\varphi_i = \frac{2\pi}{3}(h+k+l)$ and $\varphi_e = -\frac{2\pi}{3}(h+k+l)$. For $\boldsymbol{g} = 2\ 2\ 0$, we thus obtain $\varphi_i = \frac{2\pi}{3}$ and $\varphi_e = -\frac{2\pi}{3}$
For this particular reflection the intrinsic stacking fault induce a positive phase jump. As illustrated on Fig. IV.1.e the satellite spot (weakest part of the splitted Bragg peak) is located along the $[\bar{1}\ \bar{1}\ \bar{1}]$ direction, *i.e* the negative δq values with respect to the Bragg position. For an extrinsic stacking fault, the phase jump has a negative value and the same satellite spot is located along the [1 1 1] direction, *i.e* in the positive δq (Fig. IV.1.f).
Conversely, for the 2 0 0 reciprocal lattice point, the phase jumps associated to intrinsic and extrinsic stacking

faults are respectively negative and positive. In this case the position of the satellite spot is along [1 1 1] for the intrinsic stacking fault, and $[\bar{1}\ \bar{1}\ \bar{1}]$ for the extrinsic. In good agreement with previous calculations (Erhart et al. 1982, Larson & Young 1987, Nordlund *et al.* 2000), we thus demonstrated that it is possible to establish the intrinsic (vacancy) or extrinsic (interstitial) type of a large number of defects.

IV.1.2. Determination of the size of a dislocation loop

With an incoherent and large X-ray beam, even if it is not possible to determine the Burgers vectors of individual dislocation loops, or even to distinguish between Frank and prismatic loops, a lot of information can be obtained by a detailed analysis of both the HDS (Erhart et al. 1982) and the ADS (Larson & Young 1987). At large δq the scattering from interstitial and vacancy loops can be completely separated, and the dependency of the strain with the radius of the loop allows to estimate its size with the position of the scattering peak. Calculated diffuse scattering for discrete loop sizes of both type can be used to fit the experimental data and establish the type and size distribution of the loops.

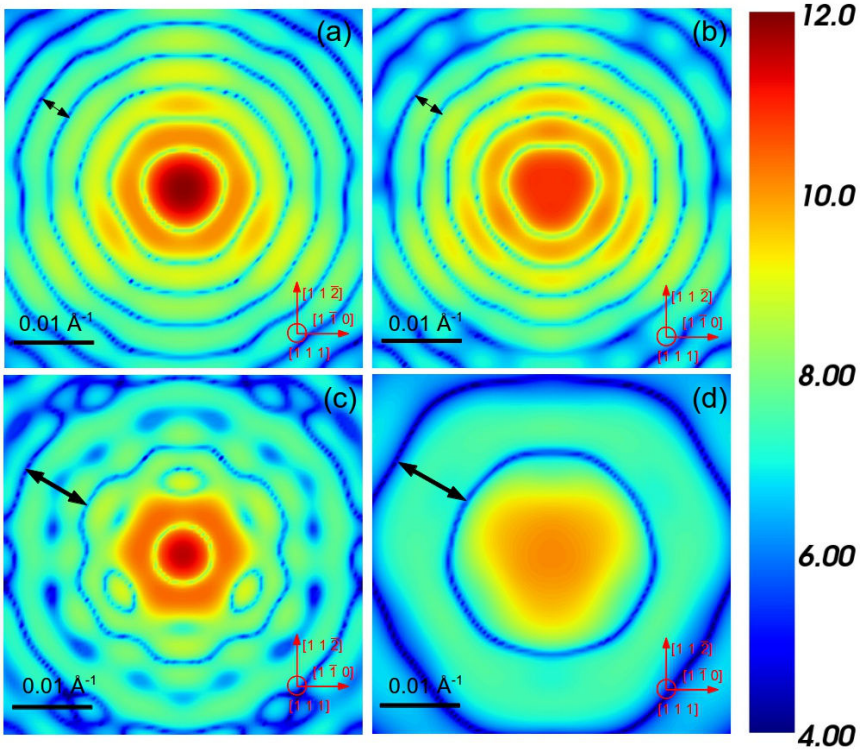

Fig. IV.2 (a) Calculated CXD pattern from a 25 nm (a) and a 10 nm (c) Frank dislocation loop with $\boldsymbol{b}$ = 1/3[1 1 1] and $\boldsymbol{g}$ // $\boldsymbol{b}$ ($\boldsymbol{g}$ = 1 1 1). Laue and total distorsion scattering from the 25 nm (b) and the 10 nm (d) dislocation loops.

A coherent X-Ray diffraction pattern also contains informations about the size of individual dislocation loops. It has been shown (Erhart et al. 1982, Zhou et al. 2005 and Kirk et al. 2006) that the size of a dislocation loop can be determined by the spacing between nodal lines of zero intensity.
According to Erhart (*Erhart et al.* 1982) they correspond to a cylinder of scattering with zero intensity at the zeros of the Bessel function that results from the coherent scattering of a circular loop. These cylinder are perpendicular to the loop axis and appear as concentric rings in a reciprocal lattice plane perpendicular to the loop axis (the (1 1 1) plane in the present study). Here, as illustrated on Fig. IV.2., the hexagonal shape of the

Frank loop is reflected in the shape of the nodal lines.
Fig. IV.2.a & IV.2.c show the calculated CXD pattern in the (1 1 1) reciprocal space plane for a 25 nm and a 10 nm interstitial Frank loop (introduced at the centre of a 30 nm Copper crystal of Wulff geometry) while Fig. IV.2.b and IV.2.d show the sum of the total distortion scattering (HDS + ADS) and of the Laue scattering (SDS) (the amplitude scattered by the perfect crystal is removed, see Eq. (IV.1)) for the same dislocation loops.
The nodal lines of zero intensity appear very clearly on Fig. IV.2.b & IV.2.d, and their spacing is inversely proportional to the size of the loop. They are also visible on the CXD patterns with the same spacing, but the situation is further complicated by the fact they also interfere with the fringes induced by the finite-size of the crystal. For the large loop (Fig. IV.2.a), the loop and the crystal are almost of the same size such that the nodal lines of zero intensity also appear very clearly on the CXD pattern. For the case of loop significantly smaller than the crystal, the periodicity of the fringes related to the size of the crystal largely differ from the periodicity of the nodal lines of zero intensity. This results in a complex interference pattern where two sets of periodic fringes are visible. Nevertheless, the nodal lines are clearly visible in both cases and can be used to calculate the size of the loop. One can notice that the total scattering (Fig IV.2.a) and the diffuse scattering (IV.2.b) patterns are very similar in the case of the large dislocation loop. The loop size (25 nm) is comparable to the size of the crystal (30 nm), and most atoms are either atoms from the loop itself (Laue scattering) or from the distorted lattice surrounding the loop (HDS and ADS scattering). Hence the limited contribution from atoms of the perfect crystal. Conversely, a significant part of the scattering comes from the atoms of the undistorted lattice in the case of the small dislocation loop. The hexagonal shape of the particle is thus clearly visible on the CXD pattern in Fig. IV.2.c.
As illustrated on table IV.1, the loop size determined by the nodal lines spacing is remarkably similar to the size measured directly on the atomistic configurations.

	Vac 125 U.C	Int 125 U.C	Vac 75 U.C	Int 100 U.C	Vac 50 U.C	Int 25 U.C
$d_{measured}$ (nm)	206.2	215.7	115.2	174	71.4	45.5
$d_{nodal\ lines}$ (nm)	204	215	112.1	171	68	43

Tab. IV. 1 *Comparison between the dislocation loops size measured from the atomistic configuration and calculated from the spacing of the nodal lines of zero intensity.* U.C denotes the number of units cells in the loops.

This approach is thus efficient to estimate the size of individual dislocation loops as well as their geometry, Burgers vector and interstitial or vacancy type and has been demonstrated experimentally with the use of a coherent electron beam by Kirk *et al.* (*Kirk et al.* 2005, *Kirk et al.* 2006).
In conventional X-ray diffuse scattering experiments, performed with an incoherent and large beam, the intensity distribution is averaged over many loops and various sizes and orientations. However, with the availability of coherent and microfocused X-ray beams and progress in focused X-ray optics, it should be possible to perform similar studies with X-rays.

IV.2. Analysis of the CXD pattern of a moderately complex system: nanoindentation of a Nickel thin film

The study of the simulated nanoindentation of a gold nanoparticle (section III.4) demonstrated the ability of coherent X-ray diffraction to determine the nature of a given individual defect (Burgers vector, dissociation plane, approximate position of the defect...). However, in the case presented in section III.4, only a single defect is present in the particle at the particular stage of the indentation process. Additionally, given the small size of the particle, the defects nucleated consist of dislocation half loops and not full prismatic dislocation loops which are susceptible to be nucleated upon indentation of a sub-micron f.c.c. particle.

A simulation by molecular dynamics of plastic indentation on a Nickel thin film made in the lab. (Chang *et al.* (2010)) is used to evaluate the informations that can be retrieved by direct analysis of CXD in a moderately complex case. The nickel thin film contains a network of prismatic dislocation loops nucleated on various slip planes. The nanoindentation was carried out along the $[\bar{1}\ \bar{1}\ \bar{1}]$ direction of a nickel f.c.c. thin film and an EAM potential was employed for nickel atoms (Mishin *et al.* 1999). The simulation cell is shown schematically in Fig. IV.3.a. The indenter is modeled by a repulsive sphere with a radius of 120 Å. The size of the crystal is $173 \times 196 \times 162$ Å^3 containing 521642 atoms. The sphere is gradually moved into the crystal in steps of 0.1 Å along the $[\bar{1}\ \bar{1}\ \bar{1}]$ direction, with the bottom atomic layer of the crystal held fixed in that direction (non deformable substrate assumption). Periodic boundary conditions are applied along the $(1\ 0\ \bar{1})$ and $(1\ \bar{2}\ 1)$ sides of the cell. Between each increment, the potential energy of the cell is minimized using a Conjugate Gradient algorithm in order to obtain a succession of quasi-equilibrium states with increasing indentation depths. Additional details about the simulation can be found elsewhere (Chang et al., 2010).

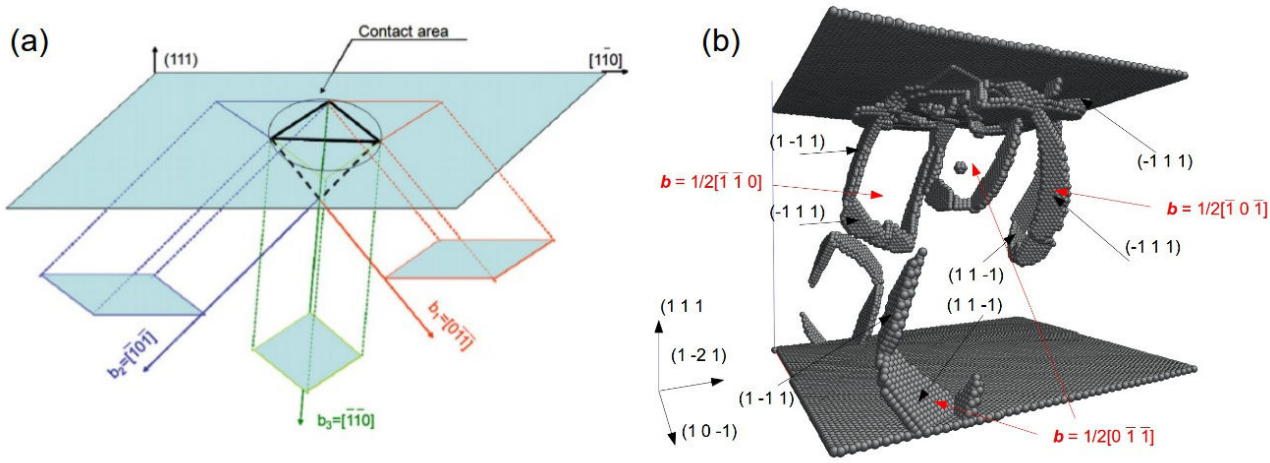

Fig. IV.3 (a) Schematic description of loop nucleation process during [1 1 1] indentation. (b) Atomistic configuration at the end of the simulated nanoindentation. Only defective atoms are shown

The nucleation process of dislocation is rather complex. Defects first appear at a few nanometers below the surface. They first evolve into dislocation lines with Burgers vectors of type ½<1 1 0> and stacking faults in a {1 1 1} plane bordered by two Shockley partials. Two dislocations segments on two slip systems sharing a common Burgers vector form an interstitial prismatic loop. The loops expand in the crystal and eventually detach from the surface. They then move away from the surface along their glide cylinder parallel to their Burgers vector. A complex network of dislocations is left near the surface beneath the indenter. Further indentation produces a more complex network from which prismatic loops are regularly emitted. At the end of the indentation simulation, four distinct prismatic loops in three equivalent variants can be found in the nickel crystal (Fig. IV.3.b). One of them with a Burgers vector of $\boldsymbol{b_1} = \frac{1}{2}[\bar{1}\ \bar{1}\ 0]$ two other with $\boldsymbol{b_2} = \frac{1}{2}[0\ \bar{1}\ \bar{1}]$ and one with $\boldsymbol{b_3} = \frac{1}{2}[\bar{1}\ 0\ \bar{1}]$. As illustrated on Fig. IV.3.a, the loops plastically accommodate a net displacement along the [1 1 1] direction of indentation and the projection of their glide cylinders covers the contact area with the indenter. Once introduced in the crystal, each prismatic loop induces plastic steps on the indented surface corresponding to a punch along its Burgers vector. The central triangle shared by the three nucleated loops is displaced along the $[\bar{1}\ \bar{1}\ \bar{1}]$ direction as a combination of the three displacements.

In the kinematic theory of diffraction, the scattering amplitude of the individual defects is given by a coherent superposition of the scattering amplitudes resulting from the defect atoms and the displaced lattice atoms in their

neighborhood. With an incoherent x-ray beam the diffuse-scattering intensity arising from a small concentration of randomly distributed lattice defects is obtained by the incoherent summation of the contributions from each defect. As already mentioned in the previous section, a detailed analysis of the diffuse scattering at large δq allows to establish the loop type and size distribution. It is however not possible to determine their detailed geometry and Burgers vector, and to distinguish between a faulted and a perfect dislocation loop.
With a coherent X-ray (or electron) beam, the defects in the probed volume interfere coherently, yielding a complex "speckled" CXD pattern. In the following we aim at establishing the possibility to determine the geometry, size, Burgers vector and interstitial or vacancy of each individual defect, when a small assembly of defects is illuminated with a coherent X-ray beam.
We apply the procedure described in section III.4 to try to determine the Burgers vector of the loops in the crystal. Since several loop with different Burgers vectors can be found in the crystallite, there are no diffraction conditions where $\boldsymbol{g}.\boldsymbol{b} = 0$ for all four loops. Additionally, the profile of the displacement field around prismatic loops is not as straightforward as in the case of perfect line dislocation (where analytical expression of the displacement field can be derived), each loop consist of two dissociated dislocation segments with Shockley partial dislocations.
As stated in section III.3.2, a dislocation is completely invisible for $\boldsymbol{g}.\boldsymbol{b} = 0$ and $\boldsymbol{g}.(\boldsymbol{b}\times\boldsymbol{t}) = 0$ ($\boldsymbol{t}$ being the dislocation line direction). This particular case only occurs for a perfect line dislocation, and when the dislocation is dissociated, a part of the displacement field surrounding the defect is necessarily projected onto the scattering vector. Hence, $\boldsymbol{g}.\boldsymbol{b} = 0$ does not imply $\boldsymbol{g}.\boldsymbol{u} = 0$. Rather than complete invisibility conditions, prismatic loops which fulfill the conditions $\boldsymbol{g}.\boldsymbol{b} = 0$ are expected to induce weak perturbations of the CXD pattern.

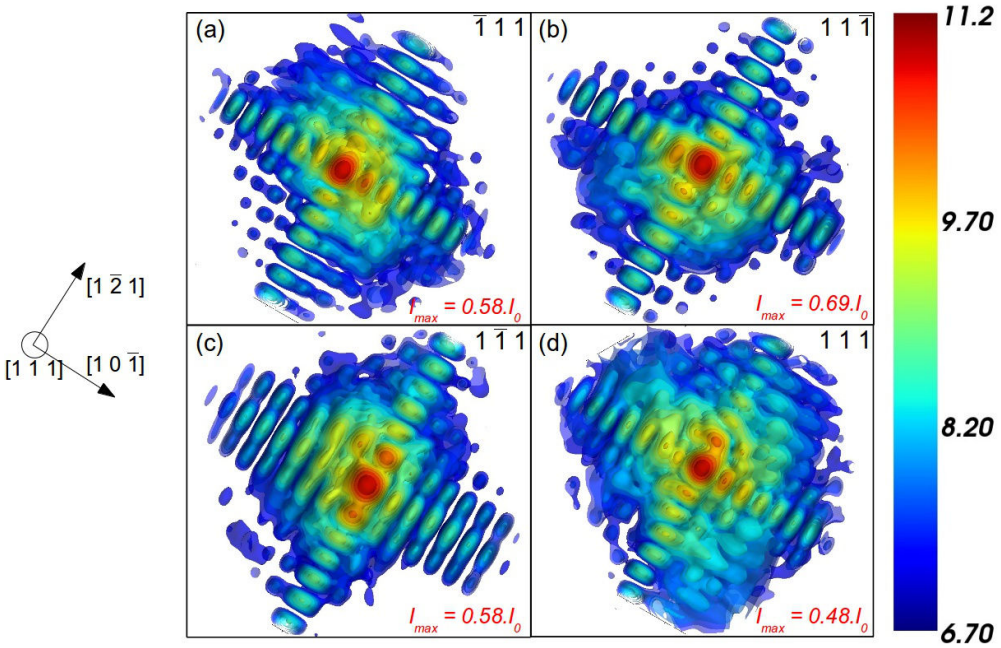

Fig. IV.4 Calculated CXD patterns from the simulated indented for four different 1 1 1-type diffraction vectors. The selected volume he reciprocal space is equal to 0.09x0.09x0.09 (1/Å)^3

We first use non-coplanar 1 1 1-type diffraction vectors. As illustrated in Fig. IV.4, the diffraction patterns displays streaks along the [1 0 $\bar{1}$], [1 $\bar{2}$ 1] and [1 1 1] directions which are fringed due to the finite size of the crystal. Strong interference effects (speckle pattern) between multiple defects can be observed in the diffuse scattering intensity.

For $\boldsymbol{g}$ = 1 1 1, all loops are visible, while only one type is visible for the other {1 1 1} vectors (Tab. IV.2). The strongest effect is thus observed for the 1 1 1 reflection (Fig. IV.4.d) with a large amount of diffuse scattering mainly along the [1 1 1] direction (out of the plane of the figure), and a maximum intensity equal to less than 50% of that of the perfect crystal.

For the other {1 1 1} reflections, the diffraction pattern is less altered with a lower amount of diffuse scattering since only one type of dislocation significantly contributes to the diffuse scattering. The largest perturbations are encountered for both $\boldsymbol{g}$ = 1 $\bar{1}$ 1 (Fig. IV.4.c) when only the dislocation loop with $\boldsymbol{b_3}$ = ½[$\bar{1}$ 0 $\bar{1}$] is visible (lower maximum of intensity: I_{max}= 0.58.I_0) and for $\boldsymbol{g}$ = $\bar{1}$ 1 1 (Fig. IV.4.a) where the two dislocation loops with $\boldsymbol{b_2}$ = ½[0 $\bar{1}$ $\bar{1}$] are visible (I_{max}= 0.58.I_0). Intuitively we would have expected the $\bar{1}$ 1 1 reflection to induce the most significant perturbations on the diffraction pattern. However it should be noted that the $\boldsymbol{b_2}$ loops are smaller than $\boldsymbol{b_3}$ and one of them is very close to the edge of the crystal. We have seen in section III.3.7 that CXD is very sensitive to the defect position and size. For a dislocation loop, it is not surprising to see that a large and central loop induce the same amount of diffuse scattering as two smaller dislocation loops with one of them close to the crystal surface. It should be noted though, that contrary to a single dislocation line, a dislocation loop does not induce a phase shift of two large volumes on each part of the dislocation line, and the position of this type of defect is expected to have a smaller influence, especially if they are small relatively to the size of the crystal (small extent of the displacement field and small size of the phase-shifted volumes).

For the last {1 1 1} reflection, $\boldsymbol{g}$ = 1 1 $\bar{1}$ sensitive to the $\boldsymbol{b_1}$ loop, the decrease of the maximum intensity is less pronounced (I_{max}= 0.68.I_0). This can probably explained by the smaller size of the loop and its position closer to the crystal surface (as compared to the $\boldsymbol{b_3}$ loop). It should be also noted that the conditions $\boldsymbol{g}$. $\boldsymbol{b}$ = 0 does not imply a complete invisibility of the defect and for each reflection the variants that fulfill the invisibility conditions also partially contribute to the perturbations on the CXD patterns. Finally, the contribution of the complex network of dislocations below the surface (rather weak due to their position close to the surface), which also depends on the diffraction conditions, should not be forgotten.

A closer look at the distribution of the intensity (Fig IV.5) of the three reflections reveals that it is mainly distributed for $\boldsymbol{\delta q}$ parallel to $\boldsymbol{g}$, *i.e* along the [$\bar{1}$ $\bar{1}$ 1] direction for $\boldsymbol{g}$ = $\bar{1}$ $\bar{1}$ 1. It is actually slightly disoriented with respect to $\boldsymbol{g}$ in a direction intermediate between $\boldsymbol{g}$ and $\boldsymbol{b}$. Such asymmetry of the scattering is characteristic of interstitial dislocation loops, and from Fig. IV.5., it is clear that all loops within the crystal are interstitial (extrinsic) prismatic dislocation loops.

The Frank or prismatic character of the dislocation loop can also be clearly determined from the analysis of the 1 1 1-diffraction pattern. Provided that the invisibility conditions are not fulfilled (see subsection III.3.3), a diffuse streak of intensity (fringed due to the finite size of the crystal) should be visible along the normal to the{1 1 1} faulted planes. No such feature can be observed on any of the calculated diffraction patterns, which indicates the prismatic nature of the dislocation loops.

The use of four 1 1 1-type reflections validate the presence of several variants of interstitials prismatic loops in the crystallite, the $\boldsymbol{b_3}$ type contributing more to the perturbations observed on the CXD patterns. In section III.3.5 it has been shown that the best conditions to evidence a prismatic dislocation loop are obtained for $\boldsymbol{g}$ // $\boldsymbol{b}$. Three 2 2 0-type reflections are used: $\boldsymbol{g}$ = $\bar{2}$ $\bar{2}$ 0, 0 $\bar{2}$ $\bar{2}$ and $\bar{2}$ 0 $\bar{2}$, respectively parallel to $\boldsymbol{b_1}$, $\boldsymbol{b_2}$ and $\boldsymbol{b_3}$.

Similarly to our observations for the 1 1 1-type $\boldsymbol{g}$ vectors, the maximum effect is observed for $\boldsymbol{g}$ = $\bar{2}$ 0 $\bar{2}$ (Fig. IV.6.b) with the largest decrease of the maximum of intensity (I_{max}= 0.31.I_0 as opposed to I_{max}= 0.37.I_0 and I_{max}= 0.38.I_0 for $\boldsymbol{g}$ = $\bar{2}$ $\bar{2}$ 0 and $\boldsymbol{g}$ = 0 $\bar{2}$ $\bar{2}$). The maximum effect is observed when $\boldsymbol{g}$ is parallel to the Burgers vector of the largest and most central dislocation loop.

As for the 1 1 1-type diffraction vectors, the diffuse intensity is stronger for $\boldsymbol{\delta q}$ parallel to $\boldsymbol{g}$ as expected from interstitial dislocation loops. If all dislocation loops had the same Burgers vector, for instance $\boldsymbol{b}$ = ½[$\bar{1}$ $\bar{1}$ 0], the diffuse scattering would be distributed along the [$\bar{2}$ $\bar{2}$ 0] direction owing to the interstitial type of the dislocation loop. Here the analysis is complicated by the presence of loops with at least three distinct Burgers vector. For a scattering vector parallel to one of them, the displacement field of the loop with $\boldsymbol{g}$ // $\boldsymbol{b}$ has the largest projection onto the scattering vector. However the displacement field from the other loop variants has also some projection on $\boldsymbol{g}$ and as a consequence, the diffuse scattering is not distributed along a specific direction, except for $\boldsymbol{g}$ = $\bar{2}$ 0 $\bar{2}$

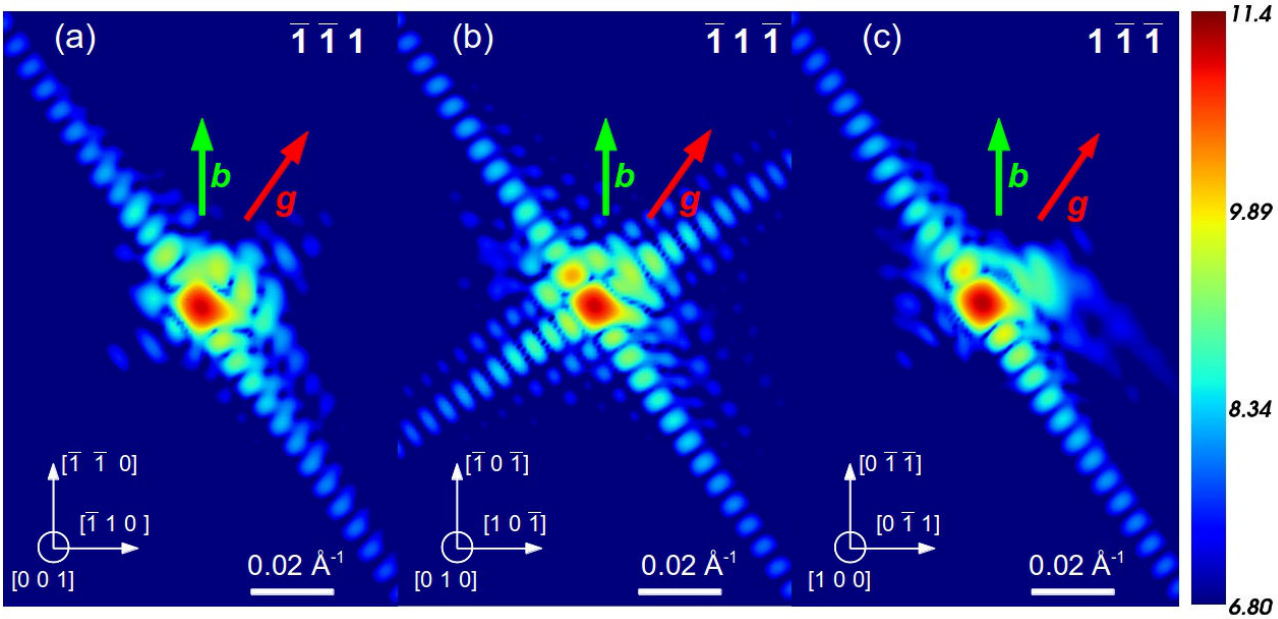

Fig. IV.5 Calculated diffraction patterns from the simulated indented nickel crystal for $\boldsymbol{g} = \bar{1}\,\bar{1}\,1$ (a), $\boldsymbol{g} = \bar{1}\,1\,\bar{1}$ (b) and $\boldsymbol{g} = 1\,\bar{1}\,\bar{1}$ (c)

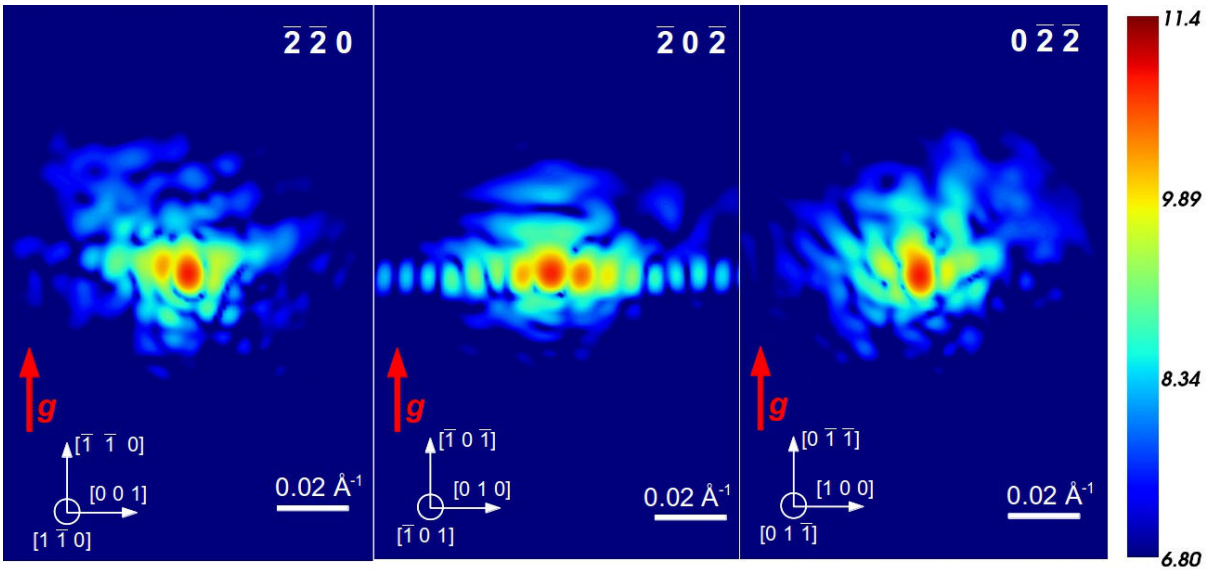

Fig.IV. 6 Calculated diffraction patterns from the simulated indented nickel crystal for $\boldsymbol{g} = \bar{2}\,\bar{2}\,0$ (a), $\boldsymbol{g} = \bar{2}\,0\,\bar{2}$ (b) and $\boldsymbol{g} = 0\,\bar{2}\,\bar{2}$ (c)

where oscillations can be observed along the $\bar{2}\ 0\ \bar{2}$ direction, another evidence that the $\boldsymbol{b_3}$ variant has the strongest contribution on the diffuse scattering. To further refine the analysis of the prismatic loop size and distribution in the crystal, we use 4 2 2-type reflections which correspond to vectors parallel to partial Burgers vector. Table 2 summarize the calculated intensities for three distinct type of scattering vectors (1 1 1, 2 2 0 and 4 2 2), and their angle with respect to the Burgers vectors of the prismatic dislocation loops. The smaller is the angle, the larger is the projection of the displacement field onto the scattering vectors. Tab. IV.2 confirms a very

$\boldsymbol{g}$	I_{max}/I_0	$\boldsymbol{b_1}$ [$\bar{1}\ \bar{1}$ 0]	$\boldsymbol{b_2}$ [0 $\bar{1}\ \bar{1}$]	$\boldsymbol{b_3}$ [$\bar{1}$ 0 $\bar{1}$]
2 2 4	0.115	54.7	30	30
2 4 2	0.150	30	30	54.7
4 2 2	0.117	30	54.7	30
$\bar{2}\ \bar{2}$ 4	0.169	54.7	73.2	73.2
$\bar{2}$ 4 $\bar{2}$	0.124	73.2	73.2	54.7
4 $\bar{2}\ \bar{2}$	0.142	73.2	54.7	73.2
$\bar{2}\ \bar{4}$ 2	0.192	30	73.2	90
$\bar{4}\ \bar{2}$ 2	0.230	30	90	73.2
2 $\bar{2}\ \bar{4}$	0.180	90	30	73.2
2 $\bar{4}\ \bar{2}$	0.234	73.2	30	90
$\bar{2}$ 2 $\bar{4}$	0.150	90	73.2	30
$\bar{4}$ 2 $\bar{2}$	0.126	73.2	90	30
1 1 1	0.479	35.26	35.26	35.26
$\bar{1}$ 1 1	0.580	90	35.26	90
1 $\bar{1}$ 1	0.583	90	90	35.26
1 1 $\bar{1}$	0.687	35.26	90	90
$\bar{2}\ \bar{2}$ 0	0.380	0	60	60
0 $\bar{2}\ \bar{2}$	0.367	60	0	60
$\bar{2}$ 0 $\bar{2}$	0.308	0	60	0

Tab. IV.2 Comparison of the decrease of intensity induced by the three variants of dislocation loop for various diffraction conditions

clear and general tendency. The $\boldsymbol{b_3}$ loop induce the largest perturbations in the CXD patterns, generally followed by the two $\boldsymbol{b_2}$ loops and the smaller $\boldsymbol{b_1}$ loop. For instance, the reduction of the maximum of intensity is much more pronounced for $\boldsymbol{g}$ = $\bar{2}$ 4 $\bar{2}$, for which the angle with $\boldsymbol{b_3}$ is the smallest (as compared to the angle with $\boldsymbol{b_1}$ and $\boldsymbol{b_2}$), than for $\boldsymbol{g}$ = $\bar{2}\ \bar{2}$ 4 (small angle with $\boldsymbol{b_1}$ and large angle with $\boldsymbol{b_2}$ and $\boldsymbol{b_3}$) . For $\boldsymbol{g}$ = 4 $\bar{2}\ \bar{2}$ (small angle with $\boldsymbol{b_2}$ and large angle with $\boldsymbol{b_1}$ and $\boldsymbol{b_3}$). the reduction of the maximum of intensity is intermediate between the two previous cases. The largest decrease of the maximum of intensity is obtained for $\boldsymbol{g}$ = 4 2 2 where the angle with $\boldsymbol{b_2}$ and $\boldsymbol{b_3}$ is minimal while the minimum decrease is found for $\boldsymbol{g}$ = 2 $\bar{4}\ \bar{2}$ normal to $\boldsymbol{b_3}$ ($\boldsymbol{g}.\boldsymbol{b_3}$ = 0) and almost normal to $\boldsymbol{b_1}$.

The detailed study of the CXD patterns from an assembly of prismatic dislocation loop using various diffraction conditions provide valuable information on the nature and content of defects. The absence of diffuse streaks of intensity along any of the <1 1 1> direction allows to determine the prismatic (perfect) nature of dislocation loops. Regarding the interstitial or vacancy type and the size distribution of the loops, Larson (Larson & Young 1987) demonstrated that the detailed analysis of the asymptotic diffuse scattering and a fitting procedure allows the determination of the size distribution and interstitial and vacancy character of an assembly of dislocation loops. To simulate realistic experimental conditions (incoherent X-ray beam), his calculations considered the presence of loops on all equivalent {1 1 1} planes and an incoherent summation of the contribution from each defect. With a coherent-X-ray beam, the interferences between multiple defects produce very complex diffraction patterns, but the interstitial character of the dislocation loops can be clearly established

from our calculations. The methodology described by Larson is clearly more adapted to an incoherent X-ray beam. However, based on the position and intensity of the asymptotic diffuse scattering peak, its methodology could in principle be applicable with a coherent X-ray beam

The use of coherent-X ray beam foresees the possibility to distinguish between various loops orientations. The presence of three different type of prismatic dislocation loops ($\boldsymbol{b_1}$, $\boldsymbol{b_2}$ and $\boldsymbol{b_3}$) is clearly established. While two $\boldsymbol{b_2}$ loops can be found in the crystal (only one $\boldsymbol{b_1}$ and $\boldsymbol{b_3}$), the largest perturbations on the CXD patterns are induced by the $\boldsymbol{b_3}$ loop which is the largest and the most central. It is thus clear that, the effect of a given crystallographic variant of dislocation loops on CXD patterns depends more on the size and central position of the loops rather than their number since a single $\boldsymbol{b_3}$ dislocation loop causes more effect than two $\boldsymbol{b_2}$.

Even with a low number of defects (only four prismatic dislocation loops in the crystal), it appears difficult to determine the number and proportion of the crystallographic variants. It is even more complicated (if not impossible) to determine the Burgers vector, geometry and position of each individual dislocation loop. Additionally, the direct analysis of the CXD patterns implies the use of at least four 1 1 1-type reflections to get useful information about the Burgers vector of the dislocation loops in the structure, and even more to refine the analysis. Measuring such a large number of reflections on the same crystal would be very challenging if not unrealistic experimentally.

IV.3. Case of a system with multiple stacking faults in equivalent slip planes

As already pointed out in Chapter III, stacking faults can be considered as strain-free defects. The signature of such defects on CXD patterns is only due to the phase jump induced by the removal or insertion of densely-packed {1 1 1} planes, and can be even evaluated analytically (subsection III.3.3). If CXD has been so far mostly limited to systems containing one or few defects, a couple of experimental studies have successfully demonstrated the ability of the technique to investigate systems containing multiple stacking faults (Favre-Nicolin *et al.* 2011, Jacques *et al.* 2013). In these two studies, the SF are distributed in only one of the {1 1 1} crystallographic planes. In the present work we aim at demonstrating that CXD can also be used for complex network of stacking faults, distributed on several {1 1 1} crystallographic planes

The atomic simulation of the liquid state dewetting of a copper island which is presented in further details in Chapter IX provides a good example of such complex network of stacking faults. Such networks are often experimentally found in strain relaxation of very thin films/small scale structure. In our simulation, driven by the high lattice mismatch between the f.c.c. copper atoms and the underlying b.c.c. tantalum substrate, partial dislocations are nucleated at the substrate particle interface. The leading partial propagate in the crystal until it reaches the top surface, leaving a stacking fault inside the particle.

Fig. IV.7. illustrates the rich and complex microstructure of stacking faults and microtwins which is formed upon the rapid cooling of the copper particle. Interestingly the partial dislocations nucleate and propagate predominantly in one slip system for the small (10.5 x 10.5 x 4.1 nm^3) particle (Fig. IV.7.a) while 2 or 3 of them (depending if the particle is annealed at high temperature before the quench) are activated in the large one (18.5 x 18.5 x 6.7 nm^3, Fig. IV.7.b). Several grains can be found in the large particle as well as disordered regions (circled in red). The microstructure of the two particles is commented in more details in chapter IX.

For both particles, the invisibility conditions established in subsection III.3.3 are applied to determine the slip planes of the partial dislocations and their proportion, directly from the analysis of the CXD pattern.

As illustrated in Fig IV.7, two slip planes can be found in the small particle: the (1 1 1) and the (1 $\bar{1}$ 1) planes, the latter being largely predominant. The invisibility conditions for these 2 faulted planes are respectively $\boldsymbol{g}$ = 1 1 1 ($h + k + l = 3n$) for the (1 1 1) plane and $\boldsymbol{g}$ = 1 $\bar{1}$ 1 ($h - k + l = 3n$) for the (1 $\bar{1}$ 1) plane.

Fig IV.8 shows the calculated CXD pattern for four non-coplanar 1 1 1-type diffraction vectors. To facilitate the analysis of the diffraction patterns, the scattering from the underlying Ta substrate has been removed.

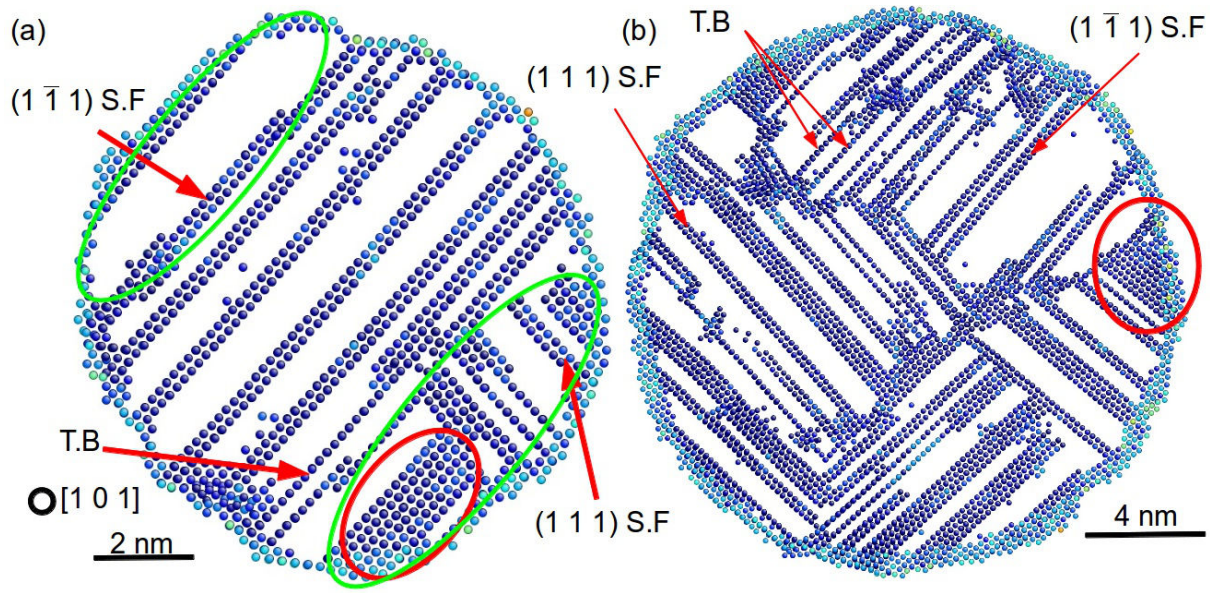

Fig. IV.7 (a) 10.5 x 10.5 x 4.1 nm and (b) 18.6 x 18.6 x 6.7 nm Copper particles dewetted on a Tantalum substrate above the melting temperature. Only the defective atoms are shown. In both particles, several intrinsic stacking faults (S.F), micro-twin boundaries (T.B) and disordered regions (circled in red) can be evidenced. Both particles are seen from the [1 0 1] direction. The two region circled in green in (a) are separated by 7 intrinsic stacking faults.

For $\boldsymbol{g}$ = 1 1 1 (Fig. IV.8.a), an intense streak of intensity can be observed along the [1 $\bar{1}$ 1] direction while no streak is observed along [1 1 1]. Conversely, for $\boldsymbol{g}$ = 1 $\bar{1}$ 1 (Fig. IV.8.b) two (1 1 1) stacking faults induce a weak streak of intensity along the [1 1 1] direction while no diffuse scattering is observed along the [1 $\bar{1}$ 1] direction. The streak display oscillations which period is equal to the invert of the distance between the two (1 1 1) intrinsic stacking faults (d = 2.1 nm). One can also notice the presence of the diffraction from the two pseudomorphic layers of copper (region circled in yellow). Of course they can not be observed experimentally since they diffract in the same position of the reciprocal space as the Tantalum substrate.

In good agreement with the calculations by Jacques *et al.* (2013), the number of stacking faults and the volume fraction of the crystal over which they are distributed have a strong influence on the decrease of the maximum intensity. Here, a large number (n = 7) and volume fraction (V~70%) of the 1 $\bar{1}$ 1 stacking faults leads to a large decrease of the maximum of intensity for $\boldsymbol{g}$ = 1 1 1 ($I_{max} = 0.16.I_0$). On the other hand the two (1 1 1) stacking faults, distributed over a small volume fraction (V~5%) induce a limited decrease of the maximum of intensity for $\boldsymbol{g}$ = 1 $\bar{1}$ 1 ($I_{max} = 0.42.I_0$). For $\boldsymbol{g}$ = 1 1 $\bar{1}$ and $\boldsymbol{g}$ = $\bar{1}$ 1 1 (Fig. IV.8.c & IV.8.d) which allow to see the signature of both stacking fault type, streaks are observed along both [1 $\bar{1}$ 1] and [1 1 1] directions, and the streak along [1 $\bar{1}$ 1] is much more intense than its counterpart along [1 1 1]. It is clear that the intensity of the streaks are driven by the number, position and volume fraction of the stacking faults. Assuming a number of stacking faults large enough to make statistics, the higher is the number of stacking faults in a given {1 1 1} plane and the larger is the volume over which they spread, the higher is the intensity of the diffuse streak normal to the stacking fault plane.

For $\boldsymbol{g}$ = $\bar{2}$ 0 2 (Fig. IV.8.e) which fulfills both invisibility conditions ($h+k+l = 3n$ and $h -k +l = 3n$), the streaks are absent in both [1 $\bar{1}$ 1] and [1 1 1] directions. Finally for $\boldsymbol{g}$ = 0 0 2, streaks are visible along both directions (Fig. IV.8.f).

It should be noted that this statistical approach proposed by Jacques *et al.* (2013), based study of the decrease of the maxima of intensity, and of the relative intensities of the streaks normal to the SF implies that the number of defects is sufficiently large and distributed over a large volume fraction. A coherent-X-ray beam is interesting for

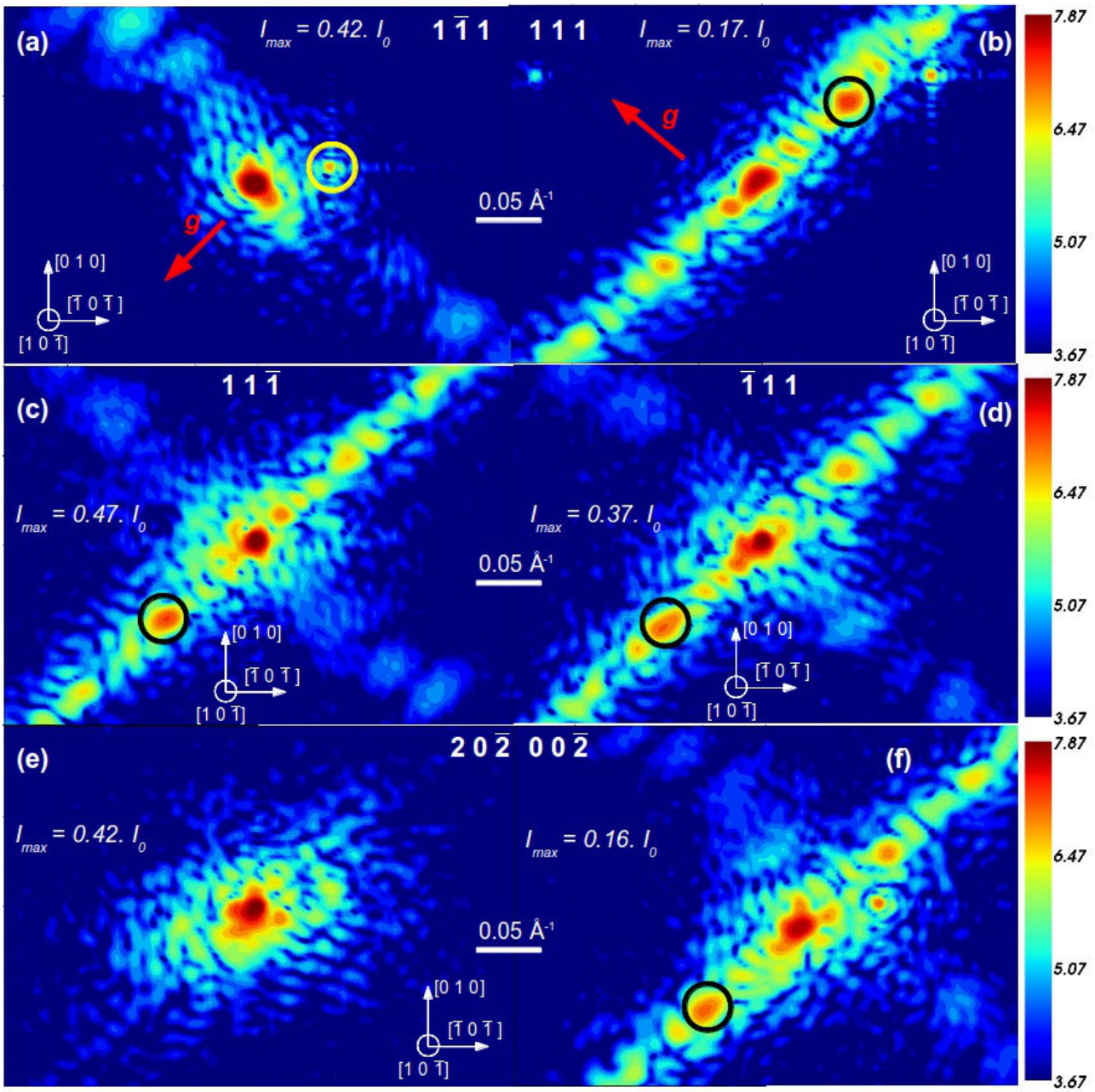

Fig. IV.8 Calculated CXD diffraction patterns from the small (10.5 x 10.5 x 4.1 nm) copper particle. (a) to (d) Calculations for four 1 1 1-type diffraction vectors. (e) for $\boldsymbol{g} = \bar{2}\ 0\ 2$ and for $\boldsymbol{g} = 0\ 0\ 2$. If possible, the direction of the diffraction vector is indicated by a red arrow. The black circle highlight the position of the satellite Bragg spot, and the yellow circle the position of the scattering from the two pseudomorphic copper layers.

the study of defective systems precisely because the defects interfere coherently, and the averaging inherent to an incoherent X-ray beam is suppressed. Here it is clear that even for a low number of defects a complex "speckle" pattern is produced by the assembly of stacking faults. The determination of the spatial distribution of the SF from the analysis of the CXD pattern appear to be far from trivial. If the analysis of the speckle pattern becomes too complicated, the interest of a coherent X-ray beam becomes questionable, especially for systems containing stacking faults. Diffraction patterns measured with an incoherent-X-ray beam does not contain any speckle, but

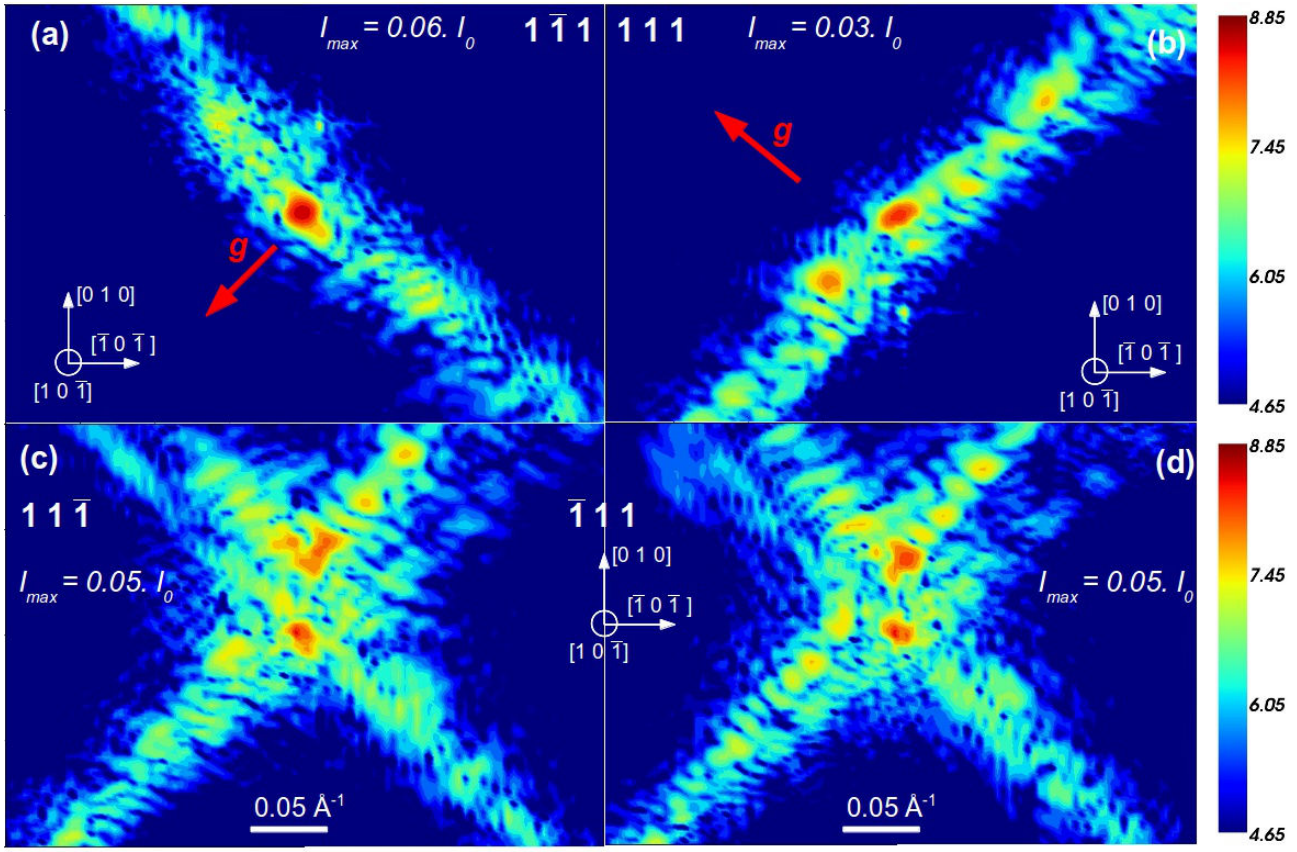

Fig. IV. 9 Calculated CXD diffraction patterns from the small (18.6 x 18.6 x 6.7 nm) copper particle. (a) to (d) Calculations for four 1 1 1-type diffraction vectors. If possible, the direction of the diffraction vector is indicated by a red arrow.

as discussed above, for a large number of defects, the informations on the spatial configuration, orientation and distribution of stacking faults in the volume are not deduced from the analysis of the speckle pattern. Only the decrease of the maximum of intensity and the orientation and intensity of the streaks normal to the stacking faults are needed, and both also appear on a diffraction pattern collected with an incoherent X-ray beam.

That being said, some features on the CXD pattern can be used to gain more insight in the precise determination of the microstructure. In the previous section it has been shown that the position of the satellite spot with respect to the reciprocal lattice point allows to determine the intrinsic or extrinsic type of a stacking fault.

As illustrated on Fig. IV.8, similar satellite spot (circled in black) can be found for an assembly of (1 $\bar{1}$ 1) intrinsic stacking faults. The stacking faults are induced by the dissociation of perfect dislocations are indeed necessarily intrinsic (see subsection III.3.3). The presence of a satellite spot for a single stacking fault located at the centre of the crystal results from a phase shift between the two parts of the crystal on each side of the stacking fault. Here we assume that this satellite spot is induced by the phase shift between the largest volumes of the crystal (circled in green in Fig. IV.7), which are separated by 7 intrinsic stacking faults. The resulting phase jump for $\boldsymbol{g}$ =1 1 1 is thus equal to: $\varphi_i = 7.\frac{2\pi}{3.}(h-k+l) = 4\pi+\frac{2\pi}{3} = \frac{2\pi}{3}$

With a positive phase jump and stacking faults in the (1 $\bar{1}$ 1) plane, the satellite spot should be located along the [$\bar{1}$ 1 $\bar{1}$] direction which is the case as illustrated on Fig. IV.8.b (circled in black). Conversely, and in good agreement with the expectations from intrinsic stacking faults, the satellite spot is along the [1 $\bar{1}$ 1] direction for

$\boldsymbol{g} = 1\ 1\ \bar{1}$, $\boldsymbol{g} = \bar{1}\ 1\ 1$ and $\boldsymbol{g} = 0\ 0\ 2$ for which $\varphi_i = -\frac{2\pi}{3}$. This confirms the intrinsic nature of the stacking faults. Of course this analysis is only possible because the number and type of the SF is already known. It also assumes that the volumes circled in green are indeed the largest volume in the crystal, and that the interferences between the other phase-shifted volumes does not induce a modification of the position of the satellite spot. It is thus clear that such interpretation would not be possible from experimental data, and unless the displacement field is reconstructed, it is not possible to determine the extrinsic or intrinsic character of each individual stacking fault for a large density of such defects.

The simulated case of dewetting of a 'large' copper particle possesses an even richer and more complex microstructure including grain boundaries, microtwin boundaries, disordered regions (circled in red) as well as two variants of intrinsic stacking faults. Similarly to the small particle, the stacking fault are located in the (1 1 1) and the (1 $\bar{1}$ 1) planes. $\boldsymbol{g} = 1\ \bar{1}\ 1$ and $\boldsymbol{g} = 1\ 1\ 1$ fulfill the invisibility conditions for the (1 $\bar{1}$ 1) and (1 1 1) stacking faults respectively. Only one streak of intensity is visible in both cases : along [1 1 1] for $\boldsymbol{g} = 1\ \bar{1}\ 1$ (Fig. IV.9.a) and along [1 $\bar{1}$ 1] for $\boldsymbol{g} = 1\ 1\ 1$ (Fig. IV.9.b). The richer microstructure produces a more speckled diffraction pattern with a very low maximum of intensity with respect to the perfect crystal and as compared to the small copper crystal ($I_{max} = 0.06.I_0$). One can also notice that the (1 $\bar{1}$ 1) stacking faults induce a larger decrease of the maximum of intensity given due to their larger number and volume fraction (60% vs 40%).

For the two other <1 1 1> reflections, streaks of diffuse intensity are visible along both directions. They also appear doubled. This is probably due to the diffraction from two distinct grains which are only slightly misoriented and diffract in almost the same Bragg conditions. Contrary to the case of the small particle, the intrinsic or extrinsic character of the stacking faults can not be determined from the analysis of the CXD patterns since no distinct satellite peak is visible. The intensities of the streaks are comparable, the [1 $\bar{1}$ 1] streak being slightly more intense owing to the larger number and volume fraction of the (1 $\bar{1}$ 1) stacking faults.

The direct analysis of CXD patterns in the case of a complex network of stacking faults proves to be an interesting approach. The use of four non coplanar 1 1 1-type reflections allows to determine without ambiguity the orientation of the faulted planes using the invisibility conditions. Even better, if several crystallographic orientations are present in the structure, the intensity of the streak normal to the faulted plane enables to estimate the relative proportion of the different orientations. The analysis of the decrease of the maximum of intensity provides a good estimation of the volume fraction over which the stacking faults are distributed in the crystallite *(Jacques et al.,* 2013).

However, it should be noted that this approach does not necessarily require the use of a Coherent-X-ray beam, since no or very few information is deduced from the speckle pattern. The complexity of the latter makes far from trivial the determination of the spatial configuration of the SF in the structure directly form the analysis of the CXD pattern. If the displacement field can not be reconstructed, the interest of a coherent X-ray beam for the analysis of a system with a large number of stacking is thus questionable.

The analysis of the CXD patterns is more adapted for a low concentration of SF where the intrinsic or extrinsic character of the stacking fault can be determined from the position of the satellite spot, and where it is even possible to determine the spacing between the stacking faults if only two of them are present along a specific orientation.

Conclusion

The case studies of the simulated nanoindentation and of the liquid state dewetting of a copper particle demonstrate that the detailed analysis of CXD patterns, using several diffraction vectors is an interesting approach for moderately-complex and realistic systems. The use of invisibility conditions is efficient in the case of the network on stacking faults. However, , the analysis of the SF content based on the decrease of the maximum of intensity and of the relative intensities of the streaks normal to the SF does not necessarily require the use of a coherent-X-ray beam.

The simulated nanoindentation appears to be even more challenging, and it is obvious that in both simulated cases the identification of each individual defects and all their characteristics (edge-screw type, burgers vector,...) although trackable is not possible through the direct analysis of the CXD patterns.
In the next Chapter we will evaluate the ability of phase retrieval methods to reconstruct the 3D displacement field from such complex objects.

Bibliography

Chang, H. J., Fivel, M., Rodney, D. & Verdier, M., (2010). *C. R. Physique* **11**, 285-292

Ehrhart, P., Trinkaus, H., & Larson, B. C. (1982). *Phys. Rev. B* 25, 834-848.

Favre-Nicolin, V., Mastropietro, F., Eymery, J., Camcho, D., Niquet, Y. M., Borg., B., Messing, M. E., Wemersson, L., Algra, R. E., Bakkers, E. P. A., Metzger, T. H., Harder, R. & Robinson, I. K. (2010). *New J. Phys.* **12**, 035013.

Jacques, V. L. R., Carbone, D., Ghisleni, R. & Thilly, L. (2013). *Phys. Rev. Lett.* **111**, 065503.

Kirk, M. A., Davidson, R. S., Jenkins, M. L. & Twesten, R. D. (2005). Phil. Mag. 85, 497-507.

Kirk, M. A., Jenkins, M. L., Zhou, Z., Twesten, R. D., Sutton, A. P., Dudarev, S. L. & Davidson, R. S. (2006). *Phil. Mag.* 86, 4797-4808.

Larson, B. C. & Schmatz, W., (1980). *Phys. Stat. Sol. B* **99**, 267-275.

Larson, B. C. & Young, F. W. (1987). *Phys. Stat. Sol. A* **104**, 273-286.

Mishin, Y., Farkas, D., Mehl, M., J., and Papaconstantopoulos, D., A. (1999). *Phys. Rev. B* **59**(5), 3393-3407

Nordlund, K., Partyka, P. R., Averback, S., Robinson, I. K. & Ehrhart, P. (2000). *J. Appl. Phys.* 88, 2278-2288.

M.-I. Richard, T. H. Metzger, V. Holý, and K. Nordlund
Phys. Rev. Lett. 99, 225504 – Published 30 November 2007

Zhou, Z., Sutton, A. P., Dudarev, S. L., Jenkins, M. L. & Kirk, M. A. (2005). *Proc. R. Soc.* A 461, 3935-3953.

Chapter V: Coherent Diffraction Imaging of single defects and of a small assembly of defects

Contents

Introduction....140
V.1. Reconstructed of the displacement field from single dislocation lines and comparison with their signature on CXD patterns....140
V.1.1. Simple case of a perfect screw dislocation....141
V.1.2 Dissociation of an edge dislocation....142
V.2. Comparison between calculated and reconstructed displacement fields and visibility of dissociated defects in experimental reconstructions....148
V.3. Single mixed dislocation in the course of nanoindentation of a gold nanoparticle 150
V.4. Displacement fields from individual dislocation loops 155
V.4.1. Frank dislocation loops....155
V.4.2. Prismatic dislocation loops....160
V.5. Case of a moderately complex system : simulated nanoindentation of a nickel thin film 162
Conclusion....167
Bibliography....168

Chapter V: Coherent Diffraction Imaging of single defects and of a small assembly of defects

Introduction

In this Chapter, we aim at testing and validating the reconstruction of the 3D CXD pattern to investigate the microstructure of isolated crystals, with single dislocation, or a moderately complex network of defects. For the case of individual dislocation it has been demonstrated that the direct analysis of CXD patterns allows to determine all its characteristics (dislocation or stacking fault, character of the line (edge/screw), Burgers vector, dissociation into partials, position...). This approach can be to some extent applied to more realistic/complex systems as shown with the case of the nanoindentation of a gold crystallite. When multiple defects are nucleated on equivalent slip planes, as in the case of the nanoindentation of the nickel thin film (Chapter IV), the interpretation of the diffraction patterns is very delicate. Rather than trying to isolate the contribution of each individual defect on such complex CXD patterns a statistical interpretation could help to characterize them, as suggested by Favre-Nicolin *et al.* (2010) and Jacques *et al.* (2013).

Ideally, the best approach would be to reconstruct the 3D displacement field around each individual defect. There are only few examples of successful reconstructions of systems with crystal defects. Takahashi *et al.* (2013) used 2D-Bragg ptychography to reconstruct a single dislocation and its associated strain field while Ulvestad *et al.* (2015) used Coherent Diffraction Imaging (CDI) to reconstruct a gold crystal with a microtwin. Recently Clark *et al.* (2015) demonstrated that CDI can be used to visualize a network of dislocations in a calcite crystal. In the following, we will demonstrate that CDI can be used to visualize both single and multiple defects in increasing order of complexity. We will also show the importance of the selection of pertinent diffraction vector to identify a given crystal defect.

By definition, a dislocation in crystals either ends at surface or form loops. Especially in fcc metals, dislocation lines are rarely straight but of mixed character. Moreover, a large number of physical process lead to the formation of closed loops of various type: prismatic for indentation or around precipitate, Frank loop in quenched or irradiated crystal, as a product of different dislocation interaction or during high temperature / creep...

Similarly to the methodology of Chapter III, we will start this section with very simple and typical single crystal defects such as screw and edge dislocations in both their perfect and relaxed state for various Bragg reflections. The use of realistic atomic scale calculations is required to take all physical effects into account: at first for the effect of dissociation into partials (physically related to the stacking fault energy of the crystal), then to have a good account of the core structure of the dislocation(s) (*i.e* where linear elasticity assumption does not apply) and finally to handle properly the boundary conditions (free surfaces / facets of a small scale free standing crystallite). At first, we will determine and analyze the displacement field expected at the vicinity of straight defect, using the atomic configurations obtained by the atomic simulations of crystallites. We will then perform reconstruction calculations of configurations of dislocation of increasing complexity: curved dislocation, loops of various type and finally a complete microstructure generated in the course of a nanoindenter penetration in an initially pristine crystallite. Finally, by analyzing the microstructure in a nickel thin film undergoing simulated nanoindentation, we will confirm that CDI can be used in a more complex system with multiple defects nucleated on several slip systems.

V.1. Reconstructed of the displacement field from single dislocation lines and comparison with their signature on CXD patterns

Note for the reader: The projections of the displacement field presented in this chapter are obtained by two distinct procedures:

- calculation of the displacements between the relaxed atomic positions and a reference perfect configuration with the same number of atoms.
- reconstruction of the displacement field using phase retrieval algorithms.

In Chapter I, phase retrieval algorithms have been used for the reconstruction of various projections of the displacement field of a perfect dislocation. The very good agreement between the reconstructed and calculated displacement field from the atomic positions has been demonstrated (section I.3.4).
In a similar way, the projections of the displacement field are reconstructed for all the cases presented in this Chapter. For the perfect dislocations, the reconstructions are very consistent with the calculations from the atomic positions. We chose not to show the comparison between the reconstructed data and the displacement field in order to avoid unnecessary overloading of the figures. All the displacement fields presented in sections V.1.1 and V.1.2 are thus calculated from the displaced atomic positions.
The agreement between calculated and reconstructed displacement fields for relaxed defects was not discussed in Chapter I and is thus evaluated in section V.2. The visibility of dissociated defects with the expected experimental resolution is also commented in the same section.
For the more complex defect structures presented in the second part of this chapter, the displacement field can not be calculated from the relaxed atomic positions (for various reasons that will be discussed in the following), hence, all the displacement fields presented starting from section V.3 are obtained by reconstruction.
The procedure used for all the reconstructions presented in this Chapter has been presented in Chapter I and is not further detailed.

V.1.1. Simple case of a perfect screw dislocation

As shown in subsection III.3.1, in the hypothesis of an infinite isotropic medium, the displacement field of a screw dislocation is parallel to its Burgers vector (and to the dislocation line) and has a very simple expression. In a Cartesian frame, where x is the line direction and y and z perpendicular to the dislocation line, $u_y=u_z=0$ and $u_x=\frac{b\theta}{2\pi}=\frac{b}{2\pi}.\tan^{-1}\frac{z}{y}$ (Hull and Bacon 1982). The displacement along the line direction increase uniformly from zero to b as the angle increase from 0 to 2π (Fig. V.1.a). Following elastic theory, the displacement field and thus the phase is continuous everywhere, except on the dislocation line where a phase jump can be observed. Here, a perfect screw dislocation (with $\boldsymbol{b}$ = ½ [1 $\bar{1}$ 0]) is introduced at the centre of a 30x30x30nm^3 gold crystallite in a Wulff geometry. In the following the various projections of the displacement field at the vicinity of dislocations generally corresponds to phase variation of more than 2π. In such cases to have a clearer picture of the displacement field, the phase is generally unwrapped (Herraez *et al.* 2002) before it is converted to lattice displacements. Here we represent the displacement and thus the phase as they would appear on a reconstruction prior to any phase unwrapping. This representation is chosen to quantify the phase jumps induced by dislocations which produce dramatic effects on the calculated CXD patterns (Chapter III & IV). As described in subsection III.3.1, the uniform increase and continuity of the phase induce a ring-shaped intensity distribution on the CXD pattern for any $\boldsymbol{g}.\boldsymbol{b} \neq 0$. The value of the phase jump depends on the component of the displacement field which is investigated. For $\boldsymbol{g}$ = 1 $\bar{1}$ 1, a phase variation of 2π corresponds to the lattice spacing between two successive (1 $\bar{1}$ 1) planes. As shown on Fig. V.1.a, if θ increases by 2π, the displacement along the [1 $\bar{1}$ 1] direction increases by a/√3 = 2.35 Å which corresponds to a phase variation of 2π. The resulting phase jump between the two parts on each side of the dislocation line is π. This results in a splitting of the Bragg peak in two contributions of equal intensity, and a zero intensity at the theoretical Bragg position.
For $\boldsymbol{g}$ = 2 $\bar{4}$ 2 an increase of θ by 2π results in a displacement of d = 2.5 Å along the [2 $\bar{4}$ 2] direction. For this particular diffraction vector, a phase variation of 2π corresponds to half the lattice spacing between two successive (1 $\bar{2}$ 1) planes *i.e* a/(2.√6) = 0.83 Å. Hence, the displacement d corresponds to a phase variation of 6π. The phase jump between the two parts on each side of the dislocation line is equal to 3π. This also results in

the splitting of the Bragg reflection with an increased spacing between the two peaks as compared to the 1 $\bar{1}$ 1 reflection. A systematic study of this splitting distance reveals that it increases with the value of the phase jump which in turn increases with the Miller indices of the reflection.

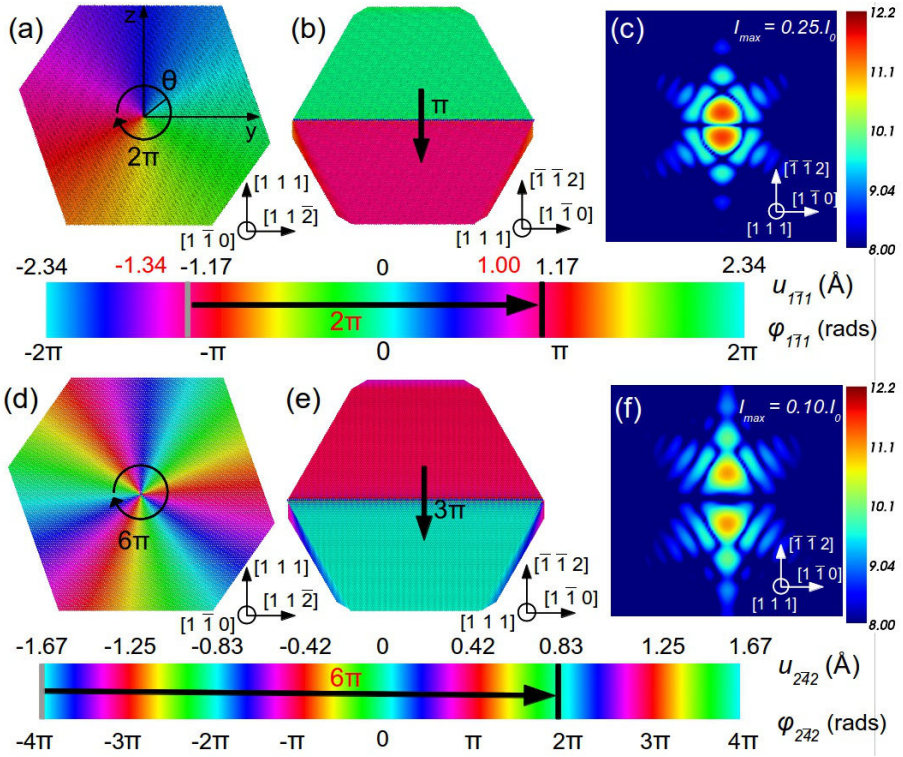

Fig. V.1 *Case of the perfect screw dislocation.* A dislocation line with $\boldsymbol{b}$ = ½ [1 $\bar{1}$ 0] is introduced at the centre of a 30x30x30nm^3 gold nanocrystal. Corresponding diffraction phase maps and diffraction patterns for $\boldsymbol{g}$ = 1 $\bar{1}$ 1 (a,b,c) and $\boldsymbol{g}$ = 2 $\bar{4}$ 2 (d,e,f). The maximum and minimum for the displacement projected onto $\boldsymbol{g}$ and the phase are indicated on the colour bar by black and gray lines. The depicted area on the CXD patterns is equal to (0.049 Å^{-1})^2

V.1.2 Dissociation of an edge dislocation

We now move on to the case of an edge dislocation to determine how the changes observed on the diffraction patterns during the dissociation of a perfect dislocation can be correlated to the variations in the displacement field. As a remind, for a perfect dislocation in the hypothesis of an infinite and isotropic medium, the displacement field $\boldsymbol{u}$ is equal to zero along the dislocation line $\boldsymbol{t}$. In a Cartesian frame (x,y,z), where the x and z-axis are the Burgers vector and line directions respectively, it can be expressed as two components:

- u_x // $\boldsymbol{b}$
- u_y // $\boldsymbol{b}$ x $\boldsymbol{t}$ sensitive to the bending planes about the z-axis caused by the extra plane forming the dislocation (see subsections I.3.4 and III.3.2, Eq. (III.2) and Eq. (III.3) for more details).

Here we introduce a perfect edge dislocation at the centre of a copper Wulff crystallite. The atomic positions are then relaxed according to the procedure described in section III.2. The atomic displacement along $\boldsymbol{b}$, *i*.e. $u_{2\bar{2}0}$ is shown for both the perfect and relaxed dislocation (Fig. V.2). The case of the perfect dislocation was already presented in Chapter I.3.4. As opposed to a screw dislocation the displacement field is not isotropic for an edge

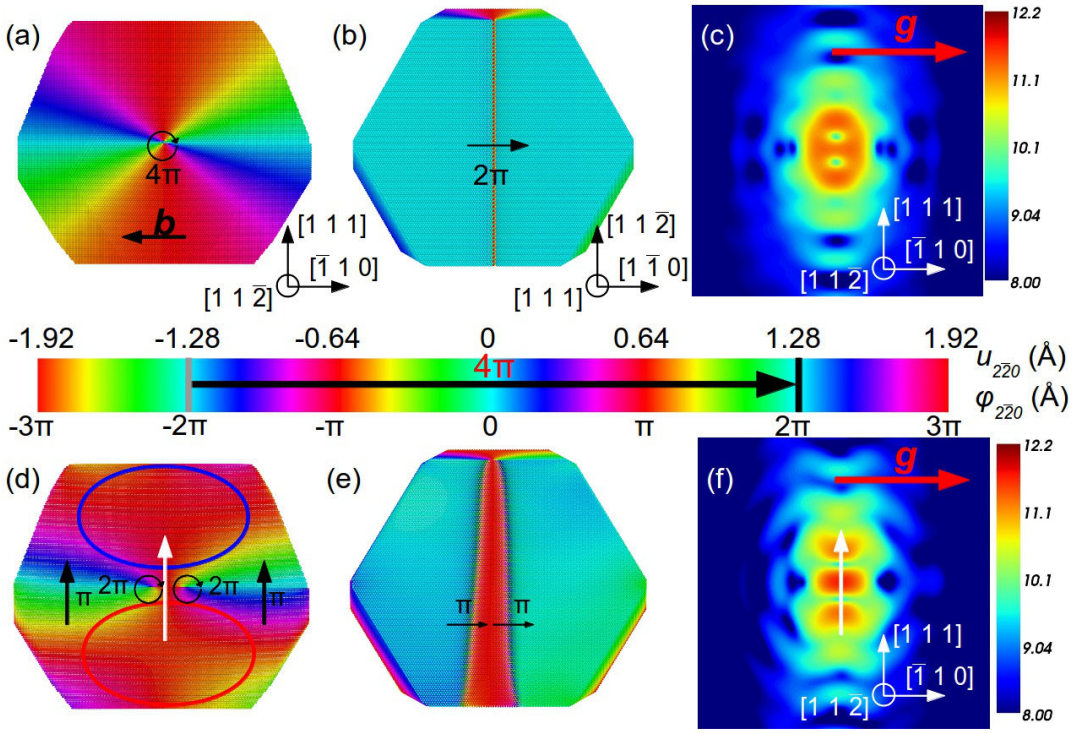

Fig. V.2 *Case of the edge dislocation line, perfect (top) and dissociated (bottom), for* $\boldsymbol{g} = 2\,\bar{2}\,0$ *(*$\boldsymbol{g}$ *//* $\boldsymbol{b}$*):* Calculated atomic displacements around single perfect and dissociated edge dislocations introduced at the centre of a 30x30x30nm^3 copper nanocrystal. The maximum and minimum for the displacement and the phase are indicated on the colour bar by black and gray lines. The left and middle panels show $\boldsymbol{g.u}$ in $(1\,1\,\bar{2})$ and $(1\,1\,1)$ planes respectively, while the CXD pattern is shown in the right panels. The depicted area on the CXD patterns is equal to $(0.055\ \text{Å}^{-1})^2$

dislocation. The origin of this anisotropy is discussed in section I.3.4. The anisotropy in the phase distribution (almost constant above and below and above the dislocation line and rapidly varying on the left and right of the dislocation line) results in an anisotropy of the diffracted intensity which is elongated along the [1 1 1] direction. As already discussed, the latter corresponds to the direction which connects the large regions of constant phase above and below the dislocation line.

For $\boldsymbol{g} = 2\,\bar{2}\,0$, a phase variation of 2π corresponds to half the lattice spacing between two $(1\,\bar{1}\,0)$ planes, *i.e* the magnitude of the Burgers vector. As shown from Fig. V.2.a , the minimum and maximum displacements along $[1\,\bar{1}\,0]$ with respect to the atomic positions in the perfect crystal are respectively -1.28 Å and 1.28 Å in the plane perpendicular to the dislocation line. The displacement amplitude is thus exactly equal to one lattice spacing between two $(1\,\bar{1}\,0)$ planes and corresponds to an overall phase variation of 4π. This implies that the phase difference between the two parts of the crystal on either side of the dislocation line is equal to 2π (Fig. V.2.b): the dislocation line does not induce any phase jump. Only the atoms on the dislocation itself are phase-shifted by π with respect to the surrounding atoms. Due to the absence of phase jump, the calculated intensity is not equal to zero at the Bragg position (Fig. V.2.c).

Upon dissociation of the dislocation, several interesting phenomena occur. As detailed in subsection III.3.3, the dissociation of the perfect dislocation in two partial Shockley dislocations leaves an intrinsic stacking fault in the (1 1 1) plane between the two partials. The two (1 1 1) planes involved in the stacking fault are shifted with respect to each other by 1.28 Å along $[1\,\bar{1}\,0]$. This results in a 2π phase jump which remains invisible, in good agreement with the invisibility conditions for a (1 1 1) stacking fault: $h + k + l = 3n$ which are fulfilled for $\boldsymbol{g} = 2\,\bar{2}\,0$. The displacements are very anisotropic in the crystal with the phase rapidly varying on the left and right of

the partial dislocation while it is almost constant on the top and bottom part of the nanocrystal. The two partial dislocations produce a pair of vortices of same chirality in the (1 1 $\bar{2}$) plane (Fig. V.2.d). A slice along the [1 1 1] direction reveals that both dislocations produce a π phase jump which results in the splitting of the Bragg peak in three spots (Fig. V.2.f.). The [1 1 1] direction of the splitting is given by the direction which connects the two regions of constant phase below and above the dislocation line (white arrow connecting the blue and red-circled areas). One can also notice the increasing of the intensity of the central spot. The region in the stacking fault ribbon is phase-shifted by π with respect to the surrounding atoms (Fig. V.2.e).

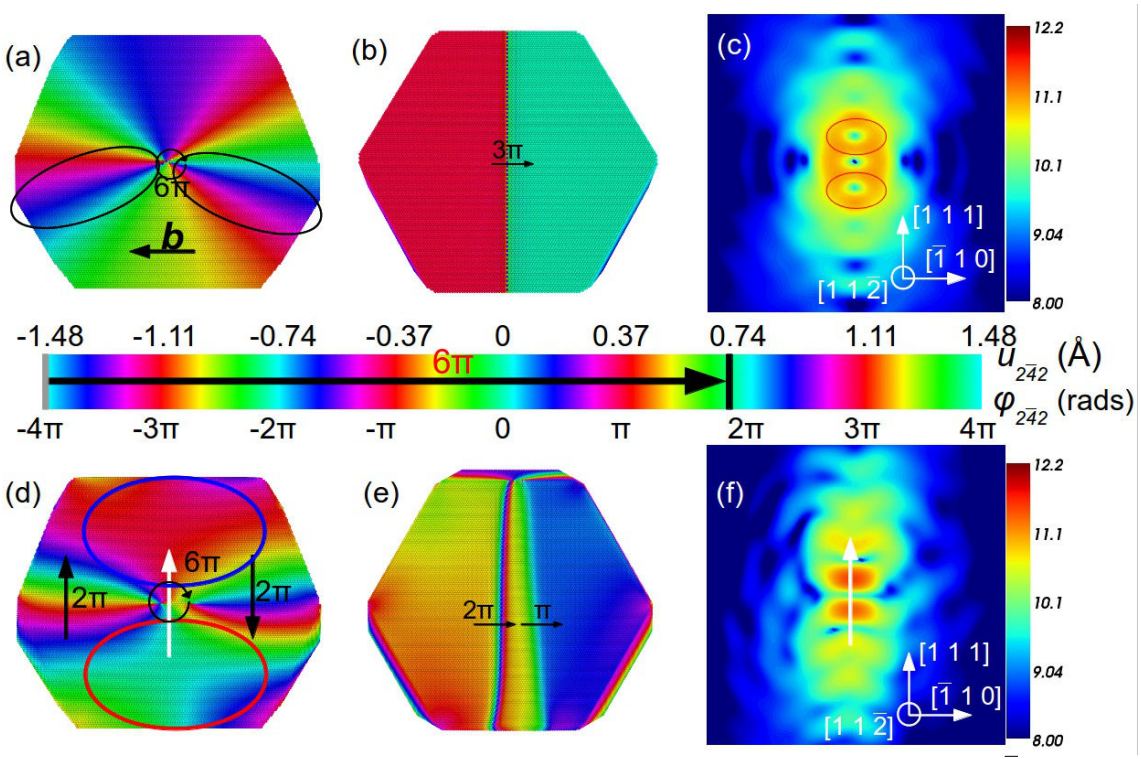

Fig. V.3 *Case of the edge dislocation line, perfect (top) and dissociated (bottom), for* $\mathbf{g} = 2\,\bar{4}\,2$ ($\mathbf{g} \,//\, \mathbf{b}_p$): Calculated atomic displacements around single perfect and dissociated edge dislocations introduced at the centre of a 30x30x30nm^3 copper nanocrystal. The maximum and minimum for the displacement and the phase are indicated on the colour bar by black and gray lines. The left and middle panels show $\mathbf{g}.\mathbf{u}$ in (1 1 $\bar{2}$) and (1 1 1) planes respectively, while the CXD pattern is shown in the right panels. The depicted area on the CXD patterns is equal to (0.055 Å^{-1})^2

Similarly to the case of the screw dislocation, the projection of the displacement onto the [2 $\bar{4}$ 2] reflection results in a phase variation of 6π in the plane perpendicular to the dislocation line (Fig. V.3.a). The phase jump between the two sides of the dislocation line is thus equal to 3π (Fig. V.3.b) that results in an intensity equal to zero at the Bragg position (Fig 3.c). Due to the anisotropy of the displacement field, the Bragg peak is also elongated along the [1 1 1] direction. The overall shape of the Bragg peak is very similar to the case of the 2 $\bar{2}$ 0 reflection. This can be explained by the fact that both reflections are insensitive to the u_y component of the displacement field. In both cases two minima of intensity (circled in red on Fig. V.3.c) are observed on each side of the Bragg position. As confirmed by calculations for other reflections, the total number of minima of intensity for an edge dislocation depends on the total phase variation in the plane perpendicular to the dislocation line. Here the total phase variation of 6π induce three minima of intensity. Similarly, for the 2 $\bar{2}$ 0 and 1 $\bar{1}$ 1 reflections respective total phase variations of 4π and 2π result in 2 and 1 minimum of intensity. When the dislocation dissociates into two partials, the phase jump induced by the stacking fault ribbon is visible but its value is not

constant over the stacking fault width (Fig. V.3.d and V.3.f). $u_{2\bar{1}2}$ becomes even more anisotropic with a similar behaviour to what has been observed for $u_{2\bar{2}0}$: very steep phase gradients on the left and right side of the dislocation line (2π variation over a very short length), almost constant phase in the top and bottom part of the nanocrystal. As illustrated in Fig. V.3.e, the 3π phase jump now decomposes in two successive phase jumps of 2π and π induced by the two partial dislocations. A closer look at Fig. V.3.d reveals that the phase undergoes very rapid variations (over 3 or 4 atoms) rather than a sharp phase jump as in the case of the perfect dislocation. The overall phase 3π shift between the left and right parts of the crystal is thus preserved. The intensity vanishes at the Bragg position and the Bragg peak splits into two parts along the [1 1 1] direction (Fig. V.3.f). Similarly to $\boldsymbol{g}$ = 2 $\bar{2}$ 0, the direction of the splitting is given by the direction which connects the two regions of constant phase below and above the dislocation line (white arrow connecting the blue and red-circled areas).

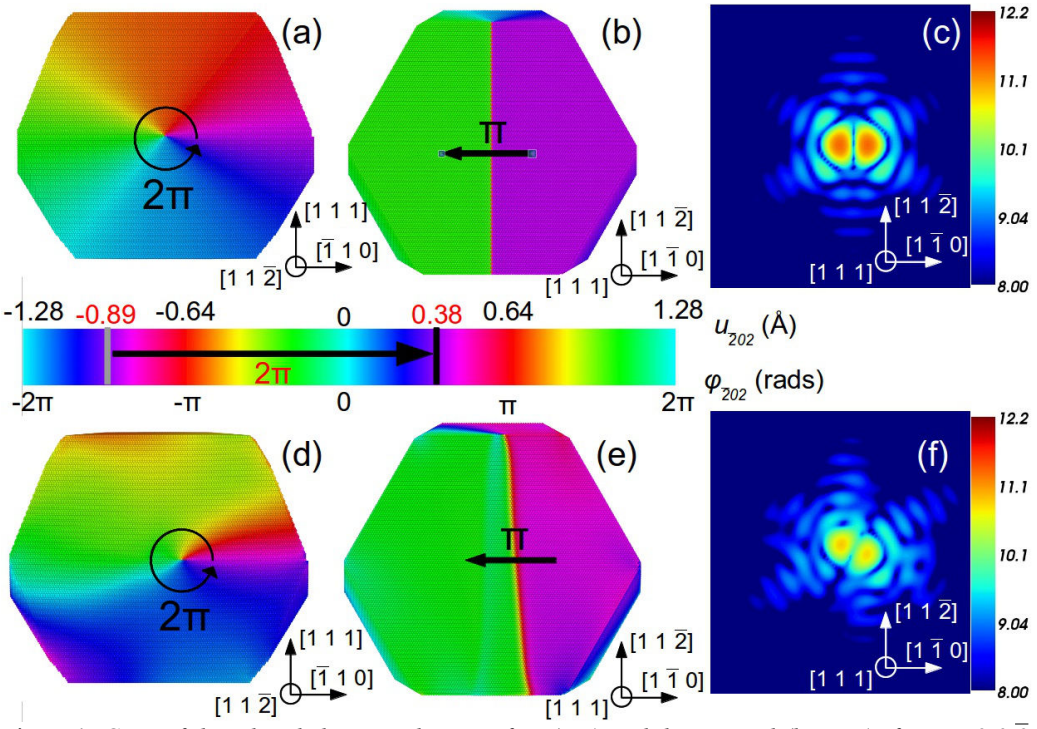

Fig. V.4 *Case of the edge dislocation line, perfect (top) and dissociated (bottom), for* $\boldsymbol{g}$ = 2 0 $\bar{2}$. Calculated atomic displacements around single perfect and dissociated edge dislocations introduced at the centre of a 30x30x30nm^3 copper nanocrystal. The maximum and minimum for the displacement and the phase are indicated on the colour bar by black and gray lines. The left and middle panels show $\boldsymbol{g.u}$ in (1 1 $\bar{2}$) and (1 1 1) planes respectively, while the CXD pattern is shown in the right panels. The depicted area on the CXD patterns is equal to (0.055 Å^{-1})^2

The case $\boldsymbol{g}$ = 2 0 $\bar{2}$ which is not perpendicular to the Burgers vector of the perfect dislocation but to the Burgers vector of one of the two partial dislocations has not been presented in the section III.3.2 but also gives interesting results.

The case of a perfect dislocation is quite straightforward as this reflection is only sensitive to the u_x component of the displacement field (parallel to the Burgers vector). The minimum and maximum displacements projected onto $\boldsymbol{g}$ = 2 0 $\bar{2}$ (with respect to the perfect crystal) in the (1 1 $\bar{2}$) plane perpendicular to the dislocation line are respectively -0.89 Å and 0.38 Å. The displacement amplitude is thus equal to 1.27 Å, *i.e.* half the distance between two successive (1 0 $\bar{1}$) planes corresponding to a phase variation of 2π (Fig. V.4.a). The dislocation line induces a discontinuity in the phase, and as illustrated on Fig. V.2.b which show $u_{20\bar{2}}$ in the (1 1 1) plane left side

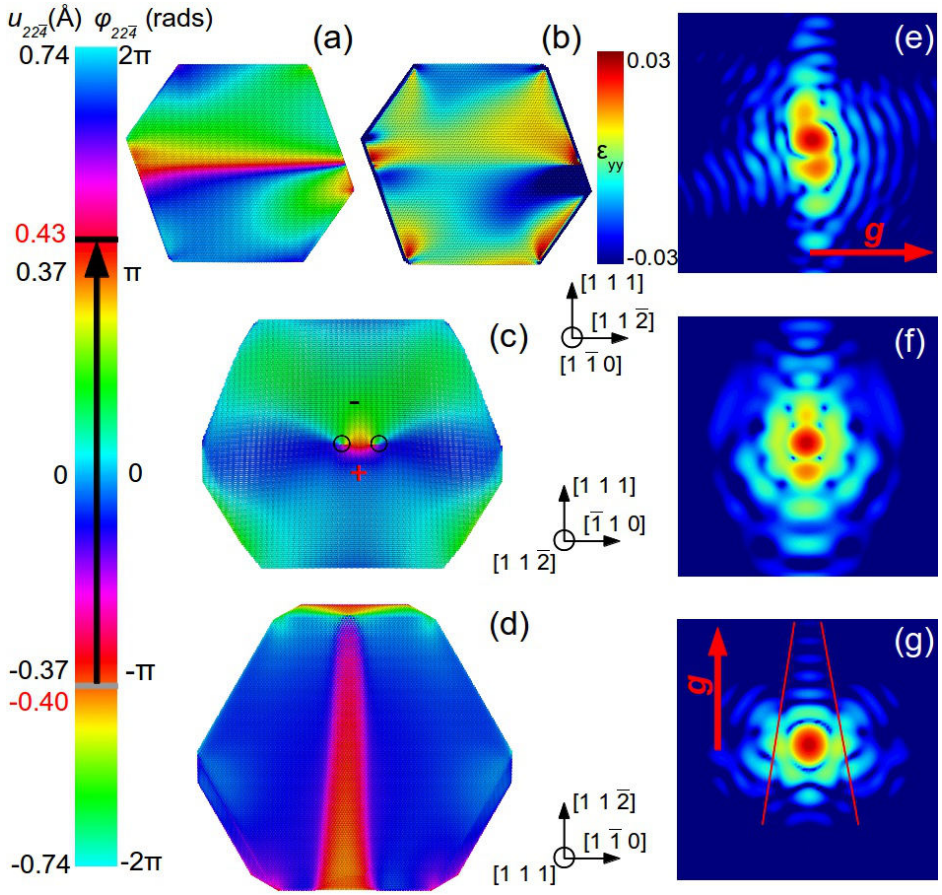

Fig. V.5 *Case of the dissociated dislocation line for* $\boldsymbol{g} = 2\,2\,\bar{4}$ *(*$\boldsymbol{g}.\boldsymbol{b} = 0$ *and* $\boldsymbol{g}.\boldsymbol{b}\boldsymbol{x}\boldsymbol{t} = 0$*).*
Calculated atomic displacements around single perfect and dissociated edge dislocations introduced at the centre of a 30x30x30nm^3 copper nanocrystal. The maximum and minimum for the displacement and the phase are indicated on the colour bar by black and gray lines .(a) $u_{22\bar{4}}$ displacement field in the (1 $\bar{1}$ 0) plane. (b) ε_{yy} (with y being the dislocation line direction). (c) $u_{22\bar{4}}$ displacement field in the (1 1 $\bar{2}$) plane. The regions of positive and negative displacements are indicated with the plus and minus signs. The black circles denote the small areas which are phase-shifted by π. (d) $u_{22\bar{4}}$ displacement field in the (1 1 1) plane. (e-f) Corresponding CXD pattern for $\boldsymbol{g} = 2\,2\,\bar{4}$, in the (1 $\bar{1}$ 0) (e), (1 1 $\bar{2}$) (f) and (1 1 1) (g) planes. The depicted area on the CXD patterns is equal to (0.055 Å^{-1})^2

of the crystal is phase-shifted by π relatively to the right side. This yields a splitting of the Bragg peak in two equal contributions along the [$\bar{1}$ 1 0] direction, and an intensity equal to zero at the Bragg position (Fig. V.4.c).
Upon relaxation, the perfect edge dislocation dissociates in two partials with Burgers vectors of $\boldsymbol{b}_{p1} = 1/6[2\,\bar{1}\,\bar{1}]$ and $\boldsymbol{b}_{p2} = 1/6[1\,\bar{2}\,1]$, the latter being perpendicular to $\boldsymbol{g}$.
As illustrated on Fig V.4.d & V.4.e, this results in a complete invisibility of $\boldsymbol{b}_{p2}$. The centre of the 2π phase vortex is now shifted to the position of the second partial with $\boldsymbol{b}_{p1} = 1/6[2\,\bar{1}\,\bar{1}]$. The atomic displacements in the vicinity of the dislocation line are again very anisotropic. The splitting of the Bragg peak is the signature of the π phase jump induced partial dislocation (Fig 4.e and 4.f.). As shown on the (1 1 1) cut of the reciprocal space, the two spots are less intense and misoriented compared to the case of the perfect dislocation. This can be attributed to the curvature of the dislocation line.
As shown in subsection III.3.2, the complete invisibility of a perfect edge dislocation can only be achieved when both invisibility conditions $\boldsymbol{g}.\boldsymbol{b} = 0$ and $\boldsymbol{g}.(\boldsymbol{b}\boldsymbol{x}\boldsymbol{t}) = 0$ are satisfied. This is only the case when $\boldsymbol{g}$ is parallel to the

dislocation line, i.e $\boldsymbol{g}$ = 2 2 $\bar{4}$. For a perfect dislocation, the displacements along the dislocation line [1 1 $\bar{2}$] are equal to zero, *i.e*. the phase is constant along this direction and the CXD pattern is similar to that of a perfect crystal for $\boldsymbol{g}$ = 2 2 $\bar{4}$. When the perfect dislocation dissociates into two partials, the small displacements along [1 1 $\bar{2}$] produce a visible effect on the CXD pattern (Fig V.5.e. to g). They consist mainly in the decrease of the maximum of intensity of the central spot, and the presence of diffuse scattering, mainly concentrated into the (1 1 $\bar{2}$) plane parallel to the dislocation line (subsection III.3.2 for more details). Both the displacement field in the real space and the diffracted intensity in the reciprocal space are symmetric with respect to the (1 1 1) plane.

Fig. V.5.a reveals that the maximum displacements are concentrated in the vicinity of the dislocation line with high positive atomic displacements just below the dislocation line and high negative displacements just above (Fig. V.5.a). The magnitude of both displacements tends to decrease with an increasing distance to the dislocation line. Converted into strain (with y being the [1 1 $\bar{2}$] direction), it results in the presence of high compressive strain (up to $6x10^{-3}$) below the dislocation line and tensile strain above the dislocation line with a lower magnitude (up to $2x10^{-3}$) (Fig. V.5.d.).

At the center of the stacking fault ribbon, the phase jump along the [1 1 1] direction is almost equal to 2π. This is in good agreement with the invisibility conditions for a stacking fault : $h+k+l = 3n$ which are fulfilled for $\boldsymbol{g}$ = 2 2 $\bar{4}$. For atoms close to the partial dislocations the phase jump decreases to a value of π. This phase jump does not produce strong effects on the CXD pattern since only a very small area just below the stacking fault ribbon (circled in black on Fig V.5.c) is phase-shifted by π with respect to the upper part of the crystal. It could explain the increase of intensity of the fringes along the [1 1 1] direction as well as the doubling of their period. Fig V.5.d reveals a shift in the phase of the atoms in the stacking fault ribbon with respect to the surrounding atoms. While the phase varies rapidly at the interface of the dislocation line, no phase jump is observed and the phase varies depending on the position on the atom on the stacking fault ribbon (Fig. V.2.d). There is no characteristic signature of this phase shift on the diffraction pattern although the increasing of the lateral width of the [1 1 $\bar{2}$] fringes could be related to the decreasing width of the stacking fault ribbon.

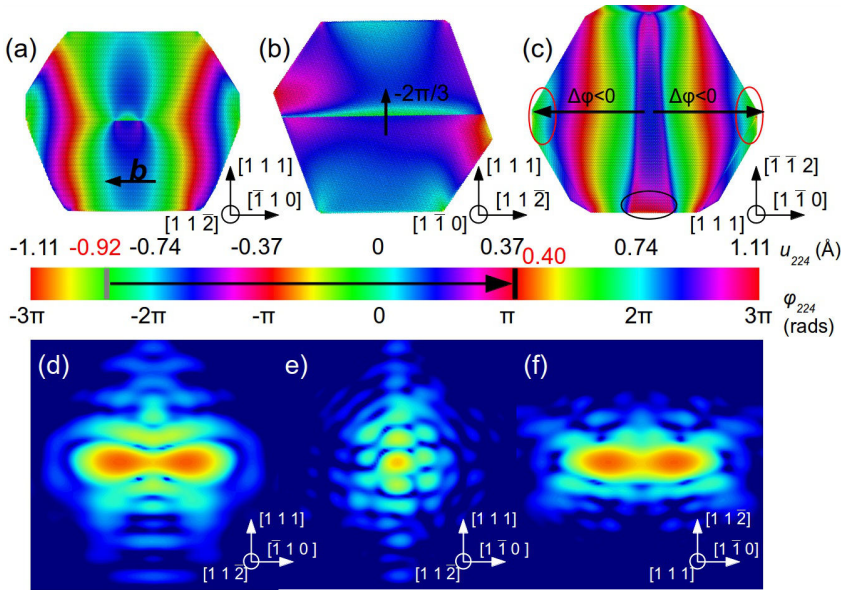

Fig. V.6 *Case of the dissociated dislocation line for* $\boldsymbol{g}$ = 2 2 4 ($\boldsymbol{g}.\boldsymbol{b} = 0$ *and* $\boldsymbol{g}.\boldsymbol{b}\boldsymbol{x}\boldsymbol{t} \neq 0$). Calculated atomic displacements around single perfect and dissociated edge dislocations introduced at the centre of a $30x30x30nm^3$ copper nanocrystal.(a) to (c) Calculated $u_{1\bar{1}1}$ displacement in the (1 1 $\bar{2}$) (a), (1 $\bar{1}$ 0) (b) and (1 1 1) planes (c). (d) to (f) Corresponding CXD patterns for $\boldsymbol{g}$ = 2 2 4 in the (1 1 $\bar{2}$) (d), (1 $\bar{1}$ 0) (e) and (1 1 1) planes (f).

We now move on to the case of a dissociated dislocation which is investigated with $\boldsymbol{g}$ = 2 2 4. Such diffraction vector is perpendicular to the Burgers vector of the dislocation but not perpendicular to the dislocation line. In subsection III.3.2 we showed that this reflection is particularly suited to evidence the dissociation of a perfect dislocation since it produce a very characteristic signature on the diffraction pattern (Fig V.6.g to V.6.i). This can be explained by the fact that diffraction vectors with high h,k,l index are sensitive to very small displacements. For the particular case of $\boldsymbol{g}$ = 2 2 4, a 2π phase variation corresponds to half the lattice spacing between two (1 1 2) planes, i.e 0.74 Å for a copper crystal. As shown on Fig V.6.a to V.6.c the total amplitude of the displacement is significant with a value of 1.32 Å which corresponds to 11.2 radians! The maximum positive displacement is found on the widest part of the stacking fault ribbon (area circled in black on Fig. V.6.c) while the maximum negative displacement is encountered on the (1 $\bar{1}$ 0) edges (regions circled in red on Fig. V.6.c.). There is thus a negative phase gradient directed along both the [1 $\bar{1}$ 0] and [$\bar{1}$ 1 0] direction (Fig. V.6.a. and V.6.c.) This phase gradient with an overall phase shift of more than 3π and produces a strong signature on the CXD pattern. It consists in an elongation of the Bragg spot along the [1 $\bar{1}$ 0] and [$\bar{1}$ 1 0] directions which has been described in subsection III.3.2 as the signature of the dissociation of the dislocation (Fig. V.6.g and V.6.j). The symmetry of the phase in the real space with the respect to the (1 1 1) plane implies the symmetry of the intensity with respect to the same plane in the reciprocal space. In Fig. V.6.a and V.6.b a sharp phase jump along the [1 1 1] direction can be observed at the vicinity of the (1 1 1) stacking fault. The 0.24 Å between the atoms above and below the stacking fault ribbon corresponds to a 2π/3 phase jump in radians, the value expected from a stacking fault since $\boldsymbol{g}$ = 2 2 4 does not fulfill the invisibility conditions. This results in an increased intensity and a doubling of the periods of the [1 1 1] fringes (Fig. V.6.g) in good agreement with the results presented in subsection III.3.2.

V.2. Comparison between calculated and reconstructed displacement fields and visibility of dissociated defects in experimental reconstructions

The excellent agreement between the calculated and reconstructed displacement fields for perfect dislocations was evidenced in Chapter I. (subsection I.4.5). In this subsection, we evaluate the agreement between calculated and reconstructed displacement fields for relaxed dissociated defects. Fig. V.7 shows the calculated (Fig.V.7.a to V.7.c) and reconstructed (Fig.V.7.d to V.7.f) displacement fields for $\boldsymbol{g}$ = 2 2 $\bar{4}$. The reconstruction is carried-out using the procedure described in Chapter I. The extent of the reciprocal space selected for the calculation gives a voxel size of 0.7x0.7x0.7 nm^3 and corresponds to a resolution of 1.5 nm, as determined from the PRTF (Chapter I, Chapman *et al.* 2006). Similarly to the case of perfect dislocations, the agreement between the calculated and reconstructed data is excellent, with a perfect reproduction of the phase variations. Note that reconstructions carried out for the projections of the displacement field presented in section V.1 are also very consistent with the calculations from the atomic positions. As discussed in the introduction of this section they are not shown to avoid overloading of the figures.

Regarding experimental considerations, it is important to understand that the voxel size along each direction is almost one order of magnitude smaller than in the experimental reconstructions presented in Chapters VI & VII. Hence the very high resolution of the reconstructions for the simulated data, which is unreachable experimentally (Chapter I). The visibility of perfect dislocations with low resolution data (10 nm) is not problematic. Sharp phase jumps are induced at the vicinity of the dislocation, and the displacement field of the dislocation has a very large spatial extent (Fig. V.1.a and V.1.b for instance). Independently on the resolution, these two features are always visible (Fig. V.8.a and V.8.c). Dissociated dislocations are potentially more troublesome. As shown in Fig. V.2, when the atomic positions are relaxed, and the defect is equilibrated in the particle, the width of the stacking fault ribbon between the two partials remains generally rather small. As a remind, the latter is material dependent and is controlled by the shear modulus μ and the stacking fault energy γ_s via the adimensional parameter $\gamma_s/\mu b_p$ (subsection III.3.3). It is in principle independent of the size of the particle but can be increased if the particle is mechanically solicited (for instance by nanoindentation, Chapter II and

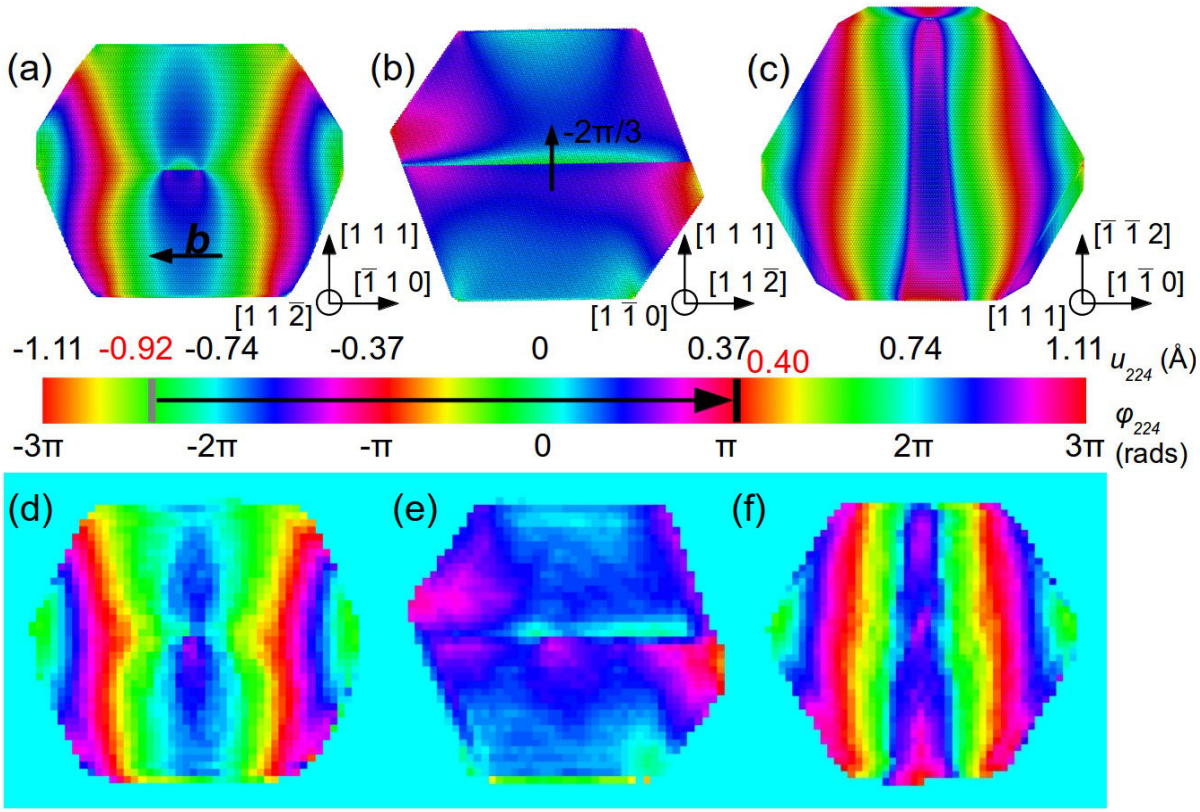

Fig. V.7 *Comparison between the calculated and reconstructed displacements around a perfect edge dislocation introduced at the centre of the reference copper nanocrystal for* $\boldsymbol{g}$ *= 2 2 4* (a) to (c) Calculated $u_{l\bar{1}l}$ displacement in the (1 1 $\bar{2}$) (a), (1 $\bar{1}$ 0) (b) and (1 1 1) planes (c). (d) to (f) Reconstructed $u_{l\bar{1}l}$ displacement in the (1 1 $\bar{2}$) (d), (1 $\bar{1}$ 0) (e) and (1 1 1) planes (f).

Chapter VI). For the Cu particle used in this section, the average width of the stacking fault ribbon is 4 nm. Hence it is smaller than the typical voxel size obtained experimentally(between 5 and 10 nm). This is generally not problematic as most of the Bragg reflections are only sensitive to one of the two Shockley partials. This is case for for instance for $\boldsymbol{g}$ = 2 0 $\bar{2}$ (Fig. V.4), but also for all the 1 1 1-
type reflections that do not fulfill the invisibility conditions (section V.3 to V.5).
For $\boldsymbol{g}$ almost parallel to $\boldsymbol{b}$ it is demonstrated in section V.1 that provided a sufficient resolution is ensured, both Shockley partials are visible. For $\boldsymbol{g}$ = 2 $\bar{2}$ 0 for instance, the 4π phase vortex around the perfect dislocation line is splitted in two 2π phase vortices with same chirality whose centres are the two Shockley partials (Fig. V.2.d, Fig. V.8.a & V.8.b). If the voxel size is larger than the dissociation length, it is clear that the two Shockley won't be resolved, and the two phase singularities will appear as a single one (Fig. V.8.d). It might be not as straightforward to determine the perfect or dissoiciated character of a dislocation from the recosntructed displacement field. That being said, perfect and dissociated dislocation yield a different phase distribution which in principle allows to differentiate them even if only phase singularity is visible in both cases (Fig. V.5.4).
As discussed above, the lower resolution of the experimental data is likely to be compensated by larger dissociation lengths. It is thus perfectly conceivable that the two phase singularities corresponding to the two Shockley partials can be resolved experimentally. For this reason we chose in the following to reconstruct the displacement field with a high resolution in the following. This choice is also obviously related to the small size of the particles (~15 → 30 nm) which readily exclude the possibility to represent them with a 5x5x5 nm^3 voxel size.

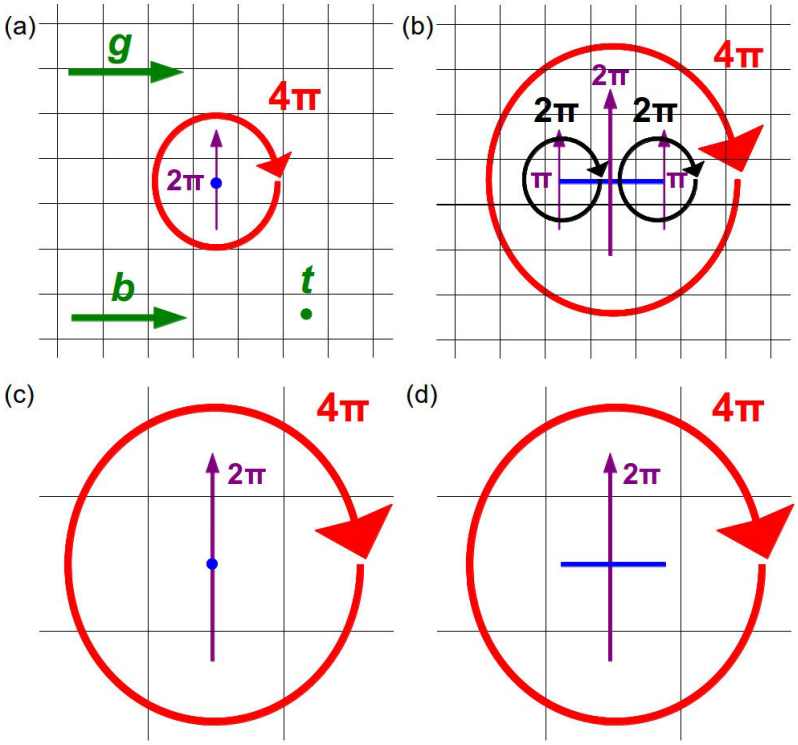

Fig. V.8 *Identification of dissociated edge dislocations with* ***g*** *//* ***b*** *for low and high real-space resolution data.* The grid represents the pixel size in the reconstruction. (a) & (c) Phase variation around a perfect edge dislocation for high (a) and low (d) resolution data. In both cases the phase vortex and sharp phase jump are visible independently on the resolution (b) Phase variation around a dissociated dislocation for high resolution data. The stacking fault ribbon is represented by a blue line. The pixel size smaller than the physical dissociation length allows to see the two phase singularities associated to the two Shockley partials. (d) Phase variation around a dissociated dislocation for low resolution data. The pixel size larger than the physical dissociation length does not allow to resolve the two phase singularities.

V.3. Single mixed dislocation in the course of nanoindentation of a gold nanoparticle

In section III.4, we demonstrated that it is possible to determine the Burgers vector and slip plane of a dissociated mixed dislocation nucleated during nanoindentation of a gold nanoparticle.
In the following we use phase retrieval algorithms to try to find more information about this single defect (width of the stacking fault ribon, orientation of the dislocation line, direct imaging...).
In the calculated CXD pattern, the signature of the dislocation is clearly visible for $\boldsymbol{g}$ = 1 1 1 and $\boldsymbol{g}$ = $\bar{1}$ 1 1 while it was invisible for $\boldsymbol{g}$ = 1 $\bar{1}$ 1 and $\boldsymbol{g}$ = 1 1 $\bar{1}$. The Burgers vector of the dislocation was determined to be ½[0 1 1] because it is the only vector that is perpendicular to the two diffraction vectors which fulfill the invisibility conditions ($\boldsymbol{g}.\boldsymbol{b}$ = 0).
Fig. V.9.a shows the indented particle viewed from the (1 1 $\bar{1}$) direction which is perpendicular to the stacking fault ribbon between the Shockley partials. The Burgers vector of the perfect dislocation and of the partial Shockley dislocations are indicated by coloured arrows (blue for the perfect and red and green for the partials)

while the direction of the indentation is indicated with a purple arrow (also on Fig. V.9.b to V.9.g). The dislocation line is mostly parallel to its Burgers vector, it has thus a dominant screw-type, however, the curvature of the dislocation line also brings an additional edge component.
From the direct analysis of the CXD pattern, it was already possible to determine the Burgers vector of the partial dislocations. The slip plane of the perfect dislocation was established from the perturbations of the fringes along the [1 1 $\bar{1}$] direction, and its Burgers vector with the invisibility conditions. With the knowledge of both slip plane and Burgers vector, the determination of the partial Burgers vector of the Shockley partial is straightforward since only one combination is possible (Hull & Bacon 1982):

$$\boldsymbol{b} = \tfrac{1}{2}[0\,1\,1] = 1/6[1\,1\,2] + 1/6[\bar{1}\,2\,1] = \boldsymbol{b}_{p1} + \boldsymbol{b}_{p2} \quad \text{(V.1)}$$

As demonstrated in the previous section, a diffraction vector perpendicular to one of the two partial Burgers vectors should in principle hide the signature of that partial The situation might be complicated here by the mixed-type of the dislocation.
Fig. V.9.b-e show the displacement field reconstructed for the four 1 1 1-type Bragg reflections that have been used to determine the Burgers vector of the dislocation. As discussed in the introduction of this chapter, the the reconstruction is carried-out following the procedure fully described in Chapter I (subsection I.3.4). The extent of the reciprocal space pattern gives a voxel size of 0.8x0.8x0.8 nm^3. This is about 8 times smaller than the typical experimental voxel size.
Similarly to Fig. V.7.a the particle is seen from the [1 1 $\bar{1}$] direction which is perpendicular to the stacking fault ribbon. Unsurprisingly, it remains invisible for $\boldsymbol{g}$ such as $\boldsymbol{g}.\boldsymbol{b} = 0$ ($\boldsymbol{g}$ = 1 $\bar{1}$ 1 and $\boldsymbol{g}$ = 1 1 $\bar{1}$, Fig 9.d and 9.e) while it appears clearly for $\boldsymbol{g}$ such as $\boldsymbol{g}.\boldsymbol{b} \neq 0$ ($\boldsymbol{g}$ = 1 1 1 and $\boldsymbol{g}$ = $\bar{1}$ 1 1) (Fig V.9.b & V.9.c) . For the latter, the decrease in the reconstructed the electron density that results from the presence of crystal defects (Takahashi *et al.* 2013, Labat *et al.* 2015) allows to determine the position and the shape of the dislocation. The density is superimposed in transparency in Fig. V.9.b, V.9.c and V.9.f. Two major differences arise between $\boldsymbol{g}$ = 1 1 1 and $\boldsymbol{g}$ = $\bar{1}$ 1 1. First, $\boldsymbol{g}$ = 1 1 1 is parallel to the displacements to the [$\bar{1}$ $\bar{1}$ $\bar{1}$] indentation direction. As seen in Fig. V.9.a, the indenter already penetrated deeply in the particle at this stage of the indentation process. As a consequence the (1 1 1) planes in the vicinity of the indenter are severely compressed which results in a steep phase gradient. The negative phase gradient in that area is consistent with a compression. For $\boldsymbol{g}$ = $\bar{1}$ 1 1 the phase in the same region is almost constant as $u_{\bar{1}\,1\,1}$ is weakly sensitive to the displacements along the [1 1 1] direction. In both cases the dislocation induce a π phase jump between the two sides of the dislocation line. However the position of the phase discontinuity differs between the two configurations.
For the $\bar{1}$ 1 1 reflection, it is located on the partial dislocation with $\boldsymbol{b}_{p1}$ = 1/6[$\bar{1}$ 2 1](the bottom one), while it is located on the second partial with $\boldsymbol{b}_{p2}$ = 1/6[1 1 2] for the 1 1 1 reflection. In the (1 1 $\bar{1}$) plane which contains the stacking fault ribbon, the phase profile is similar to the case of the dissociated edge dislocation for $\boldsymbol{g}.\boldsymbol{b}_p = 0$ ($\boldsymbol{g}$ = 2 0 $\bar{2}$, Fig. V.4.e). Although neither $\boldsymbol{g}$ = 1 1 1 nor $\boldsymbol{g}$ = $\bar{1}$ 1 1 are perpendicular to one of two partials dislocations, we observe similar phase distributions in Fig.V.9.b and V.9.c. For $\boldsymbol{g}$ = 1 1 1, almost parallel to $\boldsymbol{b}_{p2}$, $\boldsymbol{b}_{p1}$ is completely invisible (Fig. V.9.b) while the invisibility of $\boldsymbol{b}_{p2}$ is achieved for $\boldsymbol{g}$ = $\bar{1}$ 1 1 almost parallel to $\boldsymbol{b}_{p1}$ (Fig. V.9.c) .
For the two other 1 1 1-type reflections the dislocation is invisible, but some obvious differences can be observed between $\boldsymbol{g}$ = 1 $\bar{1}$ 1 and $\boldsymbol{g}$ = 1 1 $\bar{1}$. The amplitude of the phase variations just below the indenter differs between the two reflections. They are significant for $\boldsymbol{g}$ =1 $\bar{1}$ 1 (Fig. V.9.d) while the phase is almost constant for $\boldsymbol{g}$ = 1 1 $\bar{1}$ (Fig. V.9.e). The most important difference lies in the invisibility conditions for the two reflections. $\boldsymbol{g}$ = 1 1 $\bar{1}$ fulfills the total invisibility conditions for a dissociated dislocation since it is perpendicular to $\boldsymbol{b}$ and to the Burgers vectors of the partial dislocations. As a consequence, the partial dislocations are completely invisible and induce no visible change in the phase (Fig. V.9.e). For $\boldsymbol{g}$ =1 $\bar{1}$ 1 the invisibility conditions for the partial dislocation are not fulfilled, and some phase variations can be observed at the vicinity of the partial dislocations (region circled in red in Fig. V.9.d).

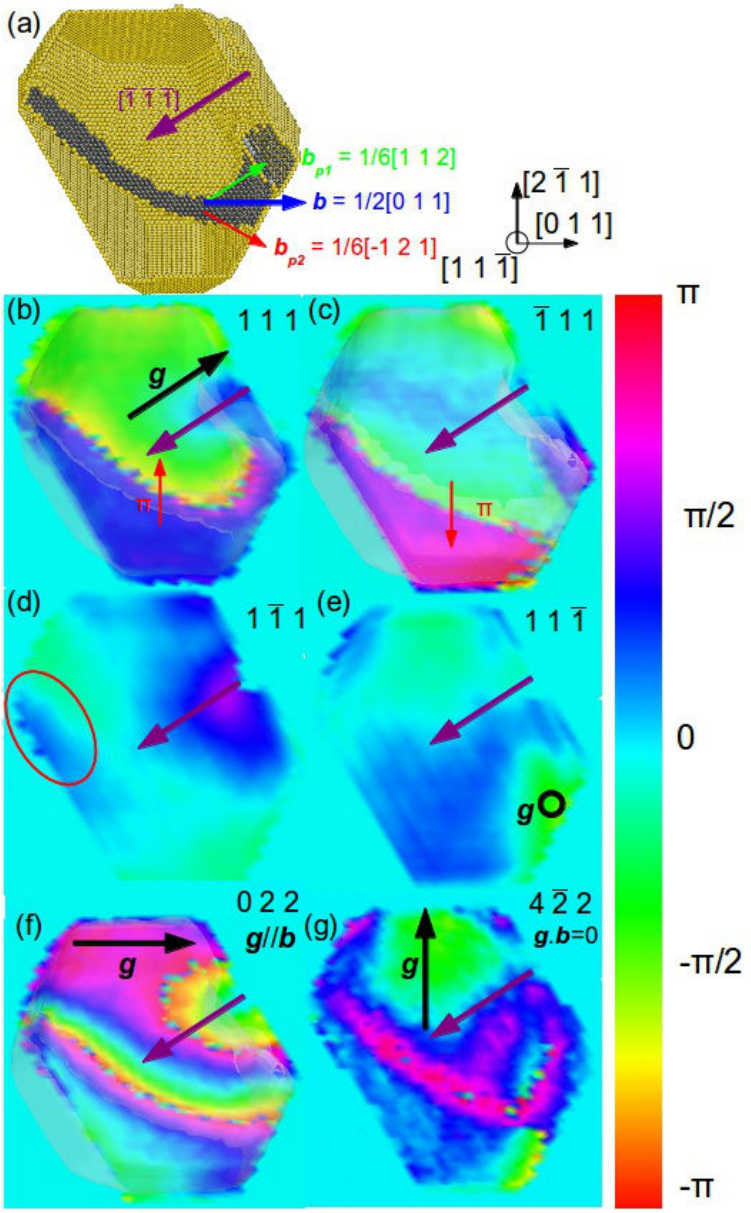

Fig. V.9 *Reconstructed displacement field of the mixed-dislocation for several* ***g*** (a) Gold nanoparticle undergoing simulated nanoindentation seen from the [1 1 $\bar{1}$] direction. Only the surface and defective atoms are shown, and the dislocation appears in grey. The direction of the Burgers vectors are indicated with a blue (perfect dislocation) and red and green arrows (partial dislocations). (b) to (g) Reconstructed displacement field in the (1 1 $\bar{1}$) dislocation slip plane, for various ***g***: 1 1 1 (b), $\bar{1}$ 1 1 (c), 1 $\bar{1}$ 1 (d), 1 1 $\bar{1}$ (e), 0 2 2 (f) and 4 $\bar{2}$ 2 (g). The direction of the ***g*** is indicated with a black arrow while the direction of the indentation is marked with a purple arrow.

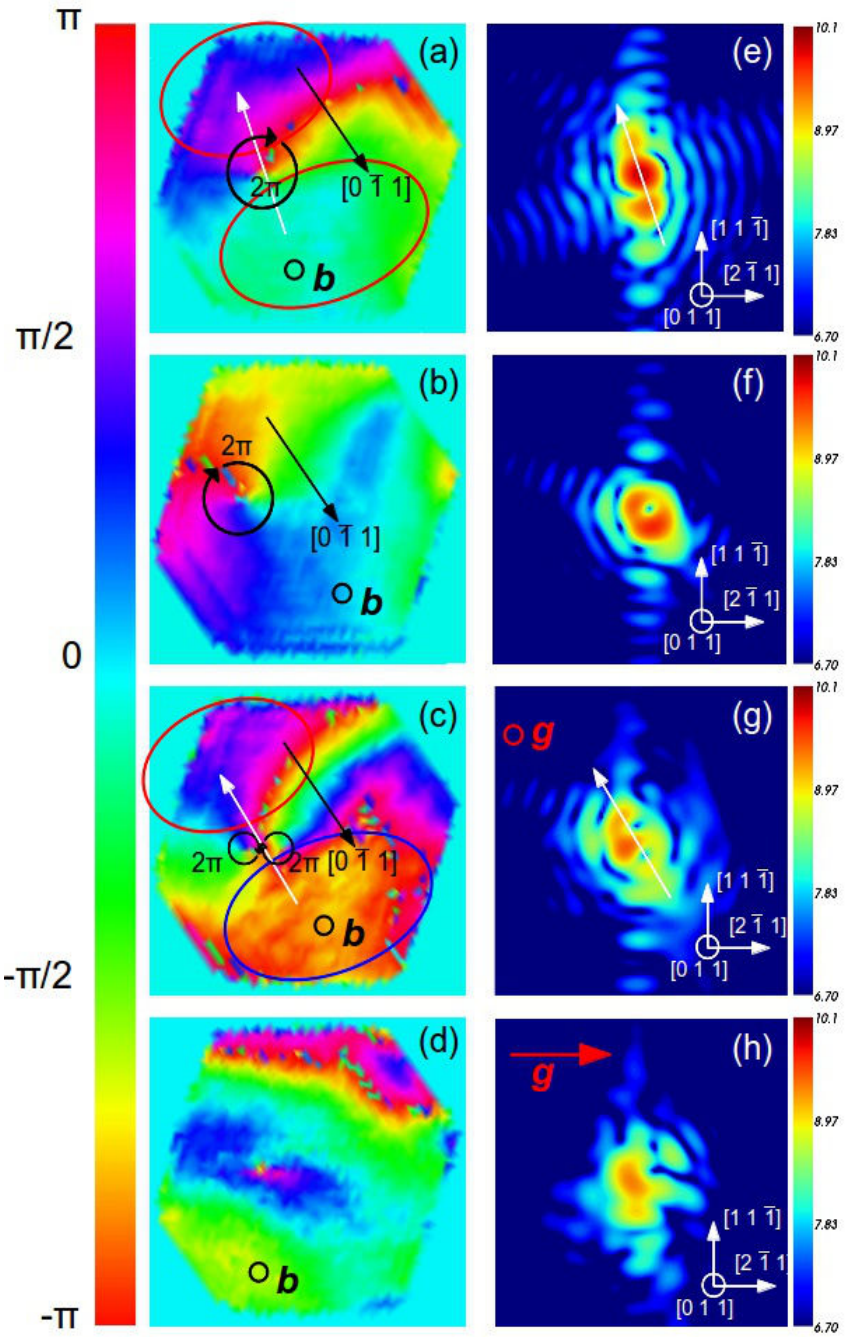

Fig. V.10 *Comparison between reconstructed displacement field and calculated CXD patterns for several* ***g*** (a) to (d) Reconstructed displacement field in the (0 1 1) plane perpendicular to ***b*** for various ***g***: 1 1 1 (b), $\bar{1}$ 1 1 (e), 0 2 2 (f) and 4 $\bar{2}$ 2 (g). The direction of the strongest phase gradient is indicated with a black arrow, while the white arrow connects the regions of almost constant phase circled in red and blue. (e) to (h) Corresponding CXD patterns in the (0 1 1) plane for the same reflections .The direction of ***g*** is indicated with a red circle (g) or a red arrow (h).

To push a bit further the analysis, the 3D displacement field has been reconstructed for two additional projections. For $\boldsymbol{g}$ = 0 2 2, parallel to $\boldsymbol{b}$, the results are similar to the case of a pure edge dislocation. The two partial dislocations induce two π phase jumps, and the phase is relatively constant for the area within the stacking fault ribbon (Fig. V.9.f). Here the (1 1 $\bar{1}$) slice is taken slightly above the staking fault ribbon, such that the phase jumps do not appear as a sharp discontinuity but as strong gradients. For the case of a pure edge dissociated dislocation, the phase outside the stacking fault ribbon is almost constant (Fig. V.2.e.). Here the phase remains quite constant below the dislocation line, while strong varations are observed for the region above the dislocation line. These phase variations can be explained by the sensitivity of $\boldsymbol{g}$ = 0 2 2 to the compression of the (1 1 1) planes by the indenter, $\boldsymbol{g}$ is indeed almost anti-parallel to the [$\bar{1}$ $\bar{1}$ $\bar{1}$] along which the displacements are the strongest.

$\boldsymbol{g}$ = 4 $\bar{2}$ 2 would be the invisibility conditions for a pure edge dislocation, but here the mixed character of the dislocation line prevents the existence of such conditions. Some similarities with the case of a pure edge dislocation can be found though. The region within the stacking fault ribbon is phase shifted compared to the rest of the crystal (Fig. V.9.g.). The value of the phase shift is approximately the same as the one observed for a pure edge dislocation (Fig. V.5.d). The indenter induce some additional perturbations in the phase. One can notice the presence of an area above the dislocation line where the phase becomes negative (area in green in Fig V.9.e.), as well as the presence of a strong phase gradient in a direction perpendicular to the direction of indentation.

As shown in Fig. V.10, the analysis of the reconstructed displacement field in the (0 1 1) plane also reveals some interesting informations. For $\boldsymbol{g}$ = 1 1 1 (Fig. V.10.a) and $\boldsymbol{g}$ = $\bar{1}$ 1 1 (Fig. V.10.b), it confirms the presence of a 2π phase vortex whose centre is one of the two partial dislocations ($\boldsymbol{b}_{p2}$ for $\boldsymbol{g}$ = 1 1 1 and $\boldsymbol{b}_{p1}$ for $\boldsymbol{g}$ = $\bar{1}$ 1 1). While the phase rotation around the dislocation line is relatively isotropic for $\boldsymbol{g}$ = $\bar{1}$ 1 1 (Fig. V.10.a), it is highly anisotropic for $\boldsymbol{g}$ = $\bar{1}$ 1 1 (Fig. V.10.b). A strong phase gradient is observed along the [0 $\bar{1}$ 1] direction which is perpendicular to the Burgers vector direction and the indentation direction (Fig. V.10.a).

The relative isotropy of the phase in real space for $\boldsymbol{g}$ = $\bar{1}$ 1 1 implies an isotropy of the intensity in the reciprocal space. A ring-shaped pattern oriented along the [$\bar{1}$ 1 1] direction is obtained as in the case of a relaxed screw dislocation (subsection III.3.1) (Fig. V.8.f). The anisotropic distribution of intensity in the ring is due to the shift of the dislocation line with respect to the particle centre (subsection III.3.7).

For $\boldsymbol{g}$ = 1 1 1, a splitting of the Bragg peak is observed instead of a ring. As already discussed, the splitting is roughly along the direction which connects the regions of constant phase (white arrow which connect the two red circled regions on Fig. V.10.a). Similarly to $\boldsymbol{g}$ = $\bar{1}$ 1 1 the anisotropy in the intensity distribution of the Bragg peak can be explained by the shift of the dislocation with respect to the particle centre.

When $\boldsymbol{g}$ is parallel to $\boldsymbol{b}$ a pair of 2π phase vortices with the same direction can be observed. As mentioned in the previous paragraph, their centre correspond to the position of the partial dislocation. Although the dislocation is of dominant screw-type, the overall phase distribution is similar to the case of a dissociated pure-edge dislocation (Fig V.8.a). Similarly to our observations for the two-1 1 1 type diffraction vectors, the phase variation is relatively isotropic around the left partial ($\boldsymbol{b}_{p1}$ = 1/6[$\bar{1}$ 2 1]) while it is highly anisotropic for the right partial ($\boldsymbol{b}_{p1}$ = 1/6[1 1 2). For the latter, the strongest phase gradient is also along [0 $\bar{1}$ 1]. The diffraction pattern in the (0 1 1) plane perpendicular to the Burgers vector and quasi perpendicular to the dislocation line is surprisingly very similar to the case of a perfect edge dislocation while we would have expected an intensity distribution similar to the case of a dissociated edge dislocation. The orientation of the Bragg peak is also roughly along the direction which connects the regions of constant phase (white arrow which connect the blue and red circled regions on Fig. V.10.c), which almost correspond to the [0 $\bar{1}$ 1] direction.

For $\boldsymbol{g}$ = 2 2 $\bar{4}$ the displacement field is not as symmetric as in the case of a pure-edge dislocation, but both the value of the phase shift and the distribution of the displacements at the vicinity of the stacking fault ribbon are quite similar (Fig. V.10.d). Due to to the strong compressive strain on the topmost (1 1 1) planes, The diffraction pattern is very “disturbed” as compared to the case of the pure edge dislocation.

The calculation of the CXD patterns and the reconstruction of the 3D displacement fields for various Bragg reflections reveal that the dislocation produces a signature which shares strong similarities with either a pure screw dislocation ($\boldsymbol{g}$ = $\bar{1}$ 1 1) or a pure edge dislocation ($\boldsymbol{g}$ = 0 2 2). This is probably due to the fact that a mixed

dislocation possesses both components.

V.4. Displacement fields from individual dislocation loops

Although the displacement field around individual dislocation loops is rather complex, some information can readily be obtained from the CXD pattern. The diffuse scattering of individual dislocation loops has been studied numerically (Erhart 1982, Zhou *et al.* 2005) and experimentally using a coherent electron beam (Kirk *et al.* 2005, Kirk *et al.* 2006). This allowed to determine both the size, the Frank or Prismatic type and the Burgers vector of individual dislocation loops. We evidenced in subsections III.3.4 (Frank), III.3.5 (Prismatic) and sections IV.1 (Frank and prismatic) that such properties can also be obtained from the analysis of CXD patterns.
The direct analysis of the CXD patterns is generally quite straightforward in the case of individual dislocation lines or stacking faults. They induce strong signature on the CXD pattern (such as a splitting of the Bragg peak) because there is generally only one phase singularity (2 in the case of partial dislocations) and as a consequence the size of the phase-shifted volumes is very large. The analysis can be complicated by the more complex nature of the displacement field around partial dislocations. However, such single defects always induce a clear and strong signature in the CXD patterns (unless the invisibility conditions are fulfilled).
In the case of dislocation loop, it is shown in the following that a large number of phase singularities are created in the nanocrystal, and that the volume in the crystal that are phase shifted with respect to each other remain generally limited. As shown in subsections III.3.4, III.3.5 and IV.1 (individual dislocation loops) and in section IV.2 (assembly of prismatic loops), the signature of dislocation loops on CXD patterns is generally quite weak. The reconstruction of the displacement field around the defect is thus needed to understand all its characteristics.

V.4.1. Frank dislocation loops

Interstitial and vacancy dislocation loops are introduced at the centre of our reference Wulff copper nanocrystal. As described in section 3.4 their Burgers vector is of type 1/3 <1 1 1> (1/3[1 1 1] in the present case) and both interstitial and vacancy loop contain stacking faults (extrinsic for the interstitial one and intrinsic for the vacancy one). Upon relaxation, the hexagonal Frank loop dissociate to produce a stair rod dislocation on each edge of the hexagon and a Shockley partial which propagates in the three other {1 1 1} slip planes.
A vacancy dislocation loop can be produced by the collapse of a platelet of vacancies while an interstitial loop can be induced by the precipitation of a close-packed platelet of interstitial atoms. In both case, the creation of such defects assume the insertion of removal of atoms within the loop. In section V.1, the atomic displacements are calculated from the reference atomic positions in a perfect crystal with the same number of atoms. Since the number of atoms is changed by the introduction of a Frank or a prismatic dislocation loop, this method of calculation is no longer applicable. Our calculation could have been modified to overcome this problem. However we evidenced in subsection I.3.4 (Chapter I) and section V.2 that the reconstructed displacement fields from the calculated CXD pattern are very reliable and consistent with the calculated displacement fields. In the following all the displacement fields shown are reconstructed from the diffraction patterns using the procedure fully described in Chapter I.
The invisibility conditions for Frank dislocation have been detailed in subsection III.3.4, they slightly differ from the case of dislocation line, since for instance there are no conditions for which $\boldsymbol{g}$ is parallel to the dislocation line. To investigate the displacement field around the dislocation loop we select diffraction conditions that can hide different contributions of the dislocation loop, *i.e.* the stacking fault or the partial dislocations for instance. For a given reflection, if the stacking fault, or the partial dislocations of the loop are visible they create a singularity in the phase. As already described in this manuscript and elsewhere (Takahashi *et al.* 2013, Labat *et*

al. 2015) these phase singularities induce a dip in the reconstructed electron density that can be used to visualize the contour of the defects using isosurfaces of density (as already shown in section V.3. of this chapter).

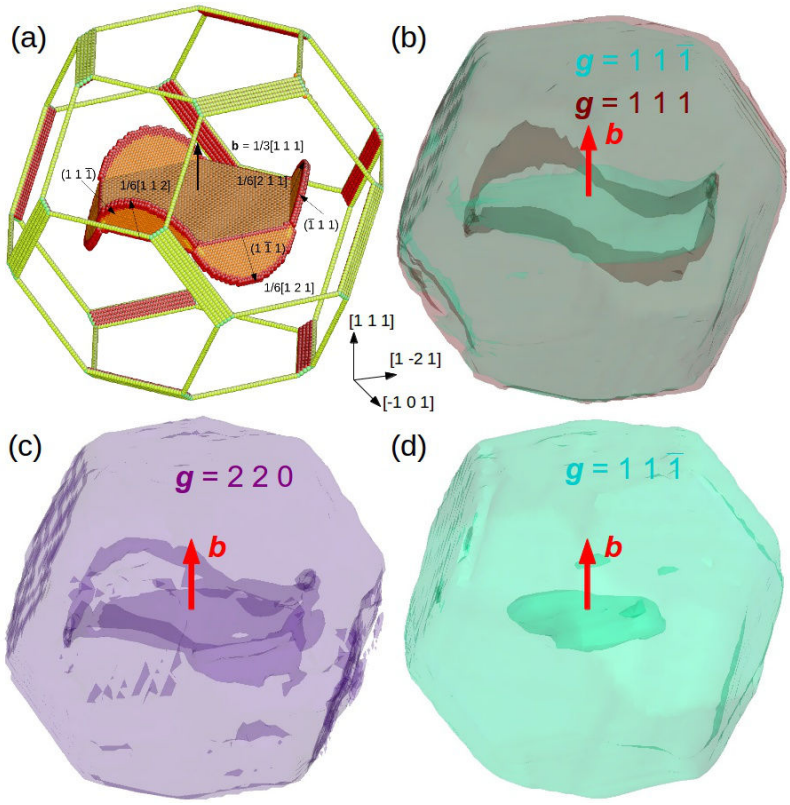

Fig. V.11 *Variations in the reconstructed electron density at the vicinity of a Frank dislocation loop* (a) Relaxed Frank dislocation loop with $\boldsymbol{b}$ = ⅓ [1 1 1] in the centre of the reference copper nanocrystal. (b) to (d) 70% isosurface of the reconstructed electron density which reveals the position of the stacking fault and of the partial dislocations. The Burgers vector of the loop is indicated with a red arrow. (b) Reconstructed electron density from a 20 nm interstitial loop for $\boldsymbol{g}$ = 1 1 $\bar{1}$ (blue isosurface) and $\boldsymbol{g}$ = 1 1 1 (red isosurface). (c) Reconstructed electron density from the same loop for $\boldsymbol{g}$ = 2 2 0. (d) Reconstructed electron density from a 13nm vacancy loop for $\boldsymbol{g}$ = 1 1 $\bar{1}$.

For $\boldsymbol{g}$ = 1 1 1, the invisibility conditions for the partial dislocations are not fulfilled, their contour is clearly visible on Fig. 11.b (red isosurface). Since $h+k+l = 3n$, the stacking fault is completely invisible.
Conversely, for all the other 1 1 1-type reflections (except the $\bar{1}$ $\bar{1}$ $\bar{1}$) the stacking fault is visible, while four out of six Shockley partials are invisible (blue isosurface in Fig 11.b). The last pair only produce few disturbances in the phase and does not appear as a phase singularity.
For $\boldsymbol{g}$ = 2 2 0 (Fig. V.11.c) which is parallel to one of the partial stair rods, none of the invisibility conditions are fulfilled and both the (1 1 1) stacking fault and the partial Shockley dislocations cause a phase jump which in turn affect the electron density. The stacking fault and all partial dislocations are visible.
Finally, for a smaller vacancy loop investigated with the same reflection, the (1 1 1) stacking fault is also visible (Fig. V.9.d). It is of course not possible to distinguish between interstitial and vacancy loop from the dip in the electron density since it is independent on the sign or magnitude of the singularity in the phase.
The vacancy or interstitial character of the loop can be easily deduced from the reconstructed displacement field.

As described in subsections III.3.3 and IV.1.1 the phase jump expected from an intrinsic or extrinsic stacking fault depends on the Bragg reflection and can be easily calculated. For $\boldsymbol{g} = 1\ 1\ \bar{1}$, a $2\pi/3$ phase jump is expected from an intrinsic stacking fault while a $-2\pi/3$ is expected from an extrinsic one. Here we introduced Frank dislocation loops with diameters of 6, 13 and 20 nm in the reference Wulff nanocrystal. The small and the large loop are interstitial loops while the intermediate one is a vacancy loop. As expected from the analytical calculations (subsection III.3.3), the latter produces a $2\pi/3$ (Fig. V.12.b) phase jump while a $-2\pi/3$ phase jump is found for the two others (Fig. 12.a and 12.c).

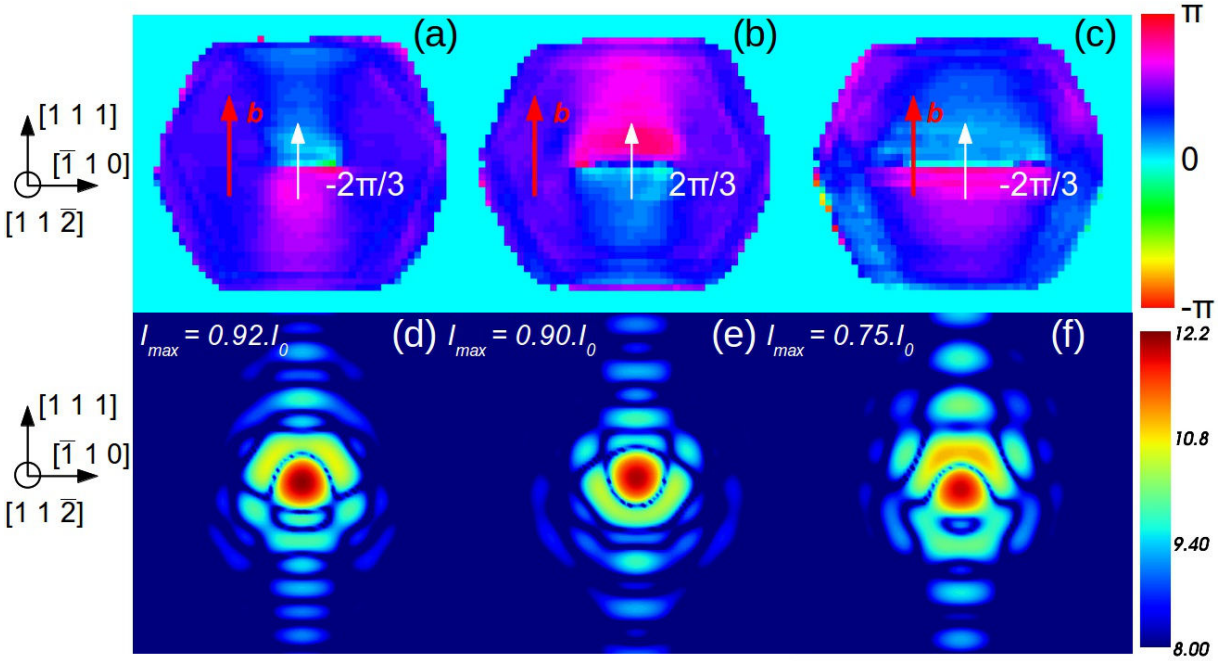

Fig. V.12 *Reconstructed displacement field from loops of varying size and type for* $\boldsymbol{g} = 1\ 1\ \bar{1}$. (a) 6nm interstitial (b) 13 nm vacancy and (c) 20nm interstitial. The direction of the burgers vector is indicated by a red arrow. (d) to (f) Corresponding CXD patterns for $\boldsymbol{g} = 1\ 1\ \bar{1}$

As already discussed in section IV.1.1, this is translated on the CXD pattern by the position of the satellite spot: above the Bragg peak for the interstitials (Fig. V.12.d and V.12.f) and below for the vacancy (Fig. V.12.e). One can also notice that the larger is the stacking fault, the more intense is the satellite peak. It will eventually become more intense than the Bragg peak when the stacking fault spreads all other the crystal volume. As mentioned in section III.3.3, the intensity of the fringes normal to the stacking fault also increases with the width of the stacking fault, while the maximum of intensity decreases. For a given loop size, we also noticed that the decrease of the maximum of intensity is always slightly larger for an interstitial loop than for a vacancy loop.
In good agreement with our observations in section IV.1.2, the spatial extent of the displacement field increases with the diameter of the loop. If some regions of the crystal remain relatively undisturbed for the small loop (Fig. V.12.a), the displacement field spreads all over the crystal for the large one (Fig. V.12.c).
For $\boldsymbol{g} = 1\ 1\ 1$ ($\boldsymbol{g}$ // $\boldsymbol{b}$) which allows to see the contribution from the partial dislocations, the displacement field around the dislocation loop is much more complex and interesting. As illustrated on Fig. 4.a and 4.b, the (1 1 1) stacking fault does not produce any visible phase jump and as a result is invisible. The partial dislocation induces singularities in the phase, and a partial dislocation line causes a π phase jump in the phase. As a consequence, for all the planes that intercept a partial dislocation, the phase around the partial dislocation forms of a vortex.
Both the $(1\ \bar{1}\ 0)$ and $(1\ 1\ \bar{2})$ plane intercept two partial dislocations and a pair of 2π vortices with opposite chirality is seen in both cases (as seen by Takahashi *et al.* 2013). One can notice that the displacements are

almost constant in between the partials, above and below the dislocation loop (region in red Fig. V.13.a & V.13.b) while the phase is varying rapidly outside the loop. The largest phase gradient is observed in the direction normal to ***g***. This is in very good agreement with the description of the strain field around an interstitial Frank loop that was made by Larson & Young (1987). The compressed area above and below the loop exhibits a remarkably constant strain, whose extent is roughly the diameter of the loop in both directions. Conversely, in the expanded area outside the loop the strain is not constant over any significant spatial extent.

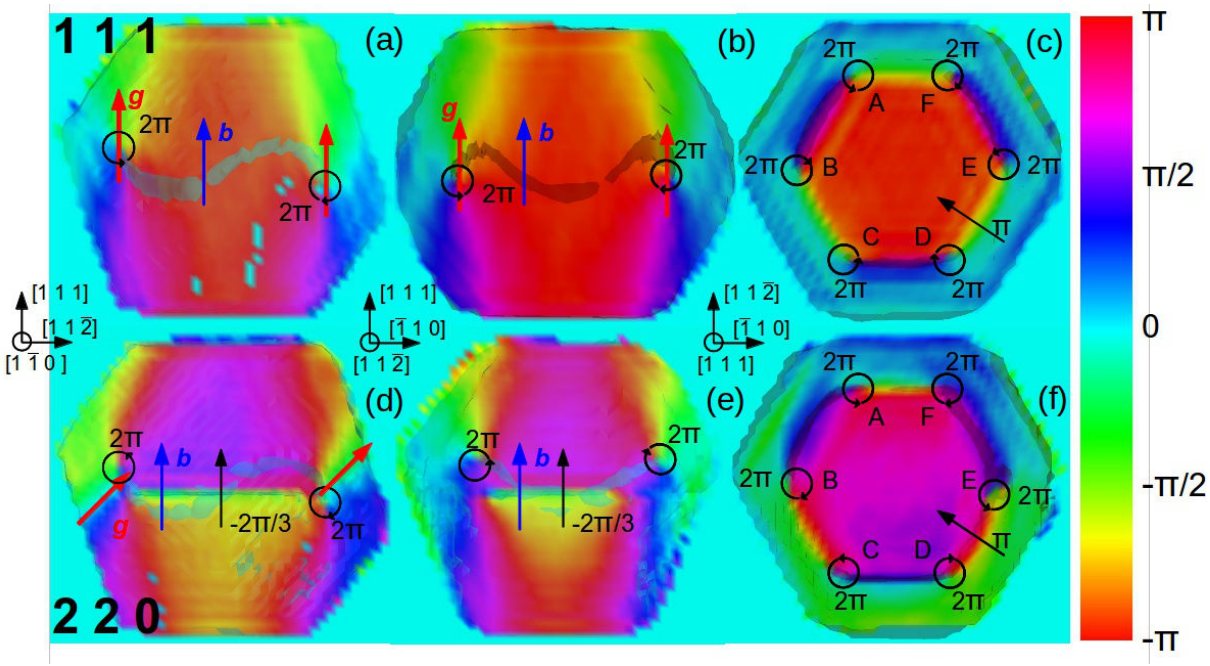

Fig. V.13 *Reconstructed displacement field from a 20 nm Frank interstitial loop for several* ***g***. The direction of ***g*** is indicated by a red arrow while the direction of the burgers vector of the loop is denoted by a blue arrow. The position of the loop is shown in transparency. (70% isosurface of the reconstructed electon density). (a) to (c) Reconstructed u_{111} displacement field in the (1 1 0) (d), (1 1 2) (e) and (1 1 1) (f) planes. (d) to (f) Reconstructed u_{220} displacement field in the (1 1 0) (d), (1 1 2) (e) and (1 1 1) (f) planes.

The (1 1 1) plane which contains the dislocation loop (Fig. V.13.c) reveals that the (1 $\bar{1}$ 0) plane is a mirror plane for the displacement field. The partial dislocations intercept the (1 1 1) plane on six different locations, and as a consequence a loop of 6 vortices of alternating chirality can be observed. The region inside the loop is phase shifted by π with respect to the surrounding region.

For ***g*** = 2 2 0, the situation is different because the stacking fault is visible (Fig. V.11.d to V.11.f) causing an additional -2π/3 phase jump phase jump owing to the interstitial nature of the loop. Apart from this phase jump, the phase is constant above and below the loop, and varies rapidly outside. As for ***g*** = 1 1 1, the (1 $\bar{1}$ 0) and (1 1 $\bar{2}$) planes intercept the partial dislocations in two points, creating a pair of opposite phase vortices. The maximum phase gradient is also normal to ***g*** =2 2 0 (red arrow in Fig. V.11.d). This phenomena are observed for both ***g*** =2 2 0 and ***g*** = 1 1 1. The displacements observed in the (1 1 1) plane (Fig. V.13.f) are very similar to the one observed for ***g*** = 1 1 1 with the (1 $\bar{1}$ 0) plane acting as a mirror plane, resulting in loop of 6 vortices of alternating chirality.

As illustrated in Fig. V.14.c, the calculated diffraction pattern from the interstitial dislocation loop for ***g*** = 2 2 0 (***g*** // $\boldsymbol{b}_{SR}$) "pseudo ring" shaped pattern with axis oriented along the [2 2 0] direction. In subsection III.3.4, a parallelism was made with the case of screw dislocation loops. The phase distribution in the case of a screw dislocation loop is fairly simple (subsection V.1.1), with a single π phase singularity at the dislocation line position and thus a 2π phase vortex in the plane perpendicular to the dislocation line. The phase distribution in

the (2 2 0) plane perpendicular to ***g*** is here much more complicated with three phase singularities: 2 vortices with opposite chirality corresponding to the two positions where the partial dislocations intercept the (1 1 0) plane, and the -2π/3 phase jump induced by the extrinsic stacking fault.
This example evidences that two completely different displacement fields around a given crystal defect can induce a relatively similar signature. To have a clear picture of the defect, it is thus necessary to reconstruct the displacement field around the dislocation loop

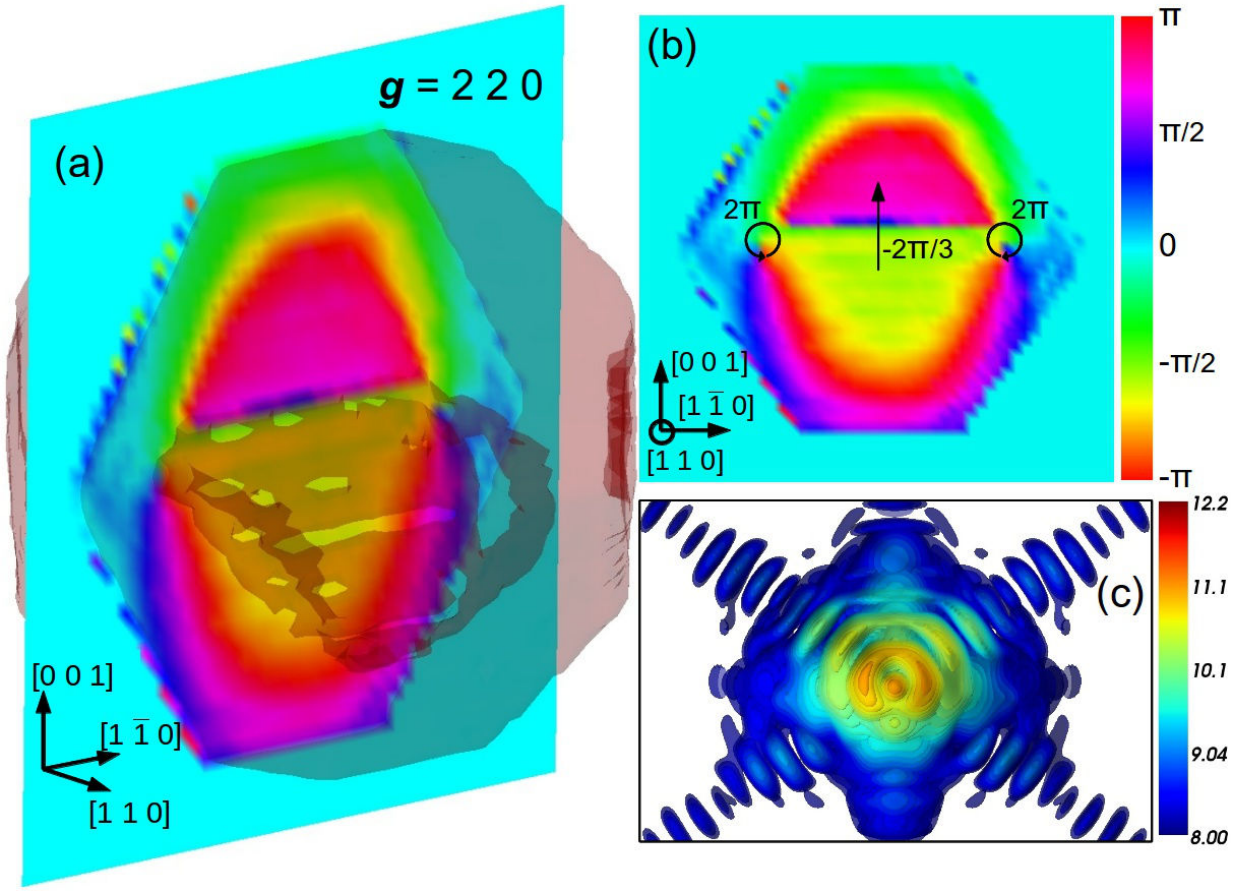

Fig. V.14 *Reconstructed $u_{2\,2\,0}$ displacement field from the 20nm interstitial loop in the (2 2 0) plane.* (a) and (b). (c) Corresponding CXD pattern for ***g*** = 2 2 0. The position of the loop is shown in transparency. (70% isosurface of the reconstructed electon density).

V.4.2. Prismatic dislocation loops

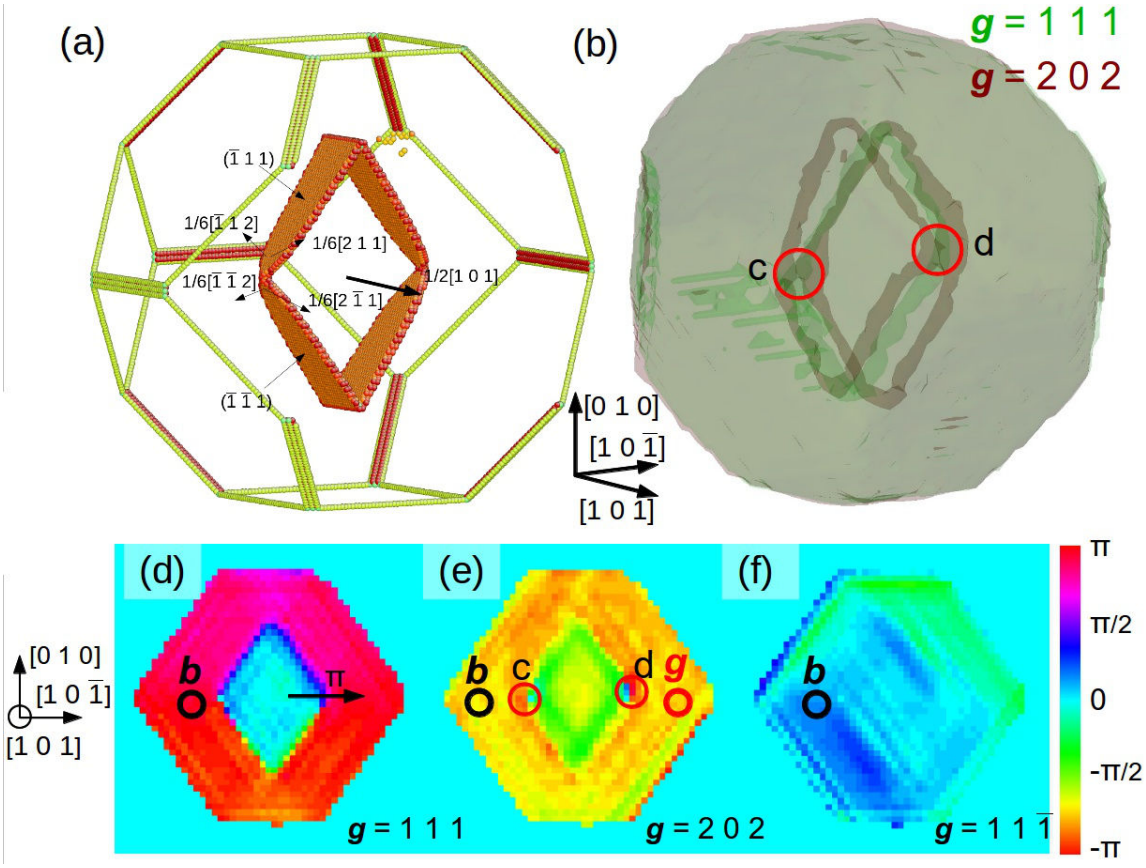

Fig. V.15 *Reconstruction of the displacement field from a diamond shaped prismatic loop for several* $\boldsymbol{g}$ (a) Relaxed 15x10 nm^2 diamond shaped prismatic dislocation loop with $\boldsymbol{b}$ = ½ [1 0 1] at the centre of the reference Wulff copper crystal. The colour code represents the coordination number, such that only the defective atoms and nanocrystal edges are shown. (b) 70% isosurface of the reconstructed electron density which reveals the position of the loop for $\boldsymbol{g}$ = 1 1 1(green isosurface) and $\boldsymbol{g}$ = 2 0 2 (red isosurface). (d) to (f) Reconstructed displacement field in the (1 0 1) plane for $\boldsymbol{g}$ = 1 1 1 (d), $\boldsymbol{g}$ = 2 0 2 (e) and $\boldsymbol{g}$ = 1 1 $\bar{1}$ (f). The orientation of the burgers vector is indicated by either a black arrow or a black circle. The letter c and d denote phase discontinuities at the interface between two dislocation segments.

In this section, the displacement field around a prismatic dislocation loop is reconstructed for several Bragg reflections. We will see that they share strong similarities with Frank dislocation loops.

As presented in subsection III.3.5, a single dislocation loop is introduced at the centre of our reference copper nanocrystal. At the end of the relaxation, the loop consists of four dislocation segments which are connected together in the form of a diamond (Fig V.15.a). The dislocation segments form stacking fault ribbons in the ($\bar{1}$ 1 1) and (1 1 $\bar{1}$) plane which are bounded by two partial dislocations.

As a consequence, a total of eight partial dislocation is present in the loop. Similarly to what has been done for the mixed dislocation (section V.3) and the Frank dislocation loop (subsection V.4.1), the visibility or invisibility of the loop can be evaluated by the absence or presence of singularities in the phase. The corresponding dips in the reconstructed density unveil the contours of the loop. Three different reflections are used to characterize the displacement field around the defect. The most interesting case probably occurs for $\boldsymbol{g}$ = 2 0 2 ($\boldsymbol{g}$ // $\boldsymbol{b}$). All eight partial dislocations induce dips in the reconstructed density (red isosurface in Fig. V.15.b). This means that they

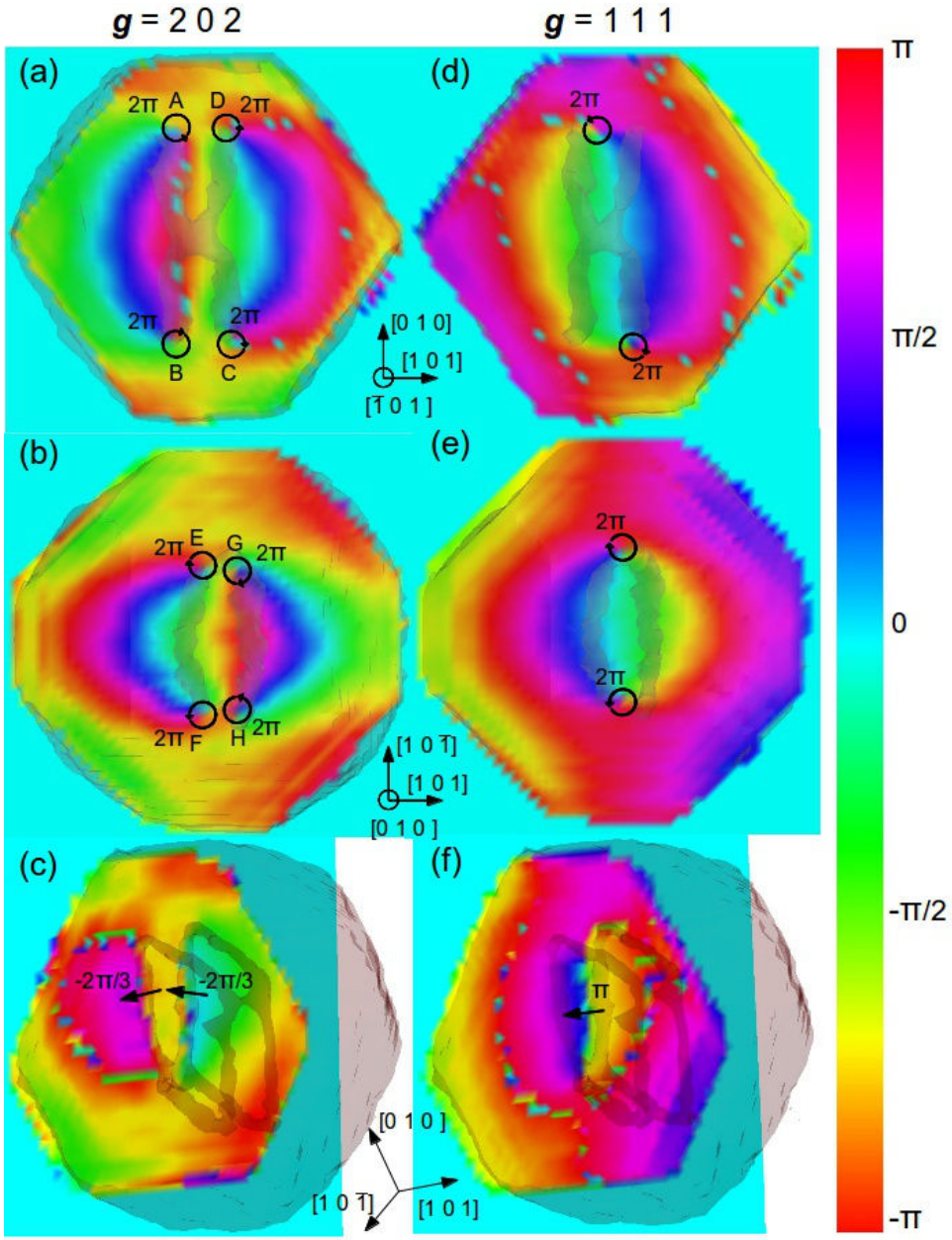

Fig. V.16 *Reconstructed displacement field from the diamond shaped prismatic dislocation loop for* $\boldsymbol{g} = 2\,0\,2$ *and* $\boldsymbol{g} = 1\,1\,1$ *in the* $(\bar{1}\,0\,1)$ *plane* : (a) and (d), the (0 1 0) plane (b) and (e) and the (1 1 $\bar{1}$) plane (c) and (f). The position of the loop is shown in transparency. (70% isosurface of the reconstructed electron density).

all create singularities in the phase.

For $\boldsymbol{g} = 1\,1\,1$, the partial dislocations are not distinguished (green isosurface in Fig. V.15.b) . This means that either this reflection is not sensitive to all the partials as in the case of a dissociated mixed dislocation) or that the dissociation can not be seen for this reflection. The dips of intensities seems to be located at the position of the partial dislocation, the first option is thus the most likely.

Fig. V.15.d to V.15.f, show the reconstructed displacements for the three reflections, in the (1 0 1) plane, perpendicular to the loop axis. For $\boldsymbol{g} = 1\,1\,1$ (Fig. V.15.d) the partial dislocations induce discontinuities in the

phase. The region inside the loop is phase-shifted by π with respect to the region outside the loop. For $\boldsymbol{g}$ = 2 2 0 the partial dislocations are seen individually, and the (1 1 0) plane intercept them only at points c and d where four partial dislocations belonging to two dislocations segments are connected. The π phase jump is only observed in the vicinity of c and d. Finally, the dislocation loop remains invisible $\boldsymbol{g}$ = 1 1 $\bar{1}$, ($\boldsymbol{g.b}$ = 0), the dislocation remains completely invisible, although some variations in the phase can be observed at the vicinity of the (1 1 $\bar{1}$) stacking fault ribbons (Fig. V.15.f). The ($\bar{1}$ 0 1) and (0 1 0) planes which are parallel to the loop axis are more suited to visualize the complex displacement field around the dislocation loop (Fig. V.16). As discussed in the previous paragraph, all eight partial dislocations are visible for $\boldsymbol{g}$ = 2 0 2 (visible in transparency on Fig.16.). The partial dislocations intercept the ($\bar{1}$ 0 1) and (0 1 0) planes in four distinct points and form on each plane two pair of vortices with opposite chiralty: A-B and C-D in the ($\boldsymbol{g}$ = 2 0 2 plane (Fig 16.a) and E-F and G-H in the (0 1 0) plane (Fig. 16.b).
A crucial difference arises compared to the case of Frank dislocation loops. In the case of a Frank loop, the phase is almost constant in the region along the loop axis and between the partial dislocations, while it varies rapidly outside the loop. In the case of prismatic loops, the exact opposite phenomenon occur: rapid phase variation are observed along the loop axis, inside the diamond shape formed by the partials, while it is almost constant in the region outside the tetrahedron . This phase profile and the absence of phase jump due to the absence of the stacking fault for a prismatic loop makes easy the distinction between a prismatic and a Frank dislocation loop.
The value of the phase jump induced by the partial dislocation can be obtained from the phase distribution in the (1 1 $\bar{1}$) plane that contains one of the stacking fault ribbon (Fig. 16.c). As seen from Fig. 16.c, the region in the stacking fault ribbon is phase shifted by 2π/3 with respect to the surrounding atoms. This value is quite surprising since it differs from the case of a dissociated edge dislocation and a mixed dislocation, where the stacking fault ribbon is phase-shifted by π with respect to the surrounding region (for $\boldsymbol{g}$ // $\boldsymbol{b}$). This is probably related to the anisotropy of the phase vortices in the planes perpendicular to the partial dislocations, so that the phase jump between the two parts on the dislocation line is not necessarily π.
For $\boldsymbol{g}$ = 1 1 1, the displacement field is less complicated. Fig. V16.d & V16.f reveals that only half of the partial dislocation are seen, since phase singularities are observed in only two points in the ($\bar{1}$ 0 1) and (0 1 0) planes. These two singularities form a pair of vortices with opposite chirality.
Similarly to $\boldsymbol{g}$ = 2 0 2 , there is a large phase gradient in the region along the loop axis, inside the tetrahedron while the phase is much more stable outside. The partial dislocation induces a π phase jump, as seen from Fig. 16.g, a value in good agreement with the cases of dissociated edge and mixed dislocations.

The complex nature of the displacement field around dislocation loop inherently produces complex signature which are difficult to analyze. Even if the distinction between a prismatic or Frank loop, the determination of its interstitial or vacancy character, or its size and Burgers vector can be determined from its signature on CXD patterns, the reconstruction of 3D field allows to obtain a richer and more complete picture of the defect. We will see in the next section that it is even more true when the crystal hosts several dislocation loops.

V.5. Case of a moderately complex system : simulated nanoindentation of a nickel thin film

We have seen in section IV.2 that an assembly of prismatic dislocation loop produces a very complex signature in the CXD pattern. Some information can be obtained on the dominant crystallographic variant from the decrease of the maximum of intensity. However, even with a low number of defects, the CXD pattern induced by the interferences between the dislocation loop is already complex, and it appears delicate to establish the number of loops and even harder to determine the Burgers vector of each dislocation loop. Additionally, the procedure described in section IV.2 is based on the use of a large number of reflections (at least four and up to twenty-two), an approach which is really not realistic experimentally.
In the following we establish that the reconstruction of the displacement field is a much more suitable approach

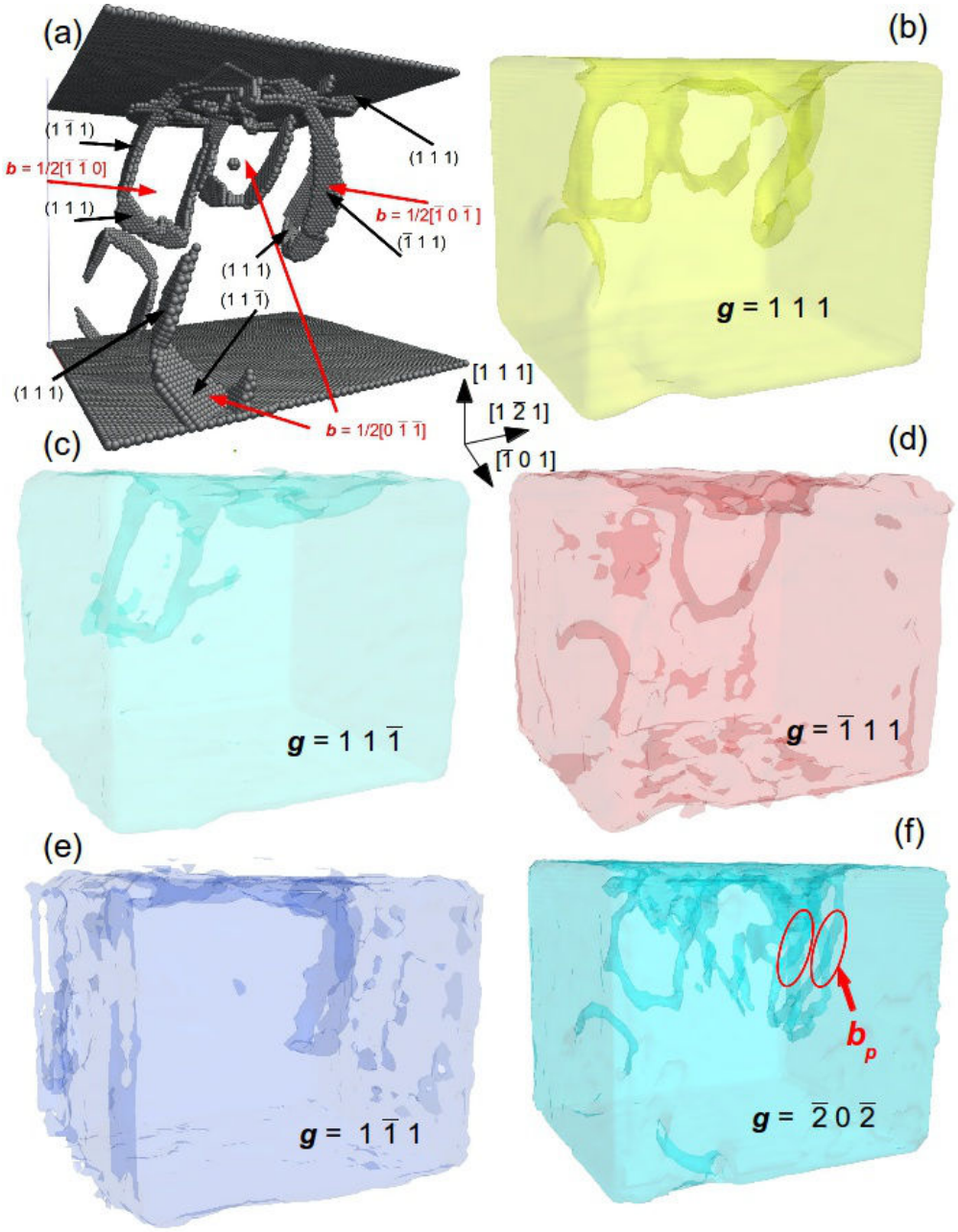

Fig. V.17 *Reconstructed electron density in the nickel thin film for several reflections* (a) Atomistic configuration at the end of the indentation of a nickel thin films. Several prismatic dislocation loops with equivalent burgers vectors can be found in the structure. (b) to (f) 65% isosurface of the reconstructed electron density which reveals the invisibility or visibility of the loops at various ***g***.

in the case of moderately complex systems. Similarly to section V.3, all the displacement fields obtained for various reflections are reconstructed from the calculated CXD patterns with the procedure described in subsection I.3.4. The system studied here is a nickel thin film that underwent a simulated nanoindentation along the [$\bar{1}$ $\bar{1}$ $\bar{1}$] direction, described in more details in section IV.2. Several dislocation loops are nucleated in the process, and at the end of the indenter penetration, four dislocation loops, with three crystallographic variants

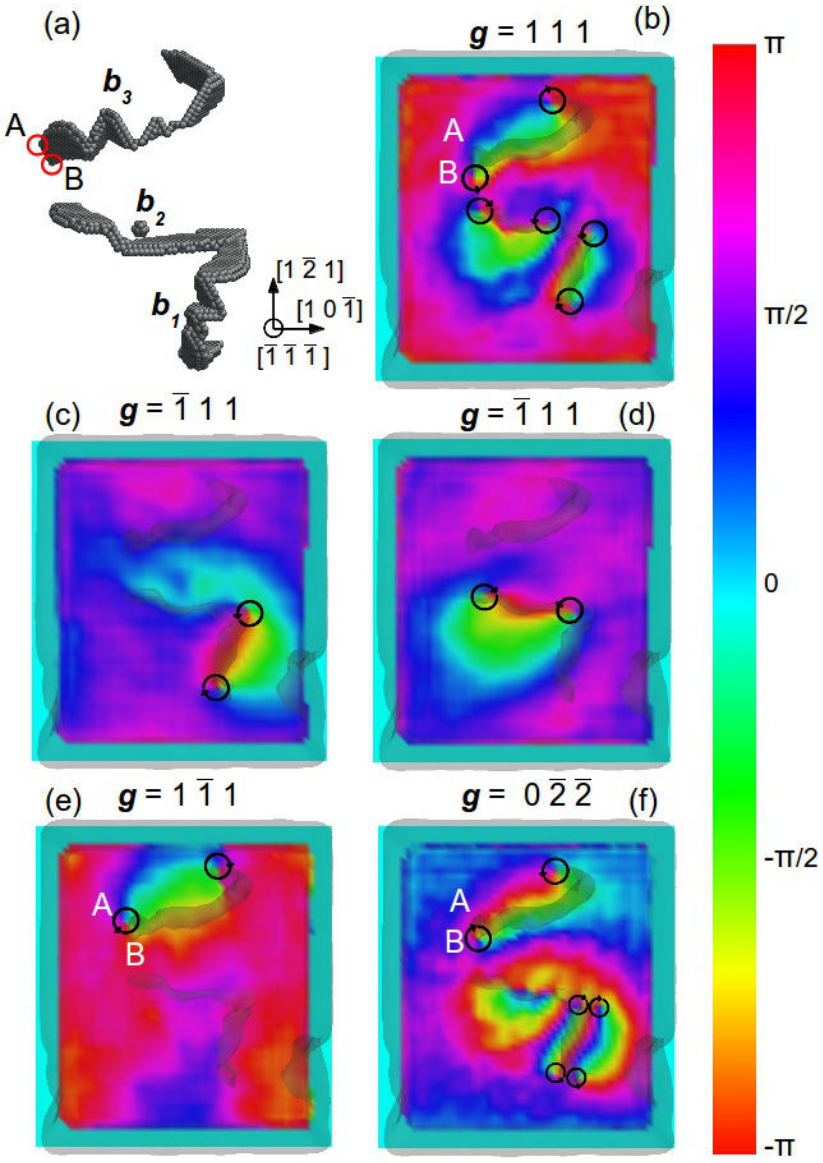

Fig. V.18 *Reconstructed displacement field in the (1 1 1) plane for several reflections* (a) Atomistic configuration seen from the [1̄ 1̄ 1̄] direction. It reveals the position of the dislocations in the structure, and the location of the (1 1 1) plane which intercept the partial dislocations and where the displacement field is reconstructed. (b) to (f) Reconstructed displacement field around the dislocation loop for four 111-type reflections: (b) $\boldsymbol{g}$ = 1 1 1, (c) $\boldsymbol{g}$ = 1̄ 1 1, (d) $\boldsymbol{g}$ = 1 1̄ 1 and $\boldsymbol{g}$ = 1 1 1̄ (e) and for $\boldsymbol{g}$ = 0 2̄ 2̄

remain in the structure: two of them with $\boldsymbol{b_2}$ = 1/2[0 1̄ 1̄], and one each with $\boldsymbol{b_1}$ = 1/2[1̄ 1̄ 0] and $\boldsymbol{b_3}$ = 1/2[1̄ 0 1̄]. An additional complex network of dislocation network is observed just below the indenter (Fig. V.17.a).

As in sections V.3-5, we use the dips in the reconstructed electron density to confirm the position and Burgers vector of the dislocations. For $\boldsymbol{g}$ = 1 1 1, none of the invisibility conditions are fulfilled, and all the dislocation loops are visible (Fig. V.17.b). This is in good agreement with the large decrease of intensity which is observed on the 1 1 1 diffraction pattern, as compared to the other {1 1 1} diffraction vectors.

$\boldsymbol{g}$ = 1 1 1 satisfies the invisibility conditions for $\boldsymbol{b_2}$ and $\boldsymbol{b_3}$ while the $\boldsymbol{b_1}$ loop should be visible. As seen from Fig. V.17.c, only $\boldsymbol{b_1}$ is visible, in good agreement with the invisibility conditions. The reconstructed density is also in good agreement with the reconstructed densities for the two other 1 1 1 diffraction vectors with only the $\boldsymbol{b_2}$ loops visible for $\boldsymbol{g} = \bar{1}\ 1\ 1$ and only $\boldsymbol{b_3}$ visible for $\boldsymbol{g} = 1\ \bar{1}\ 1$.
$\boldsymbol{g} = \bar{2}\ 0\ \bar{2}$ does not fulfill any of the aforementioned invisibility conditions so that all the dislocation loop are visible. However in good agreement with our observations in section V.4.2, the reflection parallel to $\boldsymbol{b_3}$ allows to see all the partial dislocations for this loop (circled in red on Fig. V.17.f).
In all cases, the position of the dislocation loop in the crystal match perfectly with the atomistic configuration, demonstrating that classical phase retrieval algorithms are perfectly suitable to deal with moderately complex systems, at least on simulated data. Their application to the analysis of experimental results is discussed in details in the next chapter.
Fig. V.18 shows the displacement fields around the dislocation loop for different Bragg reflections. The structure is seen from the $[\bar{1}\ \bar{1}\ \bar{1}]$ direction. The dislocation arrangement and the way they intercept the $[\bar{1}\ \bar{1}\ \bar{1}]$ plane is illustrated in Fig. V.18.a.
For $\boldsymbol{g}$ = 1 1 1 where all the dislocation loops are visible, the displacement fields obtained are in good agreement with our observations in section V.4.2. While all four partial dislocations intercept the (1 1 1) plane for the three dislocations, only two phase singularities are seen in each case, meaning that only half of the partial dislocation are seen. For the three dislocation loops, the phase singularities consist of two pair of vortices with opposite chirality, as described in section V.4.2.
Also in good agreement with the previous simulations is the strong phase gradient along the loop axis, between the partials while the phase is relatively stable outside the visible loops. Due to the irregular shape of the loops, the displacement field is not as symmetric as in section V.4.2 when the loop exhibits a diamond shape with its axis parallel to its Burgers vector (not the case here).
For the three other 1 1 1-type diffraction vectors (Fig. V.18.c-e), similar observations can be made. The displacement field around each loop is similar to the 1 1 1 reflection, with similar phase gradient and orientation, except only one of the crystallographic variant is visible. The position of the phase singularities also differ from the 1 1 1 reflection in some cases. This is particularly visible for $\boldsymbol{g} = 1\ \bar{1}\ 1$ (Fig. V.18.e) where the phase vortex is around the partial A while it is around the partial B for $\boldsymbol{g}$ = 1 1 1. Since the stacking fault ribbon between the two partials is in the $(\bar{1}\ 1\ 1)$ plane (Fig V.17.a), and since the $\boldsymbol{b_3}$ dislocation loop has a Burgers vector of $1/2[\bar{1}\ 0\ \bar{1}]$, there is only one combination of partial dislocations possible in the $(\bar{1}\ 1\ 1)$ plane : $\boldsymbol{b_{3p1}} = 1/6[\bar{1}\ 1\ \bar{2}]$ and $\boldsymbol{b_{3p2}} = 1/6[\bar{2}\ \bar{1}\ \bar{1}]$. For a given $\boldsymbol{g}$, and according to our observations in section V.3, the partial visible is the one with $\boldsymbol{b}$ almost parallel to $\boldsymbol{g}$. We can thus conclude that A, visible with $\boldsymbol{g} = 1\ \bar{1}\ 1$, has a partial Burgers vector of $1/6[\bar{1}\ 1\ \bar{2}]$ while B, visible with $\boldsymbol{g}$ = 1 1 1, has a partial Burgers vector of $1/6[\bar{2}\ \bar{1}\ \bar{1}]$.
For $\boldsymbol{g} = 0\ \bar{2}\ \bar{2}$ parallel to $\boldsymbol{b_2}$, all dislocation loop are visible. Since $\boldsymbol{g}$ is neither parallel to $\boldsymbol{b_1}$ nor $\boldsymbol{b_3}$, only half of the partial dislocations are visible for these loops, and thus only one pair of vortices in the $(\bar{1}\ \bar{1}\ \bar{1})$ plane. For the $\boldsymbol{b_2}$ variant, all the partial dislocation are visible, which results in the presence of two pairs of phase vortices with opposite chirality.
Fig. V.19 show the difference in the displacement field for the $\boldsymbol{b_3}$ loop, when the two partials are visible ($\boldsymbol{g}$ // $\boldsymbol{b_3}$, Fig. V.19.a) and only one is visible (Fig. V.19.b). Here the two pair of vortices for $\boldsymbol{g}$ // $\boldsymbol{b_3}$ (and the single pair for $\boldsymbol{g} = 1\ \bar{1}\ 1$) are not visible since the dislocation loop is not closed. Most of dislocation loop in the structure should be named half dislocation loops rather than complete dislocation loops (steps on surface were not studied in detail). As already mentioned in the beginning of this section and as best seen in Fig. V.20, for a plane normal to the loop axis (which is not necessarily the Burgers vector) and when only half of the partial dislocations are visible (typically for a 1 1 1-type reflection), the phase shift between the region inside the loop and the region outside the loop is equal to π. Fig. V.20 shows the profile of the displacement field and the π phase jump induced by the partial for all four crystallographic variants.

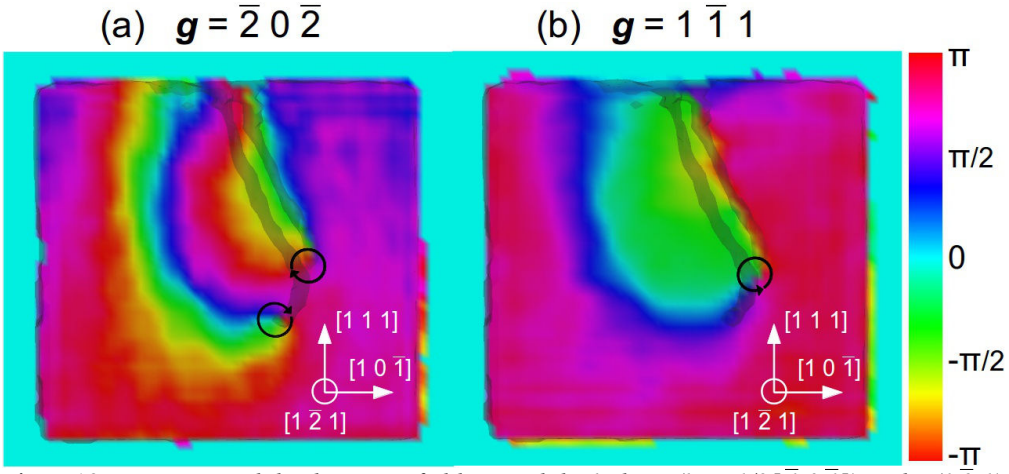

Fig.V. 19 *Reconstructed displacement field around the* $\boldsymbol{b_3}$ *loop (*$\boldsymbol{b_3}$ *= 1/2[1̄ 0 1̄]) in the (1 2̄ 1) plane*: for $\boldsymbol{g}$ = 2̄ 0 2̄ (a) and $\boldsymbol{g}$ = 1 1̄ 1 (b).

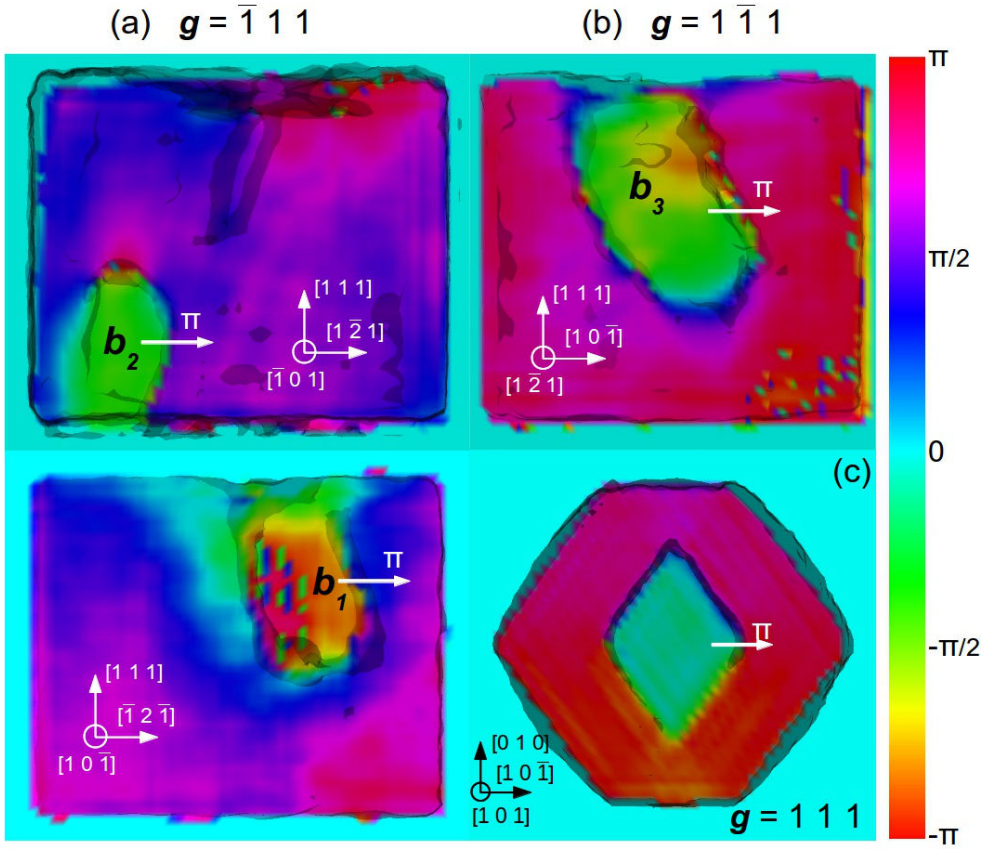

Fig. V.20 *Reconstructed displacement field from four crystallographic variants of prismatic loops* (a) $\boldsymbol{b_2}$=1/2[0 1̄ 1̄] and $\boldsymbol{g}$ = 1̄ 1 1, (b) $\boldsymbol{b_3}$=1/2[1̄ 0 1̄] and $\boldsymbol{g}$ = 1 1̄ 1, (c) $\boldsymbol{b_1}$ =1/2[1̄ 1 0] and $\boldsymbol{g}$ = 1 1 1̄ and (d) $\boldsymbol{b_3}$ $\boldsymbol{g}$ = 1 1 1 and $\boldsymbol{b}$ =1/2[1 0 1] . (a) to (c) can be found in the nickel crystal while (d) was introduced in the reference copper Wulff crystal. The displacement field is reconstructed in a plane perpendicular to the loop axis which is not necessarily the burgers vector of the loop.

Conclusion

The various cases studied in this chapter demonstrate that the Burgers vector of all dislocation loop can be easily determined with the reconstruction of the displacement field, either with the invisibility conditions of the dislocation loop (use of 111-type diffraction vector perpendicular to the Burgers vector of the loop) or the total or partial visibility of the partial dislocation loop (220-type diffraction vector parallel to one of the crystallographic variant). From the position of the phase singularities, it is even possible to determine the Burgers vector of the partial dislocations. With at most four Bragg reflections (three are in principle sufficient), the Burgers vector as well as all the characteristics of the dislocation in the structure can be determined. This procedure can thus be applied on experimental systems.

Regarding experimental parameters, it has been shown in this chapter that the signature of an individual dislocation loop on a CXD pattern is not as strong and characteristic as the signature from a dislocation line.

This is mainly due to the fact that the phase-shifted volumes does not extent over the whole crystal size as in the case of a single dislocation line, and also that their displacement field has a limited spatial extent. In all the simulations presented in chapter 3 and 4, the loop size is very large with respect to the crystal size, the signature of the loop is thus clearly visible. In experiments, dislocation loops nucleated within crystals of one order of magnitude larger are expected to produce a very weak signature on the CXD pattern.

If multiple dislocation loops are present in the structure, the CXD pattern resulting from their interferences is so far too complex to be interpreted. The reconstruction of the displacement field overcome this problem for moderately complex systems allowing to determine the number, shape, orientation, Burgers vector of all the loops within the structure with a low number of Bragg reflections. It should be also pointed out that the technique does not provide a lot of information the complex network of dislocations just below the indenter and all the aforementioned comments are only valid if the dislocations are well separated from each other.

The next chapter will aim at demonstrating that the direct analysis CXD patterns and the reconstruction of the displacement field can be used in combination in experimental systems.

We will try to understand the evolution of the microstructure in a sub-micron gold particle that undergoes in-situ nanoindentation (Zhe *et al.,* 2014). The direct analysis will be used for the live monitoring of the nucleation of defects, while the reconstruction of the 3D displacement field will allow to understand the evolution of the crystal microstructure.

Bibliography

Chapman, H. N. *et al.* (2006) *J. Opt. Soc. Am.* **A 23**, 1179–1200

Clark, J. N., Ihli, J., Schenk, A., Kim, Y-Y., Kulak, A. N., Campbell, J. M., Nisbet, G., Meldrum, F. C. & Robinson, I. K (2015) *Nature materials* **14**

Ehrhart, P., Trinkaus, H., & Larson, B. C. (1982). *Phys. Rev. B* 25, 834-848.

Favre-Nicolin, V., Mastropietro, F., Eymery, J., Camcho, D., Niquet, Y. M., Borg., B., Messing, M. E., Wemersson, L., Algra, R. E., Bakkers, E. P. A., Metzger, T. H., Harder, R. & Robinson, I. K. (2010). *New J. Phys.* **12**, 035013.

Fienup, J. R. (1982). *Appl. Opt.* **21**, 2758-2769

Herraez, M. A., Burton, D. R., Lalor, M. J. & Gdeisat, M. A. (2002) *Appl. Opt.* **41**, 7437 ;

Hull, D. & Bacon, D. J. (2001). *Introduction to dislocations,* edited by Butterworth-Heinemann, Fourth edition.

Labat. S., Richard, M-I., Dupraz, M., Gailhanou, M., Beutier, G., Verdier, M., Mastropietro, F., Cornelius, T. W., Schülli, T. U., Eymery, J. & Thomas, O. (2015) *ACS Nano*

Jacques, V. L. R., Carbone, D., Ghisleni, R. & Thilly, L. (2013). *Phys. Rev. Lett. **111**, 065503.*

Kirk, M. A., Davidson, R. S., Jenkins, M. L. & Twesten, R. D. (2005). Phil. Mag. **85**, 497-507.

Kirk, M. A., Jenkins, M. L., Zhou, Z., Twesten, R. D., Sutton, A. P., Dudarev, S. L. & Davidson, R. S. (2006). *Phil. Mag.* **86,** 4797-4808.

Labat. S., Richard, M-I., Dupraz, M., Gailhanou, M., Beutier, G., Verdier, M., Mastropietro, F., Cornelius, T. W., Schülli, T. U., Eymery, J. & Thomas, O. (2015) *ACS Nano*

Larson, B. C. & Young, F. W. (1987). *Phys. Stat. Sol.* A **104**, 273-286.

Miao, J., Sayre, D. & Chapman. H., N. (1998) Journal of the Optical Society of America 15 (6), 1662–1669.

Marchesini, S. (2003). *Phys. Rev. B* **68**, 140101

Mishin, Y., Farkas, D., Mehl, M., J., and Papaconstantopoulos, D., A. (1999). *Phys. Rev. B* **59**(5), 3393-3407

Takahashi, Y., Suzuki, A., Furukatu, S., Yamauchi, K., Kohmura,Y. & Ishikawa, T. (2013). *Phys. Rev. B* **87**, 121201.

Ulvestad, A., Clark, J. N., Harder, R., Robinson, I. K. & Shpyrko, O. G. (2015), *Nanolett.* **15**

Zhe, R., Mastropietro, F., Davydok, A., Langlais, S., Richard, M.-I., Furter, J.-J., Thomas, O., Dupraz, M., Verdier, M., Beutier, G., Boesecke, P. & Cornelius, T. W. (2014). *J. Synchrotron Rad.* **21**, 1128-1133.

Zhou, Z., Sutton, A. P., Dudarev, S. L., Jenkins, M. L. & Kirk, M. A. (2005). *Proc. R. Soc.* **A 461**, 3935-3953.

Chapter VI: Investigation of the mechanical properties of a single gold crystal by in-situ nano-indentation in combination with coherent Bragg diffraction imaging

Contents

Introduction....169
VI.1 Sample preparation....169
VI.2 Coherent X-ray diffraction experiment....174
VI.3 Selection of the gold particle and importance of the preparation conditions....176
VI.4 Simple model of the thermoelastic strain with molecular statics simulations....179
VI.5 Results....180
VI.5.1 Analysis of the CXD patterns at various iteration of the loading unloading cycle....180
VI.5.2 Reconstruction of the electron density....183
VI.5.3 Imaging of the displacement field around a prismatic dislocation loop....185
VI.5.4 Evolution of the displacement and strain fields in the particle during the loading-unloading iterations....187
Conclusion....193
Bibliography....195

Chapter VI: Investigation of the mechanical properties of a single gold crystal by *in-situ* nano-indentation in combination with coherent Bragg diffraction imaging

Introduction

Throughout Chapter III to V, we demonstrated that Coherent X-ray diffraction is a powerful tool to investigate the microstructure of isolated crystals. Individual crystal defects can be directly identified through the distinct signature they produce on CXD patterns at well chosen Bragg reflections. The use of invisibility conditions allows to determine all the characteristics of a given single defect (edge-or screw type, Burgers vector, dissociation, position,...). This method can be also applied to more realistic systems, as demonstrated by the case of the simulated nanoindentation of a gold particle, where the Burgers vector of a single mixed dislocation was clearly identified. However, this approach is far less suitable for moderately complex systems, with as few as 3 or 4 individual defects. The complex interference pattern between the defects becomes very delicate to interpret, and though some useful informations on the microstructure can be deduced through the interpretation of CXD patterns at several Bragg reflections (sections IV.2 & IV.3), the complete determination of the microstructure is completely out of reach.
As demonstrated in Chapter V with the simulated nanoindentation of a Nickel thin film, it is possible to reconstruct the displacement field around each individual defect in the structure. The variations in the electron density allows the precise determination of the defect size and position, while the phase jump and surrounding displacement field allows the unambiguous determination of the defect type. The use of the invisibility conditions enables to uncover the Burgers vector as well as all the characteristics of each defect in the structure. However, the applicability of Coherent Bragg Diffraction Imaging (CBDI) have only been demonstrated on simulated data. The reconstruction of the simulated data is much easier than the experimental one for several reasons. First, the extent of the reciprocal space that can be selected is not limited by the dynamical range of the diffraction data. As soon as the oversampling conditions (Sayre 1952) are fulfilled, an unrealistically large portion of the Brillouin zone can be selected. The resolution achieved is one order of magnitude higher in the simulation than in the experiment. Additionally, in simulation, the phase variations observed depends only on the crystal structure and are not affected by the experimental conditions. These issues have been discussed in Chapter I and are also presented in section IV.5.3. Consequently, the successful experimental demonstration of BCDI has only been achieved by a small number of research groups, and on systems containing a limited amount of defects (Takahashi *et al.* 2013, Ulvestad *et al.* 2015 and Clark *et al.* 2015)
In the following chapter, we will apply the methods described in Chapter III to V to analyze the evolution of the microstructure in an *in situ* nanoindented sub-micron gold crystal. To our knowledge, the imaging of defect by BCDI, that were nucleated by mechanical loading *in situ* has not yet been reported in the literature. We will start by describing the sample preparation, and discussing the choice of sample for this experiment. The experimental details will be given in section VI.2, while the diffraction patterns from several islands will be compared in section VI.3, to illustrate the signature of residual strain on CXD patterns. In section VI.4, a simple molecular static simulation is presented to visualize the strain distribution in the gold particle. The most interesting outcomes of the experiment are presented in section VI.5. Following the method presented in Chapters III & IV, a detailed analysis of the CXD patterns is presented in subsection VI.5.1. Subsections VI.5.2 and VI.5.3 are respectively dedicated to the analysis of the evolution of the shape of the particle under illumination by the X-ray beam, and to the visualization of the $u_{1\,1\,1}$ displacement field around a prismatic dislocation loop that is nucleated after several loading iterations. Finally, the evolution of the phase and strain field in the particle, upon emission and annihilation of prismatic dislocation loop is interpreted and discussed in the last section of this Chapter.

VI.1 Sample preparation

This experiment aims at investigating the evolution of microstructure upon indentation. In order to capture the signature of defects nucleated during the indentation process, the initial crystal needs to be as

perfect as possible. In a precedent study, the strain field in sub-micrometric Cu islands on a Ta substrate was investigated by Beutier *et al.* (2013a) and Beutier *et al.* (2013b). The detailed structure of this heteroepitaxial interface are presented in details in Chapters VIII and IX. The copper islands are strongly bounded to the tantalum substrate, such that a large amount of the thermoelastic strain generated during the cooling to the room temperature after dewetting is transmitted to the particle. This inhomogeneous strain tends to hide the features related to the shape of the crystal and can thus make difficult the clear identification of defects. Additionally, the phase retrieval of the diffraction data is always delicate in highly and heterogeneously strained systems, even if the applicability of phase retrieval algorithms on such systems has been shown by Minkevitch *et al.* (2007) and Diaz *et al.* (2010).

For the investigation of the nucleation of defects by CXD, it is preferable to select a sample with a lower amount of residual strain. Gold nanoparticles have attracted considerable interest for their various applications. In previous CXD studies, the gold particles were obtained by the dewetting of a gold thin film on a SiO_2 substrate (Williams *et al.* 2003, Robinson *et al.* 2009, Watari *et al.* 2011) such that no epitaxial relationship was found between the particle and the substrate. In this work the gold particles are grown on a c-plane oriented sapphire ((0001) single crystal α-Al_2O_3). This interface is a good example of a f.c.c. metal α-Al_2O_3 interface which are one of the most studied among the metal-ceramic interfaces. The Au-sapphire system itself is of particular interest due to its technological importance (Sadan & Kaplan 2006).

& Kaplan 2006, Sadan & Kaplan 2006b) promotes the solid state dewetting of gold particles from the substrate. The epitaxy of f.c.c. thin films with a Volmer-Weber mode (i.e 3D film growth by growth of islands) on sapphire was studied in details by Bialas & Heneka (1994). It was evidenced that several metals (Ag and Cu) can grow epitaxially on a c-plane oriented sapphire substrate. For the case of Au, the structure of the thin film was described as an intermediate stage between epitaxy and strong texture. More recently, Amram & Rabkin (2013) reported that 10 nm gold thin films grown on a cleaned and annealed α-Al_2O_3 substrate are polycrystalline with a grain size of the order of the film thickness. The films have a very strong [1 1 1] out-of plane texture with a seemingly random in-plane crystalline orientation, although some variations in the pole-figure tends to indicate a weak hetero-epitaxy for part of the grains in the film. It was concluded that the large misfit between Au and sapphire (larger than for other fcc metals) does not allow direct hetero-epitaxial growth of the thin film. This conclusion should be tempered by the results by Bialas & Heneka (1994) which evidenced the epitaxial growth of Ag on α-Al_2O_3 while its lattice mismatch with sapphire is comparable to gold (even slightly larger).

In the work by Amram & Rabkin (2013), the gold particles obtained by solid-state dewetting also exhibit a nearly random in-plane orientation. In fact, a scan along the azimuthal angle φ reveals the presence of two sets of peaks (30° apart), each being composed of six peaks 60° apart. These peaks correspond to the orientation relationship (OR) associated with a local minimum of the film-substrate interface energy. It was also stated that individual particles formed at the late stage of dewetting may rotate towards the low-energy in-plane orientation, explaining the larger degree of in-plane orientation than in the thin film. The particles grown from grains with a large disorientation do not experience this driving force towards the OR with a local minimum of interface energy and keep a random orientation.

The influence of the surface state of the sapphire substrate on the orientation of the gold thin film and of the dewetted particles has also been studied extensively in our group (Rupp 2015). It was concluded that the growth-mode of the thin film strongly depends on the substrate preparation. With an high temperature air annealed and cleaned substrate, the results are similar to Amram & Rabkin (2013) with no preferential in-plane orientation of the gold thin film, and a [1 1 1] out of plane texture. However, a larger degree of in-plane ordering is found when the substrate is just cleaned but not annealed. This orientation becomes even more pronounced after the solid state dewetting of gold particles from the substrate and suggest that the hetero-epitaxial growth of particles on the sapphire substrate. This difference between the high temperature air annealed and non annealed substrate might be attributed to surface termination. When the substrate is just cleaned, the sapphire is either terminated by an aluminium or an oxygen atom, while the annealing of sapphire leads to well defined atomic steps with an oxygen termination. The latter case not favourable to the hetero-epitaxial growth on the gold thin film due to the low affinity of Au for oxygen (Francis & Salvador 2007). Slightly different results are obtained when the substrate (epitaxy ready condition) is measured as received or is just annealed without being cleaned, but they both exhibit to some extent in-plane relationship

with the sapphire substrate, which is reinforced after the solid state dewetting. The growth mode of gold on sapphire strongly depends on the experimental conditions (temperature, atmosphere) (Kosinova *et al.* 2015) as well as the surface state of the sapphire since the thermodynamical stability of the gold on sapphire depends on the chemical potential of sapphire and of partial pressure of O. In any case both the mechanical and thermodynamical stability of a metal-ceramic interface are expected to be lower than for the case of a bimetallic interface with metal bonds. The gold particles on the ionic-like sapphire are expected to have weak bonds, and the amount of residual strain in the particle should be much lower.

The gold crystals used in this experiment were prepared at the Technion in Haifa (Israel) in the group of E.Rabkin / D.Mordehai. A gold film with a thickness of 45 nm is magnetron sputtered on a sapphire (0001) substrate under air. Upon annealing at 930 °C for 24 hours (*i.e.* below the melting point of Au), a large number of irregularly distributed Au islands is obtained by solid state dewetting (Fig. VI.3). Their typical lateral size ranges from 200 nm to 2 µm while their height varies between 100 nm and 600 nm (Fig. VI.3, see also subsection II.4.2.3). As in the case of the liquid state dewetting (Chapter VII), the formed particles are strongly faceted and exhibit a Winterbottom equilibrium shape (Winterbottom 1967). However, while the islands dewetted in the liquid phase can exhibit various out-of plane orientations (Sadan & Kaplan 2006), the islands grown by solid-state dewetting are all oriented with the Au [1 1 1] direction normal to the (0001) sapphire surface. As discussed in the introduction of this chapter, (Amram & Rabkin 2013) the gold particles also exhibit a low degree of in-plane ordering, the preferred orientation corresponding to the lowest cost in interface energy.

It should however be noted that the degree of in-plane orientation also depends on the surface state of the sapphire and on the experimental conditions for the solid state dewetting, since most of the gold particles obtained by solid-state dewetting in our group (SIMaP) exhibit a strong-degree of in-plane orientation with respect to the sapphire substrate (Fig. VI.1 & VI.2).

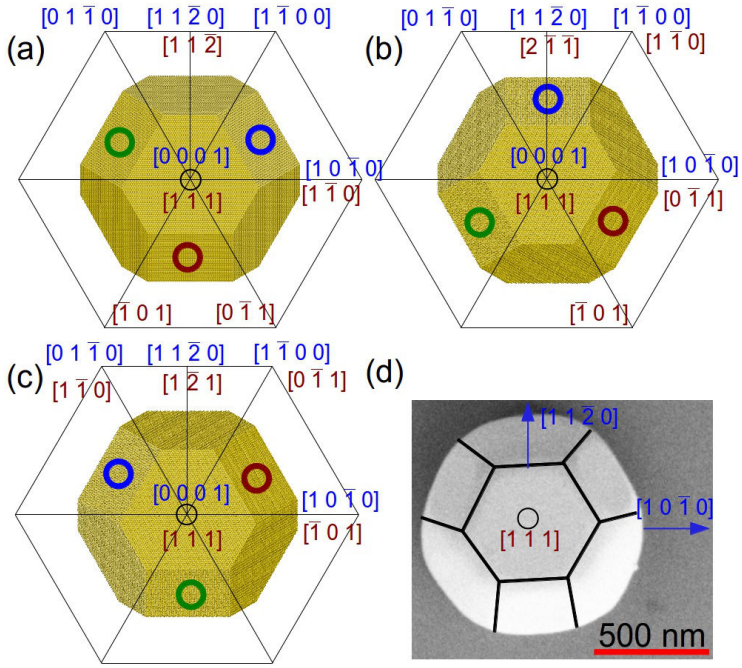

Fig. VI.1 *Summary of the possible orientation relationship between the gold particle and the sapphire substrate*. (a) Au(1 1 1)[1 $\bar{1}$ 0]||Al_2O_3(0 0 0 1)[1 0 $\bar{1}$ 0](b) Au(1 1 1)[0 $\bar{1}$ 1]||Al_2O_3(0 0 0 1)[1 0 $\bar{1}$ 0] and (c) Au(1 1 1)[$\bar{1}$ 0 1]||Al_2O_3(0 0 0 1)[1 0 $\bar{1}$ 0]. (d) SEM picture of an experimental particle which shows a slight disorientation (2-3°) with respect to the [1 0 $\bar{1}$ 0] axis of the sapphire

This well defined in plane orientation for the SIMaP particles is confirmed by laboratory X-ray diffraction

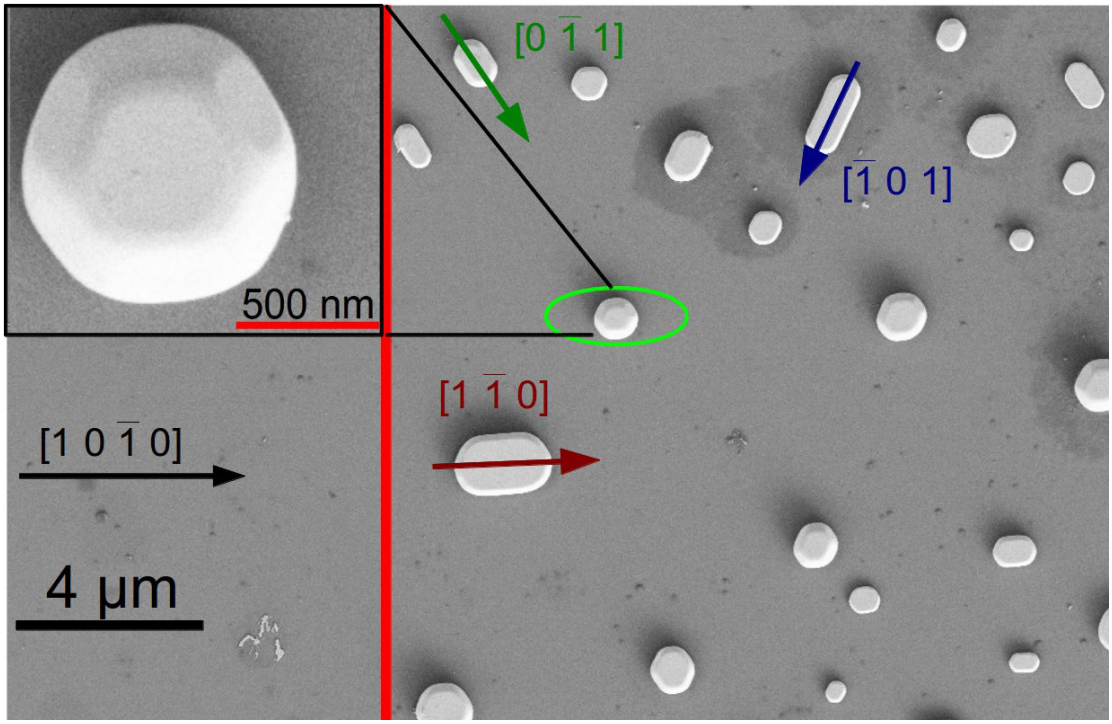

Fig. VI.2 *SEM picture of a population of solid state dewetted gold islands upon annealing of a 20 nm gold thin film at 950°C for 1h.* Both equiaxed Winterbottom particles and metastable particles elongated along one of the <1 1 0> directions can be identified. The green elipse illustrates the footprint of a 1x1 µm beam with an incident angle of 20°C while the red line defines the region where the gold particles have been removed by scratching the sample with a tweezer.

measurements (Langlais 2016, Rupp 2015). Only three distincts in plane orientations are possible (Fig VI.1 and VI.2). They are obtained by rotation of 60° along φ such that either the [1 1̄ 0], [0 1̄ 1] or [1̄ 0 1] direction of the gold particle is parallel to the [1 0 1̄ 0] crystallographic axis of the sapphire substrate.
This orientation relationship (OR) can also be seen alternatively as an alignment of the [1 1 2̄], [2 1̄ 1̄] or [1 2̄ 1] direction of the particle with the [1 1 2̄ 0] direction of the sapphire. The three equivalent relationship can thus be described as follows : Au(1 1 1)[1 1̄ 0]||Al_2O_3(0 0 0 1)[1 0 1̄ 0] (Fig. VI.1.a), Au(1 1 1)[0 1̄ 1]||Al_2O_3(0 0 0 1)[1 0 1̄ 0] (Fig. VI.1.b) and Au(1 1 1)[1̄ 0 1]||Al_2O_3(0 0 0 1)[1 0 1̄ 0] (Fig. VI.1.c) or alternatively Au(1 1 1)[1 1 2̄]||Al_2O_3(0 0 0 1)[1 1 2̄ 0] (Fig. VI.1.a), Au(1 1 1)[2 1̄ 1̄]||Al_2O_3(0 0 0 1)[1 1 2̄ 0] (Fig. VI.1.b) and Au(1 1 1)[1̄ 0 1]||Al_2O_3(0 0 0 1)[1 1 2̄ 0] (Fig. VI.1.c). These OR are in good agreement with the results on other f.c.c. metals on α-Al_2O_3 such as Nickel (Meltzman *et al.* 2012). A slight disorientation of the gold particle with respect to the sapphire substrate (of the order of 2 degrees) is revealed by XRD measurements and SEM pictures (Fig VI.2). Both the particles used during the experiment and shown in Fig. VI.2 and Fig. VI.3 are dewetted at the same temperature but annealed under different atmosphere. The particles from the Technion Inst. are annealed under a forming gas flow (Ar-10% H_2 99.999% pure) while the particles from SIMaP were annealed under air. The high degree of in-plane orientation suggests that a state closer to the equilibrium has been reached for the SIMaP particles since the described OR would correspond to the minimum of interface energy. It can not be attributed to the duration of the annealing since it is much shorter in the case of the SIMaP particles (1 hour versus 24 hours). The rotation of the particle towards the low energy orientation occurs from the beginning of the dewetting process. The differences might origin from the degree of in-plane orientation of the gold initial non dewetted thin films which is largely dependent of the sapphire surface. The SIMaP particles were dewetted from polycrystalline thin film that was not annealed. As discussed earlier it exhibits a rather large degree of in-plane orientation. Conversely, the orientation of the gold thin film for the Technion particles which was deposited on an annealed substrate is described as nearly random.
The rotation of the particle towards the low-energy OR could have also be altered by the presence of

impurities on the substrate. Although, in both cases the sample were placed in a quartz tube to avoid contaminations, they can not be totally excluded. In the case of the Technion sample, the resin mask/lithography process that was used is prone to have brought some impurities that significantly affected the sapphire surface state.

As already reported by various authors (Mordehai *et al.* 2011, Malyi *et al.* 2011) some of the particle are elongated along one of the densely packed <1 1 1> or <1 1 0> directions (Fig. VI.2). These particles are lower in height as compared to the equi-axed Winterbottom particles. It has been stated that they remain stable after elongated annealing times (up to 50 h at 900°C) and do not transform into equi-axed Winterbottom particles (Mordehai *et al.* 2011). They thus correspond to a kinetically limited metastable shape as compared to the equilibrium shape of Winterbottom particles. More recently, Malyi *et al.* (2012) reported a decreasing of the lateral dimension of the elongated particles with an increasing annealing time at higher temperature (up to 65h at 950°C). Fig. VI.2 show the SIMaP particles, grown with a very short annealing time, hence the large proportion of elongated particles than in the sample used for the experiment (Fig. VI.3). As compared with the dewetting processed in the liquid phase, the Winterbottom particles are further away from the Equilibrium Crystal Shape (ECS). Due to the partial wetting of the gold particle on the sapphire substrate the lateral size of the particles is significantly larger than their height. The particles exhibit a flat aspect ratio with enlarged (1 1 1) facet normal to the substrate (Fig. VI.2). A large amount of surface stress owing to the differential contraction of the flat facets (Watari *et al.* 2011) is expected to be found in the structure. The long annealing time combined with the high annealing temperature for the particles used in this experiment gives more time to the particles to reach their ECS and is expected to reduce the amount of surface strain.

However, and similarly to the case of copper islands on a Ta substrate, the main source of strain in the island probably results from the difference of thermal expansion coefficient between gold and sapphire $\Delta\alpha = \alpha_{Au} - \alpha_{Al2O3}$. The cooling down of $\Delta T \sim 925°C$ from the annealing temperature to the room temperature would lead to a $\Delta\alpha\,\Delta T \sim 0.8\%$ of thermal mismatch. Such mismatch would correspond to a rather large mean residual strain as in the case of copper islands, (Beutier *et al.* 2013a), but this strain can be partially relaxed through diffusion and rearrangement at the interface, such that a much lower mean residual strain may be expected in the particles. Laboratory XRD measurements allowed to obtain an estimated value of the mean residual strain of $<\varepsilon_{zz} = 0.1\%>$. Such value is significantly lower than the strain found in copper crystals on tantalum, and a strain dominated CXD pattern as in the case of copper island on a Tantalum substrate is not expected.

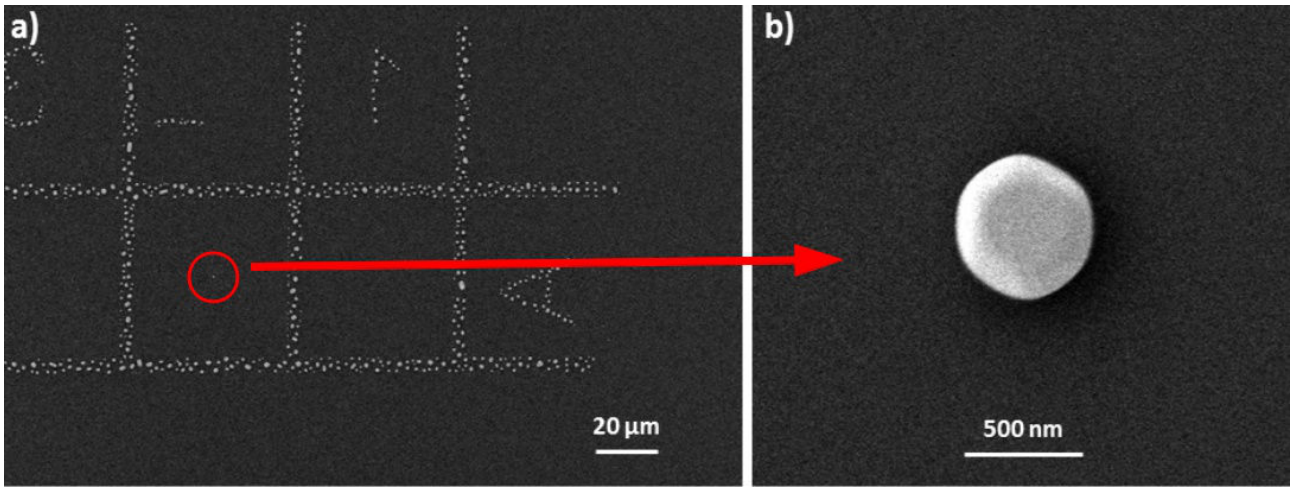

Fig. VI.3 *Solid state dewetted particles from Technion Inst.*(a) SEM picture of the solid state dewetted gold particles. The mask used for the deposition of the gold thin film allows to obtain a regular array cf crystals with a single and isolated particle at the centre of each square. (b) Zoom of the gold particle that was selected for the in-situ nanoindentation experiment

An important requirement for CXD experiments is to be able to isolate a single gold crystal. The dewetting process results in regularly distributed particles, with a spacing which appear to depend on the thermal

treatment (Langlais 2016, Rupp 2015). It has been shown in particular that a low heating rate to reach the annealing temperature favours the nucleation of small particles in between the larger ones. A larger heating rate tends to prevent this phenomena and a typical spacing of 2-3 μm between the island is generally observed (Fig. VI.2).
To enable the phase retrieval of the diffraction data, both the transverse and longitudinal coherence length of the incoming X-ray beam should exceed the dimensions of the sample. This obviously implies that the incoming X-ray beam is larger than the particle. The typical lateral size of the gold particles is of the order of 800 nm while their average height is around 400 nm (see Chapter II). The incident X-ray beam should not be smaller than these dimensions. Additionally, the relatively small value of the Bragg angles used for the collection of the diffraction data results in a enlarged footprint of the beam on the sample. For instance, for an angle incident angle of 15° which is the Bragg angle for the gold 1 1 1 reflection at 9.7 keV, and for a beam size of (FWHM ~ 0.8x0.4 μm^2 , HxV) the footprint is equal to 0.8x1.3 μm^2. The green ellipse in Fig. VI.2 show that the footprint of a 1x1 μm^2 (FWHM) which illuminates a particle with an incident angle of 20° is significantly smaller than the typical spacing between two islands. However, the tails of the beam are much larger than the FWHM such that the partial illumination of neighboring islands and the associated interferences on the CXD patterns can not be excluded. To isolate the island, a very simple and somehow rough procedure was to scratch the sample with tweezers in order to remove gold islands in some regions of the sample as described in subsection II.4.2.2. As illustrated in Fig VI.2, the particle at the vicinity of the depleted region (delimited by a red line) are well isolated.
To completely prevent the potential illumination of several particles, at the expense of substrate contamination as discussed previously, a lithography/mask process route was used during the deposition of the initial gold film. A regular array of Au crystals was prepared where an individual Au particle was located in the centre of a square formed by Au crystals (Fig. VI.3.a). The side length of this square amounted to 50 μm allowing for studying a single Au island and image it before and after the experiment by SEM. The 25 μm gap with the closest neighbour ensure that the illuminated crystal is completely isolated.

VI.2 Coherent X-ray diffraction experiment

For coherent Bragg diffraction imaging, the 8 keV X-ray beam was focused down to 500 x 300 nm^2 (HxV, FWHM) using a tungsten Fresnel zone plate with a diameter of 300 μm. The high precision slits installed in front of the FZP were closed to 60 x 300 μm^2 matching the lateral coherence lengths at the upgraded ID01 beamline. In order to fully illuminate the isolated islands, it was eventually defocused to a larger size (estimated to be 700 x 400 nm^2). A significant part of the beam time was dedicated to the selection of the best candidate for the *in situ* nano-indentation experiment. In order to select the most "perfect" crystal, a 3D CXD pattern was collected at the 1 1 1 Bragg reflection for each of the potential candidate. To do so, a series of rocking curves (subsection II.1.5) was acquired on several islands by rotating the sample by +/- 0.5° (Δq = ± 1.34 nm^{-1}). The 2D diffraction patterns were collected using a 516x516 pixels Maxipix detector (ESRF) installed at a distance of 1.3m downstream the sample. The 2D CXD patterns were then stacked together and a coordinate change was performed in order to work in the laboratory reference (subsection II.1.6).
Most of the crystals that were measured were very defective with a "speckled" CXD pattern indicating the presence of several crystal defects. However, for two of them, located in the 'A2' and 'B3' positions of the array, the diffraction pattern appeared very clean, with a single Bragg spot and a maximum intensity at the Bragg position (Fig. VI.4). The absence of splitting of the Bragg peak indicates that there are no defect in the structure that induce a phase-shift of a large volume of the crystal. Mordehai *et al.* 2011 reported by TEM investigation the presence of a small number of long sessile dislocations produced during the particle formation. Such defect would induce phase shifts between large volumes in the crystal and produce a very distinct signature on the CXD pattern. The presence of such dislocation lines or stacking faults that spread in the whole crystal volume is thus improbable, unless their Burger vectors are perpendicular to $\boldsymbol{g}$. However, the presence of small dislocation loop which can induce phase-shift of small parts of the crystal can not be excluded. If in both crystals the Bragg peak is slightly elongated along the [1 1 1] direction due to the

enlarged (1 1 1) facet normal to the sapphire substrate, it appears relatively undistorted. This, associated to the good visibility of the fringes induced by the finite size of the crystal is a good indication of the low amount of residual strain or at least of the absence of large inhomogeneous strain in the particle (Beutier *et al.* 2013a). The 'A2' island has been finally selected for the *in situ* nano-mechanical tests.

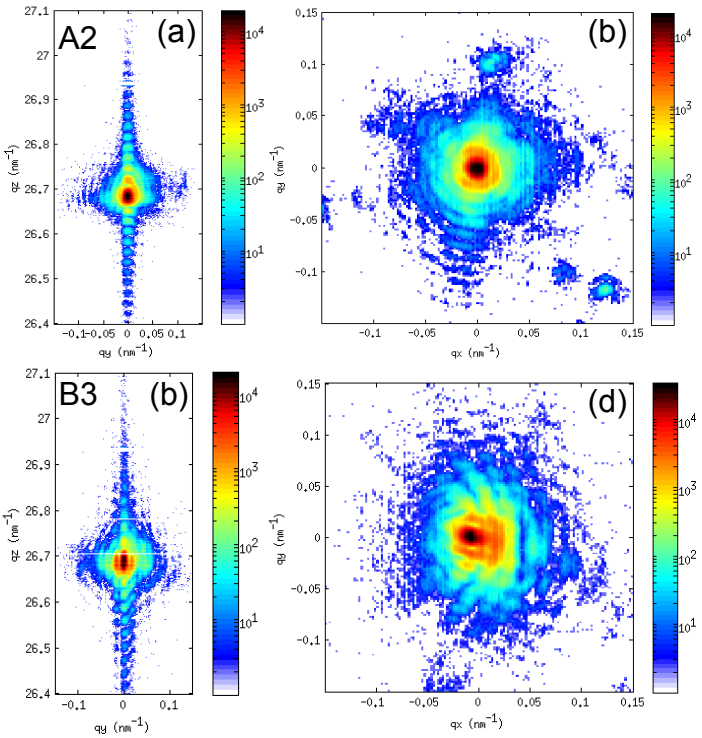

Fig. VI.4: *CXD diffraction patterns from the two crystals with the least estimated residual strain and defect content.* (a) and (b) (qy-qz) slice of the reciprocal space for the A2 and B3 crystal respectively. (c) and (d) (qx-qy) for the A2 and B3 crystal respectively

To perform the *in situ* indentation, the *in situ* AFM "SFINX" (Zhe *et al.* 2014) which have been developed within the framework of the ANR MecaNIX project was installed on the diffractometer of the upgraded ID01 beamline. The AFM-tip, the Au islands, and the focused X-ray beam were aligned with respect to each other by simultaneously recording an AFM topography image and a scanning X-ray diffraction map. The scheme of the experiment is shown on Fig. VI.5.a. After alignment, the AFM-tip was positioned above a selected Au island (Fig. VI.5.a), the feedback loop of the AFM (Fig. VI.5.b) as well as the excitation of the cantilever are switched off, and the tip was moved down with a speed of 2 nm/s indenting the island. At pre-defined loads, the AFM-tip was retracted with the same speed until it reached a position of 1 µm above the island top facet.
A total of 6 iterations of loading-unloading was performed and a 3D diffraction pattern was collected after each unloading. Finally a last diffraction pattern was recorded after 24 hours of illumination with the coherent X-ray beam. Between these two steps, diffraction patterns were collected for additional Bragg reflections: one specular 2 2 2 reflection and two off-specular 1 $\bar{1}$ 1 and 1 1 $\bar{1}$ reflections. The reconstruction of the displacement field for four different $\boldsymbol{g}$ with three of them being non-coplanar would have fully determine the microstructure inside the particle (as illustrated in sections V.3 and V.5). Unfortunately, the phase retrieval of the diffraction data was only possible for $\boldsymbol{g}$ = 1 1 1.
This failure can be explained by several reasons. The beam being of a size comparable to the sample, the complete illumination of the particle for $\boldsymbol{g}$ = 1 1 1 was only achieved because of the large footprint of the beam at low incidence angle. For the 2 2 2 reflection the larger Bragg angle did not allow to completely illuminate the crystal. As seen from the slice in the (qx,qy) plane (Fig. VI.6.a), parallel to the specular (1 1 1) facet, the contrast of the fringes along the direction of the facets is very poor. Fringes are induced by

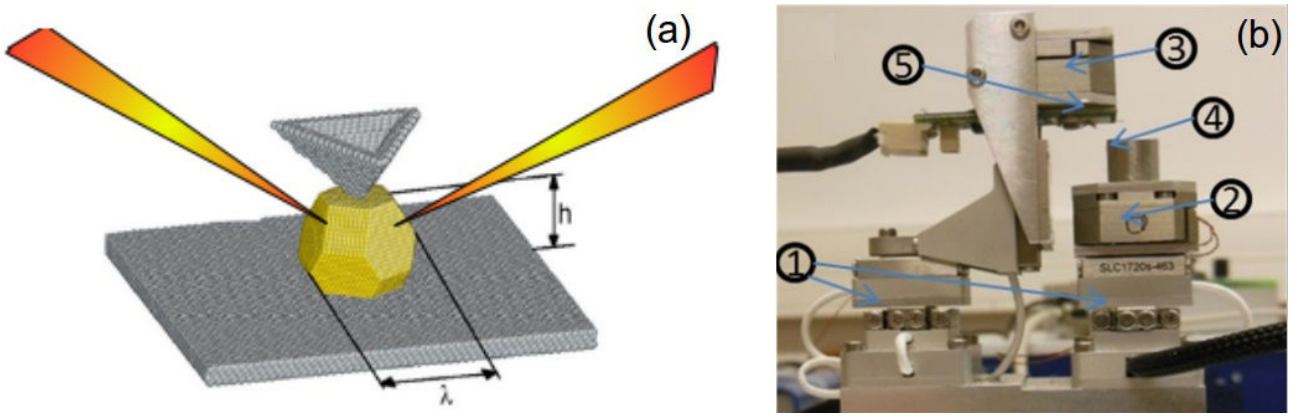

interferences between two parallel crystal facets, and the absence of contrast is either due to a weak coherence of the beam (which is not the case here) or due to the fact that the two facets are not illuminated simultaneously. The diffraction data at this Bragg reflection is thus not usable for phase retrieval.
For the off-specular reflections, the diffractometer on the ID01 beamline was not designed to routinely work in off-specular geometry. It is only possible to measure the off-specular reflections through a complex combination of motions of the diffractometer axes. The <1 1 1> reflection were only reachable at a grazing incidence angle (3°). Even with the large resulting footprint, the gap with the closest crystallite was sufficient to ensure that only the A2 crystal was illuminated. Interferences with neighbouring crystals can thus be excluded. Additionally, the rather large footprint of the beam ensured a complete illumination of the crystal. The fringes contrast is very poor for $\boldsymbol{g} = 1\ \bar{1}\ 1$ (Fig. VI.6.b) while it is more pronounced for $\boldsymbol{g} = \bar{1}\ 1\ 1$ (Fig. VI.6.c). This difference in term of fringes contrast is rather surprising since the crystal was illuminated with the same incident angle in both cases. No satisfying explanation to the failure of the phase retrieval of the diffraction data has been found so far. It may come from the asymmetry of the beam with such low incident angle.

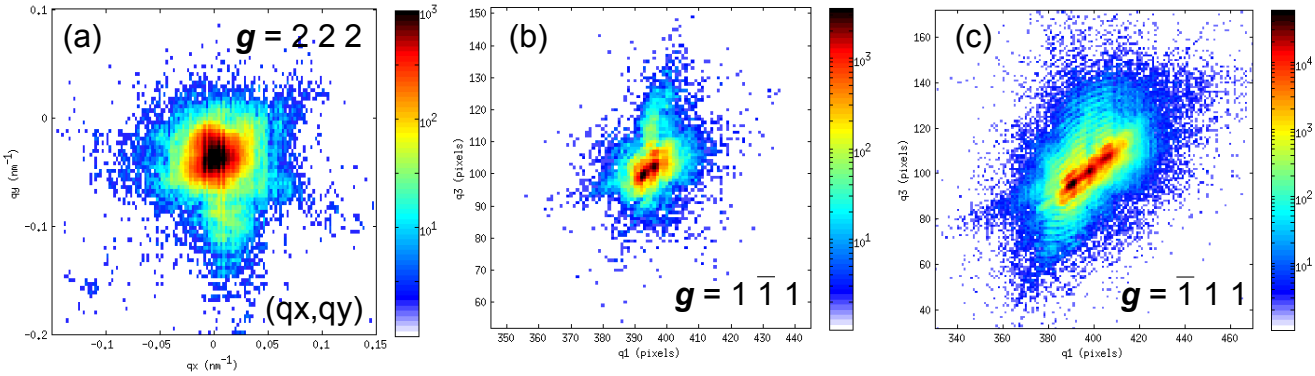

Fig. VI.6: *CXD patterns measured at other Bragg reflections.* (a) $\boldsymbol{g} = 2\ 2\ 2$ in the (qx,qy) plane of the reciprocal space. (b) $\boldsymbol{g} = 1\ \bar{1}\ 1$ (c) $\boldsymbol{g} = \bar{1}\ 1\ 1$. For (b) and (c), the coordinate transformation to work in the laboratory reference has not been performed

VI.3 Selection of the gold particle and importance of the preparation conditions

As discussed in sections VI.1 & VI.2, the pristine crystal needs to be as perfect as possible (i.e low residual strain and low defect content). The A2 crystal seems to be a particularly good candidate since both the Bragg peak and the fringes appear nearly undistorted which indicates both the absence of large residual strain and of a low defect content. As compared to previous CXD experiments with similar sample, the signature of the strain is almost invisible in the CXD pattern. Fig. VI.7 show various diffraction patterns calculated for $\boldsymbol{g} = 1\ 1\ 1$ and $\boldsymbol{g} = 2\ 2\ 2$ from particles with similar size and geometry. They all exhibit a

Winterbottom shape which is very close to the equilibrium crystal shape, and the aspect ratio between their lateral size and height is comparable (of the order of 0.5). However, they are grown with different thermal treatments, and a different surface state of the sapphire substrate. The first particle (Fig. VI.7.a) is the particle from Technion which has been measured during this experiment (A2 crystal). The other 3 particles (Fig. VI.7.e, VI.7.i & VI.7.m) are SIMaP particles whose preparation process was described in subsection II.3.1.1 and section VI.1.

For each particle, the direction of the incident X-ray beam is indicated with a green arrow, while the blue arrow show the [1 0 $\bar{1}$ 0] direction of the sapphire substrate. As shown in section VI.1, the in-plane orientation of the particle seems to be well defined for particles (e), (i) and (m) with one of the <1 $\bar{1}$ 0> direction almost parallel to the [1 0 $\bar{1}$ 0] direction of the sapphire substate. For the A2 particle, a strong in plane misorientation (approximately 15°) is observed. As discussed in section VI.1, the other particles on this substrate exhibit a spread of in-plane orientations on the sample though some degree of in-plane ordering is observed. We suggested in section VI.1 that the Technion particle is at an intermediate stage between strong texture and epitaxy while the SIMaP particle are in epitaxy with the substrate and thus exhibit a stronger binding with the sapphire substrate.

The corresponding diffraction patterns are in very good agreement with these assumptions. For the A2 particle, and as described in section VI.2, the Bragg peak is weakly distorted, suggesting a low amount of residual strain (Fig. VI.7.b to VI.7.d). We inferred in the previous section that the main of source of strain is the thermoelastic strain ($\Delta\alpha$ ΔT) induced during the cooling of the particle. Since the A2 particle has a weak binding with the substrate that would allow a better relaxation during cooling, only a very small part of $\Delta\alpha$ ΔT remains.

The diffraction patterns from the SIMaP particles show some obvious differences. The diffraction data from (e) was collected at the I13 beamline of the diamond light source, using a 9.375 keV coherent X-ray beam. The procedure described in section VI.2 was used to measure a 3D CXD pattern around the 1 1 1 Bragg reflection. The stronger binding between the particle and the substrate seem to keep unrelaxed a significant part of the thermoelastic strain to the particle and produce a very clear and distinct signature on the CXD pattern. As seen from Fig. VI.7.h, the Bragg peak is elongated along the three <1 1 1> directions which are not perpendicular to the top facet. This case is intermediate between a strain free particle, and a particle with a large and inhomogeneous interfacial strain (Beutier *et al.* 2013a). The shape of the crystal is still visible on the CXD pattern (presence of fringes along the direction of the facets), but the inhomogeneous strain induce a clear broadening of the Bragg peak.

The last two particles were measured from the same sample but on different beam lines, and with a different Bragg reflection for the last one. The 1 1 1 Bragg peak of particle (i) has been also collected at the upgraded ID01 beamline (ESRF) during a previous experimental run, using a coherent X-ray beam at 9keV. The CXD pattern from the last particle (m) was measured on the CRYSTAL beamline of the synchrotron SOLEIL, using a 8.9 keV coherent X-ray beam.

As illustrated from Fig. VI.7.l, the elongation of the Bragg peak along the <1 1 1> directions is less pronounced than in particle (e), suggesting a lower amount of residual strain. As opposite to the A2 particle, the Bragg peak does not consist of a single clean spot, but is splitted in two main parts indicating the presence of defect in structure. Particle (e) and (i) being from the same sample, one could wonder why particles with the equivalent size and shape, and grown with the same thermal treatment with the same surface state for the substrate, exhibit such large differences in term of residual strain. As discussed in section VI.1, the residual strain can be partially relaxed through the emission of dislocation that migrates to the substrate particle interface, and through the diffusion of vacancies (or of cluster of vacancies know as vacancy Frank loops) in the substrate. We can assume that the relaxation of the strain is more or less efficient from one particle to another, independently on its size and geometry.

The diffraction pattern from the last particle (m) measured for the 2 2 2 Bragg reflection is largely strain dominated. The Bragg peak is even more elongated along the <1 1 1> directions than in particle (e), due to the larger sensitivity of the 2 2 2 reflection to lattice displacements along the [1 1 1] direction. We estimate

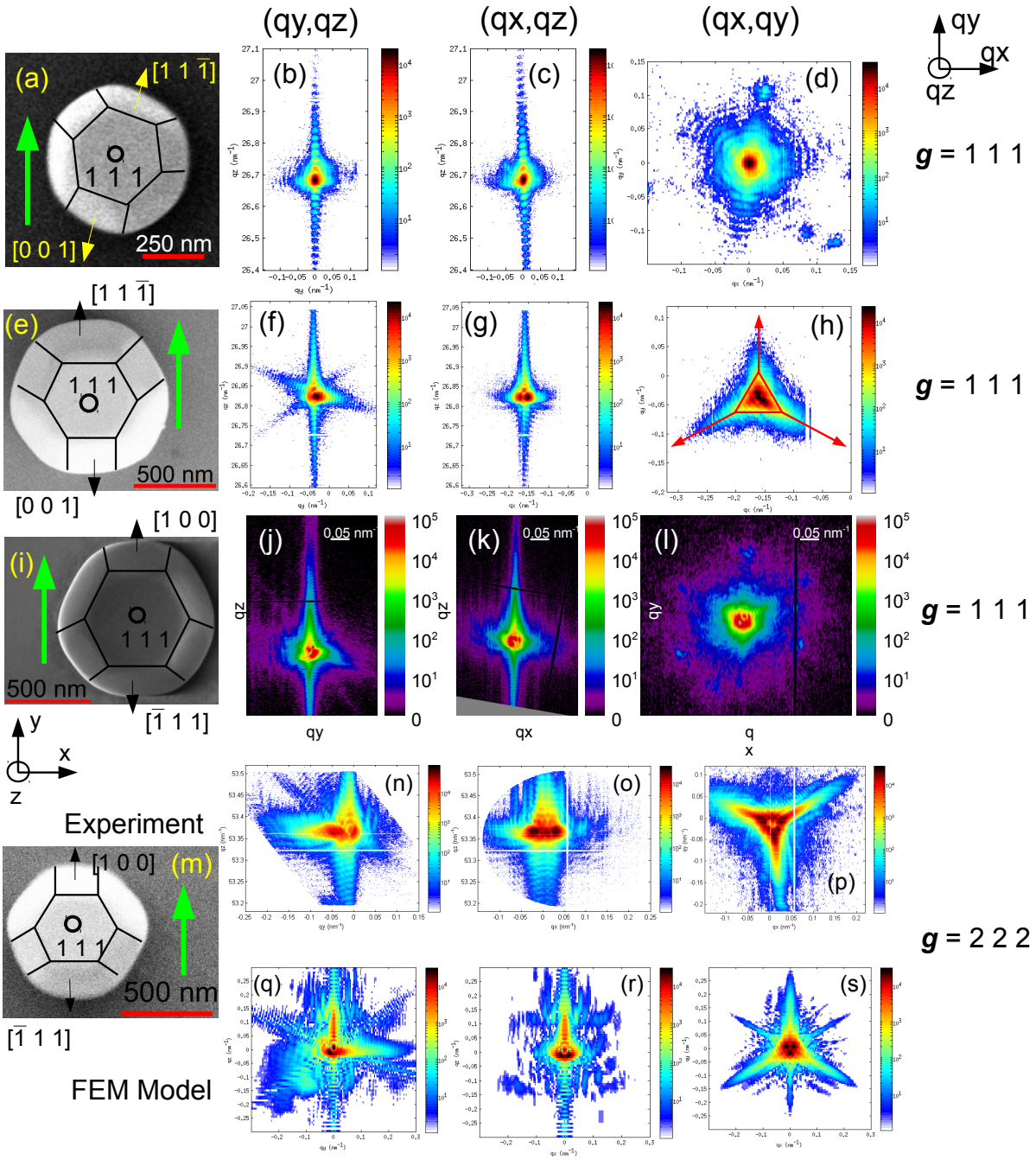

Fig. VI.7: *Signature of the thermoelastic strain on the CXD pattern.* The green arrow on figures **(a)**, **(e)**, **(i)** and **(m)** denotes the direction of the incident x-ray beam while the blue arrow indicate the [1 0 $\bar{1}$ 0] direction of the sapphire substrate. **(a)** 600x600x300 Au crystal that was measured during the present experiment with a 8 keV coherent X-ray beam. Corresponding CXD pattern around $\boldsymbol{g}$ = 1 1 1 in the (qy,qz) **(b)**, (qx,qz) **(c)** and (qx,qy) **(d)** planes of the reciprocal space. **(e)** 800x800x400 nm gold particle annealed during 1hour at 950 °C. The 1 1 1 Bragg reflection was collected at the I13 beamline of the Diamond light source, using a 9.375 keV coherent X-ray beam. Corresponding CXD pattern in the qyqz **(f)**, qxqz **(g)** and qxqy **(h)** planes. **(i)** 800x800x400 nm gold particle dewetted with the same thermal treatment as in **(e)** measured during a previous experimental run on the ID01 beamline using a 9 keV coherent X-ray beam. Corresponding CXD patterns around $\boldsymbol{g}$ = 1 1 1 in the (qy,qz) **(j)**, (qx,qz) **(k)** and (qx,qy) **(l)** planes. **(m)** 750x750x370 nm gold particle dewetted with the same thermal treatment as in **(e)** and **(i)**. The measurements were made at the crystal beamline of the synchrotron Soleil, using a 8.9 keV coherent X-ray beam. Corresponding CXD patterns around $\boldsymbol{g}$ = 2 2 2 in the (qy,qz) **(n)**, (qx,qz) **(o)** and (qx,qy) **(p)** planes. Simulated 2 2 2 Bragg reflection calculated from a gold crystal modeled with FEM in the (qy,qz) **(q)**, (qx,qz) **(r)** and (**s**) planes. The thermal mismatch corresponds an average deformation ε_{zz}~0.3%.

that the level of strain is comparable in (e) and (m) and of course much larger than in (a). A particle with size and shape comparable to particle (m) was modeled using FEM. The strain field was calculated assuming only thermoelastic deformation (no plasticity), and the $u_{2\,2\,2}$ displacement field used for the calculation of the diffracted intensity was obtained from the the strain field by integration. More details about the details of calculations of the diffracted intensity can be found elsewhere (Beutier *et al.* 2013a).
The calculated diffraction pattern (Fig. VI.7.q to VI.7.s) show some strong similarities with the experimental data, with an elongation of the Bragg peak along the <1 1 1> directions, but also along the <0 0 1> directions. (Langlais 2016). Similarly to the case of copper island, the simulation of the CXD pattern with the strain field from the FEM allows to obtain a good estimation of the mean residual strain along z (with z being the 1 1 1 direction) : $\varepsilon_{zz} \sim 0.3\%$. This value is significantly larger than the result obtained from the XRD laboratory measurements, which is a statistical average of Winterbottom and elongated crystallites. However, we have seen that the level of residual strain can be very different from one particle to another (large difference between particle (i) and (m) for instance), even if they belong to the same sample.
The comparison of the CXD patterns form the A2 patterns with CXD patterns measured during previous experiments suggests an almost strain-free and defect free particle in its pristine state. As discussed at the beginning of section VI.1, it is thus a particularly good candidate for a detailed study of defect nucleation in small size crystal.

VI.4 Simple model of the thermoelastic strain with molecular statics simulations

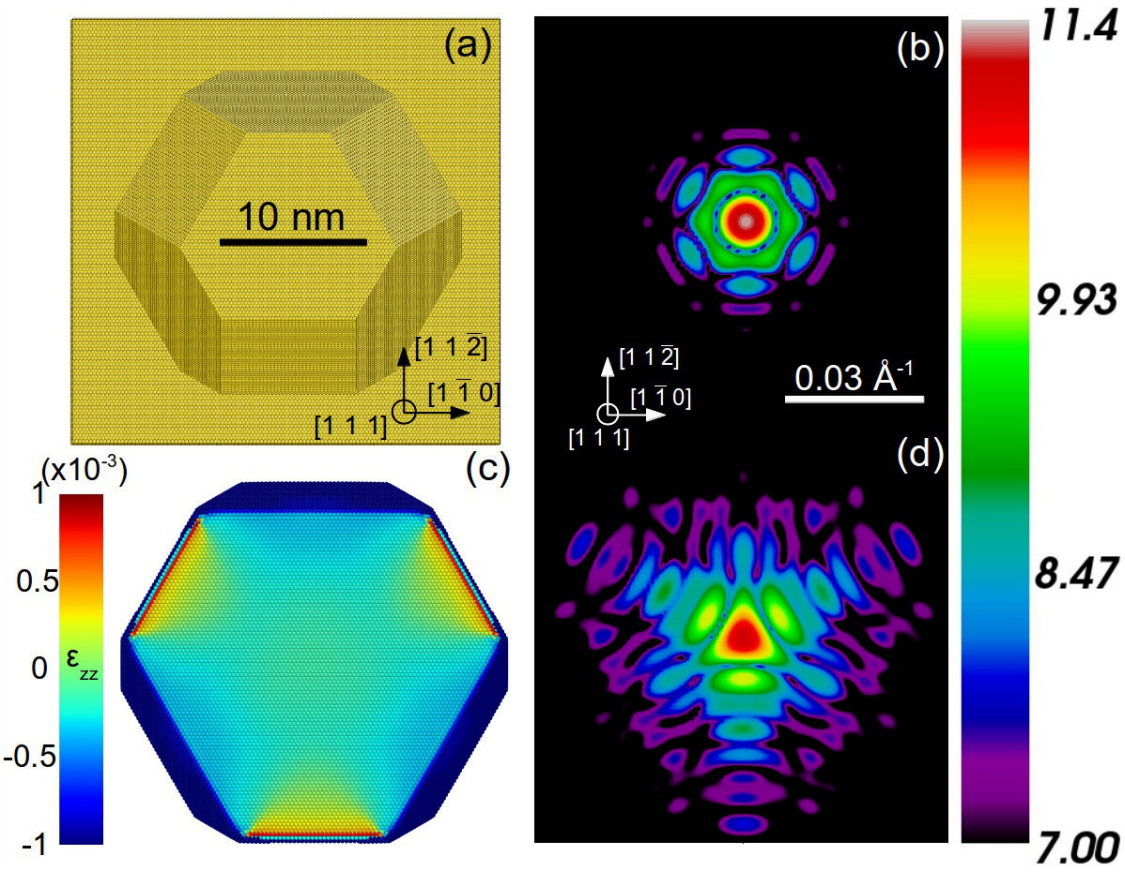

Fig. VI.8 *Thermoelastic strain modeled with molecular statics simulations.* (a) 30x30x30nm gold nanoparticle with a varying amount of thermal mismatch with the underlying substrate. (b) CXD pattern calculated around $\boldsymbol{g}$ = 2 2 2 for the unrelaxed strain-free particle. (c) ε_{zz} strain with z being the [1 1 1] direction induced by a 4.2% lattice mismatch with the substrate. (d) Corresponding CXD pattern for $\boldsymbol{g}$ = 2 2 2

The effect of thermoelastic strain on CXD patterns can also be modeled through molecular statics simulations. Of course the dimensions of the experimental particles (few hundred of nanometers) are unreachable with atomistic simulations. The results presented in this short section are purely qualitative but they provide a good description of the strain distribution in the particle.
A 30x30x30 nm_3 gold particle in a Wulff geometry was modeled using EAM potentials (Grochola *et al.* 2005) (Fig. VI.8.a) The sapphire substrate is simulated by a block of 20 layers of gold atoms frozen in their position and the thermal mismatch by imposing a displacement corresponding to compressive loading along the in-plane [1 $\bar{1}$ 0] and [1 1 $\bar{2}$] directions. For a given value of thermal mismatch, the atomic position in the particle are then relaxed, and the diffraction pattern is calculated in the kinematic approximation (Chapter III). The gold atoms mimicking the substrate are not taken into account to only capture the signature from the particle. Given the small size of the particles, the lattice mismatch has to be set to very large values in order to produce level of strain in the particle that sufficiently affect the diffraction pattern.
Fig. VI.8.b & VI.8.c show the calculated diffraction patterns in the (1 1 1) plane parallel to the (1 1 1) specular facet for $\boldsymbol{g}$ = 2 2 2. For the unrelaxed particle, the diffraction pattern is almost isotropic, the hexagonal shape of the particle is reflected in the hexagonal shape of the diffraction pattern. Both the fringes along the <1 1 1> and <0 0 1> direction are intercepted by the (1 1 1) plane, resulting in a six-fold symmetry. The diffraction pattern from the strained particle is also calculated for $\boldsymbol{g}$ = 2 2 2 for an equivalent initial imposed interfacial strain of 5.2%. As discussed in the next chapter (Chapter VII) the average lattice parameter in nanoparticles tends to decrease upon relaxation such that the value of the lattice mismatch is in fact significantly lower. Similarly to the FEM calculations, the Bragg peak evolves towards a triangular shape, and is elongated along both <1 1 1> and <0 0 1> directions. This signature of the strain is quite consistent with our observations on the experimental data. The atomic strain along [1 1 1]: ε_{zz} calculated from the atomic positions is represented on Fig. VI.8.c in the (1 1 1) plane, about half-way of the height of the particle. The elongation of the <1 1 1> and <1 0 0> fringes seems to be associated seems with alternating regions of tension and compression. The areas of compression are located close to the {1 1 1} facets while the areas of tension are close to the {1 0 0} facets.

VI.5 Results

In this section the in-situ indentation experiment are reported. A detailed analysis of both the CXD patterns and of the displacement field reconstructed from the diffraction data are provided.

VI.5.1 Analysis of the CXD patterns at various iteration of the loading unloading cycle

As presented in section VI.2, we carried out a total of 6 loading-unloading iterations. Each iteration consists in increments of an imposed total displacement of the z-piezo, with a maximum of 40 nm amplitude, once the surface is detected. During this slow loading, the tip is withdrawn as soon as a subtle variation in the diffraction pattern (actually on the detector) seem to appear. This procedure of quasi-static indentation is used so that initial irreversible change in the particle are not missed, Beutier *et al.* (2013b). In past in-situ loading, too large depth/load excursion have provoked the typical burst of defects (pop in events). The diffraction pattern presented in Fig. VI.9 are collected at four different stages of the in-situ indentation experiment: on the pristine particle, before indentation, after 3 loadings, after 4 loadings and after 6 loadings and after a 24h illumination under the beam.
The simulated nano-indentation presented in section IV.2 (for the analysis of the CXD patterns) and in section V.5 (analysis of the reconstructed displacement field) presented the detailed defect structure that should correspond to the nucleation by indentation of a sub-micron f.c.c. particle indented along the [$\bar{1}$ $\bar{1}$ $\bar{1}$] direction. Three crystallographic equivalent variants of prismatic dislocation loops are regularly emitted from the region just below the indenter with a Burgers vector of type 1/2<1 1 0>. They are thus all visible with $\boldsymbol{g}$ = 1 1 1. Under indentation load they are likely to move along their glide cylinder parallel to their Burgers vector until they are annihilated at the crystal substrate interfaces. The 3D CXD patterns are always recorded

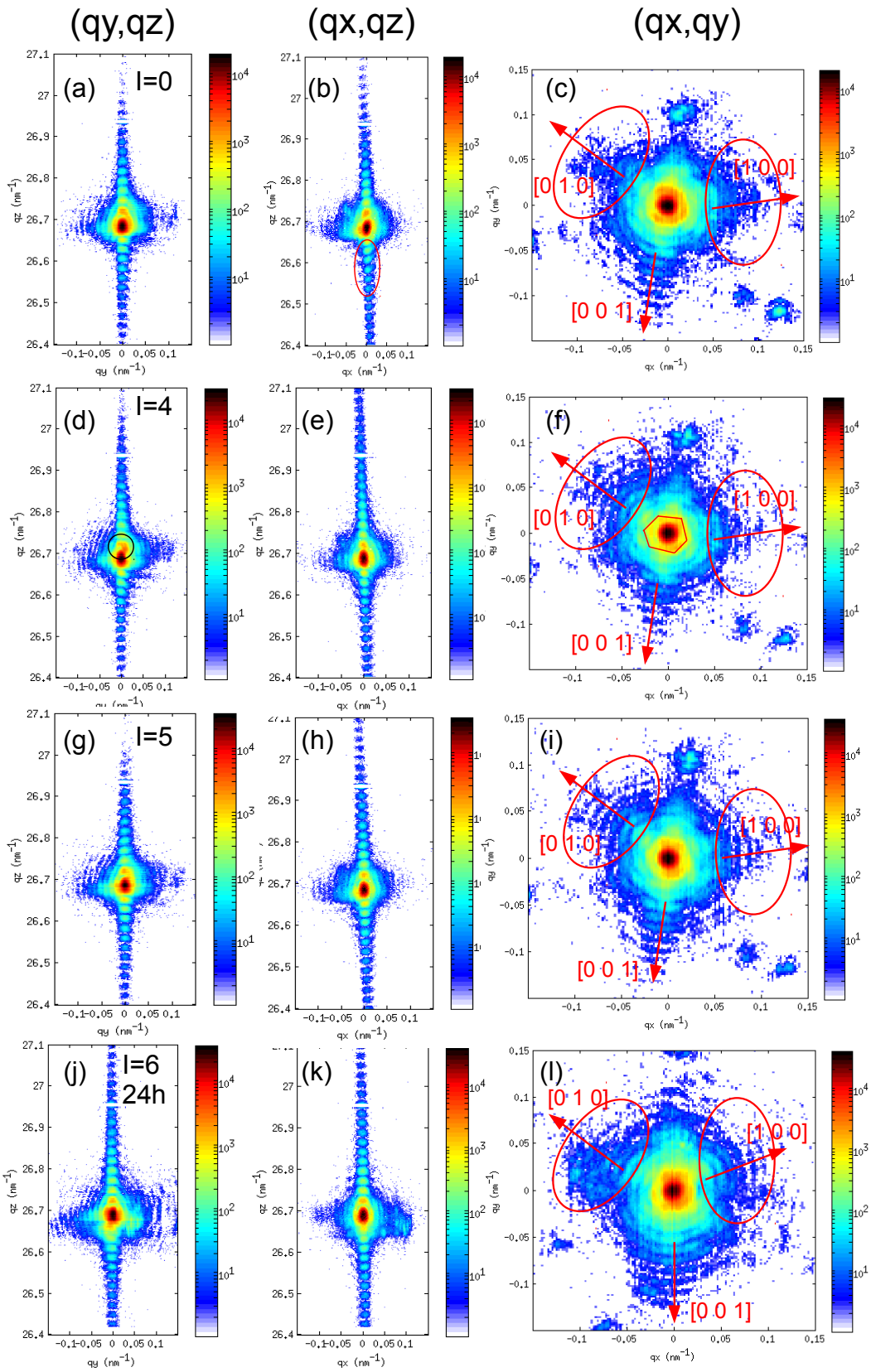

Fig. VI.9*: CXD patterns at different stages of the indentation experiment measured around* ***g*** *= 1 1 1.* (qy,qz) (a), (qx,qz) (b) and (qx,qy) (c) slices of the reciprocal space for the pristine island. Same slices of the reciprocal space after three cycles of loading-unloading (d to f), four cycles (g to I), 7 cycles and 24 hours of illumination under the X-ray beam.

after unloading, such that most of the dislocation that are created during the loading have probably left the crystal. Even if dislocation loops are present in the structure, their signature on the CXD pattern should remain rather limited. The displacement field of prismatic dislocation loops have been presented in details in sections V.4 and V.5 and it has been evidenced that the strain field around dislocation loop extends over a region that does not exceed the loop diameter. The volume of the phase shifted volumes in the crystal are small, unless the loop has a size comparable to that of the crystal which is very unlikely. As a consequence, a 20 nm loop nucleated in a 600x600x300 nm^3 crystal as the one measured experimentally is expected to create a weak signature on the CXD pattern. The diffraction pattern from the pristine island has already been described in section VI.3. The Bragg peak is weakly distorted and the fringes along the directions normal to the crystal facet are clearly visible, suggesting a low mean residual strain. A closer look at the fringes along the (1 1 1) direction in the (qx,qz) slice of the reciprocal space reveals that they are slightly distorted (area circled in red on Fig VI.9.b). This could indicate the presence of some strain in the particle. The fringes along the <0 0 1> directions can also be distinguished, but the contrast is rather poor for the fringes along [0 1 0] and [1 0 0] (Fig. VI.9.c, circled in red).

After three loading-unloading events (I=3), some visible changes can be observed (Fig. VI.9.d to VI.9.f). A close look close to the Bragg position in the (qx,qz) slice of the reciprocal space (Fig VI.9.d) reveals a slight modification of the shape of the Bragg peak (area circled in black). Since no splitting can be observed, we can infer that if some defects have been nucleated, they don't induce the phase shift of large volumes in the crystal, in good agreement with our predictions. The analysis of the (qx,qz) and (qx,qy) slices also reveals interesting informations (Fig. VI.9.e & VI.9.f). The distortion of the (1 1 1) fringes that was observed in the (qx,qz) slice has completely vanished, suggesting that some of the residual strain has been relaxed. On the (qx,qy) slice the hexagonal shape of the particle can clearly seen in the CXD pattern .We have seen in the simulations (section VI.4 for instance) that such visibility of the shape of the particle is a good indication of the absence of strain. The contrast in the fringes along the [1 0 0] and [0 1 0] directions is also enhanced as compared to the pristine particle. Overall, we notice a slight modification of the Bragg peak which could be the signature of the nucleation of defects. On the other hand, the CXD patterns looks cleaner with the almost complete vanishing of the fringes distortion and an improvement of the fringes contrast along some directions. This suggest an overall decrease the residual strain in the particle.

The diffraction pattern collected after four indentation events (I=4) tends to confirm this trend. On the (qy,qz) slice of the reciprocal space (Fig. VI.9.g), the shape of the Bragg peak is very similar to the case of the pristine particle. This could be an indication that the modifications observed for (I=3) are indeed related to the nucleation of defects. Additionally, the distortion of the (1 1 1) fringes (Fig. VI.9.g & VI.9.h) has completely vanished, and the contrast of the fringes along [1 0 0] and [0 1 0] is even further enhanced as compared to I=3. This in good agreement with our hypothesis of the decrease of the mean residual strain in the particle after few loading and unloading events.

Fig. VI.9.j to VI.9.l show slices of the CXD pattern that was collected after 6 loading-unloading iterations followed by a 24 h illumination under the beam. Some strong differences are observed with the previous stages of the indentation. They suggest a change in the particle shape. This is particularly obvious in the (qx,qy) slice (Fig. VI.9.l) where the orientation of the <0 0 1> fringes indicated by the red arrows has been clearly modified such that the (qx,qz) slice (Fig. VI.9.k) now intercept the fringes along the [1 0 0] direction. The reconstruction of the electron density should allow to visualize the detailed evolution of the particle shape. Apart from this changes, the Bragg peak still consists of a single clean spot while the (1 1 1) fringes are not distorted. The mean residual strain in the particle does not seem to have significantly increased.

The direct analysis of CXD patterns provide some useful informations. A change in the orientation of the facet fringes reveals a modification of the shape of the particle under illumination. It is also quite clear that the diffraction pattern appears more perfect after few loadings. This suggest a partial relaxation of the residual strain, by emission of dislocations also known as “mechanical annealing” (Matthews & Blakeslee 1974). As discussed in section V.5 and at the beginning of this paragraph, the signature of small dislocation loops in a large crystal volume are not expected to produce a clear signature on the CXD pattern. The variations in the shape of the Bragg peak could be attributed to the nucleation of defect in the structure, but the presence of dislocation loop in the crystal can only be confirmed through the phase retrieval of the

diffraction data.

VI.5.2 Reconstruction of the electron density

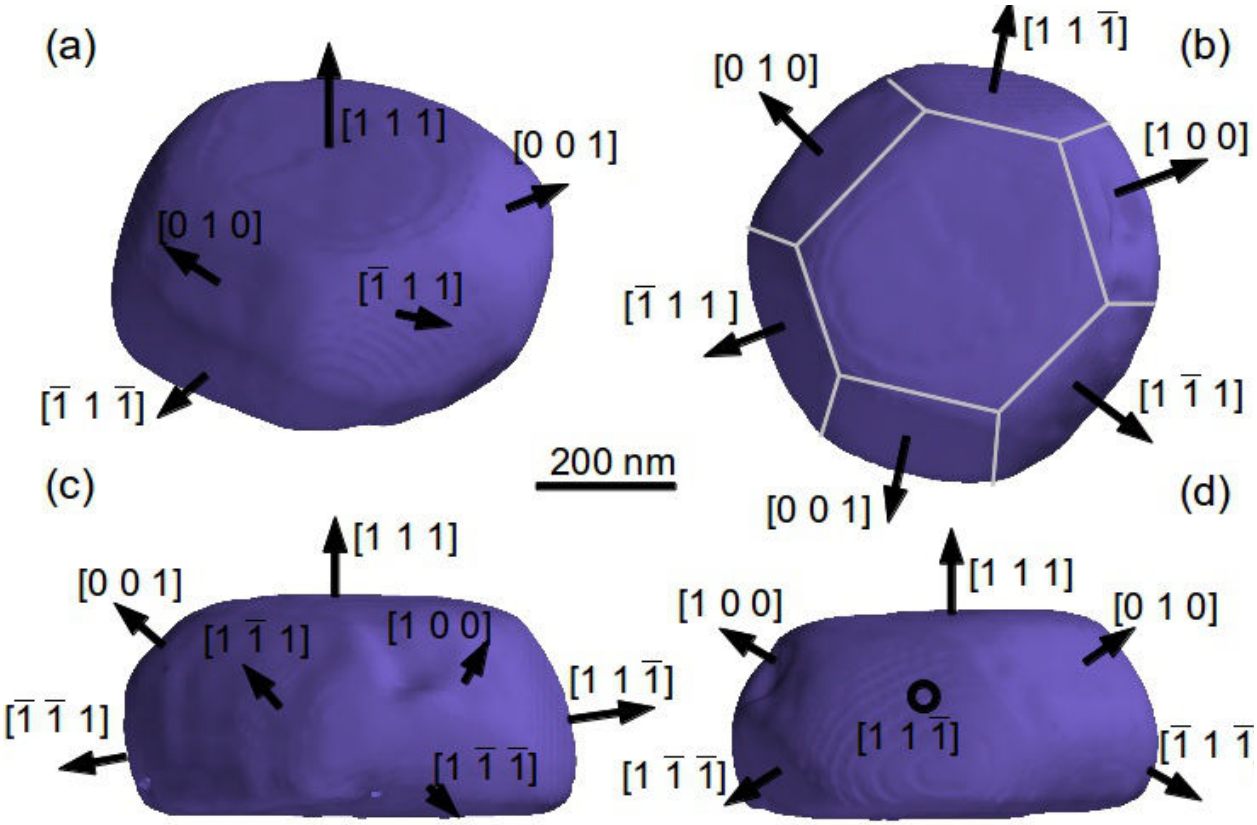

Fig. VI.10: *Reconstructed electron density isosurface drawn at 30% of the maximum density.* The density is averaged over 50 reconstruction consisting of the 10 best reconstructions at each iteration of the loading – unloading cycle for I=0 to I=4 (with i the number of loading-unloading cycles). (b) is seen from the z direction which corresponds to the [1 1 1] direction while (c) and (d) are seen from the x and y direction which are almost parallel to the [1 1̄ 0] and [1 1 2] directions.

The phase retrieval of the diffraction data was carried out using classical phase retrieval algorithms (Fienup 1982, Marchesini 2003), following the procedure described in details in Chapters I & VII. The $u_{1\,1\,1}$ displacement field was reconstructed for each iteration of the loading unloading cycle.
Similarly to the case of the twin particles, the best solution are selected according to their metric error and to the homogeneity of the electron density. For each scan, a total of 40 random starts was performed, and the 10 best solution were averaged to produce the final image of the sample.
The reconstructed electron density shown on Fig. VI.10 is averaged over 50 reconstructions: the 10 best reconstructions for the first five stages of the indentation (I=0 to I=4). Given the averaging over a large number of estimates, the isosurface drawn at 30% of the electron density appears very smooth. The voxel size given by the extent in the reciprocal space is equal to (7.4x8.45x7.75 nm^3).
In good agreement with previous observations (Sadan & Kaplan 2006, Malyi *et al* 2012) the particle is strongly faceted with a Winterbottom equilibrium shape. All the {1 0 0} and {1 1 1} facets connected with rounded interfaces can clearly be identified. The particle is wider than it is tall, suggesting that the equilibrium crystal shape (Chapter II) has not been completely reached (Watari *et al.* 2011). Fig. VI.10.b confirms the misorientation of 15° with respect to the [1 0 1̄ 0] axis of the sapphire substrate. Fig. VI.10.c and 10.d are thus seen 15° from the [1 1̄ 0] and [1 1 2̄] directions respectively. The reconstruction of the electron density at each iteration of the loading-unloading cycle reveals a remarkable reproducibility of the shape of the particle for I=0 to I=6 (Fig. VI.11.a to VI.11.g). For the latter, the density is averaged over a

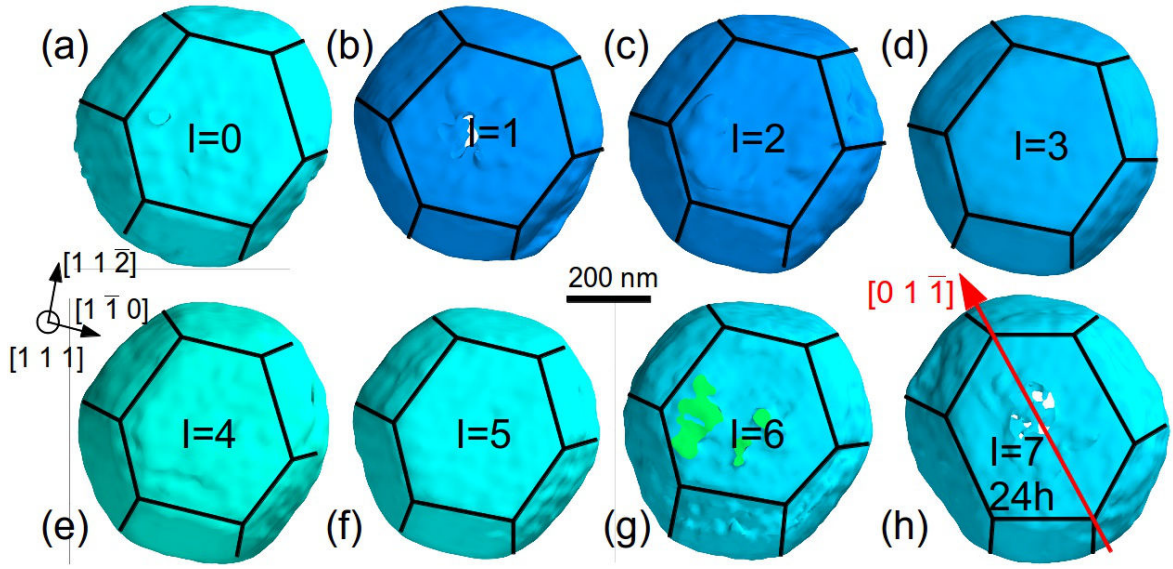

Fig. VI.11: *Reconstructed electron density isosurface drawn at 25% of the maximum density for each iteration of the loading-unloading cycle.* The density is averaged over the 10 best reconstructions after iterative mechanical loadings (a-g) and (h) after 24 h ageing at RT under the beam

fewer number of solutions such that the isosurface appears a bit rougher. Of course the footprint of the indenter on the top (1 1 1) surface can not be seen from the reconstruction since we limit the amount of plastic deformation. The remarkable similarities between each stage of the indentation and with the SEM picture is a quite good evidence of the convergence of the phase retrieval algorithms towards the good solution.

After 24 hours ageing with illumination, the shape of the particle has completely evolved (Fig VI.11.h). First, the height of the particle remains unchanged (within 20 nm upper bound resolution), but the respective area for <1 1 1> and <1 0 0> facets have dramatically evolved. Moreover, an in-plane rotation of the crystallite is clearly visible: the <1 1 0> intercepts of <1 1 1> and <1 0 0> facets have rotated (Fig. VI.11), by around 5-10° and finally, and an asymmetric elongation along [0 1 $\bar{1}$] can be observed. This change of shape is rather striking. Several mechanisms can be considered, all include surface diffusion which are not negligible at RT over 24 h:

- alteration of surface energies and their relative ratio, due for example to surface contamination (ionization phenomena of air induced by the beam). This would indeed lead to a more isotropic shape.
- free energy change (elastic stored energy of the residual strain) that induces a morphological change of the shape of the particle (Muller *et al.* 1998, see subsection II.3.1.1): the equilibrium shape of crystals (Wulff, Winterbottom...) formalism are proposed to explain the shape of crystallites from their formation (only transition from vapor/liquid to perfect crystal are considered). If additional energetical volumic contributions are added, this alters the ECS. This is the case treated by Kaishew (1952) applied to ECS by Muller *et al.* (1998) involving epitaxial strain for example. This should lead to a change of relative facets area proportion, but also the height (equilibrium wetting angle) as stated by Muller *et al.* (1998). Rotation has not been considered in their calculations, since isotropic elastic field are only considered.
- rotation induced by the crystal plasticity : if during the plastic events, an unbalanced net displacement accumulates at the interface (due to a unbalanced slip system nucleation/activation), this would produce after atomic rearrangement at the interface a net rotation. This rearrangement is not immediate, since it would have been observed during the mechanical iteration, but a 24 h annealing at RT could allow general diffusion based mechanism to modify the weak crystallite/substrate interface.

VI.5.3 Imaging of the displacement field around a prismatic dislocation loop

The strongest modification of the shape of the Bragg peak is observed after 3 loading-unloading events. We suspect that some defect could be present in the particle at this stage of the indentation.

For weakly strained systems, the phase of the retrieved complex-valued electron density $f(\mathbf{r})$ often presents some variations that can be related to the experimental conditions rather than to the crystal structure. They mainly consist of a reciprocal space offset which induces a linear phase ramp, refraction effects (Harder *et al.* 2007) presented in Chapter II and further discussed in Chapter VII and curved illumination wavefront (Chamard *et al.* 2010). Any phase ramp due to a bad centering of the diffraction data is eliminated by multiplying $f(\mathbf{r})$ by the phase ramp calculated from the centre of mass (Clark *et al.* 2015). The only other phase variations that are not related to the crystal structure are thus the refraction effect and the illumination wavefront inhomogeneities. Fig. VI.12 show the reconstructed displacement field for I=3. A region where the phase drops significantly (by almost 2 radians) can clearly be identified near the [0 1 0] and [$\bar{1}$ 1 $\bar{1}$] facets (region circled in red on Fig. VI.12.d) The linear phase variations in this region are clearly attributed to the phase of the illumination wavefront rather than the u_{III} displacement field in the crystal.

The particle was illuminated with a beam size which is only slightly larger than its lateral size and height (600x600x300 nm^3 particle versus beam size of FWHM ~700x400 nm^2 HxV). For a sample placed exactly in the focal spot of a Fresnel-Zone plate, the phase of the wavefront is expected to be flat in the focus (Schroer *et al.* 2008, Takahashi *et al.* 2009, Mastropietro *et al.* 2011). However, under such experimental conditions, and for a beam size only slightly larger than the sample, distortion of the wave front were reported to cause phase variations of as much as 0.5 radians (Diaz A. *et al.* 2009). Here the sample was not placed in the focal spot of the Fresnel zone plate and the distortions of the wave front are expected to be even larger. The retrieved phase at the sample is thus a mixing of the illumination wavefront phase with the phase of the complex sample density itself.

In order to disentangle the contribution of both phases, a 2D ptychography scan (Rodenburg *et al.* 2007) was performed at the 2 2 2 Bragg reflection to reconstruct the wavefront. Such reconstruction has not been performed yet and in the following the retrieved phase is a mixing of the illumination wavefront phase with the phase of the sample itself. Given the large phase variations observed around defects and at the substrate/particle interface, this should not be too problematic for the analysis of he evolution of the microstructure. We will indeed see in the following, that the footprint of the beam is always clearly visible on the reconstruction and does not vary from one reconstruction to another. However, given the significant contribution of the phase of the wavefront, this correction will need to be implemented in a near future. The maximum phase shift accounting from refraction effects is of the order of 0.45 radians. Its contribution to the phase variations is thus much smaller than the contribution from the distorted wavefront and can be neglected. If some of the phase fluctuations can be attributed to the experimental conditions, some phase variations can clearly be attributed to the evolution of the microstructure of the sample.

Fig. VI.12.a show the isosurface of the reconstructed electron density of the sample drawn at 25% of the maximum value of the density. A loop-shaped drop of density is seen at the centre of the particle, approximately 100 nm above the substrate-particle interface. It strongly resembles to the dips of intensity that we identified at the vicinity of dislocations in our simulations (section V.3 to V.5). The (y,z) (1 $\bar{1}$ 0) (Fig. VI.2.b), (x,z) (1 1 $\bar{2}$) (Fig. VI.2.c) and (x,y) (1 1 1) (Fig. VI.2.d) planes intercept the loop in two locations where a pair of vortices with opposite chirality can be observed. This profile of the $u_{1\,1\,1}$ displacement field around the defect (Fig VI.13.b) is very similar to the $u_{1\,1\,1}$ displacement field we observed around simulated prismatic dislocation loops (Fig. VI.13.e). Between the two phase vortices, the rapid phase variations along the loop axis are localized to a region which does not exceed the loop diameter.

In the plane that intercepts the loop perpendicularly to its axis (Fig VI.13.a and VI.13.c), the phase shift between the regions inside and outside the loop is roughly equal to π, as in simulations (Fig. VI.13.d)

The loop diameter is approximately 50 nm. As discussed in the previous section, such a small loop in a large crystal produces a very weak signature on the CXD pattern, and the identification of such defect can be achieved only through the reconstruction of the displacement field. In any case, the very strong similarities between simulation and experiment leaves little doubt on the presence of a prismatic dislocation loop in the structure at this stage of the indentation experiment.

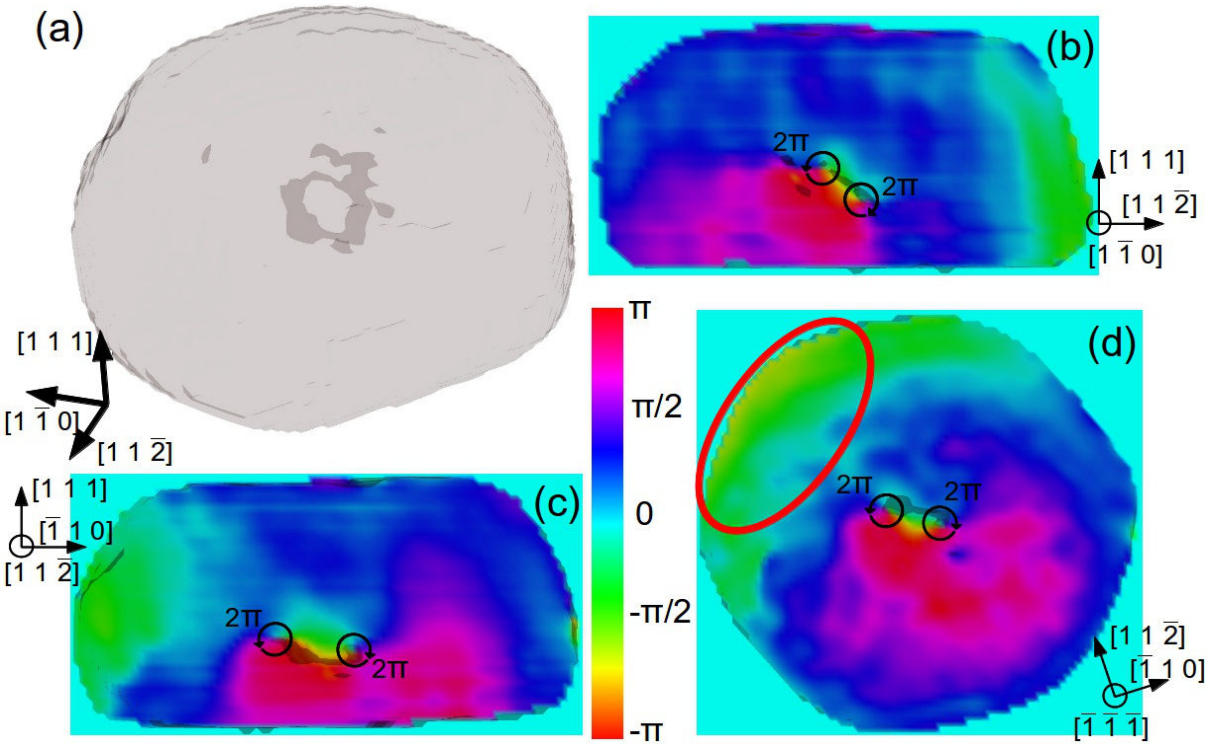

Fig. VI.12 *Reconstruction of the displacement field around a prismatic dislocation loop nucleated after four iterations in the loading-unloading cycle.* (a) Reconstructed electron density drawn at 15% of the maximum density. The drops in the electron density indicate the position of the loops. Reconstructed $u_{1\,1\,1}$ displacement field in the (1 $\bar{1}$ 0) (b), (1 1 $\bar{2}$) (c) and 1 1 1 (d) planes which are intercepted by the loop in two locations. The electron density is superimposed in transparency to locate the position of the loop with precision Red ellipse marks where the phase of the wavefront has a significant contribution - see text for more details.

What is more surprising is the presence of a single dislocation loop in the structure. As discussed earlier (section V.5), upon nano-indentation, loop are regularly emitted from the region below the indenter to accommodate plastically the area of contact of the tip, but most of them can be annihilated at the crystal surfaces. Although it can not be excluded that some dislocation loop can stabilize in the crystal after the unloading of the indenter tip, the presence of a single one rather than an assembly with equivalent Burgers vector was not necessarily expected. It could be also conceivable that some of the loops in the crystal fulfill the invisibility conditions and are thus invisible in the reconstruction. However, this hypothesis is unlikely. Upon indentation along the [1 1 1] direction, there are only three possible Burgers vectors for the nucleated dislocation loops, and none of them is perpendicular to $\boldsymbol{g}$ = 1 1 1.

The most efficient way to determine the Burgers vector of the dislocation loop is through the invisibility conditions as discussed in sections III.4.1, IV.2 & V.5. Two off specular reflections were measured during the experiment ($\boldsymbol{g}$ = $\bar{1}$ 1 1 and $\boldsymbol{g}$ = 1 $\bar{1}$ 1). The possible Burgers vector of the loop is necessarily perpendicular to one of them and possibly to the two. In any case, the use of these two reflections would have allow to determine the Burgers vector of the loop. Unfortunately, and as discussed in section V.2, the phase retrieval of the diffraction data did not converge for these two reflections.

Although it is less reliable, there is another possibility to determine the Burgers vector of the loop. It is based on the determination of the slip planes of the Shockley partials of the loop from the reconstructed electron density. The Burgers vectors of the loop being perpendicular to the slip planes of the Shockley partials, the determination of its orientation is straightforward if the slip planes are known. For the 1 1 1-type diffraction vectors, only half of the Shockley partials are visible (section V.4, & V.5). However, for the simulated data, it is quite easy to determine if a {1 1 1} plane intersect a loop or contain a part of the dislocation loop. In the latter case, this means that it is slip a plane for the Shockley partials. For the experimental data, due to the much larger voxel size and the small loop size with respect to the size of the crystal, it is more challenging to

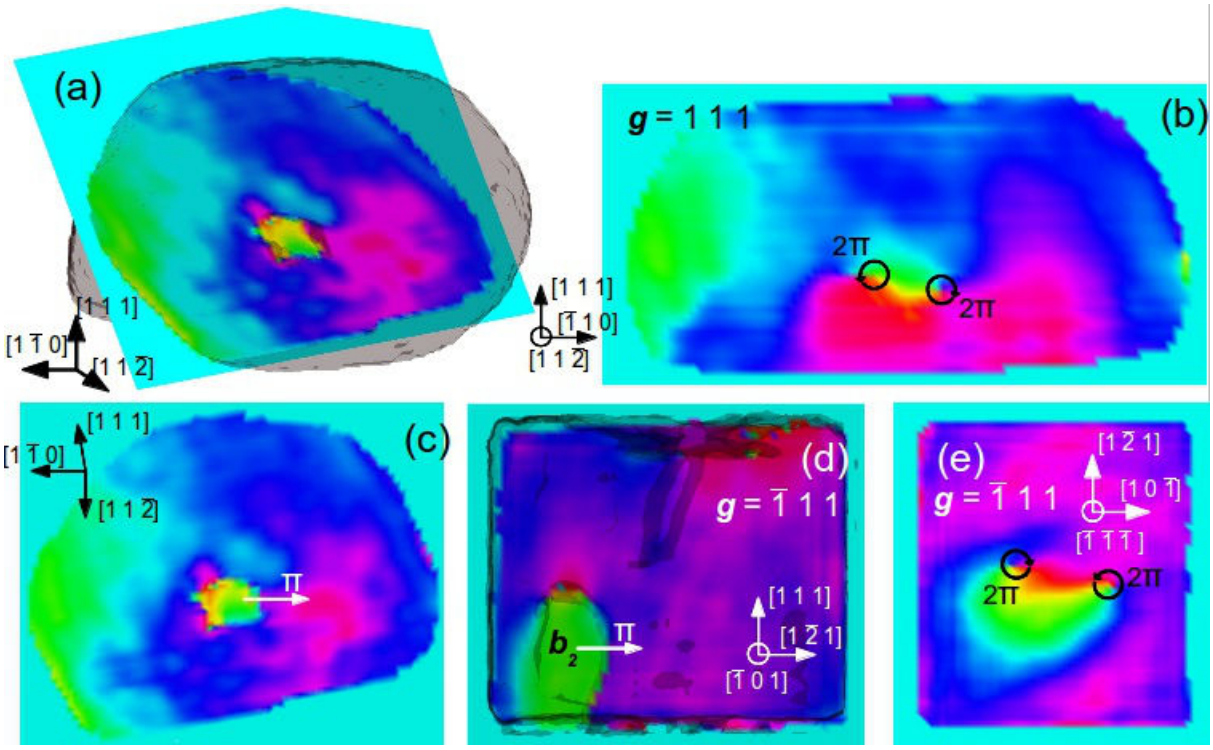

Fig. VI.13 *Comparison between the $u_{1\,1\,1}$ displacement fields from the experimental loop and from the dislocation loops nucleated during the simulated nanoindentation of a nickel thin film.* Reconstructed $u_{1\,1\,1}$ (experiment) and $u_{\bar{1}\,1\,1}$ (simulation) displacement field in planes perpendicular to the experimental (a) and (c) and simulated (d) loop axes. Same displacement field in planes intercepting the experimental (b) and simulated (e) dislocation loops.

make the distinction between a plane intersecting or containing a dislocation loop. It is nevertheless possible to establish with almost certainty that the ($\bar{1}$ 1 1) plane contain a part of the loop, while the (1 $\bar{1}$ 1) plane does not contain any part of the loop. The Burgers vector of the loop is thus the vector perpendicular to the ($\bar{1}$ 1 1) and (1 1 $\bar{1}$) plane i.e 1/2[1 0 1]. Of course this method is not very reliable, especially on the experimental data where the dislocation loop only extent over 6x6 pixels.
In summary, a planar loop of 50 nm diameter (6 pixels), with the exact phase jump of a prismatic loop is clearly evidenced. Moreover, using geometrical arguments and based on the appearance of the displacement field (stacking fault ribbon evidenced with the $g_{1\,1\,1}$) we conclude that it is a prismatic loop. Quantitative determination of its Burgers vector can not be achieved with almost certainty without reconstructions of off-specular reflections. Nevertheless, prismatic loops are well known to nucleate to accommodate the contact of area of the indenter. Moreover its diameter of around 50 nm confirm its certain nucleation from the indentation process since this corresponds to a radius of contact of 3 nm, corresponding to the initial plastic deformation stage. Again, nucleation of prismatic loops in f.c.c. metals at room temperature is generally only observed as a punching relaxation mechanisms in the crystal to accommodate imposed eigenstrain: around spherical incoherent precipitates (Ashby, giving birth to the concept of strain gradient plasticity in 1971) or around spherical/blunt indenter (Ashby 1971).

VI.5.4 Evolution of the displacement and strain fields in the particle during the loading-unloading iterations

In subsection VI.5.1, we established that the CXD patterns appeared more "perfect" after a few loading-unloading events, suggesting that the strain was partially relaxed through the emission of dislocation loops. The reconstruction of the $u_{1\,1\,1}$ displacement field allow to monitor the evolution of the strain in the particle at each stage of the indentation. On Fig. VI.13, the $u_{1\,1\,1}$ displacement field is reconstructed for five

stages of the indentation experiment. As discussed in subsection VI.5.3, the wavefront of the beam induces a large phase decrease at the vicinity of the [$\bar{1}$ 1 $\bar{1}$] and [0 1 0] facet: the top part of the crystal on the (x,y) slice, and the left part for the (y,z) and (x,z) slices. As seen from Fig VI.14.a, VI.14.d, … VI.14.m, a regular phase ramp of almost 2 radians is seen in this part of the crystal, and is observed for each reconstruction. It can not be related to the evolution of the microstructure, and won't be taken into account in our analysis. In the rest of the crystal, it is clear that the phase wavefront has a smaller contributions on the overall phase variations. We will only discuss the phase variations in this part of the crystal to comment on the evolution of the microstructure.

As demonstrated by Newton *et al.* 2010, the full strain tensor of the crystal can only be obtained with 3 non-coplanar Bragg reflections. In our case, we are able to reconstruct the displacement field for one reflection. If x, y and z are respectively the [1 $\bar{1}$ 0], [1 1 $\bar{2}$] and [1 1 1] directions , only the displacement along z and of the corresponding deformations along the z axis ε_{zz} are accessible with $\boldsymbol{g}$ = 1 1 1. The evolution of the microstructure would be best seen through the reconstruction of the 3D displacement field and of the six independent components of the strain tensor after each indentation event. However, $\boldsymbol{g}$ = 1 1 1 is sensitive to the displacements along the indentation direction and allows to detect any defect nucleated during the indentation process. The obtaining of both the displacement and strain field along z already gives a lot of information on the strain and defect content in the crystal. In the following, the evolution of the microstructure is only commented through the changes in the displacements and strain along z. The reconstructed phase presented here are averaged over the ten best solutions for the reconstruction at each iteration of the loading/unloading cycle. For I=3, where a dislocation loop has been identified in the previous section, the position of the loop slightly varies from one reconstruction to another, such that the phase jump and the displacement field around the loop are not located on the same pixels. When the 10 solutions with the lowest metric error and the most homogeneous electron density are averaged, the displacement field around the loop, those extent is limited, does not appear anymore on the reconstruction. However, some phase discontinuities are still clearly visible (Fig. VI.14.d). Their positions are consistent with the location of the loop on Fig. VI.12 & VI.13. The other consequence of the averaging is the smoother appearance of the phase, which allows to better see the phase gradients at the substrate/particle interface, and close to the particle surfaces.

In the pristine particle, the total phase variations are quite large, with an amplitude close to 2 radians (1/3 of the lattice spacing between two (1 1 1) planes). At the bottom of the particle, a positive phase gradient of approximately 1.1 radians is observed along the [1 1 1] direction (Fig VI.14.a & VI.15). This suggest the presence of compressive strain ε_{zz} at the substrate particle interface. This phase gradient changes sign at one third of the height of the particle. Between h = 100 nm and h = 300 nm (height of the specular (1 1 1) facet), a negative phase gradient of -2.2 radians is observed (Fig VI.14.a & VI.15). The overall phase variations are thus significantly larger than in the case of a twinned particle of similar dimensions (Chapter VII). These lager phase gradients can be linked to the different methods of preparation for the two particles. The twinned particle was growth by dewetting above the melting temperature of gold. In this case, the in-plane orientation is completely random and the particle has no epitaxial relationship with the substrate. Upon cooling to room temperature, only a small part of the thermoelastic strain remains in the particle, mainly at the substrate particle interface. Its contribution is of the same order of magnitude as the surface strain, induced by the relaxation of the free surfaces (Chapter VII). The large positive and negative phase gradients along the z ([1 1 1]) direction are thus attributed to the interfacial strain. It induces a weak distortion of the [1 1 1] fringes, clearly visible on the (qx,qz) slice of the reciprocal space (Fig. VI.9.c). Some phase variations can also be identified at the vicinity of several facets (regions circled in red on Fig. VI.14.a, VI.14.d & VI.14.j). For I=0 and I=3, a decrease of the phase is observed close to the [0 0 1] facet, while for I=4, I=5 and I=6, a decrease of the same order of magnitude can be identified close to the [$\bar{1}$ $\bar{1}$ 1] facet. These phase variations are localized close to the surface, and can be clearly attributed to surface strain. The latter decays rapidly in the bulk, obeying the continuum elasticity equations at a surface (Landau & Lifshift 1986). Unlike the case of the twinned particle in Chapter VII, the substrate interfacial strain outshines the surface strain and the contribution of the latter is not decisive to explain the overall strain distribution.

After 3 indentation iterations, the $u_{1\,1\,1}$ displacement field is largely modified in the particle. A positive phase gradient along z can still be identified at the substrate particle interface, however both its amplitude and Fig.

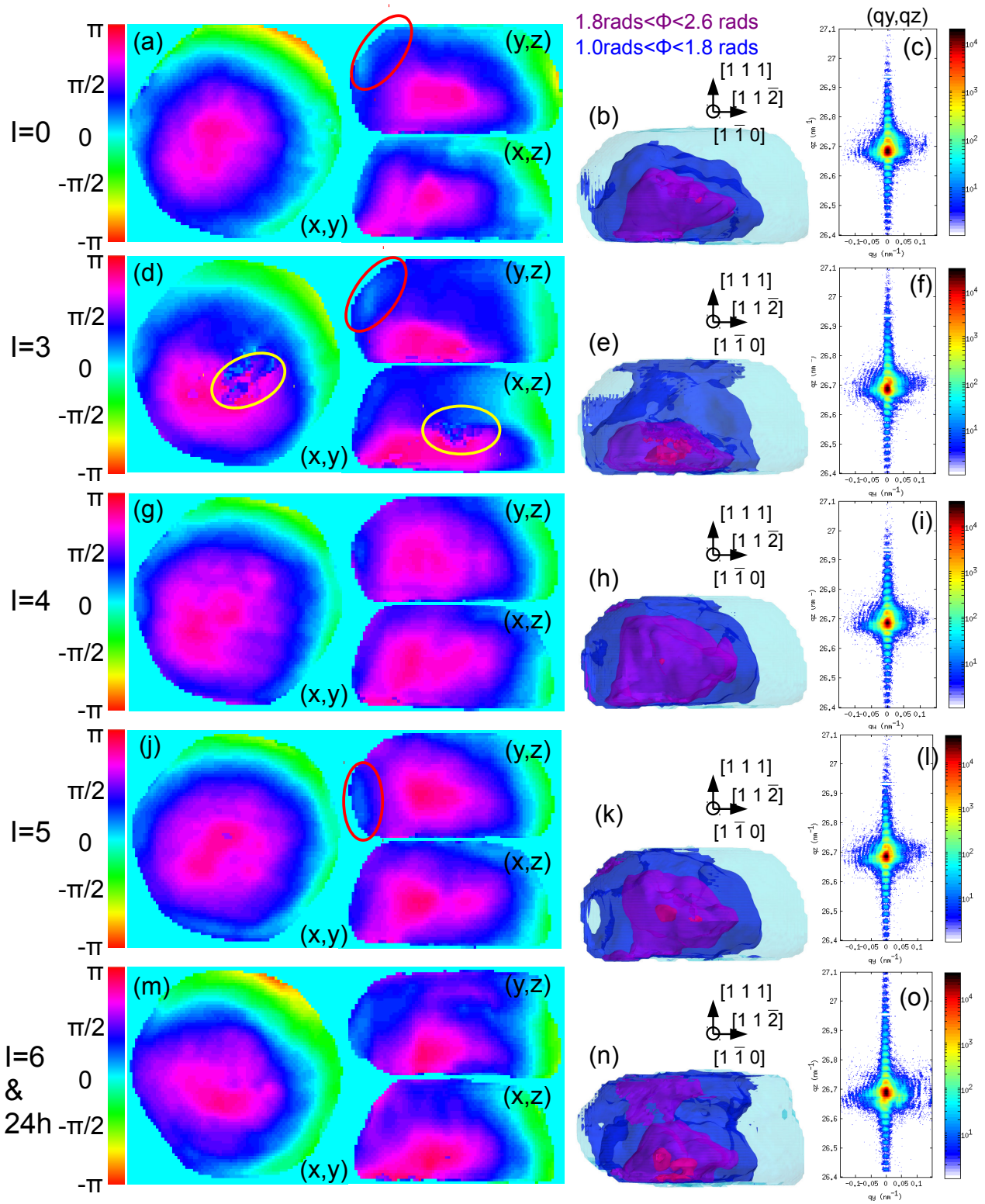

Fig. VI.14: *Reconstructed φ_{111} phase field for increasing iterations of the loading-unloading cycle.* The phase variations in the regions circled in red are attributed to the presence of surface strain (a) Reconstructed u_{111} in the (x,y), (x,z) and (y,z) planes corresponding respectively to the (1 1 1), (1 1 $\bar{2}$) and (1 $\bar{1}$ 0) planes. (d), (g), (j) and (m) phase fields in the same planes after 3, 4, 5 and 7 iterations of the loading-unloading cycle. The yellow circle in(d) denotes the position of the dislocation loop. Isosurface of the phase drawn for 1.8 rads < φ_{111} < 2.6 rads (magenta) 1.0 rads < φ_{111} < 1.8 rads (blue) in the pristine Au crystal (b), after 3 iterations (e), after four iterations (h), after 5 iterations (k) and after 7 iterations (n). Corresponding CXD patterns in the (qy,qz) plane for the pristine particle (c), after 3 iterations (f) after four iterations (l) and after 7 iterations (o)

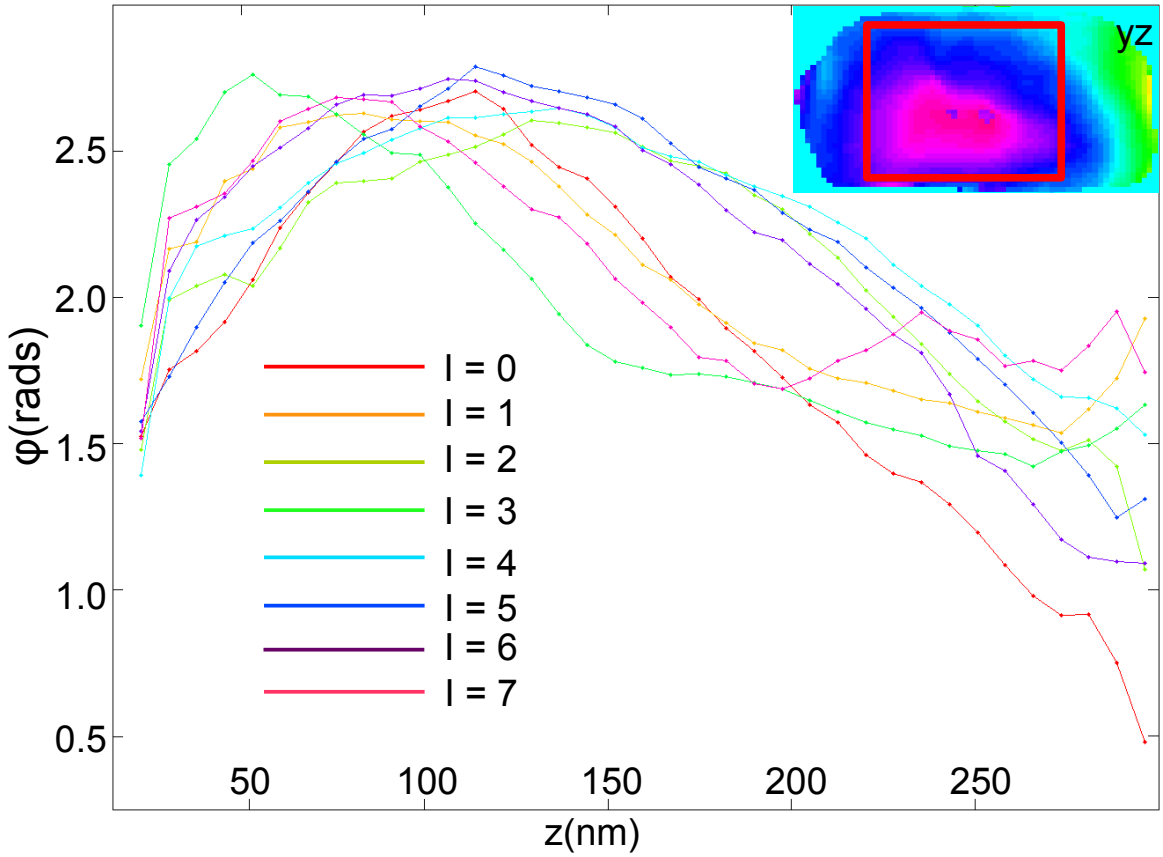

Fig. VI.15: *Phase profile along z (the [1 1 1] direction) at each iteration of the loading-unloading cycle.* The variations are averaged over the region in the red rectangle as shown on the top left figure.

spatial extent have decreased (0.8 versus 1.1 radians, and 50 nm vs 100 nm Fig. VI.14). The slope of this phase gradient is thus higher than in the pristine particle, implying an increased and more localized compressive strain at the substrate/particle interface. The inversion of the sign of the phase gradient now occurs at the approximate height of the dislocation loop, and a large and rapid decrease of the phase ($\Delta\varphi \sim 1$ rads) is observed over a spatial extent of 100 nm (between h =50 nm and h = 150 nm, Fig. VI.15). Above h = 150 nm, the phase is remarkably stable ($\Delta\varphi \sim 0.2$ rads). Although the displacement field around a dislocation loop has a limited extent, it strongly impacts the displacement field inside the particle. The phase variations are now concentrated in the vicinity of the dislocation loop, while almost constant above half-way of the particle height. Consequently, neglecting the very large phase variations located only at the vicinity of the dislocation loop, the amplitude of the phase variations that can be attributed to the interfacial strain have been divided by almost a factor 2 (1.2 radians vs 2.2 radians). In Fig VI.14.b and VI.14.e, isosurfaces of the phase are drawn for 1.8 rads < φ_{111} < 2.6 rads (magenta) and 1.0 rads < φ_{111} < 1.8 rads. As seen on Fig. VI.14.e, it is clear that the phase varies rapidly at the vicinity of the dislocation loop while it is almost constant for h >150 nm.

For I=4, the dislocation loop have left the crystal, and the phase is very homogeneous. A negative phase gradient is still present at the substrate particle interface, with similar value as in the pristine particle, but distributed over a slightly larger spatial extent (~150 nm vs 120 nm). Above h = 150 nm, the phase gradient is negative, but with an amplitude reduced by a factor 2 as compared with the pristine particle ($\Delta\varphi \sim 1$ rads, Fig. VI.14). As seen from Fig. VI.14.h, the region of the crystal where 1.8 rads < φ_{111} < 2.6 rads now extends over 4/5 of its height, while it was confined into a much smaller region in the pristine particle (Fig. VI.14.a). The homogeneity of the phase suggests that the elastic strain in the particle has been partially relaxed. This relaxation occurs through the emission of dislocation loops that accommodate the interfacial strain at the substrate/particle interface (Matthews & Blakeslee 1974).

For I=5, the strain has been already relaxed in the particle, such that the emission of dislocation loops does

not induce large variations in the phase field. The phase is still very homogeneous in the crystal. Although slightly reduced as compared to I=4, the regions of the crystal for which 1.8 rads < φ_{111} < 2.6 and 1.0 rads < φ_{111} < 2.6 are still significantly larger than in the pristine particle. However, both the positive phase gradient at the interface, and the negative phase gradient in the particle have increased in value. The relaxation of the strain in the particle was already achieved at the previous stage of the indentation, and the emission of supplementary loops that accumulate at the substrate particle interface might induce a slight increase of the strain in the particle.

As seen in sections VI.5.1 and VI.5.2, the shape of the particle is completely changed after 24 hours illumination under the X-ray beam. As a consequence, the strain distribution in the particle is changed and tends to increase. A positive phase gradient is still visible at the substrate/particle interface, which amplitude and spatial extent are similar to I=5 (Fig. VI.15). However, while the phase gradient is monotonic for h >150 nm in the previous (I=1-5) cases, $\Delta\varphi$ alternates between regions of positive and negative values after RT ageing. This implies the existence of regions of compressive and tensile strain on the top of the particle, which are completely absent for I=3 and I=4.

To provide a clearer picture of the evolution of the strain in the particle, the ε_{zz} strain component is derivated from the u_{111} displacement field through a very simple calculation:

$$\epsilon_{zz} = \frac{(\delta u_{111})}{\delta z} \qquad \text{(VII.1)}$$

For each stage of the indentation, the strain is represented in the (1 $\bar{1}$ 0) (y-z slice), (1 $\bar{1}$ 2) (x-z slice) and (1 1 1) (x-y slice) of the crystal. For the first two planes, the slice is taken close to the centre of the particle, while the slice in the (1 1 1) plane is close to the substrate/particle interface. The volumic strain distribution ε_{zz} is also represented (Fig. VI.15.b, VI.15.e …, VI.15.n). Only the regions undergoing either a large compression (ε_{zz} < -7.10^{-4}) or a large tension (ε_{zz} >7.10^{-4}) are shown, respectively with a blue and a yellow isosurface.

In summary, three different strain distribution states can be observed during the mechanical loadings, and an important evolution in both strain distribution and shape of the particle is evidenced after 24h ageing

Initial residual strain state:

The largest amount of strain is encountered in the initial state of the particle (Fig VI.16.a-c). The substrate/particle interface corresponds to a region of compression, which extends over a bit more than 50 nanometers. Close to the centre of the particle, a large region of tensile strain is clearly visible.

Presence of dislocations:

After 3 indentations events, the compressive strain at the substrate particle interface is only marginally affected, its spatial extent has slightly diminished as discussed in the previous paragraph (Fig. VI.16.d). This variation can be attributed to the presence of the dislocation loop in the crystal, which is quite close (~100 nm) to the substrate particle interface. As a consequence, this is the only scan for which the slice in the (1 1 1) plane close to the interface does not show a large region of compression (Fig. VI.16.d). Near the centre of the particle, the tensile strain has completely vanished and is now localized at the vicinity of the dislocation loop. Given the spatial extent of the strain field around the loop, we can infer that the modification of the shape of the Bragg peak (Fig VI.16.f) can be attributed to the strain field around the dislocation loop and not to the phase jump induced by the loop. The distortions observed in the [1 1 1] fringes below the Bragg peak are probably induced by this localized tensile strain, since the fringes above the Bragg peak appear relatively undisturbed.

Mechanical annealing: For I=4 and I=5, the compressive strain at the substrate/particle interface is still present, although slightly reduced in magnitude as compared to the initial state particle (Fig VI.15.g & VI.15.j). On the other hand, the region of tensile strain has almost completely vanished. This is in good agreement with our hypothesis of mechanical annealing, through the nucleation of dislocation loops.

24 h ageing:

Associated with the evolution of the shape/rotation of the particle,we observe a large modification of the strain distribution after the RT ageing. The region of compression strain is still present at the substrate/particle interface, and both its amplitude and spatial extent are comparable with the case of the

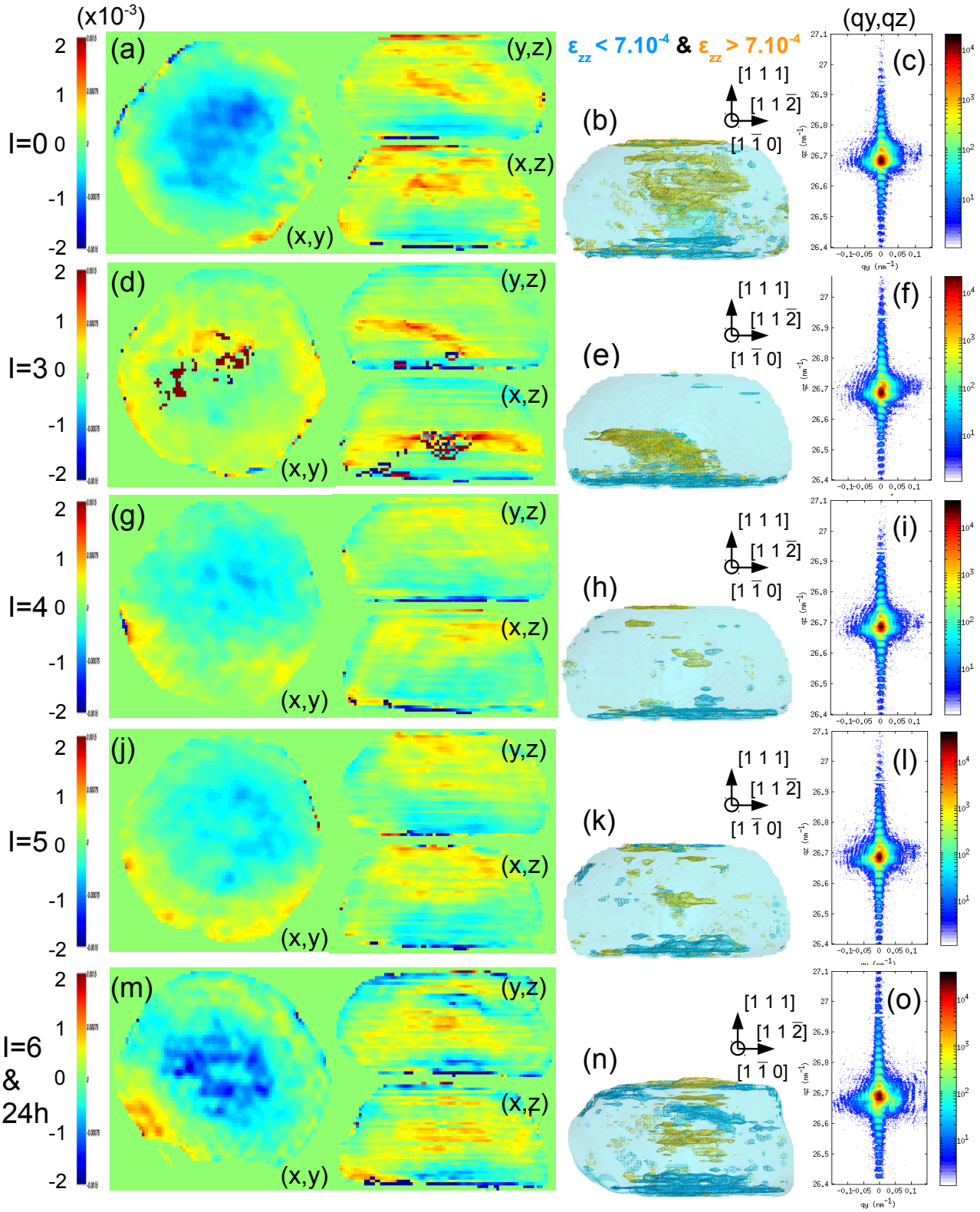

Fig. VI.16: *Reconstructed ε_{zz} strain field for increasing iterations of the loading-unloading cycle.* (a) Reconstructed ε_{zz} *strain field* in the (x,y), (x,z) and (y,z) planes corresponding respectively to the (1 1 1), (1 1 $\bar{2}$) and (1 $\bar{1}$ 0) planes. (d), (g), (j) and (m) strain field in the same planes after 3, 4, 5 and 7 iterations of the loading-unloading cycle. Isosurface of the strain drawn for $\varepsilon_{zz} < 7.10^{-4}$ (blue) and $\varepsilon_{zz} > 7.10^{-4}$ (orange) in the pristine Au crystal (b), after 3 iterations (e), after four iterations (h), after 5 iterations (k) and after 6 iterations (n). Corresponding CXD patterns in the (qy,qz) plane for the pristine particle (c), after 3 iterations (f) after 4 iterations (l) and after 6 iterations and 24 hours illumination (o)

initial state of the particle (Fig. VI.13.m and VI.13.n). Inside the particle, instead of a large region of tensile strain, alternate regions of large compressive and tensile strain are observed. The amount of elastic strain energy in the particle can be approximated by using an equivalent thin film geometry (in-plane periodic condition):

$$E_{el} = \frac{1}{2} M \sum_i \epsilon_i^2 \qquad \text{(VI.2)}$$

where M is the biaxial in plane elastic modulus. Applied to the crystallite this is a rough approximation since we only use one component of the strain tensor. On the other hand, the sum is carried out on all voxel of the reconstructed particle.

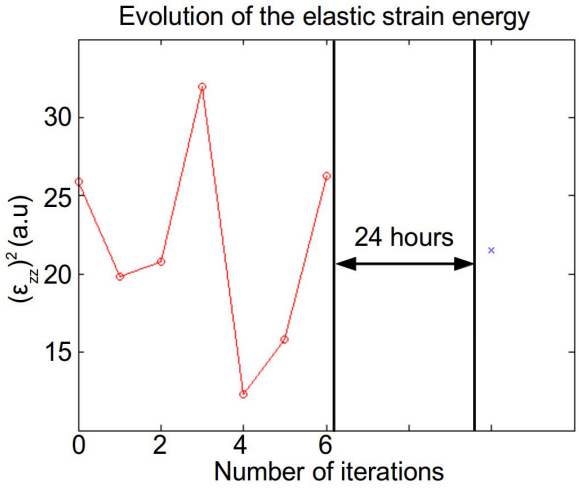

Fig. VI.17 *Evolution of the "elastic strain energy" stored in the particle versus the number of loadings of the particle*

The evolution of the curve is in good agreement with our previous observations. A relatively large amount of residual strain is present in the initial state which does not dramatically evolve in the first iterations of the indentation process (I = 0 → 2). The strain is maximal at I = 3 where a dislocation loop remain in the structure and reaches a minimum after 4 loading/unloading iterations consistent with our hypothesis of mechanical annealing. The emission of additional dislocation loops at the next loading iterations tends to increase the residual strain in the particle (in particular at I = 5). After 24 hours of ageing, the strain is partially relaxed, associated with an evolution of the particle shape and rotation. We are on the course to try to recover the full displacement field using Finite Element Method to solve the mixed boundary problem: namely, knowing the volumic shape (reconstructed electron density), the boundary conditions and one component (z) of the displacement field (reconstructed phase), the differential equation of mechanical equilibrium can be solved.

Conclusion

We applied the methodology detailed in Chapters III - V to study the evolution of the microstructure in a gold nanoparticle that was *in situ* nanoindented while illuminated by a coherent X-ray beam.
A selected gold particle with a low residual strain and defect content in its pristine state was carefully selected for the indentation experiment. Only a low degree of in-plane orientation was found for the particles used in this experiment, which suggests that the growth of the particles is not epitaxial. It is shown that the spread of in-plane orientation of the particles is highly dependent of the surface state of the substrate which in turn is driving the degree of in plane orientation of the gold thin film. A very clean CXD pattern is

observed for $\boldsymbol{g}$ = 1 1 1 for particles which are not well oriented, while a broadening of the Bragg peak is observed at the same Bragg reflection when the in-plane orientation is well defined. This broadening of the Bragg peak is attributed to the interfacial thermoelastic strain which is induced during the cooling to the room temperature. For the particles in hetero-epitaxy, the bonding with the substrate is stronger, and a larger part of the thermoelastic strain is transmitted to the particle. The particles used in this experiment exhibit a low amount of residual strain which is favorable for the identification of nucleated defects. This identification is achieved through the methods described in Chapters III-IV and V, *i.e.* the direct analysis of the reciprocal space and the reconstruction of the 3D displacement field. The direct analysis of the CXD pattern only reveals subtle changes in the microstructure of the crystal. After a few loading-unloading iterations, the CXD patterns appear more "perfect" and it is suggested that this evolution can be attributed to the relaxation of the strain in the particle. A change of the shape of the Bragg peak at a particular stage of the indentation could be an indication of the presence of defects in the structure. Finally, the modification of the shape of the particle under illumination of the X-ray beam is clearly seen through the change in the orientation of the facet fringes.

The reconstruction of the electron density and the φ_{111} phase field brings a finer analysis of the evolution of the microstructure. The shape of the particle does not evolve during the six iterations of the indentation, and is remarkably consistent with the SEM pictures. After 24 hours ageing, both shape and rotation of the crystallite is evidenced. The presence of a prismatic dislocation loop in the structure is well characterized. The remarkably good agreement of both the phase jump and displacement field around the defect with the simulated data leaves no doubt on this type of defect. The Burgers vector of the dislocation loop can be inferred from the determination of the planes of the stacking fault ribbons which are visible on the reconstructed electron density.

The analysis of both the $u_{1\,1\,1}$ displacement field and the ε_{zz} strain field confirms that the initial residual strain in the pristine particle is relaxed through the emission of prismatic loops. Their field accommodate the interfacial strain at the substrate-particle. After 4 loading-unloading events, no dislocations are present in the structure, the particle is almost strain free, as confirmed by the calculation of the elastic strain stored energy.

Although the experience was successful, there is a large room for improvement. As discussed earlier, a dislocation loop was identified at only one stage of the indentation. Most of the dislocation loops are immediately annihilated at crystal surfaces after their nucleation. A future experiment will aim at tackle this issue by recording the CXD patterns while the tip is in contact with the sample by scanning the energy of the incident X-ray beam (instead of a rocking curve after the tip retraction). The second improvement would be to achieve the reconstruction of the displacement field for off-specular reflection, which would allow a complete description of the microstructure as discussed earlier.

In summary we evidenced the nucleation of prismatic dislocation loops by in-situ mechanical loading. To the best of our knowledge, this is the first time evidencing a prismatic loop by CBDI. The relaxation of the strain in the particle, through mechanical annealing has also be clearly demonstrated.

Bibliography

Amram, D., & Rabkin, E. (2013) Acta Materiala **61**, 4113-4126

Ashby, M.F. (1971) Strengthening methods in crystals, Chapter 3, edited by Kelly A.and Nicholson R.B., John Wiley & sons, inc, New York

Beutier, G., Verdier, M., Parry, G., Gilles, B., Labat, S., Richard, M. I., Cornelius, T., Lory, P. -F., Vu Hoang, S., Livet, F., Thomas, O. & De Boissieu, M. (2013a). *Thin Solid Films* **530**, 120-124.

Beutier, G., Verdier, M., de Boissieu, M.; Gilles, B., Livet, F., Cornelius, T., Labat, S., Richard, M.-I. & Thomas,O.(2013b) *Jal of Physics : Conf. Ser., IOP,* **425**, 132003

Bialas, H., & Heneka, K. (1994) *Vacuum* **45**, 79-87

Chamard., V, Dolle, M., Baldinozzi, G., Livet, F., de Boissieu, M., Labat, S., Picca, F. , Mocuta, C. Donnadieu, P. and Metzger, T.H. (2010) *Journal of Modern Optics* **57**(9), 816–825

Chapman, H. N. *et al*. (2006) *J. Opt. Soc. Am.* **A 23**, 1179–1200 .

Clark, J. N., Ihli, J., Schenk, A., Kim, Y-Y., Kulak, A. N., Campbell, J. M., Nisbet, G., Meldrum, F. C. & Robinson, I. K (2015) *Nature materials* **14**

Diaz, A., Chamard, V., Mocuta, Stangl, J., Mandl, B., Vila-Comamala, J., Metzger, T.H. & Bauer, G. (2009) *Phys. Rev. B.* **79**, 125324.

Diaz, A., Chamard, V., Mocuta, C., Magalhaes- Paniago, R., Stangl, J., Carbone, G., Metzger, T.H., Bauer, G. (2010) *New J. Phys.* **12**, 035006.

Fienup, J. R. (1982). *Appl. Opt.* 21, 2758-2769

Francis, A.J & Salvador, P.A. (2007) *J Mater Res* **22**(89).

Grochola, G. S., Russo, P. & Snook, I. K. (2005). *J. Chem. Phys.* **123**, 204719.

Harder, R., Pfeifer, M. A., Williams, G. J., Vartaniants, I. A. & Robinson, I. K. (2007). *Phys. Rev. B* **76**, 115425

Kaishew, R., (1952), *Arbeitstagung Festkorper Physik*, Dresden, p. 81.

Kosinova, A., Kovalenko, O., Klingera, L. & Rabkin, E. (2015) *Acta Materialia* **83**, 91–101.

Labat. S., Richard, M-I., Dupraz, M., Gailhanou, M., Beutier, G., Verdier, M., Mastropietro, F., Cornelius, T. W., Schülli, T. U., Eymery, J. & Thomas, O. (2015) *ACS Nano*

Landau, L.D & Lifshitz, E. M. (1986) *Theory of Elasticity* (Pergamon 1986)

Langlais. S PHD Thesis (2015)

Malyi, O., Klinger, L., Srolovitz, D. J., Rabkin, E. (2011) *Acta Materialia* **59**, 2872–2881

Malyi, O. & Rabkin, E. (2012) *Acta Materiala* **60**, 261-268

Marchesini, S. (2003). *Phys. Rev. B* **68**, 140101

Mastropietro, F., Carbone, D., Diaz, A., Eymery, J., Sentenac, A., Metzger, T. H., Chamard, V. & Favre-Nicolin, V. (2011). *Optics Express* **19**, 20.

Matthews, J.W. & Blakeslee, A. E. (1974) *J. Crystal Growth* **27**, 118.

Meltzman, H., Mordehai, D., Kaplan, W.D (2012) *Acta Mater.* **60**, 4359-4365.

Minkevich, A.A., Gailhanou, M., Micha, J.S., Charlet, B., Chamard, V., Thomas, O. (2007) *Phys. Rev. B* **76**, 104106.

Mordehai, D., Lee, S. W., Backes, B., Srolovitz, D. J., Nix, W. D. & Rabkin, E. (2011). *Acta Mater.* **59**, 5202-5215.

Müller, P., Kern, R. (1998) *J. Cryst. Growth.* **193**, 257-270.

Newton, M. C., Leake, S., J., Harder, R. & Robinson, I., K. (2010). *Nature Materials* **9**, 120-124

Robinson, I. K. & Harder, R. (2009). *Nature Materials* **8**, 291-298.

Rupp. R Master internship (2015)

Sadan, H. & Kaplan, W. D. (2006). *J. Mater. Sci.* **41**, 5099-5107.

Sadan H. & Kaplan W. D. (2006b). *J. Mater. Sci* **41** 5371-5375.

Sayre, D. (1952) *Acta. Cryst.* 5, 843.

Schroer, C.G., Boye, P., Feldkamp, J.M., Patommel, J., Schropp, A., Schwab, A., Stephan, S., Burghammer, M., Schoder, S. & Riekel, C.(2008) *Phys. Rev. Lett.* **101**, 090801.

Takahashi, Y., Nishino, Y., Tsutsumi, R., Kubo, H., Furukawa, H., Mimura, H., Matsuyama, S.; Zettsu, N., Matsubara, E., Ishikawa, T., Yamauchi, K. (2009). *Phys. Rev. B* **80**, 054103.

Takahashi, Y., Suzuki, A., Furukatu, S., Yamauchi, K., Kohmura,Y. & Ishikawa, T. (2013). *Phys. Rev. B* **87**, 121201.

Rodenburg, J.M., Hurst, A.C., Cullis, A.G., Dobson, B.R., Pfeiffer, F., Bunk, O., David, C., Jefimovs, K. & Johnson, I. (2007) *Phys. Rev. Lett.* **98**, 034801.

Ulvestad, A., Clark, J. N., Harder, R., Robinson, I. K. & Shpyrko, O. G. (2015), *Nanoletters.* **15**

Watari, M., McKendry, R. A., Vögtli, M., Aeppli, G., Soh., Y- A., Shi, X., Xiong, G., Huang, X., Harder, R., and Robinson, I., K. .(2011), *Nature Materials* **10**, 862-866

Winterbottom, W. L. (1967). *Acta Metall.* **15**, 303.

Williams, G. J., Pfeifer, M. A., Vartanyants, I. A. & Robinson, I. K. (2003) *Phys. Rev. Lett.* **90**, 175501 .

Zhe, R., Mastropietro, F., Davydok, A., Langlais, S., Richard, M.-I., Furter, J.-J., Thomas, O., Dupraz, M., Verdier, M., Beutier, G., Boesecke, P. & Cornelius, T. W. (2014). *J. Synchrotron Rad.* **21**, 1128-1133.

Chapter VII: Investigation of the three-dimensional strain distribution in a sub-micron twinned gold island by coherent X-ray diffraction and molecular statics simulations

Contents

Abstract....198
Introduction....198
VII.1 Sample preparation....199
VII.2 CXD experiment....200
VII.2. Molecular statics simulations....204
VII.2.1 Size effects....204
VII.2.2 Influence of the boundary conditions....207
Conclusion....211
Bibliography....212

This Chapter is a draft of a paper that will be soon submitted, hence it features an abstract and the list of all the collaborators who were involved in this work.

Chapter VII: Investigation of the three-dimensional strain distribution in a sub-micron twinned gold island by coherent X-ray diffraction and molecular statics simulations

Maxime Dupraz[1,*], Guillaume Beutier[1], Simon Langlais[1], Aaron Parsons[3], Guillaume Parry[1], David Rodney[1,2], Marc Verdier[1]

[1] *SIMaP, Univ. Grenoble Alpes & CNRS, F-38000 Grenoble, France*

[2] *Institut Lumière Matière, Université Lyon 1, CNRS, UMR 5306, F-69622 Villeurbanne, France*

[3] *Diamond Light Source, Harwell Science and Innovation Campus, Didcot OX11 0DE, UK*

Abstract

The strain field of a twinned sub-micrometric gold crystal is studied with coherent x-ray diffraction and molecular dynamics calculations.
Coherent X-ray diffraction imaging is used to visualize the 3D strain distribution within the particle. The strain distribution suggest and reveals an inhomogeneous relaxation of the surface atoms.
To gain insight and understand the 3D strain distribution, crystals of a few tens of nanometers with various boundary conditions (Wulff single crystal, free-standing particle, particle constrained by a substrate...) are modeled with interatomic potentials. The calculation of their diffraction patterns and the reconstruction 3D displacement fields allows quantitative comparisons with the experimental data.
The strain distribution within the crystallite is driven by the relaxation of free surfaces to reach the equilibrium crystal shape and the interfacial strain imposed to the crystal by the thermal mismatch occuring during the preparation of the sample. This study confirms the absence of strain at the twin boundary.

Introduction

Current technological efforts in material processing have focused on nanomaterials such as nanoparticle catalysts (Lu *et al.* 2001, Waszczuck *et al.* 2002). The case of gold nanoparticles is of particular interest because of their diverse applications (Lou *et al.* 2001).
The performance of these materials is affected by the detailed structure of their shape and by the exact configuration of their surface. Surface reconstruction or surface induced strain may also affect their behaviour. Of particular interest is the structure of equilibrium crystal shape (ECS). The surface structure of an equilibrium shape is driven by the orientation dependence of the surface free energy of a crystal (Winterbottom 1967). Surface atoms have fewer interatomic bonds than their bulk counterparts and they often relax and reconstruct on extended two-dimensional surfaces. Generally the study of the displacement of the topmost atomic layers is sufficient to describe the surface contraction. The situation is complicated in the case of nanocrystals where the relaxation of the free-surfaces exhibit some coordination dependence (Huang *et al.* 2008). For instance, the contraction is stronger for edge and corner atoms which are less coordinated, and the atom relaxation must be accommodated in accordance with constraints imposed by neighbouring atoms. Understanding the relaxation of surface atoms is of great importance due to the large impact they have on surface energies and interfacial stability (Ibach 1997), and as a consequence on the resulting equilibrium crystal shape (ECS). The relaxation of free-surfaces is also likely to affect mechanical and electronic properties of nanocrystals (Gilbert *et al.* 2007, Alivisatos 1996).
On top of the surface relaxation and strain, the presence of defects and crystallographic imperfections can further alter the material properties. In particular, twin domains are of great importance in many technological challenges in particular in the understanding of plastic deformation mechanisms.
A variety of techniques are available to characterize the structure of sub-micron sized objects. Transmission electron microscopy (TEM) can achieve sub-nanometer resolution but is hindered by the low-penetration depth of electrons to thin samples, or samples which can be cut or milled to a thickness of few tens of nanometers without affecting and the shape of the structure to be studied.
Alternatively scanning electron microscopy (SEM) can be used to study the equilibrium shape of crystal as it produces a single view of the sample surface. However, the technique is limited in resolution and insensitive

to the strain or degree of crystallinity.
As demonstrated recently by Scott *et al.* (2012) and Chen *et al.* (2013), Electron tomography can be used to visualize 3D structure of a gold nanoparticle and to identify twinned regions with an atomic resolution. Although very impressive, the technique is not applicable for particles larger than 10 nanometers.
Coherent-X-ray Diffraction (CXD) taking advantage of the larger depth of X-rays can be used to image the full three-dimensional displacement field in sub-micron objects with a resolution of the order of 10 nm without requiring any complex sample preparation. The technique being able to probe deviations from the perfect lattice is not only sensitive to the defect structure, but also to all the other sources of strain in the particle: the mismatch strain at the interface for particles in epitaxy, the thermoelastic strain induced by thermal treatment and the surface strain produced by the relaxation of free surfaces.
In this chapter, the technique is used to study the 3D strain-field distribution in a twinned gold sub-micron particle which depends on all these contributions.
The preparation process of the gold crystallite and the detailed experimental CXD results are given in the first two sections. In a last part, molecular dynamics simulations are used to gain insight and understand the 3D strain distribution inside the particle. Both size effects and influence of the boundary conditions are discussed in this last section.

VII.1 Sample preparation

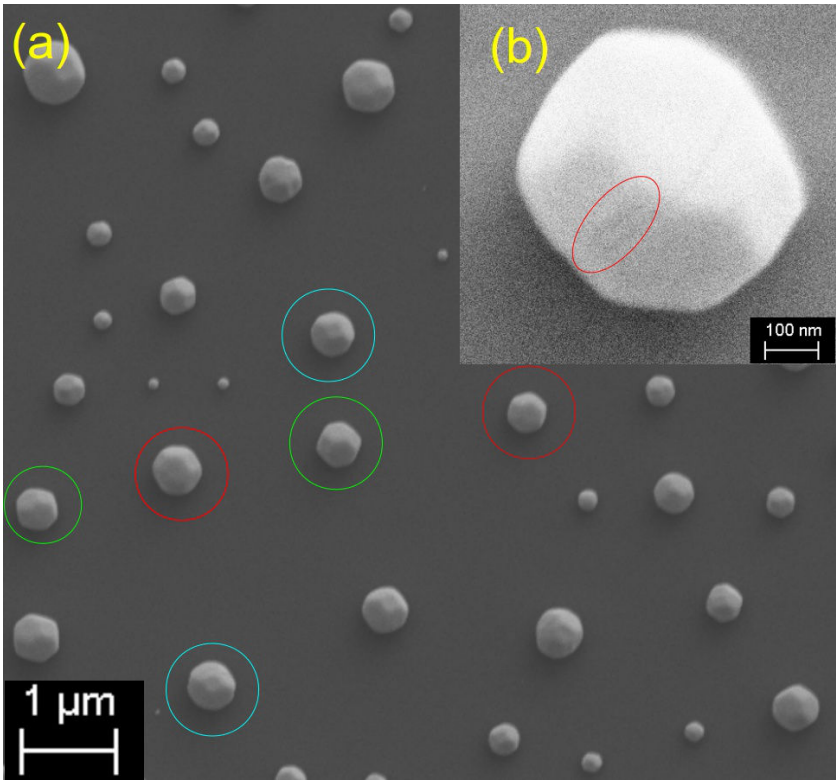

Fig. VII.1 *SEM picture of Au particles dewetted at 1100°C on a (0001) sapphire substrate.* (a) Spatial distribution of the particles. The coloured circle around the particles indicates their out-of-plane orientation with respect to the sapphire substrate. Red: Au(1 1 1)//Al_2O_3 (0 0 0 1), blue: Au(0 0 1)//Al_2O_3 (0 0 0 1), green: Au(1 1 0)//Al_2O_3 (0 0 0 1)(b) Au nanoparticle with a microtwin.

Gold nanocrystals were prepared by dewetting a thin film on a sapphire substrate, as described in details by Sadan & Kaplan (2006). A 20 nm thick film of Au is deposited on a 'epi-ready' c-plane oriented

sapphire substrate ((0 0 0 1) single crystal α-Al_2O_3). The dewetting of the thin film is carried-out by heating during 10 hours at 1100°C in air, above the gold melting point (liquid state dewetting). This temperature is reached with a fast heating rate of 50°C/min. This process results in the formation of highly faceted particles with diameter varying form 200 to 800 nm separated by a typical distance of 2 µm (Fig. VII.1). Their well known Winterbottom equilibrium shape (Winterbottom 1967) consists of {1 0 0} and {1 1 1} facets separated by rough curved surfaces (Wang & Wynblatt 1998, Heyraud & Métois 1982 Sadan & Kaplan 2006, see Chapter II for more details).

SEM observations show highly faceted particles containing fewer rough interfaces than their counterpart dewetted under UHV environment. As already reported by Sadan & Kaplan (2006), this can be explained by the preferential the segregation of impurities on the Au surface, decreasing the surface energy of the facets planes. A large proportions of particle with a grain boundary generally in the form of a twinned boundary can be observed (Fig. VII.2.a. presence of a twin boundary). For the single crystal particles, three distinct orientations with the substrate are observed: Au (1 0 0)//Al_2O_3 (0 0 0 1) (circled in blue in Fig. VII.1), Au(1 1 0)//Al_2O_3 (0 0 0 1) (circled in green in Fig. VII.1) and Au (1 1 1)//Al_2O_3 (0 0 0 1) (circled in red in Fig. VII.1), the latter being predominant. As compared to their counterparts dewetted in the solid-state, there is no indication of in-plane ordering. As pointed out by Sadan and Kaplan, most of the (1 1 1) and (1 0 0) planes parallel to the substrate surface show an inclination of the particle with respect to the surface which has been explained by the presence of an array of interfacial dislocations to reduce the strain.

VII.2 CXD experiment

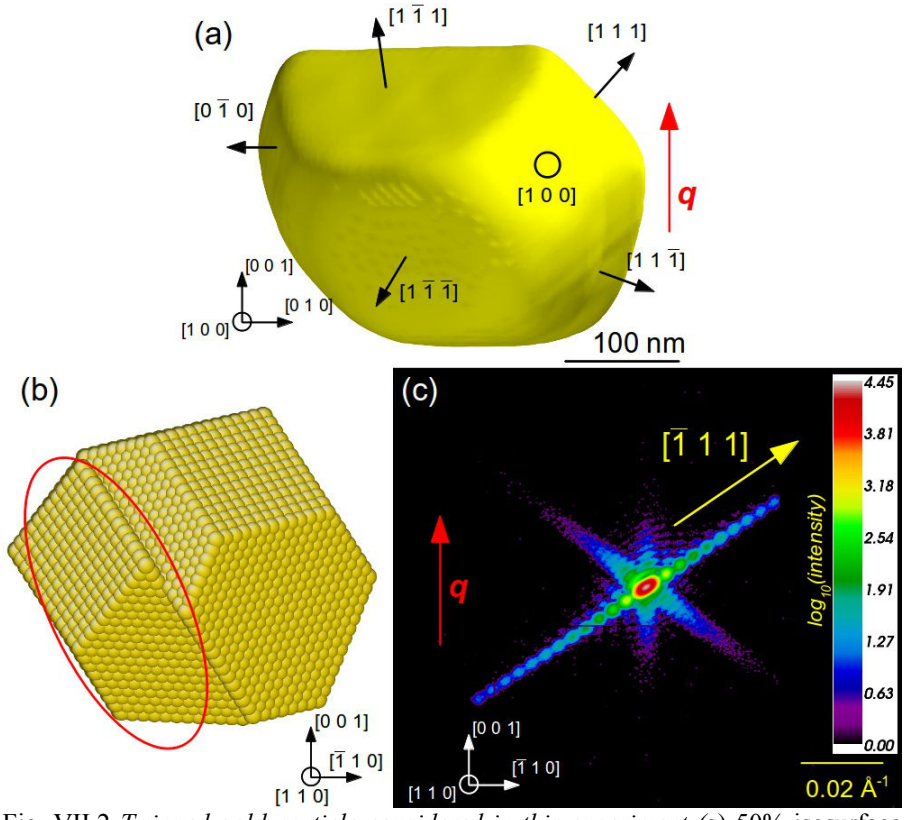

Fig. VII.2 *Twinned gold particle considered in this experiment (*a) 50% isosurface of the reconstructed electron density. (b) Modelled twin nanoparticle. The region circled in red corresponds to the grain that was measured experimentally (c) (1 1 0) cut of the coherent X-ray diffraction pattern used for the reconstruction .The direction of the scattering vector is indicated with a red arrow

The measurement of the gold islands was carried out at the I13-1 beamline of the Diamond light source. Coherent X-Rays of 9.7 keV were focused onto the sample using Kirkpatrick-Baez mirrors. The beam size on the sample was approximately 8 x 6 μm^2 on the sample.

Despite the large beam size and low separation between islands, it was possible to isolate a crystal with a (0 0 1) out-of plane orientation whose occurrence is less frequent than the (1 1 1). The 0 0 2 Bragg reflection of an individual gold island was measured in specular geometry, corresponding to a Bragg angle θ of 18.2° at 9.7 keV. The diffracted intensity was recorded with a 516x516 pixel detector MAXIPIX (pixel size of 55 μm), mounted 0.945 meters downstream from the sample. This set-up gives a resolution of 2 x 10^{-4} $Å^{-1}$ in reciprocal space. Three-dimensional maps of the Bragg reflection were collected by rocking the sample over 1° (Δq = 1 nm^{-1}) with steps of 0.005° and a 2 s exposure time per point. This procedure was repeated twice, and the 3D CXD patterns were summed together to increase the dynamical range.

Fig VII.2.d shows a cut perpendicular the (1 1 0) axis of the CXD pattern. The direction of the scattering vector $\boldsymbol{q}$ is indicated by a red arrow. The intensity is maximal at the 0 0 2 Bragg position and forms streaks along the {1 1 1} and {1 0 0} directions due to the crystal facets. These streaks are fringed because of the finite size of the crystal. The increased intensity and the doubling of the period of the fringes along the [$\bar{1}$ 1 1] direction (yellow arrow in Fig. VIII.2.c), indicates a shorter distance between the two ($\bar{1}$ 1 1) facets (as compared to the other <1 1 1> and <1 0 0> directions). This can be the signature of either a truncated single crystal particle, or a twinned particle where only one of the two grains is diffracting with the 0 0 2 Bragg conditions. The latter explanation is more consistent with the SEM observations (Fig. VII.1).

Another interesting feature of the CXD pattern is the asymmetry of the intensity around the Bragg position. In particular, along the [0 0 1] direction where the intensity of the fringes at high scattering angle (above the Bragg position) is stronger than their intensity at low scattering angle (below the Bragg position). A diffraction pattern measured from a strain free and defect free crystal would appear perfectly centrosymmetric, and a loss of the local symmetry is an indication of strain within the nanocrystal (Robinson *et al.* 2001). Huang *et al.* (2008) demonstrated that such redistribution of intensity from low to high scattering angle was the signature of surface contraction, the direction of the asymmetry being along the facet undergoing the maximum contraction (*i.e.* the (0 0 1) facet)).

The direct analysis of the diffraction data allows to obtain valuable information on the strain and defect content, however the reconstruction of the full 3D displacement field provide a more complete picture. In the past few years, Coherent X-ray Diffraction has been routinely used as an imaging technique. Provided that the crystal is isolated, and the diffraction data is oversampled by twice the Nyquist frequency (Sayre 1952) (*i.e.* at least 2 pixels per fringe on the diffraction data) the complex sample density $\tilde{\rho}(\boldsymbol{r})$ may be reconstructed from the diffraction data using phase retrieval algorithms (see Chapter I for more details). CXD is highly sensitive to internal strains within a crystal, which appears as phase changes on the complex sample density. The amplitude and the phase of the latter can be expressed as the electron density of the sample and as the projection of the displacement from the ideal crystal lattice, $\boldsymbol{u}(\boldsymbol{r})$, onto the reciprocal lattice $\boldsymbol{g}$ vector the Bragg peak chosen: $\varphi(\mathbf{r}) = -\boldsymbol{g}.\boldsymbol{u}(\boldsymbol{r})$.

Recently it has been shown that several non-coplanar vectors can be combined to extract the full displacement field $\boldsymbol{u}(\boldsymbol{r})$ (Newton *et al.* 2010, Labat *et al.* 2015). In this work we used only the 0 0 2 Bragg reflection to highlight the displacements along the [0 0 1] direction.

A coordinate change was performed on the diffraction in order to depict the 3D-reciprocal space maps in the laboratory reference (subsection II.1.6). The 512x370x512 matrix was cropped to a size of 398x370x398 and binned by a factor 2 in the three dimensions, to obtain a 199x185x199 3D matrix which was used for the reconstruction .

Three algorithms were used for the reconstruction: Error Reduction (ER) (Gerchberg & Saxon 1972), Hybrid Input Output (HIO) (Fienup 1982) and Shrink-Wrap (SW) (Marchesini 2003) (details on these algorithms are given in Chapter I of this manuscript). A strong air scattering was observed on the collected CXD patterns, since no flight-tube was placed between the sample and the detector. In order to remove this air scattering and greatly reduce the noise on the reconstructions, the diffraction data was thresholded by setting all the pixels with 4 or less photons to zero. The 'hot pixels' of the detector (high value on the pixel where no photon is present) were also set to zero (subsection II.1.2).

In the phase retrieval procedure, both reciprocal space and real space are updated at each step of the

algorithm and constraints are applied on both sides. Inputs of the algorithms are the measured intensity data and a finite size 3D support in which all the complex sample density $\tilde{\rho}(\boldsymbol{r})$ is constrained. In our case this initial support is the autocorrelation function of the object (Marchesini 2003, subsection I.4.3.5).
The procedure consists of an alterning of 50 ER and 100 HIO repeated 100 times, with an update of the support using SW at the end of every series of (100 HIO +50 ER). This method is used over 200 random starts, and the best solutions are selected according to their metric error, which quantifies the matching between the retrieved intensity and measured intensity (subsection I.4.3.4). This provide a population of solutions with equivalent metric errors. To discriminate between these solutions, the standard deviation of the electron density is used (Labat *et al.* 2015). The final image is averaged over the 20 solutions with the lowest metric error and the most homogeneous electron density.
To avoid any linear phase ramp in $\tilde{\rho}(\boldsymbol{r})$ induced by the bad centering of the diffraction data, its Fourier transform, $F(\boldsymbol{q})$ is re-centred (to the nearest pixel) using the centre of mass of $|A(\boldsymbol{q})|^4$ as suggested by Clark (Clark et al. 2015). Sub-pixel shifting is done by multiplying $\tilde{\rho}(\boldsymbol{r})$ by the appropriate phase ramp calculated from the centre of mass.
Fig. VII.2.a shows the reconstructed electron density of the crystal as a yellow isosurface drawn at 50% of the maximum density. The twinned region is rotated out of the 0 0 2 Bragg condition and is thus missing. As estimated from the shape of the particle close to the ECS, approximately 40% of the particle is reconstructed. In good agreement with the SEM observations, the reconstructed particle is highly faceted, with reduced rough curved area in between the {1 0 0} and {1 1 1} facets. The atomic model in Fig. VII.2.b illustrates the estimated relative proportion of the two grains. As stated earlier, the equilibrium shape of the particle is known as the Wulff equilibrium shape (Winterbottom et al. 1967, Chapter II) which is achieved by the minimization of the surface energy by an optimization of the surface area of different crystallographic plane. In the case of a partial wetting of the underlying substrate, the equilibrium shape is a truncated Wulff shape known as the Winterbottom shape (Winterbottom et al. 1967) : the (0 0 1) facet on which the particle sits is more extended than the two others {1 0 0} facets (subsection II.3.1.2). The latter are very small compared to the surrounding {1 1 1} facets, suggesting the crystal has not completely reached the ECS.
Fig. VII.3 shows the reconstructed displacement field within the gold particle. The maximum phase variation in the nanocrystal is 1.2 radians. In the particular case of $\varphi_{002} = -g_{002}.u_{002}$, a phase variation of 2π corresponds to half the lattice spacing between two consecutive (0 0 1) planes, *i.e.* 2.04 Å. Here the displacements involved are thus very small and of the order of 0.4 Å in the [0 0 2] direction.
Given the size of the crystal and the relatively weak strain, the data has been corrected for refraction (Harder *et al.* 2007). The shape of the crystal being almost spherical (with the twinned part), the phase shift from x-rays scattering at its center (when the refraction, is expected to be maximal) is given by $\Phi_0 = kd\delta$, where the diameter of the particle d = 350 nm, the wave vector k = 49.1 nm^{-1} and the refraction index $\delta = 3.19 \times 10^{-5}$. Close to its centre, a spherical particle of such diameter has a phase shift of: $\Phi_0 = 0.55$ rads (corresponding to a $u_{002} \sim 0.18$ Å).
This phase shift due to refraction can be calculated in each point of the crystallite $\boldsymbol{r}$ according to the equation given by (Harder *et al.,* 2007):

$$\Phi = \frac{\Phi_0}{2} \sum_{j=i,f} \left(\hat{\boldsymbol{k}}_j . \rho - \sqrt{1 - |\hat{\boldsymbol{k}}_j . \rho|^2 - |\rho|^2} \right) \qquad \text{(VII.1)}$$

where $\hat{\boldsymbol{k}}_j$ are units vector pointing toward the centre of the sphere in the direction of the incident and diffracted wave vectors, $\rho = \frac{\boldsymbol{r}}{r_0}$ is a fraction of the crystal radius r_0 = d/2 including the non-diffractive grain.
In order to apply the refraction correction, the shape of the particle has to be known precisely. In particular, it is clear from Eq. (VII.1) that the calculated phase shift at each point of the crystallite depends on the definition of the centre of the particle. In our case, less than a half of the particle is reconstructed, but the centre of the particle can be estimated quite precisely from the 3D reconstruction. The spherical approximation is also reasonable since the particles are perfectly spherical in the liquid phase (slightly

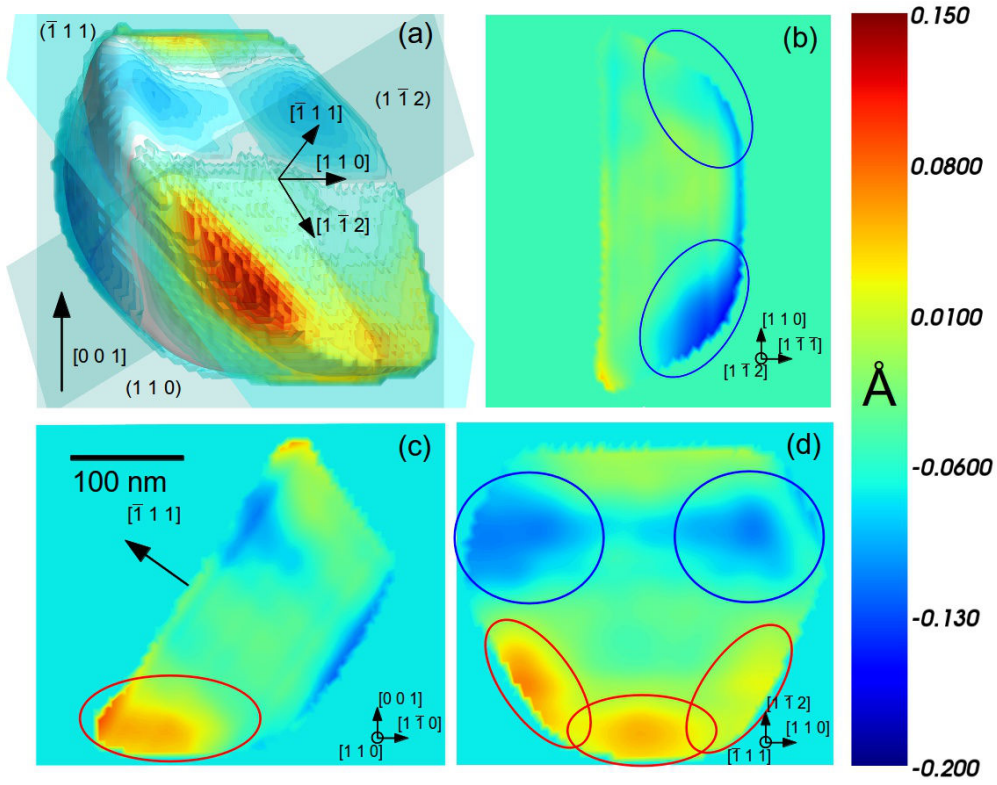

Fig. VII.3 *Reconstructed electron density and $u_{0\ 0\ 2}$ displacement for the twinned gold particle.* (a) Isosurfaces of the $u_{0\ 0\ 2}$ component of the displacement field. Central cross sections of the displacement field along the [1 $\bar{1}$ 2] (b) [1 1 0] (c) and [$\bar{1}$ 1 1] d directions.

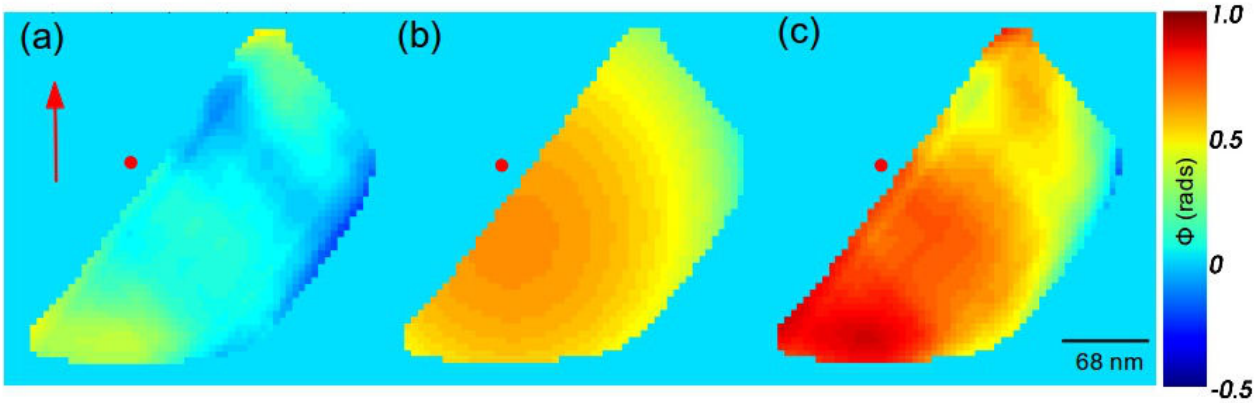

Fig. VII.4 *Effect of the correction for refraction.* Cross section of the phase map perpendicular to the beam direction: phase map before correction for refraction (a). Refraction phase only (b) and phase map after correction for refraction (c). The direction of the scattering vector is indicated by a red arrow. And the approximated centre of the particle

truncated because of the partial wetting of gold) before faceting upon solidification.

Fig. VII.4 shows a phase map before (left) and after (right) the refraction correction. The section of the crystal displayed is perpendicular to the beam direction. As illustrated in Fig. VII.4.b, the maximum phase shift is encountered for a point slightly below the particle centre with a value of 0.58 radians while the phase shift is equal to zero only for the points on the top (0 0 1) facet lying in the direction of the ***q*** vector. The top (0 0 1) facet does not exist in the reconstructed grain, and the minimum phase shift here is thus equal to 0.12 radians. The maximal phase difference induced by refraction is thus estimated to be of the order of 0.45

radians (corresponding to a displacement of 0.15 Å, it contributes significantly to the reconstructed displacement field and is thus taken into account in the reconstructions.
After correction for refraction, the average phase inside the crystallite is calculated and set to zero, meaning that the reference for the displacements shown in Fig VII.3 is the average displacement along the [0 0 1] direction. Note that this procedure is not performed in Fig. VII.4.c, explaining the high positive values for the data corrected for refraction.
It has been shown by Watari *et al.* (2011) that the facet and the curved areas of sub-micron gold particles undergo a differential contraction. The same observations was made by Huang *et al.* (2008) on smaller particles (~ 5 nm). In particular, he evidenced the differential contraction of the {1 1 1} and {1 0 0} surface planes, the latter being more pronounced. As a general tendency, upon relaxation surface atoms tend to contract towards the bulk. The driving force for this contraction is attributed to the smoothing of the electron surface density resulting in an electrostatic force which pulls surface ions towards the bulk (Smoluchowski 1941 and Howe 1997). This contraction being dependent on their coordination number, it is maximal for rough surface (Howe 1997), such as the edge and corner. Interplanar spacings of at least the first three atomic planes have been experimentally measured for several low-index surfaces of unreconstructed thin film of gold, see MacLaren, et al. (1991): in brief, they report outward displacement for {1 1 1 } top layer, no net displacement for {0 0 1} and larger inward but oscillating for the rough {0 1 1} surface.
The reconstruction of the displacement field projected onto the 0 0 2 Bragg reflection reveals that such behaviour is also visible on larger crystals. Most of the {1 1 1} facets tend to be in expansion while the {1 0 0} facets are in contraction. The maximum contraction is observed for the lateral {1 0 0} facets (the (0 $\bar{1}$ 0) and (1 0 0), (circled blue areas in Fig. VII.3.b), while the net positive displacement on the (0 0 1) facet (Fig. VII.3.c) suggests that it might be constrained by the underlying substrate. Most of the {1 1 1} facets are in expansion (Fig VII.3.a,c,d), this expansion being maximal on the edge of the lateral {1 1 1} facets in contact with the twin boundary (Fig VII.3.a & VII.3.d, red circled areas). Interestingly, the (1 $\bar{1}$ $\bar{1}$) surface plane, parallel to the twin-boundary undergoes contraction, also possibly due to the fact that the particle is constrained by the substrate.
The displacement profile on the twin boundary (($\bar{1}$ 1 1) facet) is more complex, with alternating areas of contraction (mostly on the top most part) and expansion (mostly at the substrate/particle interface (Fig. VII.3.d). Cut along ($\bar{1}$ 1 1) (Fig. VII.3.d) and (1 $\bar{1}$ 2) planes (Fig. VII.3.d) reveals that the displacement is symmetrical with respect to the [1 $\bar{1}$ 2] and [$\bar{1}$ 1 1] axis.

VII.2. Molecular statics simulations

VII.2.1 Size effects

To understand the strain distribution within the crystallite, we simulated the twinned crystal using Molecular Statics (MS) with Embedded Atom Method (EAM) potentials (Grochola *et al.* 2005), that reproduce accurately surface energies and elastic properties. The geometry employed here also consists in the Wulff geometry which minimizes the surface energy. The determination of the surface area of each crystallographic plane corresponding to the Wulff equilibrium shape is calculated by using 2 ratio of surface energies $\gamma_{111}/\gamma_{100}$ and $\gamma_{110}/\gamma_{100}$ calculated from relaxed surfaces. This method yields a crystallite with {1 0 0} and {1 1 1} facets separated by sharp edges.
The surface area of the crystallographic planes is then adjusted to fit the shape of the experimental particle. To match the experimental shape, surface area of all {1 1 1} surfaces are increased implying a reduction of the surface area of the (0 $\bar{1}$ 0) and (1 0 0) facets. This is a good evidence that the particle measured experimentally has not reached its full equilibrium shape, probably due to the fact that no equilibration was performed below the melting temperature. The (0 0 1) facet, parallel to the substrate is also enlarged due to the partial wetting of the gold particle (subsection II.3.1.1).
The simulated and experimental gold particles feature two main differences. The first one being that the rough curved areas between the {1 0 0} and {1 1 1} facets have not been taken into account. As observed from the reconstruction of the electron density (Fig. VII.2.b) and confirmed by the SEM pictures (Fig. VII.1

and VII.2.a), their extent is rather limited compared to the flat facets. Nevertheless, their contribution to the surface strain has been clearly demonstrated (Watari *et al.* 2001), and should induce some discrepancies in the strain distribution. It has been also evidenced by Huang et *al.* (2008) that the contraction of surface atoms is coordination dependent, implying a strong contraction of the edge and corner atoms compared to atoms located at the centre of a facet. Due to the absence of sharp edges, these effects are rather limited on the experimental particle.

More evident is the difference of scales between experimental and simulated crystals. The dimensions of the reconstructed grain are approximately 360x270x270 nm^3. This represents approximately 1.4 billions atoms, a number unreachable with our current computational power.

To capture the size effect on the strain distribution, several free-standing gold nanoparticles are modeled with radius varying from 25 nm to 170 nm (respectively 15 times and twice smaller than experimental particle). The nanocrystals are equilibrated at 0 K by energy minimization until they reach their equilibrium. The relaxation is performed on the full particle in its Wulff equilibrium shape. At the end of the relaxation, the particle is cut along its ($\bar{1}$ 1 1) twin plane.

In the following, the diffraction patterns are calculated in the kinematic approximation (justified by the small size of the crystals) using the software PyNX (Favre-Nicollin 2010, subsection I.3.3). The simulated diffraction patterns are inverted with the similar procedure as described in subsection I.4.5, providing a macroscopic view of the strain in the simulated particle. The excellent agreement between the reconstructed and calculated displacement fields from the atomic positions have been demonstrated in Chapter V of this manuscript. Here we chose to use the reconstructed displacement fields rather than the calculated one. This choice is primarily justified by the fact that the software OVITO (Stukowski 2010) used the visualization of the atomic configuration and the calculation of the atomic displacements has difficulties to handle very large crystal sizes (> 100 nm). Additionally, using this enables a visualization of the displacement field consistent with the experimental data.

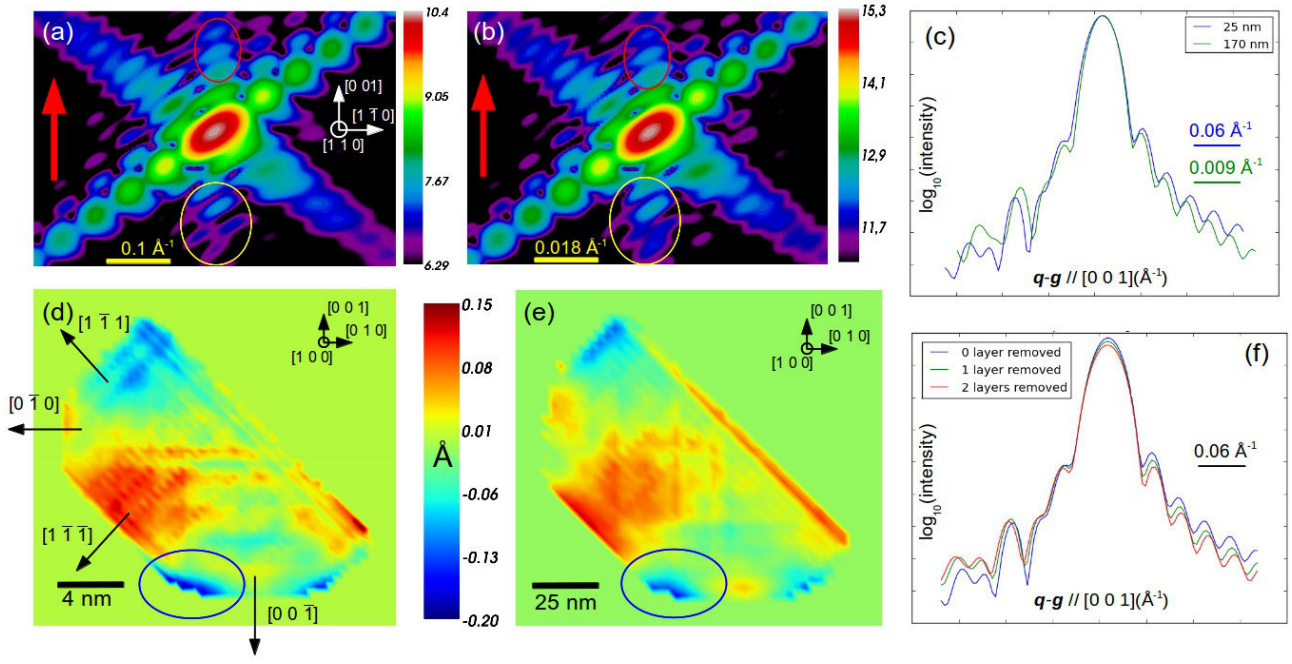

Fig. VII.5 *Influence of the size of the particle on the calculated CXD patterns and the reconstructed $u_{0\,0\,2}$ displacement fields.* Calculated CXD patterns for a 25nm (a) and 170nm (b) gold nanoparticle. Intensity profile along the [0 0 1] direction for both particle. Projected displacement field for the 25nm (d) and 170 nm (e) particles. (f) Intensity profile along [0 0 1] for a varying number of surface layers removed

Fig VII.5.a and VII.5.b show the calculated diffraction patterns for the 25 nm and 170 nm particles. The reciprocal space area shown is inversely proportional to their size. They look very similar, suggesting a

similar distribution of the strain within the nanocrystal. The main difference lies in the asymmetry of the Bragg peak. The redistribution of intensity from low to high scattering angle is clearly visible on both CXD patterns (Fig VII.5.a-c), but it is more pronounced on the smaller particle (Fig VII.5.c). It is directed along the [0 0 1] perpendicular to the facet undergoing the maximum contraction.

The measurement of the lattice spacing between the first few surface planes (25 nm particle) for the {1 1 1} and {1 0 0} orientations reveals respective lattice contraction of 3.8% and 5.9%. Also interesting is the oscillatory behaviour of this relaxation. The contraction of the first surface plane is indeed followed by an expansion of the underlying plane and then a damped contraction of the third plane (this pattern slightly differs depending on the orientation). This surface distortion can be described in the form of Rayleigh wave that die off exponentially (1/e) into the bulk with a decay length of $L/2\pi$ where L the period of the wave along the surface is twice the width of the facet (Landau & Lifshitz 1986, Harder *et al.* 2007). The smaller is the crystal, the faster is the decay. It is also quite obvious that the smaller is the crystal, the larger is the contribution of the surface atoms as compared to their bulk counterpart. The average lattice parameter, measured from the position of the Bragg peak, for the 25 nm and 170 nm particles are respectively 4.67 nm (0.31% contraction compared to the bulk value) and 4.73 nm (0.17% contraction).

Fig. VII.5.f shows the contribution of the first few surface layers to the CXD pattern, by removing the first surface layers of the 25 nm particle. The overall shape of the Bragg peak does not dramatically change, but the distribution of intensity becomes more symmetric. A similar effect can be observed on the 170 nm particle, but less pronounced. It is thus clear that larger is the crystal, the smaller is the contribution of the first few surface layers and the smaller is the asymmetry of the Bragg peak. Apart from the signature of the contraction of the surface atoms, both the diffraction patterns and reconstructed 3D maps of the displacement field are remarkably similar (Fig VII.5.c & VII.5.d) .

The surface strain decay depends on the facet size and a crystal of different size but with a similar size ratio between its facet, *i.e.*, the same equilibrium shape, will present an equivalent phase distribution. It is thus clear that for a free standing particle, the 3D displacement field only depends on the equilibrium crystal shape (ECS), *i.e*, the distribution of the surface area between its {1 1 1} and {1 0 0} facet. Obviously, the smaller is the particle, the larger is the strain, since the same amount of displacement is distributed in a much smaller volume.

The particle is modeled with the lattice parameter of the bulk gold (a = 4.08 Å), and upon relaxation it undergoes an overall coordination dependent contraction of the surface atoms. If the reconstructed displacement map was computed relatively to the bulk lattice parameter, we would *only observe negative net displacements corresponding to different levels of contraction*. It is thus important to understand that the positive net displacements on the displacement maps (Fig VII.5.c & VII.5.d) are relative to the average lattice constant in the particle. The areas which appear in expansion (positive net displacement) *are also in contraction for a reference crystal with the lattice constant of bulk gold.*

A cut along the {1 0 0} direction reveals that the maximum contraction (~ 0.2 Å) is observed for the corner and edge atoms located on the (0 0 1) facet (blue circled area in Fig. VII.5.d & VII.5.e). All three {1 0 0} facets are in contraction (with a higher contraction of the surface atoms), while all the {1 1 1} facets, except the top $(1\ \bar{1}\ 1)$ are in tension. The bottom of the $(\bar{1}\ 1\ 1)$ large facet, which is not a free surface, is in tension, while its top undergoes contraction.

It is clear from both the diffraction pattern and the reconstruction of the displacement field that the agreement between the experimental data is far from perfect. In particular, the $(1\ \bar{1}\ \bar{1})$ facet which induces contraction in the experiment displays expansion in the simulated particle. Conversely, the $(1\ \bar{1}\ 1)$ facet produces tension experimentally while contraction in the simulation. The relaxation of the free surfaces alone can not explain the profile of displacement field in the experimental particle.

This suggests the presence of another source of strain resulting from processing: the crystallite/substrate interfacial strain. An upper bound calculation can be obtained from the difference $\Delta\alpha = \alpha_{Au} - \alpha_{Al2O3}$ of thermal expansion between gold and sapphire. The particle being cooled down from melting to room temperature, a large $\Delta\alpha\Delta T \sim 0.9\%$ of residual tensile strain can be present -geometry considered here as a film on a substrate. In the case of 3D islands, the residual strain is expected to be significantly lower than a 2D film.

VII.2.2 Influence of the boundary conditions

To determine the influence of the substrate and of the twin boundary on the strain distribution, 50 nm gold nanocrystals are equilibrated with various boundary conditions. The first case is an unrelaxed Wulff crystal, *i.e.*, similar in geometry as compared to the experimental particle, but without relaxation of the atomic positions. The second particle named Wulff (c) is obtained following the procedure described in the previous section: relaxation of a single crystal Wulff particle which is cut along the ($\bar{1}$ 1 1) plane after equilibration. The third particle, (d) is a twinned particle, *i.e.*, the ($\bar{1}$ 1 1) plane is a twin boundary, and the relaxation is performed on this twinned particle. (c) and (d) aim at establishing the amount of strain is induced at the vicinity of a twin boundary. (e) is similar to (b), except that the particle is cut along its ($\bar{1}$ 1 1) plane before energy minimization. The ($\bar{1}$ 1 1) plane is thus a free surface. Finally, (f) aims at simulating the effect of interfacial strain. The (0 0 1) facet of a single crystal Wulff particle is parallel and in contact with a gold substrate. The atoms of the substrate are frozen and the lattice parameter of this underlying substrate is set to impose a defined amount of thermoelastic/interfacial strain. The corresponding lattice mismatch is calculated from the in-plane lattice parameter of the (0 0 1) surface atoms in a free-standing and equilibrated Wulff particle. A value of a = 4.069 nm is obtained.

The calculated CXD pattern from the unrelaxed crystal (Fig. VII.6.b.) exhibits some significant difference with the experimental diffraction pattern. Since no strain is present in the unrelaxed crystal, its diffraction pattern is perfectly centrosymmetric . The signature of the strain in the experimental CXD pattern (Fig. VII.6.a.) is reflected in the asymmetry of the diffraction pattern. The asymmetry of the intensity distribution along the [0 0 1] direction is not as distinct as pronounced as in simulations, due to the larger size of the crystal (360 nm vs 25 to 170 nm).

The free-standing truncated Wulff and twinned particle produce very similar diffraction pattern. In both cases, the shape of the Bragg peak is strongly affected by the relaxation of the free-surfaces. The Bragg peak becomes asymmetric, and the periodicity of the fringes along the [1 $\bar{1}$ 1] is disturbed, especially at low scattering angles (below the Bragg peak). The signature of the strain induced by the twin boundary is far from obvious, except from slight variations of intensities, the calculated diffraction patterns is almost indistinguishable from its Wulff counterpart. This is not a surprising result, considering that a twin boundary is a coherent interface and should not generate strain.
As illustrated on Fig VII.6.f, this is a completely different story when the ($\bar{1}$ 1 1) plane is a free surface. The shape of the Bragg peak is strongly affected due to the fact that this large facet undergoes strong contraction. This is another confirmation that the particle measured is a twinned crystal, and not a single crystal cut along its ($\bar{1}$ 1 1) plane.

When the particle is constrained by an underlying substrate (e), the agreement with experimental data is much better. Both the increased intensity and elongation of the “arm” above the Bragg peak and decreased intensity of the “arm” below the Bragg peak are accurately reproduced. The periodicity of the fringes along the [1 $\bar{1}$ 1] direction appears less disturbed, though it is not as periodic as in the experiment. Overall the simulated diffraction pattern appears less symmetric than its experimental counterpart. It should be also noted that the amount of mismatch strain needed to match the experimental data depends on the size of the particle. The smaller is the particle, the larger needs to be the lattice mismatch to simulate the interfacial strain. The value of the lattice mismatch employed here were respectively 1.2%, 0.8% and 0.5% for a 25 nm, 50 nm and 75 nm particle. The experimental particle being significantly larger than these sizes, the estimated interfacial strain in the particle is assumed to be much smaller than 0.5%. As discussed in the previous section, a value of 0.1% is a realistic estimation and would be in good agreement with the weak distortion observed in the CXD pattern (subsection VI.1.3).

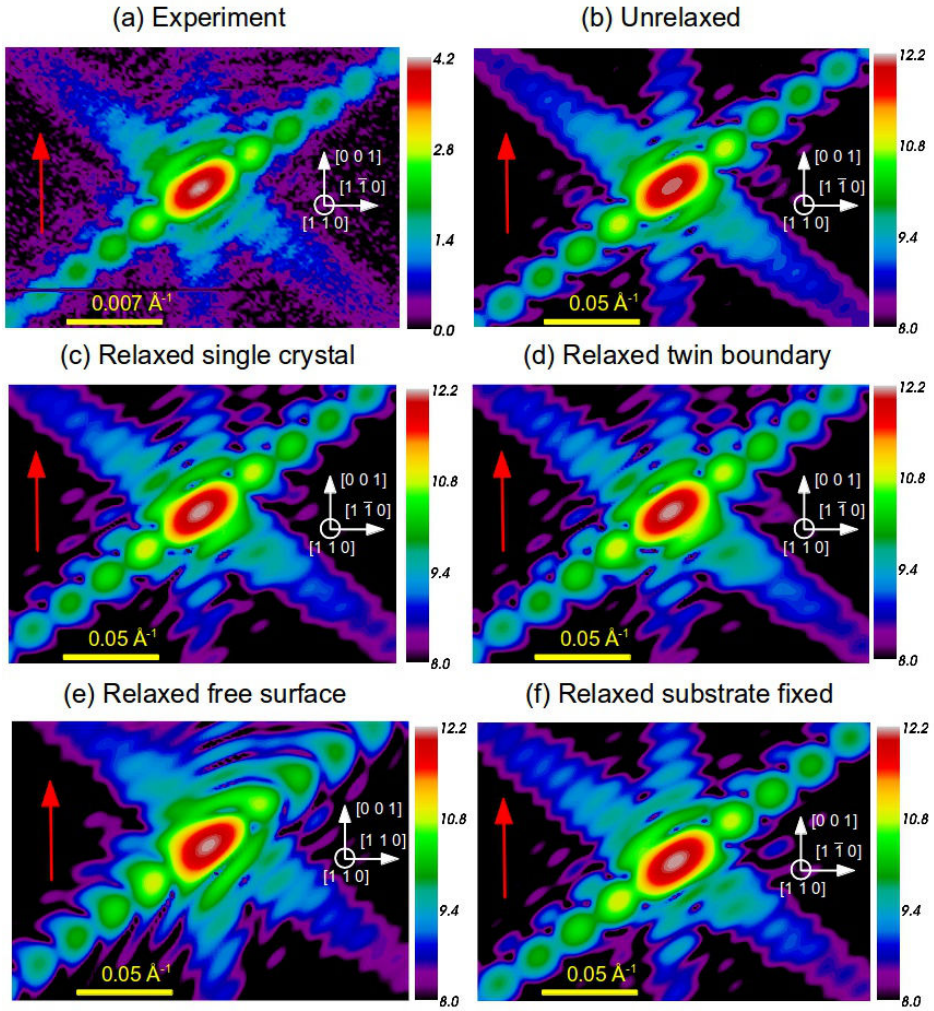

Fig. VII. *6 Dependence of the CXD patterns for* ***g*** *= 0 0 2 on the boundary conditions.* CXD patterns for the experimental particle (a) and simulated particles (b-e). (b) CXD pattern calculated before relaxation (no strain). (c) Relaxed free-standing (no substrate strain) Wulff particle. (d) Relaxed free-standing Twinned particle. (e) Relaxed free-standing with the twin boundary considered as a free-surface. (f) Relaxed Wulff particle constrained by an underlying substrate

The $u_{0\,0\,2}$ displacement fields of the simulations, as obtained by the inversion of the simulated CXD are in good agreement with the analysis of the CXD patterns.

As already discussed in subsection VII.2.1, the relaxation of the free surfaces alone does not provide a satisfying agreement with the experiment data, even if some similarities can be found. The contraction of both the lateral {1 0 0} facets and of the corner and edge atoms of the (0 0 1) facet are well reproduced.

As expected from their similar CXD patterns, the reconstructed displacements for the single Wulff crystal (Fig. VII.7.b) and the twinned crystal (Fig. VII.7.c) are very similar.

The expansion or contraction of the free surfaces is equivalent, but some slight differences arise. In particular, a positive displacement of the lateral {1 1 1} facets can be observed in both cases, but it is more intense at the twin boundary (red circled area in Fig. VII.7.c).

Similar behaviour is observed experimentally, suggesting that the corner atoms are strained at the interface.

When the twin boundary is considered as a free surface (Fig. VII.7.d), the reconstructed displacement is dominated by the contraction of the ($\bar{1}$ 1 1) surface atoms which is three times larger than the maximum -

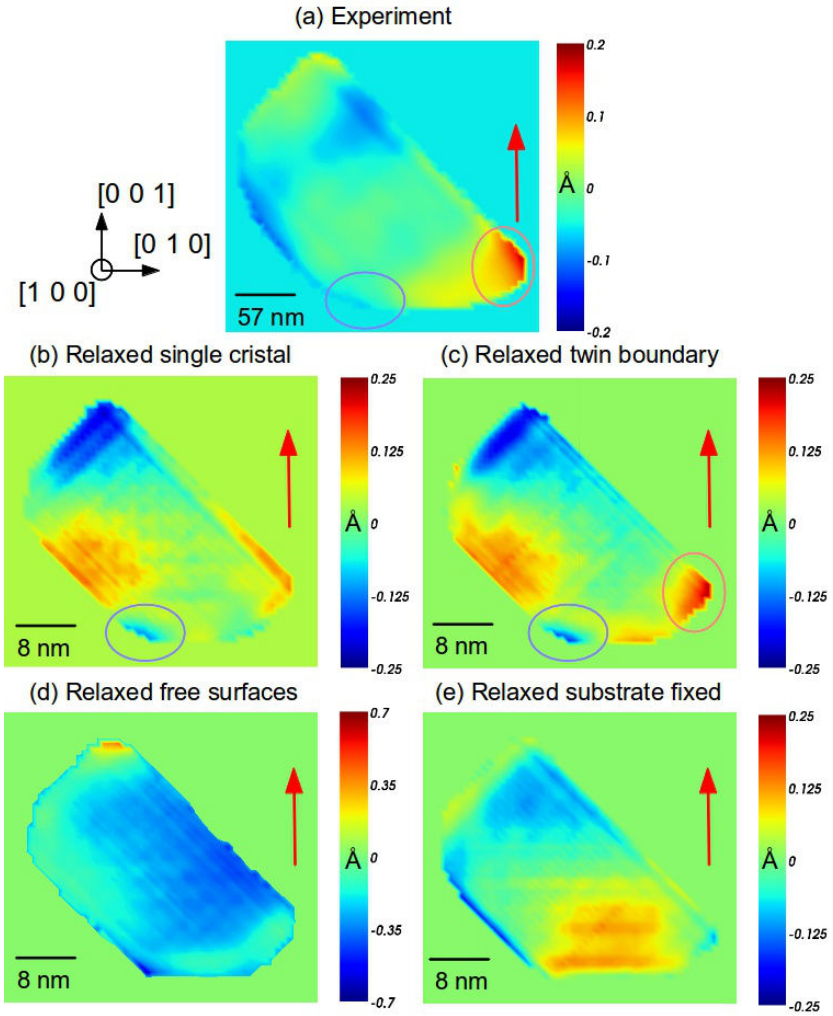

Fig. VII.7 *Distribution of the $u_{0\,0\,2}$ displacement field depending on the boundary conditions.* Cross section of the projected displacement field for (a) The experimental particle. (b) Relaxed free-standing (no substrate strain) Wulff particle.(c) Relaxed free-standing Twinned particle. (d) Relaxed free-standing Twinned particle.(e) Relaxed free-standing with the twin boundary considered as a free-surface. (f) Relaxed Wulff particle constrained by an underlying substrate

- contraction observed in the other cases (about 0.7 Å as compared to 0.25 Å).

The best agreement can be found when some interfacial strain is added to the equation (Fig VII.7.e). Fig. VII.8, shows a comparison between the experiment and a smaller particle which is constrained by its substrate. Cuts perpendicular to the 3 <1 0 0> axis reveal a good agreement with the experimental data. The contraction of the lateral {1 0 0} facets is particularly well reproduced (blue circled area in Fig. VII.8.b and 8.d), so is the expansion in the red circled area in Fig. VII.8.b & VII.8.d. The interfacial strain is clearly visible at the substrate/particle interface in the simulated particle (Fig VII.8.e). This lattice expansion at the substrate/particle interface is also visible on the experimental particle although less pronounced.

The maximum tensile strain observed on the edges of the {1 1 1} facet in contact with the twin boundary is not found in the simulated particle (red circled area in Fig. VII.8.a & VII.8.c). This discrepancy is probably due to the fact that the relaxation is performed on a perfect Wulff single crystal which is cut afterwards and not on a twinned particle.

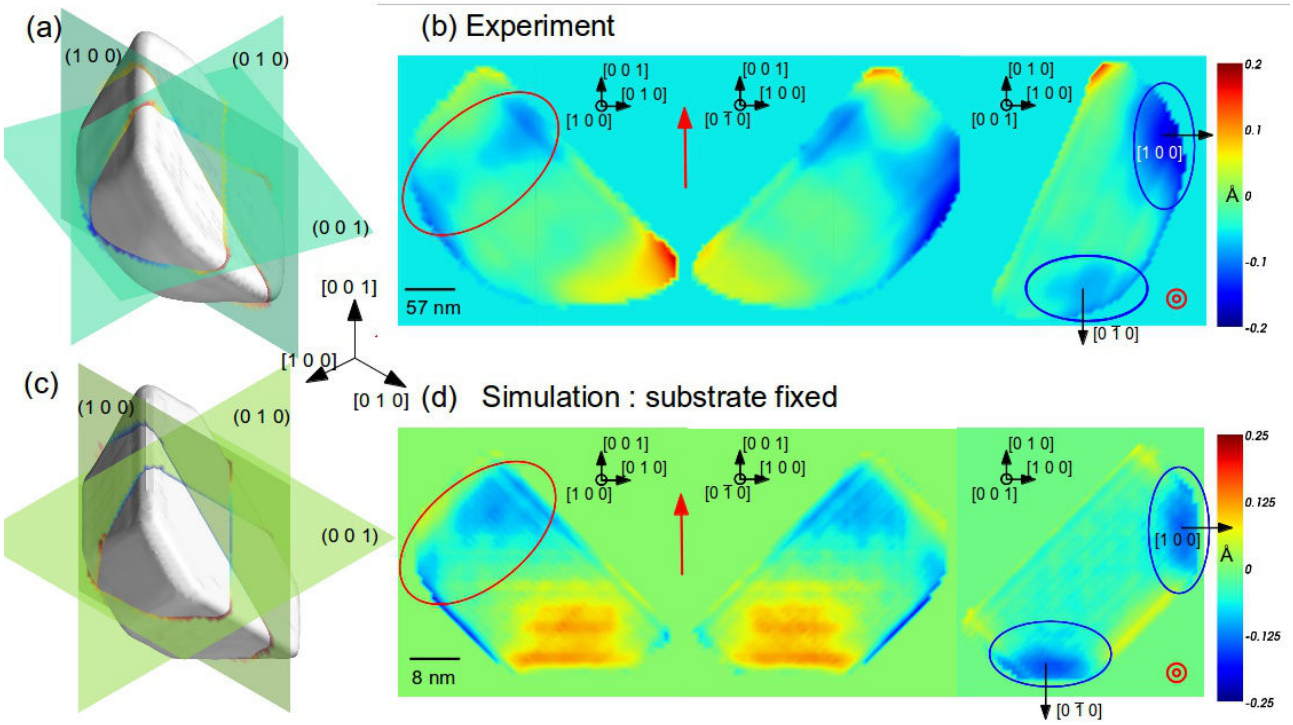

Fig. VII.8 *Comparison between experimental and simulated reconstructions.* Reconstructed electron density (50%) for the experimental (a) and simulated (c) particles which indicate the position of the cross sections of the displacement field. (100), (010) and (001) cross sections of the displacement field for the experimental (b) and simulated particle (d)

	Experiment	Wulff	Twin	Wulff free surfaces	Wulff + substrate
(0 0 1)	Expansion + contraction of the corner atoms	Contraction (stronger for the corner atoms)	Contraction (stronger for the corner atoms)	Contraction (stronger for the corner atoms)	Expansion + slight contraction of the corner atoms
(1 0 0) & (0 1 0)	Contraction	Contraction	Contraction	Contraction	Contraction
(1 $\bar{1}$ $\bar{1}$)	Contraction	Expansion	Expansion	Expansion	Contraction
($\bar{1}$ 1 1) (twin boundary)	Expansion (bottom) Contraction (top)	Expansion (bottom) Contraction (top)	Expansion (bottom) Contraction (top)	Strong contraction	Expansion (bottom) Contraction (top)
{1 1 1} lateral facets	Expansion (stronger for the edge atoms)	Expansion	Expansion (stronger for the edge atoms)	Contraction	Expansion
(1 $\bar{1}$ 1) top facet	Expansion	Contraction	Contraction	Expansion (edge atoms) Contraction (facet)	Expansion + Contraction

Tab. VII.1. Contraction or expansion associated with facets.

Conclusion

We have studied the 3D displacement field of a twinned gold sub-micrometric crystallite using coherent X-ray diffraction and molecular dynamics simulation. The loss of symmetry in the diffraction pattern suggests the presence of inhomogeneous strain inside the particle. The reconstruction of the electron density reveals a highly faceted particle with {1 0 0} and {1 1 1} and relatively small curved areas between the facets. The particle is truncated due to the partial wetting of gold on sapphire and has almost reached its equilibrium crystal shape. The reconstruction of the 3D displacement field reveals an alternating pattern of inward and outward lattice displacement with a general tendency of contraction for the {1 0 0} facets and expansion for the {1 1 1} facets (relatively to the average lattice contraction). It also suggest the presence of a weak amount of interfacial strain.

Molecular Statics simulations are carried out to explore the strain distribution in the particle. It is shown that the displacement field (both magnitude and distribution) in a free standing crystallite is driven by its geometry rather than its size. The size effect is revealed by the anisotropy of the intensity distribution in the diffraction patterns. The calculation of the diffraction patterns from the relaxed particles with various boundary conditions shows that the best agreement with our experimental data is found for a particle strained by an underlying substrate.

Bibliography

Alivisatos, A. P. (1996). *Science* **271**, 933–937

Beutier, G., Verdier, M., Parry, G., Gilles, B., Labat, S., Richard, M. I., Cornelius, T., Lory, P. -F., Vu Hoang, S., Livet, F., Thomas, O. & De Boissieu, M. (2013). *Thin Solid Films* **530**, 120-124.

Chen, C.-C., Zhu, C., White, E. R., Chiu, C.-Y., Scott, M. C., Regan, B. C., Marks, L. D., Huang, Y., Miao, J. (2013). *Nature* **496**, 74−77.

Clark, J. N., Ihli, J., Schenk, A., Kim, Y-Y., Kulak, A. N., Campbell, J. M., Nisbet, G., Meldrum, F. C. & Robinson, I. K (2015) *Nature materials* **14**

Fienup, J. R. (1982). *Appl. Opt.* **21**, 2758-2769

Freund, L. B. & Suresh, S. (2003) Thin Film Materials: Stress, Defect Formation and Surface Evolution, edited by Cambridge University Press, Cambridge, England

Gerchberg, R. W. & Saxton, W. O. (1972). Optik (Stuttgart) 35, 237–246 .

Gilbert, B., Huang, F., Zhang, H., Waychunas, G. A. & Banfield, J. F. (2004). *Nanoparticles: Strained Stiff. Sci.* **305**, 651–654.

Grochola, G. S., Russo, P. & Snook, I. K. (2005). *J. Chem. Phys.* **123**, 204719.

Harder, R., Pfeifer, M. A., Williams, G. J., Vartaniants, I. A. & Robinson, I. K. (2007). *Phys. Rev. B* **76**, 115425

Heyraud, J. C. and Métois, J. J. (1982) *Surf. Sci* **128**, 334

Howe J. M. (1997) Interfaces in materials, edited by John Wiley & Sons, Inc.

Huang, W. J., Sun, R., Tao, J., Menard, L. D., Nuzzo, R.G. & Zuo, J. M. (2008). *Nature Materials* **7**, 308-313.

Ibach, H. (1997). *Surf. Sci. Rep.* **29**, 195–263.

Labat. S., Richard, M-I., Dupraz, M., Gailhanou, M., Beutier, G., Verdier, M., Mastropietro, F., Cornelius, T. W., Schülli, T. U., Eymery, J. & Thomas, O. (2015) *ACS Nano*

Landau, L.D & Lifshitz, E. M. (1986) Theory of Elasticity edited by Pergamon

Lou, Y., Maye, M. M., Han, L., Luo, J. & Zhong, C. J. (2001). *Chem. Comm., 473-474*

Lu, Z., Liu, G., Phillips, H., Hill, J., M., Chang, J. & Kydd, R. A. (2001) *Nanolett.* **1**(12), 683-687

MacLaren J.M., Pendry J.B., Rous P., Salinn D., Somorjai G., Van Hove M., Surface Crystallographic Information Service, A Handbook of Surface Structures, D.Reidel, Dordrecht

Marchesini, S. (2003). *Phys. Rev. B* **68**, 140101

Matthews, J.W. & Blakeslee, A. E. (1974) J. Crystal Growth 27, 118.

Newton, M. C., Leake, S. J., Harder, R. & Robinson, I. K. (2010). *Nature Materials* **9**, 120–124.

Robinson, I. K. & Vartanyants, I. A. (2001). *Applied Surface Science* **182**, 186-191.

Sadan, H. & Kaplan, W. D. (2006). *J. Mater. Sci.* **41**, 5099-5107.
Sayre, D. (1952). *Acta. Cryst.* **5**, 843.

Scott, M. C., Chen, C.-C., Mecklenburg, M., Zhu, C., Xu, R., Ercius, P., Dahmen, U., Regan, B. C., Miao, J. (2012). *Nature* **483**, 444− 447.

Smoluchowski, R. (1941). *Phys. Rev* **61**, 661 .

Stukowski, A. (2010). *MSMSE* **18**(1)

Uchic *et al,* (2004). Science **305**, 986

Ulvestad, A., Clark, J. N., Harder, R., Robinson, I. K. & Shpyrko, O. G. (2015), *Nanoletters* **15**

Wang, Z., Wynblatt, P. (1998), *Surf. Sci.* **398**, 259-266

Waszczuck, P., Barnard, T. M., Rice, C., Masel, R. I. & Wieckowski, A. (2002) *Electro. Comm.* **4**(7), 599-603.

Watari, M., McKendry, R. A., Vögtli, M., Aeppli, G., Soh., Y- A., Shi, X., Xiong, G., Huang, X., Harder, R., and Robinson, I., K. .(2011), *Nature Materials* **10**, 862-866

Winterbottom, W. L. (1967). *Acta Metall.* **15**, 303.

Chapter VIII : Study of an heterogeneous bi-metallic interface (Cu-Ta) investigated by surface diffraction, ab-initio and molecular dynamics calculations

Contents

Introduction....214
VIII.1. Experiment....215
VIII.1.1. Experimental details....215
VIII.1.2. Comparisons between different surface states....218
VIII.2. Density Functional theory calculations....219
VIII.2.1. Computational method....219
VIII.2.2. Supercell configuration....219
VIII.2.3. Calculation of the excess interface energies....220
VIII.2.4. Calculation of the structure factors....221
VIII.2.5. Fitting of the experimental data....224
VIII.3. Atomistic simulations with an angle-dependent potential for the Cu-Ta system....225
VIII.3.1. Calculation of the excess interface energies....226
VII.3.2. Calculation of the structure factors....228
VIII.3.3. Testing the potential....230
VIII.3.4. Application to the solid state dewetting of a Cu thin film....231
Conclusions....233
Bibliography....235

This chapter is a draft of article to be submitted shortly as "Structure of the wetting layer of copper on a Tantalum (100) surface, Dupraz et al".It is self-consistent and a short introduction, sometimes redundant with previous chapters, as well as the necessary references, are included.

Chapter VIII : Study of an heterogeneous bi-metallic interface (Cu-Ta) investigated by surface diffraction, ab-initio and molecular dynamics calculations

Introduction

Copper is nowadays a widely used interconnected metal in integrated circuits (IC) devices. However, the rapid diffusion of copper through silicon and its poor adhesion to silicon oxide led to the investigation of reliable diffusion barrier metal to isolate the copper interconnects from the silicon chips. Among the diffusion barrier metals Tantalum is one of the most interesting candidates and the past two decades have seen an increasing interest on the study of the Cu/Ta system (Holloway *et al.* 1992, Laurila *et al.* 2000). On top of its technological interest, Cu/Ta is also a prime example of a strongly heterogeneous film-substrate system with almost zero mutual solubility (Massalski 1986), different crystal structure (f.c.c. Cu vs b.c.c. Ta), different lattice parameters as well as many other properties. An atomic scale understanding of the growth mode, structure and thermal stability of Cu thin films on Ta substrates is thus of both fundamental and technological importance

As a misfitting system, the Cu/Ta interface is a good example of a bi-metallic system with a Stranski-Krastanov (SK) growth mode (Rodriguez & Goodman 1991). It combines features of the Volmer-Weber growth mode (film growth by growth of islands) and the layer-by-layer growth mode known as the Frank-van-der-Merve (FM) growth mode and can be described as a growth of 3D islands on top a thin film. The structure and morphology of the Cu/Ta interface is however difficult to predict and the study of the stability and wetting behaviour of thin Cu films deposi ted on a Ta substrate has been the subject of several experimental investigations and controversial observations over the past few years.

Kuhn *et al* (1993) studied ultra thin Cu films deposited on a Ta(1 1 0) substrate. They established that ultrathin Cu films form a stable pseudomorphic (PM) layer on top of the Ta substrate for a coverage up to 1.22 monolayers (ML). Chen *et al.* (2000) studied the influence of impurities on the wetting behaviour of ultrathin Cu films on Ta(1 1 0). They reported the stability of a Cu sub-monolayer on a clean Ta(1 1 0) substrate for temperatures up to to 1000K, a temperature at which diffusion into the bulk occurs. More recently, Fillot *et al.* (2007) reported the dewetting of Cu from Ta (1 1 0) substrates, leaving exactly one stable Cu monolayer on top of which 3D islands of Cu form. In 2009 Venugopal *et al.* investigated the stability of Cu thin films with varying thickness deposited on clean Ta(1 1 0) and Ta(1 0 0) substrates at room temperature. They described the agglomeration of the thin film into islands at a temperature which depends on the film thickness. The out-of-plane and in-plane orientation islands differ for the two substrate surfaces, and the presence of a wetting layer of 1 or 2 ML was reported for both orientations.

Atomistic simulations were also helpful to provide some new insights in the formation and structure of Cu film growth on Ta substrate. Klaver and Thijsse (2003) used Molecular Dynamics (MD) calculations to simulate the deposition of copper on b.c.c. Ta (1 0 0) and Ta (1 1 0) and β-Ta (0 0 1). For the deposition of Cu on the Ta(1 0 0) substrate they describe the formation of a stable PM ML, on top of which grains with f.c.c. (1 1 1) out-of plane orientation and two different in-plane orientations are formed. These grains have mobile grain boundaries, and upon further deposition, the smaller grains are absorbed by the larger grains to form an almost defect free monocrystalline films with (1 1 1) orientation. Following this work, large scale MD simulations of Cu deposition on Ta(1 0 0) were performed by Lazic *et al.* (2010). They reported a quite rich and complex microstructure. The Cu thin film forms a first stable PM layer, on top of which it grows in the form of a superstructure of 26 atoms misfit supercells which upon relaxation breaks up into islands. The third layer and above are f.c.c. (1 1 1) planes with grain boundaries as main defects. The thermodynamical and mechanical stability of Cu films on Ta (110) has also been investigated by Hashibon, Elsässer *et al.* (2008), using Density Functional Theory (DFT) in the local density approximation, and later with M D calculations (Hashibon, Lozovoi *et al.* 2008). The DFT study reported the stability of an incoherent ML of Cu on Ta. The MD simulations showed the stability of a Cu pseudomorpic ML with mismatch occurring along the [0 0 1] direction of the Ta substrate. Thicker Cu films are unstable and agglomerate into islands,

leaving a stable Cu ML on the surface.
If the atomic structure of the Cu ML on top of a Ta (1 1 0) substrate remains quite controversial, there are several experimental studies as well as DFT and MD simulation that report the presence of a single stable Cu ML of a Ta(1 1 0) surface. The growth mode and wetting behaviour of Cu thin films on Ta(100) is not as well documented. The dewetting of Cu thin films deposited on Ta(1 0 0) has been reported in several studies (Kim *et al* 2005, Venugopal *et al.* 2009). There is also some experimental evidences of the presence of a wetting layer covering the Ta(1 0 0) surface, between the dewetted islands (Venugopal *et al.* 2009). Venugopal estimated the thickness of this layer to less than 5 Å, corresponding to 1 or 2 ML. However, the precise number of ML and their crystal structure remains so far unknown.
Surface X-ray diffraction (SXRD) is a powerful probe of the structure of crystalline surfaces (Robinson & Tweet, 1992). Sharp interfaces give rise to Crystal Truncation Rods (CTR) in reciprocal space (Andrews & Cowley, 1985, Ribinson 1986, see subsection II.2.1). CTRs can be used to go beyond a 2D description of the surface structure (Robinson 1986) and are particularly useful to evidence pseudomorphic wetting layers (Ball *et al.* 2002). Indeed, the scattering amplitude from a PM wetting layer is enhanced by interference with the scattering amplitude from the substrate in the vicinity of the Bragg reflections of the latter, allowing, with synchrotron radiation, a quantitative characterisation of the structure of the PM layer. This is precisely the experimental method used in this report, to shed light on the nature of the copper on tantalum (100) interface.
In this study we measured CTRs of a clean Ta (1 0 0) surface while performing an *in situ* dewetting of copper thin film. The results provide atomic details on the Ta surface termination and in particular allow us to determine the number of PM Cu layers on top of the Ta(1 0 0) surface as well as their interplanar spacing. All the experimental details and results are presented in section VIII.1.
To gain a new insight in the experimental results, DFT calculations in the local density approximation are presented in section VIII.2. The thermodynamic stability of several thin Cu films on a Ta(100) surface, with a varying number of ML and crystal structure (f.c.c or PM (b.c.c.)), is investigated by the calculation of the excess interface energy. In order to determine the number of PM Cu layers as well as their inter planar spacing from the measured CTR, the structure factors of the relaxed configuration are calculated and compared to the experimental data. The agreement between the predictions from excess interface energy calculation and the experimental results are discussed.
In the last section some complementary calculations are performed with an Angular Dependant Potential (ADP) developed by Hashibon, Elsässer *et al.* (2008) . The excess interface energy is calculated for a variety of thin Cu film on Ta (100) interfaces and compared to the results from DFT calculations. The structure factor of the film/substrate structure of lowest energy is then calculated and compared to the experimental data. The use of this potential to work on larger systems, in particular to study the dewetted 3D islands on top of the thin wetting Cu layer is finally discussed at the end of this section.

VIII.1. Experiment

VIII.1.1. Experimental details

The experiment was carried out at the ESRF on the BM32 SUV (CRG-IF) beamline. It is equipped with a large UHV chamber mounted on a four circle diffractometer. The UHV chamber itself features several evaporation sources for *in situ* epitaxial deposition. It is also equipped with a high temperature furnace. However the preparation of a clean Ta(1 0 0) requires the flash annealing of the Ta substrate at very high temperatures (above 2000K) which can not be reached with the set-up on the beamline. The first stage of the surface preparation was thus performed in our laboratory UHV chamber.
A high purity (more than 99.9999%) Ta crystal, cut and polished to less than 0.1° along the (0 0 1) plane was purchased from MaTecK. The surface is prepared by repeated cycles of Argon sputtering and flash annealing above 2000 K to remove all the oxygen and carbon contamination (Musket *et al.* 1982). The atomic flatness of the surface is monitored by Low-Energy Electron Diffraction (LEED), and the absence of oxygen or carbon contamination is checked by X-ray Photoelectron Spectrometry (XPS). A protective 5 nm copper layer is then deposited to protect the Ta surface during the transfer under primary vacuum to the

beamline chamber. The sample is shortly exposed to air during the introduction in the beamline chamber. This obviously leads to a significant oxygen and carbon surface contamination as illustrated on Fig. VIII.1.a. To clean the Ta surface, the sample is annealed during 8 hours at 300°C and the copper is then evaporated at

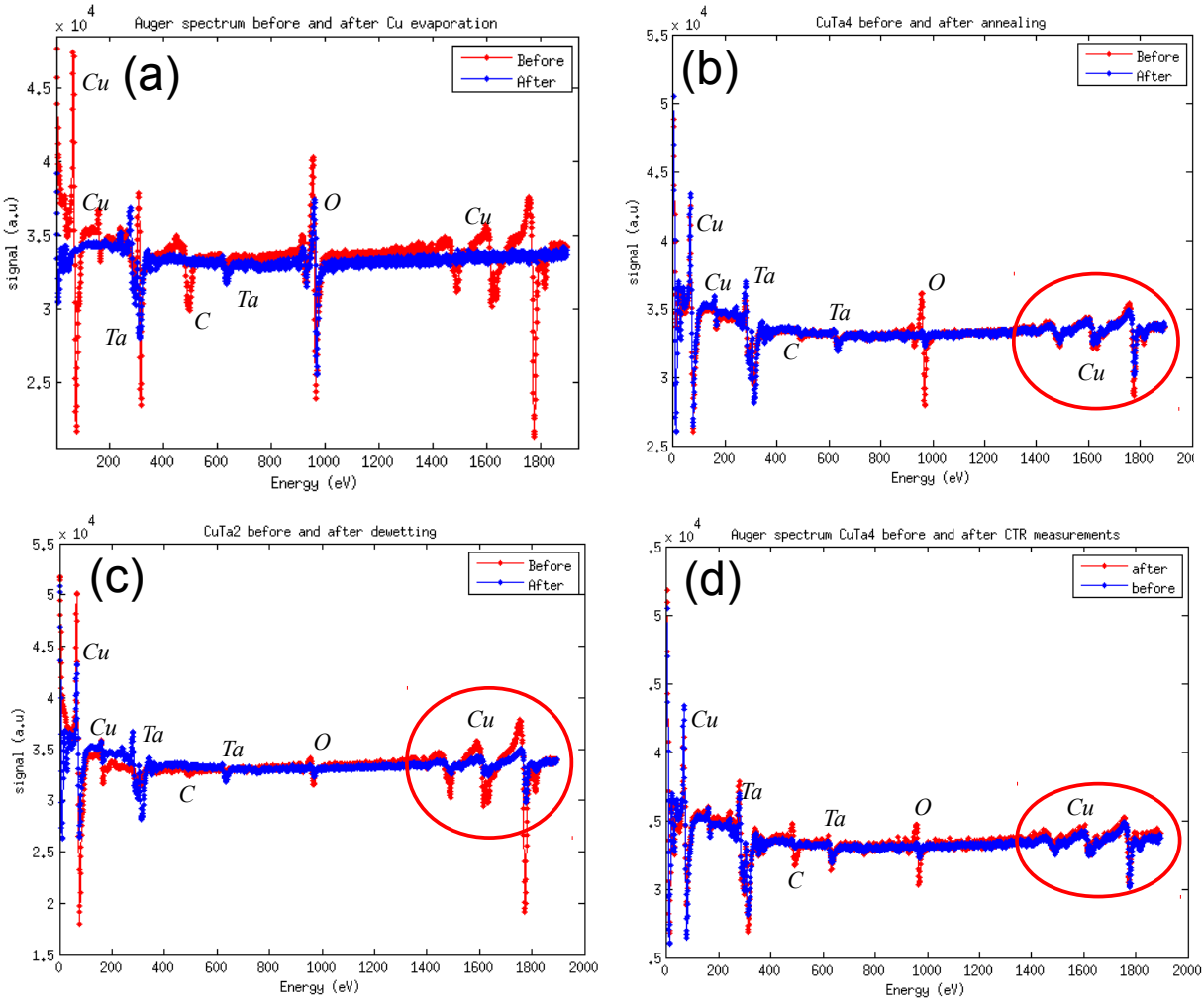

Fig. VIII.1 *Auger spectra showing the surface contamination at various stages of the experiment* a) before and after Cu evaporation . b) before and after Cu annealing and Ar bombardment. c) before and after Cu dewetting. d) before and after CTR measurements

1100°C during 3 minutes. This procedure has been repeated 4 times during two different experimental runs and has proven to be efficient to prevent the Ta surface from a high level of contamination. For both experiments no carbon contamination is observed after Cu evaporation. However for the second experimental run, the oxygen contamination of the Ta surface remains significant after Cu evaporation (Fig. VIII.1.a). The conditions of preparation of the Ta surface, and the Cu deposition and dewetting then differ depending on the sample and the experimental run.

For the first Ta substrate which was used during the first experimental run (thereafter CuTa1), the Cu deposition was done by sputtering during 5 minutes, allowing the deposition of approximately 9 nm of Cu. The surface was then cleaned during 20 minutes by Ar bombardment. To perform the dewetting, the sample was then heated during 20 minutes at 750° when the dewetting occurs. As illustrated in Fig. VIII.1.b, this preparation procedure allowed to obtain a clean Ta surface.

During the dewetting, the temperature was monitored with a pyrometer and the base pressure into the chamber was carefully checked to avoid any copper evaporation. The thickness of the Cu film was controlled by monitoring the FWHM of the rocking curve for the Cu 2 0 0 reflection. The beginning of dewetting is

reflected in the sharp increase of the peak intensity and the diminution of its FWHM. The analysis of the Auger spectrum reveals that the ratio between low energy electron and high energy electrons increase after the Cu dewetting. This can be explained by the presence of a thin wetting layer in-between the islands (Fig. VIII.1.c).
For the second experimental run, the sample was prepared with 3 different procedures. For the first one, named CuTa2, the copper was deposited at a deposition rate of 1 ML(1.8 Å)/5'20" during approximately two hours. The estimated thickness of the Cu thin film was approximately 22 ML *i.e.*, 4 nm. The Cu dewetting was performed at 800 °C during 5 minutes and the sample is further heated at 830°C during 1 minute. This procedure lead to reasonably low level of oxygen and almost no carbon contamination.
For CuTa3 the Ta surface and the Copper deposition and dewetting were performed under the same conditions. The substrate surface was restored in the laboratory between CuTa2 and CuTa3, using the procedure described above. Before the CTR measurements, the Auger spectrum, did not show no sign of carbon contamination, and a low oxygen contamination.
A last measurement was done on this sample (CuTa4). To get rid of the significant oxygen and carbon contamination that occurred during the CTR measurement, Cu was evaporated at 1100°C during 3 minutes. A single Cu ML was then deposited at room temperature. After the measurement of one CTR, two additional Cu ML were deposited. The sample was then heated 30 minutes at 430°C, 5 minutes at 670°C and the dewetting was performed at 780°C during 1 minute. As illustrated in Fig. VIII.2.b, this procedure turned out to be particularly efficient to reduce the oxygen contamination and allowed to obtain an almost clean Ta surface.
Overall we managed to obtain reproducibly a clean Ta surface for all 4 CTR measurements, although a low oxygen contamination was observed for the 2nd experimental run (Fig VIII.1.c). However, it is also clear from Fig. VIII.1.d that most of the carbon and oxygen contamination occured during the CTR measurements and that the surface contamination for a given rod is strongly correlated to the time elapsed between the dewetting of the Cu thin film and the CTR measurement.
Tab. VIII.1 summarizes the Ta surface state, before and after the CTR measurements, and time elapsed (in hours) between the dewetting and measurement.

	Oxygen contamination		Carbon contamination		CTR 11L	CTR 10L
	Before CTR	After CTR	Before CTR	After CTR		
CuTa1	No	Yes	No	Yes	3.5	0.5
CuTa2	Low	Yes	No	Low	2	3.5
CuTa3	Low	Low	No	Low	0.5	3.5
CuTa4	Very low	Yes	No	Yes	0.5	3.5

Tab. VIII.1: *Surface contamination of the Ta(100) surface before and after CTR measurements*

For the rod 1 0 L the cleanest surface state is obtained for CuTa1 followed by CuTa4, CuTa3 and CuTa2. For the rod 1 1 L it is achieved for CuTa4 followed by CuTa3, CuTa2 and CuTa1.

CTR measurements were performed with the sample mounted in the so called z-axis geometry described in more details in subsection (II.2.3) and elsewhere (Bloch 1985, Vlieg 1998).
The energy of the incoming monochromatic X-ray beam was set to 22 keV and the size of the beam on the sample was approximately (0.5x0.3 mm FWHM). The scattered intensity was recorded on a 2D pixel detector placed 50 centimetres away from the sample.
In order to reduce the Thermal Diffuse Scattering (TDS) from the bulk, the penetration of X-ray into the sample has to be kept as small as possible. This can be achieved by using a low glancing angle α of the incoming X-ray beam. In the present it was set to 0.6°, a value slightly above the critical angle of total external reflection (respectively 0.194° and 0.154° for Cu and Ta at 22 keV). The sample was carefully aligned in order to put the surface normal exactly parallel to the axis for azimuthal rotation ω, *i.e.*, the

scattering angle is independent of the ω rotation. The rod scans were then performed by a combined movement of ω rotation of the sample and of the detector which can be moved out to the surface plane by an angle β in order to probe different exit angles to the surface of the diffracted beam (section II.2.3 for more details).

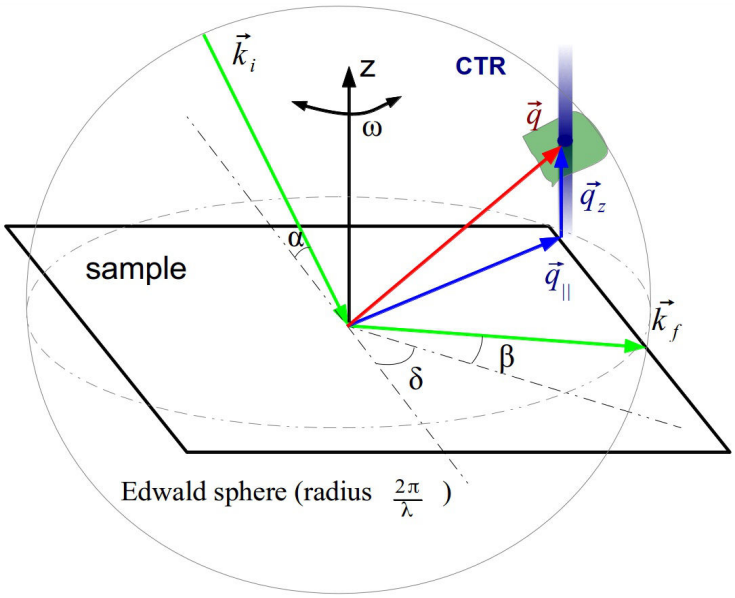

Fig. VIII.2 Geometry of the experiment

The atomic structure within a crystal unit cell can then be determined from the structure factors. A very accurate determination of structure factors can be obtained from the integrated intensities of a reflection (Vlieg 1997). The integrated intensities along the CTR were measured thanks to angular ω scan of the reflection over a range of ± 5° and steps of 0.1°. This relatively large range was selected to ensure the accurate measurement of the background level. To obtain a precise value of the integrated intensities, this background needs to be properly subtracted. This is done thanks to the software ANA (Vlieg 1997, Vlieg 2013) which enables the background subtraction, integrated intensities calculation and conversion of the latter into structure factors.

VIII.1.2. Comparisons between different surface states

A respective total of 8, 5, 6 and 4 rods were measured for CuTa1, CuTa2, CuTa3 and CuTa4 with different states of surface contamination. Both CTR 1 1 L and 1 0 L shown on Fig. VIII.3.a and VIII.3.b are averaged over 2 symmetry-equivalent reflections (1 1 L and 1 $\bar{1}$ L for the 1 1 L, 1 0 L and 0 1 L for the 1 0 L rod).

The CTR 1 1 L was measured on an almost clean surface with no carbon contamination and a very low oxygen contamination for CuTa3 and CuTa4, while the surface contamination (for both oxygen and carbon) was significant for CuTa1. As illustrated in Fig. VIII.3, the 1 1 L CTR for CuTa3 and CuTa4 are almost equivalent and some differences can be observed for CuTa1. The peak at L = 0.7 is smoother and shifted to an higher exit angle, and the bump observed between L = 1.1 and L = 1.5 for CuTa3 and CuTa4 is less prominent on CuTa1. Given that 1 1 L rods measured on a clean Ta surface (CuTa3 and CuTa4) are very reproducible, the differences observed for CuTa1 are likely to be related to surface contamination.

Similar conclusions can be drawn for the CTR 1 0 L, where the clean surface was measured for CuTa1 and the contaminated surface for CuTa3 and CuTa4. The rod profiles are again very similar for an equivalent state of surface contamination, while differences can be observed with the case of a clean Ta surface (CuTa1). The profile of the rods are very similar with a drop of the structure factor amplitude for L = 2.1 and

a bump observed between 2.2 and 2.6 . The main difference lies in the structure factor amplitudes for high exit angles which are significantly lower for the contaminated surfaces (CuTa3 and CuTa4).
From these four distinct CTR measurements with different sample, preparation process and surface state, we can conclude that the CTR are reproducible. Although visible, the effect of the surface contamination is weak.

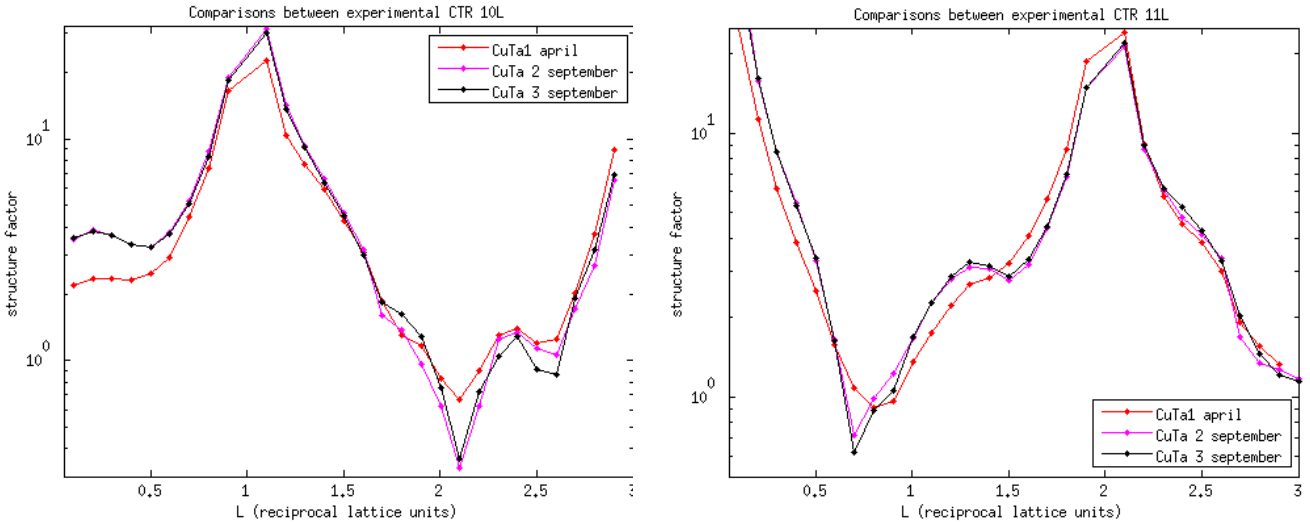

Fig. VIII.3 *Comparison of the 1 0 L rod (a) and 1 1 L rod (b) for two different experimental runs with different state of surface contamination.* Error bars have been omitted to facilitate the vizualization.

VIII.2. Density Functional theory calculations

From the measured CTRs, the precise determination of the structure of the interface is in principle obtained by the fitting of the experimental data. However, in this work, DFT calculations are performed to gain further insight in the experimental results. The agreement between the interfaces predicted from the experimental data and the DFT calculations is quantified and discussed in extensive details.

VIII.2.1. Computational method

Total energy calculations are performed using the local-density approximation to the exchange and correlation and norm conserving Martins-Troullier pseudopotentials (Troullier & Martins 1993) as implemented in the PWSCF code (Giannozzi *et al.* 2009). The wavefunction and charge density cutoffs are taken as 90 Ry and 360 Ry, respectively. Atomic relaxation is performed until forces on atoms are less than 0.03 eV/Å. The bulk structures of b.c.c Ta and f.c.c Cu are fully optimized using a 12x12x12 Monkhorst-Pack grid (Monkhorst & Pack 1976) for the integration of the irreducible Brillouin zone leading to a_{Cu} = 3.5538 Å and a_{Ta}= 3.235 Å. The slab calculations of a few pseudomorphic Cu layers described in the following section employ 12x12x1 Monkhorst-Pack grid while the Cu f.c.c interface is computed employing the Gamma point only.

VIII.2.2. Supercell configuration

In order to determine the stability and structure of a Cu thin film on Ta(1 0 0), the following interfaces systems are modeled using a periodic slab configuration: 1 to 5 PM layers of Cu on top of Ta, a

single Cu f.c.c. layer on top of Ta and a f.c.c layer on top of 2 PM layers of Cu on a Ta substrate.
For the PM Cu layers, *i.e.* adopting a b.c.c. structure coherent with the Ta substrate, 14 Ta (1 0 0) planes are considered and 1 to 5 b.c.c Cu layers are located on on both sides of the slab leading to two equivalent Cu/Ta interfaces. Each layer is modeled using one atom per unit cell by taking advantage of periodic boundary conditions along the y and x direction. A thick vacuum region of about 15 Å is considered along z between the two Cu films in order to ensure a negligible interaction between the two free surfaces. The structural relaxation is computed by relaxing the z coordinate of all atoms within the supercell.
The calculation of f.c.c. Cu requires a significantly larger cell. The orientation relationship of the thin film with respect to the substrate is Cu(0 0 1)[1 1 0]//Ta(0 0 1)[1 0 0] inducing an in-plane misfit strain of ε_{xx} = 31.4% (calculated from the computed lattice parameters of the corresponding bulk) if the Cu is strained to the nominal value of the bulk Ta lattice parameter. This in plane strain was minimized by creating a supercell of 9x9 Cu f.c.c. atoms on top of 7x7 Ta b.c.c. (Fig VIII.4.b). The corresponding lattice mismatch for 9 Cu atoms on top of 7 Ta atoms is about 0.13%.

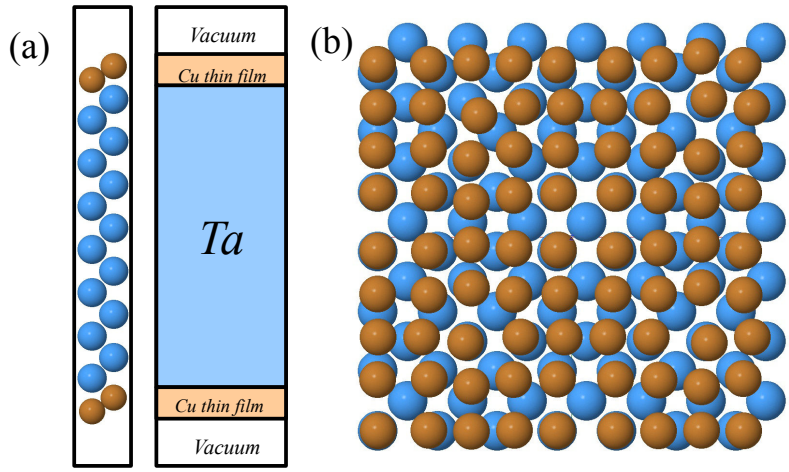

Fig. VIII.4 *Configurations considered for the DFT calculations* (a) Periodic slab configuration to model the relaxation of a varying number of PM Cu layers. (b) 9x9 Cu /7x7 Ta supercell used to model the relaxation of thin fcc films on top of the bcc Ta substrate

Fig. VIII.4: (a) Periodic slab configuration to model the relaxation of a varying number of PM Cu layers. (b) 9x9 Cu / 7x7 Ta supercell used to model the relaxation of thin fcc films on top of the bcc Ta substrate

Given the large size of the supercell, a smaller number of Ta planes is considered here. For the single f.c.c. layer, 6 Ta planes are used (6 Ta/1 Cu f.c.c.) leading to a 375 atoms supercell while for the f.c.c. layer on top of 2 PM layers only 5 Ta planes are used (5 Ta / 2 Cu PM / 1 Cu f.c.c., 424 atoms). In all cases only the z coordinates of all Cu atoms plus the first 3 interfacial Ta planes are relaxed to reduce the computational cost of the calculations.

VIII.2.3. Calculation of the excess interface energies

The thermodynamical stability of Cu thin films is evaluated by computing the excess interface energy as the energy difference between the fully relaxed configuration for each model and the configuration with the same number of atoms in their bulk environments. It can thus be written as:

$$\gamma = (E_{supercell} - (E_{Ta\,bulk} + E_{Cu\,bulk}))/2A \qquad \text{(VIII.1)}$$

where $E_{supercell}$ is the total energy of the slab calculation and A is the surface area (considered twice for the two

Cu/Ta interfaces). The excess interface energy described in Eq. (VIII.1) is the sum of the film/substrate interface energy, γ_i, and the free surface energy of the thin film, γ_f, *i.e.* $\gamma = \gamma_i + \gamma_f$. As the number of layers of the film increases, the strain contribution ($1/2E\varepsilon^2h$) becomes implicitly contained in Eq. (VIII.1) and this term dominates the trend. In order to evaluate the stability and growth mode of a film on a substrate, the energy difference between the free surface and the interface configurations needs to be considered. This is given by (Freund & Suresh 2003, Wuttig & Liu 2004) :

$$\delta = \gamma_i + \gamma_f - \gamma_s \qquad \text{(VIII.2)}$$

where γ_i and γ_f are described above and and γ_s is the free surface energy of the substrate. For $\delta < 0$ the film/substrate interface is thermodynamically stable and a complete coverage of the substrate by the thin film is obtained. When this condition is satisfied, a layer-by-layer growth, known as the Frank-van-der-Merwe mode is OBSERVED(Frank & Van der Merve 1949, Van der Merve 1963). Starting from $\delta = 0$, the Stranski-Krastanov growth is obtained, which corresponds to a 3D growth on the top of the thin film.
The excess interface energies calculated up to 6 Cu PM layers are reported in Tab. VIII.2.

	1PM	2PM	3PM	4PM	5PM	6PM
γ (J/m^2)	2.50	2.19	2.63	2.78	3.13	3.32

Tab. VIII.2 *: Comparison of the excess interface energy calculated for 1 to 6 PM Cu layers.*

Our computed free surface energy γ_f is 3.18 J/m^2 which is larger than the experimental value of 2.5 J/m^2 (Tyson & Miller 1977), but close to other theoretical values of 3.10 J/m^2 (Vitos *et al.* 1998) and 3.14 J/m^2, (Aqra & Ayyad 2011). The free Ta (100) surface energy exceeds the excess interface energy, resulting in $\delta < 0$, for up to 5 PM layers. As mentioned above, the increase in γ found for increasing number of layers, reflects the increase in strain energy.
The configuration with 2 PM layers on the top of the substrate corresponds to the most stable configuration for a thin film of Cu on Ta(1 0 0) while 1, 3, 4 and 5 Cu PM layers are metastable. Therefore, our calculations indicate that a Frank-van-der-Merwe growth mode is awaited up to 5 PM layers above which a Stranski-Krastanov mode should be expected. This result is consistent with experimental data which reported the presence of 1 or 2 wetting layers (Venugopal *et al.* 2009). For all the PM configurations, the high in-plane tensile strain induce a compensative high out-of-plane compressive strain among the Cu layers. The precise interplanar spacing and strain level for the case of 2 PM layers are presented in more details in the next subsection.
The excess interface energies for the two configurations involving Cu f.c.c. layers are not available from our calculations. Our attempt to relax a single Cu f.c.c. monolayer on Ta(1 0 0), as described in the previous section as the 6 Ta / 1 Cu f.c.c. configuration, did not converge to a reasonable structure, although we see the tendency to form at least a first PM layer. Our attempt to check for the possible stability of a single f.c.c. layer on top of the 2 PM layers also failed, as we observe a structural modulation of the f.c.c. structure out of plane indicative of periodic boundary conditions leading to non-zero strain.
As a comparison, we computed the wetting behaviour of Cu on Ta(1 1 0) and found that 1 pseudomorphic layer is thermodynamically the most stable configuration, while 2 pseudomorphic layers are metastable. The computed free surface energy of Ta(1 1 0) is 2.98 J/m^2 while the excess interface energy is 2.34 J/m^2 and 2.74 J/m^2, respectively. This result is at variance with the work of Hashibon & Elsässer *et al.* (2008) but consistent with several experimental works (Kuhn *et al.* 1993, Chen *et al.* 2000) reporting the observation of a PM monolayer.

VIII.2.4. Calculation of the structure factors

According to our DFT calculations, the configuration which has been found to be the most thermodynamically stable is 2 PM Copper layers on top of the (1 0 0) Ta surface. The agreement between DFT simulations can be demonstrated by calculating the structure factors of the relaxed configurations.
These calculation are performed using the software ROD(Vlieg 1999) according to Eq. (VIII.3):

$$F_{hkl}=\sum_j f_j e^{-B_j Q^2/(16\pi^2)} e^{2\pi i(hx_j+ky_j+lz_j)} \qquad \text{(VIII.3)}$$

where f_j is the atomic scattering factor of atom *j*, *B* the Debye-Waller parameter, *(hkl)* the diffraction indices and $(xyz)_j$ the position of atom *j* in fractional coordinates.
Fig. VIII.5. presents several comparisons between CTR measured from the clean Ta surface (CuTa4), and the simulated CTR for 1, 2 and 3 PM Cu layers. For both 1 1 L and 0 1 L it is clear that the best agreement and by far can be found for 2 PM layers. It is also interesting to notice that the structure factors are systematically overestimated at high exit angles. Despite this discrepancy, the 2 PM model manage to reproduce accurately all the peaks and curves inflection observed on the experimental data. It should be also pointed out that the best agreement between the simulated CTR and the measured one is systematically found for the cleanest Ta surface demonstrating the effect of surface contamination discussed in section VIII.1.

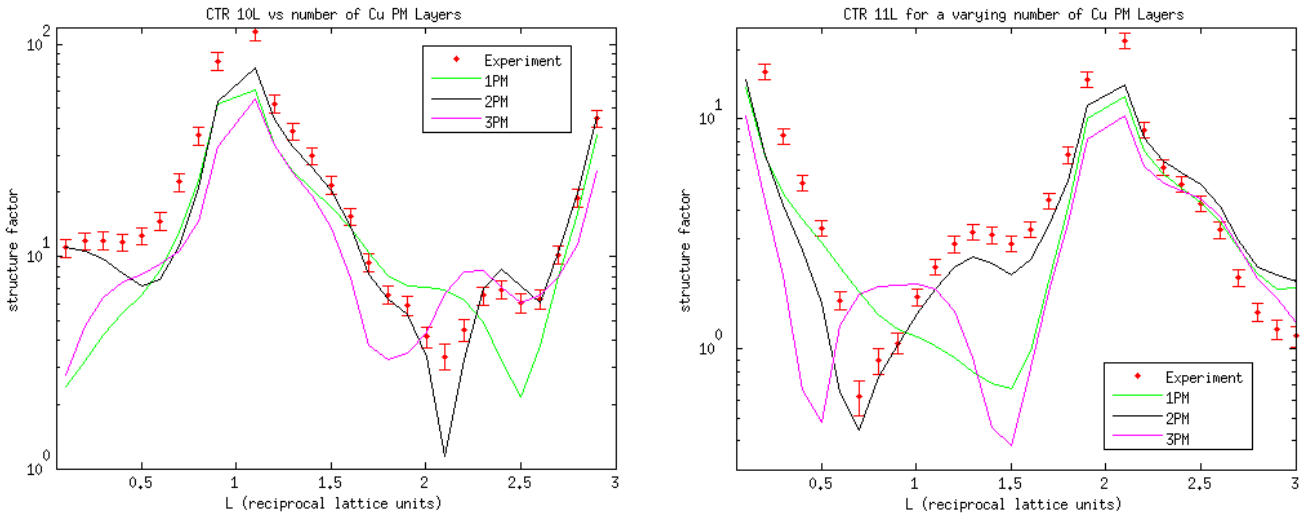

Fig. VIII.5 *1 0 L (a) and 1 1 L(b) calculated structure factors for a varying number of PM Cu layers compared with experimental data*

The position of the Cu layers for the configuration which manage to reproduce accurately the experimental data are illustrated in Fig. VIII.6. The high lattice mismatch between Copper and Tantalum induces an in-plane strain ε_{xx} of 31.4%. This results in a reduced Cu interplanar direction along the (0 0 1) direction by almost 36% for the 2nd Cu plane and 11% for the 1st Cu plane. The Tantalum atoms are also affected by the presence of neighbouring Cu atoms, and a strong relaxation can be observed for the first 3 Tantalum planes. The first two Ta interfacial planes are compressed by respectively 3.9 and 2.5% for Ta_{-1} and Ta_{-2}. To compensate for this compression the spacing between Ta_{-2} and Ta_{-3} significantly increase (by 2.3%). It is interesting to notice that the relaxation of Ta atoms is mostly limited to the first 3 interfacial planes. The spacing between Ta_{-4}, and Ta_{-5}, Ta_{-5} and Ta_{-6}, and Ta_{-6} and Ta_{-7} is indeed close to the bulk nominal value of Ta (respective variations of -0.3%, -0.45% and 0.24%).
To quantify the importance of the Ta relaxation and provide an accurate description of the Cu-Ta interface and surface, the structure factor of 4 different systems has been calculated and compared to the experimental data. In the first case, the relaxation of the Cu atoms is taken into account whereas the atomic positions for Ta are equal to their unrelaxed bulk values. In the 2nd, 3rd and 4th case, the relaxation of Cu is taken in account and the relaxation of the Ta atoms is restricted respectively to 2,3 and 7 Ta planes.
As illustrated in Fig. VIII.7, for up to 3 Ta planes, the number of Ta planes taken into account for relaxation has a very strong influence on the calculated structure factors. In all cases and independently of the number of relaxed Ta planes, the positions of the minima of amplitude are accurately reproduced for both CTR. However, the agreement between the calculated structure factors and the experimental data is not very good for less than 3 relaxed Ta plane. For the 1 0 L CTR, all 4 configurations manage to reproduce the drop of

intensity around L = 2.1, however the bump which is observed in the 2.2 < L < 2.6 region is only accurately

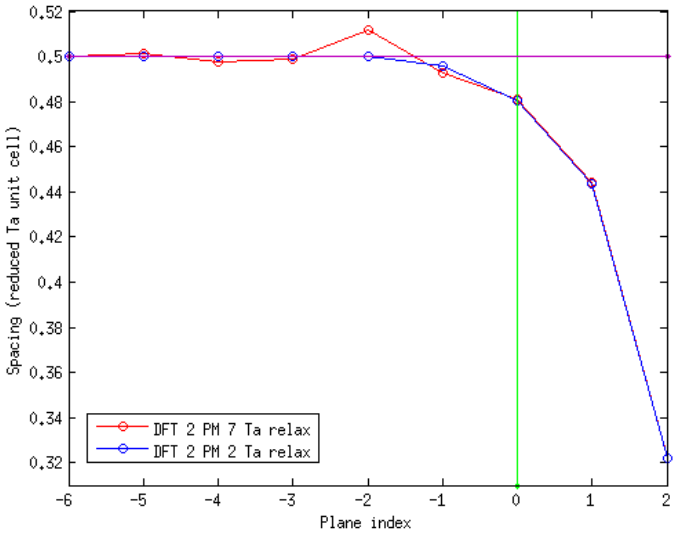

Fig. VIII.6 *Interplanar spacing versus plane index for 2 and 7 relaxed Ta planes.* The positions are expressed in reduced coordinates relatively to the Tantalum unit cell.

reproduced for Ta $\geq$ 3. Similar conclusions can be drawn for the 1 1 L CTR where the configurations with 0 and 2 relaxed Ta planes fail to reproduce the curve inflection in the 1 < L < 1.5 and 2.3 < L < 2.7 regions. The drop of amplitude for L = 0.7 is also strongly overestimated when the number of relaxed Ta planes is inferior to 3. The simulated CTR for 3 and 7 relaxed Ta planes exhibit a remarkable similarity. This tends to confirm that the relaxation of the Ta planes is mostly limited to the first 3 interfacial planes and is consistent with the small value of displacements found for the Ta planes further away from the Cu-Ta interface.

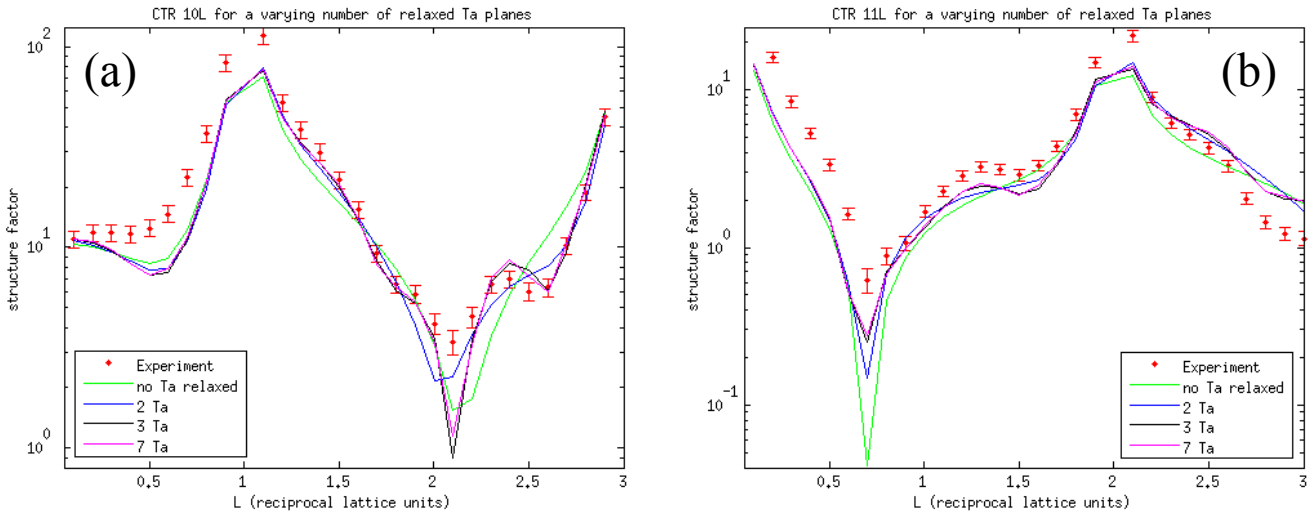

Fig. VIII.7 *Influence of the number of relaxed Ta planes on the calculated 10L (a) and 11L(b) structure factors*

Comparison between experimental data and calculated structure factors allowed to determine the number of stable PM layers and to provide a precise estimation of the interplanar distance for the surface atoms.
If the calculated structure factor from the model structure described in subsection VIII.2.2 is in good agreement with the experimental data, it should be pointed out that the measurements carried out at ESRF were only sensitive to PM layers, since the scans are done along the Ta CTRs. However the presence of

f.c.c. copper on top of the PM Cu layers can not be excluder and is likely to modify the interplanar spacing between the Cu layers.

VIII.2.5. Fitting of the experimental data

The calculated structure factor is a sum of the bulk contribution and the surface contribution (Vlieg 1999):

$$F_{tot} = SR\left[(1-f_s)\sum_j \alpha_j F_{b,j}^2 + f_s \sum_j \alpha_j \left(F_{b,j}+F_{s,j}\right)^2\right]^{1/2} \quad \text{(VIII.4)}$$

where S is the scale, R the roughness parameter, f_s the fraction of the crystal covered by a surface layer, α_j is the occupancy of domain j, $F_{b,j}$ and $F_{s,j}$ are respectively the structure factors of the j^{th} domain of the bulk and of the j^{th} domain of the surface unit cell.
According to Eq. (VIII.3) and (VIII.4), there is a total of 6 parameters can be fitted in order to improve the agreement with the experimental data: the scale, the roughness, the surface fraction, the occupancy, the interplanar spacing and the Debye-Waller factor. Fig. VIII.8. shows a comparison between the experimental data and the DFT calculations before and after fitting. The parameters used for the fit are listed in Tab. VIII.3. A readily reasonable agreement can be found between DFT calculations and experimental data by fitting only the scale.

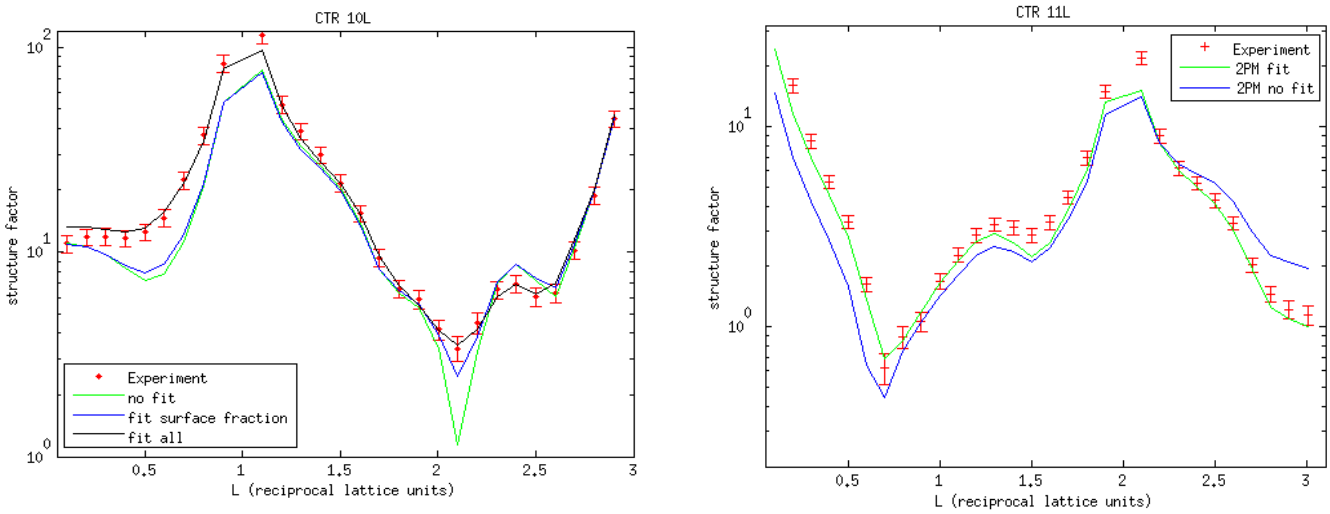

Fig. VIII.8: *1 0 L(a) and 1 1 L(b) calculated structure factors, before and after fitting*

For the 1 0 L CTR, the fit is done on the first data set (CuTa1) since it has presumably the lowest level of surface contamination. As shown in Fig. VIII.8, fitting only one experimental parameter, the surface fraction allows a much better agreement with the experimental data.
To further improve the fit the inter planar spacing and the Debye Waller factor of the surface atoms are relaxed. The displacement obtained expressed in reduced coordinates remain very small, demonstrating that the inter planar spacing is accurately predicted by DFT calculations. The Debye-Waller factors obtained from the fit are significantly larger than the bulk value especially for the second Cu layer, however, they are in the right order of magnitude.
The fit of the 1 1 L CTR is done on the fourth data set (CuTa4). One can notice that the surface fraction is significantly higher than the one found for CuTa1. This can probably be explained by the differences in the surface preparation detailed in subsection VIII.1.1.
Similarly to the 10L CTR, a good agreement with the experimental data is obtained by applying rather large Debye-Waller factors (even larger than for the 10L CTR), while the calculated displacements are very small and in good agreement with the DFT calculations.

	1 0 L	1 1 L
Scale	0.4713	0.1561
Roughness	0.014	0.0173
Surface fraction	0.9396	0.9805
Spacing Ta_{-2} Ta_{-3}	-0.0048	
Spacing Ta_{-1} Ta_{-2}	-0.0041	
Spacing $Ta_0$$Ta_{-1}$	-0.0005	0.0041
Spacing Cu_1 Ta_0	0.0108	0.0056
Spacing Cu_2 Cu_1	-0.0207	0.0094
Debye-Waller Ta_{-1}	0.9886	
Debye-Waller Ta_0	1.1877	4.1520
Debye-Waller Cu_1	2.4648	4.3292
Debye-Waller Cu_2	8.0034	8.0562

Tab. VIII.3 *Parameters used for the fitting of the structure factors.*

VIII.3. Atomistic simulations with an angle-dependent potential for the Cu-Ta system

The DFT calculations provide a very good agreement with the experimental data. Both calculations of the excess interface energy and of the structure factor confirm that the most stable interface consists of 2 PM layers of Cu on the Ta (1 0 0) surface. However, the high computational cost of DFT simulations limits the size of the simulations. It is already difficult to evaluate the stability of f.c.c. layers of Cu on top of the b.c.c. Ta surface, given the number of atoms involved in the simulation. For the same reason, the prediction of the growth mode above the first PM layers can not be achieved with DFT calculations. The study of the dewetting of the Cu thin film on the Ta surface that will be presented in the next section can only be achieved through large-scale atomic simulations. These simulations relies on the use of interatomic potentials.

Large-scale atomic simulations can provide new insights in the understanding of the structure of bimetallic interfaces. However, the lack of reliable cross interatomic potentials for binary systems prevented their use in a large range of systems. Most of them are based on the embedded-atom method (EAM, Daw & Baskes 1984). If reliable EAM potentials have been developed for f.c.c. metals such as Cu (Mishin *et al.* 2001), they are less adapted for b.c.c metals due to the angular dependency of the interatomic forces. An EAM potential for the Cu-Ta system has been developed (Johnson 1990) and applied to simulations of Cu-Ta interfaces (Klaver and Thijsse 2003, Lazić *et al.* 2010), but this model lacks an accurate description of the atomic bonding as it does not take into account their angular dependence.

This lack of reliable cross potentials for the Cu-Ta system has been eventually overcome in 2008, by the development of an angle-dependent potential (ADP) (Hashibon, Lozovoi *et al.* 2008). This potential was modeled by crossing two existing potentials for pure Cu (Mishin *et al.* 2001) and Ta (Mishin & Lozovoi 2006). It was tested against first-principle energies (Hashibon, Elsässer *et al.* 2008) and applied to molecular dynamics simulations of wetting and dewetting of Cu and Ta. It was found that a Cu thin film placed on top of a Ta(1 1 0) surface dewets from it, forming a Cu droplet on top of a stable Cu monolayer, while a drop of liquid Cu placed on a clean Ta(1 1 0) surface spreads over it as a stable monolayer.

These results are in good agreement with experiments (Kuhn *et al.* 1993, Chen *et al.* 2000) and first-principle calculations (Hashibon, Elsässer *et al.* 2008). They validate the potential for describing the Cu-Ta interface on a Ta (1 1 0) surface. We have seen in the previous sections, that the wetting behaviour and structure of the Cu ML on top of a Ta (1 0 0) are very different from what has been observed on a Ta (1 1 0)

surface. In the following, the validity of the potential potential to describe the Cu-Ta(1 0 0) interface is discussed extensively.

VIII.3.1. Calculation of the excess interface energies

To evaluate the accuracy of the potential, the structures described in section I.2 have been modeled and relaxed using the ADP potential. The relaxation is performed at 0 K by energy minimization, using a quench dynamical algorithm (Rodney *et al.* 2005). The excess interface energies are calculated at the end of the relaxation using Eq. (VIII.1), and the structure factor are calculated from the atomic positions obtained in the relaxed configuration. Due to the very low computational cost for Molecular Statics (MS) on such small systems, the stability of a larger range of configurations has been evaluated. 1 to 6 Cu ML are put on top of the Ta (1 0 0) substrate. For a given number of ML, all the possible combinations of f.c.c and PM layers, with all the PM layers between the substrate and the f.c.c. layers, are tested. For instance for 2 ML, three cases are evaluated: 2 PM layers, 1 PM layer and 1 f.c.c. and 2 f.c.c. layers.
For the f.c.c layers, the in-plane strain is minimized by creating a supercell of 22 x 22 Cu atoms on top of 17 x17 b.c.c. Ta. This corresponds to an in-plane strain of -0.07% (-7.10^{-4}) with a_{Cu} =3.615 Å and a_{Ta} =3.3058 Å (bulk values). This value is sufficiently low to consider that the system is almost strain free before relaxation.
Table 2 presents some of the results obtained for up to 6 ML of Cu. Contrary to the results presented for molecular statics (MS) simulations, the atoms are relaxed in all directions of space, such that a reorganization of the atomic structure is possible. To allow meaningful comparisons with the DFT calculations, the values of excess interface energies when only the relaxation of the z position is authorized are also given.

	1 PM	1 f.c.c	2 PM	1 PM / 1 f.c.c	2 f.c.c	3 PM	1 PM / 2 f.c.c	5 PM	1 PM / 4 f.c.c	3 PM / 2 f.c.c	6 PM	7 PM	1 PM / 6 f.c.c
γ(J/m^2)	0.89 0.89	1.08 2.25	0.92 0.93	1.27 2.08	1.64 3.02	1.65 1.66	1.78 2.53	1.90 2.12	2.05 2.55	2.08	1.95 2.33	2.00 2.57	2.10 2.55

Tab. VIII.4 *Comparison of the excess interface energies, calculated with the ADP potential for 1 to 6 Cu ML.* The values in black (in red) are calculated for a relaxation of x,y and z positions (of the z position only)

The first comment that can be made from these values is the overall tendency of the excess interface energies to be very low, as compared to the values obtained from the first-principle calculations.
For the sake of comparison, the free surface energies of the Ta (1 0 0) and Ta (1 1 0) have been calculated. They are equal respectively to 2.24 J/m^2 and 2.06 J/m^2 which is much lower than the values obtained for the first-principle calculations (3.18 J/m^2 for Ta(1 0 0) and 2.98 J/m^2 for Ta(1 1 0)) but quite close to the experimental value of 2.5 J/m^2 (Tyson & Miller 1977). The surface energies of relaxed Cu (1 1 1) and (1 0 0) surfaces are calculated to be respectively 1.24 J/m^2 and 1.34 J/m^2, values significantly lower than the experimental value of 1.8 J/m^2 (Tyson & Miller 1977).
Since the values of the free surface energies are clearly underestimated, it is not surprising to calculate very low values for the excess interface energies. However, it should be noticed though that the values obtained for 1 and 2 PM layers are unexpectedly low as compared to the free surface energy of Ta (1 0 0). If we compare the ratio between the excess interface energy for 1 PM layer and the free surface energy of Ta (1 0 0), a value of only 0.41 is obtained for the ADP potential as compared to 0.78 for the first-principle calculations. Above 3 PM layers, the agreement is much better with 0.74 for the ADP potential and 0.82 for the first-principle calculations. These values for 1 and 2 PM are discussed in more details in subsection VIII.3.3.
Regarding the stability of the ML, the results also slightly differ as compared to the DFT calculations. While the latter clearly points to a larger stability of the 2 PM layers, the trend is less clear with the ADP potential. The excess interface energies are indeed comparable between 2 PM and 1 PM, with the latter being slightly lower. It should be noted that a sharp increase of γ occurs between 2 and 3 PM while it increases more steadily above 3 PM. It is thus clear that the maximum number of PM layers is strictly inferior to 3.

It is also obvious from the calculations that for few Cu layers, the f.c.c. structure is far less stable than the b.c.c. structure. For one PM layer, the relatively low excess interface energy found for 1 f.c.c as compared to 1 PM can be attributed to a transformation of the f.c.c. layer to a b.c.c. layer upon relaxation. The f.c.c. layer being more densely-packed than the PM layer, the atoms that can not fill the first PM layer decorate the 2nd plane (Fig. VIII.9.a). When the relaxation is constrained to the z direction, the transformation into b.c.c. is not possible, and the highly unstable f.c.c. layer forms ripples (Fig. VIII.9.b). Its excess interface energy is even larger than the free surface energy of Ta (0 0 1), suggesting that this layer is unstable.
For up to five layers, the f.c.c. layers with a (0 0 1) orientation are not stable. Depending on the initial number of f.c.c layers, 1 or 2 PM layers generally form at Cu/Ta interface, with highly defective and disordered planes on top of them (Fig. VIII.9.c).

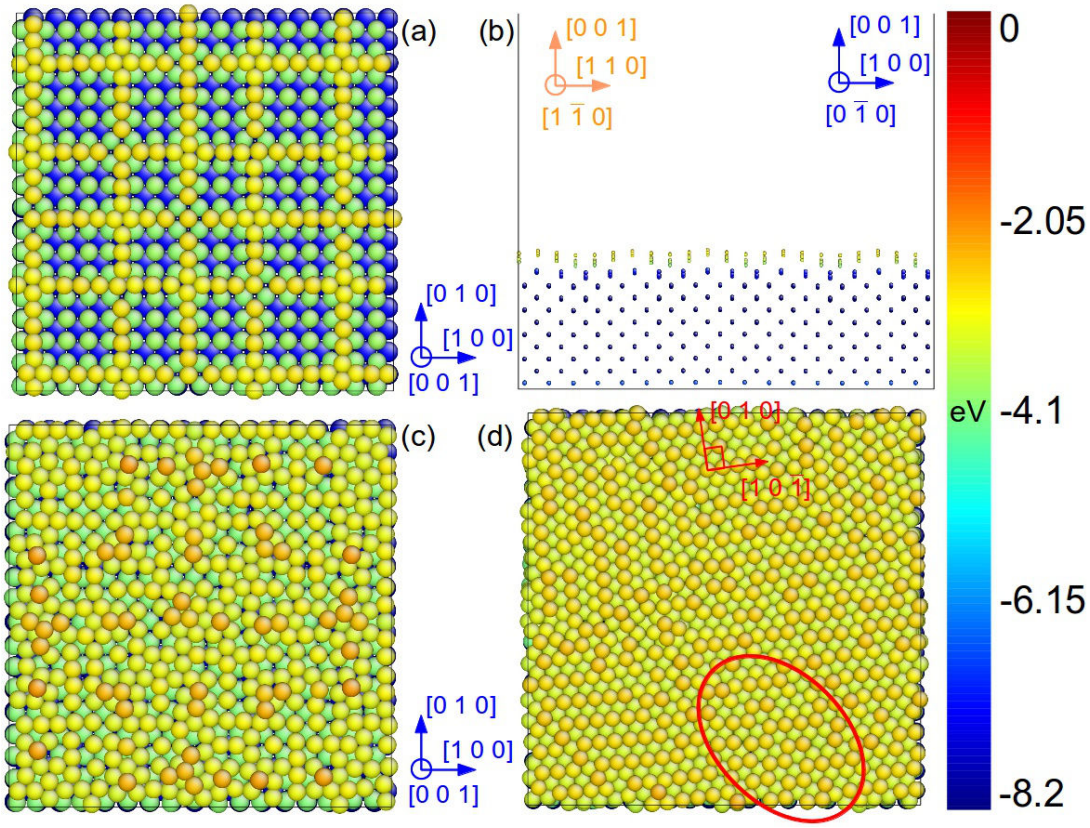

Fig. VIII.9: *Atomic structures from a different set of initial Cu thin films obtained by energy minimization at 0K with the ADP potential.* The color coding corresponds to the energy of the atoms. The axis directions in blue indicate the orientation of the Ta substrate while the ones in orange indicate the orientation of the Cu atoms. (a) 1 f.c.c Cu layer on top of a (0 0 1) Ta surface relaxed by energy minimization in all three directions of space (b) side view of the same f.c.c layer relaxed only along the z ([0 0 1]) direction (c) 2 f.c.c Cu layers on top of a (0 0 1) Ta surface relaxed in all three directions of space (d) 7 P.M Cu layers on top of a (0 0 1) Ta surface relaxed by energy minimization in all three directions of space. The crystal structure in the region circled in red can be described as a fish bone structure (see text for more details)

Conversely, the PM structure is very stable for few Cu layers but unstable for a large number of layers.
For up to 3 PM layers, the relaxation of the structure is only achieved through a decrease of the interplanar distance. Indeed, the excess interface energies have exactly the same values for a relaxation in three dimensions and a relaxation along z only. Above 5 PM, the structure is not stable anymore, as illustrated by the divergence between the excess energies calculated for a relaxation along z and for a relaxation in three dimensions (Tab. 4). The strain contribution which is extremely large for a PM layers increases linearly with the number of layers ($\frac{1}{2}E\varepsilon_0^2h$), causing their instability above 5 layers. This instability is reflected in the

calculated excess interface energies. It exceeds the Ta (1 0 0) free surface energy for $n_{layers} > 5$ when the atomic reorganization of the layer is not allowed (relaxation only along z). This is in very good agreement with the DFT calculations for which the number of metastable PM layers is found to be exactly the same.
For a larger number of PM layers, a stable structure is achieved through the transformation of the PM planes into several grains with a pronounced (1 1 0) texture on top of two stables PM layers.
At the grain boundaries, the atomic structure resembles to the fish-bone structure (region circled in red) that was found by Klaver and Thijsse 2003 for a simulated growth of a Cu thin film on a (0 0 1) Ta surface.
In summary, when the atoms are relaxed in all directions, for up to 7 layers and independently of the proportion of f.c.c and PM layers, all the calculated excess interface energies are lower than the free surface energy of the (1 0 0) Ta surface. The stability of the thin film is achieved through a reorganization of the atomic structure. For a low number of Cu layers, the f.c.c. structure is not stable and the presence of a few f.c.c layers on top of the 2 PM layers that were measured experimentally is thus highly improbable.
Similarly to the DFT calculations, the maximum number of stable PM layers is found to be 5. Above this limit, the stability of the structure is achieved through the transformation of the PM layers into highly disordered f.c.c. layers with a (1 1 0) texture. The preferred orientation for the 3D islands is not clearly determined at this point, and will be the object of the next chapter.

VII.3.2. Calculation of the structure factors

As in subsection I.2.4 for the DFT calculations, the agreement of the experimental data and the ADP calculations can be evaluated through the calculation of the structure factors for the relaxed atomic positions. Fig. VIII.10. presents a comparisons between the 1 1 L CTR measured from the clean Ta surface (CuTa4), and the simulated CTR for 1, 2 and 3 PM Cu layers (a) and for a varying number of relaxed Ta planes.

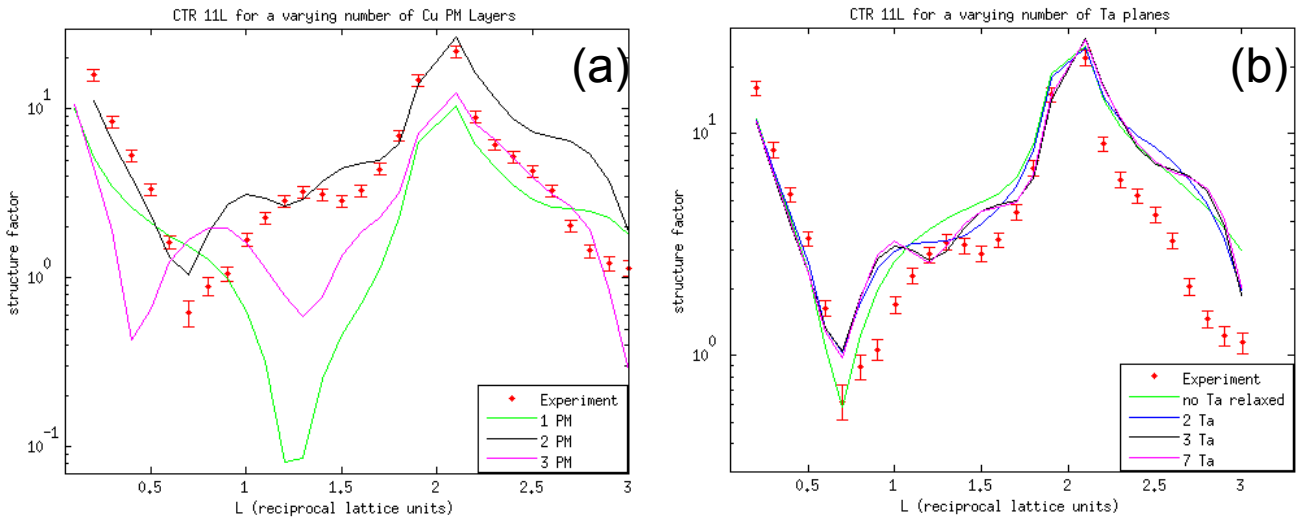

Fig. VIII.10: *Calculated structure factors with the ADP potential* (a) 1 1 L calculated structure factor for a varying number of PM Cu layers compared with experimental data (b) Influence of the number of relaxed Ta planes on the calculated 1 1 L structure factor

The agreement is not as good as for the DFT calculations where a very good conformity was found for 2P M layers, even without fitting the data. Here the "best" agreement is also clearly found for 2 PM, but the peaks and inflections of the curve are not well reproduced. If the minimum and maximum of the structure factors are in reasonably good correspondence (respectively for L = 0.7 and L = 2 in both cases), the agreement is particularly bad in the $1 < L < 1.5$ region. The bump observed at L = 1.3 on the experimental data, which was attributed to the relaxation of the topmost planes of the Ta substrate, corresponds to a dip for the ADP calculations. Conversely, two bumps are observed for L = 1.0 and L = 1.6 on the simulated data, which are absent on the experimental one.
Similarly to the DFT calculations, it is clear that the relaxation of the Ta planes plays an important role on the

calculated structure factor.
Surprisingly, the best agreement is found when the relaxation of the Ta planes is not taken into account. The agreement with the experimental data is in this case particularly good for the low exit angles. This suggest that the relaxation of the Ta planes is not accurately reproduced by the ADP potential.
To confirm this hypothesis, the spacing between the surface layers is plotted in Fig.VIII.11 and compared with the positions obtained from the DFT calculations.

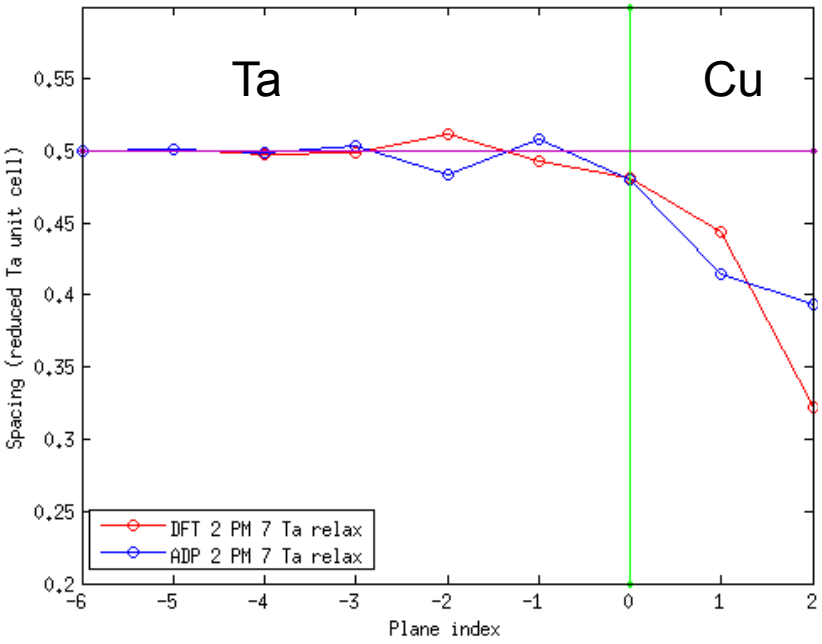

Fig. VIII. 11*: Interplanar spacing versus plane index for the ADP and DFT calculations*

The discrepancy between the ADP and DFT calculations is significant.The two Cu surface planes both undergo contraction, but the contraction of the topmost Cu plane is largely underestimated with the ADP potential (-21% contraction vs -36%), while the contraction of the 1st Cu layer is significantly overestimated (-17% vs -12 %). For the Ta planes, the agreement is even worse. For the topmost Ta plane (Ta_0), a similar level of contraction is found for the ADP and DFT simulations (respectively -4 and -3.8%). On the other hand, where the 2nd and 3rd were found to be respectively in contraction (-1.5%) and expansion (+2.3%) for the DFT simulations, a completely opposite behaviour is found for the ADP potential with respective expansion of +1.5% and contraction of -3.3%. The level of contraction or expansion for the two Cu surface planes, and for the five topmost Ta planes is summarized in Tab. VIII.5.

	Ta_{-4}	Ta_{-3}	Ta_{-2}	Ta_{-1}	Ta_0	Cu_1	Cu_2
DFT	-0.5%	-0.3%	+2.3%	-1.5%	-3.8%	-11%	-36%
ADP	-0.3%	+0.8%	-1.5%	+3.3%	-4%	-17%	-21%

Tab. VIII.5 : *Summary of the contraction and expansion of the surface planes for the DFT and ADP simulations*

In both cases, it is clear that the relaxation of the Ta substrate is essentially limited to the three closest planes to the interface. This is in good agreement with Fig. VIII.7 & VIII.10.b where almost no difference is observed for the structure factors calculated for 3 relaxed Ta planes and 7 Ta planes.
The origin of the extra bumps at L = 1.0 and L = 1.6 for the 1 1 L CTR (ADP simulations) is also clearly related to the relaxation of the Ta planes. It is thus clear that the ADP potential mostly fails to predict the precise atomic structure at the Cu-Ta interface, even though the best agreement is found for 2 PM layers like the DFT calculations.

VIII.3.3. Testing the potential

Both the unexpectedly low values calculated for the excess interface energies and the poor ability of the potential to predict the precise atomic structure at the Cu-Ta interface question the accuracy of the potential for the prediction of the Cu-Ta(1 0 0) interface. In the work by Hashivon, Lozovoi *et al.* (2008), the potential was extensively tested against first-principle calculations. The phase diagram of the Cu-Ta system practically shows zero mutual solubility between Cu and Ta and does not contain any intermetallic compound or other solid phases (Massalski 1986). To use this potential for the study of the Cu-Ta interface, it is thus a requisite that it does not produce any stable Cu-Ta compounds at any composition or temperature. The relative formation energy ΔE of several artificial f.c.c.-based layered structures containing stacking sequences of CuCuTa and CuTaTa (1 1 1) was calculated and compared to the equilibrium f.c.c. Cu (1 1 1) and b.c.c. Ta (1 1 0) around the energy minimum. In each case the relative formation energy was found to be positive, indicating that all the compounds were instable. The agreement between the ADP calculations and the first-principles calculations was reasonably good, indicating that the potential is suitable for atomistic simulations of this system.
Here we extend the calculations by Hashibon by calculating the relative formation energies for artificial layered structured representing possible atomic arrangements at the Ta (0 0 1) // Cu (0 0 1) interface. The stability of several stacking sequence is evaluated for both the f.c.c. (0 0 1) and the b.c.c. (0 0 1) structures.
To ensure the validity of our calculations, the formation energies of stacking sequences with a (1 1 1) f.c.c orientation are also calculated and compared to the results obtained by Hashibon. Finally, the stability of the CuCuTaTa b.c.c (1 1 0) sequence which was not tested by Hashibon is also evaluated.
Tab. VIII.6 summarizes the equilibrium formation energies of these compounds obtained by ADP calculations :

Structure	ΔE (eV)
CuCuTa / f.c.c (1 1 1)	0.171 (0.172)
CuCuCuTaTaTa / f.c.c (1 1 1)	0.356 (0.351)
CuTaTa / f.c.c (1 1 1)	0.304 (0.294)
CuCuTaTa / b.c.c (1 1 0)	-0.020
CuCuCuTaTaTa / b.c.c (0 0 1)	-0.030
CuCuCuTa / b.c.c (0 0 1)	0.153
CuCuTaTa / b.c.c (0 0 1)	0.033
CuCuCuTaTaTa / f.c.c (0 0 1)	0.252

Tab. VIII.6: Equilibrium formation energies (in eV per atom, relative to f.c.c Cu and b.c.c Ta) of Cu-Ta compounds obtained with ADP potential. The value in brackets are the values calculated by Hashibon for the same structure

The formation energies calculated for the 1 1 1 f.c.c compounds are equivalent to the values found by Hashibon. That was expected since the same ADP potential is used and confirm the validity of our calculations. Way more problematic, it appears that the potential can form some stable Cu-Ta compounds.
For the Ta (0 0 1) surface, very low but positive formation energies are found for the CuCuCuTa / b.c.c (0 0 1) and CuCuTaTa/ b.c.c (0 0 1) structure. However the formation energy is found to be negative for the CuCuCuTaTaTa / b.c.c (0 0 1) compound which is obviously not expected for a system with zero-mutual solubility. A similar negative formation energy for the CuCuCuTaTaTa / b.c.c. (1 1 0) compound. On the other hand all the compounds with a f.c.c structure (either (1 1 1) or (0 0 1)) have a formation energy which is largely positive and comparable to the DFT calculations (at least for the (1 1 1) orientation).
It is thus obvious that the stability of the b.c.c Cu atoms (*i.e.* the Cu PM layers) is largely overestimated for both the (0 0 1) and (1 1 0) orientation.

This explains the unexpectedly low excess interface energies that were found for 1 and 2 PM Cu layers, while the energy of the single f.c.c layer was in the expected range. The excess interface energy for a single PM Cu layer on top of a Ta (1 1 0) surface is found to be 0.43 J/m^2 as compared to the 2.34 J/m^2 obtained from the DFT calculations. Converted into ratio with respect to the Ta(1 1 0) free surface energies, respective values of 0.21 and 0.78 are found for the ADP and DFT calculations. It confirms that the problem is not restrained to the (0 0 1) orientation which is surprisingly not discussed by Hashibon in his paper.

We conclude that excess interface energies for very few monolayers calculated with the ADP potential are largely wrong and the ability of this potential to finely predict the Cu-Ta interface appears very questionable. That being said, the tendencies obtained with the potential are in good agreement with the DFT calculations. The same number of stable PM layers is predicted, and the presence of 2 PM layers on top of the (0 0 1) Ta surface appear to be very favourable energetically. However, contrary to the DFT calculations, it can not be clearly asserted that 2 PM layers are more stable than a single one.

VIII.3.4. Application to the solid state dewetting of a Cu thin film

While the ADP potential fails to predict the precise atomic structure at the Cu-Ta interface for a few atomic layers, it correctly predicts the instability of a single Cu atomic layer and of thicker thin films on the Ta(110) surface, in agreement with experimental observations (Kuhn et al. 1993, Chen et al. 2000) and DFT calculations (Hashibon, Elsässer et al. 2008). It is thus possible that the potential can accurately predict the wetting or dewetting behaviour of Cu thin films on top of a (1 0 0) Ta surface and even provide a precise description of the atomic structure at the interface between the Ta substrate and the 3D islands grown on top of the 2 PM layers.

In the two examples presented in this section we aim at simulating the solid state dewetting of the Cu thin film on a Ta(0 0 1) surface. This topic is the object of Chapter IX, and the structure of the islands and of the CuTa interface shall not be detailed. With this simulation, we seek to demonstrate that the potential predicts the correct number of the PM layers between the Cu islands. To this end we examine two different initial configurations, with a similar structure of the thin film but a different number of PM layers. Given that the simulation is done below the melting point of Cu, the diffusion of the Cu atoms is not sufficient to achieve the solid state dewetting from a continuous thin film in a reasonable amount of time. The starting point of the simulation consists of a truncated Cu thin film with sharp boundaries along the [1 1 0] and [1 $\bar{1}$ 0] corresponding to the [1 0 0] and [0 1 0] directions of the Ta substrate (Fig. VIII.12.a & VIII.12.c). As seen on Fig. VIII.12.a, the first initial structure sits on the bare Ta substrate, while it is deposited on a single PM layer for the second one. The Cu thin film composed of 11 f.c.c layers and the orientation relationship with respect to the Ta substrate has been described in subsection VIII.2.2 : Cu (0 0 1)[1 1 0] || Ta (0 0 1)[1 1 0]. The in-plane strain is minimized by adjusting the lateral width of the thin film. The minimum value of in-plane strain of -0.07% is obtained for 23 atoms of Cu on top of 18 atoms of Ta. The first initial structure contains 6348 atoms while the second one contains 6973 atoms owing to the extra PM layer structure (Fig. VIII.12.c). The Ta substrate is composed of 10 planes of 25x25 = 625 atoms each corresponding to a total number of 6250 Ta atoms. As shown in Fig. VIII.12.a and 12.c, the substrate is significantly larger than the Cu thin film to leave sufficient space for the Cu atoms to diffuse on the Ta surface. Periodic boudaries are applied along the in-plane x and y directions.

The evolution of the two configurations is studied at 1040 K, way below the melting temperature of the bulk Cu (1357 K), but quite close to the melting point in this simulation given the small number of Cu atoms in the the thin film (Yeshchenko et al. 2007, Attarian Shandiz et al. 2007)). This temperature was also chosen because it is consistent with the temperature at which the solid state dewetting is performed experimentally (1073K).

For the first initial configuration, the thin film is annealed during 23.5 ns at 1040K. This annealing is followed by a quench to room temperature (RT, 300K), and an energy minimization at 300K to suppress the thermal noise.

For the 2nd configuration, the annealing time is shorter and equal to 8.64 ns. It is also followed by a quench from the annealing temperature to the RT in 0.8 ns and a subsequent energy minimization.

As stated previously, the microstructure of the dewetted island and particularly the structure of the Cu-Ta interface will be discussed in extensive details in Chapter IX. For this section we are mainly interested in the structure of the interface outside the island. We evidenced experimentally the presence of two 2PM on top of the Ta (1 0 0) surface, and a number of PM layers consistent with the experiment would be encouraging and would increase our conviction that the potential can predict the good Cu-Ta interface, despite the limitations mentioned in subsections VIII.3.2 & VIII.3.3

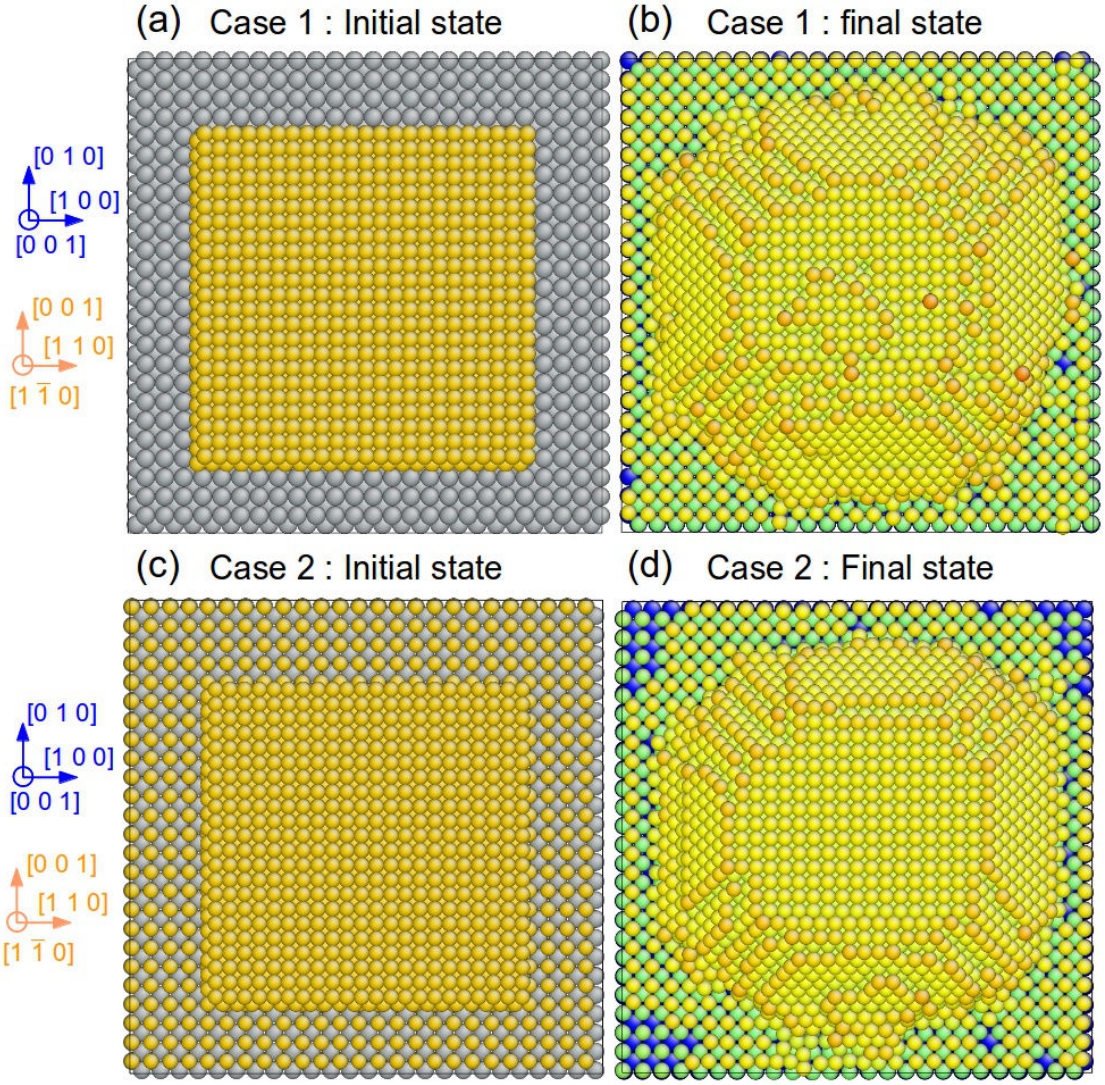

Fig. VIII.12 *Simulation of the solid state dewetting of Cu islands on a (0 0 1) Ta surface for a varying number of PM layer in the initial configuration.* (a) f.c.c. (0 0 1) Cu thin film on top of the (0 0 1) Ta substrate. (b) Dewetted island on top of 2 PM layers after 23 ns at 1040K. (c) f.c.c. Cu thin film on top of a single PM layer (d) Dewetted island on top of 2 PM layers after 8.64 ns at 1040K.

As illustrated in Fig. VIII.12.b & VIII.12.d, the final shape of the island is remarkably reproducible (Chapter IX for more details) and two PM copper layers are covering the Ta substrate in the final stage of both simulations. For the configuration with no PM layer in the initial state, the complete coverage of the first layer is almost completely achieved after 13 ns while the coverage of the second one is completed in about 20 ns. It should be also noted that the coverage of the 2nd layer begins at early stages of the simulation, and long before the coverage of the first-layer is completed. No start of the initiate of the covering of a third layer can be evidenced at any stage of the simulation. For the second simulation, the substrate is entirely covered by a single PM layer in the initial state, and a second layer starts forming at early stages of the simulation

and is almost achieved after 8.5 ns.
The reproducibility of this interface and its consistency with the experimental data is very encouraging. Despite the lack of accuracy of the potential in the precise description of the Cu-Ta interface (bad prediction of the relaxation of the topmost Ta planes), and the limitations highlighted in section VIII.3.3, the ADP potential manages to accurately reproduce the number of PM layers outside the islands, independently of their initial number. This and the fact that is clearly the best potential to describe the Cu-Ta interface justify its use in Chapter IX for the prediction of the Cu-Ta interface in the dewetted islands.

Conclusions

We have presented a detailed study of the Cu(0 0 1)/Ta(0 0 1) interface by surface X-ray diffraction and DFT and MD calculations. For the experimental part, the solid-state dewetting of a copper thin film on a carefully prepared Ta surface was performed *in situ* during two successive experimental runs. Several crystal truncation rods were measured after the dewetting of the thin-film to determine the precise structure of the Cu-Ta interface. It was evidenced that the CTR measurements are strongly influenced by the level of surface contamination. A careful preparation procedure allowed to obtain an almost contamination free Ta surface after dewetting, but it was clearly demonstrated that most of the contamination occurred during the CTR measurements. Since several samples were measured, the CTR were measured for different level of surface contaminations and a very good reproducibility was found for a similar level of surface contamination.
The DFT calculations allowed to gain a new insight in the experimental results. From the calculation of the excess interface energies, up to 5 ML of PM Cu were found to be metastable on top of the Ta (1 0 0) surface. The most stable interface was found to be 2 PM layers. The agreement with the experimental data was evaluated through the calculations of the structure factors from the relaxed atomic positions, and for a varying number of PM layers and of relaxed Ta planes. The best agreement was found to be by far for 2 PM layers, in good agreement with the calculations of the excess interface energies. It was also evidenced that the relaxation of the interfacial Ta planes plays a large role in the calculated structure factor and that a precise description of the interface is only achieved if the first three Ta planes are relaxed. The agreement between the experimental data and the DFT calculations was found to be very good without any fitting of the experimental data, but a fitting of the experimental data was performed to reinforce this agreement.
The study of the dewetting of the Cu thin film on the Ta surface that will be presented in Chapter IX can only be achieved through large-scale atomic simulations. These simulations relies on the use of interatomic potentials. To ensure of the ability of the ADP potential to predict the interface between the substrate and the dewetted islands, it was tested against the DFT calculations and the experimental data.
The calculation of the excess interface energies revealed some discrepancies with the DFT calculations. They were found to be unexpectedly low, especially for a low number of PM layers. Additionally, the superior stability of the 2 PM layers as compared to a single PM layer was not clearly established. On the other hand, the potential predicted the metastability of up to 5 PM layers as in the DFT calculations. The large difference of excess interface energies between n=2 and n=3 PM layers also demonstrates that the potential predict a number of PM layers strictly inferior to 3.
The precise description of the precise Cu-Ta interface (spacing between the layers) was found to be much less satisfying than with the DFT calculations. In particular, the relaxation of the Ta substrate was quite badly reproduced.
To understand these discrepancies, the potential was tested by calculating the equilibrium formation energy of several compounds consisting of alternating layers of Cu and Ta with both f.c.c. and b.c.c. structure. The equilibrium formation energies was found to be unexpectedly low for all the b.c.c compounds, and even negative for some of them. This is a clear evidence that the stability of the cu b.c.c. layers are clearly overestimated with the potential, and it explains why such low excess interface energies were found for a low number of PM layers.
In the last section the potential was applied in MD simulations of the solid state dewetting of a Cu thin film on a Ta (1 0 0) surface for various initial configurations. At the end of the simulated dewetting an encouragingly reproducible number of 2 PM layers was found independently of the initial configuration. This result is consistent with both the DFT calculations and the experimental data, and demonstrate that the potential can predict the good interface for the thin film outside the islands. The shape of the island is also

very reproducible and very consistent with the experimental observations and will be discussed in Chapter IX. Despite the evident limitations pointed out in sections VIII.3.2 andVIII.3.3 this potential will thus be used to predict the interface between the Ta (0 0 1) and the dewetted islands.

Bibliography

Attarian Shandiza , M., Safaeia , A., Sanjabia, S., Barberb, Z.H. (2007) *J. Phys. Chem. Sol.* **68**, 1396-1399.

Aqra, F. & Ayyad, A. (2011) *Appl. Surf. Science* **257***,* 6372-6379

Andrews, S. R. & Cowley, R. A. (1985) *J. Phys. C* **18**, 6247

Ball, M. J., Lucas, C. A., Markovic, N. M., Stamenkovic, V. & Ross, P. N. (2002) *Surface Science* **518**, 201.

Bloch, J.M. (1985) *J. Appl. Cryst.* **18***,* 33

Chen, L., Magtoto, N., Ekstrom, B. & Kelber, J. (2000) *Thin solid films* **376**, 115

Daw, M. S. & Baskes, M., I. (1984) *Phys. Rev. B* **29**, 6443 (1984).

Feidenhans'l, R. (1989) *Surface Science Reports* **10**, 105-188

Fillot, F., Tőkei, Zs. & Beyer, G. P. (2007) *Surf. Science* **601**, 986

Frank, F. C. & Van der Merwe, J. H. (1949) *Proc. R. Soc. London*, *Ser. A* **198**, 205

Freund, L. B. & Suresh, S. (2003) Thin Film Materials: Stress, Defect Formation and Surface Evolution, edited by Cambridge University Press, Cambridge, England

Hashibon, A. , Elsässer, C., Mishin, Y. & Gumbsch, P. (2008) *Phys. Rev. B* **76,** 245434.

Hashibon, A., Lozovoi, A. Y., Mishin, Y., Elsässer, C. & Gumbsch, P. (2008) *Phys. Rev. B* **77**, 0941131.

Giannozzi, P., Baroni, S., Bonini, N., Calandra, M., Car, R., Cavazzoni, C., Ceresoli, D., Chiarotti, G. L., Cococcioni, M., Dabo, I., Dal Corso, A., Fabris, S., Fratesi, G., De Gironcoli, S., Gebauer, R., Gerstmann, U., Gougoussis, C., Kokalj, A., Lazzeri, M., Martin-Samos, L., Marzari, L., Mauri, F. Mazzarello, R., Paolini, S., Pasquarello, A., Paulatto, L., Sbraccia, C., Scandolo, S., Sclauzero, G. Seitsonen, A. P., Smogunov, A., Umari, P. & Wentzcovitch, R. M. (2009) *J. Phys.: Condens. Matter* **21**, 395502

Holloway, K., Fryer, P. M., Cabral, Jr., C., Harper, J. M. E., Bailey, P. J. & Kelleher, K. H (1992) *J. Appl. Phys.* **71**, 5433

Johnson, R.A (1990) *Phys. Rev. B* **41**, 9717.

Klaver, T. P. C. & Thijsse, B. J. (2003) *J. Comput.-Aided Mater. Des.* **10**, 61

Kim, H., Koseki, T., Ohba, T., Ohta, T., Kojima, Y., Sato, H. & Shimogaki, Y. (2005) *J. Electrochem. Soc.* **152***,* G594

Kuhn, K. W., Campbell, R.A. & Goodman, W.D. (1993), *J. Phys. Chem* **97**, 446-453

Laurila, T., Zeng, K., Kivilahti, J. K Molarius, J. & Suni, I. (2000) *J. Appl. Phys.* **88**, 3377

Lazić, I., Klaver, P. & Thijsse, B. (2010) *Phys. Rev. B* **81**, 045410

Massalski, T.B (1986) *Binary Alloy Phase Diagrams* edited by Materials Park, OHMassalski, T.B (1986)

Binary Alloy Phase Diagrams edited by Materials Park, OH

Mishin, Y., Mehl, M. J., Papaconstantopoulos, D. A., Voter, A. F. & Kress, J. D. (2001) *Phys . Rev. B* **63***,* 224106

Mishin, Y. & Lozovoi, A. Y. (2006) *Acta Mater.* **54***,* 5013.

Monkhorst, H. J. & Pack, J. D. (1976). *Phys. Rev. B* **13***,* 5188.

Musket, R.G, McLean, W., Colmenares, C.A., Makowiecki, D. M. & Seikhaus, W. J (1982) *Appl. of Surf. Sci.* **10**, 143-207.

Robinson, I. K. (1986) *Phys. Rev. B.* **33**(6)

Robinson, I.K & Tweet, D. J. (1992) *Rep. Prog. Phys.* **55***,* 599-651 .

Rodney, D., Fivel, M. & Dendievel, R. (2005). *Phys. Rev. Lett.* **95**, 108004.

Rodriguez, J.A. & .Goodman, D.W (1991) *J. Phys. Chem.* **95**, 4196-4206

Troullier, N., Martins, J. L. (1991) *Phys. Rev. B* **43**, 1993

Tyson, W. R. & Miller, W. A. (1977). *Surf. Sci.* **62**(1), 267-276.

Van der Merwe, J. H. **1963** *J. Appl. Phys.* **34**, 123.

Venugopal, V. & Thijsse, B. J. (2009) *Thin solid Films* **517***,* 5482-5488.

Vitos, L., Ruban, A. V., Skriver, H., L. & Kollár, J. (1998) *Surface Science* **411***,* 186-202.

Vlieg, E. (1997) *J. Appl. Cryst.* **30***,* 532.

Vlieg, E. (1998) *J. Appl. Cryst.* **31***,* 198.

Vlieg, E. (2000) *J. Appl. Cryst.* **33***,* 401-405

Vlieg, E. (2013) *A concise rod manual*

Wuttig, M. & Liu, X. (2004) Ultrathin Metal Films*,* edited by Springer-Verlag, Berlin

Yeshchenko ,O.A, Dmitruk, I. A., Alexeenko, A. A. & Dmytruk, A. M. (2007) *Phys. Rev. B* **75**, 085434.

Chapter IX: Interface of copper islands dewetted in the solid state on the Tantalum (0 0 1) surface studied by coherent X-ray diffraction and molecular dynamics simulations

Contents

Introduction....237
IX.1. Sample preparation and description....238
IX.2. Molecular dynamics simulations of the Cu-Ta interface using the angle-dependent potential....239
IX.2.1. Simulation of the solid-state and liquid-state dewetting....239
IX.2.2. Interfaces obtained with simulated experimental conditions....244
IX.2.3. Evolution of the interface for longer annealing times....245
IX.3. HR-TEM observation of the Cu-Ta interface....247
IX.4. Influence of the atomic structure of the interface on the distribution of the displacement field. .248
Conclusion....254
Bibliography 255

Chapter IX: Interface of copper islands dewetted in the solid state on the Tantalum (0 0 1) surface studied by coherent X-ray diffraction and molecular dynamics simulations

Introduction

In Chapter VIII we investigated the atomic structure of the Cu wetting layer on a (0 0 1) Ta surface. The analysis of the intensity along the crystal truncation rod allows to precisely determine the spacing between the surface layers relative to the bulk as well as the surface termination. DFT calculations are able to predict a Cu-Ta interface which is remarkably consistent with experimental results. Due to the large number of atoms that would be involved in the simulation, it is unfortunately not possible to use *ab initio* calculations to determine the atomic-structure of the Cu-Ta interface in the islands. For such a large number of atoms, large-scale atomic simulations using inter-atomic potentials can provide new insights in the prediction of the atomic structure of the interface. The ability of the Cu-Ta ADP potential developed by Hashibon & Lozovoi *et al.* (2008) to predict an interface for the wetting PM layers has been evaluated in Chapter VIII. Some issues were evidenced with the potential. It clearly underestimates the excess interface energy, and predicts the stability of some Cu-Ta compounds (while the Cu-Ta system practically shows zero mutual solubility, Massalski 1986)! Additionally, a poor agreement is found between the structure factors calculated from the relaxed atomic positions with molecular dynamics (MD) and the XRD experimental data. In particular, the prediction of the relaxation of the interfacial Ta planes, which plays a large role in the calculated structure factors was found to be quite badly reproduced.

On the other hand, the potential reproduces the correct number of stable PM layers in good agreement with the surface diffraction data and the DFT calculations. The MD simulations of solid state dewetting also reproducibly predicts the presence of two wetting pseudomorphic (PM) layers, independently of the initial conditions of the simulation (number of PM layers, size of the particle, wetting or dewetting process…).

Despite its limitations, it is clear that the ADP potential provided by Hashibon is the best cross-potential to simulate the Cu-Ta interface. As discussed in section VIII.3, the other existing potentials (Johnson 1990) based on the embedded atom method (EAM, Daw & Baskes 1984) do not provide a sufficiently accurate description of the atomic bonding for the b.c.c. atoms (they do not take into account the angular dependence). In any case, the development and fitting of a new potential for the Cu-Ta system was out of scope of this work.

As discussed in the introduction of Chapter VIII, the solid state dewetting of Cu thin films on a Ta (0 0 1) surface has been little studied in the literature. It is reported by Venugopal *et al.* (2009) who evidence the presence of a wetting layer at the substrate/particle interface by He desorption experiments. The thickness of this ultra-thin film is then estimated to be smaller than 5 Å corresponding to 1 or 2 Cu monolayers (ML).

Surface diffraction experiments combined with DFT calculations provided a precise description of this wetting layer (Chapter VIII). On the other hand, the atomic structure of the islands has not been reported yet, and this is the focus of this chapter.

In a first part, we detail the sample preparation, describe the geometry of the dewetted island, and discuss the influence of the large interfacial strain induced during the dewetting thermal treatment.

In a second part, the molecular dynamics simulations of the solid-state and liquid-state dewetting are presented. The orientation and equilibrium shape of the particles is discussed and compared to the shape of the experimental islands. The influence of the initial conditions for the simulation (temperature, boundary conditions, size of the particle) on the equilibrium shape of the particle is also evaluated. The interfaces obtained with the simulated experimental conditions and the evolution of their atomic structure for long annealing times are presented in sub-sections X.2.2 & X.2.3 respectively. After that, the interfaces obtained by MD simulations are compared with the experimental interfaces imaged by high resolution transmission electron microscopy. Finally, the influence of the atomic structure of the interface on the distribution of the displacement field in the particle is discussed in the last section of this chapter.

IX.1. Sample preparation and description

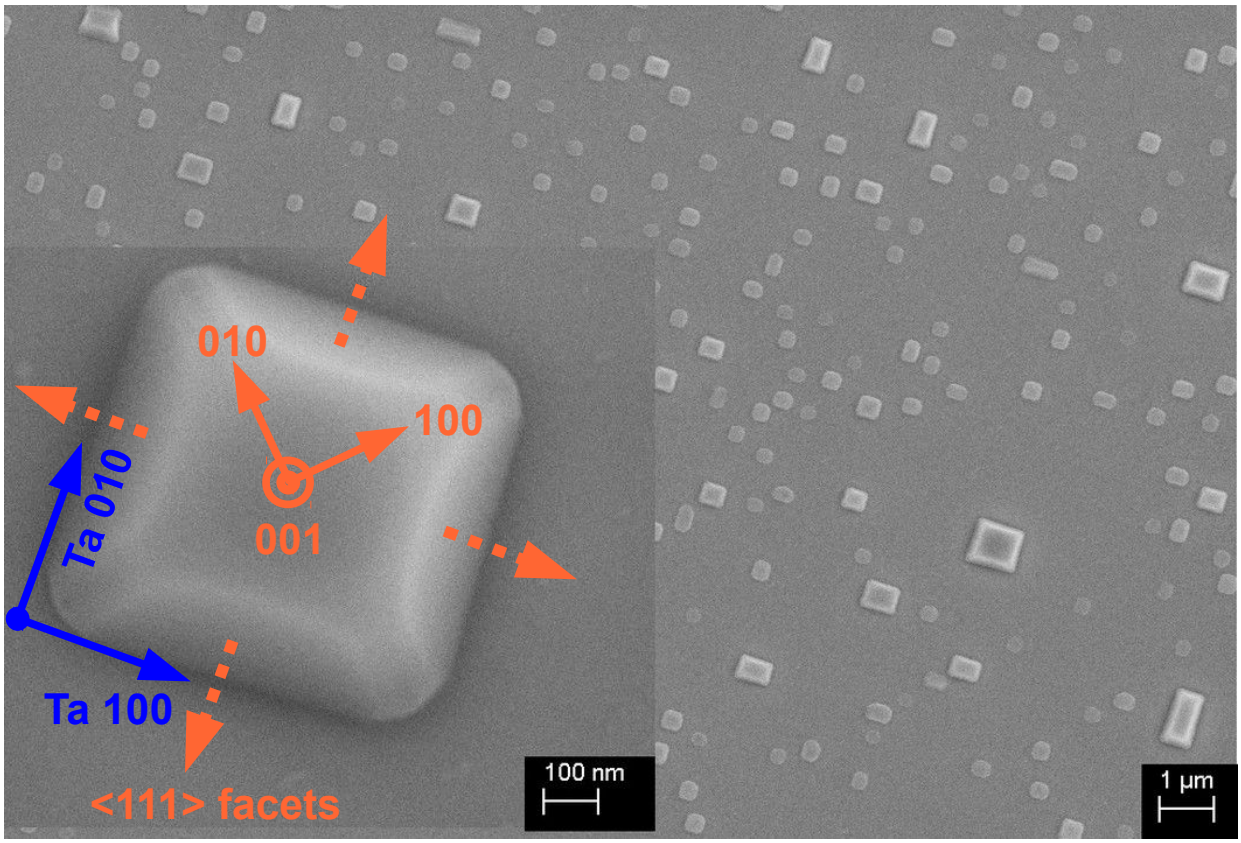

Fig. IX.1: *Secondary Electron Microscopy of the solid state dewetted copper islands.* The enlargement in the insight shows the crystallographic axes. (from Beutier *et al* 2013a)

The Cu particles are obtained by the solid-state dewetting procedure detailed in Chapter II (section II.3.1.1). It requires a careful preparation in UHV of the Ta surface (Musket *et al.* 1982), a topic that is addressed in sub-sections VIII.1.1 and VIII.1.2. The islands are dewetted in a UHV environment by heating a 5 nm Cu thin film at 800°C during five minutes. Fig. IX.1 shows typical dewetted Cu crystallites which display a variety of size and shapes. Their lateral dimensions varies between 200 nm and 1 µm and their height usually ranges between 100 and 400 nm (as measured with Atomic Force Microscopy).

The shape of the particles consists of a largely truncated Wulff equilibrium shape (Winterbottom 1967) with a (0 0 1) specular facet and 4 lateral {1 1 1} facets connected with rounded edges. They exhibit a unique crystalline orientation relationship (OR) with respect to the Tantalum substrate: Cu (0 0 1)[1 1 0] // Ta (0 0 1)[1 0 0] as confirmed by Electron Backscatter diffraction (Beutier *et al.* 2013a).

This very well defined orientation and the flat (0 0 1) specular facet make them good candidates for *in situ* nano-indentation experiments combined with coherent X-ray diffraction (CXD) to monitor the evolution of the microstructure (3D strain and nucleation of defects (Beutier *et al.* 2013b)).

The strain field in these islands has been studied by Beutier *et al.* (2013a) and it has been found to be particularly large ($\varepsilon_{zz} \sim -0.65\%$) and heterogeneous, inducing large perturbations in CXD patterns. The large residual strain in the island is solely due to the interfacial strain. It is of the same order as the thermal strain induced by the difference $\Delta\alpha = \alpha_{Cu} - \alpha_{Ta}$ of thermal expansion coefficients between Ta and Cu from cooling. It is estimated that the cooling of the particle from the annealing temperature (AT) to room temperature (RT) leads to a large amount of tensile thermoelastic strain: $\Delta\alpha\Delta T \sim 0.82\%$. A large part of the thermoelastic strain remains in the particle,

with a value of $\Delta\alpha\Delta T \sim 0.4\%$. Indeed the precise temperature at which dewetting is finished to leave isolated crystallites is not yet determined on Ta(001); however one can assume strain free interface at this critical temperature (experimentally completed at 400°C in 30 min., so between 500-800°C (Verdier 2008)).
The presence of a wetting layer consisting of 2 PM layers has been established in chapter VIII and it is also reasonable to assume a network of dislocations to be present at the substrate-particle interface since a theoretical mismatch of as much as 31.4% needs to be accommodated along both in-plane directions. The question of the structure of such an interface is puzzling, even more intriguing if one realizes that the crystallite looks defect free: TEM cross sections evidence no dislocation in the bulk of crystallite and CXD patterns are qualitatively very close to the strain field obtained by only elastic calculations modelled by Finite Element Method (Beutier *et al* 2013a). Since interfacial dislocations do not produce any phase jump in the crystal, they can not be directly apparent on Coherent-X-ray Diffraction (CXD) pattern. On the other hand, since the technique is sensitive to the displacement field it is pertinent to search for a signature of the structure of this interface. The influence of the structure of the interface on the displacement fields and strain field distribution is addressed in further details in section IX.4 of this chapter.

IX.2. Molecular dynamics simulations of the Cu-Ta interface using the angle-dependent potential

IX.2.1. Simulation of the solid-state and liquid-state dewetting

The potential used for the MD simulations is the same as in chapter VIII, namely the ADP potential developed by Hashibon, Lozovoi *et al.* (2008). We have seen previously that despite its strong limitations (addressed in sections VIII.3.2 and VIII.3.3 and in the introduction of this chapter), it is surprisingly able to predict the stability and the correct number of PM layers at the Cu-Ta interface. More importantly it predicts the correct number of wetting layers (2 PM) outside the islands, independently on the initial conditions of the simulation. Due to the very limited physical time accessible in MD for the size of simulation we investigate (a few ns) it is not realistic to perform MD simulations of the complete solid-state dewetting from a continuous Cu thin film. To overcome this limitation, two configurations have been selected to simulate the dewetting of the Cu particles on top of a Ta (0 0 1) surface.
The first approach is to perform the dewetting above the melting temperature of Cu while the second one is to carry out the dewetting at temperatures comparable to the experiment, below the Cu melting point. We will see in the following that for the latter are not properly speaking solid-state dewetting simulations.
Using the same potential, Hashibon, Lozovoi *et al.* (2008) demonstrated the instability of two f.c.c. (1 1 1) Cu layers on top of a b.c.c. (1 1 0) Ta substrate. Upon heating at 1400°C, the uniform thin film rapidly breaks up and agglomerates in droplets with a (1 1 1) f.c.c structure. Prior to this work, it was numerically tested if similar behaviour is observed for Cu thin-films on top of a Ta (0 0 1) surface. This initial configuration consists in of 5 Cu f.c.c. (0 0 1) layers. Upon heating at 1500 K it is observed that the film breaks up and agglomerates in several small droplets with a f.c.c. structure, leaving 2 PM layers at the Cu-Ta interface (not shown here). This simulation thus demonstrates that the instability of thick Cu films on top of Ta (0 0 1) surfaces is also well reproduced with the potential. It was noticed that the process was significantly longer than in the case of a Ta(1 1 0) surface, and that the dewetted islands are very small (a few nanometres).
Larger sizes of islands are simulated by changing the initial conditions of the simulations. In order to dewet a single and large island in the simulation cell, two types of initial configurations are considered. The first consists of the thin film which sharp truncations along both in-plane directions and is already described in section VIII.3.4. As illustrated in Fig. IX.2.a it appears like a parallelepiped volume of Cu atoms. The second initial configuration is an island which shape is similar to the top truncated pyramidal one as in the experiment, except that the lateral {1 1 1} facets are connected with sharp boundaries instead of rounded edges. In the latter case, if

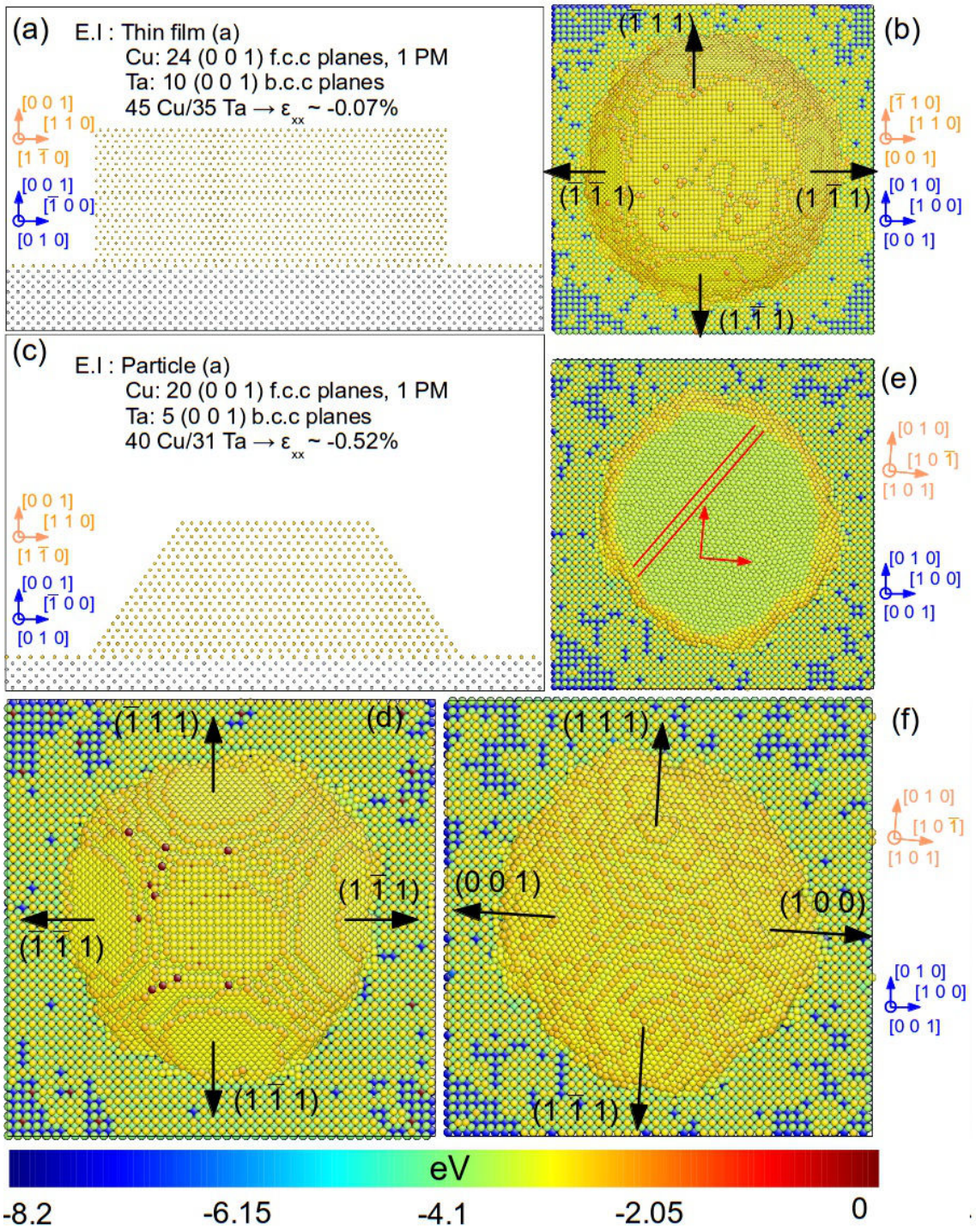

Fig. IX.2 *Comparison of the simulated solid state and liquid state dewetting for various initial configurations.* The atoms are coloured according to their potential energy, using the scale at the left of the figure (a) f.c.c. (0 0 1) thin film on top of a single PM Cu layer. (b) Evolution of the atomic configuration after annealing at 1200 K for 14 ns, and quench from AT to RT in 1 ns (c) f.c.c. (0 0 1) island on top of a single PM Cu layer. (d) Atomic configuration after annealing at 1150 K for 15 ns and quench from AT to RT in 1 ns. (e) (f) Atomic configuration after annealing at 1500 K for 5 ns and quench from AT to RT in 1 ns. The parallel lines on (e) denote the presence of an intrinsic stacking fault.

the temperature of the simulation is below the Cu melting point, the simulation can be described as a relaxationof the particle at a finite temperature. It allows to monitor evolution of both the shape of the island and of the Cu-Ta interface without the need to perform time consuming simulations.

Fig. IX.2.a shows one of the initial "thin film" configurations used for both solid-state and liquid state dewetting simulations. This configuration named thin-film (a) in the following consists of 24 f.c.c. (0 0 1) layers, and an interfacial Cu PM layer on top of a Ta(0 0 1) surface. Similarly to the configurations described in section VIII.3.4, the in-plane strained is minimized by adjusting the lateral width of the thin film. The minimum value of -0.07% lateral strain is obtained for 45 Cu atoms on top 35 Ta atoms with a_{Cu} = 3.615 Å and a_{Ta} = 3.3058 Å at 0 K. The substrate is made of eight Ta (0 0 1) layers so that the system contains 51409 Cu atoms and 33708 Ta atoms. The thin film has the orientation relationship (OR) with the substrate defined previously *i.e.* Cu(0 0 1)[1 1 0] // Ta(0 0 1)[1 0 0]. When it reaches its equilibrium shape, the particle measures 11.5 x 11.5 x4.5 nm^3.

The solid-state dewetting simulation is performed by setting the thin film at T = 1200K, which is below the melting temperature of bulk Cu, but above the experimental temperature (~1070K). Additionally and as discussed in section VIII.3.4, this temperature is expected to be close to the melting point of Cu for such a small nanoparticle (Yeshchenko *et al.* 2007, Attarian Shandiz *et al.* 2007). This elevated temperature is primarily selected to increase the mobility of the Cu atoms and thus reduce the computing time needed to reach the equilibrium shape for the particle. The particle is annealed for 14 ns, then quenched from AT to RT in 1 ns and a subsequent energy minimization is carried out. It should be noted that the energy minimization is done at 300 K. At this temperature, both lattice parameters increase, in agreement with the thermal expansion coefficients, to values of a_{Cu} = 3.6297 Å and a_{Ta} = 3.3156 Å. However, the lattice parameter of Ta is here constrained by the periodic boundary conditions, and is thus equal to the 0 K value.

With 45 f.c.c. atoms on top of 35 PM atoms, the coincidence is not as perfect at 300 K, and the in-plane mismatch strain is only minimized to a value of -0.47%. Upon annealing, the atoms at the sharp edges diffuse to the surface, and the thin film rapidly lose its squared shape. The flat (1 1 0) facets gradually transforms into {1 1 1} facets interconnected by rounded rough surfaces (Fig. IX.2.b). The fraction of the curved areas is significantly larger than in the experimental particle (Fig. IX.3.a). This is attributed to the higher annealing temperature, close to the melting temperature of copper. After 4 ns the shape of the particle does not change much, and on the initial Ta surface around the particle, a 2nd wetting layer is gradually formed by diffusion of atoms out of the crystallite . Both out-of plane and in-plane OR do not evolve upon further annealing.

To evidence the influence of the initial configuration on the equilibrium shape of the particle, another series of simulations are considered, with an island already close to its equilibrium shape as a starting point (Fig. IX.2.c). The simulations are performed above and below the melting point to compare the results from solid-state and liquid state dewetting. The initial configuration, named particle (a) in the following, is slightly smaller thin film (a) with 20 f.c.c. (0 0 1) planes on top of a single PM layer. The substrate consists only of 6 Ta planes so that the number of atoms is significantly lower than in thin film (a) with 21295 Cu atoms and 10525 Ta. This corresponds to dimensions of 10.2 x 10.2 x 3.8 nm^3. The supercell consists of a different number of Cu on Ta atoms (40/31 vs 45/35) which leads to a larger value of compressive in-plane strain of -0.52% and -0.93% at 0 and 300 K.

In order to obtain an equilibrium shape in a better agreement with the experimental shape, the annealing temperature is lowered to 1100 K for the dewetting in the solid phase. It is equivalent to the experimental annealing temperature but still close to the Cu melting point for such small particle size. Similarly to thin film (a), a 1 ns quench followed by an energy minimization is performed after the annealing.

The annealing time is similar to thin film (a) (15 ns) so that the coverage of the 2nd Cu ML (Fig. IX.2.d) is comparable (Fig. IX.2.b). Upon annealing, the sharp boundaries gradually transform into rough rounded surface. After 15 ns of annealing, the equilibrium shape of the particle shape is remarkably similar to the equilibrium shape observed experimentally, the large spatial extent of the spherical areas relative to the flat facets is again attributed to the equilibration temperature closer to the Cu melting temperature.

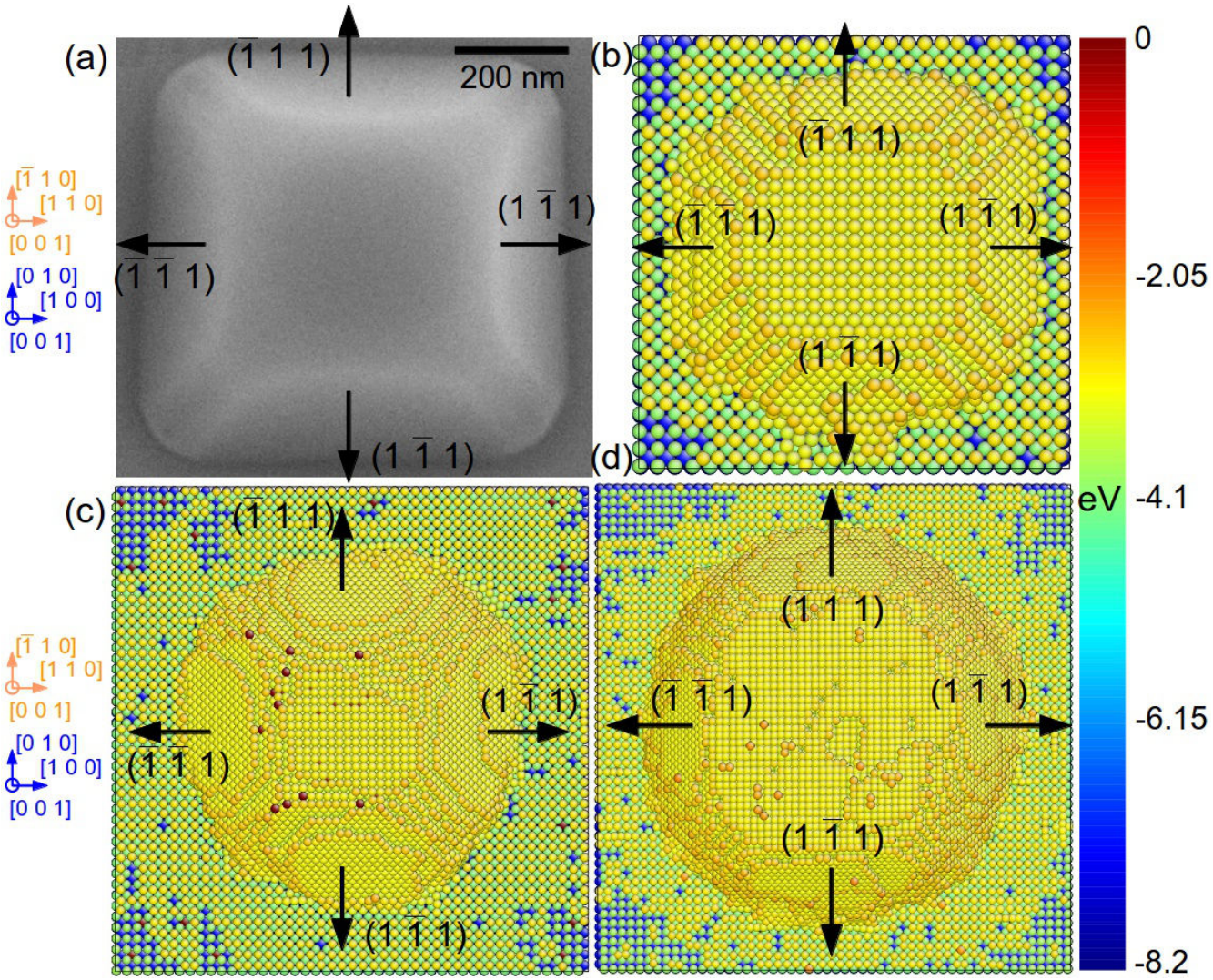

Fig. IX.3 *Comparisons of the shape of experimental and simulated particles obtained by solid-state dewetting.* The atoms are coloured according to their potential energy, using the scale at the left of the figure (a) SEM picture of a 750x750x350 nm^3 solid-state dewetted copper island. (b)-(c)-(d) Simulated copper islands obtained from various initial configurations (b) Annealing of a f.c.c. (0 0 1) thin film (thin film (b)) on top of a single PM layer at 1040 K and for 8.64 ns. (c) Annealing of particle (a) at 1150K for 15 ns. (d) Annealing of thin film (a) at 1200K for 14 ns.

As illustrated in Fig. IX.3, independently of the initial configuration (thin film or particle), the number of PM layers at the Cu-Ta interface or of the size of the particle, the experimental equilibrium shape is remarkably well reproduced. The equilibrium shape is achieved by the minimization of the surface energy by an optimisation of the surface area of different crystallographic plane (Winterbottom *et al.* 1967). It is thus clear that the potential predict Cu surface energies in relative good agreement with the experimental observations.

One important question is to determine if the same crystal structure is obtained when the dewetting is performed above the melting temperature. There are only few experimental studies of the dewetting of a Cu thin film on a Ta(0 0 1) surface and none of them was performed above the Cu melting temperature. The requirement of a clean Ta surface state implies to perform the dewetting in an UHV environment with a base pressure of the order of 10^{-8} to 10^{-9}, which is much lower than the vapor pressure of pure liquid Copper (of the order of 10^{-6} at 1400 K, McCormack *et al.,* 1965). This poses experimental difficulties, which can be eventually overcome by performing

the dewetting under a small pressure of nitrogen or Argon gas. In any case, the liquid state dewetting of a Cu islands has not been reported experimentally and the crystal structure of the islands is unknown.
The simulation of the liquid state dewetting is achieved by heating the thin film at 1500 K (way above the Cu melting point) for 5 ns. Similarly to previous simulations, the annealing is followed by a quench from AT to RT in 1 ns followed by a subsequent energy minimization. As illustrated in Fig. X.2.e & X.2.f, the crystal structure obtained for the dewetted particle completely differs from the previous simulations, performed below the Cu melting point. Fig. IX.2.e reveals the complexity of the microstructure in the-island. A f.c.c. structure is still obtained but with a different (1 0 1) out-of-plane orientation. The particle is highly defective and contains 7 intrinsic stacking fault (one of them is indicated by parallel red lines), and a grain boundary as a result of the solidification process during the numerical quench process
The main grain occupies 95% of the volume of the particle, the [1 0 $\bar{1}$] direction is slightly misoriented with the [1 0 0] axis of the Ta substrate. The OR relationship can thus be defined as Cu (1 0 1)[1 0 $\bar{1}$] // Ta (0 0 1)[1 0 0].
The surface of the crystallite is also completely different. First-of all, the particle has a (1 0 1) out of plane orientation and it is well known that the low-densely packed (1 0 1) free surface is highly unfavourable energetically as compared to the (0 0 1) and (1 1 1) free surface (Vitos *et al.* 1998). The potential reproduce quite well this trend since the potential energy of a (1 0 1) surface atom is found to be significantly higher (-2.87 eV/atom) than the one obtained for a (1 0 0) surface atom (-3.02 eV/atom) or a (1 1 1) surface atom (-3.11 eV/Atom). As a consequence, the particle does not exhibit a specular (1 0 1) facet that would be too costly energetically. Some changes are also visible in the orientation of the lateral facets. They do not consist any more in four low-energy {1 1 1} facets but in a set of two {1 1 1} and two {1 0 0} facets. Overall the crystal surface is very rough, with a lot of terraces and the facets are not well defined as in the case of the solid state dewetted particle. It is clear that the equilibrium particle shape has not been achieved. Long equilibration time below the melting point would probably allow the particle to get closer to its equilibrium shape.
The fact that a different orientation from the liquid state dewetting is observed poses several questions. Considering the issues with the potential highlighted section VIII.3.2 and VIII.3.2, the fact that it leads to two different orientations depending on the temperature of the simulation is worrisome. It is clear and well reproducible that the experimental solid state dewetting promotes a (0 0 1) out-of plane orientation, and there is so far no experimental data for the liquid state dewetting to validate or contradict the simulation. It is thus difficult from only these simulations to determine whether if the variation of orientation is a real physical phenomenon or just an artefact / quench effect.
Our solid-state dewetting simulations are in agreement with the experimental results but the OR found at the end of the simulation is already present in the initial configuration. It is thus possible that the (1 0 1) orientation corresponds to an absolute minimum of energy for this potential. Below the Cu melting point, the atoms do not have enough mobility to reach this orientation and the (0 0 1) orientation only corresponds to a local minimum. In such case, the potential would clearly contradicts the experimental results.
The excess interface energy used in Chapter VIII is a relevant criterion to evaluate the stability of an interface.
This parameter has been calculated for several Cu-Ta interfaces with the two orientations and a varying number of PM layers. Detailed calculations are reported in Appendix. I. In summary it is shown that the (0 0 1) orientation is the most stable starting from n = 13 Cu planes and above, in good agreement with the experimental observations. For this orientation, two interfaces with a different number of PM layer are found to be equivalent energetically. In both cases the large lattice mismatch is accommodated by only two transitions plane : 1 b.c.c. and 1 f.c.c. that differ in position depending on the initial configuration: if the latter consists of 1 PM layer, these transitions layers correspond to the 1st and 2nd Cu planes starting from the interface. This interface is called the 1 PM configuration in the following. For 2 PM layers in the initial configuration, these layers are observed in the 2nd and 3rd Cu planes starting from the interface. This interface is named the 2 PM configuration in the following.
A detailed study of these transition planes (Appendix A1.2) reveal that they consist of of elementary cells separated by a network of orthogonal dislocations (Fig. IX.4.). This network of orthogonal dislocation allows an almost complete relaxation of the initial mismatch strain. The position of the transition planes determine the position of the core of the interfacial dislocations. For the 1 PM and 2 PM configurations, it is located

respectively in the first and second Cu planes. In both case, The dislocations are regularly spaced (every 4 or 5 planes), hence the average spacing between two dislocations for both configurations is reproducible, independent on the size of the particle and equal to 1 dislocation every 4.5 Cu plane.

IX.2.2. Interfaces obtained with simulated experimental conditions

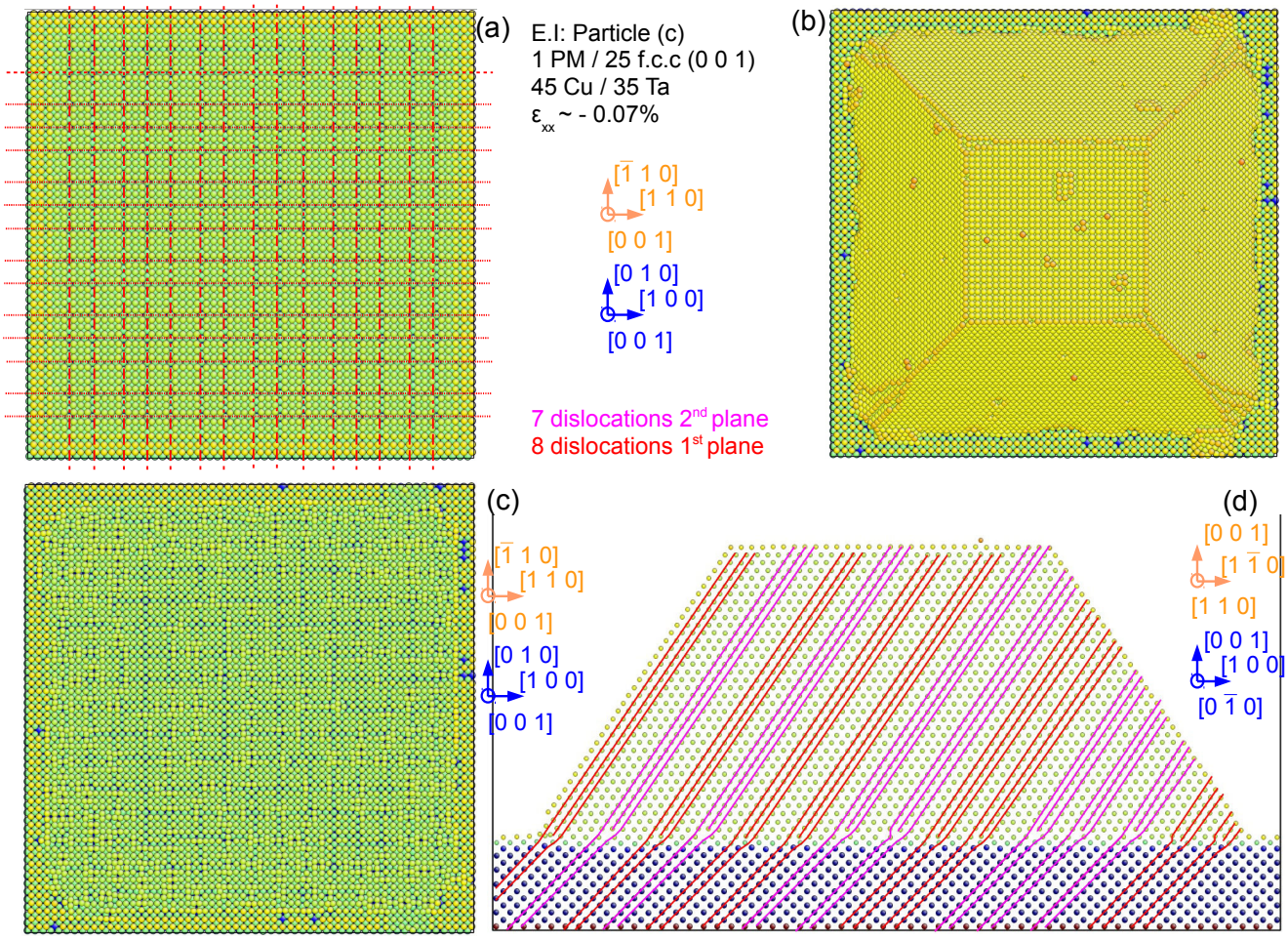

Fig. IX.4: *Evolution of the structure of the interface of particle (c) after 1 ns of annealing at 1000K. The atoms are coloured according to their potential energy. The scale not indicated here is the same as in previous figures.* (a) Atomic structure of the 2nd Cu layer with 2 sets of periodic cells: 5Cu/4Ta and 4Cu/3Ta along both in-plane directions. (c) Evolution of the particle shape (particle (c) after one second of annealing at 1000 K followed by a 1 ns from AT to RT and a subsequent energy minimization. (c) Evolution of the structure of the 2nd Cu layer after annealing. (d) Evolution of the network of interfacial dislocation. Two variants of interfacial dislocations can be found in the structure

The interfaces described briefly in the previous sub-section and in extensive details in Appendix A1 are the most stable energetically as determined from the excess interface energy criterion. They are obtained by energy minimization at 0K and thus rare not necessarily representative of the experimental Cu-Ta interface. The study of the atomic structure of the interface of the crystallites presented in section IX.1 should provide a clearer picture of the structure of the interfaces that can be obtained experimentally.
The particle shown in Fig. IX.4 is the particle (c) described in Appendix A1.1. The particle consists of 2 PM and

37 f.c.c. layers in the initial configuration. Similarly to the configurations presented in section X.2.1, the Cu/Ta ratio is adjusted so that the in-plane strain is minimize (67/52 atoms corresponding to ε_0 = -0.07%). The particle sits on 12 Ta planes which gives a 99553 Cu atoms and 38998 Ta atoms in total. This corresponds to a size of 17.1x17.1x7 nm^3.
The aim of the simulation is to capture the effect of short annealing time on the evolution of both particle shape and atomic structure of the interface. Particle (c) is thus annealed at 1050K for 1 ns and then quenched to room temperature in 1 ns. As usual this quench is followed by an energy minimization (at 300 K) . It should be noted that the starting point of the simulation is not the unrelaxed particle, *i.e.* the particle before the nucleation of the strain relieving dislocations, but the relaxed particle with the array of dislocations described in the previous sub-section (again, see Appendix A1.1. and A1.2 for more details). As seen from Fig. IX.4.a, this array of two families of orthogonal dislocations is clearly visible in the transition b.c.c. plane (2nd Cu layer). Even for short annealing times, the particle shape rapidly evolve (Fig. IX.4.b). The transformation of the sharp edges between {1 1 1} lateral facets, into rough rounded interfaces is already initiated and starts from the bottom of the particle.
The evolution of the atomic structure of the Cu-Ta interface is even more rapid and interesting. As illustrated on Fig. IX.4.b some degree of ordering can still be observed in the 2nd Cu plane, and the 4x4, 3x4 (…) elementary cells are still visible in some regions. However, the atomic structure can not be described as a b.c.c. structure since the number of atoms have significantly increased so that the arrangement of atoms in some regions is closer to a f.c.c. structure. Similarly, for the above Cu plane which was usually described as the transition f.c.c. plane (not shown here), the presence of the 5x4 elementary cells can not be as distinctly established as in the ideal case of the energy minimization at 0 K. The side view of the structure provides a clearer picture of the modification of the interface. The array of orthogonal dislocations is still present in the structure, but unlike the energy minimization at 0 K, the dislocations cores are now located either in the 1st Cu plane or in the 2nd Cu plane. This is in good agreement with our observations on the 2nd Cu plane which was described as an intermediate structure between f.c.c. and b.c.c. The number of dislocations and the average interval between them is kept, with one dislocation every 4.5 Cu plane (15 dislocations for 67 Cu planes).
In Fig. IX.4.c, the regions close to the crystal edges are more densely-packed, and have thus a dominant f.c.c structure where a majority of 1st plane dislocations are nucleated. Conversely, in the less densely-packed b.c.c regions (around the crystal centre), a majority of 2nd plane dislocations is observed. It should be emphasized that these calculations are in very good agreement with the results from the excess interface energies calculation which are not able to determine whether the 1 PM or the 2 PM interface is the most stable. It is thus not surprising to obtain an interface which combines the characteristics of both configurations.

IX.2.3. Evolution of the interface for longer annealing times

Similarly to the equilibrium shape, the atomic structure of the interface is prone to evolve upon longer annealing times. The evolution of the interface, is illustrated through two examples, a small particle obtained from thin-film (b) that was used to evaluate the potential in section VIII.3.4 and a larger one obtained from thin-film (a) (section IX.2.1). Thin film (b) sits on the bare Tantalum in the initial configuration and is annealed for 23.5 ns at 1040 K (see section VIII.3.4). The thermal treatment for thin film (a) is described in details in section IX.2.1. As a reminder the latter sits on a single PM plane in the initial configuration. Fig. IX.5 shows the atomic structure of the 2nd Cu plane for the small and the large particle after respective annealing times of 23 and 15 ns. As illustrated on Fig. IX.5.a, the structure of the 2nd plane for the small particle exhibit a large degree of ordering. The crystal structure is again intermediate between b.c.c and f.c.c but the latter clearly dominates the trend, and several 5 f.c.c/4 P.M and 4 f.c.c/3 P.M (see Appendix A1) can be identified, mostly at the particle centre. Fig. IX.5.b confirm that the 1st plane interfacial dislocations are predominant in the structure.
For the larger particle, the 2nd Cu plane is clearly intermediate between f.c.c. and b.c.c. (Fig. IX.5.c), and the 2nd plane variant seems to be slightly predominant as illustrated on (Fig. IX.5.d).
At the interface inter-diffusion of atoms occurs, and some interstitial Ta atoms are observed in the first-Cu layer (circled in red), while several Cu atoms diffuse in the substrate. The Cu and Ta having almost zero mutual

solubility (Massalski 1986), such behaviour is not expected and is probably related to the issues with the potential highlighted in subsections VIII.3.2 and VIII.3.3.

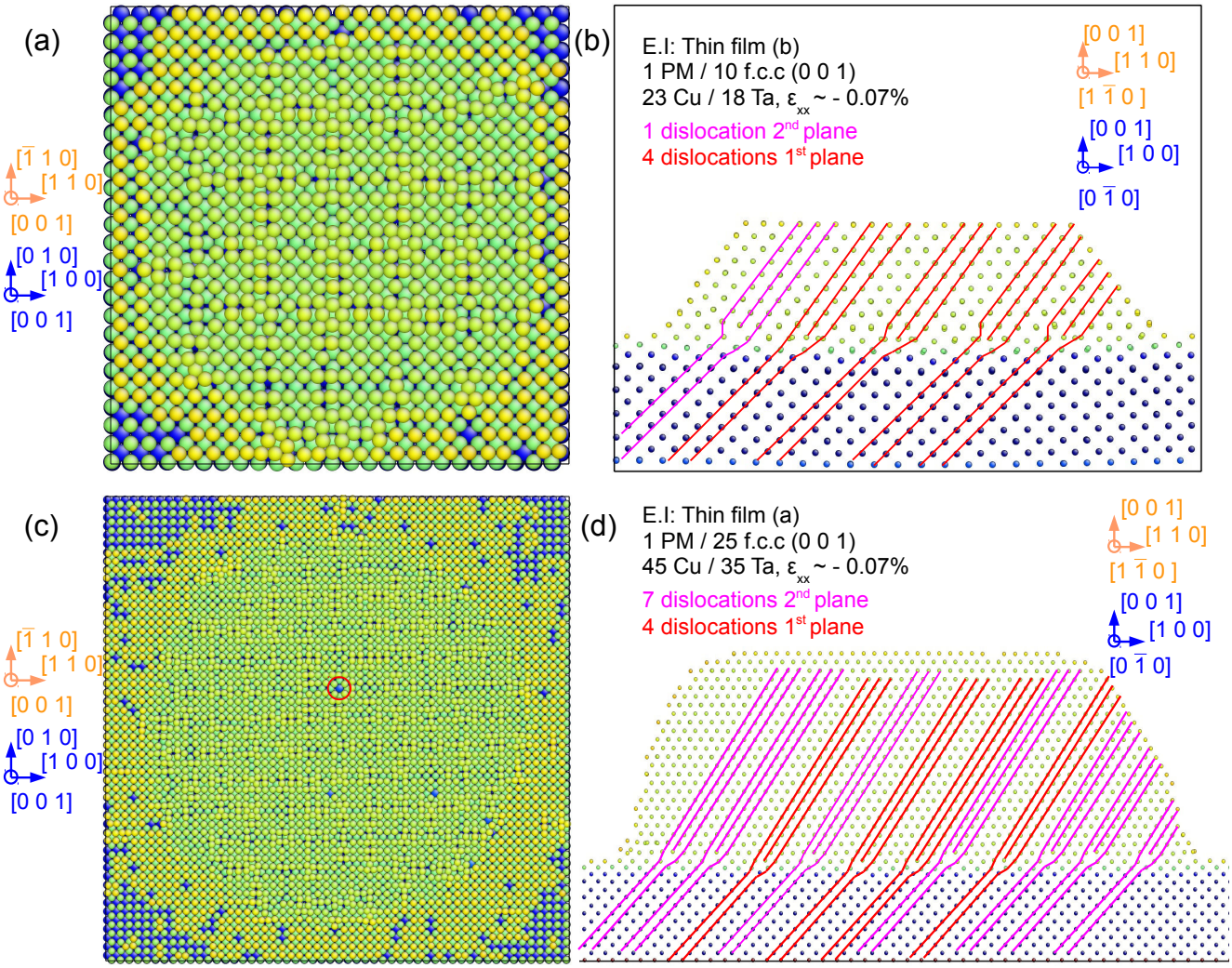

Fig. IX.5: *Size dependency of the Cu-Ta interface. The scale not indicated here is the same as in previous figures.* (a) Atomic structure of the 2nd Cu layer of a small particle (obtained by annealing of thin film (b)). It is highly disordered but with a dominant f.c.c. (0 0 1) structure. (b) Side view of the Cu-Ta interface, the interfacial dislocations starting from the first Cu layer are predominant. (b) Atomic structure of the 2nd Cu layer of a larger particle (obtained by annealing of thin film (a)). (d) Side view of the Cu-Ta interface, the interfacial dislocations starting from the second Cu layer are predominant.

In summary, all the atomic configurations presented in section IX.1 to X.3 that are annealed below the Cu melting point, leads to very reproducible Cu-Ta interface. An array of two families of orthogonal dislocations is always obtained, with a regular interval between them. Neither the number of PM layers (0, 1 or 2), nor the boundary conditions in the initial configuration have a significant effect on the final equilibrium shape of the particle or on the atomic structure of the interface. Similar results are indeed obtained for the thin-film and the particle as a starting point for the simulation. The interval between dislocations is also very reproducible and is always equal to 4 or 5 Cu planes (except for thin-film (a) where intervals of 3 Cu planes can be found). For all

particles, the density of dislocations is exactly the same with one dislocation every 4.5 Cu plane.
Regarding the size of the particle, a possible size effect might be observed with the tendency of the 1st plane dislocations to be predominant in small particles while the 2nd plane dislocations are more present in the larger ones. However we have not carried out a systematic size study to draw any conclusion at this stage.

IX.3. HR-TEM observation of the Cu-Ta interface

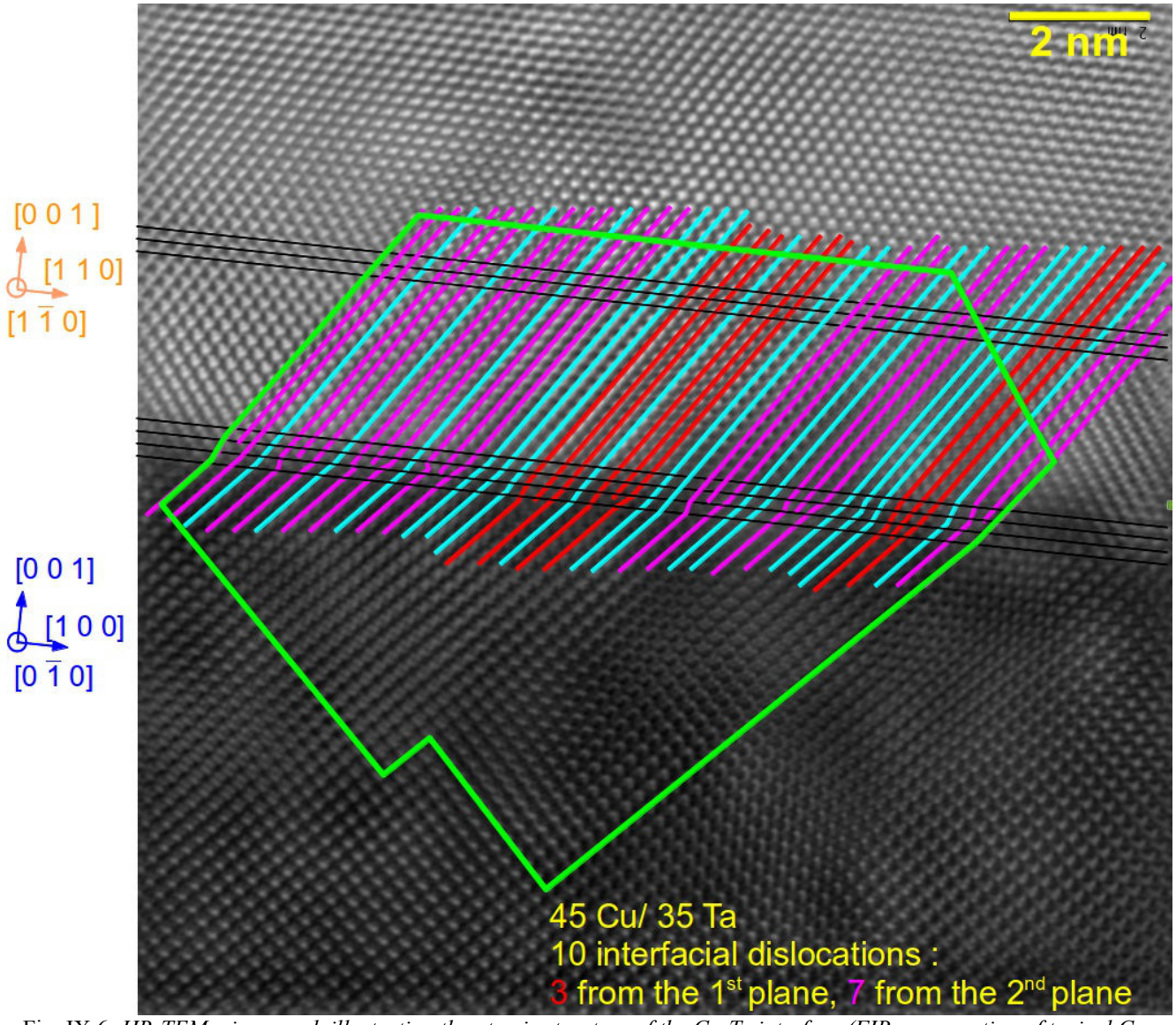

Fig. IX.6: *HR-TEM micrograph illustrating the atomic structure of the Cu-Ta interface (FIB cross section of typical Cu island)*

Below the Cu melting point, the Cu-Ta interface obtained with the Cu-Ta potential is very reproducible, but this does not mean that it is a structure consistent with the experimental interface.
If it is possible to determine the detailed atomic structure of the Cu-Ta interface for the wetting layer outside the islands, by measuring the crystal truncation rod (CTR) of a clean Ta (1 0 0) surface in a synchrotron. The

measurement of the integrated intensities along the Bragg rods enables to determine the height of the surface atom relative to the Bulk layer (Robinson 1986, Feidenhans'l 1989 and Robinson & Tweet 1992).
The determination of the precise in-plane structure, which was not discussed in Chapter VIII is also possible. By using grazing incidence and exit angles to the surface, the scattering vector (momentum transfer) (see Chapter VIII) can be kept nearly parallel to the surface, which allows the determination of the in-plane structure that is the 3D surface structure projected onto the surface plane. However, here the situation is complicated by the presence of bulk f.c.c atoms on top of the interfacial planes, which make difficult the use of surface diffraction techniques, since the signal from the first planes will be shadowed by the bulk atoms.
Coherent X-ray diffraction (CXD), gives access to the 3D displacement field in isolated objects and is very sensitive to the presence of dislocations. However, the latter are only detected if they produce a phase shift between the neighbouring regions of the crystal separated by a dislocation. This is not the case for interfacial dislocations, which do not produce any phase shift in the Cu island. The technique is however sensitive to the inhomogeneous strain field at the vicinity of the dislocations and a modification of the atomic structure of the interface is expected to induce a modification in the distribution in the strain field, which can be investigated by CXD. This is the object of section IX.4.
For the study of interfaces with atomic resolution, high-resolution transmission electron microscopy (HR-TEM) is a good alternative to X-ray diffraction techniques. It allows the direct imaging of the sample with atomic resolution (Spence 1980). Fig. IX.6 shows the detailed atomic structure of the Cu-Ta interface, as seen from the [0 $\bar{1}$ 0] direction of the Ta substrate (corresponding to the [1 $\bar{1}$ 0] direction of the island). It is confirmed that the large mismatch strain is accommodated by misfit dislocations.
The interval between the dislocations is remarkably consistent with the predictions from the ADP simulations. They are indeed mostly distributed every 4 or 5 Cu planes, even if spacings of 6 planes which were not found in the simulations are also observed. The region delimited by the green contour corresponds to 45 Cu planes and 35 Ta planes. This corresponds to the optimum ratio that was found for the minimization of the in-plane strain with the potential at 0 K. With the experimental lattice parameters of a_{Cu} = 3.6149 Å and a_{Ta} = 3.3013 Å this also corresponds to a very low value of in-plane mismatch strain of -0.2 %. The presence of 10 extra-Cu planes implies the presence of 10 edge dislocations in the green volume. The value of one dislocation every 4.5 Cu planes that was predicted by the potential is observed experimentally. Even more interesting, it appears that all the dislocations core are not located on the same Cu plane as predicted by the MD simulations. As illustrated on Fig. IX.6, the atomic resolution is not completely achieved at the Cu-Ta interface, and the atoms appear very blurry. The precise determination of the core of the dislocations is rather delicate. However, from the estimated position of the interface planes (black lines) it is possible to establish that there are at least two different starting planes. The variant in magenta which is defined as the second plane variant seems to be predominant, in good agreement with the prediction of the MD simulations for large particles.

In summary, despite the tendency of the potential to overestimate the stability of the PM layer, and despite the fact that he predicts a lower interface energy for the (1 0 1) orientation (explaining why this orientation is promoted for the liquid state dewetting simulations), the potential is able to predict a Cu-Ta interface and an equilibrium shape of the particle that seems to be consistent with the experiment. The atomic structure of the interface and the ECS predicted from the solid-state dewetting simulations are remarkably reproducible, independently on the initial conditions for the simulation (number of PM layers or boundary conditions for the particle). Unfortunately, experimental liquid state dewetting of Copper was not successful.

IX.4. Influence of the atomic structure of the interface on the distribution of the displacement field

As discussed in section X.1 and this chapter, the residual strain field in the island is large and heterogeneous. In the paper by Beutier *et al.* (2013a), it is claimed that this strain field mainly originate from the

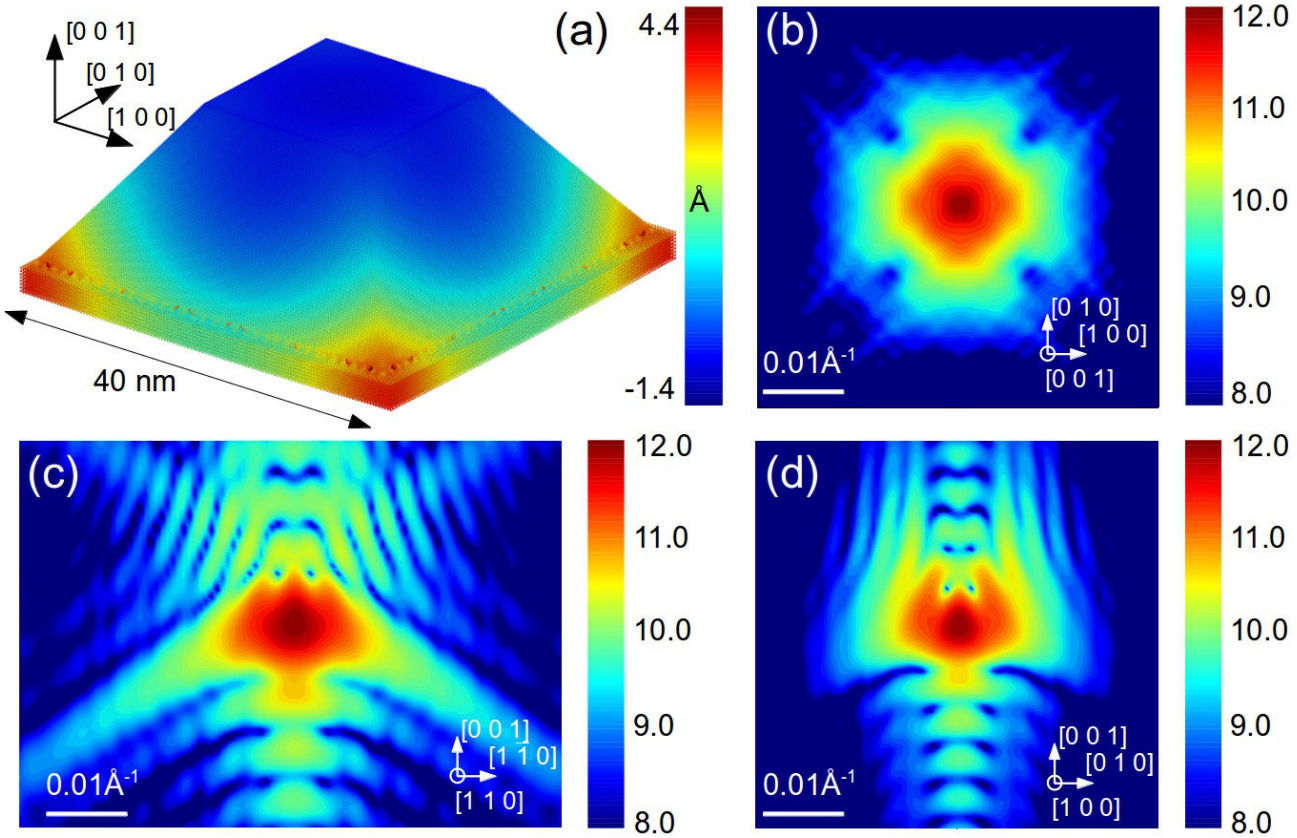

Fig. IX.7: (a) Distribution of the u_z displacement field in a 40x40x15 Cu particle relaxed by energy minimization. (b)-(c)-(d) Slices of the 0 0 2 Cu reflection computed for the u_z displacement field (b) (0 0 1) slice, (c) (1 1 0) slice and (d) 0 0 1 slice

the interfacial strain estimated to be of the order of 0.4%, corresponding to $\varepsilon_{zz} \sim -0.65\%$. Although quite large these values are two order of magnitude smaller than the nominal mismatch strain $\varepsilon_0 \sim 31.4\%$ for the Cu / Ta system which indicate that it is almost completely relaxed by the structure of the interface.

The strain in the relaxed particles have several origins: the thermoelastic strain that is generated during the cooling of the particle, the interfacial strain (including pseudomorphic layers and misfit dislocation to adapt the f.c.c./b.c.c. crystals) and the surface strain connected to the relaxation of the free-surfaces to reach the equilibrium crystal shape. It is also established by Beutier *et al.* (2013a) that the residual strain is only half the $\Delta\alpha\Delta T$ value that is calculated for a cooling down of the particle from the dewetting temperature to the RT. The presence of the 2 wetting PM layers certainly plays a role in the relaxation of both the initial mismatch strain, and of the thermal mismatch strain (thermoelastic strain). To explore the properties of such an unusual interface, we carried out various MD simulations.

In the following we consider particles of two sizes. They are significantly larger than the particles presented in the previous section but still at least one order of magnitude smaller than the typical experimental particle. Here the small particle measures 40x40x15 nm^3 and the large 74x74x27.5 nm^3. Unlike the FEM simulations by Beutier *et al.* (2013a), this difference of scale between simulation and experiment implies that the results presented in this section do not allow to estimate a quantitative value of the residual strain in the particle.

The aim of this section is to understand how the strain distribution in the particle can be affected by the network of interfacial dislocation. We also seek at demonstrating if the two stable interfaces lead to a different strain distribution and thus induce a different signature in CXD patterns.

For both sizes the two most stable interfaces, corresponding to 1 PM and 2PM Cu layers are modelled. The total

interfacial strain is modelled by adjusting the lateral dimensions of the particle in order to induce a certain amount of mismatch strain. For the small particle, a mismatch strain of 1.14% is achieved by a ratio of 156 Cu f.c.c atoms on top of the 122 PM atoms. The substrate contains 16 Ta planes and the simulation cell contains a large number of atoms: 1196863 Cu atoms and 262144 Ta for the 1 PM configuration and 1208063 Cu atoms for the 2 PM configuration, with the same number of Ta atoms.

For the large particle, a similar mismatch strain is obtained by a ratio of 281 f.c.c atoms on top of 219 PM atoms. The substrate is thicker with 50 Ta planes, for a total of 6774136 Cu atoms and 3125000 Ta atoms for the 1 PM configuration, and 6819736 Cu atoms with the same number of Ta atoms for the 2 PM. The value selected for the simulated thermoelastic strain is significantly larger than the experimental value of 0.4% (Beutier *et al.* 2013a), in order to make sure that the interfacial strain has a significant contribution to the residual strain in the particle, and produce a distinct signature on the calculated CXD patterns.

The relaxed configuration is obtained by energy minimization at 0 K. The relaxation of the atomic positions is allowed in the three directions of the space. The bottom most last Ta planes is not fixed, but its relaxation is allowed only along the z direction. Fig. IX.7.a shows the distribution of the u_z displacement field in the small particle and the underlying substrate at the end of the relaxation. The particle has 1 PM layer in the initial configuration and the displacements are calculated relatively to the atomic positions in the initial configuration. Though they are not clearly visible on Fig. IX.7.a, the network of orthogonal dislocations which was described previously is present at the substrate particle interface. Since the simulation is performed at 0 K, the interface correspond to the ideal 1 PM case with all dislocations separated by 4 or 5 Cu planes and starting from the 1st Cu plane (transition b.c.c plane). Large displacements can be identified at the vicinity of the dislocations, but they have very limited spatial extent.

The largest negative displacements are obtained close to the centre of the particle, while the largest positive displacement are found on the corners of the particle, at the sharp intersections between the lateral {1 1 1} facets. Overall, the presence of interfacial dislocation does not seem to have much effect on the distribution on the displacement field. It has been shown by Beutier *et al.* (2013a) that large and heterogeneous interfacial strain have a very strong signature on CXD patterns. In a 800 nm particle a $\Delta\alpha\Delta T \sim 0.4$ % (corresponding to $\varepsilon_{zz} \sim$ -0.65%) residual strain leads to a CXD pattern which is largely strain dominated so that the features related to the shape of the particle (fringes induced by the finite shape of the crystal) tend to disappear. The effect of the strain on CXD patterns is discussed in extensive details in section VI. 3. The 3D CXD patterns are calculated in the kinematic approximation. More details on the calculation procedure are found in section Chapter III, and elsewhere (Favre-Nicolin 2011). As expected from a particle which exhibits a large amount of heterogeneous residual strain, the CXD pattern is largely strain dominated. A large broadening of the Bragg peak is observed and shape of the Bragg peak can be more or less be described as a square-based pyramid (Fig. IX.7.b). Some features related to the shape of the particle are still visible. Periodic fringes (with a spacing invert to the height of the particle) are observed along the specular (0 0 2) reflection (Fig. IX.7.c & IX.7.d). They are bended due to the heterogeneity of the strain. The fringes along the {1 1 1} direction are still visible above the Bragg peak (Fig. IX.7.c), below the Bragg peak they form diffuse streaks of intensity.

Fig. IX.8 show a comparison between the Cu 0 0 2 Bragg reflection calculated from the MS simulations and the same reflection measured from a typical Cu islands and calculated from FEM simulations of an island with size comparable to the experimental particle. Details on the FEM simulations are given in (Beutier *et al.* 2013a). A qualitative good agreement is found between the molecular statics (MS) simulations the experimental data and the FEM simulation. The 3D Bragg peak exhibits the same pyramidal shape, and the bending of the (0 0 1) fringes is also observed (Fig. IX.8.c & IX.8.g). However, although a larger thermal mismatch strain was applied (1.1% vs 0.4%) it is clear that the CXD pattern is less strain dominated. Some features of the shape are still

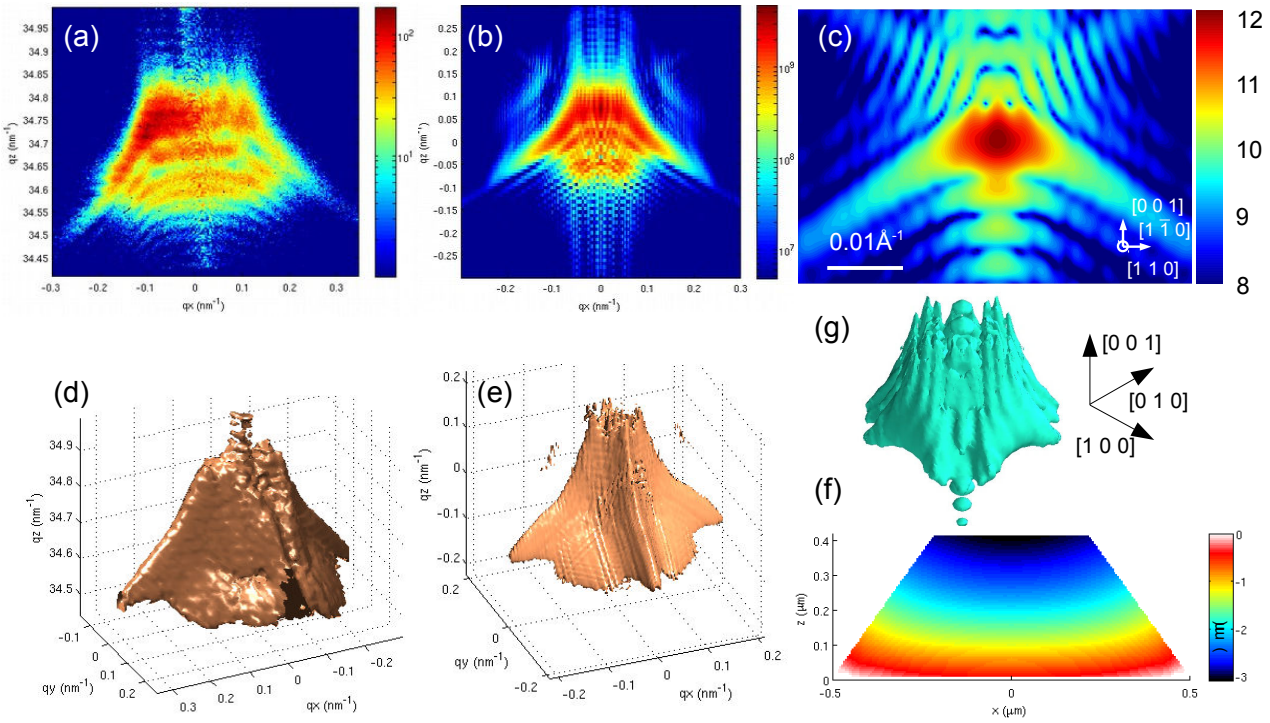

Fig. IX.8: *Comparison of the 0 0 2 Bragg reflection from a typical experimental island, from FEM simulations and from MS simulations.*(a) – (b) – (c) (qx,qz) slices of the 0 0 2 Bragg reflection measured experimentally (a), calculated from the FEM simulations (b) calculated from the MS simulations (c). (d) – (e) – (g) Isosurface of the Cu (0 0 2) Bragg reflection, measured experimentally (d), calculated from the FEM simulations (e), calculated from the MS simulations (g). (f) (x,z) slice through a Cu island with size comparable to the experimental particle showing the displacement field u_z for interfacial strain of 0.4% by FEM

clearly apparent, and the broadening of the Bragg peak is much less pronounced. In both the experimental data and the FEM simulations, the diffracted intensity is spread over a large area, and it is difficult to define a region which corresponds to a maximum of intensity (Fig. IX.8.a & IX.8.b). For the MS simulations, the maximum of the Bragg peak is still clearly visible and consists of a single clean spot though elongated due to the inhomogeneous strain (Fig. IX.8.c). No evidence of the presence of dislocations (splitting of the Bragg peak, chapter III) can be observed on the CXD pattern. As already discussed, the interfacial dislocations does not produce any phase discontinuities, and the extent of the displacement field around the dislocations seems to be very limited. The weaker signature of the strain on the CXD pattern can be clearly attributed to the small size of the particle.

Fig. IX.9 shows the distribution of the ε_{zz} strain in a (1 1 0) slice taken at the centre of the 40x40x15 nm^3 particle with 2 PM layers in the initial configuration.

It is clear that the non-uniform strain distribution introduced by the dislocations has a very limited spatial extent. It is thus not surprising that it does not produce any distinct signature on the CXD pattern. The analysis of the atomic strain reveals that the topmost Ta layer and the 1st PM Cu layer undergo a large compressive strain of the order of -11 to -17%, depending on the position of the atoms. The strain is partially relaxed in the 2nd PM plane by the nucleation of dislocations, with values of the order of 1 to 2%.

The 1st f.c.c layer (3rd Cu plane) undergoes a large tensile strain (of the order of 14%), which is reduced close to the dislocation positions (to a value of 7%). It then rapidly decreases, starting from the 2nd f.c.c layer.

The ε_{zz} strain is relatively low and homogeneous in the rest of the island. It is slightly negative close to the interface while it increases with the height of the particle to become positive in a region below the (0 0 1)

specular facet. The contribution of the surface strain induced by the relaxation of the free-surfaces to reach the equilibrium shape is also visible (see Chapter VII for more details). The first-two surface planes undergo compressive strain. This is especially visible on the top (0 0 1) facet where respective contractions of 1.5% and 0.5% of the first two surface layers are observed, while a positive tensile strain of about 0.7% is observed in the underlying region.
It is well known that a contraction of the first few layers is observed during the relaxation of metallic surfaces (Howe 1997). In particles close to the ECS, (Huang *et al.* 2008) evidenced a coordination dependent contraction of the surface atoms. The largest out-of plane contraction occur for the edge and corner atoms (respectively 3 and 4.5% contraction), with the lowest coordination number. For the same reason, a differential contraction of the {1 1 1} and {1 0 0} facets is observed, the latter being more pronounced.

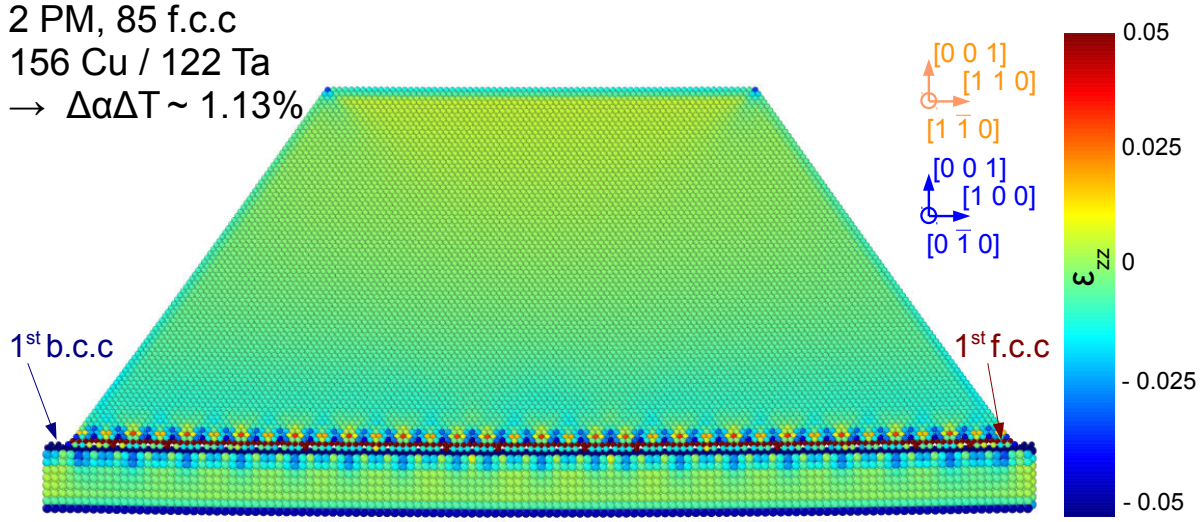

Fig. IX.9: *(x,z)* slice through a 40x40x15 nm Cu island showing the strain field ε_{zz} for $\Delta\alpha\Delta T = 1.13\%$

The continuum elasticity (Landau & Lisfitz 1986) theory predicts that the surface distortions die off exponentially (to 1/e) in the bulk with a decay length of $L/2\pi$. Where L is the period of the wave on the surface which corresponds approximately to twice the width of the facets (Harder *et al.* 2007). The surface strain thus decays very rapidly in the structure.

The last remaining question was to determine whether or not the structure of the dislocations at the interface has a strong influence on the strain distribution in the particle. Here the $u_{0\,0\,2}$ displacement field is calculated for the two interfaces (1 or 2 PM in the initial configuration) and for two particle sizes exhibiting the same amount of thermal mismatch strain (1.1%). As illustrated in Fig. X.10.a & X.10.b, the distribution of the displacement field is very similar for the two interfaces. The core location of the interfacial dislocations does not play a significant role, and the spatial extent of the non-uniform strain field around the dislocations does not vary from one interface to the other. As a consequence, the 0 0 2 Bragg reflection is very similar for the two interfaces (Fig. X.10.e and Fig. X.10.f). For the 2 PM case, the Bragg peak is slightly more elongated (Fig. X.10.f). It appears thus impossible to differentiate the two interfaces from the CXD pattern alone.
Similar conclusions can be drawn for the large (74x74x27.5) particle. Both the $u_{0\,0\,2}$ displacement fields and corresponding CXD patterns are very similar (Fig. X.10.c & X.10.d). Some variations can be observed in the [0 0 1] fringes above the Bragg peak, but they remain very limited.

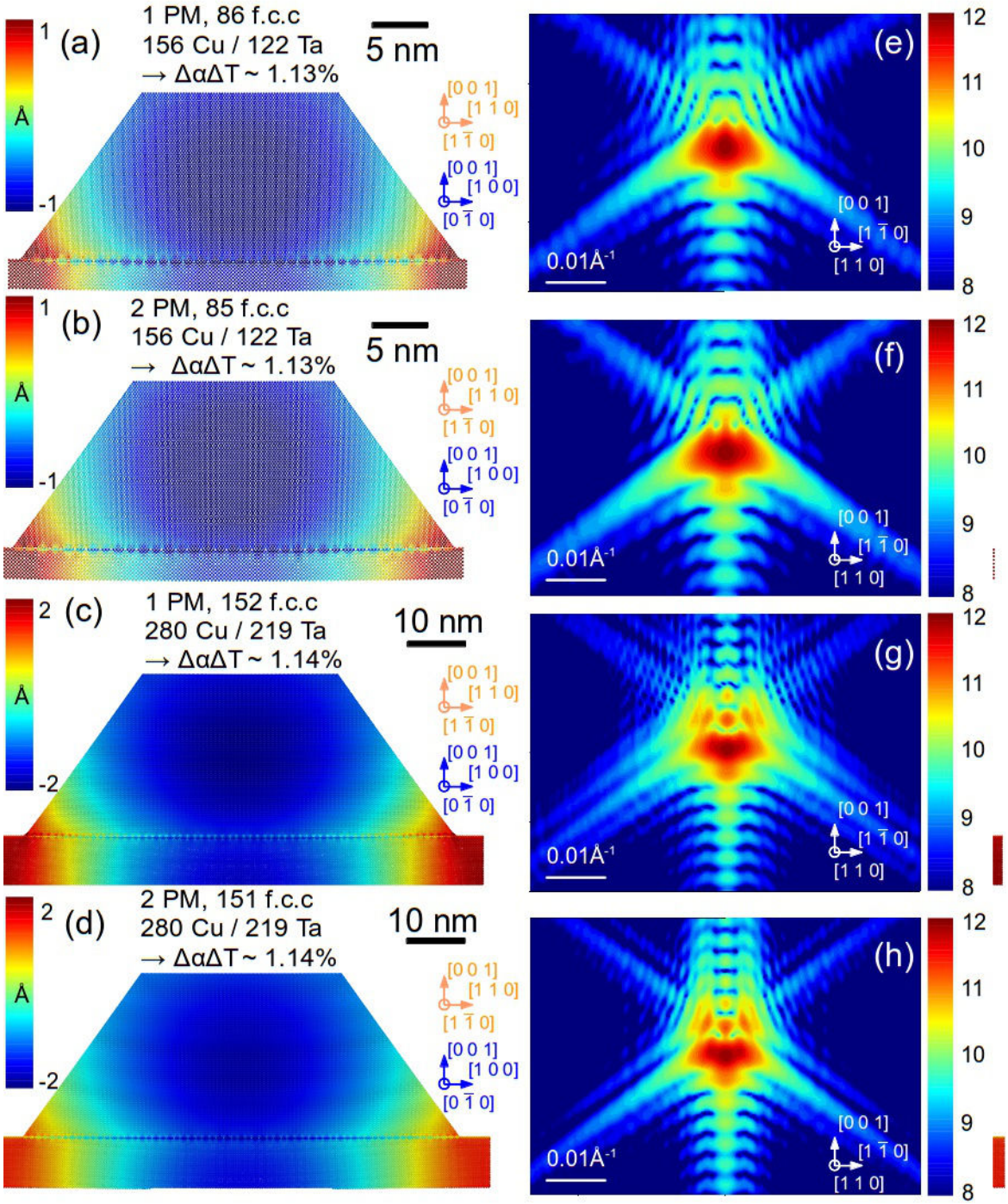

Fig. IX.10 *Comparison of the distribution of the u_z displacement field for the 1 PM and 2 PM configurations* (a) – (b) – (c) – (d) (x,z) slice through Cu islands with various sizes and number of PM layers in the initial configuration. showing the displacement field u_z for ΔαΔT = 1.13% (a) 40x40x15 nm^3 particle, 1 PM layer, (b) 40x40x15 nm^3 particle, 2 PM layers (c) 73x73x27.5 nm^3 particle, 1 PM layer, (b) 73x73x27.5 nm^3 particle, 2 PM layers. (e) – (f) - (g) – (h) (qx,qz) slices of the 0 0 2 Bragg reflection computed for the same u_z displacement field.

Due to the larger size of the particle, the amplitude of the displacement are larger for the same amount of thermal mismatch strain. The CXD pattern differs from the small particle, and the broadening of the Bragg peak is more pronounced. This suggest that CXD patterns similar to the experiment and to the FEM calculations would be observed if it was be possible to relax particles of similar size with the ADP potential. With our computational power (cluster of 60 cores/384 Gb) we are able to relax particles containing more than 10^7 atoms, which corresponds to a size of 140x140x53 nm. The length scale involved in the experiment should thus be accessible in a near future. It should be also noted that when the scattering vector is parallel to the surface (for instance the 2 2 0 reflection), the difference between the two interfaces is much more obvious (not shown here), however this kind of geometry is not adapted to a CXD experiment.

Conclusion

Large scale atomistic simulations using a ADP Cu-Ta potential have proven to be an efficient tool to predict the atomic structure of the interface between the Ta b.c.c. (0 0 1) surface and a solid state dewetted island with a (0 0 1) f.c.c. orientation. Both the predicted atomic structure of the interface and the equilibrium shape of the particle are reproducible below the melting point of Cu, independently on the initial conditions for the simulation (number of PM layers, size of the particle, boundary conditions...) and are very consistent with the shape and interface obtained experimentally.

A different orientation was predicted for the liquid state dewetting simulations; unfortunately, due to unsuccessful experiments , it is not clearly established if this orientation would exist.

CXD is a powerful tool to investigate 3 D displacement field in isolated objects, however it is clear that the technique can not provide much insight on the atomic structure of the Cu-Ta interface, since the calculated CXD patterns from the two most stable interfaces appear very similar as their residual strain is nearly equivalent.

Bibliography

Attarian Shandiza , M., Safaeia , A., Sanjabia, S., Barberb, Z.H. (2007) *J. Phys. Chem. Sol.* **68**, 1396-1399.

Beutier, G., Verdier, M., Parry, G., Gilles, B., Labat, S., Richard, M. I., Cornelius, T., Lory, P. -F., Vu Hoang, S., Livet, F., Thomas, O. & De Boissieu, M. (2012). *Thin Solid Films* **530**, 120-124.

Beutier, G., Verdier, M., De Boissieu, M., Gilles, B., Livet, F., Richard, M. I., Cornelius, T. W., Labat, S. & Thomas ., O. (2013). *J. Phys .Conf. Series* 425, 132003.

Daw, M. S. & Baskes, M., I. (1984) *Phys. Rev. B* **29**, 6443 (1984).

Favre-Nicolin, V., Richard, M. I. & Renevier, H. (2011). *J. Appl. Cryst.* **44**, 635-640.

Feidenhans'l, R. (1989) *Surface Science Reports* **10**, 105-188

Freund, L. B. & Suresh, S. (2003) *Thin Film Materials: Stress, Defect Formation and Surface Evolution,* edited by Cambridge University Press, Cambridge, England

Giannakopoulos ,K. P., & Goodhew, P. J (1998) *J. Crystal Growth* **188**, 26-31.

Hashibon, A., Lozovoi, A. Y., Mishin, Y., Elsässer, C. & Gumbsch, P. (2008) *Phys. Rev. B* **77**, 0941131

Howe J. M. (1997),. *Interfaces in materials,* edited by John Wiley & Sons, Inc.

Huang, W. J., Sun, R., Tao, J., Menard, L. D., Nuzzo, R.G. & Zuo, J. M. (2008). *Nature Materials* **7**, 308-313.

Johnson, R.A (1990) *Phys. Rev. B* **41**, 9717.

Jonsdottir, F. (1995) *Mat. Res. Soc. Symp. Proc.* **356,** 45-51

Massalski, T. B. (1986) *Binary Alloy Phase Diagrams* edited by Materials Park, OH

Matthews, J.W. & Blakeslee, A. E. (1974) *J. Crystal Growth* **27**, 118.

Matthews J.W. & Blakeslee, A. E. (1975) *J. Crystal Growth* **29,** 273.

McCormack, J. M., Myers, J. R. & Saxer, R. K. (1965) *J. Chem. Eng. Data* **10**(4), 319-321.

Musket, R.G, McLean, W., Colmenares, C.A., Makowiecki, D. M. & Seikhaus, W. J (1982) *Appl. of Surf. Sci.* **10**, 143-207.

Pinnington, T., Lavoie, C. & Tiedje, T. (1997) *J. Vac. Sci. and Tech.* **B 15**, 1265-1269

Robinson, I. K. (1986) *Phys. Rev. B.* **33**(6)

Robinson, I.K & Tweet, D. J. (1992) *Rep. Prog. Phys.* **55***,* 599-651

Rodney, D. & Phillips, R. (1999) *Phys. Rev. Lett.* **82**, 1704

Rodney, D. & Martin, G. (2000) *Phys. Rev. B* **61**, 8174

Rodney, D., Fivel, M. & Dendievel, R. (2005) *Phys. Rev. Lett.* **95**, 108004.

Spence, J. C. H (1988) [1980] *Experimental high-resolution electron microscopy*. Edited by New York: Oxford U. Press.

Springholz, G. (1999) *Applied Physics Letters* **75**, 3099-3101.

Venugopal, V. & Thijsse, B. J. (2009) *Thin solid Films* **517***,* 5482-5488

Verdier M (2008) ANR n°06-NANO-051 CRISTAL processing report

Vitos, L., Ruban, A. V., Skriver, H., L. & Kollár, J. (1998) *Surface Science* **411***,* 186-202

Winterbottom, W. L. (1967). *Acta Metall.* **15**, 303.

Yeshchenko ,O.A, Dmitruk, I. A., Alexeenko, A. A. & Dmytruk, A. M. (2007) *Phys. Rev. B* **75**, 085434.

Chapter X: Investigation of the three-dimensional distribution of Polar Inversion Domain Boundary in GaN wires

Contents

X.1 GaN nanowires and Inversion Domain Boundaries 257
X.2 CXD experiment.....258
Conclusion.....260
Bibliography.....261

Chapter X: Investigation of the three-dimensional distribution of Polar Inversion Domain Boundary in GaN wires

X.1 GaN nanowires and Inversion Domain Boundaries

As seen in previous chapters, f.c.c. metals are difficult to grow without a high density of defect and are thus well applied for their shaping / working ability. Conversely, semiconductors in general and GaN in particular can be grown with nearly no structural defects (dislocations), due to their high melting point and covalent bonding. This is fortunate, since their technological use is dedicated to functional properties, such as electron transport properties or optoelectronic: the presence of structural defects is a major drawback. Nevertheless, an old mechanical problem, the so called the Eshelby twist (Eshelby 1954), has been revisited in the 2000's thanks to the technological progress of nanowire growth: the presence of one or a group of screw dislocations stabilized at the core of the wire. These dislocations are usually bent to the side wall surface along a distance of the order of magnitude of the diameter (Chen *et al.* 2011)

The initial objective in the ANR MecaNIX project was to use such an isolated screw dislocation for Coherent Diffraction Imaging (CDI) experiments on these model structures. A dedicated synchrotron experiment has been unsuccessful to find a wire with a trapped dislocation. This would have left a clear Bragg splitting on the experimental CXD pattern.

Nevertheless, the detailed data analysis of theses measurements reveals an equally interesting microstructure. Instead of phase vortices, constant phase jumps between domains of homogeneous phase are observed.

These constant phase jumps between domains are related to the presence of planar defects in the (0 1 $\bar{1}$ 0) planes. The latter are very flat and remain parallel to the [0 0 0 1] growth direction. These planar defects are known as Inversion Domain Boundaries (IDB, Northrup *et al.* 1996): locally the occupation of the Ga and N sublattices is inversed (Fig. X.1), and the GaN polarity (defined by the Ga-N bonding, see Appendix. A2) is reversed between each side of the boundary, hence the name polar IDB.

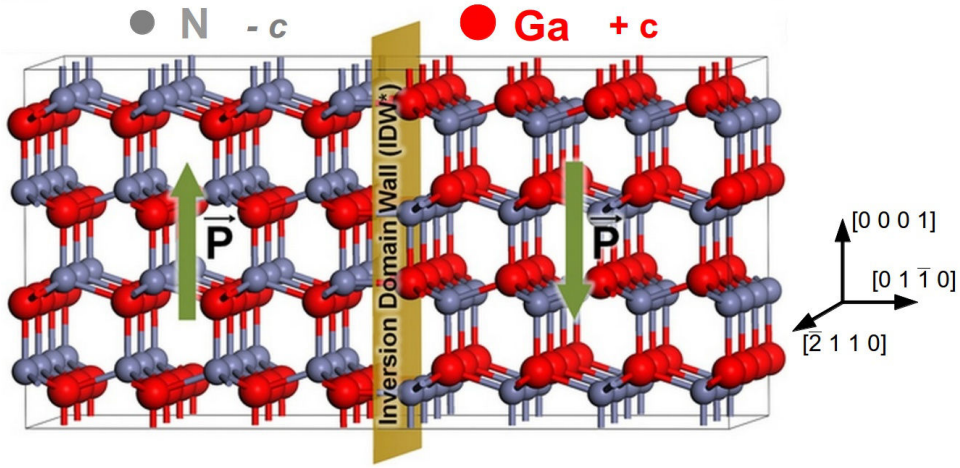

Fig. X.1 *3D representation of an Inversion Domain Boundary or Wall (IDB) in the [0 1 $\bar{1}$ 0] separating two-oppositely polarized GaN domains.* The left and right domains are respectively N-polar oriented (-c orientation) and Ga-polar oriented (+c orientation)

IDBs can be imaged by SEM after chemical etching of the wire, for example as shown in Fig. X.2.b. Under H_2 carrier gas, -*c* (nitrogen terminated) GaN surface stays flat, whereas the +*c* (Ga-Terminated) surface is -

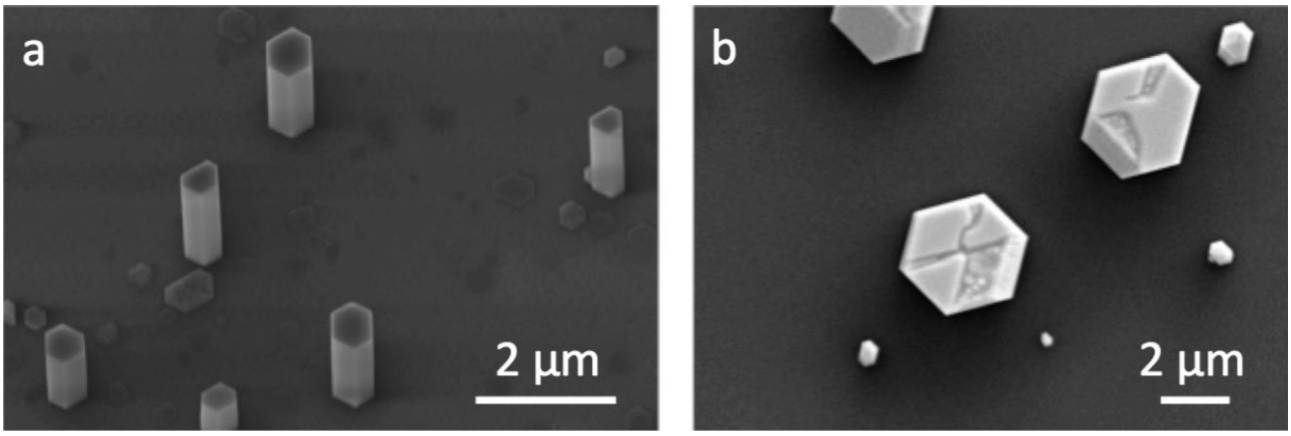

Fig. X.2 *Scanning electron microscopy pictures of GaN wires obtained by MOVPE.* (a) 25° - tilted view taken at the centre of the wafer showing single crystal wires. (b) top view taken at the wafer edge for a sample etched under H_2 carrier gas to underline polarity inversion domain boundaries

- roughened and exhibits small faceted pyramids (Fig. X.2.b). Nevertheless, a non destructive characterization of these wires (in the 100 nm – µm diameter size) to reveal the spatial distribution can also be achieved.
As discussed above it relies in the use of Coherent X-ray Diffraction which was used in the previous chapters to investigate the microstructure of sub-micron f.c.c. crystals..
It is particularly relevant for the study of IDBs since the latter can indeed be described as low-energy, coherent and thus strain-free interfaces.
The absence of inhomogeneous strain or structural defect that could alter the phase distribution makes this system particularly suitable for CDI. Using this technique, it is possible to access the precise atomic structure of the IDB. The high resolution of the phase allows to probe atomic displacements as small as a few picometres.
Annex A2 (Labat *et al*, 2015), is dedicated to the investigation of such domains. Using several reflections, it is demonstrated that picoscale displacements along and across the wire can be extracted from several non-coplanar reflections using CDI. In this study, the absolute polarity of each domain is also unambiguously identified.
The data analysis in Annex A2 is carried out in 2 dimensions so that the eventual variations of the IDB along the c-axis are not investigated. The reconstruction of the 3D displacement field can provide some insight in the evolution of the domain sizes and distributions along the wire axis. This unpublished complementary work is the purpose of this very brief Chapter.

X.2 CXD experiment

The GaN wires in this study are grown by Metal Organic Vapor Phase Epitaxy (MOVPE) on a c – oriented (0 0 0 1) sapphire substrate. Details on the sample preparation are found in Appendix A2. The growth conditions promote a vertical growth and hexagonal wires with average diameter of 600 nm and height of 3-5 µm are obtained (Fig. X.1.b). A low wire density is required for individual analysis with a micro-focused beam. For the sample of interest, a typical spacing of 5-10 µm is achieved between the wires (Fig. X.1.b) which is ideal for individual analysis of the nanowires with a CXD beam.
The collection of the diffraction data is performed around the 0 0 4 reflection, corresponding to a Bragg angle of $\theta = 32°$ at 9 keV. A single wire is illuminated by a 0.8 x 0.4 (HxV) μm^2 coherent beam focused by a Fresnel Zone Plate (FZP). The diffracted intensity is collected by a 516x516 pixels MAXIPIX detector (pixel size of 55 μm) placed 1.3m downstream from the sample. Further experimental details are found in the supplementary information of Appendix A2.

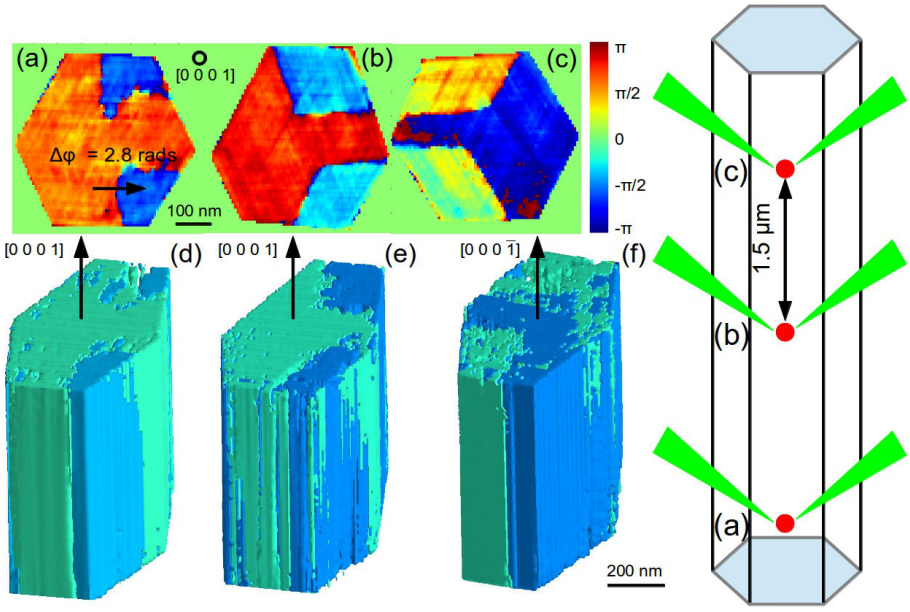

Fig. X.3 *2 D and 3 D reconstruction of the $u_{0\,0\,4}$ displacement field at several positions along the GaN wire.* 2D & 3D reconstruction carried out at the base (a & d), centre (b & e) and top (c & f) of the NW. (f) Schematics of the wire where the positions at which the measurements have been performed are indicated by a red dot.

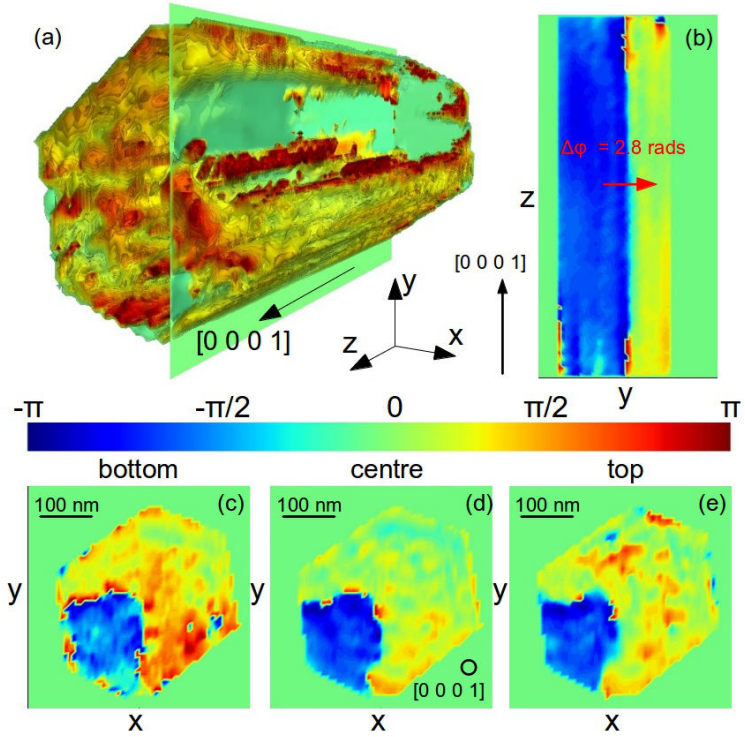

Fig. X. 4 *Evolution of the relative proportion and position of the interface between two IDB along the c-axis.* (a) 3D distribution of the phase revealing two IDB. (c) y-z slice showing the abesnce of variation in the relative proportion of the two domains. (c) Evolution of the position of the interface at varying height.

The wire of interest is 400 nm thick (as measured by the reconstruction) and approximately 5 μm high. The latter is estimated by scanning the wire along its height, using the *z* piezo-stage, while recording the diffracted intensity at each position of the scan. The measurement of the CXD patterns is carried out at 3 distinct positions along the wire, close to its base, at the centre and close to the top. The three positions are separated by approximately 1.5 μm. For each position, 3D CXD patterns are collected by rocking the sample over a range of 1.28° by steps of 0.005°.

Similarly to the approach described in Appendix A2, 2D intensity maps are first extracted from the 3D data in order to reconstruct a 2D image of the sample (Fig. X.3.a-c). The latter corresponds to the projection of the measured volume along the *c*-axis. The reconstruction is carried out using the procedure described in previous Chapters (Chapter VI & VII), consisting of alternating cycles of Error Reduction (ER) and Hybrid Input Output (HIO) with a regular upgrade of the support by Shrink Wrap (SW).

The 2D reconstructions reveal that a constant phase jump of 2.8 radians consistent with the measurements presented in Appendix A2 is observed for the three positions. The distribution of the IDB is slightly modified along the *c*-axis. Note that the reconstruction shown for the top position correspond to a complex-conjugated solution $\tilde{\rho}(\boldsymbol{r})$ explaining why both phase values and domain positions are inverted as compared to the other reconstructions.

These 2D reconstructions at various heights of the wire show that the inner structure is not completely invariant. The remaining question is to determine if the latter is invariant at small scale, in the illuminated volume (~0.4 μm in height). The 3D reconstruction of the diffraction data can address this question.

The results of the 3D reconstructions are shown in Fig. X.3.d-f. Note that smooth edges are normally expected at the boundaries of the illuminated volume since the latter is defined by the beam. Here we arbitrarily define a support with sharp boundaries which is a rough approximation. The support shape is determined from the 2D reconstruction and extended along the *c*-axis. It is not updated by SW during the phase-retrieval procedure. A reasonably good convergence of the procedure is achieved with this fixed support.

Fig. X.3.d-f shows that the relative proportion of the different domains is not significantly modified with the position along the *c*-axis. This is confirmed by measurements carried out on a different wire, with a different distribution of IDBs. The position of the interface and the relative proportion of the two polar IDB is found to be practically constant over a height of 0.8 μm. The calculated phase-jump between the two domains is determined to be 2.8 rad, in good agreement with data gathered on other wires.

Conclusion

The 3D reconstructions reveals that the inner structure does not undergo strong modifications along the wire axis. It is shown that the structure of the IDB is significantly modified over the whole wire length, but that the variations are very small within the volume illuminated by the X-ray beam.

The 3D reconstruction is thus not necessarily needed to understand the microstructure since the 2D projections already provides most of the interesting information.

Bibliography

Chen, X. J., Hwang, J.-S., Perillat-Merceroz, G., Landis, S., Martin, B., Le Si Dang, D., Eymery, J. & Durand, C. (2011) *J. Cryst. Growth* **322**, 15–22.

Eshelby, J. D. (1954) *J. Appl. Phys.* **25**, 255.

Labat. S., Richard, M-I., Dupraz, M., Gailhanou, M., Beutier, G., Verdier, M., Mastropietro, F., Cornelius, T. W., Schülli, T. U., Eymery, J. & Thomas, O. (2015) *ACS Nano*

Northrup, J. E., Neugebauer, J., & Romano, L. T. (1996) *Phys. Rev. Lett.* **77**, 103–106.

Chapter XI: Investigation of the magnetic structure and dynamics of sub-micron magnetic elements using Fourier Transform Holography

Contents

Introduction....262
X.1 Fourier Transform Holography....263
X.1.1 Basics of Fourier Transform Holography....263
X.1.2 Experimental set-up....265
XI.1.3 Magnetic contrast polarization and interference....266
XI.1.4 Investigation of in-plane magnetic scattering....270
XI.1.5 Extended reference....271
XI.2 Investigation of the in-plane magnetization of nanostructures and their dynamics....273
XI.2.1 Determination of the magnetic structure of a permalloy thin film....273
XI.2.2 Experimental considerations and correction of the experimental data....276
XI.2.3 Field dependence measurements....279
XI.2.4 Time resolved imaging of the magnetic vortex dynamics....281
XI.2.5 Observation of the resonance gyration of the magnetic vortex in a nano-contact spin torque oscillator....285
Conclusions....287
Bibliography....288

Chapter XI: Investigation of the magnetic structure and dynamics of sub-micron magnetic elements using Fourier Transform Holography

Introduction

In the previous chapters we demonstrated the interest of X-ray diffraction (XRD) techniques, and in particular of coherent X-ray diffraction, to investigate the structural properties of sub-micrometer objects. However, XRD techniques are not limited to the study of structural properties and are also relevant for the investigation of functional properties. Among them are the magnetic properties which also exhibit some size dependence.

Patterned and self-organized magnetic nanostructures are currently the subject of much interest due to their great potential in future nanotechnology (Wolf *et al.* 2001), including spintronics applications in which control of the spin orientation opens up a large range of perspectives in magnetoelectronic devices. One of the distinctive examples is the synchronized arrays of spin-torque oscillators (STO), a novel type of nanoscale source of microwaves (Slavin *et al.* 2009). Characterization of the magnetic states on the submicroscopic scale is however still a challenge, precluding advances in understanding and utilization of the properties of such new materials.

Since its first demonstration more than 20 years ago by McNulty *et al.* (1992) soft X-ray Fourier Transform Holography (FTH) has attracted considerable attention for imaging of nanostructured materials. Its high spatial resolution and independence from optical aberration are very beneficial for experimental studies of material properties. By exploiting the circular dichroism of soft x-ray resonant magnetic scattering (SXRMS), Eisebitt *et al.* (2004) demonstrated the application of the technique to magnetic materials. Magnetic holography combines the advantages of conventional FTH (nanometre spatial resolution, straightforward image reconstruction, sensitivity to buried layers,..) and XMCD (magnetic and element contrast). In the last decade, it has developed into a mature magnetic imaging technique. It is now well established for the study of in-plane magnetization (Tieg *et al.* 2010) and can be also used under applied electric and magnetic fields (Hellwig *et al.* 2006, Tieg *et al.* 2010). This feature is of particular interest as traditional imaging techniques such as magnetic force microscopy (MFM) are less suited for such measurements since they employ magnetic probes which are influenced by the external field. More recently, the technique took advantage of the ultrashort coherent X-ray pulses of a free electron laser to investigate ultrafast magnetization dynamics (Korff von Schmising *et al.* 2014).

In this chapter we first present the basics of Fourier Transform Holography and its application to the imaging of magnetic structures. In the following section, we detail the specificities of the experimental set-up that was used to perform most of the magnetic holographic experiments. To image the in-plane magnetization we employ a particular holographic imaging technique named HERALDO. The relevance of this technique and its advantages as compared to traditional FTH are exposed in section XI.1.4. The second part of this chapter is dedicated to the presentation of the synchrotron experiments carried-out during this PhD work. In this experimental part the key aspects to achieve a successful reconstruction are also discussed. In the first section of this second part, we use HERALDO to image the in-plane magnetization of a Fe/Ni element. The magnetic structure consist of a vortex closure domain which motion can be induced by a magnetic field. The study of the field-induced motion of this vortex is presented in section XI.2.3. The understanding of the magnetization dynamics of magnetic nanostructures is of particular technological interest. In the last part of this chapter, we investigate the magnetization dynamics of two types of objects. Section XI.2.4 presents an experiment dedicated to the imaging of the precession of the vortex in Permalloy (Py) elements in time-resolved mode. Section XI.2.5 investigates the magnetization dynamics of the so-called spin-torque oscillators.

X.1 Fourier Transform Holography

X.1.1 Basics of Fourier Transform Holography

We have seen in Chapter I that a coherent scattering pattern contains only half of the information on the illuminated object, as only intensities and not the phase of the scattered waves are measured. Using iterative phase retrieval algorithms (Gerchberg & Saxton 1972, Fienup 1982, Fienup 1987) it is however possible to retrieve the sample complex density numerically (Chapter I).
As no optical elements are used in this approach, the spatial resolution achievable with the technique is not limited by optical aberrations. Provided that sufficient oversampling is achieved, the resolution only depends on the maximum of the scattering vector, hence the term "lensless imaging method" to designate the technique.
Phase retrieval algorithms are not the only option to address the phase problem, and in some cases, an holographic method can be used. It relies on the fact that, if a reference wavefield from a suitable scatterer interferes at the detector plane with the wave scattered by the sample, the phase information can be sufficiently preserved such that an image of the object can be reconstructed from the measured intensity pattern.
This method named holography was first established in the visible spectral range using lasers, and was introduced by Gabor (1948) to improve the resolution of electron microscopes.
In the in-line geometry proposed by Gabor, a so-called Gabor-Leigth hologram is recorded at the detector plane. The latter results from the interferences between the wavefield from the sample of interest and a reference scatterer which is in this case the incident wavefield (Fig. X.1.a).
Almost two decades later, Stroke (1965) demonstrated that the high resolution required for lensless imaging techniques can be achieved by the use of a point reference in the plane of the object. The interference hologram recorded at the detector plane is defined as a lensless Fourier-Transform Hologram (Fig. X.1.b).

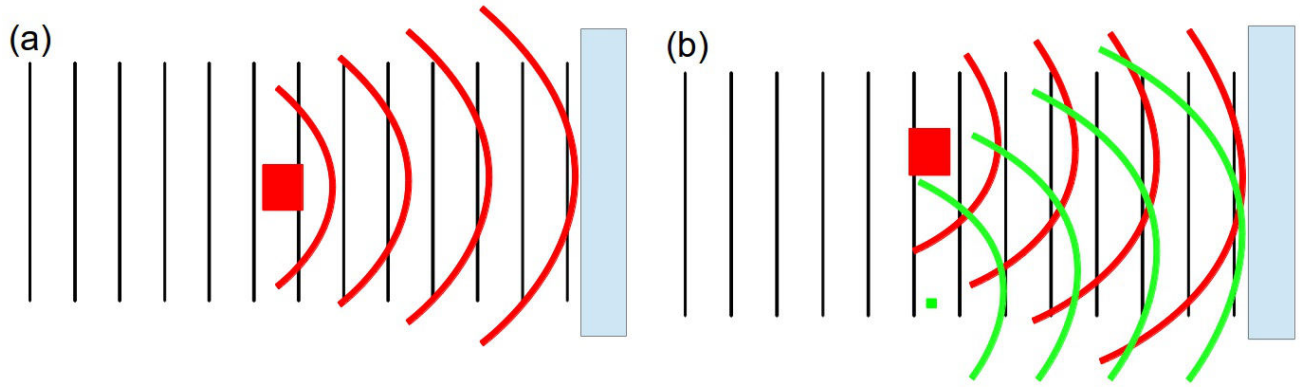

Fig. XI.1 *Schematics of the interferences between the wavefront scattered by the object and a reference wavefront.* (a) Gabor in line geometry → black : incident/reference wavefront , red : wavefront scattered by the sample. (b) Lensless Fourier Transform geometry → green : wavefront scattered by a point reference located in the same plane as the object.

This approach is a very elegant and simple way to address the phase problem. The phase of the object wave-field is encoded by the reference wave-field in the far-field scattered intensity collected by an area detector.
Both amplitude and phase of the complex image of the object are obtained using a single inverse Fourier transform.
The mathematical formalism of Fourier Transform Holography (FTH) can be expressed as follows. The scattered wave-field in the far field regime $A(q_x, q_y)$ can be represented by the sum of the wave-field $O(q_x, q_y)$ scattered by the object $o(x,y)$ and the wave-field $R(q_x,q_y)$ scattered by a point reference $r(x,y)$, where x and y are the Cartesian transverse coordinates in the real space, and q_x and q_y are the Cartesian transverse coordinates in the reciprocal space:

$$|A(q_x,q_y)|^2 = |FT\{r(x,y)+o(x,y)\}|^2 = |R(q_x,q_y)+O(q_x,q_y)|^2$$
$$TF^{-1}\{|A(q_x,q_y)|^2\} = f\otimes f = o\otimes o+r\otimes r+o\otimes r+r\otimes o \quad \text{(XI.1)}$$

We have seen in Chapter I that the inverse Fourier Transform of the far field intensity pattern is equal to the spatial autocorrelation of the scattering object (also known as a Patterson map). Here this function can be decomposed in four terms as illustrated in Fig. XI.2. The central part of the autocorrelation contains the object-object and reference-reference autocorrelations which are not of interest. The sample–reference cross correlations are seen on opposite sides of this central structure. They correspond to the complex object image and its complex conjugate and are located around ***r*** and ***-r*** where ***r*** is the vector from the reference to the object. The spatial resolution achievable in the object image is equal to the size of the reference scatterer.
If the technique was primarily demonstrated in the visible spectral range using lasers, the availability of coherent X-ray beams made possible its transposition to the soft X-ray range (McNulty *et al.* 1992, Eisebitt *et al.* 2004). It has also been implemented in Bragg geometry with hard X-rays (Chamard *et al.* 2010).

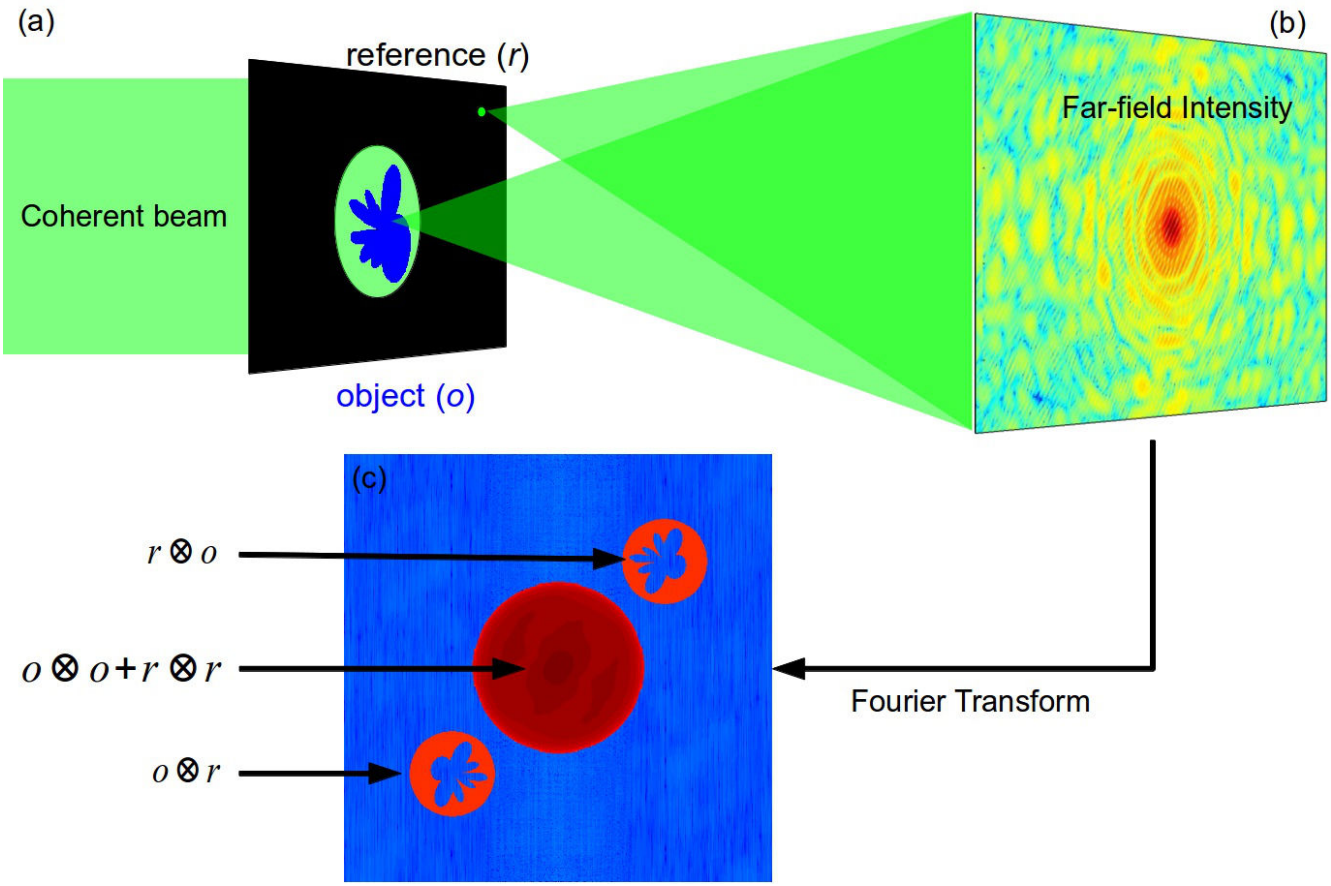

Fig. XI.2 *Schematics of the Fourier Transform Holography (FTH) technique.* (a) Sample and point-reference illuminated by a coherent X-ray beam. (b) Far-field intensity interference pattern (hologram) recorded by an area detector (c) Two dimensional Fourier transform of the hologram where the complex image of the sample appear in the cross-correlation terms.

The limitation in spatial resolution can be seen as a drawback in comparison to the iterative phase retrieval approach, where the resolution is only limited by the spatial extent of the far-field intensity pattern. To improve

the spatial resolution, the technique can be used in combination with phase retrieval algorithms. In this case, the image obtained by FTH is used to define the finite support and the starting guess of the phase retrieval procedure (Eisebitt *et al.* 2003).

X.1.2 Experimental set-up

The magnetic holography experiments presented in this work were carried-out on three beamlines at three different synchrotron facilities: I06 at Diamond Light Source, SEXTANTS SOLEIL and ID32 at the European Synchrotron Radiation Facility.

The three beamlines share some common points. The source of the X-ray beam is an undulator to provide a high brilliance and are designed to operate in the soft X-ray energy range (typically 0.05 → 1.8 keV for SEXTANTS, 0.1 → 1.5 keV for I06 and 0.4 → 1.6 keV for ID32). This energy range contains the $L_{2\text{-}3}$ absorption edges of 3d-transition metals, which is essential for the experiments presented in the following.

Additionally, since most of the experiments carried out on these beamlines involve magnetic elements, an important feature of the undulators is that they can provide variable polarization of the incident X-ray beam (either circular or linear, see section XI.1.3). The monochromatization of the beam is ensured by a plane grating monochromator which gives an energy resolution of $\Delta E/E \sim 10^{-4}$.

For coherent scattering experiments, the beam is refocused using toroidal mirrors placed between 1.5 and 3 m upstream the sample. Beam sizes of 200 (H) x 20 (V) μm^2, (FWHM) and 80 (H) x 50 (V) μm^2 are obtained for the I06 and SEXTANTS beamline respectively.

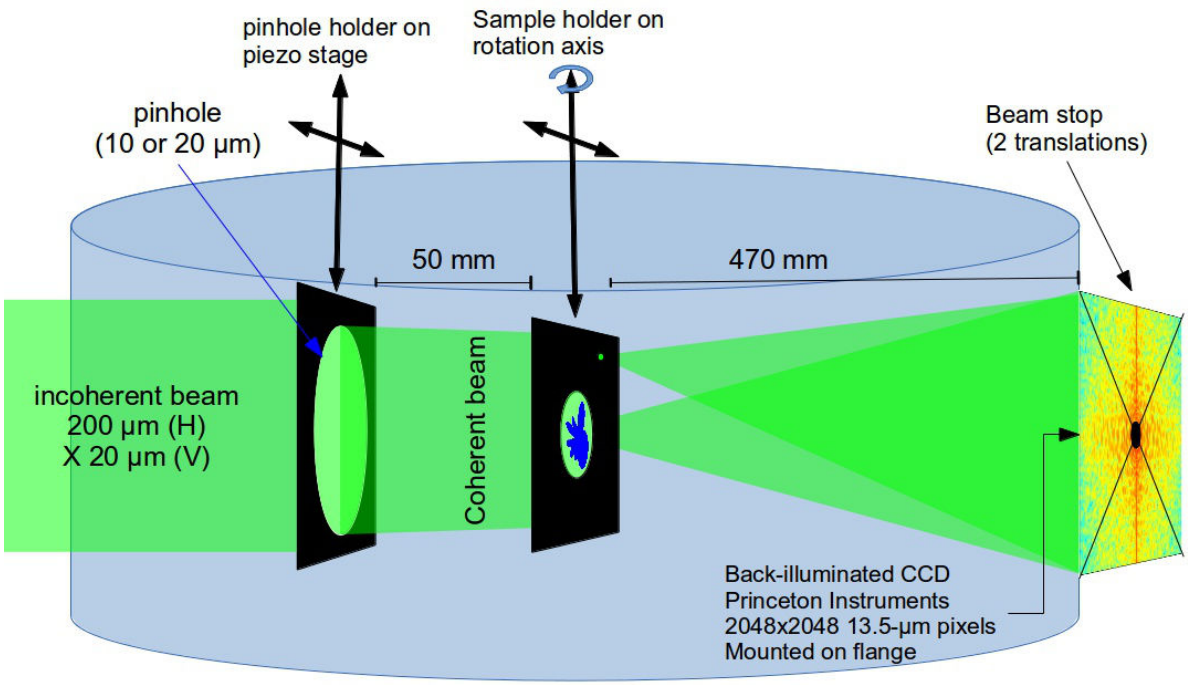

Fig. XI.3 *Schematics of the experimental set-up on the I06 beamline (Diamond Light Source)*

Fig. XI.3 shows the holographic set-up in the experimental hutch of the I06 beamline. Note that the strong absorption of soft X-rays in air requires to carry the experiment in an UHV chamber. Generally, it is not necessary to work in UHV conditions (< 10^{-9} mbar), and the base pressure in the chamber during the experiment is typically of the order of 10^{-6} mbar.

The energy range used for these experiments (700-850 eV) is one order of magnitude smaller than that of the CXD experiments in Bragg geometry. According to Eq. (I.4)(Chapter I), the transverse coherence length are expected to be larger than in the hard X-ray regime. However, the 200(H) x 20(V) μm^2 beam is not fully coherent, at least in the horizontal direction. To extract the coherent part of the beam, a circular pinhole is placed 50 mm upstream the sample. Pinholes of variable diameters have been used for the holographic experiments, the typical diameter being 20 μm. Note that for the ID32 beamline (ESRF) where the sample is located 120 meters downstream the source, larger transverse coherence lengths are obtained and larger pinhole diameters (50 μm) can be used without degrading the coherence properties. Due to the diffraction from the pinhole, a reduced pinhole size such as a 10 μm pinhole implies a larger beam size in the sample plane than a 20 μm one.
As illustrated in Fig. XI.3, the holographic experiments are carried out in a forward scattering geometry; the sample plane is perpendicular to the incident X-ray beam. Both sample and pinhole are mounted on holders for alignment in the beam. For the pinhole holder, piezo-actuators are used to ensure a precise positioning. The sample holder is mounted on a rotation axis, such that the sample can be tilted with respect to the incident X-ray beam. This feature is essential for the investigation of in-plane magnetization (see section XI.1.4).
The scattering intensity is collected by a back-illuminated CCD (BI-CCD) from Princeton Instruments. The CCD chip consists of 2048x2048 pixels of size 13.5 μm. The camera is mounted on a flange, hence the sample/detector distance can not be reduced below 47 cm. A beamstop prevents exposing the CCD camera in the direct beam.
As discussed in the previous section, the real space resolution of FTH is limited by two parameters: the size of the reference, and the extent of the reciprocal space pattern. In the case of the forward scattering geometry, the decay of intensity with q is not as pronounced as in the case of the Bragg geometry such that a large extent of the reciprocal space is in principle accessible. For the samples used in this work, the aperture of the reference slit (see section XI.2.1) is generally of the order of 20 nm, which gives the limit of the resolution accessible by FTH. The extent of the reciprocal space accessible is given by the angular acceptance of the area detector which depends on the sample-detector distance D :

$$r_{limit} = \frac{\lambda . D}{n_{pixels} . s_{pixels}} \qquad \text{(XI.2)}$$

where λ is the X-ray wavelength, n_{pixels} is the number of pixels of the CCD camera and s_{pixels} is their size. We will see in the next section that the experiments were carried out at the absorption edge of 3d-transition metals which corresponds to 700-850 eV. The pixel size of 13.5 μm gives a resolution limit of 30 nm with the I06 set-up. It turns out that the resolution is here limited by the extent of the reciprocal space. In order to improve the spatial resolution, it is thus necessary to increase the angular acceptance of the area detector, for instance by decreasing the sample-detector distance.
The camera being mounted on a flange at the I06 end-station, it is so far not possible with this set-up to bring the detector closer to the sample. As a comparison, the set-up on the ID32 and SEXTANTS beamlines allows to decrease the sample/detector to a value of 30 cm. With a similar detector, this gives a resolution limit of 17 nm.

XI.1.3 Magnetic contrast polarization and interference

In this PhD work, FTH is used to investigate magnetic structures in transition metals exploiting the circular dichroism of soft X-ray resonant magnetic scattering (SXRMS) in forward scattering geometry. The term dichroism is used to to reflect the dependence of photon absorption of a material on polarization. It originates in anisotropies in the charge or the spin in the material. In the latter case we speak of magnetic dichroism.
Metals are usually ferromagnetic and their magnetic properties are best studied with circular dichroism. Circularly polarized X-rays are sensitive to the projection of the magnetic moments onto the propagation

direction, both in the absorption and in the scattering cross-section. In FTH, we use the circular dichroism to image the magnetic moments along the propagation vector: it is similar to X-ray Magnetic Circular Dichroism (XMCD), which is an absorption spectroscopy, but in (small angle) scattering geometry.
In the photon absorption process, core electrons are excited into empty states and thereby probe the electronic and magnetic properties of the empty valence levels. For the case of 3d transition elements such as Fe, Ni and Co which magnetic properties are largely determined by the 3d valence electrons.

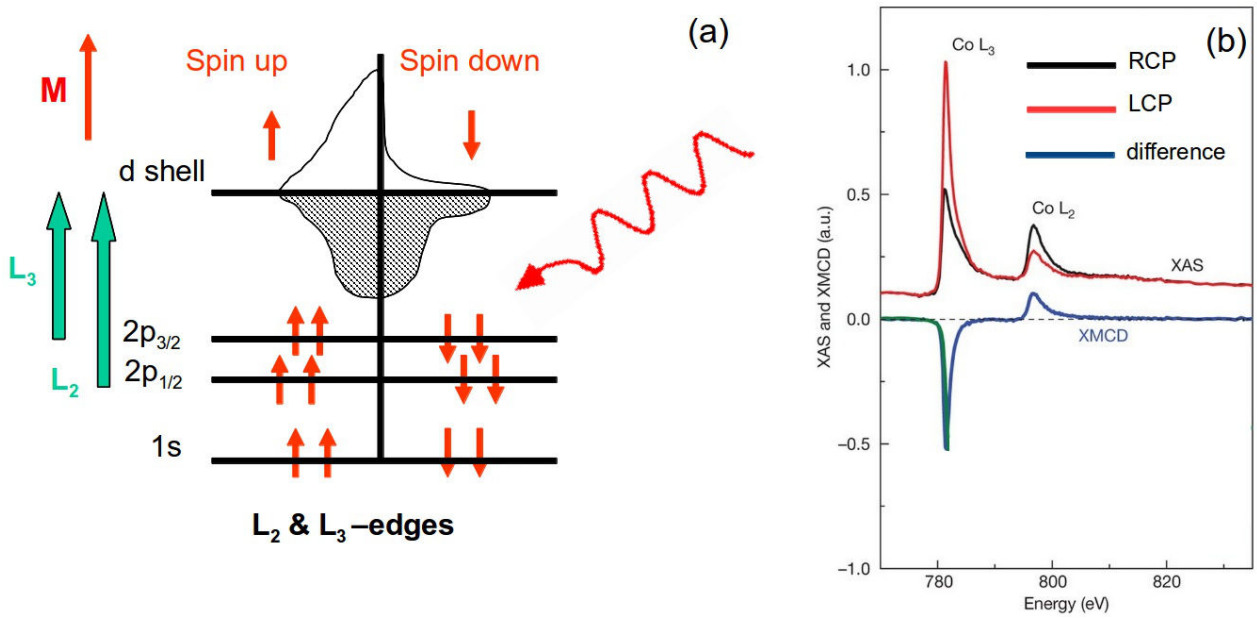

Fig. XI.4 *Illustration of the X-ray circular magnetic dichroism (XMCD)* (a) Electronic transitions in L-edge X-ray absorption for circular magnetic dichroism. The transition occurs between the split 2p core level and the empty spin polarized 3d states. (c) L-edge absorption spectra of Co in the presence of XMCD.

To access their magnetic properties it is thus interesting to excite 2p core electrons to use 2p → 3d dipole transitions ($L_{2,3}$ absorption edges). Band structure plays an important role in the shape of the absorption spectra of 3d transition metals. The photo-electron is excited from the spin-orbit split $2p_{3/2}$ and $2p_{1/2}$ levels to empty d valence states (L_3 and L_2 edges respectively, Fig. XI.4.a).
In XMCD spectroscopy pioneered by Schültz 1987, the L_3 and L_2 resonant intensities can be linked with the number of empty d states (holes). For a magnetic material the electronic shell has a spin moment which is given by the imbalance of spin-up and spin-down electrons (or spin-up and spin-down holes). This difference between the number of spin-up and spin-down hole can be measured if the X-ray absorption process becomes spin dependent. The photoelectron carries the transferred angular momentum of the photon as a spin or angular momentum or both (Stohr & Wu 1994). If the photo-electron originates from a spin-orbit split level, for instance the $2p_{3/2}$ level (L_3), the angular momentum can be transferred in part to the spin through the spin-orbit coupling. Right Circularly Polarized (RCP) and Left Circularly Polarized (LCP) photons carries an angular momentum with opposite direction, hence photo-electrons with opposite spins are created in the two cases. As illustrated in Fig. XI.4.b, this results in different absorption for the two polarizations at the L_2 and L_3 edges. The technique has thus both a chemical sensitivity and electron shell sensitivity.
Soft X-ray resonant magnetic scattering combines X-ray scattering with XMCD or X-Ray Magnetic Linear Dichroism (XMLD) and is used in this PhD work to study magnetic structures. Usually, X-ray scattering is weakly sensitive to magnetism, and the non-resonant magnetic scattering which can be defined as the scattering from the orbital and spin moment of the electron is much weaker than the charge scattering. The situation is

changed when the incident photon energy is tuned close to an absorption edge where for the reasons described above (spin-orbit coupling of the core electrons), X-ray scattering becomes very sensitive to magnetization.
The polarization dependence in charge and resonant magnetic scattering is expressed in the following representation of the complex scattering factors f_n for a scattering centre n (Hannon *et al.* 1988, Lovesey & Collins 1996)

$$f_n = F_0(\hat{\epsilon}_f^* . \hat{\epsilon}_i) - iF_1(\hat{\epsilon}_f^* \times \hat{\epsilon}_i) . \hat{m} + F_2(\hat{\epsilon}_f^* . \hat{m})(\hat{\epsilon}_i . \hat{m}) \quad \text{(XI.3)}$$

where $\hat{m}$ is the local magnetization unit vector and ε_i and ε_f the polarisation of the incident and scattered photons respectively. F_0 , F_1 and F_2 depend on the energy E of X-rays. The F_0 term gives the charge scattering and contains anomalous terms $f_c' + i f_c''$ which are large near the absorption edge. This term allows to study the charge order. The F_1 term is the magnetic scattering $f_m' + i f_m''$ which depends linearly on the magnetization direction and can become comparable to F_0 near $L_{2,3}$ and $M_{4,5}$ absorption edges (Fig. XI.5). The third term F_2 has a quadratic dependence in the magnetization direction and is thus sensitive to orbital order, but it is usually much smaller than F_0 and F_1. For the 3d transition metals at the $L_{2,3}$ absorption edge, the resonant magnetic scattering is comparable in amplitude to the charge scattering.

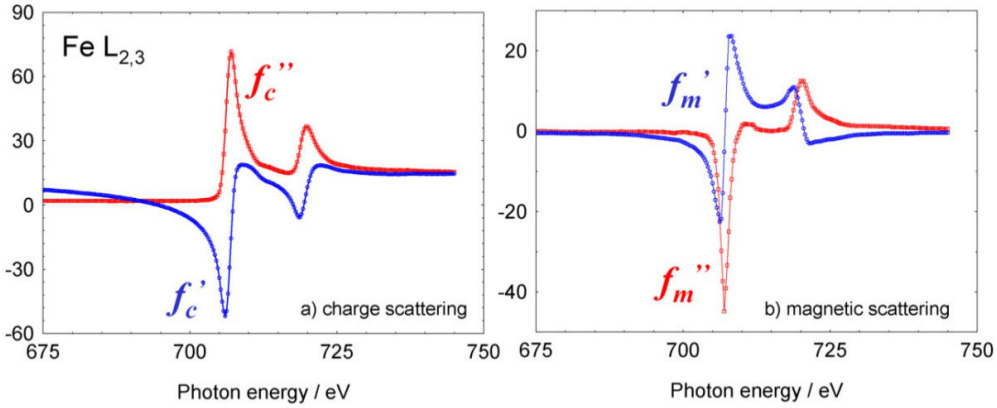

Fig. XI.5 *Real and imaginary parts of (a) the charge scattering F_0 and (b) the magnetic scattering F_1 at the Fe $L_{2,3}$ edges* (from Van der Laan, 2008)

The magnetic scattering intensity is a function of both the photon energy and the wave-vectors $\boldsymbol{k_i}$ ($\boldsymbol{k_f}$) of the incident (scattered) X-ray beam: this can be shown from Eq. (XI.3) (Hill & McMorrow, 1995). The scattering intensity is given by:

$$I(E, \boldsymbol{q}) \propto \left| \sum_n f_n(E) e^{i\boldsymbol{q}.\boldsymbol{r}_n} \right|^2 \quad \text{(XI.4)}$$

where the summation over the scatterer n runs over a coherence volume in the sample. The magnetic terms f_n containing F_1 and F_2 in Eq. (XI.3) give rise to circular and linear X-ray magnetic dichroism in the scattered or absorbed X-ray intensity.

By taking the Fourier transforms $\bar{\rho}$ and $\hat{\boldsymbol{M}}$ of the charge density and of the unit magnetization vector, Eq. (XI.3) can be rewritten as

$$F(\boldsymbol{q}) = F_0(\hat{\epsilon}_f^* . \hat{\epsilon}_i)\bar{\rho}(\boldsymbol{q}) - iF_1(\hat{\epsilon}_f^* \times \hat{\epsilon}_i) . \hat{\boldsymbol{M}}(\boldsymbol{q}) = M_c(\boldsymbol{q}) + M_m(\boldsymbol{q}) \quad \text{(XI.5)}$$

where $M_c(\boldsymbol{q})$ and $M_m(\boldsymbol{q})$ refer to the Fourier transform of the charge and magnetic contributions. Note that for the sake of simplicity we discarded the third term of Eq. (XI.3), F_2, which is much smaller in amplitude than F_0 and F_1.

In interference experiments such as holography, the ability to interfere depends on the polarization state of the interfering beams. Following the formalism introduced by Hill & McMorrow (1996), the polarization dependence of the magnetic scattering cross-section can be reformulated in term of linear polarization states, perpendicular and parallel to the scattering plane.
It is convenient to write the geometry factors $(\hat{\epsilon_f}^*.\hat{\epsilon}_i)$ and $(\hat{\epsilon_f}^*\times\hat{\epsilon}_i).\hat{m}$ as a 2 x 2 matrix,

$$\begin{pmatrix} \sigma\rightarrow\sigma' & \pi\rightarrow\sigma' \\ \sigma\rightarrow\pi' & \pi\rightarrow\pi' \end{pmatrix} \tag{XI.6}$$

representing the different scattering channels, where the linear polarization perpendicular and parallel to the scattering plane is denoted σ and π polarization respectively. The primes refer to the scattered beam.

Using the unit vectors $\hat{\boldsymbol{k}}_i$ and $\hat{\boldsymbol{k}}_f$ along the incident and scattered beams respectively. The Fourier transform of the complex resonant scattering factor can be expressed as follows:

$$F(\boldsymbol{q}) = F_0\begin{pmatrix} 1 & 0 \\ 0 & \hat{\boldsymbol{k}}_f.\hat{\boldsymbol{k}}_i \end{pmatrix}\bar{\rho}(\boldsymbol{q}) - iF_1\begin{pmatrix} 0 & \hat{\boldsymbol{k}}_i \\ -\hat{\boldsymbol{k}}_f & (\hat{\boldsymbol{k}}_f\wedge\hat{\boldsymbol{k}}) \end{pmatrix}.\hat{\boldsymbol{M}}(\boldsymbol{q}) \tag{XI.7}$$

The first term, which does not have off-diagonal elements, keeps the polarization state unchanged, *i.e.* an $\epsilon_{i\|}$ photon is scattered into an $\epsilon_{f\|}$ photon (π → π' scattering) and $\epsilon_{i\perp} \rightarrow \epsilon_{f\perp}$ (σ → σ ' scattering). On the other hand, the magnetic scattering term allows both σ → π' scattering and σ' → π as well as π → π' scattering while σ → σ' is forbidden. Note that the off-diagonal elements are $\hat{\epsilon_{i\|}}.\hat{\epsilon_{f\perp}} = \hat{\boldsymbol{k}}_i$ and $\hat{\epsilon_{i\perp}}.\hat{\epsilon_{f\|}} = -\hat{\boldsymbol{k}}_f$. In other words, Eq. (XI.6) shows that the magnetization component parallel to the scattering plane rotates the polarization channel while the magnetization component perpendicular to the scattering plane appears in the π → π' channel.
In forward small-angle scattering, where $\hat{\boldsymbol{k}}_i \approx \hat{\boldsymbol{k}}_f$, Eq. (XI.6) can be simplified :

$$F(\boldsymbol{q}) = F_0\bar{\rho}\begin{pmatrix} 1 & 0 \\ 0 & 1 \end{pmatrix} - iF_1\begin{pmatrix} 0 & \hat{\boldsymbol{k}} \\ -\hat{\boldsymbol{k}} & 0 \end{pmatrix}.\hat{\boldsymbol{M}} \tag{XI.7}$$

It comes that in forward scattering geometry, the only interference term between charge and magnetism vanishes with linear polarization. It was also the only term probing magnetic component perpendicular to the scattering plane and thus to the propagation vector. Circular polarization is thus needed to access the magnetic contrast.

Let us consider now a magnetic sample with a point reference (a pinhole) in a forward scattering geometry. At the absorption edge, the resonant scattering from the sample interfere with the unscattered wave propagating from the pinhole.
For an incident X-ray beam with linear polarization, the scattering intensity collected by the CCD camera is expressed as follows.

$$I_{\text{lin}}(\boldsymbol{q}) = |F(\boldsymbol{q})|^2 = |F_0\bar{\rho}(\boldsymbol{q})|^2 + |F_1|^2|\hat{\boldsymbol{k}}.\hat{\boldsymbol{M}}(\boldsymbol{q})|^2 \simeq |F_0\bar{\rho}(\boldsymbol{q})|^2 \tag{XI.8}$$

There is an interference between the charge scattering from the sample and the unscattered reference wave propagating from the pinhole, and a charge hologram is recorded. However, no interference is recorded between the magnetic scattering and the reference wave. It can be understood by the fact that for linearly polarized radiation, the magnetic scattering term is maximized when the plane of polarization is rotated by $\pi/2$ (see Eq. (XI.7)) while the diffraction from the pinhole does not change the polarization of the X-ray beam. Unscattered and magnetically scattered X-rays go into orthogonal polarization channels and can not interfere. The magnetic contrast is thus not accessible in forward scattering geometry with linearly polarized X-rays.
With circularly polarized X-rays, right and left circular polarized X-rays are scattered into the same polarization state and can interfere with the pinhole wave at the detector plane. The scattering intensity collected by the CCD camera is expressed as follows;

$$I_{\text{circ}}(\boldsymbol{q}) = |F_0\bar{\rho}|^2 + |F_1|^2 |\hat{\boldsymbol{k}}.\hat{\boldsymbol{M}}|^2 \pm 2\Re[F_0 F_1 \bar{\rho}\,\hat{\boldsymbol{k}}.\hat{\boldsymbol{M}}] \quad \text{(XI.9)}$$

A charge-magnetic interference term appears in Eq. (XI.9) which sign depends on the helicity of the incident X-rays. From Eq. (XI.9) it also comes that if the coherent scattering intensities measured with right and left circular polarization are added, the magnetic-interference term vanishes, and the intensity distribution obtained is exactly the same as the intensity distribution with linear polarization (Eisebitt *et al.* 2003). Linear polarization can thus be thought as the coherent superposition of right and left circular polarization.

The intensity difference is much more interesting. As seen from Eq. (XI 10), the difference between the two polarizations leads to the cancellation of the pure charge scattering and magnetic scattering terms. The difference hologram is proportional to the reference - magnetic interference term alone:

$$I_{XMCD}(\boldsymbol{q}) = 4\Re[F_0 F_1 \bar{\rho}(\boldsymbol{q})\hat{\boldsymbol{k}}.\hat{\boldsymbol{M}}(\boldsymbol{q})] \quad \text{(XI.10)}$$

The difference of two opposite helicity images can thus be used to enhance the magnetic contrast and suppress any non-magnetic contributions.
It turns out that by exploiting the circular dichroism of SXRMS it is possible to turn conventional FTH into a magnetic imaging technique. As discussed previously, the use of the technique for magnetic systems was pioneered by Eisebitt *et al* in 2004 and has developed into a mature magnetic imaging technique in the last decade.

XI.1.4 Investigation of in-plane magnetic scattering

In the field of magnetic imaging FTH has been primarily applied to systems with out-of-plane magnetization (Eisebitt *et al.* 2004). The most typical structures are based on [Co/Pd]or [Co/Pt] multilayers. This limitation is owing to the sample mask structure and the angular dependence of the XMCD effect. FTH samples are usually prepared on the back side of a Si_3N_4 membrane while the front side carries the mask to define the sample and reference beams. This common sample-mask design has a fixed field-of-view.
Tieg *et al.* (2010) demonstrated the possibility of imaging the in-plane magnetization by adapting the mask and scattering geometry to record holograms at off-normal incidence. In this geometry, the reference beam is defined by an inclined hole. (Fig. XI.6.a from Tieg *et al.* 2010)
From Eq. (XI.10) it comes that the magnetic contrast in FTH using XMCD is proportional to the projection of the magnetization onto the incident wave vector : $\hat{\boldsymbol{M}}.\hat{\boldsymbol{k}}_i$. In a forward scattering geometry, the in-plane magnetized samples can thus be only imaged with a tilt angle α. Fig. XI.6.a shows the off-normal geometry employed by Tieg to image the in-plane magnetization. An inclined reference hole is milled by Focused Ion Beam (FIB) at 20° with respect to the surface normal. Note that the hole has a quite large opening angle which allow FTH imaging at ± 15° with respect to the milling angle. The increase in the magnetic contrast with the

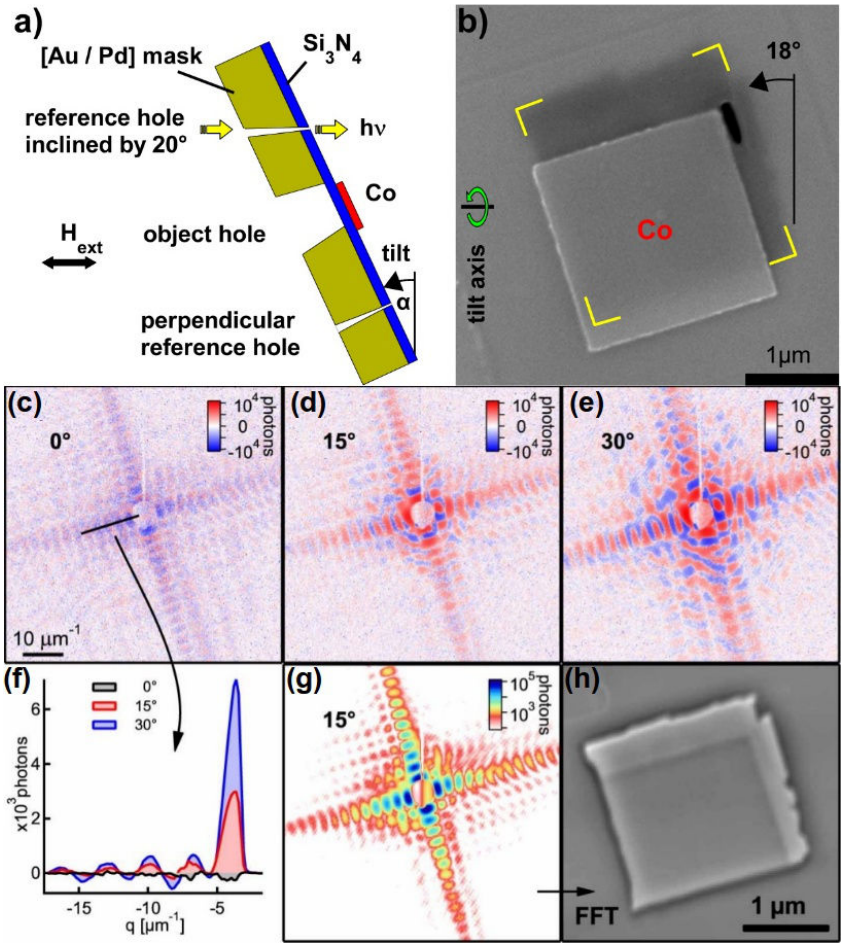

Fig. XI.6 *Imaging the in-plane magnetisation with FTH* (a) Cross section of the sample-mask assembly with an inclined and conically shaped reference hole. (c) 2x2 µm^2 Co element, the square object hole is indicated by yellow corners. Holograms from the Co element measured at tilt-angles α of 0° (c), 15°(d) and 30°(e). Images (c-e) show difference holograms for opposite helicities and (g) gives the sum of both helicities. (f) Line scan showing that the intensity in the difference hologram scales with the projection of the magnetization on the incoming beam direction. (h) Reconstruction of the sample using (g)

tilting angle is clearly visible (Fig. XI.6.c & XI.6.f). As discussed above, the larger is the tilt angle, the larger is the projection of the sample onto the plane normal to the beam, and the larger is the projection of the in-plane magnetization along the beam direction.
We will see in the next-sections that we mainly investigated in-plane magnetic structures in this PhD work, hence the off-normal geometry was generally employed.

XI.1.5 Extended reference

A recent development in the Field of FTH has reduced the restrictions on the reference size to allow a wider range of possibilities, and more flexibility during the holographic experiments.
The technique known as Holography with Extended Reference by Autocorrelation Linear Differential Operator

(HERALDO) enables the use of extended objects references without compromising and even enhancing the spatial resolution. It was introduced by Guizar & Fienup (2007) and first demonstrated experimentally a year later (Guizar & Fienup 2008). Its lensless imaging capabilities have also been extended to the soft-X-ray regime, (Zhu *et al.* 2010) and to femto second imaging (Gauthier *et al.* 2010). More recently, it has been applied to the imaging of out-of-plane (Duckworth *et al.* 2011) and in-plane (Duckworth *et al.* 2013) magnetic structures.
In HERALDO the reference wave emerges from a sharp feature or an edge on an extended structure, and the image is differentially encoded in the autocorrelation of the coherent far-field intensity pattern, *i.e.* the Fourier transform of the recorded hologram. The reconstruction procedure is based on the application of linear differential operators to the Fourier transform of the hologram.
In the experiments presented in this manuscript we used a linear slit as extended reference around the magnetic sample (Fig. XI.7.a). The latter induce an intense streak of intensity on the recorded hologram (Fig. XI.7.b). The differential filter to be multiplied to the hologram is defined by the directional derivative of the edges from the extended reference (Fig. XI.7.d). Prior knowledge of the slit orientation is unnecessary as it is determined from the slit that it forms on the hologram (Fig. XI.7.b)

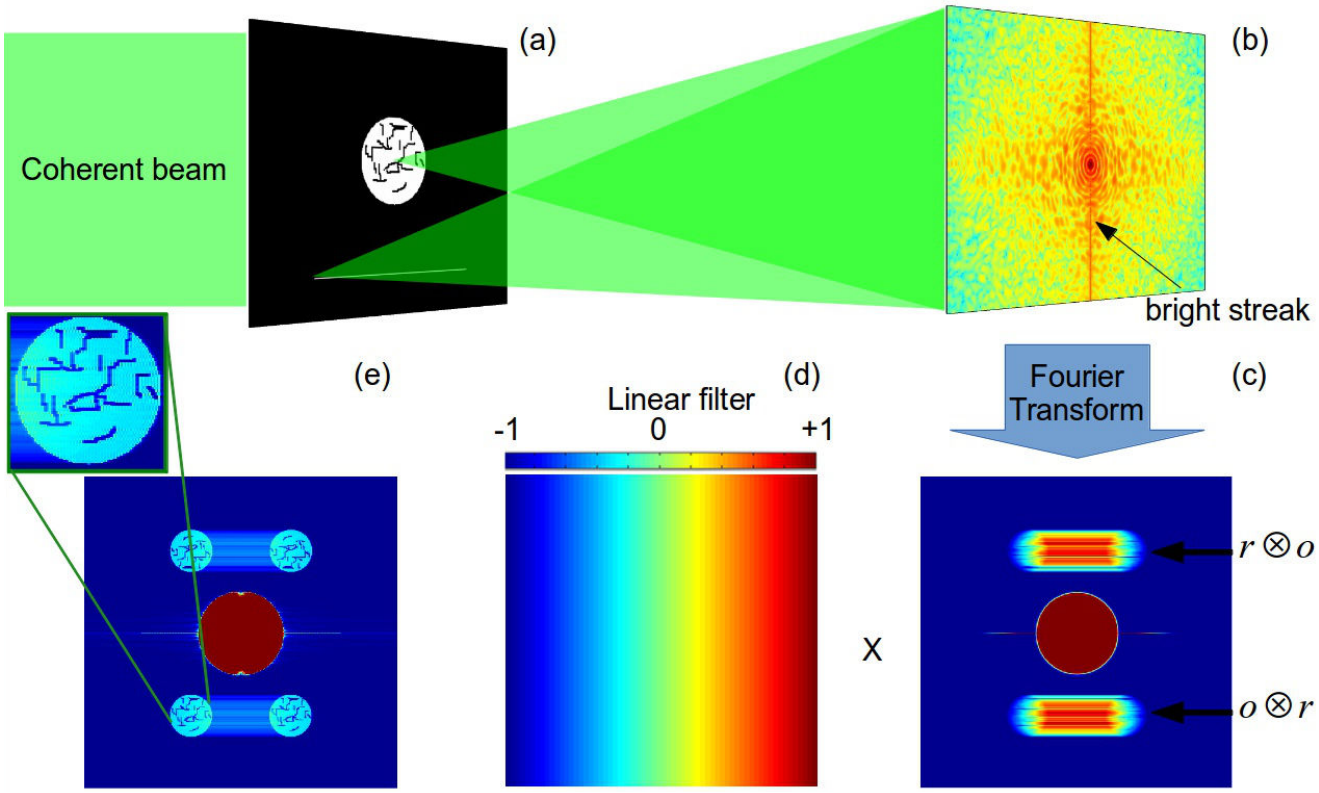

Fig. XI.7 *HERALDO* schematics (a) Object and extended reference illuminated by a coherent X-ray beam. (b) Far field intensity hologram recorded by an area detector. The bright streak is induced by the diffraction from the slit. (c) Fourier transform of the differential hologram. (d) Differential filter applied to the hologram. (e) Reconstructed hologram after application of the differential filter.

With a slit used as a reference, the reference waves emerge from the sharp edges on the slits, providing two independent reconstructions. Note that in order to obtain two independent reconstructions, the two ends of the slits must satisfy the HERALDO separation conditions defined by Guizar-Sicairos & Fienup (2007). In short, a sufficient distance must be ensured between the magnetic sample and the slit and between both ends of the slits. If these conditions are not satisfied, *i.e.* the edges of the slits are too close, the two reconstructions overlap.

Similarly to the case of a point-reference, a complex conjugate image is obtained for the two reconstructions. The resolution is non longer determined by the size of the reference but rather by the quality of the sharpness features.
The use of an extended reference has several advantages. In standard FTH, there is a compromise in the determination of the size of the reference point-source between two requirements: the resolution given by the reference size and the flux through the reference for observing interference fringes with a good contrast. The hologram of the fringe visibility depends on the relative amplitude of the wave-fields diffracted by the object and by the reference. It is thus maximum when these amplitudes are equal (Gauthier *et al.* 2010, Szoke 1997).
With an extended reference the flux is no longer limited by the size of the reference. The wavefields diffracted by the object and the reference become comparable in intensity. This yields an increased fringe visibility, especially at large scattering angles (corresponding to higher resolution) where the scattering is generally weak and a potential enhancement of the resolution as compared with a point source reference.
The second advantage is more specific to the experiments presented in this work, where the in-plane magnetization is investigated. As shown in the previous section, the contrast in the in-plane magnetization depends on the projection of the latter onto the wave-vector of the X-ray beam. It is thus only accessible if the sample is tilted with respect to the incident X-ray beam. As shown by Tieg *et al.* 2010, the point-reference (pinhole) needs to be milled with an inclination with respect to the surface normal. Beyond the experimental difficulties of milling an inclined hole with FIB, the main limitation with this configuration is its lack of versatility. Only a limited angular range is reachable, and to image the sample in normal geometry (sample normal parallel to the direction of propagation), two holes need to be milled. The use of a slit as an extended reference overcome these limitations, and FTH can be imaged with good contrast within a large range of tilt angles (± 45° with the I06 experimental set-up).

XI.2 Investigation of the in-plane magnetization of nanostructures and their dynamics

During this PhD, I was involved in several FTH experiments aiming at imaging magnetic structures and their dynamics. If I did not participate to the sample preparation, my contribution was significant for the measurement and the analysis (*i.e.* the reconstruction) of the experimental data. The most interesting results of the holography experiments carried out during this PhD are presented in this section.

XI.2.1 Determination of the magnetic structure of a permalloy thin film

In this work, FTH was primarily used for the investigation of the in-plane magnetization in permalloy (Fe/Ni) thin films. The preparation procedure of the sample is briefly described in the following. Note that additional details on the preparation procedure can be found elsewhere (Duckworth *et al.* 2011)
The processing starts by depositing a 50 nm thick Py film onto the front side of 100 nm thick Si_3N_4 membrane. The sample is protected with a 2 nm Ta capping layer. On the reverse side of the membrane, a 600 nm Au layer is deposited to act as an X-ray opaque mask. FIB milling is used to pattern a square 3.0 μm field of view (FOV) into the mask, milled down as far as the membrane. FIB is then used to cut out the material from the continuous thin film on the other side of the membrane, such that an isolated Py element remains within the FOV aperture (Fig. XI.8.a & XI.8.b). The lateral dimensions of the Py element are generally selected between 400 nm and 1 μm (Fig. XI.8.a). Note that larger dimensions have been used for the study of the magnetization dynamics presented in section XI.2.3 (around 2 μm). The geometry of the Py element has been also varied and both square and disc elements were used. The Py element is positioned to one side of the FOV aperture in accordance to the geometry of the experiment to avoid the Au mask blocking soft-X-rays from passing through the Py element when the sample is illuminated and rotated in the X-ray beam (Fig. XI.8.d).

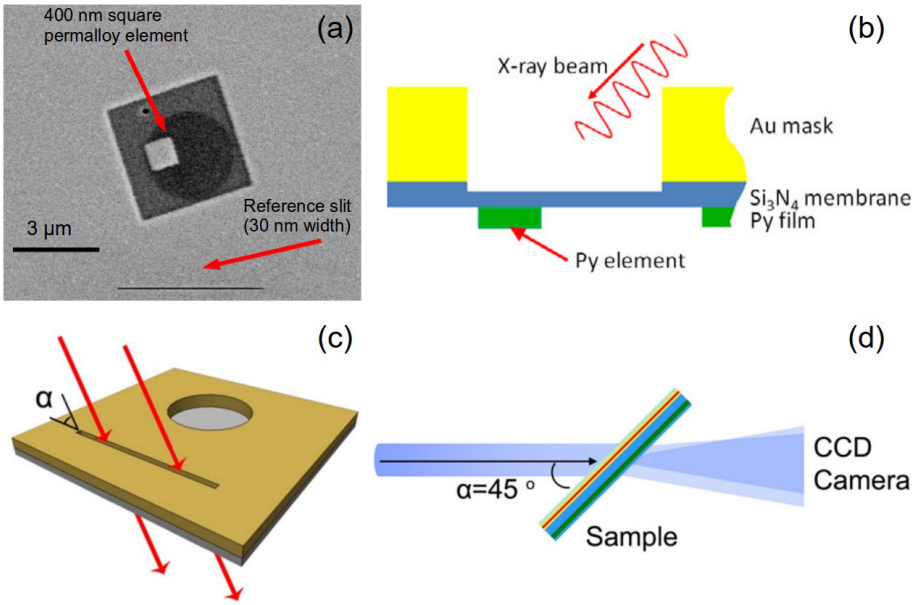

Fig. XI.8 *Imaging the in-plane magnetisation in a Py square element* (a) SEM picture of the 400 nm square Py element. The black circular area is the aperture in the gold mask to allowing the x-rays to go through the sample. The reference slit is located 5 µm away from the sample. (b) Schematics of the sample. (c) Sample design, the front side of the SiN membrane is covered with gold mask blocking the X-rays everywhere apart from the circular aperture and the reference slit. (d) geometry of the experiment, the sample is rotated in the X-ray beam to image the in-plane magnetisation.

Measurements of the Py sample were performed at several synchrotron facilities listed in section XI.1.2 of this chapter. Here we focus on the experiment carried out on the I06 beamline at the Diamond light source whose set-up is described in section XI.1.2.

To investigate the magnetization in the Py element, the normal to the sample is rotated by 30° and 45° with respect to the direction of propagation of the X-ray beam. The off-normal geometry is similar to the setup reported by Tieg *et al.* (2010) except that the reference slit allows to image the magnetic structure at larger tilt angles, hence the larger projection of the magnetization onto the wave vector of the x-ray beam, and the expected enhanced magnetic contrast.

The photon energy is usually tuned to the L_3 absorption edge of Fe (~708 eV). Note that holograms were also taken at the Ni L_3 edge where the magnetic contrast was not as good.

Holograms are collected using both helicities of circularly polarized X-rays. Typically, 100 holograms are recorded for each polarization. The exposure time for each hologram depends on the available flux, but is usually around 5s with minimum and maximum values of 2 and 10 s respectively (note that much shorter exposure time are used for the experiment presented in section XI.2.5). The exposure time needs to be sufficiently large to maximize the Signal to Noise (S/N) ratio at high scattering angle but sufficiently small to avoid saturation of the CCD camera. The Princeton camera used for most of the FTH experiments can hold a maximum of 65 000 electrons per pixel. Usually, the exposure time for a single frame is set such that the number of electrons stored into the most exposed pixels is just below the maximum value. The 100 individual frames for each polarization are accumulated in order to further reduce the S/N ratio and enhance the resolution. The accumulated holograms recorded for both polarizations are then subtracted from each other. According to Eq. (XI.10) this allows to remove the effects of the charge scattering and maximize the magnetic contrast.

Fig. XI.9 shows the holograms recorded at the tilt angle α of 0°, 30° and 45°. Fig XI.9.a-c correspond to the

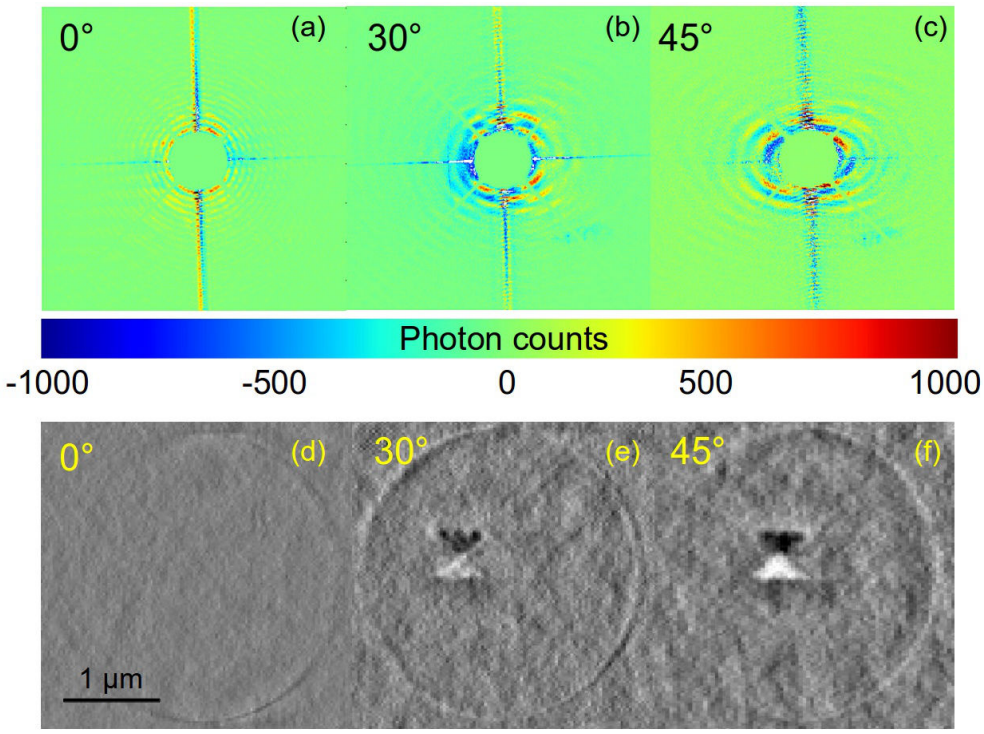

Fig. XI.9 *Influence of the tilt angle for the imaging of the in-plane magnetisation.* Difference holograms for opposite photon helicities measured at tilt angles α of 0° (a), 30° (b)and 45°(c). (d-f) Corresponding reconstructions showing an increase of the magnetic contrast with the tilt angle.

difference betweens the holograms recorded with opposite photon helicities, while Fig. XI.9. d-f show the reconstructed magnetic structure from the different holograms. Note that the figures show only the centre of the holograms. For the reconstruction, the full data covering a wave vector range of 0.21 nm^{-1} was used.

In normal geometry, the sample is orthogonal to the incident X-ray beam, the in-plane magnetization has no projection onto the beam. Consequently, since the measurement is only sensitive to the out-of plane magnetization, no structure is revealed in this geometry. As seen from Fig. XI.9.a, the difference between the two polarizations is not exactly equal to zero. This could be due to a small misalignment of the sample, which result in a very small sensitivity to the in-plane magnetization (Tieg *et al.* 2010). However it is more likely that this small remaining intensity results from the fact that the right and left polarization does not yield the same flux on the sample plane. Consequently the difference between the two polarization in the absence of magnetic scattering is not exactly equal to zero, and the charge scattering terms in Eq. (XI.9) and (XI.10) are not completely canceled in the difference hologram.

Of course, this can be corrected by normalization of the positive and negative helicities as discussed in the next sub-section. Here this correction was applied before reconstruction of the hologram by inverse Fourier Transform such that the magnetic hologram appears very clean (Fig. XI.9.d). A faint outline of the circular aperture is visible. If the normalization was perfect, this contour which is clearly a charge scattering effect should completely vanish.

The sensitivity to the in-plane magnetization in off-normal geometry is well illustrated in Fig. XI.9.b & XI.9.c where additional features appear on the hologram. These features completely vanish when the photon energy is detuned, confirming their magnetic nature. The corresponding reconstruction assess the dependence of the magnetic contrast with the tilt angle. Due to the increasing projection of the in-plane magnetization along the beam direction, the best contrast is obtained for the larger tilt angle, *i.e.* 45°. In both cases, the reconstruction

reveals a Landau ground state which is typical for Py elements of this size. In the square element it consists of four triangular domains with the static magnetization abruptly rotating in domain walls aligned along the diagonals of the square (Fig. XI.10). In Fig. XI.10., the Landau ground state is reconstructed for a larger 2 x 2 μm^2 Py element. A remarkable agreement is found with the micromagnetic simulations (left part of Fig. XI.10). The magnetic structure is also referred as a vortex domain closure, since a 30 nm vortex with out-of plane magnetization is located at the intersection of the four triangular domains. We will see in the next sections that the position vortex core can be displaced with the application of an external magnetic field.

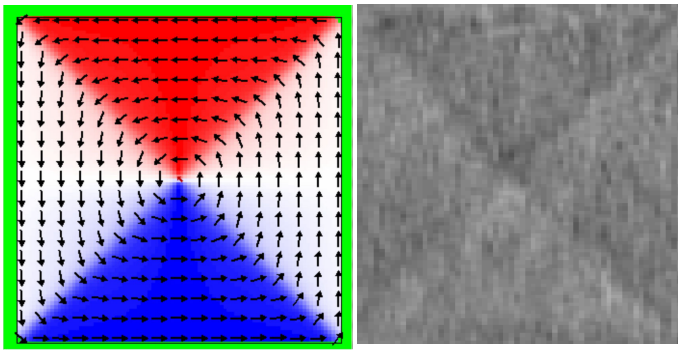

Fig. XI.10: *Vortex closure domain in a Py square element at the remanence obtained from micromagnetic simulations (left) and experimentally from a 2x2 μm^2 Py square element.*

XI.2.2 Experimental considerations and correction of the experimental data

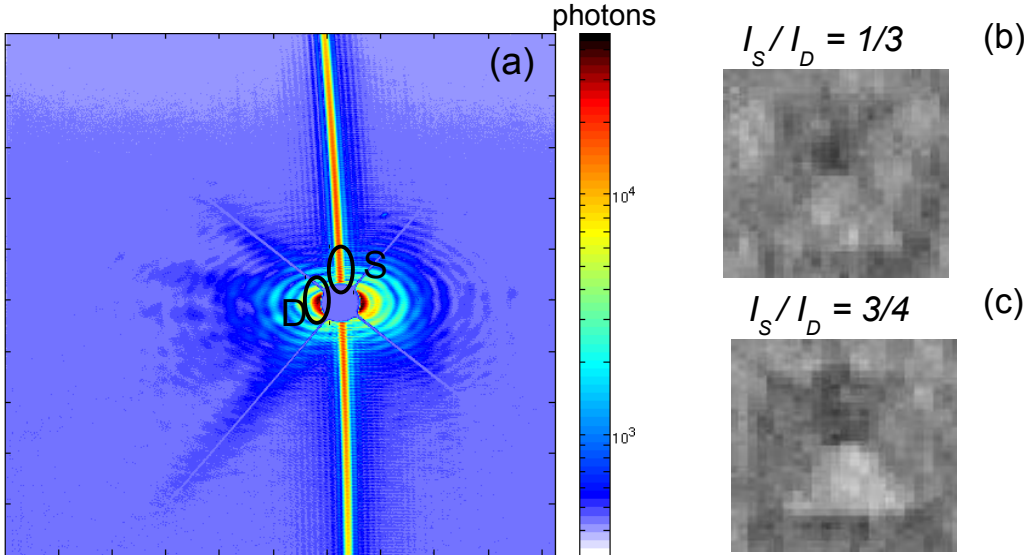

Fig. XI.11: *Influence on the ratio between the intensity scattered by the slit and the sample.* (a) Hologram from a 700x700 nm^2 Py square element measured at tilt angle α of 45°. (b-c) Reconstructed hologram for two different ratio between the intensity scattered by the slit and the sample. (b) I_S / I_D=1/3, (c) I_S / I_D= 3/4

From the various holographic experiments performed in this PhD work we realized that the quality of

the reconstructed data is highly dependent on the quality of the experimental set-up. Of course, some corrections which are described in the following can be applied, but if a "good" hologram is not recorded from the beginning, only little can be done to improve the quality of the data.

Ratio between the intensity scattered by the slit and the sample

As discussed by Gauthier *et al.* (2010), the hologram fringe visibility is maximum when the amplitude of the wave field diffracted by the object and the slit are equal. For this reason, the quality of the image reconstruction can potentially be enhanced as compared to a point-source reference. In the experiments presented in this manuscript, the size of the beam is defined by the pinhole placed in front of the sample. For the I06 experiments a 20 µm pinhole was used, and the distance between the sample and the slit is of the order of 5 to 10 µm. Consequently, depending on the position of the beam on the sample, either the scattering from the slit or from the sample is reinforced. This ratio needs to be optimized. The slit induce an intense streak of intensity on the hologram, experimentally, the ratio was calculated by taking the maximum intensity of the pixels in region S (scattering from the slit, Fig. XI.11.a) and region D (scattering from the device). With a 20 µm pinhole, the optimum ratio was determined experimentally to be between $½ < I_S / I_D \sim ¾$ (Fig. XI.11.c). Note that for the ESRF experiment presented in section XI.2.4, a 50 µm pinhole is used. Due to the resulting larger beam size, the ratio is less dependent on the beam position, and these considerations are less critical.

Calibration of the undulator(s)

Another very important point is the calibration of the helical undulator. It is essential that the two circular polarizations yield the same flux on the sample. As discussed thereafter, differences in intensity for the two polarizations can be usually corrected. However, the larger is the difference, the more difficult is the correction of the experimental data (see below, *Normalization*). This typically occurred for the experiments on the I06 beamline, hence the importance of a good calibration of the undulator. For the experiments carried-out on the SEXTANTS and ID32 beamline, the undulator was very well calibrated, yielding the same flux for both polarizations. In this case and provided a good stability of the experimental set-up, the differential holograms are very clean (almost no charge scattering) and don't need any correction (except the optimization of the phase of the complex image discussed in the following)

Stability of the optics and of the monochromator

Since the acquisition time for the holograms is rather long (typically 500 to 1000s per polarization), a high stability in the beamline optics and in particular of the monochromator is required. During the first experimental runs on the I06 beamline, large variations in the beam intensity and position on the sample were noticed during the collection of the holograms. They resulted in large difference in the intensity collected for the two polarizations. Beyond the fact that it is particularly tiresome to realign the sample in the beam in between two measurements, the data analysis is complicated by the large difference of intensities between the two polarizations, as discussed in the previous paragraph.

Saturation of pixels on the CCD camera

To achieve the best resolution possible, it is essential to probe a large extent of the reciprocal space. Increasing the exposure time improves the S/N ratio at high *q,* however it is critical to avoid the saturation of the pixels in the central area surrounding the beamstop. Beyond the fact that it can damage the camera, these saturated pixels create artifacts in the reconstruction which are difficult to remove. The usual strategy we employed to obtain a good S/N ratio while avoiding overexposure was to set the exposure time in order to obtain the largest possible dynamical range (without saturation of the pixels in the central region) for a single frame,

and to accumulate a large number of frames in order to improve the S/N ratio (typically a 100 for each polarization)

Detector correction

The detector correction was already discussed in section II.3.2. The main issue lies in the presence of "hot pixels" in the hologram. These pixels can be removed by hand when they are not too numerous. This was generally the case for most of the experiments we carried-out.
A more elegant way (and probably more efficient) would be to use the droplet algorithm proposed by Livet (2000), this algorithm can handle both hot pixels and cosmic X-rays. It was not implemented in our reconstruction procedure.

Normalization

The acquisition of an hologram which allows to access the magnetic contrast supposes the measurement of both helicities. As discussed above, if the helical undulator is not properly calibrated, the available flux on the sample can change between the two circular polarizations. An even more problematic issue is the drift of the X-ray beam during the measurement due to the lack of stability of the experimental set-up. The latter can cause large intensity variations during the acquisition of the hologram. In this case, the difference between the two polarization contains some contributions of the charge scattering. The charge contributions can be removed by normalization of the two polarizations. A reliable method is to plot an histogram of the intensities of all the pixels on the hologram for both polarizations. If the histograms coincide for the two polarizations, there is no need for normalization. If the two histograms don't overlap, a correcting factor is applied.
This correction is generally efficient, but as discussed above, the larger is the difference in intensity between the two polarizations, the more difficult is the correction of the experimental data (difficulty to remove some charge scattering artifacts).

Beamstop correction

The beamstop used to block the direct beam can be potentially problematic for the reconstruction. The usual strategy to deal with the beamstop is to mask all the pixels within the circular area defined by the beamstop, *i.e.* to set the the pixels value to zero in the region. This method creates sharp variations of intensity between the region within the beamstop where all the pixels are set to zero and the surrounding region where the scattering is maximal. These sharp variations can create artifacts in the reconstruction. To limit these artifacts the beamstop was generally convoluted with a Gaussian in order to obtain a "smooth" beamstop.
It should be noticed although that this correction is not critical for the quality of the reconstruction, especially when using HERALDO. Indeed, the differential filter applied on the differential autocorrelation is typically a high pass filter, *i.e.* the information is preferentially encoded at large scattering angles (Zhu *et al.* 2010). The loss of the central part of the data is thus not essential for achieving high quality reconstructions. From our experiment, when a lot of artifacts can be found in the reconstructed image, masking a large central part of the data can even be a basic but efficient way to improve the quality of the reconstruction.

Phase correction

Generally, in the reconstructed complex image, the magnetic contrast is "shared" between the real and the imaginary part of the phase. As shown from Eq. (XI.10), the charge magnetism interference term is real. Hence all the magnetic contrast should be contained in the real part of the phase. The optimization of the magnetic contrast is done by rotating the phase by a certain amount which corresponds to the maximum contrast for the real part and the minimum contrast of the imaginary part. The optimization of the rotation angle can be

done using by monitoring the reconstructed images (Fig. XI.12.a-d) while rotating the phase. Alternatively, a reliable method is to draw a line profile through the magnetic domains, and to adjust the phase angle in order to yield a maximum contrast for the real part and the minimum for the imaginary part (Fig. XI.12.e-f).

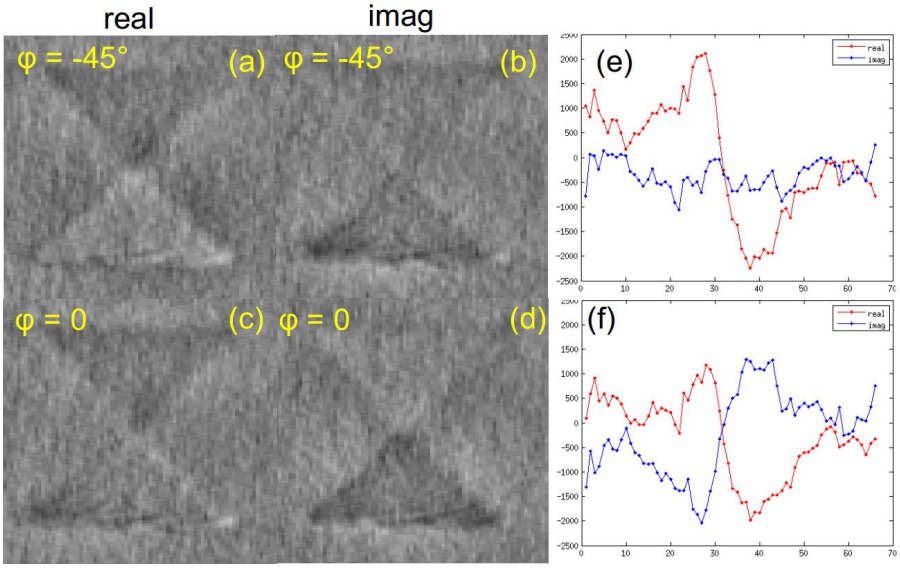

Fig. XI.12 *Effect of the "phase optimization".* Real and imaginary part of the reconstructed magnetic structure in a Py square element. (a) and (c) Real part with and without the phase optimization. (b) and (d) Imaginary part with and without the phase optimization. (f) and (e) Line scan along the magnetic element before (f) and after (e) the phase optimization.

XI.2.3 Field dependence measurements

In the previous section, the suitability of HERALDO to image the vortex domain closure at the remanence was well established for several Py elements with various sizes and geometry (disc or square element). Before trying to image complex vortex motions in a time-resolved mode, it was necessary to confirm that relatively simple and well understood displacement of the vortex core can be imaged with the technique. In that optic, the dependence on the vortex core position on an external magnetic field was investigated.

The schematic drawing of the experiment is shown in Fig. XI.13.a. An external magnetic field is applied to the tilted sample (by typical values of 30 to 45°) to image the evolution of the in-plane magnetic structure with an increasing external field which is applied along the direction indicated in Fig. XI.12.e.

Fig. XI.13. b shows the magneto-optical Kerr effect (MOKE) Kerr hysteresis loop of a single Py square obtained from micromagnetic (OOMMF) simulations. When the magnetic field is decreased from the saturated state, the Kerr signal (M/M_{sat}) gradually decreases (1) until it reaches a so-called nucleation field H_n where a single magnetic vortex is formed on the Py square element (2). The nucleation of the magnetic vortex is reflected by an abrupt jump in the Kerr signal. In the remanent state, the vortex stays at the square centre, and when a magnetic field is applied the vortex is shifted perpendicular to the magnetic field to increase the net magnetization along the field. At the annihilation field H_{an}, the vortex vanishes and the magnetization state turns out to be a single domain (3). The reversal of the magnetization of the square element is thus accompanied by nucleation and annihilation of the single vortex (Guslienko *et al.* 2002). The study of the field dependent displacement of the vortex has been carried-out on the I06 beamline. The sample of interest is a square Py element with relatively large lateral dimensions (900 nm).The external magnetic field is applied with a permanent magnet and the photon energy is tuned at the L_3 Fe absorption edge (706 eV in this experiment). The imaging of the magnetic

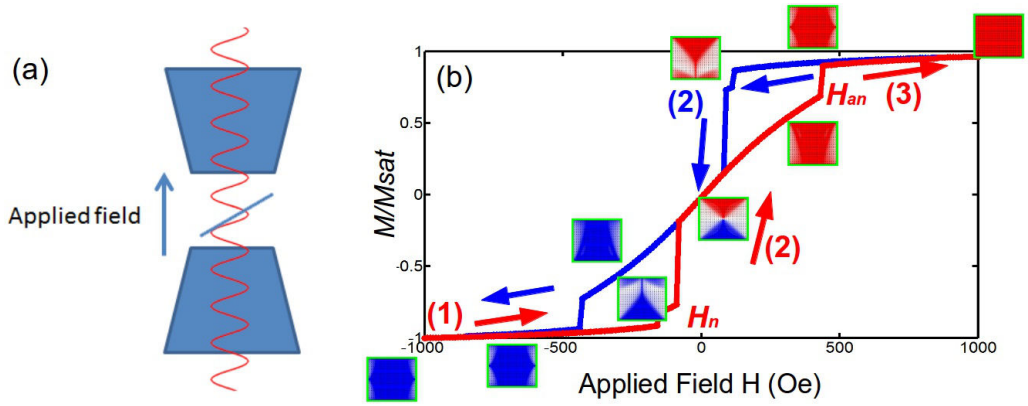

Fig. XI.13: *Kerr-hysteresis loop in square Py element* (a) Schematic drawing of the application of the field on the magnetic sample. (b) Micomagnetic simulation showing a hysteresis loop of a Pu square element. Several positions along the loop are marked with simulated images of the domain pattern at different field values

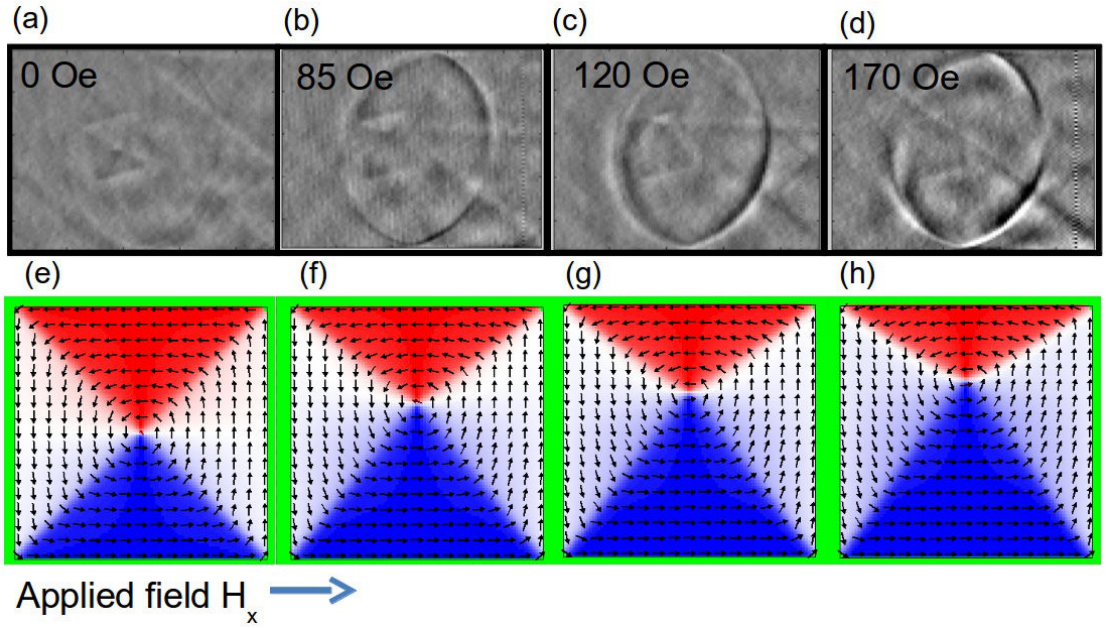

Fig. XI.14 *Field-induced displacement of the vortex core and comparisons with micromagnetic modeling.* The square Py element is imaged at several field values. (a) Landau domain structure which formed at remanence (b-d) Displacement of the vortex core perpendicularly to the applied field. The shift increases with the applied field (e-f) Micromagnetic simulations of (a-d).

structure for each field value is achieved following the procedure described in section XI.2.1: accumulation of 100 holograms for each polarization with a 6s exposure time for each frame. At zero field, similarly to our previous observations, a Landau ground state is observed. The vortex core is roughly at the centre of the square element (Fig. XI.14.a), in good agreement with the micromagnetic simulations. As discussed above, when a magnetic field is applied, the vortex is shifted perpendicularly to the field to increase the net magnetization along the field (Fig XI.14.b and XI.14.c). At 170 Oe, the field is close to the annihilation field, and the vortex has almost completely vanished.

Despite the poor quality of the reconstruction, the field-induced displacement of the vortex in the square Py

element is clearly visible and is in reasonably good agreement with the micromagnetic simulations. The discrepancy between the simulations and the experimental data could result from the idealistic nature of the model.

XI.2.4 Time resolved imaging of the magnetic vortex dynamics

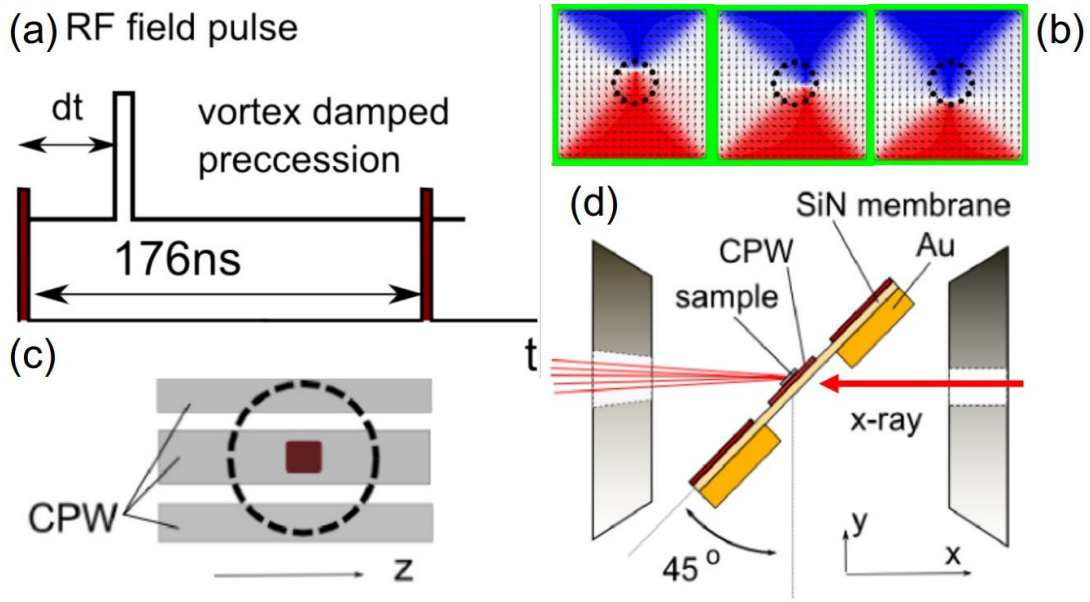

Fig. XI.15: *Schematics of the time-resolved experiment* . (a) Stroboscopic imaging in pulsed excitation in 16 bunch operating mode. The magnetic pulse is triggered by the X-ray bunch and delayed by *dt.* (b) OOMMF calculation of the gyration of the vortex core in a 500x500 nm^2 Py square element for three different stages of the precession (c) Py element and coplanar waveguide (CPW) tracks on the other side of the membrane behind the circular aperture. (d) Orientation of sample with respect to the X-ray beam.

In the previous sub-sections we mainly employed the Py elements as model objects to demonstrate the suitability of FTH coupled with XMCD to investigate in-plane magnetic structures. However, and as discussed previously these elements also have a great technological interest, and understanding the magnetization dynamics of such objects is of prime importance. The vortex domain closures can perform a number of functions ranging form non-volatile high-density data storage to microscopic microwave generators (Madami *et al.* 2011, Pribiag *et al.* 2007). The latter has recently attracted particular attention when it has been shown that a vortex can be excited with DC current and perform as a microwave oscillator (Pribiag *et al.* 2007). It has been predicted that if a macroscopic pattern of isolated vortices could be coupled to obtain phase synchronized precession, the generated power would be sufficient for wireless communication of microwave radiation in localised macroscopic regions (Sugimoto *et al.* 2011).

The technological exploitation of vortex oscillators supposes a detailed understanding of their magnetization dynamics. We have demonstrated in the previous section that holographic imaging can provide the precise in-plane structure of Py elements and is well suited to study the displacements of the vortex core induced by a magnetic field. In this section, the technique is used in time resolved mode, to investigate the precession of the vortex core induced by short magnetic pulses.

The experiment has been carried-out on the upgraded ID32 beamline at ESRF on 2 x 2 μm^2 Py squares (Fig. XI.10). The Py sample are processed using the procedure described in section X.2.1 and elsewhere

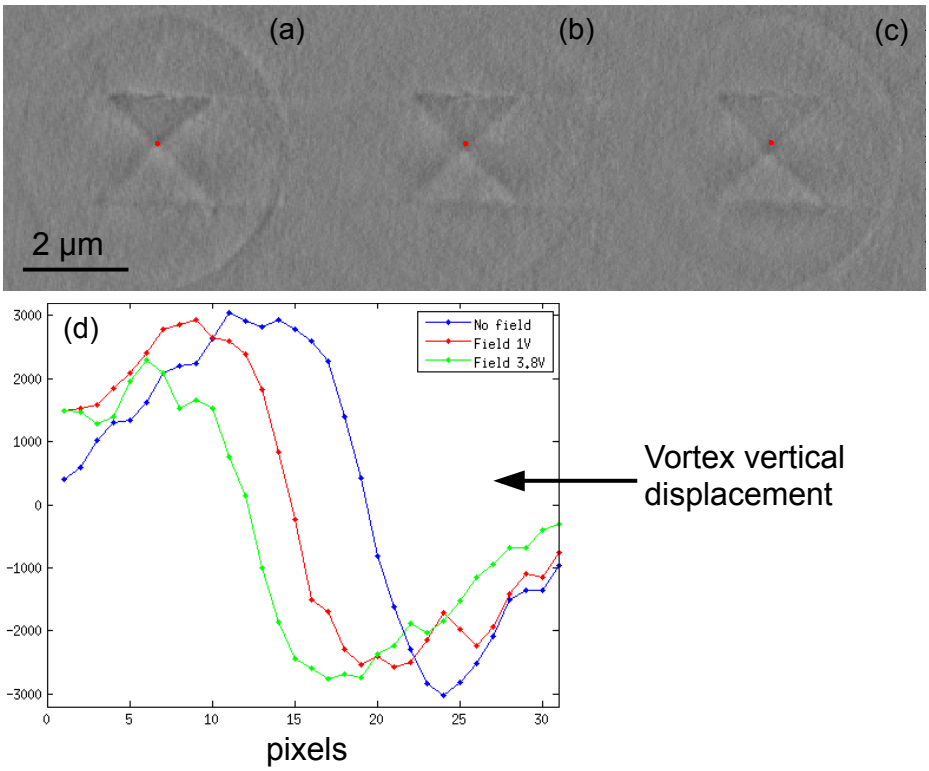

Fig. XI.16: *Field induced displacement of the vortex core.* The red dot incicate the position of the vortex core in the Landau ground state (a) Reconstruction of the Landau ground state at the remanence (no field applied) for the 2x2 μm^2 Py element. (b) and (c) Shift of the vortex perpendicularly too the applied field with increased field values. (d) Line profile through the vortex core revealing the vertical displacement of the vortex core.

(Duckworth *et al.* 2011). To provide the RF field, coplanar waveguides (CPW) are integrated on the Si_3N_4 membrane using lithographic procedures (Fig. XI.15.c). In some experiments not presented in this manuscript, the size of the Py elements was generally chosen to match the resonant frequencies (sub-gigahertz range) of the vortex oscillation (the later being determined by micromagnetic (OOMMF) simulations). In this experiment this knowledge is not required since the vortex is excited at its eigenmodes.

The principle of the experiment is shown in Fig. XI.15.d, the sample is rotated by 45° to image the in-plane magnetization. The holograms for both polarizations are recorded following the procedure described in section XI.2.1 with some adjustments corresponding to the particularities of the beamline. The main difference between the I06 and SEXTANTS beamline and the ID32 beamline lies in the distance between the source and the sample. The latter is much larger for the ID32 beamline. As a consequence, larger transverse coherence lengths are obtained, and larger pinhole diameters are used (50 µm instead of 20 µm). The flux on the sample is thus increased thanks to the larger pinhole diameter, but on the other hand, the 16 bunch operating mode yield an inherent decrease of the available flux. As a consequence, the counting time for both polarizations was equivalent to the I06 experiments (500-800s per polarization).

The set-up allows to bring the CCD camera closer to the sample (~33 cm), but on the other hand a different type of CCD camera is used, with a smaller chip (1340x1300 pixels) and a 20 µm pixel size. Using Eq. (XI.2), the resolution limit depending on the extent of the reciprocal space is calculated to be 22 nm as compared to the 30 nm obtained with the I06 set-up.

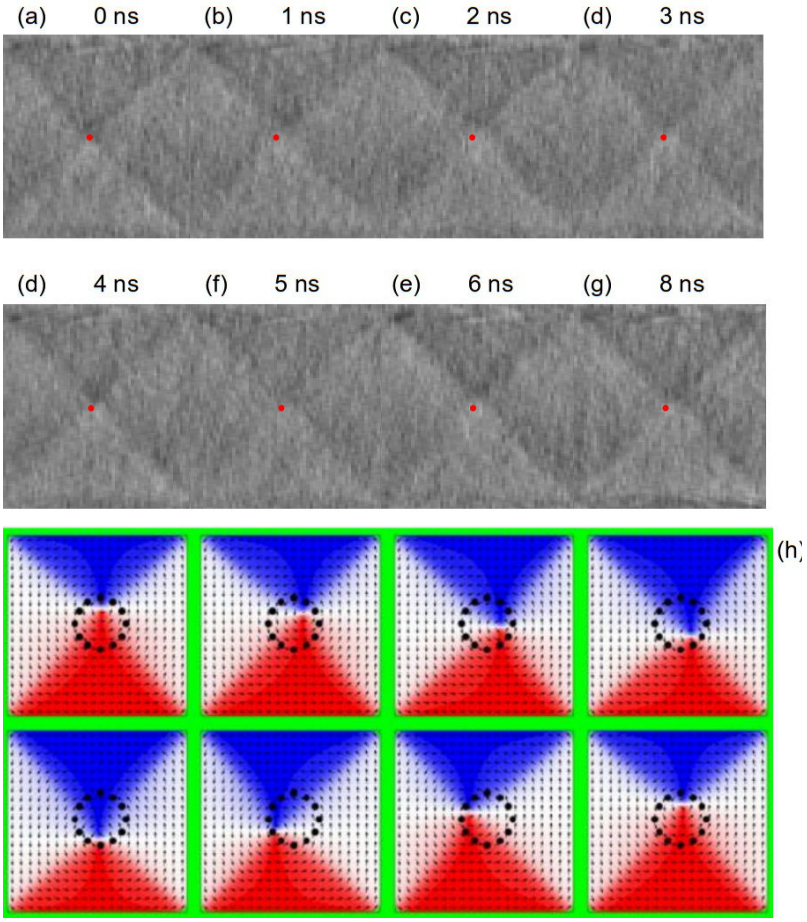

Fig. XI.17 *Reconstruction of the magnetic flux closure for different delays from the rise point of the magnetic pulse.* (a) – (g) Position of the vortex core for increasing delay times. The red dot indicates the initial position of the vortex core (dt = 0). (h) OOMMF calculation of the gyration of the vortex core in a Py square element for three different stages of the precession

To confirm that the waveguide is able to provide the RF field, measurements were first carried out with a static magnetic field, to check the field-induced displacement of the vortex core. These measurements were also a good opportunity to evaluate the quality of the reconstruction provided by the set-up.

Fig. XI.16 show the reconstructed in-plane magnetization at the remanence (zero-field, Fig. XI.16.a) and for two different field-values (Fig. XI.16.b & XI.16.c). A very good quality reconstruction is obtained. The vortex closure domain is perfectly visible, and the vortex core is located at the centre of the square element. The contributions from the charge scattering are very weak (faint contour of the aperture is visible) even without normalization of the data: the two polarizations yield a similar intensity thanks to a good calibration of the undulator and the very good stability of the experimental set-up. Knowing the dimensions of the Py square (2 x 2 μm^2) it is possible to evaluate the resolution of the data by counting the number of pixels in the Py element. Pixel sizes of 24 µm and 36 µm in the vertical and horizontal directions of the hologram are found respectively. The larger pixel size along the horizontal direction is explained by the fact that the 45° tilt angle leads to a projection of the sample onto the plane normal to the beam, which causes a contraction (by sin 45°) of the real space images along the horizontal direction.

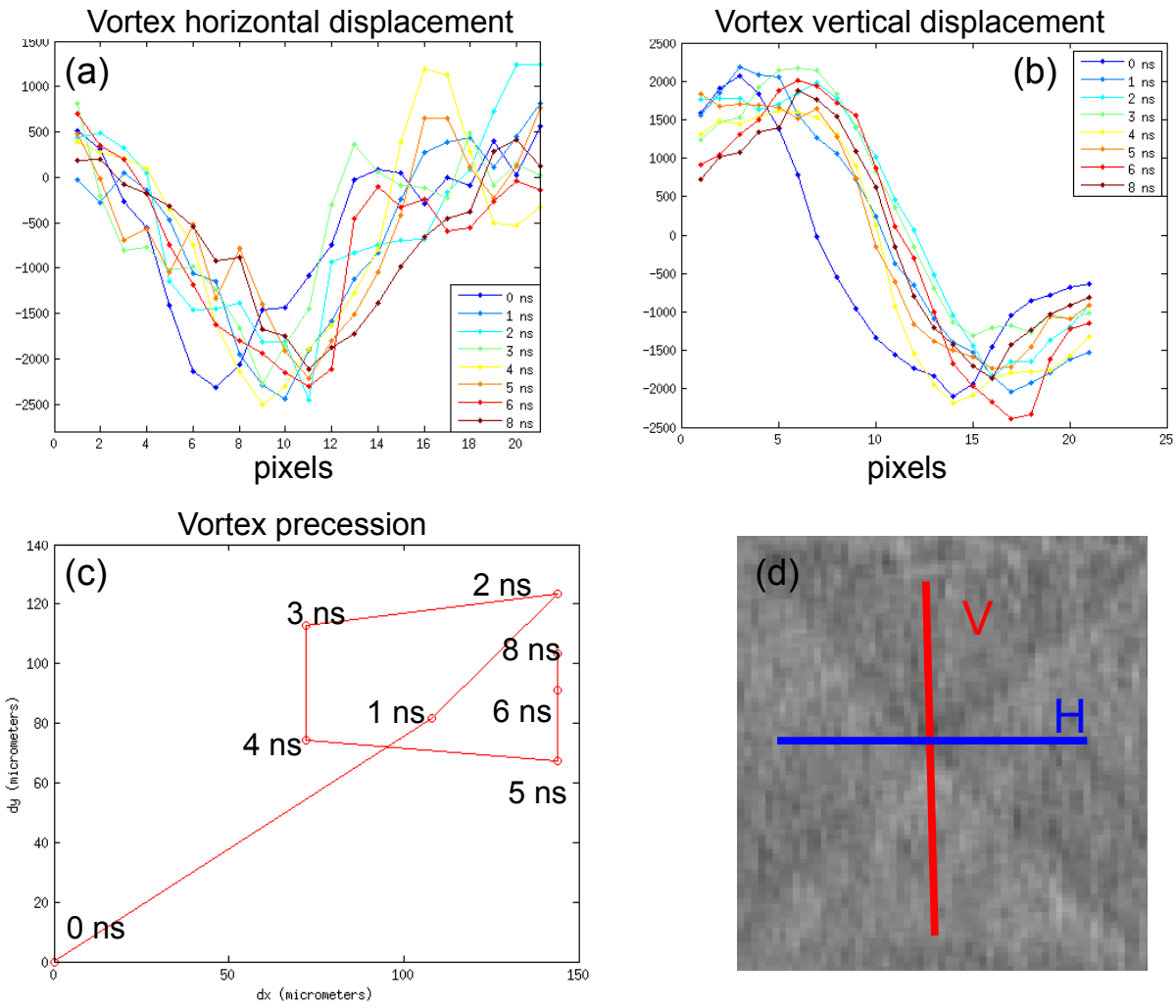

Fig. XI.18: *Position of the vortex core for different stages of the precession.* (a) and (b) Line profiles through the vortex core showing the evolution of the vertical and horizontal positions of the vortex core. The line profiles are taken at positions indicated in (d). (c) Position of the core for various delay times.

When the field is applied, one can notice that the vortex is shifted perpendicularly to the field in order to increase the net magnetization along the field. This displacement increases with the applied field, as illustrated in Fig. XI. 16.b,c where the red dot indicates the position of the vortex core in the ground state. Respective displacements of 100 and 170 nm are found along the vertical direction for the small and large field value. Note that the vortex displacements remain rather limited, indicating that the Py element is far from saturation.

In any case, the displacement of the vortex core indicates that the CPW is able to provide the RF field and that the time resolved measurement can be performed.

To investigate the magnetization dynamics of vortices, the measurements are performed in stroboscopic mode by using an RF pulsed excitation. The X-ray pulses are provided by the 16 bunch filling mode with 176 ns between bunches (Fig. XI.15.a). The pump field pulses are used to induce a damped vortex precession while the X-ray probe pulses can image a particular phase of the precession (Fig. XI.15.b) and serve as triggers for the pump (Fig. XI.15.a). The 176 ns delay between the bunches is in principle sufficiently long for each gyration to be dumped before the next one is excited. Overall we imaged 7 frames with delay times starting from 0 to 8 ns. The delay time correspond to the delay between the front edge of the pump pulse and the X-ray probe pulse.

Fig. XI.17.a to g shows the evolution of the vortex core position for different delays. The initial position of the vortex core is indicated by a red dot. From Fig. XI.17, it is clear that the largest oscillations are observed at the beginning of the precession. The displacement of the vortex core is indeed obvious between 0 and 1 ns (Fig XI.17.a & XI.17.b) and between 1 and 2 ns (Fig. XI.17.b & XI.17.c). After 2 ns, the displacements are much more difficult to see on the reconstructed images. It should be noted that the amount of displacement is less than predicted by the micromagnetic simulations (Fig. XI.17.h).
To precisely quantify the displacement of the core, vertical and horizontal profiles (Fig. XI.18.a & XI.18.b) are drawn though the vortex core, along the directions indicated in Fig. XI.18.d. The variations of the core position are more obvious on the line profiles, and allows to determine the position of the core for each delay. Fig. XI.18.c shows how the position of the core moves from the beginning of the oscillation towards the end when the excitation is dumped. The displacement of the core and its cyclic motion is clearly visible, as predicted from simulations. No satisfying explanation was found so far to explain the small amplitude and the higher asymmetry of the gyration as compared to the simulations or experimental results with other techniques (Jung *et al.* 2011). These effects can either arise due to particular structure of the pulse (for instance, slow rise time), or coupling effects induced by the periodic pattern of magnetic vortex oscillators (Ogrin *et al.* 2015).
In any case and as discussed by Ogrin *et al.* 2015, this experiment is to our knowledge *the first successful attempt of using x-ray time resolved holography for imaging in-plane magnetized materials.*

XI.2.5 Observation of the resonance gyration of the magnetic vortex in a nano-contact spin torque oscillator

Prior to the ESRF experiment presented in the previous sub-section, most of our first tentatives to image the magnetic vortex dynamics in the Py element were unsuccessful. Two experiments were performed on the I06 beamline to try to resolve temporal magnetic configurations of the magnetic vortex and to explore their resonant gyration. The main objective of these experiments was to study the resonance characteristics of the gyration as a function of the geometric external parameters of the system, including the bias field and applied radio frequency (RF) power. Unfortunately, it was found that for all the Py elements tested, no distinguished RF magnetic signal from them could be obtained. It was thus decided to use another type of samples, exhibiting vortex dynamics but generated by the Spin Transfer Torque (STT) phenomena (Slonczewski 1996).
The samples are based on nano-contact spin-torque oscillator (NC-STO) and utilises STT to excite ferromagnetic resonance (FMR) in which the damping is balanced by the torque of the spin-polarised current, creating auto-oscillations or damping-free precession of magnetisation (Pribiag *et al.* 2007).
The samples were manufactured at KTH by J. Åkerman group who also provided the RF characteristics. In previous experimental studies, it was shown that a microwave signal can be generated from this system with the amount of power and the line width comparable with those produced in giant magneto-resistance (GMR) systems. The observed effect has a relation to the magnetisation dynamics in the NiFe layer (Fig. XI.19.a), but the exact nature of it is not completely understood. Given the large range of generated microwaves (from 250 MHz to 3 GHz), it was suggested that the effect must involve a complex behaviour based on a vortex-antivortex (V-AV) pair (Petit-Watelot *et al.* 2012).
We investigated these dynamics with HERALDO, which was found to be suitable for imaging both in-plane and out-of-plane components of the magnetisation with a very good spatial resolution (20-30 nm). The technique is particularly relevant for the study of magnetic vortices because their dynamics can be generally described as the combination of these two components.
The experiment was carried-out on the SEXTANTS beamline. Details on the setup for coherent-scattering experiments (including holographic experiments) can be found elsewhere (Sacchi *et al.* 2012). Both out-of-plane and in plane magnetization were investigated by varying the tilt angle of the sample (from 0 to 45°).

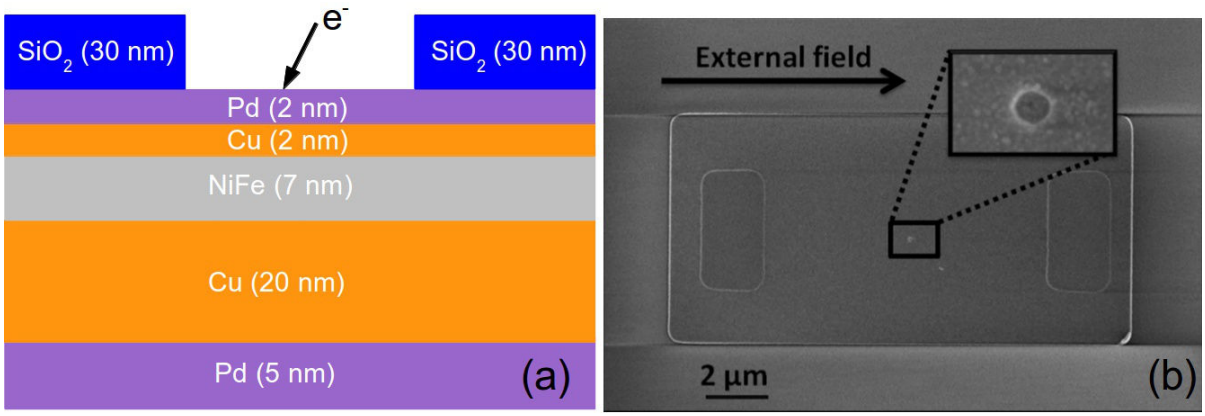

Fig. XI.19 *Nano-contact spin torque oscillator (STO)* (a) Scheme of the "single" layer Nanocontact spin-torque oscillator. (b) SEM view of the nanocontact (image taken from Sani *et al.* 2013)

The main advantages of the set-up as compared to the I06 beamline are the very good calibration of the undulators, the high stability of the set-up (no normalization needed), and the possibility to bring the CCD camera closer to the sample (less than 30 cm). The resolution limit with this set-up is 17 nm, a value which is confirmed by our reconstructions (Fig. XI.20).

The sample is a NC-STO single layer vortex device which consists of a stack of Pd5-Cu20-NiFe7-Cu2-Pd2 (in nm, Fig. XI.19.a). It is grown on the same mask structure that has been used for the experiments with the Py elements

The vortex gyration is excited with a DC current in the region 0-35 mA, using an integrated CPW with a ~ 100 nm nanocontact which is shown in Fig. XI.19.b. As discussed previously, one of the main advantage of the sample is that the dynamic effects can be observed in a continuous spectrum of excitation frequencies, roughly proportional to the DC current supplied to the sample. The measurements have been performed on two samples with different sizes of the nanocontact for different values of the DC current and different tilt-angles.

Fig. XI.19 show the recorded holograms and the corresponding reconstructions for different values of DC currents (no current applied, -26 mA and 26 mA) and with the photon energy tuned to the Fe L_3 edge.

The strategy to record the holograms is slightly different as compared to the previous experiments. The single-frame exposure is very short (~ 60 ms) but a larger number of frames is accumulated (typically 800).

As shown from Fig. XI.20. a-c the magnetic contrast is readily visible on the holograms. In particular, it is clear that the current of opposite signs lead to a different magnetic contrast.

The reconstructed holograms (Fig. XI.20.d-f) confirm that the system exhibit a vortex like magnetic system formation that depends on the current and changes chirality of in-plane vector rotation depending on the orientation of the current. Note that the imaging was not performed in time-resolved mode, and the gyration of the vortex is thus averaged over time. The reconstructed images show the trace of this gyration. The latter is coloured according to the projection of the magnetisation components in the vortex structure onto the direction of the wave vector of the incident-beam. Note that the vortex formation occurs on the edge of the 'rim' corresponding spatially to the aperture of the gold layer.

Based on the fact that the vortex structure is observed away from the nanocontact, it is expected that at this value of the current, the vortex structure was initially formed underneath the contact, but was then displaced due to the large variation of the potential and the magnitude of the current.

Our first interpretation is that the vortex gets eventually pined on the boundary of the rim. It is indeed likely that the magnetic layer is highly stressed at these points because of the physical removal of the gold layer behind the Si_3N_4 membrane. The mechanical stress along the rim is likely to cause a sharp variation of the potential energy density (due to anisotropic effects) which can play a role of a pinning site where the vortex is likely to get trapped. The fact this result can be produced by both orientations of the current suggest that this effect is due to

the magnetic field generated by the DC current rather than the Spin-Transfer-Torque. The latter is still present but can not be distinguished, unless the vortex is free to move.
This observation is very interesting since it allows to image the vortex system which otherwise would likely to dissipate or run off from the nanocontact area. On the other hand, the pinning site adds additional potential which inhibit the dynamic properties. In a future experiment, it is planned to find an optimal condition, in order to observe the vortex dynamics and eventually apply time resolved measurements.

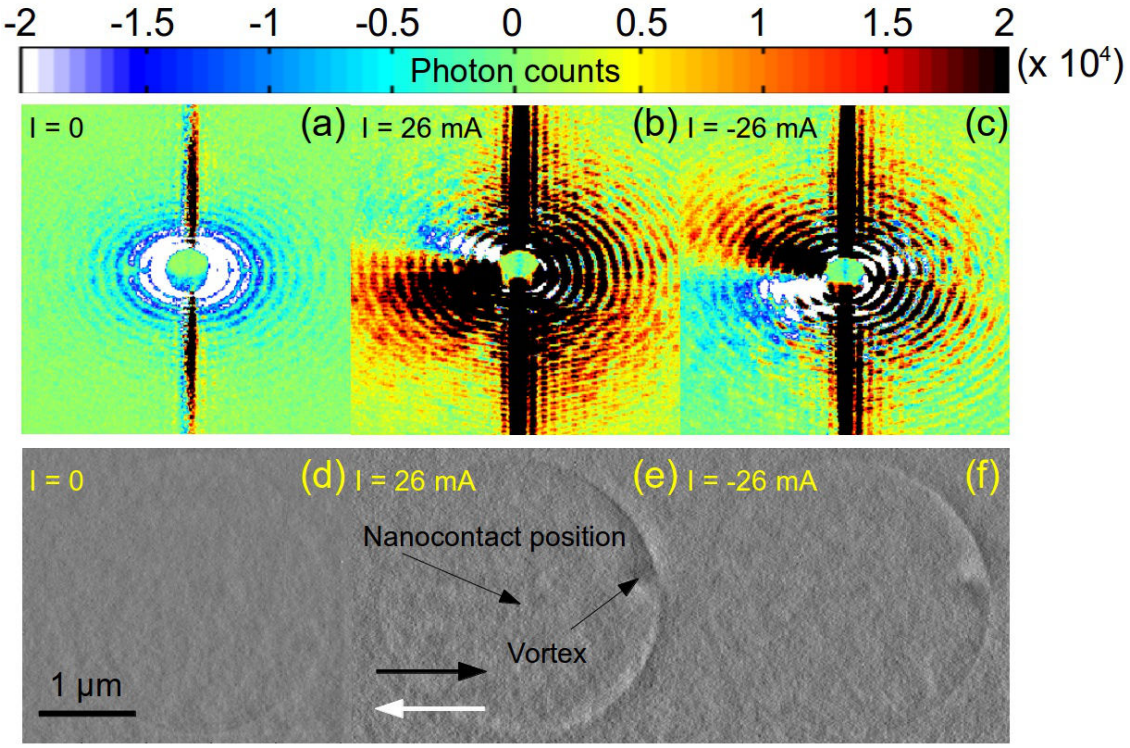

Fig. XI.20 *HERALDO reconstructed image of the magnetisation in the single layer structure for several DC currents applied.* (a-c) Difference holograms for opposite photon helicities and different values of DC current; (a) I =0, (b) I = -26 mA (c) I = 26 mA. (d-f) Corresponding reconstructions revealing the in-plane magnetic structure. The contrast indicates black (right) and white (lef) direction of the in-plane magnetisation component

Conclusions

In summary it is demonstrated in this chapter that Fourier transform holography applied to magnetic systems is a very powerful technique to investigate the magnetic structure and dynamics in sub-micrometer magnetic elements. The use of an extended reference can enhance the resolution of the reconstructed data and allows to image easily both in-plane and out-of plane magnetization.
In the experimental part of this chapter, it is shown that the in-plane magnetic structure of several magnetic systems can be determined with magnetic HERALDO. More importantly, the technique can be used to investigate the magnetization (in plane and out-of-plane) dynamics in sub-micrometer structures. The demonstration of the ability of the technique to provide new insight in the understanding of magnetization dynamics of vortex domain closures in Py element and of Spin Torque oscillator is a very interesting contribution to the field. It is believed that these results could be of great value in developing promising technologies for computation and communication applications.

Bibliography

Chamard., V, Dolle, M., Baldinozzi, G., Livet, F., de Boissieu, M., Labat, S., Picca, F. , Mocuta, C. Donnadieu, P. and Metzger, T.H. (2010) *Journal of Modern Optics* **57**(9), 816–825

Duckworth, T. A., Ogrin, F., Dhesi, S.S., Langridge, S., Whiteside, A., Moore, T., Beutier, G. & Van der Laan G (2011) *Optics Express* **19**, 16223.

Duckworth, T. A., Ogrin, F., Beutier, G., Dhesi, S.S., Cavill, S. A., Langridge, S., Whiteside, A., Moore, T.G., Dupraz, M., Yakhou, F. &Van der Laan G (2013) *New J. Phys.* **15**, 023045.

Eisebitt, S. , Lörgen, M., Eberhardt, W., Lüning, Stöhr, J., Rettner, C., T., Hellwig, O., Fullerton, E. E. & Denbeaux, G. (2003). *Phys. Rev. B.* **68**, 104419

Eisebitt, S., Luning, J., Schlotter, W. F., Lorgen, M.; Hellwig O., Eberhardt, W. & Stohr, J. (2004) *Nature* **432**, 885

Eisebitt, S. , Lörgen, M., Eberhardt, W., Lüning, J., Andrews, S., Stöhr, J. (2004). *Appl. Phys. Lett.* **84**, 3373

Fienup, J. R. (1982). Appl. Opt. 21, 2758–2768.

Fienup, J. R. (1987). J. Opt. Soc. Am. A **4**, 118

Gabor, D. A. (1948). Nature 161, 777-778.

Gauthier, D., Guizar-Sicairosn, M., Wu, B., Scherz, A., Acremann, Y., Tyliszczak, Fischer, P., Friedenberger, N., Ollefs, K., Farle, M., Fienup, J. R. & Stöhr, J. (2010). *Phys. Rev. Lett.* **105***,* 043901.

Gerchberg, R. W. & Saxton, W. O. (1972). Optik (Stuttgart) 35, 237–246 .

Guizar-Sicairos, M. & Fienup, J. R. (2007) *Opt. Express* **15**, 17592 .

Guizar-Sicairos, M. & Fienup, J. R. (2008) *Opt. Letters* **33**(22), 2668-2670 .

Guslienko, K., Yu, Novosad, V., Otani, Y., Shima, Y. & Fukachimi, K. (2002). *Phys. Rev. B* **65***,* 024414.

Hannon, J. P., Trammell, G. T., Blume, M. & Gibbs, D. (1988) *Phys. Rev. Lett.* **61**, 1245.

Hellwig, O., Eisebitt, S., Eberhardt, W., Schlotter, W. F., Luning, J. & Stöhr, J. (2006). *J. Appl. Phys.* **99**, 08H307.

Jung, H. *et al.* (2011). *Scientific Reports* **1**, 59

Livet, F. Bley, F. Mainville, J. Caudron, R., Mochrie, S. G. J., Geissler, E., Dolino, G., Abernathy, D., Grubel, G. & Sutton M. (2000) *, Nucl. Instr. Meth.* Phys Res. **451**(3), 596–609.

Lovesey, S. W. & Collins, S. (1996) *X-Ray Scattering and Absorption by Magnetic Materials* edited by Oxford University Press Inc., New York,

Madami, M., Bonetti, S., Consolo, G., Tacchi, S., Carlotti, G., Gubbiotti, G., Mancoff, F. B., Yar, M. A. & Åkerman, J. (2011) *Nature Nanotech.* **6**, 635-638.

McNulty, I., Kirz, J., Jacobsen, C., Anderson, E. H., Howells, M. R. & Kern, D. P (1992). *Science* **256**, 1009–1012

Ogrin, F. Y. *et al.* (2015) *Experimental report HC1569*

Petit-Watelot, S. et al. (2012) *Nature Physics* **8**, 682

Pribiag, V. S., Krivotov, I. N., Fuchs, G. D., Braganca, P. M., Ozatay, O., Sankey, J. C., Ralph, D. C. & Buhrman, R. A. (2007) *Nature Phys.* **3**, 498-503.

Sacchi M, Popescu H, Jaouen N, Tortarolo M, Fortuna F, Delaunay R and Spezzani C 2012,
Opt. Express 20 9769

Sani, S. R., Durrenfeld, P., Mohseni, S. M., Chung, S. & Åkerman, J. (2013) *IEEE Trans. Magn*. **49**(7).

Schultz, G., Wagner, W., Wilhelm, W., Kiekle, P., Zeller, R., Frahm, R. & Martelik, G. (1987) *Phys. Rev. Lett.* **58**, 737

Slavin, A. (2009). *Nature Nanotech.* **4**, 479.

Slonczewski, J. (1996). *J. Mag. Mag. Mat.* **159**, L1–L7.

Stöhr, J. & Wu, Y. (1994) *New Directions in Research with Third-Generation Soft X-Ray synchrotron Radiation Sources,* edited by A. Schlachter, F. J. Wuilleumier (Kluwer, Netherlands)

Stroke, G. W. (1965) *Appl. Phys. Lett.* **6** (10), 201-202.

Sugimoto, S., Fukuma, Y., Kasai, S., Kimura, T., Barman, A. & Otani, Y. (2011), *Phys. Rev. Lett.* **106***,* 197203.

Tieg, C., Frömter, R., Stickler, D., Hankemeier, S., Kobs, A., Streit-Neirobisch, S., Gutt, C., Grübel, G. & Oepen, H. P., *Opt. Express* **18**, 27251.

Von Korff Schmising, C., Pfau, B., Schneider, M., Günther, C. M., Giovannella, M. Perron, J. Vodungbo, B. Müller, L., Capotondi, F. Pedersoli, E. Mahne, N., Lüning, J. & Eisebitt, S. (2014) *Phys. Rev. Lett.* **112**, 217203

Wolf, S.A., Awschalom, D.D., Buhrman, R.A., Daughton, J. M., Von Molnár, S., Roukes, M. L., Chtchelkanova A. Y., Treger D. M. (2001). *Science* **294**, 1488

Zhu, D., Guizar-Sicairos, M., Wu, B., Scherz, A., Acremann, Y., Tyliszczak, T., Fischer, P., Friedenberger, N., Ollefs, K., Farle, M. & Stöhr, J. (2010) *Phys. Rev. Lett.* **105**, 093901

Conclusions and perspectives

The perspective chosen for this work is taken from the metal physics / metallurgy approach (Materials Science) to establish the properties of complex system formed by a very large number of atoms in crystalline state. It is classically based on the study and understanding of the interrelationship between microstructure of defects, physical properties and processing. In this framework, we use a specific experimental tool, synchrotron radiation, more specifically, coherent X-Rays diffraction techniques to address some fundamental and topical questions. There is indeed a good convergence between the range of length scale accessible by CXD for metals and the one concerning size effects on structural and mechanical properties questioning.

Structural defects and size effect on mechanical properties

The mechanical response of crystals stems from the nature, density and behaviour of crystal defects. Compared to bulk scale, submicron size samples have a different response because of some modification of the predominant mechanisms of deformation. This modification is not linked with the apparition of a new type of defect, which is still dislocation based, but in their detailed character and production. What dictates the selection of a given mechanism of deformation is a matter of the internal state of stress (elastic stored energy is the driving force) and the ability to nucleate a specific type of dislocation/source (kinetic).

- The residual internal stress level in small structure is strongly modified as compared to the bulk: first the closer proximity to boundary conditions (role of free surfaces, spatial extent of interfacial strain more or less relaxed) raises its magnitude, but also its spatial heterogeneity. Second, depending on the processing route, a same geometrical object can be in a more or less relaxed state of residual strain. A big challenge is to measure this internal state and to identify the possible stress generator: density of defects and interface relaxation essentially.
- The next question concerns the nucleation mechanism: what character/structure of dislocation would be able to relax and in what proportion an external loading condition superimposed on an initial state of strain. This dictates critical level of mechanical loading for which the object undergoes irreversible deformation.

We have in this work made several steps to answer these questions.

Quantitative defect identification and imaging:

- a first requirement is to demonstrate the ability of CXD technique to quantitatively identify all type of dislocation-related defects, and the requirements to do so. In an comprehensive way, we developed in Chapter III and IV method and numerical tools to list the pertinent signature on the diffraction pattern characteristic of most characters of dislocation (perfect, dissociated and partial), including stacking fault ribbon. It includes configurations associated with the physical variation of stacking fault energies covering all f.c.c metals. Moreover the effect of arrangement in pertinent dislocation loop type, as experimentally encountered in thermal quench, irradiation and indentation is also achieved. Best contrast, condition of visibility and the associated relevant choice of the Bragg diffraction vector is established and discussed for each case.
  It turns out, that within the kinematic approximation, CXD technique is as much pertinent as TEM contrast imaging to quantitatively identify defect. The requirements of using several $\boldsymbol{g}$ vector is as much as in TEM for example to unambiguously determine a Burgers vector. Practically speaking, since both techniques are based on the long range strain field generated by the defect, this can be achieved for 'isolated' defects. For example in TEM defect imaging, absolute determination of defect nature can only be made on a part of a thin foil where the line/structure stands isolated (50nm -100nm thickness) and

where internal strain is rather low (e.g. impossible in tangled dislocation lines / large variation of due to other sources of strain). The application of defect determination by CXD on atomitic realistic configuration is demonstrated Chapter IV.

- The imaging capacity by phase and electron density reconstruction is a powerful technique that in our opinion can fill the absence in CXD (lens less technique by nature) of multi-beam contrast techniques as in TEM (weak beam mode for example).
  Using reconstruction, we established for the first time on a exhaustive list of defects a methodology that quantitatively identifies the geometrical and physical nature of the defect:
  - the local electron density contrast resolves the location of a dislocation line,
  - the reconstructed phase magnitude (quantitatively defined by the product of $\boldsymbol{g}$ with the defect phase jump) and chirality defines unambiguously the nature of the defect.

  Due to the long rang strain field of the defects and the localisation of the phase jump on the defect, this can be achieved with a spatial resolution of the reconstruction smaller than the physical size of the object. Finally, it can (with the pertinent choice of the diffraction vector) already be applied on 2D reconstruction.

- The extreme sensitivity to crystalline imperfection in CXD pattern is a powerful tool to quickly evaluate the quality of a crystallite. We show a large variation of crystallite quality for equivalent shape structures (as observed by AFM / FEG-SEM) obtained by the dewetting process. The non destructive nature of CXD characterization allow to make sure that any mechanical characterization is carried out on equivalent initial state, which is compulsory for investigating size effects on mechanical response.
  Fast mapping of large collection of samples (a few thousands gold crystallites per area) has been carried out as well as complementary characterization (AFM) of same area: this opens the perspective for statistical measurements of mechanical response as function of size and crystallite quality, an on going work at the lab. with a dedicated SEM in-situ nanoindentation system.

- An original *in situ* deformation experiment of indentation on a pristine gold crystallite is presented and by applying our methodology, successful determination of the nucleated stage is demonstrated. Using 3D reconstructions at different stages of mechanical loading:
  - a prismatic loop generation is clearly identified: this mechanism is in good agreement with atomic simulations previously reported.
  - We demonstrate the interplay of nucleated defects with interfacial strain leading to 'mechanical annealing'
  - More surprisingly, strong recovery mechanisms operate after ageing modifying the global shape and orientation of the deformed crystallite.

  This successful experiment paves the way for exploring different mechanical loading on our model samples.

Interfaces and boundary conditions have also successfully been explored on various systems :

- In a pristine twinned part of gold crystallite, we were able to probe the high sensitivity of the phase reconstruction to measure the effect of free surface relaxation. At first, we checked that the coherent interface (twin) is not exhibiting a long range strain field, and help to isolate the diffracted part of the crystal from the substrate interfacial strain. This 'free standing like' diffracted crystallite allow us to have access to local measurement of the free surface relaxation. I,n this configuration, we interpret the phase gradient close to <100> and <111> facets as their respective expected atomic surface strain relaxation.

- A more complex case of interface in bimetallic system has been revisited. The f.c.c/b.c.c Cu[001]/Ta[001] system studied in the laboratory is confirmed to be of Stransky-Krastanov type. Namely we quantitatively measured by in-situ XRD the wetting layer to consist in two pseudomorphic Cu atomic layers on Ta. It shows excellent agreement with extensive ab-initio calculations. The CXD pattern of the f.c.c highly strained crystallite is discussed in terms of the f.c.c/b.c.c interfacial structure and evaluated with the help of extensive and large scale Molecular Statics simulations.

- Finally, successful 3D reconstruction is demonstrated to obtain the microstructure of inversion polarity domain along a GaN wire.

As a final note, we can draw a general perspective about 3D strain imaging in the framework of mechanics and structural stability including size effects: the combination of measuring quantitatively, *in situ*, even in buried structure, both microstructural defects and internal displacement field makes CXD as a unique tool to solve fundamental mechanical problems. The most advanced theory to incorporate size effect in continuum model is based on strain gradient plasticity. It lacks however of some experimental validation, for example to evaluate quantitatively the back stress against an interface. CXD can also address some long standing question like for example the understanding of plastic deformation by twining mechanism and fracture/plastic relaxation problems.
At last, a field not yet fully addressed with this technique concerns studies of phase transformations in small system.

Magnetic configuration and time resolved dynamics

- In a model micrometer dot of permalloy (Fe-Ni), size effect on complex magnetic configuration is successfully demonstrated, using our reconstruction of Fourier Transform Holography. Moreover, time-resolved dynamics of magnetic vortices at the nanosecond is demonstrated in this micromagnetic model system. This opens the perspective to study coupling effects in small scale systems, particularly concerning the ferroelectric-ferromagnetic coupling induced in multilayers made of multiferroelectric materials with magneto-strictive metallic layers.

The challenging scientific perspectives we presented shall benefit from constant improvements of coherent X-rays sources, particularly some actual or available or in a very near future. Higher brilliance sources bring increased resolution in reconstruction due to probing larger portion of reciprocal space. Programmed upgrades at standard synchrotron sources shall bring a x10 factor in that respect. Even more spectacular are the characteristics of X-ray free electron lasers, where up to 9 decades in brilliance is available. Access to exceptional time resolved experiments, as already demonstrated in magnetic holography by von Korff Schmising et al. (2014) or by Clark et al. (2013) for acoustic wave imaging in crystallite have been demonstrated.

Clark, J. N. *et al.* (2013). *Science* **341,** 56–59

Von Korff Schmising, C. *et al.* (2014) *Phys. Rev. Lett.* **112**, 217203

Appendix A1: Study of the Cu/Tantalum (0 0 1) interface

Contents

A1.1 Calculation of the excess interface energies for several Cu-Ta interfaces.....293
A1.2 Atomic structure of the Cu-Ta interface in solid state dewetted particles.....301
Bibliography 305

A1.1 Calculation of the excess interface energies for several Cu-Ta interfaces

The excess interface energy was introduced in Chapter VIII and used to evaluate the thermodynamical stability of Cu thin film. In this chapter it is used to check the stability of several Cu-Ta interfaces. As a remind it can be expressed as following :

$$\gamma = \left(E_{supercell} - \left(E_{Ta\ bulk} - E_{Cu\ bulk}\right)\right) / A \quad \text{(A1.1)}$$

where $E_{supercell}$ is the sum of the potential energies of the atoms in the atomic configuration, and $E_{Ta\ bulk}$ and $E_{Cu\ bulk}$ are the cohesion energies for Ta and Cu multiplied by the respective number of Ta and Cu atoms in the configuration and A is the surface area of the thin film. With this potential, the cohesion energies for the bulk Ta atoms and bulk Cu atoms are respectively -3.54 eV/atom and -8.1 eV/atom.
Equation (IX.1) depends on the energy of the Cu-Ta interface, the free surface energy of the Cu thin film, and of a strain contribution, and the excess interface energy is also given by:

$$\gamma = \gamma_i + \gamma_f + \frac{1}{2} E \epsilon_0^2 h \quad \text{(A1.2)}$$

where γ_i is the energy of the interface, γ_f the free surface energy of the Cu surface and $1/2E\ \varepsilon_0^2 h$ is the elastic strain contribution which increases linearly with the height of the thin-film. In a strain free surface, the excess interface energy would be simply the sum of γ_i and γ_f, and it is straightforward to understand that the sum of these two contributions, which is the most adapted criteria to evaluate a stability of an interface, is the y-intercept of $\gamma = f(h)$.

In the following, γ is calculated for 6 distinct interfaces (0 PM, 1PM and 2PM for each orientation), and various height of thin films. The geometry considered in these simulations is not a particle close to the equilibrium shape, but a thin film. Periodic boundary conditions are thus applied along x and y. (Fig. A1.1.a). To simulate a semi-infinite substrate, the bottom layer of the Ta substrate is fixed in all three directions of space. The energy of the atoms in this plane are set to zero and not considered in the excess interface energies calculation.
The determination of the atomic structure and of the excess interface energy for each interface is achieved through an energy minimization of the structure at 0K using using a quenched dynamical algorithm (Rodney *et al.* 2005). The force between atoms are minimized until they are less than 2.10^{-5} eV/Å. It is important to understand that the atomic structure of each interface strongly evolves upon relaxation since the atoms are relaxed in all three directions. In particular, the atomic structure of the Cu-Ta interface with 0 Cu PM layer is likely to evolve due to the thermodynamical stability of the PM structure on a Ta (0 0 1) surface.
The in-plane strain for the (0 0 1) orientation is minimized to the value of -0.07% with the supercell already described in Chapter VIII which consists of 22x22 Cu atoms on top of 17x17 Ta atoms.
The relaxation of the strain in the thin film clearly depends on the width of the substrate. The strain at the Cu-Ta interface is indeed partially relaxed in the Ta substrate. From Eq. (A1.2) it is clear that larger values of strain in the thin film leads to an increased excess interface energy. For a low number of Ta planes ($n < 4$), the mismatch strain in the interface can not be relaxed in the substrate and the relaxation of the interface is achieved through a modification of the atomic structure in the thin film. As the number of substrate planes increase, the strain of the interface is more efficiently released in the substrate. A decrease of γ is observed for an increasing number of substrate planes for up to 9 Ta planes. Above this value, it is almost independent on the thickness of the Ta substrate. In order to make quantitative comparisons between interface with different atomic structure, it is important to make sure that a low thickness of the substrate does not induce a modification of the strain distribution in the thin film. The Cu-Ta interface was modeled with a sufficiently large number of Ta planes (n=12).

The minimization of the in-plane strain for the (1 0 1) orientation is achieved through a slightly different Cu/Ta ratio. As discussed in the previous section the OR relationship for this orientation can be described as follows: Cu(1 0 1)[1 0 $\bar{1}$] || Ta (0 0 1)[1 0 0]. This means that the [1 0 $\bar{1}$] axis of the Cu thin film is aligned with the [1 0 0] direction of the Ta substrate, while the [0 1 0] direction of the thin film is aligned with the [0 1 0] direction of the Ta substrate.
Along the [1 0 $\bar{1}$] direction which will be called the x direction in the following, the minimization of ε_{xx} to a value of -0.07% is achieved through the ratio described in the previous paragraph (22 Cu/17 Ta). Along the y direction, the nominal value of the mismatch strain is equal to $2*(a_{Cu} - a_{Ta})/(a_{Ta} + a_{Cu}) \sim 8.9\%$. This value significantly lower than ε_{xx} is minimized to 0.02% by a ratio of 32 Cu atoms on top 35 Ta atoms. Overall, the supercell for the (1 0 1) orientation consists of 22x32 Cu / 17x35 Ta atoms.
For both orientation, the in-plane strain is minimized to such low values that the strain contribution in Eq. (A1.2) is expected to be very small. As a consequence the excess interface energy should be nearly independent on the height of the Cu thin film.

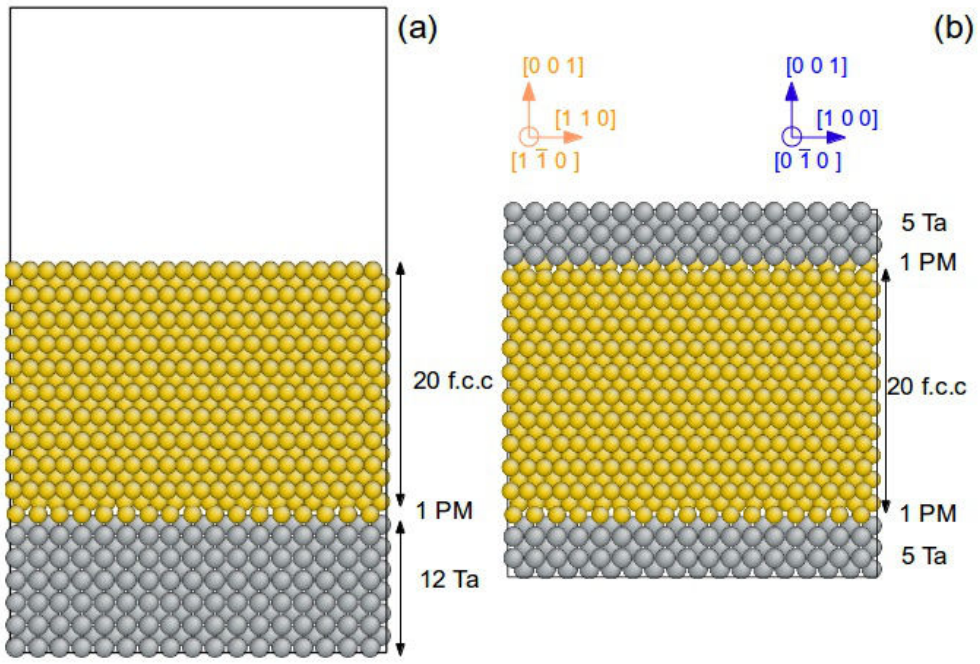

Fig. A1.1 *Geometries considered in the simulations. The copper atoms are coloured in yellow, and the Ta atoms in grey* (a) Thin-film simulation with periodic boundary conditions along x and y and a large vacuum region along z. (b) Simulation cell with periodic boundary conditions along x, y and z to calculate the interface energy

The excess interface energies are calculated for the six interfaces with a number of Cu planes varying between 9 and 100. Below this number, the structure of the thin film is too defective to obtain reliable values of γ.
As expected the latter is mostly independent of the number of Cu planes, except for a low number of layers with the (1 0 1) orientation where the value of γ rapidly increase with the number of Cu planes, when this number is below about 20. Above n = 20 planes, a transition occurs, and γ becomes independent of the number of Cu planes. This transition will be explained in the following.
For the (1 0 1) orientation, γ_0, *i.e* the y-intercept of the curve which represents the sum of the interface energy and of the free surface energy of the Cu thin film is calculated from the slope of the curve after the transition (*i.e* for n> 20). From Fig. A1.2, it appears that a low value of γ is obtained for three distinct interfaces, namely f.c.c.

(0 0 1) / 1 PM, f.c.c. (0 0 1)/ 2 PM and f.c.c. (1 0 1) / 1 PM.
For the two orientations, the largest values of γ are obtained for 0 PM layers in the initial configuration. As described previously, when the first Cu layer has a f.c.c structure in the initial configuration, it undergoes a f.c.c to b.c.c. (0 0 1) transformation. The latter is less densely-packed and the extra-atoms that can not fill this first b.c.c. layer are distributed in the overhead planes and form a complex structure which is intermediate between f.c.c. and b.c.c. in the 2nd and 3rd Cu planes. In the 4th Cu plane and above for the (1 0 1) orientation (5th and above for the (0 0 1)), defect free f.c.c planes are obtained (not shown here). These interfaces are highly unfavorable energetically and they are not likely to be formed experimentally.
The important outcome of these simulations is that the (0 0 1) orientation appears to be more stable than the (1 1 0) above n = 13 Cu planes. Of course this number is largely inferior to the height of the observed experimental islands which ranges between 100 and 400 nm so this is in good agreement with the experimental observations.

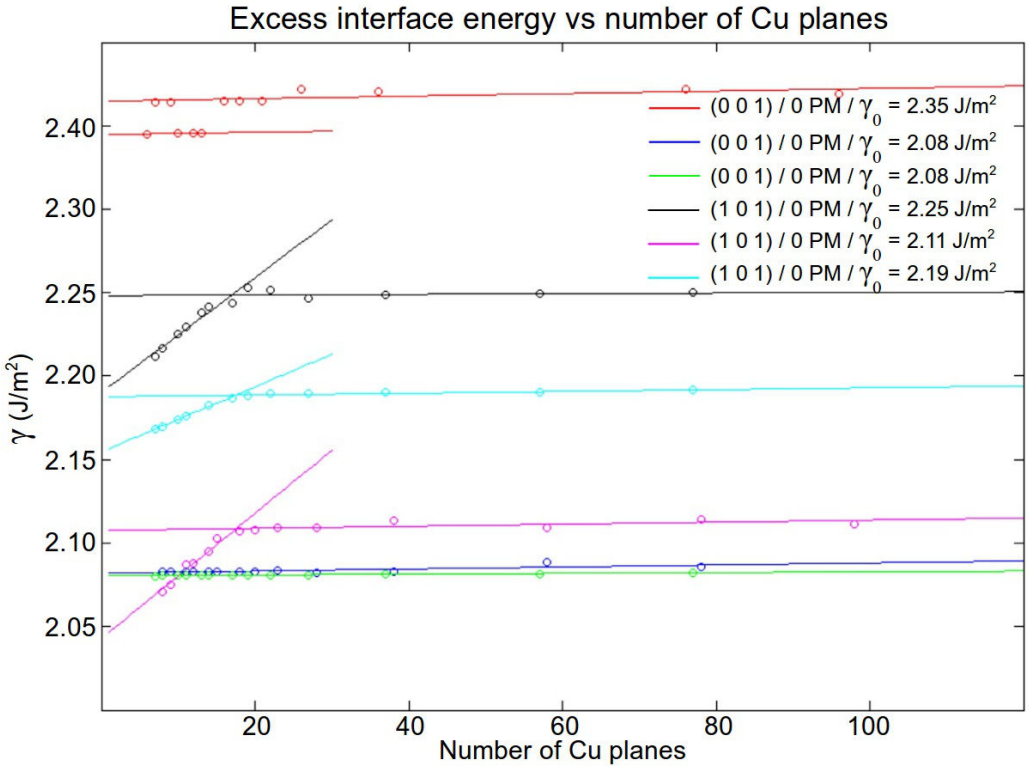

Fig. A1.2 *Excess interface energies calculated from various Cu-Ta interface, with a (1 0 1) or (0 0 1) orientation and a varying number of PM layers in the initial configuration.*

At this stage it is not clear if 2 PM layers in the initial configuration leads to a more stable interface than a single PM layer since the excess interface energies are found to be equivalent for the two configurations. This suggests the existence of two interfaces which are very close energetically. However it should be also noted that these results contradict liquid state dewetting simulations we performed with this potential, where a (1 0 1) orientation was obtained for as much as 55 Cu planes.
The discrepancy between these two results can be explained quite easily. As evidenced in the previous section, and contrary to their (0 0 1) counterparts, the crystallites dewetted with the (1 0 1) orientation exhibit a very rough surface. No (1 0 1) specular facet is present on top of the particles, free surfaces with this orientation are indeed very unfavorable energetically. In the current simulations, the structures consist of thin film of varying thickness with a large (1 0 1) free-surface for the (1 0 1) orientation. Since the excess interface energy is the sum of the free-surface energy of the thin film and of the interface energy, it is normal that the value of γ_f is largely

superior for the (1 0 1) orientation. It is also likely that the potential predicts lower values of interface energies for the (1 0 1) orientation, which would explain why the (1 0 1) orientation is promoted for liquid state dewetted particles.
To calculate the value of the interface energy, a different geometry is considered. Instead of a thin film, the simulation cell is periodic along the x,y,z directions with two equivalent Cu-Ta interfaces (Fig. A1.4.b). The supercell is created with the same Cu-Ta ratio to ensure an almost strain-free configuration.
Similarly to the thin film simulations, the interface energy is obtained by energy minimization at 0 K . The values of γ_i for the four most stable interfaces are presented in table. I.

	(1 0 1) / 1 PM	(1 0 1) / 2 PM	(0 0 1) / 1 PM	(0 0 1) / 2 PM
γ_{int} (J/m^2)	0.64	0.75	0.79	0.82

Tab. A1.1: Comparison of the interface energies respectively to the bulk Cu and bulk Ta values

These calculations confirm that the (1 0 1) orientation leads to lower interface energies, explaining why this orientation is promoted for the liquid state dewetted particles. It does not necessarily contradict the experimental results since the particles dewetted experimentally exhibit a shape close to the ECS with large (1 1 1) and (1 0 0) free-surfaces. The present calculations evidence that the (1 0 1) orientation is the most stable only if the particle is far from the equilibrium crystal shape (ECS) and does not contain any (1 0 1) free surfaces. For particles which are close to the ECS, it is thus clear that the potential will favour the (0 0 1) orientation, in good agreement with the experimental results.

Fig. A1.3 shows the atomic structure of the three most stable Cu-Ta interfaces. For the values of mismatch strain considered, ($\varepsilon_{xx} = \varepsilon_{yy} \sim 31.4\%$ for the (0 0 1) orientation, $\varepsilon_{xx} \sim 31.4\%$ and $\varepsilon_{yy} \sim 8.9\%$ for the (1 0 1) orientation) it is clear that the thickness of the thin film is largely above the critical thickness for dislocation misfit generation (Matthews & Blakeslee 1974), so that the large elastic mismatch strain will be partially relaxed by introducing misfit dislocations.
If the initial configuration has a (0 0 1) orientation and contains a single PM layer, the structure of the first Cu layer does not change upon relaxation, and a b.c.c. structure is still observed. However, the position of the atoms is significantly modified (Fig. A1.3.a). They form elementary cells of 3 or 4 atoms along both in-plane directions (4x4, 4x3 and 3x4 and 3x3 atoms, see Fig. A1.3 where these elementary cells are separated by red dashed lines). The second Cu plane has a f.c.c. structure but it is clear from Fig. A1.3.b that the atoms are not regularly distributed. They also form elementary cells of 4 or 5 atoms along both in-plane direction. In fact, 5 f.c.c atoms can be found on top of 4 PM atoms, while 4 f.c.c atoms are placed on top of 3 PM atoms. The 4 f.c.c Cu atoms on the 3 PM Cu atoms are in tension ($\varepsilon_{xx} \sim 3.04\%$) while the 5 f.c.c Cu atoms on the 4 PM atoms are in compression ($\varepsilon_{xx} \sim -3.40\%$). Although significantly lower than the nominal value of $\varepsilon_{xx} \sim 31.4\%$, it should be noted that this value is almost two orders of magnitude larger than the strain obtained with the ratio 22 Cu / 17 Ta. The 5 Cu/4 Ta and 4 Cu/ 3 Ta elementary cells are separated by two families of orthogonal edge dislocations which are aligned along the substrate x and y directions. In contrast to the initial mismatch strain, they give rise to a nonuniform strain distribution that will discussed in the next sub-section and in the final section of this chapter.
For 2 PM layers in the initial configuration, the first plane is a perfect b.c.c. plane (Fig. A1.3.d), on top of which a second b.c.c. plane with 4x4, 4x3 and 3x4 and 3x3 elementary cells (Fig. A1.3.e) is observed. This plane is equivalent to the first-Cu plane in the 1 PM configuration. On top of this b.c.c. plane, a f.c.c. plane which corresponds to the 2nd Cu plane for the 1 PM configuration can be found (Fig. A1.3.f) For the 4th layer and above a perfect f.c.c structure is obtained (not shown here).

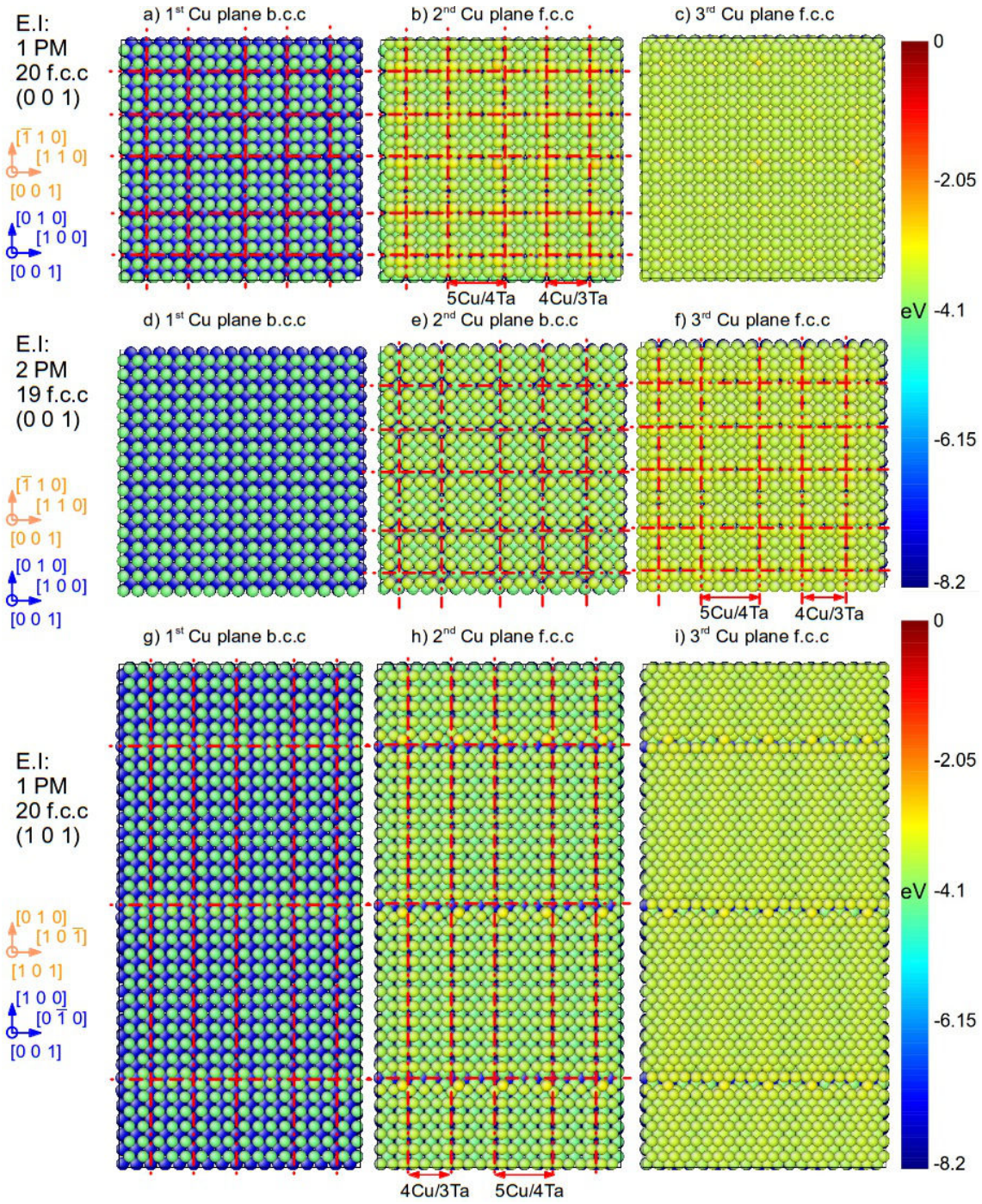

Fig. A1.3 *Structure of the most stable Cu-Ta interfaces determined from the values of the excess interface energies.* The atoms are coloured according to their potential energy, using the scale at the left of the figure Atomic structure of the first three Cu planes, obtained by energy minimization of the structures at 0K, for various initial configurations. (a)-(b)-(c) E.I : 20 f.c.c (0 0 1) planes / 1 PM / 12 Ta planes. (d)-(e)-(f) E.I : 19 f.c.c (0 0 1) planes / 2 PM / 12 Ta planes. (g)-(h)-(i) E.I : 20 f.c.c (1 0 1) planes / 1 PM / 12 Ta planes.

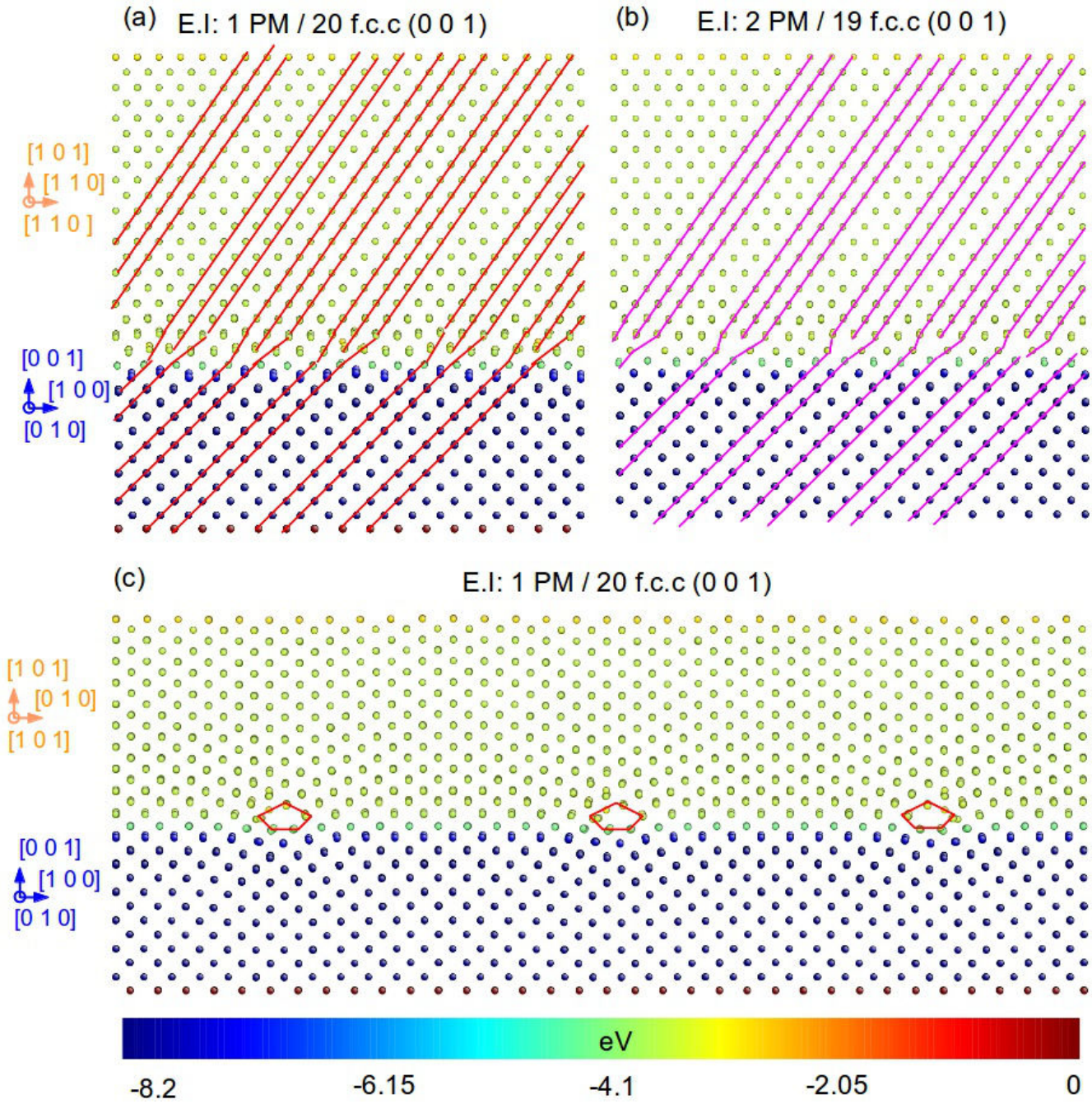

Fig. A1. 4 *Network of interfacial dislocations for the most stable Cu-Ta interfaces after energy minimization of the structure at 0 K.* The atoms are coloured according to their potential energy, using the scale at the left of the figure (a) E.I 20 f.c.c (0 0 1) / 1 PM / 12 Ta. (b) E.I 19 f.c.c (0 0 1) / 2 PM / 12 Ta. (c) E.I 19 f.c.c (1 0 1) / 1 PM / 12 Ta.

Unsurprisingly, the atomic structure of the first Cu planes is largely different for the (1 0 1) orientation with a single PM layer in the initial configuration. The first plane is also b.c.c but it is clear from Fig. A1.3.g that atoms also form elementary cells. Along the x [1 0 $\bar{1}$] they consist of 3 or 4 Cu atoms, while a strong decrease of the spacing between two successive rows of atoms is observed every 10 or 11 rows of atoms along the [0 1 0] direction. On top of this first transition b.c.c. plane, a transition f.c.c. plane is found. Along the x direction, and

similarly to the (0 0 1) orientation, 5 f.c.c atoms are found on top of the four PM, while 4 f.c.c atoms are on top of 3 PM atoms.
Along the [0 1 0] direction, the ε_{yy} is minimized by two supercell configurations: 9 f.c.c atoms on top of 10 PM and 10 f.c.c / 11 PM which corresponds respectively to in-plane strain values of -0.6 and -1.6%. These values are significantly smaller than the nominal in-plane strain value of 8.9%, but 30 and 80 times larger than the in-plane strain achieved through the creation of a 32x35 supercell. Similarly to the (0 0 1) orientation with 1 PM layer, perfect f.c.c layers are observed for the third layer and above.
These three interfaces share some common points. The very large lattice mismatch between the Ta b.c.c and the Cu f.c.c is accommodated with only two transition planes, one b.c.c and one f.c.c. This accommodation is done through the creation of small elementary cells which does not correspond to the optimum ratio for the reduction of the in-plane strain. However, it should be noted that all the supercells that minimize the in-plane strain along a <1 1 0> direction are obtained by a summation of 5/4 and 4/3 elementary cells (Fig. A1.3 separated by red dashed lines). For instance, a minimum is observed for 13 f.c.c and 10 P.M planes which can be decomposed in (5/4+4/3+4/3). Similarly, 22/17 can be decomposed in (5/4+4/3+4/3+5/4+4/3). The optimum ratio for the minimization of the in-plane strain are listed in table 2 for up to 35 Cu atoms and 27 Ta (or PM Cu atoms)

ratio	4/3	5/4	9/7	13/10	22/17	30/23	31/24	35/27
ε_0 (%)	-3.05	3.41	0.59	-0.52	-0.07	-0.85	0.12	-0.23

Tab. A1.2 *List of the Cu/Ta ratio that minimize the in-plane strain at 0 K.*

In order to have a clearer picture of the dislocation network, Fig. A1.4 show a side view of the interfaces. For the 1 PM configuration, the alternating pattern of 4 f.c.c/3 PM atoms and 5 f.c.c/4 PM atoms is clearly visible.
interfacial dislocations can be evidenced along both in-plane directions. The extra half plane is along a <1 1 1> direction. They all start from the first Cu plane which was described as a transition b.c.c. plane previously.
A similar structure of the interface is observed for 2 PM. The network of interfacial dislocations has the same spacing and in order to accommodate the large mismatch strain, as much as five dislocations are found in the structure. Unlike the 1 PM configuration, they do not start at the Cu-Ta interface, but at the 2nd Cu plane, since both b.c.c and f.c.c transition are shifted one plane above for a relaxation from the initial 2 PM configuration.
For the (1 0 1) orientation with 1 PM layer, the dislocation network is similar to the (0 0 1) orientation along the [1 0 $\bar{1}$] orientation, with regularly spaced dislocations starting from the the Cu-Ta interface (not shown on Fig.7). Along the [0 1 0] direction, the dislocation structure is largely different. The dislocations at the interface exhibit a pentagonal core similar to the Lomer-Cotrell dislocations described by Rodney & Phillips (1999), Rodney & Martin (2000).
For the three orientation, the very large mismatch strain is accommodated by the creation of elementary cells separated by dislocations. The nature of the dislocations depends on the nature of the interface, and different type of dislocations are nucleated for the (1 0 1) orientation. As already stated, for the most energetically favorable interfaces, the lattice mismatch is accommodated by only two transition planes (1 f.c.c. and 1 b.c.c.). Below and above these planes, perfect b.c.c. and f.c.c. layers are observed. For the case of 1 and 2 PM layer in the initial configuration, similar interfaces are obtained and the number of PM layers only influence the position of the transition layers (1st and 2nd Cu planes for 1 PM and 2nd and 3rd Cu planes for 2 PM). For the (0 0 1) orientation, the two interfaces are energetically equivalent.

As illustrated in Fig. A1.2, the excess interface energy for the (1 0 1) orientation depends on the number of Cu layers for n < 20 Cu layers. Since the in-plane strain strain is minimized through the creation of supercells, the origin of this thickness dependency for very thin Cu films is unclear.
To understand this behaviour, the interfaces of a thin (9 f.c.c layers and $h \sim 1.15$ nm) and a thick Cu film (20 f.c.c layers and $h \sim 2.6$ nm) are compared for the (1 0 1) orientation.
As illustrated on Fig. 8.a and 8.b the atomic structure of the 2nd plane differs between the thin and the thick Cu

film. As described in the previous paragraph, a large gap is observed every 9 or 10 Cu atoms, which corresponds to the pentagonal core of the dislocations. For the thick Cu film, the gap is free of atoms while the presence of atoms is observed at the junction of the [1 0 $\bar{1}$] supercells for the thin Cu film.
The side view of the interface (Fig. 8.c and 8.d) provides a better picture of the evolution of the atomic structure of the Cu film. For the thin Cu film, the core of the dislocations is filled with an extra-atom while it remains empty for the thick one. A closer look at the surface plane reveals the presence of periodic ripples associated with this modification of the atomic structure of the interface in the Cu thin film. These periodic ripples, that can be described as a surface waviness (roughness), are related to the presence of misfit dislocations. As discussed by Freund & Suresh (2003), a thin film of height h that is epitaxially bonded to a thick substrate is uniformly strained and has a flat surface before any strain-relieving dislocations are formed at the substrate/film interface. The chemical potential can indeed be considered as spatially uniform over the surface of the film so that the flat surface is an equilibrium shape. The condition of uniform chemical potential are not fulfilled once misfit dislocations are formed at the film-substrate interface. The magnitude of the average elastic strain along the surface is reduced by the formation of dislocations, and the strain distribution becomes spatially non-uniform. The non-uniform strain field has a several consequences, in particular it implies that the surface
chemical potential becomes nonuniform. As a consequence, there is a configurational force acting on the nominally flat surface tending to change its shape: the film exhibits periodic fluctuations in surface shape.
In our case, the periodicity of the fluctuations is clearly correlated with the position of the misfit dislocations.
Such correlations in the fluctuations of the surface shape correlated in position with misfit dislocations on the interface have been observed by Pinnington *et al.*(1997), Giannakopoulos and Goodhew (1998) and Springholz (1999) in partially relaxed thin film. A commonly reported idea is that a strained surface will roughen and that the nonuniform strain along the surface will lead to formation of dislocations at the highest concentration sites (Freund & Suresh 2003). In such materials, the strain energy field arises mainly from three sources: the initial uniform lattice mismatch strain, the strain associated with the interface misfit dislocations which partially relax the elastic mismatch strain and an additional contribution due to the waviness of the surface (Jonsdottir 1994).
In our simulations an array of two families of orthogonal dislocations is obtained for both orientation. All dislocations have a Burgers vector of magnitude b. They are distributed at the Cu-Ta interface at a distance h of the film surface at intervals p and q in the x and y directions. The full relaxation of the mismatch strain only occurs when (Jonsdottir 1995):

$$\frac{p}{h} = \frac{b}{\epsilon_{xx} d \sqrt{2}}, \qquad \frac{q}{h} = \frac{b}{\epsilon_{yy} d \sqrt{2}} \tag{A1.3}$$

For the thin Cu film, q/h = 3 while the second term is equal to 0.78. It is thus clear that the mismatch strain is not completely relaxed by misfit dislocations and the roughness of the surface is thus expected.
It has been established that the amplitude of the fluctuations and thus the degree of roughness of the interface can be determined by the fraction of the elastic mismatch strain that is relaxed by formation of misfit dislocations (Jonsdottir 1995). For a given mismatch strain and film thickness, the amplitude of the fluctuation decreases with the decrease of the dislocation spacing (Freund & Suresh 2003, Jonsdottir 1995). In our case i the fluctuations are more pronounced along the [0 1 0] orientation where the spacing between dislocations is much larger than along the [1 0 $\bar{1}$] but the nominal mismatch strain along both in-plane direction
differs by a factor 3, so that it can not be established if our simulations follow this trend. It has been also reported by Freund & Suresh (2003) that the magnitude of the elastic strain at the film surface due to dislocations is typically on the order of b/h. This gives values of respectively 5% and 11.1% for the thick and thin Cu films respectively. For the latter, this value is even larger than the mismatch strain along y, and the large amplitude of the fluctuations of the surface plane is not surprising. For the thick Cu film (Fig. A1.5.d), the mismatch strain is only twice the value of the elastic strain due to the dislocations, but the latter is not sufficient to induce large perturbations at the surface plane. The lower magnitude of the elastic strain due to dislocations at the surface, the

higher is the uniformity of the chemical potential. The flat surface is less prone to change its shape.
This is very clear in our simulations where the surface completely vanishing in the thick Cu film resulting in an almost perfectly flat (1 0 1) free-surface.
The flatness of the surface is confirmed by the calculation of the atomic positions in the thin film with respect to the atomic positions in a very thick Cu film (n=129 f.c.c Cu planes).
For n = 9 f.c.c. oscillations are observed for the x, y and z atomic positions. For the z position, the amplitude of the oscillations increase for atoms closer to the surface (atoms with higher index on Fig. A1.5.e). For n = 24, no such oscillations are observed, and the atomic position are similar to that of a thick film, even when the atoms are close to the surface. An indirect consequence of the fluctuations of the surface shape is a reduction of the free-surface energy of the (1 0 1) surface. We have seen previously that a large (1 0 1) free surface is very unfavourable energetically as compared to the more densely-packed (1 0 0) and (1 1 1) free surfaces. As a remind, with this potential, the chemical potential of a (1 0 1) surface atom is equal to -2.87 eV/at while it is equal to -3.02 eV/at for a (1 0 0) surface atom.
Here the surface fluctuations locally reduces the spacing between the atoms along the y direction so that it get closer to the value along the x direction. In other words, the starting of a transition from a tetragonal unit-cell (corresponding to the (1 0 1) orientation) to a cubic unit cell ((0 0 1) orientation) is locally observed.
The minimum spacing along the y direction is observed for the atoms above the pentagonal dislocations (regions circled in red). In this region, the spacing between two atoms in the unit cell is still equal to $a_{Cu}/\sqrt{2}$ along the [1 0 $\bar{1}$] while along the [0 1 0] direction the lower is the number of Cu planes, the larger is the compression of the unit cell. For 10 f.c.c Cu planes, the lattice spacing is reduced to 3.40 Å corresponding to a compression of 6%. The unit-cell is still tetragonal, but the reduced asymmetry between the two in-plane directions induce a decrease of the atom energy of 0.04 eV (-2.91 eV vs -2.87 eV). Of course the compression of the rows above the Lomer dislocations implies a compensative expansion of the neighbouring atoms, and the lattice spacing is increased by up to 2.7% in the region between the dislocations. This of course induce an increase of the atom energies but by only 0.015 eV.
Overall these alternating regions of expansion and compression lead to a decrease of the free-surface energy of the (1 0 1) surface. The lower is the number of Cu planes the larger is the amplitude of the oscillations, and the larger is the subsequent decrease of the free-surface energy. Conversely, an increasing thickness of the thin film causes a damping of the oscillations which completely vanishes above 20 f.c.c planes. The free-surface energy becomes independent of the number of Cu planes for n > 20 explaining the flat slope of the curve in this region in Fig. A1.2. Nevertheless it should be noted that the ultrathin Cu films are very defective, inducing an overall increase of the excess interface energy.

A1.2 Atomic structure of the Cu-Ta interface in solid state dewetted particles

In section A.1.1 we evaluated the stability of several Cu-Ta interfaces in thin-film structures. However, this chapter aims at determining the atomic structure of the Cu-Ta interface for the Cu particles.
As discussed in the introduction of this chapter, in the presence of mismatch strain, there is a natural tendency for thin films to agglomerate into islands in the presence of mismatch strain, for sufficiently high temperature. It is clear that the total free energy of the system will be affected in forming any particular island arrangement from a strained thin-film. As discussed by Freund & Suresh (2003), it might result in a positive or negative net change whether the surface energy increase or the elastic energy reduction dominates the process.
In the case of the solid state dewetting of the Cu islands, it is clear that the island maintains the epitaxial bond with the substrate so that the mismatch strain is probably not affected by dewetting. However, the relaxation of the free-surface to reach the ECS might affect the structure of the Cu-Ta interface.
In a first step, the idea is to evaluate the agreement between the interface structures obtained for a thin film and for and island. Two initial configurations with 1 and 2 PM Cu layers and a varying number of f.c.c (0 0 1) layers are considered. In both case, the initial shape of the particle is already close to the ECS. Similarly to the thin film

simulations, the relaxed atomic structure of the two interfaces is obtained by energy minimization at 0K.
The 1 PM island is composed of 24 f.c.c planes and the supercell consists of 45x45 atoms which are on top of 35x35 Cu PM atoms (ε_0 = -0.07%). The substrate contains 12 Ta planes for a total of 30584 Cu atoms and 27500 Ta atoms (Fig. 9.a). This gives a size of 11.2x11.2x4.5 nm^3 for the relaxed particle.

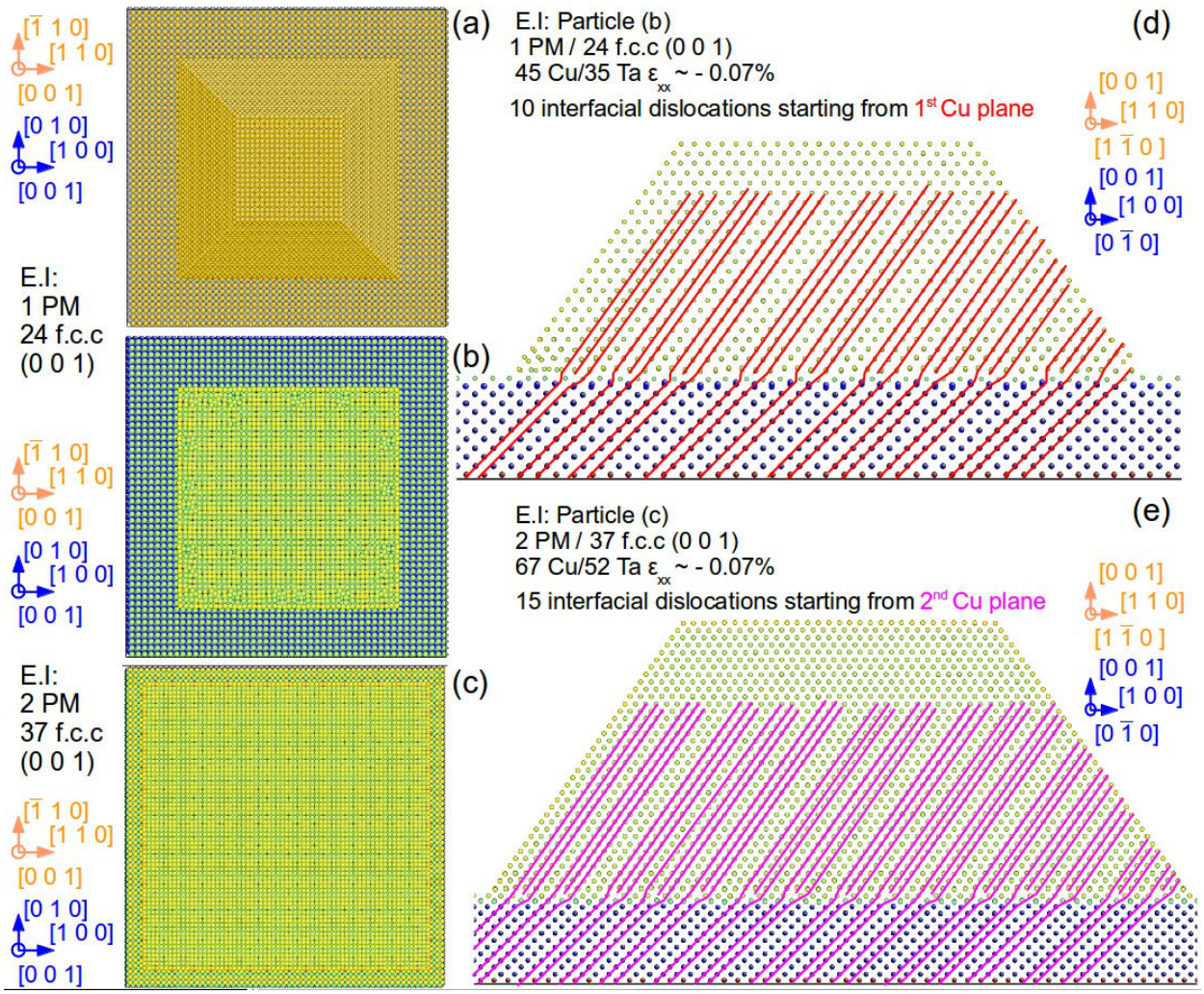

Fig. A1.5 *Network of interfacial dislocations in the dewetted islands, for a varying number of PM layers.* Atoms are colour coded according to their potential energy. The scale not indicated here is the same as in previous figures. (a) Initial configuration: 24 f.c.c. planes/ 1PM/ 12 Ta (b) Atomic arrangement of the 2nd Cu plane after energy minimization at 0K. (c) Atomic arrangement of the 3rd Cu plane after energy minimization at 0K at 0K. (b) Side view of the relaxed Cu-Ta interface in particle (b) The particle hosts a network of dislocation which start from the first Cu plane. (c) Side view of the relaxed Cu-Ta interface in particle (c). The particle hosts a network of dislocation which start from the second Cu plane.

The 2 PM island is slightly larger (37 f.c.c) planes, while maintaining the same Cu/Ta ratio (67/52, ε_0 = -0.07%) and the same number of Ta planes (99553 Cu atoms and 38998 Ta atoms in total). This corresponds to a size of 17.1x17.1x7 nm^3.
The atomic structure of the relaxed interfaces is presented on Fig. A1.6.b & A1.6.c. The relaxation of the mismatch strain is achieved by the nucleation of the same network of orthogonal families of edge dislocations,

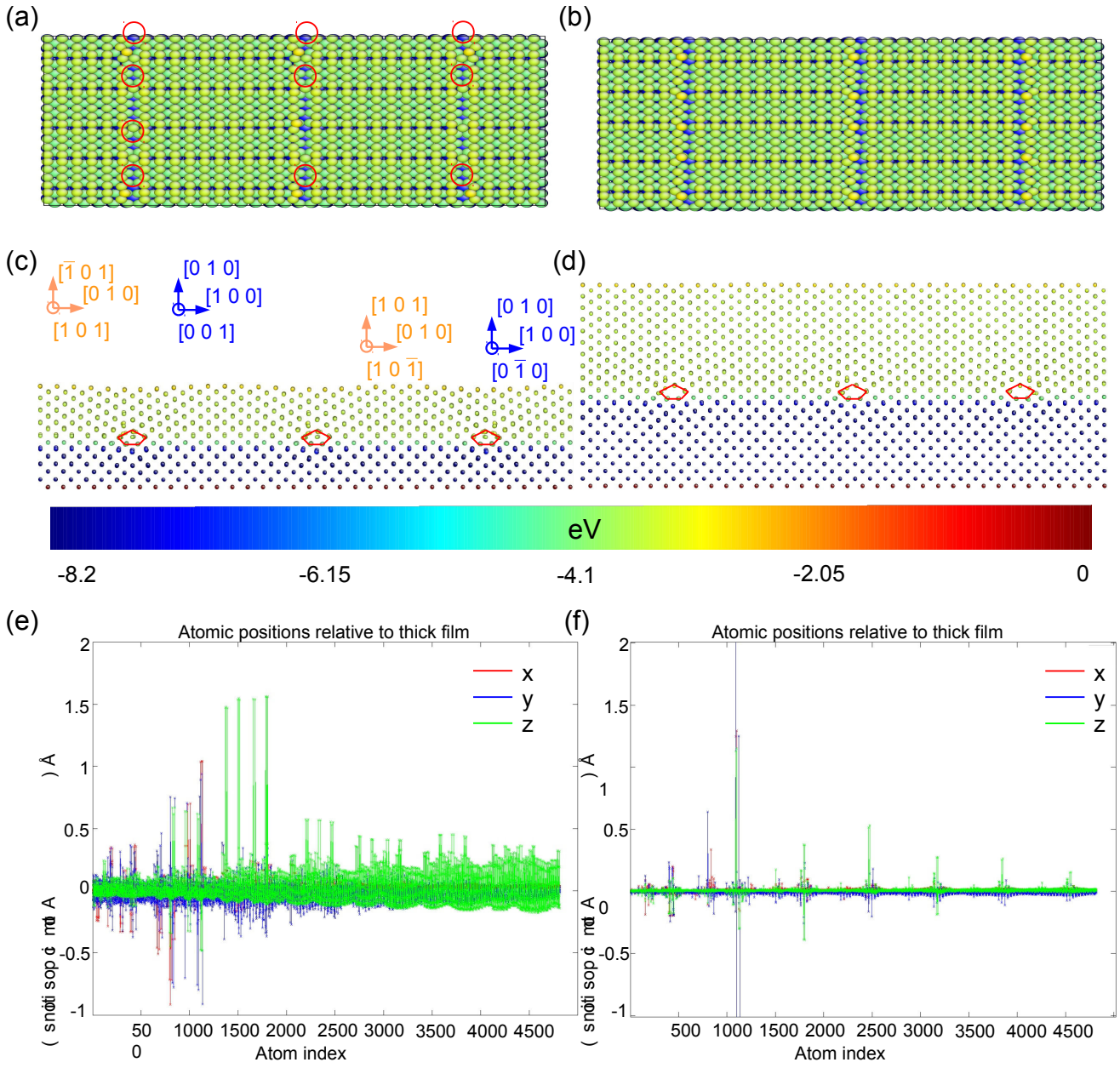

Fig. A1.6 *Explanation of the presence of two regimes in the excess interface energy vs number of planes curve for the (1 1 0) orientation.* The atoms are coloured according to their potential energy, using the scale at the left of the figure (a) Atomic structure of the 2nd Cu plane for n = 9 f.c.c planes. The red circled indicate the location of the supplementary atoms (b) Atomic structure 2nd Cu plane for n = 21 f.c.c planes. (c) and (d) Side view of the Cu-Ta interface for n = 9 and n =21 f.c.c planes. (e), (f) Variations of the x, y and z atomic positions for n= 9 f.c.c and n = 21 f.c.c planes, relatively to the positions in a thick Cu film (n=129 planes)

which act as boundaries for the 5 f.c.c / 4 P.M and 4 f.c.c / 3 P.M elementary cells. For both particles, the dislocations are regularly spaced, with intervals equivalent to the thin-film simulations (every 4 or 5 Cu planes). For the 1 PM particle, 10 dislocations are distributed in 45 Cu planes and for 2 PM, 15 dislocations are distributed in 67 planes. This gives the exact same ratio of one dislocation every 4.5 Cu plane.

For the 2nd PM dislocation, the interval between dislocations always corresponds to Cu/Ta ratio which minimize the in-plane strain at 0K. If the left-most dislocation is located in plane 0, the next dislocation is found in plane 4. From the left to the right of the particles, dislocations are found at positions 13, 17, 22, 26, 31, 35, 39, 44 … They all correspond to ratio that minimize the in-plane strain (Tab. A1.2). To a certain extent, the alterning of 5/4 and 4/3 elementary cells is thus not random, and aims at building larger supercells which minimize the in-plain strain to even lower values.

For the 1 PM particle, all the dislocations originate from the 1st Cu plane (namely the transition b.c.c. plane). As illustrated on Fig. A1.6.b, the 2nd Cu layer, namely the f.c.c transition layer, is not as perfect as in the case of a thin film. Several disordered regions are observed at the vicinity of the crystal free surface and of the particle-substrate interface. In these regions atoms undergo large strain values, and the interaction of the surface strain, the strain form the misfit dislocation and the residual misfit strain might explain this relative disorder.

For the particle with two 2 PM layers in the initial configuration, the interface is not affected by the boundary conditions, *i.e* the relaxed free surfaces of the crystallite. Similarly to the thin-film simulation, the dislocation array starts from the b.c.c transition plane, *i.e* the second Cu plane.

From these two simulations, it appears the boundary conditions of the simulations have a limited effect on the atomic structure of the interface, and the obtained interfaces are similar to the case of the thin-films, although it is slightly more disordered for 1 PM layer in the initial configuration.

Bibliography

Attarian Shandiza , M., Safaeia , A., Sanjabia, S., Barberb, Z.H. (2007) *J. Phys. Chem. Sol.* **68**, 1396-1399.

Beutier, G., Verdier, M., Parry, G., Gilles, B., Labat, S., Richard, M. I., Cornelius, T., Lory, P. -F., Vu Hoang, S., Livet, F., Thomas, O. & De Boissieu, M. (2012). *Thin Solid Films* **530**, 120-124.

Beutier, G., Verdier, M., De Boissieu, M., Gilles, B., Livet, F., Richard, M. I., Cornelius, T. W., Labat, S. & Thomas ., O. (2013). *J. Phys .Conf. Series* 425, 132003.

Daw, M. S. & Baskes, M., I. (1984) *Phys. Rev. B* **29**, 6443 (1984).

Favre-Nicolin, V., Richard, M. I. & Renevier, H. (2011). *J. Appl. Cryst.* **44**, 635-640.

Feidenhans'l, R. (1989) *Surface Science Reports* **10**, 105-188

Freund, L. B. & Suresh, S. (2003) *Thin Film Materials: Stress, Defect Formation and Surface Evolution,* edited by Cambridge University Press, Cambridge, England

Giannakopoulos ,K. P., & Goodhew, P. J (1998) *J. Crystal Growth* **188**, 26-31.

Hashibon, A., Lozovoi, A. Y., Mishin, Y., Elsässer, C. & Gumbsch, P. (2008) *Phys. Rev. B* **77**, 0941131

Howe J. M. (1997),. *Interfaces in materials,* edited by John Wiley & Sons, Inc.

Huang, W. J., Sun, R., Tao, J., Menard, L. D., Nuzzo, R.G. & Zuo, J. M. (2008). *Nature Materials* **7**, 308-313.

Johnson, R.A (1990) *Phys. Rev. B* **41**, 9717.

Jonsdottir, F. (1995) *Mat. Res. Soc. Symp. Proc.* **356,** 45-51

Massalski, T. B. (1986) *Binary Alloy Phase Diagrams* edited by Materials Park, OH

Matthews, J.W. & Blakeslee, A. E. (1974) *J. Crystal Growth* **27**, 118.

Matthews J.W. & Blakeslee, A. E. (1975) *J. Crystal Growth* **29,** 273.

McCormack, J. M., Myers, J. R. & Saxer, R. K. (1965) *J. Chem. Eng. Data* **10**(4), 319-321.

Musket, R.G, McLean, W., Colmenares, C.A., Makowiecki, D. M. & Seikhaus, W. J (1982) *Appl. of Surf. Sci.* **10**, 143-207.

Pinnington, T., Lavoie, C. & Tiedje, T. (1997) *J. Vac. Sci. and Tech.* **B 15**, 1265-1269

Robinson, I. K. (1986) *Phys. Rev. B.* **33**(6)

Robinson, I.K & Tweet, D. J. (1992) *Rep. Prog. Phys.* **55***,* 599-651

Rodney, D. & Phillips, R. (1999) *Phys. Rev. Lett.* **82**, 1704

Rodney, D. & Martin, G. (2000) *Phys. Rev. B* **61**, 8174

Rodney, D., Fivel, M. & Dendievel, R. (2005) *Phys. Rev. Lett.* **95**, 108004.

Spence, J. C. H (1988) [1980] *Experimental high-resolution electron microscopy*. Edited by New York: Oxford U. Press.

Springholz, G. (1999) *Applied Physics Letters* **75**, 3099-3101.

Venugopal, V. & Thijsse, B. J. (2009) *Thin solid Films* **517***,* 5482-5488

Verdier M (2008) ANR n°06-NANO-051 CRISTAL processing report

Vitos, L., Ruban, A. V., Skriver, H., L. & Kollár, J. (1998) *Surface Science* **411***,* 186-202

Winterbottom, W. L. (1967). *Acta Metall.* **15**, 303.

Yeshchenko ,O.A, Dmitruk, I. A., Alexeenko, A. A. & Dmytruk, A. M. (2007) *Phys. Rev. B* **75**, 085434.

Appendix A2 : Inversion Domain Boundaries in GaN Wires Revealed by Coherent Bragg Imaging

Appendix A2 is the paper published by Stéphane Labat and co-workers in ACS Nano earlier this year. I was significantly involved in both the synchrotron experiments and the data analysis (reconstruction).

Inversion Domain Boundaries in GaN Wires Revealed by Coherent Bragg Imaging

Stéphane Labat,[*,†] Marie-Ingrid Richard,[†,‡] Maxime Dupraz,[§,∥] Marc Gailhanou,[†] Guillaume Beutier,[§,∥] Marc Verdier,[§,∥] Francesca Mastropietro,[†] Thomas W. Cornelius,[†] Tobias U. Schülli,[‡] Joël Eymery,[⊥,#] and Olivier Thomas[†]

[†]IM2NP UMR 7334, Aix Marseille Université, CNRS, Université de Toulon, F-13397 Marseille, France, [‡]ID01 ESRF, F-38043 Grenoble, France, [§]Université Grenoble Alpes, SIMAP, F-38000 Grenoble, France, [∥]CNRS, SIMAP, F-38000 Grenoble, France, [⊥]Université Grenoble Alpes, F-38000 Grenoble, France, and [#]"Nanophysique et Semiconducteurs" Group, CEA, INAC-SP2M, F-38000 Grenoble, France

ABSTRACT Interfaces between polarity domains in nitride semiconductors, the so-called Inversion Domain Boundaries (IDB), have been widely described, both theoretically and experimentally, as perfect interfaces (without dislocations and vacancies). Although ideal planar IDBs are well documented, the understanding of their configurations and interactions inside crystals relies on perfect-interface assumptions. Here, we report on the microscopic configuration of IDBs inside n-doped gallium nitride wires revealed by coherent X-ray Bragg imaging. Complex IDB configurations are evidenced with 6 nm resolution and the absolute polarity of each domain is unambiguously identified. Picoscale displacements along and across the wire are directly extracted from several Bragg reflections using phase retrieval algorithms, revealing rigid relative displacements of the domains and the absence of microscopic strain away from the IDBs. More generally, this method offers an accurate inner view of the displacements and strain of interacting defects inside small crystals that may alter optoelectronic properties of semiconductor devices.

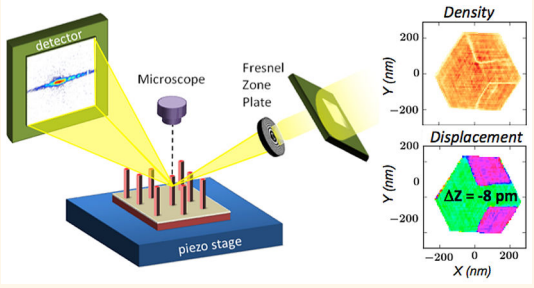

KEYWORDS: GaN wires · inversion domain boundary · coherent X-ray Bragg imaging · displacement field

The physical properties of crystals are strongly affected by the presence of defects: dislocations, stacking faults and twins have a prominent role in the mechanical behavior, vacancies are crucial in the diffusion process and electrical, and optical properties are widely affected by defects too.[1] The detailed knowledge of defects distribution in crystals is thus a prerequisite for understanding how physical properties are affected. For many years, methods based on transmission electron microscopy (TEM) have been unchallenged for investigating defects in crystals and have provided numerous essential results.[2−6] But recently, a new lensless imaging technique using coherent X-ray diffraction has emerged, which is able to determine the atomic displacement field in a crystal from the measurement of Bragg reflections.[7] This technique is called Coherent Bragg Imaging (CBI). Up to now, it has been mainly used, however, for imaging perfect crystals with very small strain.[7−10] Very few works use it for materials containing defects.[11−13]

Here, we report on the first study of the displacement field induced by several Inversion Domain Boundaries in Gallium Nitride (GaN) wires with a spatial resolution better than 10 nm and a displacement accuracy of a few picometres. Nitride materials are studied intensively and their growth mastering has opened the way to blue-light emission[14] and power devices applications. Since defects in GaN wires are a key issue,[15] such results give new insights into the optoelectronic properties of nitride semiconductors.

RESULTS AND DISCUSSION

The GaN wires of this study were grown by Metal Organic Vapor Phase Epitaxy (MOVPE) on a *c*-oriented sapphire substrate. A sample with a low wire density was prepared

* Address correspondence to stephane.labat@im2np.fr.

Received for review June 24, 2015 and accepted August 31, 2015.

Published online August 31, 2015
10.1021/acsnano.5b03857

© 2015 American Chemical Society

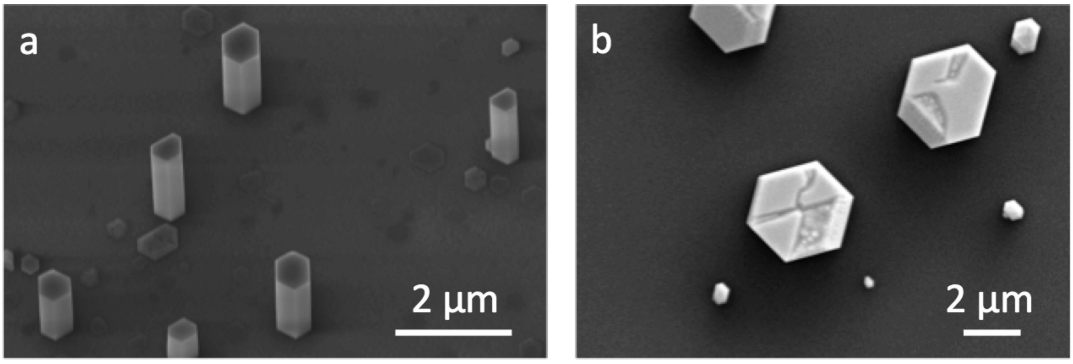

Figure 1. Scanning electron microscopy images of GaN wires obtained by MOVPE. (a) A 25°-view taken at the center of the wafer showing single crystal wires and (b) top view taken at the wafer edge for a sample etched under H_2 carrier gas to underline polarity inversion domain boundaries. The growth conditions (mostly flows and materials supply) are changed in the 2 mm outer edges.

in order to ease the individual analysis with the microfocused X-ray beam: specific surface annealings and growth conditions (detailed in the Methods section) promote the 'vertical' growth (*i.e.*, perpendicular to the surface of the substrate) of hexagonal wires with average diameter of 600 nm and length of 3−5 μm (Figure 1a).

They have their *c*-axis parallel or antiparallel to the growth axis and smooth lateral $\{1\bar{1}0\}m$-plane facets. The wires are in epitaxial relationship with the sapphire as confirmed by grazing incidence X-ray and electron diffraction: $[1\bar{1}0]_{GaN}//[0\bar{1}0]_{Al203}$ and $[00\bar{1}]_{GaN}//[001]_{Al203}$ with twist and tilt misorientations of less than half a degree.[16] TEM studies have shown that "defect-free wires" are single crystalline with a flat top surface and have no extended defects along the length, except for threading dislocations nucleated at the lattice mismatched interface. These dislocations are usually bent to the sidewall surface along a distance of the order of magnitude of the diameter.[5,17] Polarity in non-centrosymmetric wurtzite crystal is defined with standard notations: the bond pointing from the Ga cation to the N anion defines the polar axis *c* labeled [001] also called Ga-polar orientation. Within the selected growth conditions, the wires are mostly N-polar oriented, *i.e.*, along −*c* axis. Nevertheless, IDBs separating +*c* and −*c* crystal orientation domains have been observed in the core of guided wires close to the holes of patterned masks.[5,18] The lateral overgrowth tends to favor the occurrence of IDBs nucleating on the surface defects of the SiN_x seed layer.[19] In this paper, we select "defective" wires close to the wafer edge in order to increase the probability of occurrence of IDB defects and to benefit from an even lower wire density. This defective character has been checked by etching a sample at the end of the growth under H_2 to reveal selectively the −*c* and +*c* orientation domains (note that similar results can be obtained *ex situ* by wet KOH solutions[20]): under H_2 carrier gas, −*c* (nitrogen-terminated) GaN surface stays flat, whereas the +*c* (gallium-terminated) surface is roughened and exhibits small faceted pyramids. This procedure is demonstrated in Figure 1b. IDBs are clearly observed and show complex structures separating flat (−*c*) and rough (+*c*) surfaces. Note that facets can be visible at some wire edges. This faceting provides also a signature of +*c* GaN growth as evidenced by previous TEM studies.[5]

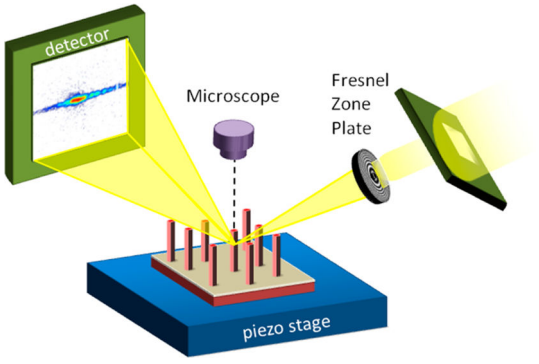

Figure 2. Sketch of the experimental setup for coherent X-ray Bragg imaging.

The CBI technique was used to investigate the arrangement of the IDBs inside the GaN wires and the displacement field generated by these defects. The very good epitaxial relationship of the wires with the substrate eases the otherwise tedious alignment procedure of a known wire with the microfocused X-ray beam (Figure 2).

When a crystal is fully illuminated by a coherent X-ray beam, the scattered waves from all parts of the sample interfere in the diffraction pattern. The intensity scattered by the sample is measured in far field and a real space image of the sample may be reconstructed from the intensity pattern thanks to phase retrieval algorithms. When the intensity pattern is measured close to a Bragg peak, a complex-valued image of the sample (named $\rho(\mathbf{r})$) is retrieved, which is related to the structure factor $F(\mathbf{G},\mathbf{r})$ and the displacement field $\mathbf{U}(\mathbf{r})$ by the expression:

$$\rho(\mathbf{r}) = F(\mathbf{G}, \mathbf{r})\, e^{-i2\pi \mathbf{G}.\mathbf{U}(\mathbf{r})} \quad (1)$$

where **G** corresponds to the scattering vector of the Bragg Peak. Note that the sign convention used to

describe the plane wave e^{ikr} implies a minus sign in the Fourier transform of eq 1. The spatial resolution or pixel size of the reconstructed image of the object is inversely proportional to the extension of the intensity measurements around the Bragg peak. Extended diffraction pattern measurements provide small pixel sizes in the reconstructed sample images. Because of the steep decrease of intensity away from the Bragg peaks, the pixel size in the sample image is rarely smaller than 10 nm. For the sake of clarity, the modulus $M(\mathbf{r})$ and phase $\phi(\mathbf{r})$ of the reconstructed object will be displayed in two separate images. From eq 1, $M(\mathbf{r})$ and $\phi(\mathbf{r})$ can be written as

$$M(\mathbf{r}) = |F(\mathbf{G},\mathbf{r})| \quad \text{and} \quad \phi(\mathbf{r}) = \psi_F(\mathbf{G},\mathbf{r}) - 2\pi\mathbf{G}.\mathbf{U}(\mathbf{r}) \quad (2)$$

where ψ_F corresponds to the phase of the complex structure factor $F(\mathbf{G},\mathbf{r})$. In the case of GaN wires containing inversion domains, the same moduli are expected for the two types of domain, but different phases will be observed including the effects of the structure factors and the displacement field. Thus, one expects a homogeneous modulus map $M(\mathbf{r})$ and an inhomogeneous phase map $\phi(\mathbf{r})$. Each Bragg peak is sensitive to the displacement field $\mathbf{U}(\mathbf{r})$ projected onto the scattering vector $\mathbf{G}$, *i.e.*, $\mathbf{G}.\mathbf{U}(\mathbf{r})$. To extract the full displacement vector field $\mathbf{U}(\mathbf{r})$, at least three noncoplanar Bragg peaks are needed. In this work, we measured five Bragg peaks: 004, 014, 104, 112, and 203. The redundancy is expected to improve the reliability of the retrieved vector field $\mathbf{U}(\mathbf{r})$. The intensity measurements were done while illuminating a slab (~400 nm thick) at mid-height of the wire. Each of the five diffraction patterns was measured in three dimensions by recording a stack of frames of an area detector while rocking the sample across the reflection. In all three-dimensional diffraction patterns, the measured intensity is concentrated in an (h,k)-plane perpendicular to the l-axis. This means that the inner structure of the measured slab is constant along the wire axis. 2D intensity maps were thus extracted from the 3D data sets in order to reconstruct a 2D image of the sample (Figure 3a). The latter is therefore a projection of the measured slab along the c-axis, which provides a good image of the inner structure in this translation-invariant sample.

In all five diffraction patterns, the 6 streaks observed along directions separated by an angle of 60° clearly demonstrate the hexagonal shape of the wire. Each diffraction pattern was used independently to reconstruct an image of the inner structure of the wire with different displacement field components. The sample is reconstructed with a pixel size of 6×6 nm^2 because of the extent of the measured intensity in the reciprocal space. Phase retrieval of the diffraction data was carried out using standard algorithms[21,22] based on Fourier transforms going back and forth between the direct space (sample image) and the reciprocal space (diffraction patterns).

The reconstruction procedure (see Methods and Supporting Information S1) is carried out a thousand times with random initial phases for each diffraction pattern. Two criteria were used to identify the best reconstructions: the agreement with the measured intensity and the homogeneity of the modulus map. The best solutions, which fulfill these two criteria, are used to determine the accuracy of the results (see Supporting Information S1). Then, we are still left with two solutions, $\rho(\mathbf{r})$ and $\rho^*(-\mathbf{r})$, which fulfill equally the two criteria (Figure 4).

For this specific 2D case, $\rho^*(-\mathbf{r})$ corresponds to a 180° rotation of $\rho(\mathbf{r})$ with phases of opposite sign. However, they can be distinguished by considering the optical path length inside the sample. Indeed, the waves scattered by atoms at the surface and inside the wire travel along different optical paths because of the shape of the wire: the travel inside the crystal from the entrance to the scatterer and from the scatterer to the exit is less for atoms at surfaces. In the crystal, the refractive index n is slightly different from 1, which means that the phase velocity is not the same as in the air. For 9 keV X-rays in GaN, $n = 1 - \delta + i\beta$ with $\delta = 1.356 \times 10^{-5}$ and $\beta = 2.5 \times 10^{-7}$ (ref 23). δ and β imply a phase shift and an absorption, respectively. Thus, for a diameter of 500 nm, the phase shift between the surface and the center of the wire is around 0.3 rad, which is not negligible. By contrast, the absorption is less than 1% and will be neglected. According to the Fourier transform convention mentioned in eq 1, the plane wave of the incident and diffracted beam is written e^{ikr}, where $k = 2\pi/\lambda$ is the wave vector of the plane wave in vacuum and λ the wavelength of the X-ray beam. After a traveled distance d inside the crystal, the phase of the beam is shifted negatively by $-k\delta d$. A negative curvature of the phase is therefore expected in the middle of the wire, which is clearly identified in one of the two possible reconstructed objects (Figure 4).

Moreover, the specific fingerprint of the phase shift coming from the optical path length cannot be confused with a displacement field inside the wire. In particular, the phase is curved only in the direction transverse to the scattering plane (X), and is flat along the longitudinal one (Figure 4). Note that we neglect the curvature of the incident wavefront, which is mostly flat at this scale for our setup.[24] In conclusion, the identification of the optical path length effect allows the unambiguous determination of the correct solution $\rho(\mathbf{r})$, from which we can deduce the polarity of each domain.

Figure 3b displays the best reconstructed images of the wire for the 5 Bragg peaks including the optical path length correction. All five solutions converge to the same shape and inner structure. The average diameter of the wire is estimated at (490 ± 10) nm. The reconstructions clearly evidence the presence of

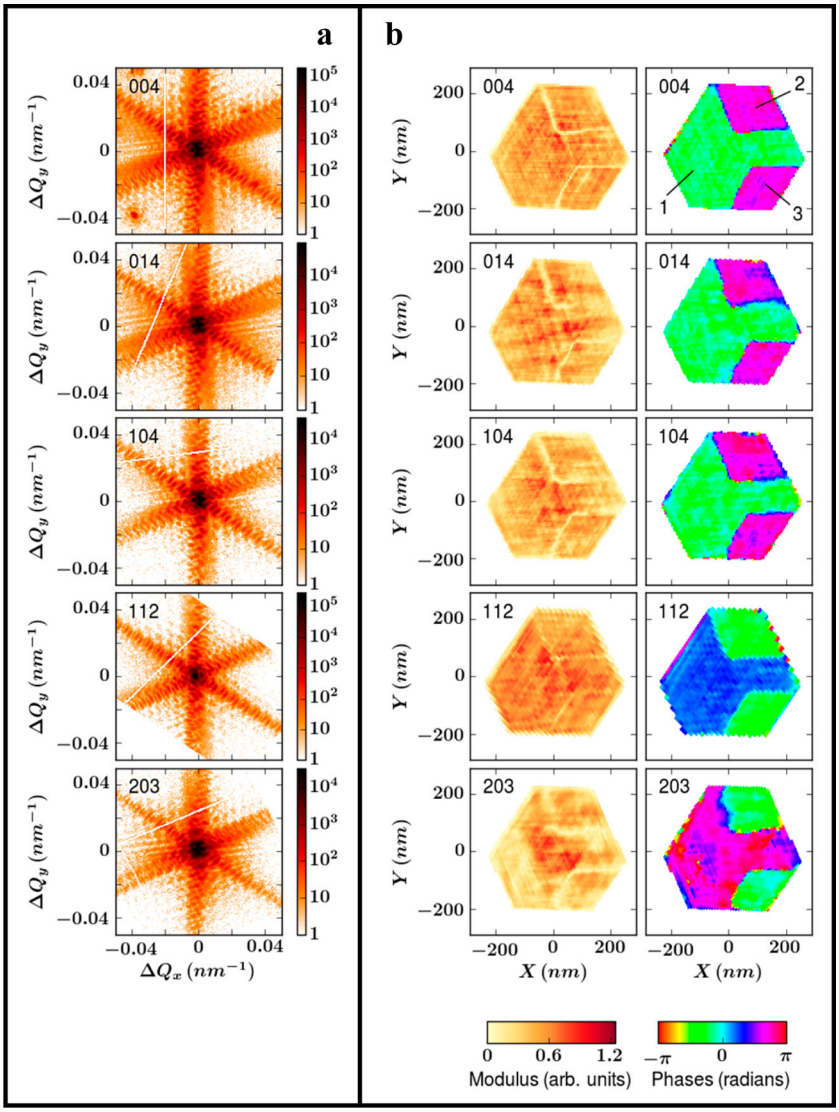

Figure 3. Coherent X-ray diffraction measurements of five Bragg reflections of a single GaN wire and the corresponding real space reconstructions (modulus and phase). The (*hkl*) planes are indicated in the top left corner of the figures. (a) Intensities are shown in counts with a log scale. (b) The real space reconstructions (modulus and phase), the (*X*,*Y*,*Z*) axis correspond to the crystallographic directions([$\bar{2}$10],[010],[001]).

three domains: one large and two smalls. The phase values (Figure 3b) are constant inside the domains and the two small domains show the same phase value for all reconstructions. In the following, the three domains will be called domains 1, 2, and 3 as mentioned in Figure 3b. The IDBs, separating the domains, correspond to the {100} planes, which have been reported in many studies.[25,26] In the modulus maps of the reconstructed samples (Figure 3b), a gap clearly appears at the position of the IDBs. This is an artifact of the Fourier transform caused by data truncation. Indeed, numerical test demonstrates that an ideal sample with homogeneous modulus map and a phase shift between domains cannot be reconstructed without such an artifact, since only a small part of the reciprocal space is used for reconstruction. In the present study, the measured reciprocal space corresponds to the 20th of the reciprocal space unit cell. Such a partial reciprocal space measurement implies an artifact in the modulus of the reconstructed object.

The homogeneity of the phase inside the domains denotes the absence of significant strain variation. The first column of Table 1 reports the experimental difference in the phase values between domains 1 and 2−3 at different Bragg reflections. These differences originate in the phase difference of the structure factor ψ_F between Ga and N-terminated GaN domains and a homogeneous displacement of the domains between each other. For the calculations of ψ_F, the internal parameter u_c is equal to 0.377 (ref 27) and the analytical atomic scattering factors of Ga and N were taken from the work of Waasmaier and Kirfel.[28] This work assumes a spherical electron density around atoms, which is not perfectly true for the GaN wurtzite since the Ga−N

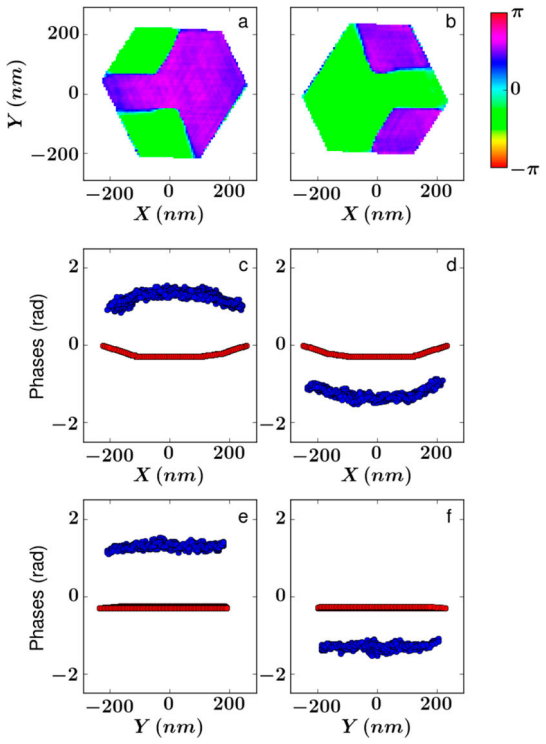

Figure 4. Effect of the optical path length. (a and b) Two phase maps of reconstructed objects giving the same 004 diffraction patterns. The phase changes along the *X* and *Y* directions in the reconstructed objects (blue dots) are compared to the expected phase changes originated in the optical path lengths (red dots): (c and e) for the solution shown in (a) and (d and f) for the solution shown in (b). This confirms solution (b) as the correct one.

TABLE 1. Phase Difference between the Domains 1 and 2−3[a]

(*hkl*)	$\Delta\phi$ experimental (rad)	$\Delta\psi$ theoretical (rad)	$\Delta\phi$ (rad) with $U_z = (c/2 + 8)$ pm and $U_{x,y} = 0$ pm
(004)	-2.80 ± 0.05	3.07	−2.79
(014)	-2.75 ± 0.1	3.07	−2.79
(104)	-2.85 ± 0.1	3.07	−2.79
(112)	1.50 ± 0.1	1.24	1.45
(203)	2.80 ± 0.2	−0.63	2.81

[a] For the two last columns, domains 1 and 2−3 are related to $-c$ and $+c$ GaN crystal, respectively.

bonds have a strong ionic character. However, the difference with the structure factor determined from convergent beam electron diffraction or from electron densities calculated using density functional theory does not affect ψ_F by more than a few hundredths of a radian.[29] The theoretical difference of the structure factor ($\Delta\psi_F$) between $-c$ and $+c$ domains are reported in the second column of Table 1, supposing that the 1 and 2−3 domains are $-c$ and $+c$ oriented, respectively. It clearly shows a disagreement with experimental values. One has to introduce a rigid displacement of the atomic lattice in the *z* direction of $(c/2 + 8)$ pm of the $+c$ with respect to the $-c$ domains (see third column of Table 1) to match the experimental values. The error bar of this value is estimated to be 1 pm from the accuracy of the phase shift. The theoretical values do not fit the experimental ones, when the polarities of the 1 and 2−3 domains are mutually exchanged, meaning that the 1 and 2−3 domains are $+c$ (Ga-terminated) and $-c$ (N-terminated) oriented crystals, respectively. Thus, it is possible to assert that the largest domain is $-c$ (N-terminated) and the two small domains are $+c$ (Ga-terminated), in agreement with the usual tendency of this type of wire growth.[5,20] Moreover, the displacement of the atomic lattice between the $-c$ and $+c$ inversion domains along the *z* direction implies that the Ga atomic network of the $+c$ domains is 8 pm higher than the N atomic network of the $-c$ domain. In the (*x*,*y*)-plane, no displacement is needed to fit the experimental phase values. Nevertheless, the accuracy of the displacement in this plane is worse than the one along the *z* axis. It is estimated to 4 pm. This implies that atoms from domains 2−3 are shifted by less than 4 pm in the (*x*,*y*)-plane with respect to the atoms of domain 1.

Four different models of the {100}, IDB structure have been reported in the literature.[30,31] One of them, the IDB* structure proposed by Northurp *et al.*,[30] is by far the best match with our measurements. It can be formed by translating one side of an IDB by *c*/2 along the [001] direction and contains 4-fold and 8-fold rings of bonds that prevent Ga−Ga and N−N bonds. It has been demonstrated that the IDB* structure is the most energetically favorable one and the one experimentally observed in thin films.[26] However, the IDB* structure differs from our results in two ways. On the one hand, the displacement along the *z* axis is *c*/2 for the IDB* and our measurements in the GaN wire reveal an additional shift of +8 pm. On the other hand, the 10 pm displacement perpendicular to the IDB* predicted by Northrup *et al.* is not observed in our wire. However, it can be noted that this experimental work corresponds to a more complicated situation: this wire contains several IDBs* which interact with each other and with the surfaces. Such a configuration can affect the equilibrium structure of the IDB*, which has been calculated for an isolated defect in an infinite media by Northrup and coworker.[30] Moreover, in a wire containing several IDBs* with different orientations, the displacements perpendicular to the IDBs* have to relax to accommodate each other. Interestingly, our molecular statics calculations with Tersoff-Brenner potential failed to reproduce the displacement field found experimentally, even though the complex configuration of domains had been taken into account (Supporting Information S3).

It is worth noting that the 004 reflection has been measured at mid-height of several GaN wires (see Supporting Information S2). Different domain configurations were observed, but the retrieved phase shift between inversion domains is always the same.

Therefore, we conclude that the 8 pm displacement along the *c*-axis, determined with an accuracy of 1 pm, is not due to a particular domain configuration, but a general feature of the IDB* structure. The in-plane components of the displacement field were measured only for the wire of Figure 3, which suggests that the in-plane components must be smaller than the accuracy of our measurements in that plane (~4 pm).

A possible explanation, yet to be verified, to the discrepancy between experimental and numerical results, is the segregation of silicon atoms in the IDBs. Indeed, the growth is performed with a high Si-dopant concentration (above 10^{20} cm^{-3} in the wire bulk[16]), and it is known that the presence of silicon at an IDB perpendicular to the *c*-axis modifies the bond length at the interface.[32] The present case of these prismatic IDBs has not been reported yet.

CONCLUSIONS

In conclusion, the inner structure of GaN wires containing a complex arrangement of inversion domains has been investigated by CBI with a spatial resolution of 6 nm and a displacement field accuracy of 1 pm along the *c*-axis and 4 pm in the (001) plane. The absolute polarity of the domains is unambiguously revealed and the microscopic structures of the IDBs characterized: the Ga-terminated domains undergo a rigid relative displacement with respect to the N-terminated domain of $(c/2 + 8)$ pm along the *c*-axis and almost zero in the (001) plane. Such a surprising displacement field cannot be explained by atomistic simulations and may originate in the high Si-dopant concentration. Finally, let us point out that this study demonstrates that the CBI technique offers the possibility to get a very precise inner view of the microstructure of small crystals in the presence of interacting defects. This work opens the way to the nondestructive characterization of various defects inside small crystals. This technique can be also applied in a straightforward manner to materials under complex environment or *operando* as found in microelectronics and optoelectronics devices.

METHODS

Sample Preparation. The growth of self-catalyzed GaN wires has been performed on *c*-plane sapphire substrates by metal organic vapor phase epitaxy (MOVPE) in a 3 × 2 in. closed-coupled showerhead reactor. As described by R. Koester *et al.*,[16] the substrate is cleaned under H_2 at high temperature and annealed under ammonia to promote the formation of an Al(O)N layer (~1.5 nm thick according to X-ray reflectivity measurement) before the deposition of a thin SiN_x layer (~2 nm thick) playing the role of a selective growth layer with respect to GaN.[33] Another ammonia annealing stabilizes the surface stoichiometry and induces the formation of composition fluctuations or thinner areas that can be punched through by GaN deposition to achieve epitaxy with sapphire. The GaN polarity and the shape of the objects are directly determined by the atomic stacking of the Al(O)N layer.[25] A high Si-dopant concentration (induced by silane diluted in a majority N_2 carrier gas) and a small V/III molar ratio (ammonia to trimethylgallium) promote the vertical wire growth (see details in ref 16). By adjusting the growth conditions for CBI studies, we obtained 3−5 μm wire length for 150 s of growth with quite low density (about 10^6 cm^{-2}) as illustrated by the scanning electron microscopy view of Figure 1a.

Experiment. X-ray Coherent Bragg Imaging was performed at the ID01 beamline of the European Synchrotron Radiation Facility. A coherent portion of the monochromatic (9.0 keV) beam was selected with high precision slits by matching their horizontal and vertical gaps with the transverse coherence lengths of the beamline: 20 μm (horizontally) and 60 μm (vertically) close to the sample position. The coherent beam was then focused to 0.8 μm × 0.4 μm using a Fresnel Zone Plate (diameter of 300 μm), in order to illuminate a single GaN wire (Figure 2). Diffraction was measured by a two-dimensional detector (516 × 516 pixels of 55 μm placed at 1.307 m from the sample). 3D data sets were recorded by rocking the sample over a range of 1.28° by steps of 0.005°.

Reconstruction. Three standard algorithms were used: Error Reduction (ER), Hybrid Input-Output (HIO) and Shrink Wrap (SW).[21,22] At each step, constraints are applied in the reciprocal space and in the direct space. A custom version of the SW method has been used to determine the support region, *i.e.*, the shape of the object. The SW procedure is stopped when the shrinking process slows down. The support or shape of the object is then adapted manually to get the best homogeneous modulus map. With these supports, a procedure mixing ER and HIO is done 1000 times with different initial random phases associated with the measured intensity. The modulus was left completely free inside the support.

Conflict of Interest: The authors declare no competing financial interest.

Supporting Information Available: The Supporting Information is available free of charge on the ACS Publications website at DOI: 10.1021/acsnano.5b03857.

Additional information on the reconstruction process, the measurements on other wires and molecular statics simulations (PDF)

Acknowledgment. The authors are grateful to ESRF for allocating beamtime on the ID01 beamline. This work has been funded by the French National Research Agency through the project ANR-11-BS10-01401 MecaniX. All the authors took part in the X-ray experiments. O.T. supervised the project. The paper was written by S.L., M.-I.R., G.B., J.E., M.G. and O.T. J.E. prepared the wires. S.L conducted the phase retrieval in collaboration with M.-I.R., G.B., and M.D. S.L., G.B., and M.G carried out the analysis. F.M. helped with the wavefront calculation. M.G. conducted the molecular static calculations.

REFERENCES AND NOTES

1. Yu, P. Y.; Cardona, M. *Fundamentals of Semiconductors—Physics and Materials Properties*, 4th ed.; Springer: Berlin, 2010.
2. Hirsch, P.; Horne, R.; Whelan, M. Direct Observations of the Arrangement and Motion of Dislocations in Aluminium. *Philos. Mag.* **1956**, *1*, 677–684.
3. Bourret, A.; Desseaux, J. Dislocations at Atomic Scale. *Nature* **1978**, *272*, 151–152.
4. Hytch, M. J.; Putaux, J.-L.; Pénisson, J.-M. Measurement of the Displacement Field of Dislocations to 0.03 Å by Electron Microscopy. *Nature* **2003**, *423*, 270–273.
5. Chen, X. J.; Hwang, J.-S.; Perillat-Merceroz, G.; Landis, S.; Martin, B.; Le Si Dang, D.; Eymery, J.; Durand, C. Wafer-Scale Selective Area Growth of GaN Hexagonal Prismatic Nanostructures on c-Sapphire Substrate. *J. Cryst. Growth* **2011**, *322*, 15–22.

6. Tessarek, C.; Bashouti, M.; Heilmann, M.; Dieker, C.; Knoke, I.; Spiecker, E.; Christiansen, S. Controlling Morphology and Optical Properties of Self-Catalyzed, Mask-Free GaN Rods and Nanorods by Metal-Organic Vapor Phase Epitaxy. *J. Appl. Phys.* **2013**, *114*, 144304.
7. Pfeifer, M. A.; Williams, G. J.; Vartanyants, I. A.; Harder, R.; Robinson, I. K. Three-Dimensional Mapping of a Deformation Field Inside a Nanocrystal. *Nature* **2006**, *442*, 63–66.
8. Newton, M. C.; Leake, S. J.; Harder, R.; Robinson, I. K. Three-Dimensional Imaging of Strain in a Single ZnO Nanorod. *Nat. Mater.* **2010**, *9*, 120–124.
9. Yang, W.; Huang, X.; Harder, R.; Clark, J. N.; Robinson, I. K.; Mao, H.-K. Coherent Diffraction Imaging of Nanoscale Strain Evolution in a Single Crystal Under High Pressure. *Nat. Commun.* **2013**, *4*, 1680.
10. Cha, W.; Jeong, N. C.; Song, S.; Park, H.-J.; Pham, T. C.P.; Harder, R.; Lim, B.; Xiong, G.; Ahn, D.; McNulty, I.; et al. Core−Shell Strain Structure of Zeolite Microcrystals. *Nat. Mater.* **2013**, *12*, 729–734.
11. Takahashi, Y.; Suzuki, A.; Furutaku, S.; Yamauchi, K.; Kohmura, Y.; Ishikawa, T. Bragg X-Ray Ptychography of a Silicon Crystal: Visualization of the Dislocation Strain Field and the Production of a Vortex Beam. *Phys. Rev. B: Condens. Matter Mater. Phys.* **2013**, *87*, 121201(R).
12. Clark, J. N.; Ihli, J.; Schenk, A. S.; Kim, Y.-Y.; Kulak, A.; Campbell, J. M.; Nisbet, G.; Meldrum, F. C.; Robinson, I. K. Three-Dimensional Imaging of Dislocation Propagation during Crystal Growth and Dissolution. *Nat. Mater.* **2015**, *14*, 780–784.
13. Ulvestad, A.; Clark, J. N.; Harder, R.; Robinson, I. K.; Shpyrko, O. G. 3D Imaging of Twin Domain Defects in Gold Nanoparticles. *Nano Lett.* **2015**, *15*, 4066–4070.
14. Nakamura, S.; Senoh, M.; Iwasa, N.; Nagahama, S. High-Brightness InGaN Blue, Green and Yellow Light-Emitting Diodes with Quantum Well Structures. *Jpn. J. Appl. Phys.* **1995**, *34*, L797–L799.
15. Kirste, R.; Collazo, R.; Callsen, G.; Wagner, M. R.; Kure, T.; Reparaz, J. S.; Mita, S.; Xie, J.; Rice, A.; Tweedie, J.; et al. Temperature Dependent Photoluminescence of Lateral Polarity Junctions of Metal Organic Chemical Vapor Deposition Grown GaN. *J. Appl. Phys.* **2011**, *110*, 093503.
16. Koester, R.; Hwang, J. S.; Durand, C.; Le Si Dang, D.; Eymery, J. Self-Assembled Growth of Catalyst-Free GaN Wires by MOVPE. *Nanotechnology* **2010**, *21*, 015602.
17. Hersee, S. D.; Sun, X. Y.; Wang, X. The Controlled Growth of GaN Nanowires. *Nano Lett.* **2006**, *6*, 1808–1811.
18. Coulon, P. M.; Mexis, M.; Teisseire, M.; Jublot, M.; Vennéguès, P.; Leroux, M.; Zuniga-Perez, J. Dual-Polarity GaN Micropillars Grown by Metal Organic Vapour Phase Epitaxy: Cross-Correlation between Structural and Optical Properties. *J. Appl. Phys.* **2014**, *115*, 153504.
19. Chen, X. J.; Perillat-Merceroz, G.; Sam-Giao, D.; Durand, C.; Eymery, J. Homoepitaxial Growth of Catalyst-Free GaN Wires on N-polar Substrates. *Appl. Phys. Lett.* **2010**, *97*, 151909.
20. Alloing, B.; Vézian, S.; Tottereau, O.; Vennéguès, P.; Beraudo, E.; Zuniga-Perez, J. On the Polarity of GaN Micro- and Nanowires Epitaxially Grown on Sapphire (0001) and Si (111) Substrates by Metal Organic Vapor Phase Epitaxy and Ammonia-Molecular Beam Epitaxy. *Appl. Phys. Lett.* **2011**, *98*, 011914.
21. Fienup, J. R. Phase Retrieval Algorithms: a Comparison. *Appl. Opt.* **1982**, *21*, 2758–2769.
22. Marchesini, S. X-Ray Image Reconstruction from a Diffraction Pattern Alone. *Phys. Rev. B: Condens. Matter Mater. Phys.* **2003**, *68*, 140101.
23. Henke, B. L.; Gullikson, E. M.; Davis, J. C. X-Ray Interactions: Photoabsorption, Scattering, Transmission, and Reflection at E = 50−30000 eV, Z = 1−92. *At. Data Nucl. Data Tables* **1993**, *54*, 181–342.
24. Mastropietro, F.; Carbone, D.; Diaz, A.; Eymery, J.; Sentenac, A.; Metzger, T. H.; Chamard, V.; Favre-Nicolin, V. Coherent X-Ray Wave Front Reconstruction of a Partially Illuminated Fresnel Zone Plate. *Opt. Express* **2011**, *19*, 19223–19232.
25. Liu, F. D.; Collazo, R.; Mita, S.; Sitar, Z.; Duscher, G.; Pennycook, S. J. The Mechanism for Polarity Inversion of GaN *via* a Thin AlN Layer: Direct Experimental Evidence. *Appl. Phys. Lett.* **2007**, *91*, 203115.
26. Liu, F. D.; Collazo, R.; Mita, S.; Sitar, Z.; Pennycook, S. J.; Duscher, G. Direct Observation of Inversion Domain Boundaries of GaN on c-Sapphire at Sub-Ångstrom Resolution. *Adv. Mater.* **2008**, *20*, 2162–2165.
27. Schulz, H.; Thiemann, K. H. Crystal Structure Refinement of AlN and GaN. *Solid State Commun.* **1977**, *23*, 815–819.
28. Waasmaier, D.; Kirfel, A. New Analytical Scattering-Factor Functions for Free Atoms and Ions. *Acta Crystallogr., Sect. A: Found. Crystallogr.* **1995**, *51*, 416–431.
29. Jiang, B.; Zuo, J. M.; Holec, D.; Humphreys, C. J.; Spackman, M.; Spence, J. C. H. Combined Structure-Factor Phase Measurement and Theoretical Calculations for Mapping of Chemical Bonds in GaN. *Acta Crystallogr., Sect. A: Found. Crystallogr.* **2010**, *66*, 446–450.
30. Northrup, J. E.; Neugebauer, J.; Romano, L. T. Inversion Domain and Stacking Mismatch Boundaries in GaN. *Phys. Rev. Lett.* **1996**, *77*, 103–106.
31. Moon, W. H.; Choi, C. H. Molecular Dynamics Study of Inversion Domain Boundary in W-GaN. *Phys. Lett. A* **2006**, *352*, 538–542.
32. Liu, Z.; Wang, R.-Z.; Liu, L.-M.; Yan, H.; Lau, W.-M. Si Doping at GaN Inversion Domain Boundaries: an Interfacial Polar Field for Electron and Hole Separation. *J. Mater. Chem. A* **2014**, *2*, 9744–9750.
33. Gibart, P. Metal Organic Vapour Phase Epitaxy of GaN and Lateral Overgrowth. *Rep. Prog. Phys.* **2004**, *67*, 667–715.

Résumé de thèse

Les propriétés physiques à petite échelle de longueur diffèrent fortement de celles du matériau massif, typiquement en deçà du micromètre. Par exemple, la résistance mécanique augmente quand la taille diminue et de fortes contraintes résiduelles liés aux procédés d'élaboration sont présentes au sein de nanostructures. Il existe ainsi un besoin d'une meilleure compréhension de la relation entre la microstructure et les propriétés des matériaux aux échelles sub-micrométriques. La diffraction des rayons-X cohérents (CXD) est une technique émergente de synchrotron qui est très sensible aux champs de déformation et à la présence de défauts structuraux. En principe, une image 3D de la microstructure de l'échantillon peut-être obtenue à partir des données de diffraction cohérente. De plus , les rayons X cohérents peuvent être aussi utilisés pour l'imagerie par holographie de domaines/structures magnétiques. Ces deux techniques sont mises en pratique dans ces travaux de thèse. Tout d'abord, nous démontrons que la CXD permet d'identifier quantitativement dans l'espace réciproque tous les types de dislocations, dans le cas d'arrangements simples. Pour des structures plus complexes de défauts, la reconstruction numérique de la densité électronique et de la phase permet de déterminer leur nature et microstructure 3D. Ces deux méthodologies, *i.e.* l'analyse de la signature des défauts dans l'espace réciproque et la reconstruction dans l'espace réel, sont appliquées au cours d'une expérience de déformation *in situ* d'une micro-cristallite d'or par nano-indentation. En s'appuyant sur les reconstructions 3D à différents stades de la sollicitation mécanique, la germination une boucle de dislocation prismatique est clairement identifiée. L'interaction entre les défauts germés et la déformation résiduelle dans la cristallite, conduit à une relaxation équivalente à un "recuit mécanique". De plus la sensibilité de la technique est évaluée dans le cas d'interfaces (surface libre, mâcle, hétéro-épitaxie). L'holographie magnétique est utilisée pour déterminer les structures magnétiques dans des plots micrométriques de permalloy (FeNi) qui prennent la forme de vortex. De plus leur dynamique sous champ magnétique est résolue en temps (à la nanoseconde).

Abstract

Physical properties at small length scale deviate strongly from the bulk counterpart, typically below the micrometer. For instance, mechanical strength increases with reducing size, large residual strain due to processing are present in nanostructures. Thus a better understanding of the physical properties in relationship with the microstructure is needed for sub-micrometer materials. Coherent X-ray Diffraction (CXD) is an emerging synchrotron technique very sensitive to strain fields and structural defects that allows the detailed measurement of the crystal structure,including strain field and defects, of micro/nano-objects. In principle, a 3D image of the microstructure of the sample can be obtained from the CXD data. X-ray coherent beam can also be used with holographic techniques to image magnetic domains/structures. Both techniques are applied in this work. First, we demonstrate that CXD can quantitatively identify in reciprocal space all type of dislocation related defects in simple arrangements. In more complex defects structures, numerical reconstruction of electron density and phase allow to determine their nature and 3D microstructure. Both methodologies, *i.e.* reciprocal space analysis and real space reconstruction are applied during an original *in situ* nanoindentation experiment of a gold crystallite. Using 3D reconstructions at different stages of the mechanical loading, nucleation of a prismatic dislocation loop is clearly identified. The interplay of nucleated defects with the initial residual strain leads to a relaxation equivalent to a "mechanical annealing" process. Moreover, sensitivity of the technique is evaluated for the case of interfaces (free surface, twin, heteroepitaxy). We successfully use magnetic holography to determine the magnetic structures in micrometric permalloy (FeNi) dots, as vortices. Moreover, time-resolved of their dynamics at the nanosecond is demonstrated.